IntechOpen

Updates in Volcanology

From Volcano Modelling to Volcano Geology

Edited by Karoly Nemeth

UPDATES IN VOLCANOLOGY - FROM VOLCANO MODELLING TO VOLCANO GEOLOGY

Edited by **Karoly Nemeth**

Updates in Volcanology - From Volcano Modelling to Volcano Geology
http://dx.doi.org/10.5772/61961
Edited by Karoly Nemeth

Contributors

Yuruo Shi, Boris Chako Tchamabé, Karoly Nemeth, Gabor Kereszturi, Gerardo Carrasco-Núñez, Angelo Paone, Sung-Hyo Yun, Fabio Dioguardi, Tobias Dürig, Samantha L. Engwell, Magnus T. Gudmundsson, Susan C. Loughlin, José García-Antón, Ramón Fernández Domene, Rita Sanchez-Tovar, Bianca Lucas-Granados, Clara Escriva Cerdan, Rafael Leiva Garcia, Peter Vajda, Carles Soriano, Tonci Balic-Zunic, Anna Garavelli, Sveinn Peter Jakobsson, Athanasios Katerinopoulos, Kristjan Jonasson, Konstantinos Kyriakopoulos, Pasquale Acquafredda, Shigekazu Kusumoto, Hidetsugu Yoshida, Viktor Dvigalo, Alina Shevchenko, Ilya Svirid, Cindy Young, Jennifer Telling, Steffi Burchardt, Olivier Galland

Notice

First published in Croatia, 2016 by INTECH d.o.o.
eBook (PDF) Published by IN TECH d.o.o.
Place and year of publication of eBook (PDF): Rijeka, 2019.
IntechOpen is the global imprint of IN TECH d.o.o.
Printed in Croatia

Legal deposit, Croatia: National and University Library in Zagreb

Additional hard and PDF copies can be obtained from orders@intechopen.com

Updates in Volcanology - From Volcano Modelling to Volcano Geology
Edited by Karoly Nemeth

p. cm.

Print ISBN 978-953-51-2622-5

Online ISBN 978-953-51-2623-2

eBook (PDF) ISBN 978-953-51-5079-4

Meet the editor

Dr. Karoly Nemeth is an associate professor at the Institute of Agriculture and Environment of the Massey University, Palmerston North, New Zealand. His areas of expertise include sedimentology, volcanology, and geoheritage. Nemeth's research is centered on understanding monogenetic volcanism and volcanic field evolution in Argentina, Chile, China, Hungary, Idaho (USA), Japan, Korea, Libya, New Zealand, Saudi Arabia, and SW Pacific. He has been a member of the executive committee of the International Association of Volcanology and Chemistry of the Earth's Interior (2011–2015). He is an editorial board member of *Bulletin of Volcanology* and JVGR and Editor-in-Chief for *Advances in Volcanology*. He was leading the Commission on Monogenetic Volcanism, and he is currently leading the Commission on Volcanic Geoheritage and Protected Volcanic Landscapes.

Contents

Preface

It is a pleasure to present this new volcanology book to a broad readership. This book is part of the initiative of InTech Open Publisher, collecting the latest research results for specific research fields on the basis of book chapter proposals. This volcanology book was proposed about a year ago that shortly followed potential authors to be asked to propose a book chapter that could represent their research expertise and the advances of researches associated with volcanoes, volcanic modeling, and volcanic hazard studies. Owing to an effective communication with potential authors, we have received many promising offers ; the total submitted official book chapter proposals were 17. From these 17 book chapter offers, 16 have been invited to develop a full book chapter. The review process of each chapter involved at least one expert review and a review by the book editor. In case some ambiguity appeared, additional reviewers were called in. In the end, we have received revised book chapters from 13 author groups. These revised book chapters have been accepted to be included in the book. During the submission-revision-resubmission process, we enjoyed great support from the InTech technical editor who maintained and fine-tuned the gradually evolving editorial and reviewer system of the publishing house. As a result, we can state that each of the accepted book chapter went through proper peer-review process.

This new book contains high-quality research outputs, and it reflects a snapshot of research activity relevant to volcanology.The chapters made in this book reflect perfectly the diversity of researches associated with volcanology in recent years. This book creation method also justifies that volcanology is a very diverse and very dynamically developing science combining multiple research fields to provide complex research outputs. The title reflects that this book does not intend to provide some specific subject-centered collections of research outputs, but rather providing a snapshot on volcanic research in 2016. This is reflected in the book title as it has been retained as *Updates in Volcanology* similarly as it was in two previous similarly prepared books published in 2010 (*Updates in Volcanology – A Comprehensive Approach to the Volcanological Problems*) and in 2013 (*Updates in Volcanology – New Advances in Understanding Volcanic Systems*). This current book title such as *Updates in Volcanology: From Volcano Modeling to Volcano Geology* reflects well to the collection of its 13 chapters guiding the reader from the modeling and geophysical aspects of volcanology to a more volcanic geology and field-based researches. This process reflects well to the current trends in volcanology putting strong emphasis on the volcanic process modeling, numerical aspects, and geophysical approaches but at the same time showing an elevated appreciation of classical field-based researches targeting to understand the volcanic geology behind the preserved pyroclastic and coherent volcanic rocks that form the geological record of volcanoes. This later process is in perfect concert with the recent progress to build strong awareness of volcanic geology in volcanology researches establishing a new commission in the International

Association of Volcanology and Chemistry of the Earth's Interior (IAVCEI) as Commission on Volcanic Geology. Overall, I can offer this book to anyone who is interested in this healthy and growing research area with great dynamism that is promising. Volcanology and volcanoes are increasingly important research subjects due to the fact that volcanic hazards in general are more directly relevant to our everyday life than ever before due to the population growth on Earth. The diversity of researches in addition shows clearly that volcanic systems are complex, and multidisciplinary approaches from numerical modeling to field-based geological researches together can bring holistic understanding of how volcanoes work. Finally, we also thank all of our reviewers who contributed in the review process.

Dr Karoly Nemeth (Associate Professor)
Massey University,
Institute of Agriculture and Environment
Ag-Hort Bldg, Riddet Road, Turitea Campus
Palmerston North
New Zealand

Introduction

Chapter 1

Introductory Chapter: Updates in Volcanology – From Volcano Modeling to Volcano Geology

Károly Németh

Additional information is available at the end of the chapter

http://dx.doi.org/10.5772/64734

The book "*Updates in Volcanology*: *From volcano modelling to volcano geology*" is composed of 13 book chapters provided by authors from a great variety of disciplines. Each of the book chapter genuinely reflects the diversity of volcanological researches in recent years and documents new look at geological problems associated with volcanism and volcanic hazard research. The chapters from this book represent perfectly the current trends in volcanology as a merging research directions from geophysical aspects of volcanology and its traditional field-based methods. The book chapters have been grouped into three sections.

Section 1 is titled "Understanding the volcano system from petrology, geophysics to large-scale experiments" and provides a total of five chapters covering geophysical aspects of volcanic researches including their geochemical perspectives. The section starts with a comprehensive summary on the volcanic plumbing systems we know today and their relevance to understand the volcanic behavior from the magmatic source to a magma fragmentation that provides pyroclasts to be transported and deposited away from their source. Volcanic plumbing systems commonly defined as a network of various magmatic intrusive bodies (sheet- or dyke-like) and diverse size and shape of magmatic storage places (chambers) that located between the primary source and the surface anywhere the geological conditions allow to stall magma migration toward the surface [1–7]. The magmatic plumbing system of a volcano is a complex array of injected melts where various chemical processes take place that are strongly or loosely linked to the primary melt source and/or interact with the wall rocks. This book chapter provides a detailed summary of the methods recently applied to harvest information about these complex system feeding volcanoes on the surface. This chapter provides a summary on the potentials and the limitations of each applied methodology commonly used in magmatic plumbing system studies and highlight the fact that magmatic plumbing systems are complex geo-environments where physical and

geochemical processes interact and create a complex 3D array of solidified melts that can then be traced in the geological record as igneous rocks.

Following the detailed summary of the melt generation and migration toward the surface, the next chapter takes the reader to the "surface" and provides a methodological summary on the power of photogrammetric surveys in volcanology. This chapter not only provides an exciting and new read on a traditional method to define volcanic morphology and their temporal changes during volcanic eruptions but it also takes the reader to a very active volcanic zone—Kamchatka—that produced several of the most spectacular volcanic eruptions in the last centuries including the Bezymianny 1955 and other [8, 9], Great Tolbachik 1975 [10–13] and recent 2012 events [14, 15] (**Figure 1**), Karymsky-lake Surtseyan eruption 1996 [16] or the Klyuchevskoy [17], Shiveluch [18], Ksudach [19], Mutnovsky, or Karymsky (**Figure 2**) volcanoes ongoing eruptions. Many of these eruptions not only provided new insight to volcanic eruption processes but also gave new conceptual models for gold recycling beneath volcanoes [20] or let us discover new minerals such as the tolbachite ($CuCl_2$) [21] and other unique minerals [22] or special rock names such as avachites a high-magnesian basalt group documented from the Avachinsky volcano [23]. This chapter looks back 100 years of research history and provides some forgotten images and documents from an area largely unknown for the majority of volcanologists. The chapter through its critical review and global comparison also provides a way forward for the development of the photogrammetric method in volcanology.

Figure 1. Strombolian style explosive eruption through a fissure vent at the Tolbachik volcano in Kamchatka (2012) [Photograph by Dmitry Melnikov, Institute of volcanology and seismology FEB RAS, Petropavlovsk-Kamchatsky, Russia].

Linked to the previous chapter, the third chapter provides a critical review with some original data and research about the role of volcano gravimetry. Volcano gravimetry has developed dramatically in recent years and became a fundamental tool to understand activity changes

http://dx.doi.org/10.5772/64734

inside a volcano and hence use collected in situ or near real-time data to estimate volcanic alert status in active volcanoes [24–29]. Gravimetry studies also been used to detect various volcanic structures such as maar-diatreme volcanoes and establish the geological origin of sediment field terrestrial basins, which indeed not as simple process as we might think [30–33]. Similarly, gravimetry has been applied successfully to describe the internal architecture of large volcanoes [34] as well as relatively small-scale features as cavities in lava flows [35]. This chapter provides an easy to understand review of the science behind gravimetry studies then provides an evaluation for the future of gravimetry research on volcanoes.

Figure 2. Summit activity on the Karymsky strato-volcano in Kamchatka [Photo by Dmitry Melnikov, Institute of volcanology and seismology FEB RAS, Petropavlovsk-Kamchatsky, Russia].

The fourth chapter takes the reader to Kyushu in Japan and provides a state-of-art research report with a high-value review of the methods applied to understand the gravity gradient tensor in active volcanic regions in southern Japan. Southern Japan is a home of several post-Pliocene calderas that define the landscape today and the style of expected volcanism in the region [36]. The Kagoshima Bay and its surrounding is in particular one of the region where the highest frequency of silicic caldera-forming eruptions is known on Earth that produced multiple large (10 km<) across calderas and associated ignimbrite and silicic pyroclastic tephra sheets [37]. The large number of volcanoes in these regions alongside with the thick deposits made difficult to see the internal structure of many of these complex volcanoes and their structural relationship to the regional and volcano-tectonic structures; hence, geophysical methods are useful to provide data. This book chapter provides an introduction to the applicability of special gravity gradiometry survey with a new technique to define gravity gradient tensors. The chapter provides clear example to demonstrate that this method capable to locate structural elements such as caldera walls as it has been tested across the Aso caldera [38] hence offer some new avenue to explore for others in other complex volcanic terrains such as the caldera-pitted North Island in New Zealand [39, 40].

The fifth and closing chapter of this section of the book provides a summary of large-scale experiments to understand the source conditions and controlling parameters of explosive eruptions. This chapter is a valuable summary of the methods applied for large-scale experiments written by a group of researchers pioneered experimental volcanology through large-scale experiments; hence, the reader can get a very genuine view of such researches limitations and extent [41, 42]. In addition, the author group is also strongly linked to field-based research on pyroclastic deposits of pyroclastic density currents; therefore, this chapter provides well-established ideas and concepts [43]. In general, large-scale experiment to model various types of explosive processes, magma fragmentations, crater formation, and their numerical modeling is probably one of the most dynamic parts of volcanology in recent years [44–56]. In this chapter, different methodologies for investigating eruptive source conditions and the subsequent evolution of the eruptive plumes are presented. The methodologies range from observational techniques to large-scale experiments and numerical models. The chapter also poses fundamental research questions that can only be answered if we follow the proposed techniques to define the effect of unsteady flow conditions at the source on the eruptive column dynamics and the interaction between a convective plume and wind.

The second section of the book "volcanic eruptions and their impact to the environment" consists of five chapters. Each of these chapters provides various aspects of volcanism from their hazard and consequence perspective. The opening chapter of this section sum up the volcanological information associated with one of the less known volcano that produced one of the largest set of eruptions in the past 10 ka. Baekdusan volcano that is located in the frontier between China and North Korea is a volcano that has a basaltic shield capped by a trachyte-dominated sequence and a large caldera [57]. This chapter highlights the fact that Baekdusan volcano is an active and very complex volcano as its volcanic seismicity, ground deformation, and volcanic gas geochemistry yields indicate that a magmatic unrest takes place in the period between 2002 and 2006. The geological record and the recent volcano monitoring data suggest that the Mt. Baekdusan is an active volcano [58]; hence, proper volcanic hazard studies are needed to estimate the potential volcanic eruption scenarios a new eruption would follow.

The second chapter in this section takes the reader to Japan where an analysis of the magnitude-frequency distribution of slope failures was studied. The statistical data provided in this chapter are based on many years of research, and this chapter gives a very useful summary to the readers how to apply similar method to their fields. Interestingly, this chapter provides a relatively simple equation for the magnitude-frequency distribution of slope failures for larger than 10^7 m^3 volumes. The chapter concludes that this magnitude-frequency may applicable over several thousands of years of record making possible for future large-scale volcanic failure predictions. It is an alarming conclusion however, that larger than 10^9 m^3 mega collapses can occur in every 1000–2000 years period; hence, such mega events cannot be looked at as a rare events in Japan. Volcanic debris avalanches are common volcanic processes that generate a specific volcanic sedimentary successions and geomorphological disturbances; hence, their study is important [59, 60]. Such large-scale failures of volcanic edifices need to be studied in similar way as this chapter demonstrated to be able to provide magnitude-frequency distribution relationships in volcanic terrains prone to collapse.

The third chapter of this section deals with a research area of volcanic aerosol behavior developing dynamically in recent years to provide functioning models to volcanic aerosol effect to radiation in the Arctic. This chapter claims that despite the suspected perturbance of volcanic aerosols to the Arctic radiation balance, we know very little about their radiative impacts in the Arctic. It is also poorly understood partially due to the limited attention, this process has received what the effects of other aerosol types that are often present in the region [61], both natural and anthropogenic [62–64]. The link between volcanic events and their potential climatic impact is one of the subjects reach beyond the limits of volcano sciences and commonly connected to social studies, history, and art [65–69]. Research activity to understand volcanic aerosol behavior over the Arctic has also increased in recent years [70–72]; hence, this chapter provides a very useful summary of the current state of knowledge. The chapter points out that the Arctic environment is both unique and complicated, and the perturbations caused by volcanic aerosol need to be examined in a regional context. Due to the harsh environment, more data are derived from remote sensing; hence, this chapter provides a comprehensive summary of remotely sensed data collection techniques. The numerous models presented in this chapter show the strengths and shortcomings of volcanic ash transport and dispersion models in general [73–75] and calling future targeted research specifically designed for Arctic conditions. Among many, the authors claim that the effect of ash aggregation such as accretionary lapilli formation [76, 77] not many cases considered in ash transport and deposition models in spite their huge effect on the potential distribution pattern their deposition can show [78].

The fourth chapter in this section takes a reader to a fairly new research area that studies the link between corrosion effects on various alloys in a volcano-polluted seawater. Corrosion damage in human-built environment caused by volcanic processes can cause significant economic loss especially in marine steel infrastructures such as bridges, wharfs, platforms, and pipeline systems. While understanding the corrosion in general relatively well documented in subaerial conditions such as volcanic ash and acid rain effect on man-made structures [79–81]. Similar studies in a subaqueous environment are relatively rare [82]. This chapter provides an interesting overview of the world of corrosion including the description of techniques that can measure their rates. The results of the study of corrosion in volcanic-polluted waters can contribute to understanding of the volcanic hazards and associated risks of such processes that can act on human-built environments.

The final chapter in this section deals with the mineral assemblages recorded in various fumarolic systems across the most famous fumarole fields in Europe. This chapter provides a descriptive overview of the mineral phases recorded from various fumarolic systems focusing on examples from Italy and Greece. Fumarolic systems viewed as important environments where rare elements can concentrate even in economically significant amount [20]. The mineral variations associated with fumarolic systems are great, and such systems often act as harvesting ground to identify previously unknown minerals [10, 83]. Fumarolic systems are also viewed as a window to the magmatic system; hence, they commonly studied with an aim to understand the magma behavior provides the heat beneath such systems [84–86]. This chapter takes examples from well-known fumarolic systems such as those at Vulcano Island in Italy

to raise some awareness among researchers on the significance of fumarolic systems in volcanic regions.

The final, third section of the book consists of three chapters dealing with volcanic geology problems that can be applied to older volcanic successions. The section starts with an exhaustive summary of the recent results on the study of subaqueous explosive and effusive volcanism in the Cabo de Gata region in SE Spain. Subaqueous volcanism in recent years became the center of volcanic researches [87] partially due to the racing to identify reliable evidences of presence of water or ice on extra-terrestrial regions commonly associated with volcanism [88, 89] and understand ore-forming processes in volcanic regions located or closely linked to subaqueous environments [90, 91]. It is just an addition to the increase of research activity that in the geological record, volcanic rocks are commonly associated with subaqueous sedimentary rocks; hence, there is a need to understand well the limitations of identification of various eruptive environment hence using volcanic rocks for paleoenvironmental (eruptive environment) reconstructions. Identification of peperites [92] for instance became a trademark to contribute to the eruptive environment discussions such as establishing subaqueous versus subaerial conditions [93]. Similarly, new researches on distinguishing explosive versus effusive non-explosive fragmentation of magma to feed large volume of hyaloclastite piles provided useful tools to use these deposits for paleoenvironmental reconstruction of rock units in the geological record [94, 95]. As a result of these research activities, a new commission called Commission of Subaqueous Volcanism of the International Association of Volcanology and Chemistry of the Earth's Interior was established in 2016. Cabo de Gata is probably one of the most perfectly exposed regions where the eruptive products (effusive and explosive) of subaqueous volcanism can be accessed along coastal sections [96]. This chapter provides a very detailed summary for the research results of the study of the Cabo de Gata volcanic rocks based on many previous research works [97].

Figure 3. The AD 1256 fissure eruption site near the city of Al Madinah in Saudi Arabia, a potential geosite in the proposed Al Madinah Volcanic Geopark.

The second chapter in this section addresses a question: how polygenetic are monogenetic volcanoes? This question sounds strange as the two word, monogenetic versus polygenetic are opposing and negating each other. The authors take the reader to a journey to demonstrate the difficulty to define monogenetic volcanism especially if we are looking at volcanic successions preserved in a geological record. Such problem has been addressed recently in many places arguing that in old but partially preserved and eroded successions, the distinction between volcanic rock units formed in a single and short volcanic process can look very similar to those that formed over longer time without significant evidence of erosional surfaces in the rock units. This chapter draws again the attention to view small-volume volcanoes as a system that functions as a source to surface model [98]. *In such model, the timing, longevity, and the total eruptive volume of individual eruptive episodes and the total volcanic activity can produce complex volcanic facies architecture composed of multiple eruptive units commonly forming such small-volume volcanoes* [99, 100]. This chapter explores the volcanic facies architecture of small-volume volcanoes that carry obvious signs of complex eruptive history that commonly can be translated to relatively long eruptive history and an elevated volume of magma involvement [101–103]. This chapter is useful to understand the gradual transition of small to large volcanoes, hence to see the link between monogenetic and polygenetic volcanism [104].

The final chapter of this section and the entire book takes the reader to a volcanic region in Inner Mongolia, China, where volcanic rocks help to understand the evolution of the Central Asian Orogenic Belt [105–108]. While this region is not directly considered as a locality of volcanological studies, its geological history documents significant magmatological processes associated with terrane accretion and associated volcanic processes [109]. The region is also a home of advanced studies of adakite magmas, and hence, it is inferred that magmatism resulted from intermediate to felsic magmas that carry geochemical characteristics indicative for the melt to be sourced by partial melting of the altered basalt that is subducted below volcanic arcs [110]. This chapter also highlights the methods need to be applied to recognize various stages of terrain accretion and petrogenetic processes associated with a complex plate margin process.

The book overall provides a great diversity of subjects relevant to volcanic researches. While the book purely a result of "blue sky" attempt to collect new research outputs reflecting the current trends in volcanic researches, the selection of chapters reflects well the dynamic nature of volcanological researches. The book naturally cannot provide a balanced summary of the current advances in volcanology. Large and dynamically developing segments of current volcanological research are not covered in this book. Reports on the advances of crater formation based on analog experiments [47, 50], experimental volcanological studies [76, 111–113], lava flow dynamic modeling through experiments and numerical codes [114, 115], developing new methods for eruption forecasting especially the eruptions' economic impact [116–119], experimental and field-based studies of maar-diatreme volcanism [48] or new advances in understanding magma fragmentation, vesiculation, and their internal and external controlling parameters are among many new research fields this book has not provided overviews. Also, recently, IAVCEI has established a new commission called Commission on Volcano Geoheritage and Protected Volcanic Landscape, which is a clear sign

that geoeducation, geoconservation, and geotouristic researches and programs associated with volcanism claiming their own place among volcanic sciences [120] (**Figure 3**). It is hoped that in a future "volcanology" book, reports on these field's research results will be incorporated. Until that please enjoy this book!

Author details

Károly Németh

Address all correspondence to: k.nemeth@massey.ac.nz

Volcanic Risk Solutions, Massey University, Palmerston North, New Zealand

References

[1] Allard, P., et al., Mount Etna 1993–2005: Anatomy of an evolving eruptive cycle. Earth-Science Reviews, 2006. 78(1–2): p. 85–114.

[2] Cartwright, J. and D.M. Hansen, Magma transport through the crust via interconnected sill complexes. Geology, 2006. 34(11): p. 929–932.

[3] Holt, S.J., S.P. Holford, and J. Foden, New insights into the magmatic plumbing system of the South Australian Quaternary Basalt province from 3D seismic and geochemical data. Australian Journal of Earth Sciences, 2013. 60(8): p. 797–816.

[4] Kavanagh, J.L., D. Boutelier, and A.R. Cruden, The mechanics of sill inception, propagation and growth: Experimental evidence for rapid reduction in magmatic overpressure. Earth and Planetary Science Letters, 2015. 421: p. 117–128.

[5] Gudmundsson, A., Strengths and strain energies of volcanic edifices: Implications for eruptions, collapse calderas, and landslides. Natural Hazards and Earth System Sciences, 2012. 12(7): p. 2241–2258.

[6] Geshi, N., S. Kusumoto, and A. Gudmundsson, Effects of mechanical layering of host rocks on dike growth and arrest. Journal of Volcanology and Geothermal Research, 2012. 223: p. 74–82.

[7] Geshi, N., K. Németh, and T. Oikawa, Growth of phreatomagmatic explosion craters: A model inferred from Suoana crater in Miyakejima Volcano, Japan. Journal of Volcanology and Geothermal Research, 2011. 201(1–4): p. 30–38.

[8] Belousov, A., Deposits of the 30 March 1956 directed blast at Bezymianny volcano, Kamchatka, Russia. Bulletin of Volcanology, 1996. 57(8): p. 649–662.

[9] Belousov, A., et al., Pyroclastic surges and flows from the 8-10 May 1997 explosive eruption of Bezymianny volcano, Kamchatka, Russia. Bulletin of Volcanology, 2002. 64(7): p. 455–471.

[10] Chaplygin, I., et al., Native gold from volcanic gases at Tolbachik 1975–76 and 2012–13 Fissure Eruptions, Kamchatka. Journal of Volcanology and Geothermal Research, 2015. 307: p. 200–209.

[11] Fedotov, S.A., A.P. Khrenov, and A.M. Chirkov, Tolbachik Great Fissure Eruption of 1975, kamchatka. Doklady Akademii Nauk Sssr, 1976. 228(5): p. 1193–1196.

[12] Fedotov, S.A., et al., Major Tolbachik Fissure Eruption in Kamchatka, South Break of 1975–1976. Doklady Akademii Nauk Sssr, 1977. 237(5): p. 1155–1158.

[13] Budmikov, V.A., Y.K. Markhinin, and A.A. Ovsyannikov, The quantity, distribution and petrochemical features of pyroclastics of the Great Tolbachik Fissure Eruption., in The Great Tolbachik Fissure Eruption, S.A. Fedotov and Y.K. Markhinin, Editors. 1983, Cambridge University Press: Cambridge. p. 41–56.

[14] Lundgren, P., et al., Dike model for the 2012–2013 Tolbachik eruption constrained by satellite radar interferometry observations. Journal of Volcanology and Geothermal Research, 2015. 307: p. 79–88.

[15] Volynets, A.O., et al., Monitoring of the volcanic rock compositions during the 2012–2013 fissure eruption at Tolbachik volcano, Kamchatka. Journal of Volcanology and Geothermal Research, 2015. 307: p. 120–132.

[16] Belousov, A. and M. Belousova, Eruptive process, effects and deposits of the 1996 and the ancient basaltic phreatomagmatic eruptions in Karymskoye Lake, Kamchatka, Russia. Special Publication of the International Association of Sedimentologists, 2001. 30: p. 35–60.

[17] Koulakov, I.Y., et al., Magma sources in the mantle wedge beneath the volcanoes of the Klyuchevskoy group and Kizimen based on seismic tomography modeling. Russian Geology and Geophysics, 2016. 57(1): p. 82–94.

[18] Belousov, A.B., The Shiveluch volcanic-eruption of 12 November 1964—Explosive eruption provoked by failure of the edifice. Journal of Volcanology and Geothermal Research, 1995. 66(1–4): p. 357–365.

[19] Braitseva, O.A., et al., The caldera-forming eruption of Ksudach volcano about cal AD 240: The greatest explosive event of our era in Kamchatka, Russia. Journal of Volcanology and Geothermal Research, 1996. 70(1–2): p. 49–65.

[20] Zelenski, M., V.S. Kamenetsky, and J. Hedenquist, Gold recycling and enrichment beneath volcanoes: A case study of Tolbachik, Kamchatka. Earth and Planetary Science Letters, 2016. 437: p. 35–46.

[21] Vergasova, L.P. and S.K. Filatov, A new mineral Tolbachite, CuCl2. Doklady Akademii Nauk Sssr, 1983. 270(2): p. 415–417.

[22] Pekov, I.V., et al., New zinc and potassium chlorides from fumaroles of the Tolbachik volcano, Kamchatka, Russia: Mineral data and crystal chemistry. III. Cryobostryxite, $KZnCl_3 \bullet 2H_2O$. European Journal of Mineralogy, 2015. 27(6): p. 805–812.

[23] Portnyagin, M.V., et al., Petrology of avachites, high-magnesian basalts of Avachinsky volcano, Kamchatka: I. General characteristics and composition of rocks and minerals. Petrology, 2005. 13(2): p. 99–121.

[24] Delgado, F. and A. Pavez, New insights into La Pacana caldera inner structure based on a gravimetric study (central Andes, Chile). Andean Geology, 2015. 42(3): p. 313–328.

[25] Crossley, D., J. Hinderer, and U. Riccardi, The measurement of surface gravity. Reports on Progress in Physics, 2013. 76(4):046101. doi: 10.1088/0034-4885/76/4/046101.

[26] Battaglia, M., et al., 4D volcano gravimetry. Geophysics, 2008. 73(6): p. WA3–WA18.

[27] Behncke, B., et al., Ground deformation and gravity changes on the island of Pantelleria in the geodynamic framework of the Sicily Channel. Journal of Volcanology and Geothermal Research, 2006. 150(1–3): p. 146–162.

[28] Pingue, F., et al., Ground deformation and gravimetric monitoring at Somma-Vesuvius and in the Campanian volcanic area (Italy). Physics and Chemistry of the Earth Part A: Solid Earth and Geodesy, 2000. 25(9–11): p. 747–754.

[29] Saibi, H., J. Gottsmann, and S. Ehara, Post-eruptive gravity changes from 1999 to 2004 at Unzen volcano (Japan): A window into shallow aquifer and hydrothermal dynamics. Journal of Volcanology and Geothermal Research, 2010. 191(1–2): p. 137–147.

[30] Sesulka, V., et al., Identification of a buried Late Cenozoic maar-diatreme structure (North Moravia, Czech Republic). Geologica Carpathica, 2014. 65(6): p. 471–479.

[31] Nickschick, T., H. Kaempf, and T. Jahr, The "Triasscholle" near Greiz, Germany-a volcanic origin? Bulletin of Volcanology, 2014. 76:806. DOI 10.1007/s00445-014-0806-x.

[32] Valenta, J.J., et al., Problems and challenges in detection of pre-Mesozoic maar volcanoes: Example from the Principalek Volcano in the Permian Krkonose Piedmont Basin. Journal of Geosciences, 2014. 59(3): p. 169–181.

[33] Flechsig, C., et al., Integrated geophysical and geological methods to investigate the inner and outer structures of the Quaternary Mytina maar (W-Bohemia, Czech Republic). International Journal of Earth Sciences, 2015. 104(8): p. 2087–2105.

[34] La Delfa, S., G. Patane, and J.C. Tanguy, Kilometer-scale heterogeneities inside volcanoes revealed by using a set of geophysical methods: Variable stress field at Mount Etna, Sicily. Physics of the Earth and Planetary Interiors, 2000. 121(1–2): p. 157–173.

[35] Deroussi, S., et al., Localization of cavities in a thick lava flow by microgravimetry. Journal of Volcanology and Geothermal Research, 2009. 184(1–2): p. 193–198.

[36] Suzukikamata, K. and H. Kamata, The proximal facies of the Tosu Pyroclastic-flow deposit erupted from Aso Caldera, Japan. Bulletin of Volcanology, 1990. 52(5): p. 325–333.

[37] Aramaki, S., Formation of the Aira caldera, southern Kyushu, approximately 22,000 years ago. Journal of Geophysical Research, 1984. 89(NB10): p. 8485–8501.

[38] Miyabuchi, Y., Post-caldera explosive activity inferred from improved 67–30 ka tephrostratigraphy at Aso Volcano, Japan. Journal of Volcanology and Geothermal Research, 2011. 205(3–4): p. 94–113.

[39] Wilson, C.J.N. and J.V. Rowland, The volcanic, magmatic and tectonic setting of the Taupo Volcanic Zone, New Zealand, reviewed from a geothermal perspective. Geothermics, 2016. 59: p. 168–187.

[40] Cole, J.W., et al., Okataina Volcanic Centre, Taupo Volcanic Zone, New Zealand: A review of volcanism and synchronous pluton development in an active, dominantly silicic caldera system. Earth-Science Reviews, 2014. 128: p. 1–17.

[41] Dioguardi, F. and P. Dellino, PYFLOW: A computer code for the calculation of the impact parameters of Dilute Pyroclastic Density Currents (DPDC) based on field data. Computers and Geosciences, 2014. 66: p. 200–210.

[42] Duerig, T., et al., A new method for the determination of the specific kinetic energy (SKE) released to pyroclastic particles at magmatic fragmentation: Theory and first experimental results. Bulletin of Volcanology, 2012. 74(4): p. 895–902.

[43] Mele, D., et al., Hazard of pyroclastic density currents at the Campi Flegrei Caldera (Southern Italy) as deduced from the combined use of facies architecture, physical modeling and statistics of the impact parameters. Journal of Volcanology and Geothermal Research, 2015. 299: p. 35–53.

[44] Ross, P.S., et al., Experimental birth of a maar-diatreme volcano. Journal of Volcanology and Geothermal Research, 2013. 260: p. 1–12.

[45] Mader, H.M., et al., Dynamics of explosive degassing of magma: Observations of fragmenting two-phase flows. Journal of Geophysical Research-Solid Earth, 1996. 101(B3): p. 5547–5560.

[46] Roche, O., D.C. Buesch, and G.A. Valentine, Slow-moving and far-travelled dense pyroclastic flows during the Peach Spring super-eruption. Nature Communications, 2016. 7.

[47] Macorps, E., et al., The effects of the host-substrate properties on maar-diatreme volcanoes: Experimental evidence. Bulletin of Volcanology, 2016. 78:26. DOI 10.1007/s00445-016-1013-8.

[48] Valentine, G.A., et al., Experiments with vertically and laterally migrating subsurface explosions with applications to the geology of phreatomagmatic and hydrothermal explosion craters and diatremes. Bulletin of Volcanology, 2015. 76:15. DOI 10.1007/s00445-015-0901-7.

[49] Sweeney, M.R. and G.A. Valentine, Transport and mixing dynamics from explosions in debris-filled volcanic conduits: Numerical results and implications for maar-diatreme volcanoes. Earth and Planetary Science Letters, 2015. 425: p. 64–76.

[50] Sonder, I., A.H. Graettinger, and G.A. Valentine, Scaling multiblast craters: General approach and application to volcanic craters. Journal of Geophysical Research-Solid Earth, 2015. 120(9): p. 6141–6158.

[51] Graettinger, A.H., et al., Facies distribution of ejecta in analog tephra rings from experiments with single and multiple subsurface explosions. Bulletin of Volcanology, 2015. 77:8. DOI 10.1007/s00445-015-0951-x.

[52] Valentine, G.A., et al., Experimental craters formed by single and multiple buried explosions and implications for volcanic craters with emphasis on maars. Geophysical Research Letters, 2012. Vol. 39, L20301, doi:10.1029/2012GL053716.

[53] Doronzo, D.M., et al., Numerical analysis of the effect of topography on deposition from dilute pyroclastic density currents. Earth and Planetary Science Letters, 2010. 300(1–2): p. 164–173.

[54] Doronzo, D.M., et al., Dust storms, volcanic ash hurricanes, and turbidity currents: Physical similarities and differences with emphasis on flow temperature. Arabian Journal of Geosciences, 2016. 9:290. DOI 10.1007/s12517-016-2351-8.

[55] Roche, O., Nature and velocity of pyroclastic density currents inferred from models of entrainment of substrate lithic clasts. Earth and Planetary Science Letters, 2015. 418: p. 115–125.

[56] Lube, G., et al., Synthesizing large-scale pyroclastic flows: Experimental design, scaling, and first results from PELE. Journal of Geophysical Research-Solid Earth, 2015. 120(3): p. 1487–1502.

[57] Yun, S.-H. and J. Koh, Petrochemical characteristics of volcanic rocks of historic era at Mt. Baekdusan. Journal of the Geological Society of Korea, 2014. 50(6): p. 753–769.

[58] Park, K., Research Trends on Mt. Baekdu Volcano - Is She Dormant or Active? Journal of The Korean Geomorphological Association, 2013. 20(4): p. 117–131.

[59] Tost, M., S.J. Cronin, and J.N. Procter, Transport and emplacement mechanisms of channelised long-runout debris avalanches, Ruapehu volcano, New Zealand. Bulletin of Volcanology, 2014. 76(12).

[60] Procter, J.N., S.J. Cronin, and A.V. Zernack, Landscape and sedimentary response to catastrophic debris avalanches, western Taranaki, New Zealand. Sedimentary Geology, 2009. 220(3–4): p. 271–287.

[61] Iwi, A.M., et al., Mechanisms linking volcanic aerosols to the atlantic meridional overturning circulation. Journal of Climate, 2012. 25(8): p. 3039–3051.

[62] VanCuren, R.A., et al., Aerosols and their sources at Summit Greenland – First results of continuous size- and time-resolved sampling. Atmospheric Environment, 2012. 52: p. 82–97.

[63] Scalabrin, E., et al., Amino acids in Arctic aerosols. Atmospheric Chemistry and Physics, 2012. 12(21): p. 10453–10463.

[64] Allen, R.J. and S.C. Sherwood, The impact of natural versus anthropogenic aerosols on atmospheric circulation in the Community Atmosphere Model. Climate Dynamics, 2011. 36(9–10): p. 1959–1978.

[65] Toohey, M., et al., Climatic and societal impacts of a volcanic double event at the dawn of the Middle Ages. Climatic Change, 2016. 136(3–4): p. 401–412.

[66] Miller, G.H., et al., Abrupt onset of the Little Ice Age triggered by volcanism and sustained by sea-ice/ocean feedbacks. Geophysical Research Letters, 2012. Vol. 39, L02708,doi:10.1029/2011GL050168.

[67] Timmreck, C., Modeling the climatic effects of large explosive volcanic eruptions. Wiley Interdisciplinary Reviews-Climate Change, 2012. 3(6): p. 545–564.

[68] Meronen, H., et al., Climate effects of northern hemisphere volcanic eruptions in an Earth System Model. Atmospheric Research, 2012. 114: p. 107–118.

[69] Zhong, Y., et al., Centennial-scale climate change from decadally-paced explosive volcanism: A coupled sea ice-ocean mechanism. Climate Dynamics, 2011. 37(11–12): p. 2373–2387.

[70] Kravitz, B. and A. Robock, Climate effects of high-latitude volcanic eruptions: Role of the time of year. Journal of Geophysical Research-Atmospheres, 2011. Vol. 116, D01105, doi:10.1029/2010JD014448.

[71] Harris, B.M. and E.J. Highwood, A simple relationship between volcanic sulfate aerosol optical depth and surface temperature change simulated in an atmosphere-ocean general circulation model. Journal of Geophysical Research-Atmospheres, 2011. Vol. 116, D05109, doi:10.1029/2010JD014581.

[72] Robock, A., L. Oman, and G.L. Stenchikov, Regional climate responses to geoengineering with tropical and Arctic SO_2 injections. Journal of Geophysical Research-Atmospheres, 2008. Vol. 113, D16101, doi:10.1029/2008JD010050.

[73] Wilkins, K.L., et al., Using data insertion with the NAME model to simulate the 8 May 2010 Eyjafjallajokull volcanic ash cloud. Journal of Geophysical Research-Atmospheres, 2016. 121(1): p. 306–323.

[74] Mulena, G.C., et al., Examining the influence of meteorological simulations forced by different initial and boundary conditions in volcanic ash dispersion modelling. Atmospheric Research, 2016. 176: p. 29–42.

[75] Stevenson, J.A., et al., Big grains go far: Understanding the discrepancy between tephrochronology and satellite infrared measurements of volcanic ash. Atmospheric Measurement Techniques, 2015. 8(5): p. 2069–2091.

[76] Mueller, S.B., et al., Experimental volcanic ash aggregation: Internal structuring of accretionary lapilli and the role of liquid bonding. Earth and Planetary Science Letters, 2016. 433: p. 232–240.

[77] Van Eaton, A.R., et al., Hail formation triggers rapid ash aggregation in volcanic plumes. Nature Communications, 2015. 6:7860. DOI: 10.1038/ncomms8860.

[78] Folch, A., A. Costa, and G. Macedonio, FPLUME-1.0: An integral volcanic plume model accounting for ash aggregation. Geoscientific Model Development, 2016. 9(1): p. 431–450.

[79] Wilson, G., et al., Vulnerability of laptop computers to volcanic ash and gas. Natural Hazards, 2012. 63(2): p. 711–736.

[80] Watanabe, M., et al., Corrosion of copper and silver plates by volcanic gases. Corrosion Science, 2006. 48(11): p. 3759–3766.

[81] Kelestemur, O. and B. Demirel, Corrosion behavior of reinforcing steel embedded in concrete produced with finely ground pumice and silica fume. Construction and Building Materials, 2010. 24(10): p. 1898–1905.

[82] Morinaga, Y., et al., Comparative Study of Corrosion Resistance and Corrosion Products in Hot Spring, Seaside, and Other Environments Between Zn and Zn-7Al Alloy-Coated Steel. Corrosion, 2008. 64(12): p. 929–938.

[83] Jacobsen, M.J., et al., Oskarssonite, AlF3, a new fumarolic mineral from Eldfell volcano, Heimaey, Iceland. Mineralogical Magazine, 2014. 78(1): p. 215–222.

[84] Caliro, S., G. Chiodini, and A. Paonita, Geochemical evidences of magma dynamics at Campi Flegrei (Italy). Geochimica Et Cosmochimica Acta, 2014. 132: p. 1–15.

[85] Tassi, F., et al., Geochemical and isotopic changes in the fumarolic and submerged gas discharges during the 2011-2012 unrest at Santorini caldera (Greece). Bulletin of Volcanology, 2013. 75:711. DOI: 10.1007/s00445-013-0711-8.

[86] Paonita, A., et al., The episodic and abrupt geochemical changes at La Fossa fumaroles (Vulcano Island, Italy) and related constraints on the dynamics, structure, and compo-

sitions of the magmatic system. Geochimica Et Cosmochimica Acta, 2013. 120: p. 158–178.

[87] Cas, R.A.F. and G. Giordano, Submarine Volcanism: A review of the constraints, processes and products, and relevance to the Cabo de Gata volcanic succession. Italian Journal of Geosciences, 2014. 133(3): p. 362–377.

[88] Bernhardt, H., et al., Photogeologic mapping and the geologic history of the Hellas basin floor, Mars. Icarus, 2016. 264: p. 407–442.

[89] Zealey, W.J., Glacial, periglacial and glacio-volcanic structures on the Echus Plateau, upper Kasei Valles. Planetary and Space Science, 2009. 57(5–6): p. 699–710.

[90] Large, R.R., Australian volcanic-hosted massive sulfide deposits—features, styles, and genetic models. Economic Geology and the Bulletin of the Society of Economic Geologists, 1992. 87(3): p. 471–510.

[91] McPhie, J., et al., Origin of the supergiant Olympic Dam Cu-U-Au-Ag deposit, South Australia: Was a sedimentary basin involved? Geology, 2011. 39(8): p. 795–798.

[92] Skilling, I.P., J.D.L. White, and J. McPhie, Peperite: A review of magma-sediment mingling. Journal of Volcanology and Geothermal Research, 2002. 114(1–2): p. 1–17.

[93] Rosa, C.J.P., J. McPhie, and J.M.R.S. Relvas, Distinguishing peperite from other sediment-matrix igneous breccias: Lessons from the Iberian Pyrite Belt. Journal of Volcanology and Geothermal Research, 2016. 315: p. 28–39.

[94] Jutzeler, M., J. McPhie, and S.R. Allen, Explosive destruction of a Pliocene hot lava dome underwater: Dogashima (Japan). Journal of Volcanology and Geothermal Research, 2015. 304: p. 75–81.

[95] Allen, S.R. and J. McPhie, Products of neptunian eruptions. Geology, 2009. 37(7): p. 639–642.

[96] Biber, J.L. and T. McCann, Peperite development in a Miocene-age carbonate succession, Cabo de Gata volcanic area (Agua Amarga/Carboneras basins), SE Spain - The Breche Rouge revisited. Zeitschrift Der Deutschen Gesellschaft Fur Geowissenschaften, 2014. 165(2): p. 229–245.

[97] Soriano, C., et al., Facies architecture, emplacement mechanisms and eruption style of the submarine andesite El Barronal complex, Cabo de Gata, SE Spain. Journal of Volcanology and Geothermal Research, 2013. 264: p. 210–222.

[98] Canon-Tapia, E., Reappraisal of the significance of volcanic fields. Journal of Volcanology and Geothermal Research, 2016. 310: p. 26–38.

[99] Muirhead, J.D., et al., Monogenetic volcanoes fed by interconnected dikes and sills in the Hopi Buttes volcanic field, Navajo Nation, USA. Bulletin of Volcanology, 2016. 78:11. DOI: 10.1007/s00445-016-1005-8.

[100] Lefebvre, N.S., J.D.L. White, and B.A. Kjarsgaard, Arrested diatreme development: Standing Rocks East, Hopi Buttes, Navajo Nation, USA. Journal of Volcanology and Geothermal Research, 2016. 310: p. 186–208.

[101] Sheth, H.C. and E. Canon-Tapia, Are flood basalt eruptions monogenetic or polygenetic? International Journal of Earth Sciences, 2015. 104(8): p. 2147–2162.

[102] Jankovics, M.E., et al., A complex magmatic system beneath the Kissomlyo monogenetic volcano (western Pannonian Basin): Evidence from mineral textures, zoning and chemistry. Journal of Volcanology and Geothermal Research, 2015. 301: p. 38–55.

[103] Brenna, M., et al., Co-located monogenetic eruptions similar to 200 kyr apart driven by tapping vertically separated mantle source regions, Chagwido, Jeju Island, Republic of Korea. Bulletin of Volcanology, 2015. 77:43. DOI: 10.1007/s00445-015-0928-9.

[104] Nemeth, K. and G. Kereszturi, Monogenetic volcanism: Personal views and discussion. International Journal of Earth Sciences, 2015. 104(8): p. 2131–2146.

[105] Zhao, Y., et al., The Dunhuang block is a Paleozoic orogenic belt and part of the Central Asian Orogenic Belt (CAOB), NW China. Gondwana Research, 2016. 30: p. 207–223.

[106] Shi, Y., et al., Zircon ages and Hf isotopic compositions of Ordovician and Carboniferous granitoids from central Inner Mongolia and their significance for early and late Paleozoic evolution of the Central Asian Orogenic Belt. Journal of Asian Earth Sciences, 2016. 117: p. 153–169.

[107] Li, H., et al., Ordovician intrusive rocks from the eastern Central Asian Orogenic Belt in Northeast China: Chronology and implications for bidirectional subduction of the early Palaeozoic Palaeo-Asian Ocean. International Geology Review, 2016. 58(10): p. 1175–1195.

[108] Xiao, W. and M. Santosh, The western Central Asian Orogenic Belt: A window to accretionary orogenesis and continental growth. Gondwana Research, 2014. 25(4): p. 1429–1444.

[109] Liu, J., et al., The tectonic setting of early Permian bimodal volcanism in central Inner Mongolia: Continental rift, post-collisional extension, or active continental margin? International Geology Review, 2016. 58(6): p. 737–755.

[110] Castillo, P.R., Adakite petrogenesis. Lithos, 2012. 134: p. 304–316.

[111] Kueppers, U., et al., Fragmentation efficiency of explosive volcanic eruptions: A study of experimentally generated pyroclasts. Journal of Volcanology and Geothermal Research, 2006. 153(1–2): p. 125–135.

[112] Daniels, K.A. and T. Menand, An experimental investigation of dyke injection under regional extensional stress. Journal of Geophysical Research-Solid Earth, 2015. 120(3): p. 2014–2035.

[113] Dioguardi, F., P. Dellino, and S. de Lorenzo, Integration of large-scale experiments and numerical simulations for the calibration of friction laws in volcanic conduit flows. Journal of Volcanology and Geothermal Research, 2013. 250: p. 75–90.

[114] Kereszturi, G., et al., Emplacement conditions of the 1256 AD Al-Madinah lava flow field in Harrat Rahat, Kingdom of Saudi Arabia - Insights from surface morphology and lava flow simulations. Journal of Volcanology and Geothermal Research, 2016. 309: p. 14–30.

[115] Del Negro, C., A. Cappello, and G. Ganci, Quantifying lava flow hazards in response to effusive eruption. Geological Society of America Bulletin, 2016. 128(5–6): p. 752–763.

[116] Bebbington, M. and R. Zitikis, Dynamic Uncertainty in Cost-Benefit Analysis of Evacuation Prior to a Volcanic Eruption. Mathematical Geosciences, 2016. 48(2): p. 123–148.

[117] Sobradelo, R., et al., Probabilistic approach to decision-making under uncertainty during volcanic crises: Retrospective application to the El Hierro (Spain) 2011 volcanic crisis. Natural Hazards, 2015. 76(2): p. 979–998.

[118] Kereszturi, G., et al., Influences on the variability of eruption sequences and style transitions in the Auckland Volcanic Field, New Zealand. Journal of Volcanology and Geothermal Research, 2014. 286: p. 101–115.

[119] Runge, M.G., et al., Integrating geological and geophysical data to improve probabilistic hazard forecasting of Arabian Shield volcanism. Journal of Volcanology and Geothermal Research, 2016. 311: p. 41–59.

[120] Moufti, M.R. and K. Nemeth, The intra-continental Al Madinah volcanic field, Western Saudi Arabia: A proposal to establish Harrat Al Madinah as the first volcanic Geopark in the Kingdom of Saudi Arabia. Geoheritage, 2013. 5(3): p. 185–206.

Section 2

Understanding the Volcano System from Petrology, Geophysics to Large Scale Experiments

Chapter 2

Studying Volcanic Plumbing Systems – Multidisciplinary Approaches to a Multifaceted Problem

Steffi Burchardt and Olivier Galland

Additional information is available at the end of the chapter

http://dx.doi.org/10.5772/63959

Abstract

Magma transport and storage beneath active volcanoes occurs in the so-called volcanic plumbing system (VPS), a network of different magmatic sheet intrusions and magma reservoirs. The complex physical and chemical processes, which occur in the volcanic plumbing system, are key parameters that control the occurrence of an eruption, as well as type and size of the eruption. It is therefore imperative to assess plumbing system processes and their dynamics. Traditionally, plumbing system research is done as a part of various scientific disciplines, each with its own research questions, methods, and terms. As a consequence, there is often little overlap and communication between the disciplines. In this chapter, we give an overview of the history of plumbing system research and outline the state of the art of the main scientific disciplines involved. We summarise the potential and limitations of each discipline and then discuss three key components to foster multidisciplinary research—namely communication, information, and education—which are essential to promote a better understanding of the complexity of volcanic plumbing systems.

Keywords: volcanic plumbing system, magma transport, magma storage, multidisciplinary research, volcanology

1. Introduction

Volcanic plumbing systems (VPS) form a plexus of magma channels and reservoirs that are governed by complex interactions of chemical and mechanical processes that control how magmas are emplaced and how they propagate through the Earth's crust to an eventual eruption (**Figure 1**; [1]). Volcanic plumbing systems thus set the stage for volcanic eruptions and govern

the style and magnitude of eruptive activity including dramatic volcano–tectonic phenomena, such as caldera and sector collapses.

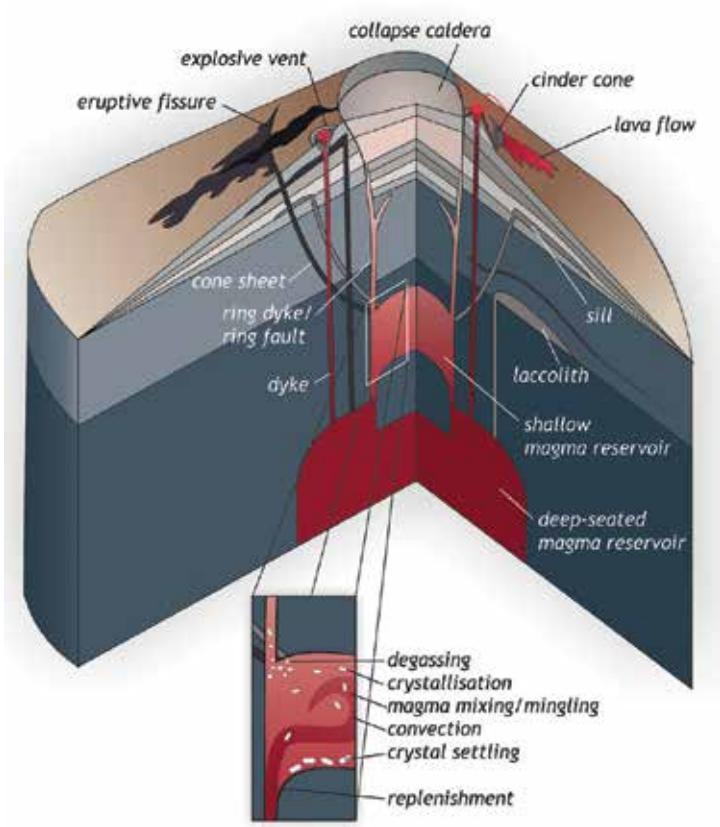

Figure 1. Schematic sketch of different components of volcanic plumbing systems, highlighting the complexity of the different types of magma channels and reservoirs. The inset illustrates the processes that may occur within magma bodies.

Traditionally, however, the study of the plumbing system components, such as dykes, sills, and larger magma bodies (**Figure 1**), as well as their dynamics is strongly method-based, for example, focussing exclusively on the composition of plutonic bodies or the seismicity of magma ascent. To date, relatively few bridges between the distinct disciplines exist. In this chapter, we will give a short overview of the historical development of the main concepts on volcanic plumbing systems and the diversification of research disciplines that study plumbing systems. We then proceed to outline the aims and approaches, as well as the potential and limitations, of the main disciplines, namely field and structural analysis, igneous petrology and geochemistry, geophysics, geodesy, and modelling. We will then discuss challenges and opportunities of combining approaches from different disciplines to overcome some of the limitations and contribute to a better understanding of the complex and dynamic processes within active volcanoes.

http://dx.doi.org/10.5772/63959

2. History of the study of volcanic plumbing systems

While naturalists of the eighteenth century debated the origin of basalt, James Hutton was the first to propose that dykes and sills formed by the solidification of "subterraneous lava" and that even granite was once in a molten state [2]. Hutton's views were based on meticulous field observations of magmatic intrusions exposed at the Earth's surface. Performing one of the first systematic petrological experiments, Sir James Hall [3] delivered supporting evidence by melting and cooling volcanic glass and basalt to produce a variety of crystallinity in the experimental products.

By the time the first petrological classifications of igneous rocks had been established and microscopy and experimental petrology had started to emerge as distinct approaches in the second half of the nineteenth century, field mapping had become more focused on the shapes and structures of igneous intrusions [4]. Studies of igneous rock bodies from that time added laccoliths [5], batholiths [6], and other intrusion geometries to the previously described dykes, veins, and sills. Based on his observation of deformation in the rocks surrounding igneous intrusions in the Henry Mountains in Utah, Gilbert [5] started to study the mechanics of magma emplacement to unravel why magma at some occasions gets trapped in the crust or erupts at other occasions. In the following decades, researchers such as Daly [7] found evidence for different types of magma emplacement mechanisms. These mechanisms were gradually linked to specific types of intrusive bodies, a classification of which was established in the early twentieth century [8]. By this time, field observations in the eroded volcanic complexes of the British Isles had identified ring dykes and cone sheets as specific intrusion types [9, 10].

Petrologists of the early twentieth century focused in turn on fractional crystallisation and magma differentiation in sills and layered intrusions [11–14]. Hence, from the first half of the twentieth century, field-based research concerning volcanic plumbing systems was conducted in parallel as part of the disciplines of igneous petrology, structural geology, and volcanic geology, as well as by distinct communities studying granitic plutons, fossil subvolcanic complexes, and extrusive rock suites in volcanic areas.

The second half of the twentieth century saw major advances in the understanding of volcanic deposits and eruptions, as well as how these are linked to the underlying volcanic plumbing system. One of the most influential researchers of this time is George P. L. Walker who, together with his students, and based on systematic observations and quantitative mapping of extinct volcanic complexes in the British Isles and Eastern Iceland, fundamentally advanced our understanding of magma transport in dykes and the architecture of shallow magma plumbing systems in central volcanoes [15, 16].

Apart from the subdiscipline of experimental petrology, even other types of modelling have been employed to study volcanic plumbing systems. Analogue modelling (or laboratory modelling) of intrusive and volcanic processes became an increasingly important method (see Section 3.5), particularly after Hubbert [17] and later Ramberg [18, 19] had introduced the principle of scaling to ensure similarity between geological and model systems [20]. Numerical modelling of plumbing systems, on the other hand, is rooted in the analytical solutions of

mostly fluid-dynamic and stress-field problems within classical structural geology. Development of computer software that is often originally designed for materials science simulations and the ever increasing computational capacity have led to a boost in numerical modelling studies of—among many other Earth science topics—volcanic plumbing systems.

The second half of the twentieth century was also the beginning for geophysical studies of volcanic plumbing systems. While gravimetric methods are nowadays routinely applied to study granitic plutons and subvolcanic complexes [21, 22], geophysical monitoring techniques have become a standard in active volcanic areas (see Section 3.3). In addition, since the launch of satellites and satellite-based mapping of the Earth's surface in the 1960s, geodesy has become an increasingly popular method to infer processes related to magma transport in active volcanoes (see Section 3.4).

The history of plumbing system research reflects the methodological and conceptual development and diversification of the Earth sciences in general. Since the days of the early naturalists who described natural phenomena as a whole, our understanding of volcanic plumbing systems has deepened considerably. However, at the same time, as we started to dig deeper into specific aspects, we mostly lost our view of the big picture. Currently, volcanic plumbing system research is carried out in the disciplines of igneous petrology, structural geology, volcanology, geophysics, and geodesy, employing methods such as field mapping, major and trace element analysis, seismology, analogue modelling, and interferogrametry of radar measurements from satellites. Section 3 gives an overview of the state of the art of the most important approaches.

3. Methods commonly used to study volcanic plumbing systems

3.1. Field geology and structural analysis of volcanic plumbing systems

Field based studies of volcanic plumbing systems have initially aimed at a qualitative description of intrusive phenomena and focused on a classification of intrusion lithologies and morphologies to understand how magma is transported, stored, and evolves in the crust [23]. With time, field work has become increasingly quantitative, producing a detailed record of the compositions and structures associated with magmatic intrusions [24]. Analyses of the composition, absolute and relative ages, and dimensions of the components of magmatic plumbing systems have produced a more and more systematic view of the emplacement and evolution of plumbing systems [25, 26]. Besides the recording of variations in lithology and emplacement-related structures, mapping of magmatic intrusions often includes the study of magmatic fabrics recorded within the igneous rocks [27], such as preferred orientation of phenocrysts and of magnetic minerals using their so-called anisotropy of magnetic susceptibility (AMS; [28, 30]). Recently, classical methods, such as field mapping with paper maps and compass, have become complemented by modern digital mapping techniques using global positioning system (GPS) and smart phones (**Figure 2**). At the same time, the possibilities to analyse structural data collected in the field become more and more sophisticated. In addition

http://dx.doi.org/10.5772/63959

to thorough statistical analysis and stereographic projection [31, 32], three-dimensional (3D) structural modelling is used to visualise, reconstruct, and interpret structural field data [33–35].

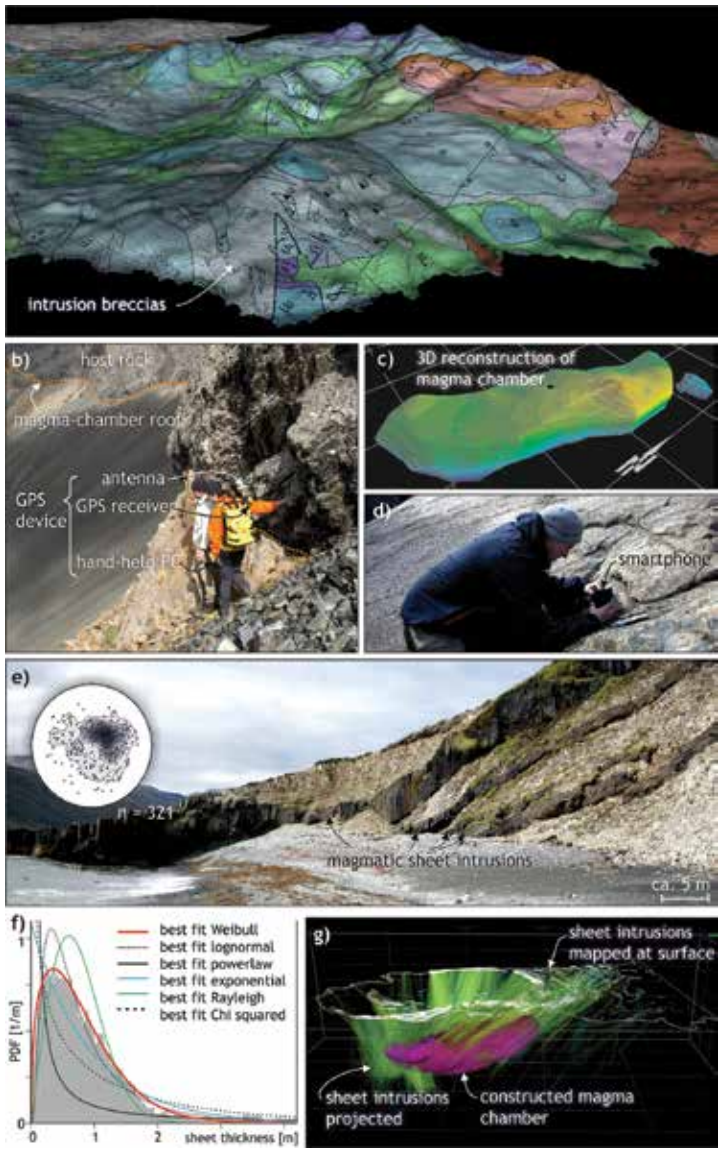

Figure 2. Examples of field and structural studies of volcanic plumbing systems. (a) Geological map of the Isle of Rum draped over a Digital Elevation Model. Map modified from Scottish Natural Heritage 1:20,000 map; © SNH. (b) High-precision GPS mapping of the roof of a granitic pluton (cf. [40, 41]). (c) Result of 3D reconstruction of a granitic pluton based on GPS mapping. (d) Measuring fractures in a granitic intrusion using a smart phone and Field Move Clino app by Midland Valley Ltd. (e) Outcrop of basaltic inclined sheets and corresponding projection of poles to orientation planes and density of 321 such sheet intrusions in an equal area, lower hemisphere plot (cf. [42]). (f) Probability Density Function (PDF) of the thickness of magmatic sheets, such as shown in (e) compared to a selection of statistical distributions. (g) 3D structural model of the plumbing system of the Ardnamurchan central complex, Scotland, produced using Move by Midland Valley Ltd (modified from [34]).

Igneous plumbing systems in outcrops regularly extend over several kilometres. Such wide extents represent a substantial challenge for (1) having a correct overview understanding of the structure of the exposed VPS and (2) completing structural field surveying in a manageable time. In addition, numerous field areas of interest are hardly reachable for direct observations, such as very steep mountains and crevasses. Recent technologies, including LiDAR scanners, drones, and robots, have recently started overcoming these challenges. The one hand, LiDAR scanners have been used to produce high-precision and high-resolution textured virtual outcrop models [36]. Such digital models allow detailed, quantitative 2D and 3D fracture mapping of extensive, mostly subvertical outcrops [37]. On the other hand, drone surveys combined with photogrammetric tools are very helpful to produce virtual outcrop models and orthorectified images of extensive subhorizontal or gently dipping outcrops, and provide new observational perspectives for extensive structural mapping [38]. Finally, robots equipped with monitoring tools can explore the Earth's interior that is inaccessible for humans [39]. The data produced by these modern tools allow new possibilities for post-field digital mapping of extensive areas, thus shortening the field campaigns.

Therefore, field studies of exhumed plumbing systems form the foundation of our conceptual understanding of the individual components of volcanic plumbing systems, their morphologies, sizes, and emplacement mechanisms, as well as of characteristic structures in the host rock associated with the evolution of magmatic intrusions. Field work in eroded volcanic areas is therefore of critical importance, because it provides us with fundamental information that may be used to benchmark numerical and laboratory models (see Section 3.5) and to interpret geophysical and geodetic data (see Sections 3.3 and 3.4).

The main limitation of the field-based approach to study volcanic plumbing systems is that fossil and eroded volcanic plumbing systems represent a snapshot of the final state of the magmatic system only, while active volcanoes do not permit a detailed look inside their VPS. An outcrop in an eroded volcano is essentially a snapshot of the sum of all superimposed processes a suite of rock has experienced. It is thus not always straightforward to extract accurate age relationship between individual units or even distinct boundaries at times, as well as to deduce what dynamic processes were contributing to the final picture.

3.2. Petrological and geochemical studies of volcanic plumbing systems

Igneous petrology and geochemistry are among the classic approaches used to characterise volcanic plumbing systems (see also Section 2) and aim to describe the conditions, time scales, and characteristics of the chemical evolution of magma. This characterisation is generally based on the mineralogy and textures of igneous rocks, as well as their major and trace element composition (e.g. **Figure 3**). In order to study the minerals, textures, and compositions of rock samples collected in the field, igneous petrologists employ a wide range of analytical techniques, which have been developed simultaneously with, and strongly facilitated, an increasing understanding of the chemical evolution of minerals and melts. These analytical techniques have emerged in a rapid succession and have become increasingly precise since igneous petrology was established as a discipline and the first microscopes were built in the second half of the nineteenth century (see Section 2). Today, rock textures and the type and associations

http://dx.doi.org/10.5772/63959

of minerals in thin sections of rock samples are studied using a variety of microscopes. The bulk, or whole-rock, composition of an igneous rock that mostly comprises the quantity of major elements or their oxides can be derived through, for example, exposing a powdered sample of a rock to X-rays (X-ray fluorescence (XRF)). Other analytical techniques, such as mass spectrometry, can quantify the isotopic composition of the major and trace elements of a sample.

Data on the mineralogy and composition of igneous rocks are probes into the chemical evolution of volcanic plumbing systems and can be used in many ways. In many cases, the whole-rock composition is characteristic of the geodynamic setting and origin of a magma and can also be used to discriminate processes in the plumbing system, such as fractional crystallisation (e.g. [43, 44]). The concentration of trace elements can be used in geochemical modelling to quantify processes in the volcanic plumbing system, such as assimilation of country rocks into the magma (e.g. [45]). The decay of radiogenic isotopes is used as a standard tool to determine the absolute age of a rock sample, which has led to detailed insights into the time scales of magma emplacement in volcanic plumbing systems (e.g. [46]).

At the scale of individual crystals, crystal size distributions, chemical zoning, and textures can serve as records of the chemical and thermal evolution of their host magmas (e.g. [47–49]). Crystal growth rates and chemical diffusion across crystal zones can furthermore be used to quantify the time scales of, for example, magma storage or replenishment (e.g. [50]). Moreover, pressure and/or temperature dependent mineral compositions can be used as so-called geobarometers and/or geothermometers that reveal the depth and conditions at which certain minerals grew, which usually corresponds to magma reservoir depths (e.g. [51, 52]).

In order to quantify the chemical evolution of minerals and magmas *in situ*, petrological experiments are used to simulate, for example, the influence of pressure and/or temperature on mineral compositions [53] and the reaction of magma with crustal rocks [54, 55].

Petrological and geochemical studies of volcanic plumbing systems are thus the foundation of our understanding of the chemical and thermal processes during magma storage and offer insight into the time scales of magma transport and evolution. Estimates of the depth of magma storage provide valuable constraints on the interpretation of geodetic and geophysical monitoring data of active volcanoes (see Sections 3.3 and 3.4). Furthermore, a characterisation of the types of magma erupted from a volcano and an understanding of the processes of magma evolution in the plumbing system allow evaluating the probable type of eruption in the future.

The main limitation of the petrological and geochemical approaches is that magma samples from active volcanic plumbing systems are generally not available. Although many of the processes of magma evolution can be constrained based on petrological experiments, the major and trace element compositions of rocks and minerals can in many cases not be attributed to any specific process. The contribution of each individual process is often difficult to quantify. Moreover, the insights derived from petrological and geochemical approaches apply to the geological past of the plumbing system only. It is therefore not always straightforward to conclude on the present state.

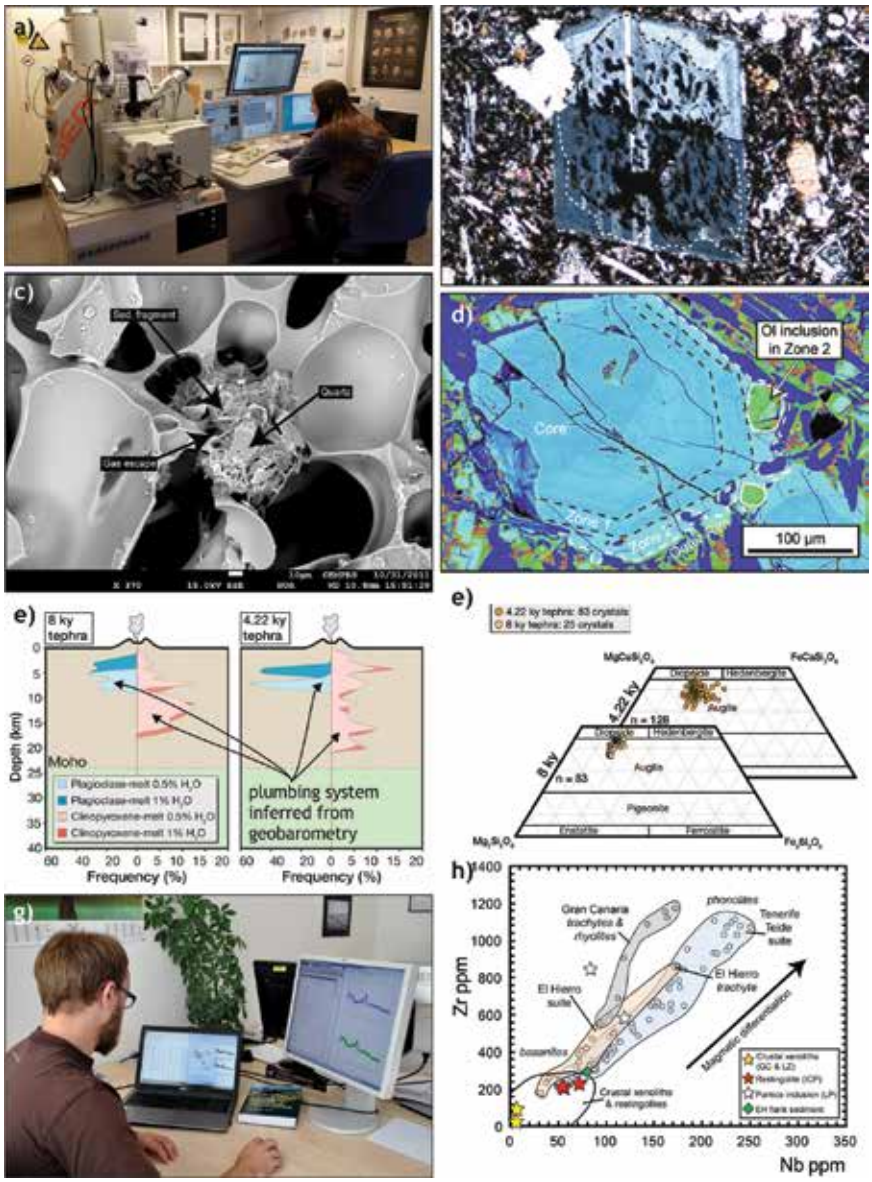

Figure 3. Examples of petrological and geochemical studies of volcanic plumbing systems. (a) High-precision chemical analysis and element mapping using a field emission gun electron probe microanalyser. (b) Thin section of a zoned plagioclase crystal (zonation indicated by dashed line) in basalt of the 2015 Holhraun eruption. Crossed polars. Crystal ca. 1 mm across. Crystal textures can be used to reconstruct processes in the volcanic plumbing system [57]. (c) Scanning electron microscope (SEM) image of vesiculated xenolith erupted offshore El Hierro [56]. (d) False-colour SEM image of a zoned clinopyroxene crystal in lava erupted at Holuhraun, Iceland. Zones and inclusions can be used to reconstruct processes in the volcanic plumbing system [58]. (e) Results of geobarometric modelling of plagioclase and clinopyroxene in tephras from Katla volcano, Iceland [58]. (f) Mineralogy of pyroxene crystals in Katla tephras [58]. (g) Analysing trace-element contents in igneous rocks. Image courtesy of Christophe Galerne. (h) Zr versus Nb plot of igneous rocks and xenoliths from the Canary Islands, Spain. Trace element compositions can be used to understand the origin of, and relationships between, rock groups [56].

http://dx.doi.org/10.5772/63959

3.3. Geophysical studies of volcanic plumbing systems

Geophysical studies of volcanic plumbing systems employ a variety of methods (**Figure 4**) that detect and quantify either the physical properties of different geomaterials, such as magma versus solid rock or igneous versus sedimentary rocks, or the effects of active physical processes, such as seismicity caused by the movement of magma through the crust. Geophysical methods are therefore applied to study both active volcanoes and extinct subsurface or eroded plumbing systems.

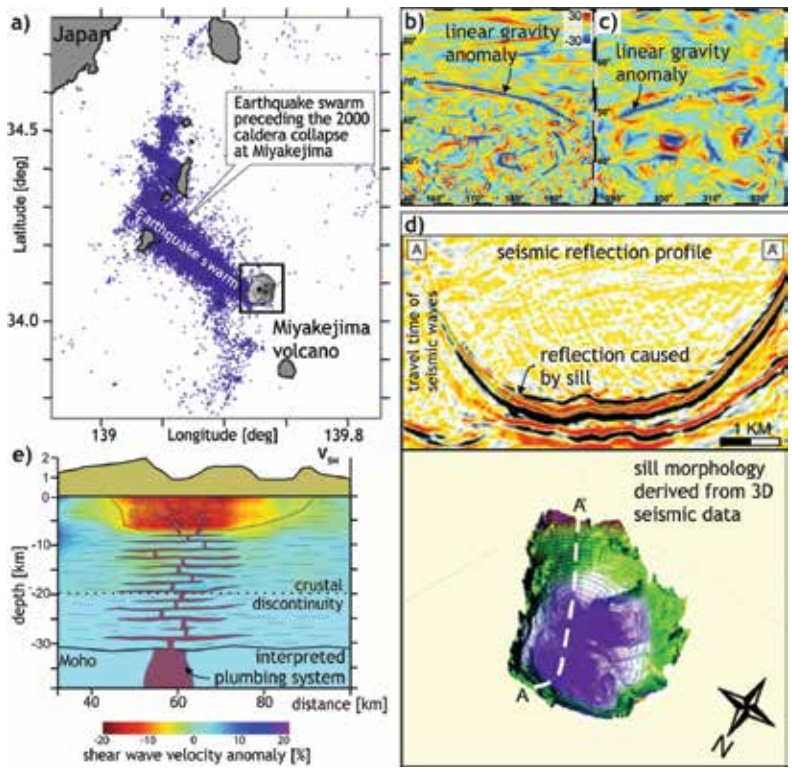

Figure 4. Examples of geophysical studies of volcanic plumbing systems. (a) Seismicity related to the emplacement of a dyke preceding caldera collapse in Miyakejima volcano, Japan, in 2010 [62]; see references therein for source data). (b) and (c) Linear gravity anomalies (marked by black dots) interpreted to be related to dykes on the Moon [59]. (d) Above: Vertical section of a 3D seismic dataset showing the signal related to a sill. Below: 3D seismic image of the same saucer-shaped sill [63]. (e) Volcanic plumbing system of the Toba caldera inferred from seismic tomography [64].

In order to characterise physical properties of different materials in the crust, a wide range of geophysical methods, such as gravimetry, magnetometry, and electrics, are commonly applied to map volcanic plumbing systems and associated hydrothermal systems. These methods detect anomalies in the Earth's gravimetric, magnetic, and electrical resistivity fields. The anomalies are caused by the presence of rock types with properties contrasting to those of the surrounding country rocks, for example, higher or lower density, resistivity etc. Depending on the type and size of target, for example, mapping a granitic intrusion, and the expected

depth range of the target, appropriate methods, and acquisition techniques are chosen. Instruments may be mounted on airplanes and satellites or installed in arrays at the Earth's surface. Acquired geophysical data can then be used to map the physical properties of the Earth's crust. Such maps allow locating the extent and map the outline of magmatic intrusions, which is extremely useful for large-scale reconnaissance and mapping in poorly exposed or inaccessible areas, such as moons or other planets (e.g. [59]). The spatial resolution of the data mainly depends on the contrast in physical properties between the target and the country rock. The acquired data on geophysical anomalies can also be used in inversion models that infer the subsurface distribution of a particular physical property by reproducing the pattern and magnitude of the anomaly making simple assumptions about the geology, for example, homogeneity and isotropy of the involved rocks. For instance, the results of inversion models can be applied to determine the subsurface shape and volume of a granitic intrusion (e.g. [60, 61]). The main limitation of geophysical mapping at depth using inversion modelling is that the data are acquired at the Earth's surface (more or less in 2D) is then used to interpret the 3D distribution of physical properties. Moreover, inversion modelling that often produces as very similar solutions in spite of different input parameters. Hence, the number of fitting solutions may be infinite, and thus, model interpretations are often non-unique.

Geophysical methods are also frequently applied to study active volcanoes in order to locate magma storage levels and to infer processes related to magma movement. For instance, microgravimetry monitoring can be applied to detect magma flow into the plumbing system by monitoring changes in the local gravimetric field, a method often combined with geodetic monitoring [65]. In the brittle crust, volcano-tectonic earthquakes that are interpreted to be related to magma movement are studied in the subdiscipline of volcano seismology [66]. Using a network of seismometers, seismicity in active volcanoes can be monitored, for example, to trace propagating sheet intrusions, which gives valuable insight into dyke emplacement mechanisms [67, 68]. The properties of seismic waves (frequencies, wave forms, etc.) can be interpreted to derive information about processes such as the rise of magma in a conduit or the intrusion of a cryptodome [60]. Travel times of seismic waves through the crust beneath a volcano can be used as input parameters for inversion models, a technique called seismic tomography. The seismic velocity structure of a volcano can be used to map subsurface areas with an increased percentage of melt, potentially corresponding to magma reservoirs [69, 51]. However, the detection limit of seismic tomography for magma bodies is on the order of several hundred metres, depending on the seismic array and acquisition conditions on the one hand and the structure of the individual volcano on the other. Therefore, most parts of the volcanic plumbing system, such as average sized dykes and sills, may be undetectable using seismic tomography.

During the last decade, seismic reflection and refraction have been extensively implemented to image volcanic plumbing systems in sedimentary basins [70, 71]. While all geophysical methods described earlier employ passive measurements of natural rock properties, seismic reflection and refraction methods represent active geophysical surveying: acoustic waves are sent into the subsurface and reflected and refracted at interfaces between rocks of contrasting impedance. Thus, the resulting seismic images are a direct echography of subsurface structures

http://dx.doi.org/10.5772/63959

and not the result of data inversion. Initially designed for studying the structure of sedimentary basins and hydrocarbon exploration, seismic data proved essential to document the presence of voluminous sill and laccolith complexes in numerous basins worldwide [73, 74]. On seismic images, igneous intrusions are very prominent because of the strong impedance contrast between igneous and sedimentary rocks. The main advantages of seismic data are that (1) they can image the shapes of entire intrusions in three dimension [74, 75], which can potentially constrain magma flow directions [64, 76], and (2) it is possible to constrain the intrusion-scale deformation induced by magma emplacement [77, 78, 83] and intrusion-fault interactions [79]. The main limitations of seismic data are (1) the limited spatial resolution (about 20 to 40 m), (2) the limited possibility to image subvertical features, such as dykes, (3) seismic artefacts that produce interpretable features that do not exist, and (4) the availability of the seismic data, as they are often kept confidential by oil companies.

Geophysical methods are thus powerful tools to study physical properties and signals produced by processes of volcanic plumbing systems. Despite their limitations, these methods are often the only way to derive information about the location and properties of plumbing systems at depth.

3.4. Geodetic studies of volcanic plumbing systems

Volcano observatories monitor active volcanoes with a combination of techniques, including seismic networks, temperature, and gas monitoring, as well as geodetic techniques (www.wovo.org; **Figure 5**). Geodetic monitoring of the deformation of the Earth's surface relies mainly on ground-based tiltmeters, GPS networks, and satellite-based Interferometry of Synthetic Aperture Radar (InSAR). A network of GPS stations has to be deployed and maintained in the field and typically delivers daily data for each station. Continuous monitoring can provide surface deformation data with an accuracy of about 1 mm/yr, but the data quality strongly depends on the station network density [80]. On the other hand, InSAR records surface deformation in the line of sight of the satellite at 10–40 days intervals. So, InSAR can reach accuracies of less than 1 cm for a stack of interferograms. Apart from disturbances due to vegetation and glaciation, InSAR allows geodetic monitoring of volcanoes worldwide, irrespective of accessibility [80]. Thanks to InSAR monitoring data, we now know of more than 140 currently deforming volcanoes (http://www.globalvolcanomodel.org).

The corrected and processed surface deformation data are interpreted using geodetic volcano-deformation modelling, which reproduces the pattern and magnitude of the surface signal with analytical models based on fluid and solid mechanics [84]. The results of geodetic models have been used to interpret volcano deformation in many volcanoes worldwide [85–87] and have led to a better understanding of magma movements. Even though surface deformation in volcanoes is not always related to an imminent eruption, geodetic monitoring, and modelling have become standard tools for eruption forecasting [88–90].

Geodetic models are analytical or numerical solutions that comprise three components: A. a deformation source representing the VPS, B. a static process in the deformation source, and C. the model crust bounded by the free surface and characterised by a rheological law. The combination of A, B, and C produces deformation of the model surface, which is compared to

the measured surface deformation. As the solution of geodetic models with highly different input parameters can produce very similar results [91, 92], the geodetic modeller is left with an infinite number of possible, non-unique solutions. Non-linear inversion is thus applied to select likely source parameters, to estimate uncertainties, and to compare the goodness-of-fit of different models [93, 94]. When comparing the fit of models, the simplest one, which reproduces the recorded data best, is usually preferred, even though it may be geologically implausible for the studied volcano.

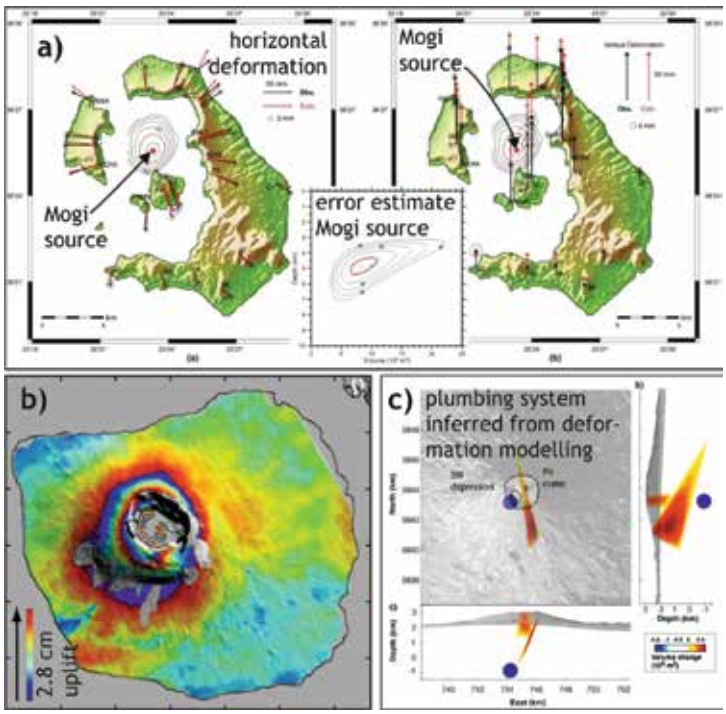

Figure 5. Examples of geodetic studies of volcanic plumbing systems. (a) GPS data (black arrows) and results of Mogi models (red arrows) of ground deformation of Santorini. The Mogi source (red dot) is given with confidence intervals in per cent [81]. (b) Post-eruptive deformation of Fernandina volcano, Galapagos islands, measured with InSAR [82]. (c) Structure of the volcanic plumbing system of Nyamulagira volcano, Congo, inferred from InSAR and stress modelling [83].

Since it is impossible to quantify the uncertainties of geodetic model results on active geological processes that occur in the subsurface, it is important to constrain the models by using model input parameters provided by depth and location of earthquakes related to moving magma [86], earthquake "shadows" around magma reservoirs (see Section 3.3; [69]), or by volcanic eruption volumes and volcanic plume heights [95]. However, these methods miss small- and medium-sized magma chambers, as well as the shape of the plumbing system. Furthermore, geobarometry (see Section 3.2) may indicate the depth and duration of long-term magma storage, but cannot resolve levels of short-time storage [51]. More importantly, however, the lack of collaborative work between different disciplines that study volcanoes has so far

http://dx.doi.org/10.5772/63959

prevented a more realistic interpretation of surface deformation in volcanoes. So in practice, deformation source geometries are often arbitrarily chosen without geological validation.

3.5. Laboratory, theoretical, and numerical modelling of volcanic plumbing systems

Since active volcanic plumbing systems are located within the crust and therefore not accessible for direct observations and even the shallowest parts, that is, volcanic vents, are extremely

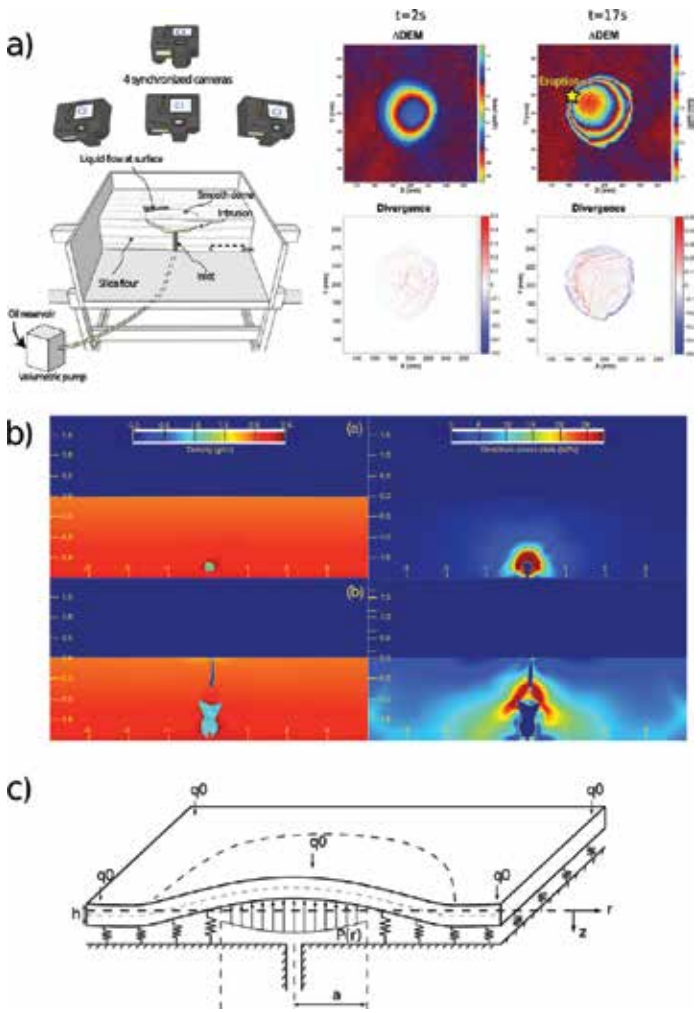

Figure 6. Examples of modelling studies of volcanic plumbing systems. (a) Experimental set-up (left) and characteristic laboratory modelling results (right) of ground deformation induced by shallow magma emplacement [96]. Results are differential DEMs (top row) and divergence maps (bottom row) calculated from horizontal displacement maps at two times of an experiment; positive divergence means dilation (tensile cracks), whereas negative divergence means compression (reverse faulting). (b) Numerical results displaying the evolution of density cross sections (left column) and deviatoric stress cross sections (right column) calculated from 2D finite volume simulations of explosive venting [97]. (c) Set-up and boundary conditions of a theoretical model of flat-lying intrusion of radius a, emplaced at the base of an elastic plate of thickness *h* and weight q0 [98]. The magma has a heterogeneous pressure *P*(*r*).

hazardous to approach, our understanding of the dynamic processes at work in VPS is based on either direct observations of extinct plumbing systems (field geology; see Section 3.1) or indirect observations through geophysics, geodetic surveys, and geochemistry and petrology of volcanic products (see Sections 3.2 to 3.4). However, these approaches are insufficient to identify and quantify the physical parameters and laws that dominantly control the dynamics of VPS.

To overcome these limitations, modelling techniques, such as laboratory, theoretical, and numerical modelling are employed to study processes in volcanic plumbing systems (**Figure 6**). By definition, modelling implies simulating processes in a model system to understand the dynamics of the same processes in nature. However, as the model system is a crude simplification of a part of nature, we cannot expect the model to represent the full complexity of natural processes. The assumptions and simplifications we make when setting up the model, will have a large impact on the model outcome. It is therefore important to keep in mind that models are models, and not nature, and that model results are only as good as the input data. Consequently, modelling of volcanic plumbing systems should always use input data from plumbing systems in nature, for example, field data, and should always be validated against observations in nature.

3.5.1. Laboratory modelling

The aim of laboratory modelling is to simulate processes in volcanic plumbing systems at manageable scales, such as laboratory lengths (sand boxes of a few metres length maximum) and time scales (minutes to days) (**Figure 4a–c**; [20]). In the nineteenth and early twentieth centuries, laboratory models were phenomenological only and used as source of inspiration and/or proof of concepts to demonstrate the existence of a phenomenon [99]. The main limitations of these models were their applicability to geological systems. Laboratory models entered a new era after Hubbert [17] introduced the scaling theory that established scale relationships between laboratory-scale model and geological-scale system. However, these scale relationships address the similarity between the two systems only, that is, they cannot be used to understand the physics behind the modelled processes. Hence, the development of the dimensional analysis concept within the field of physics was a breakthrough for laboratory modelling. Dimensional analysis identifies fundamental physical laws, so-called scaling laws, that are simple relationships between dimensionless parameters, that is, their validity is scale independent ([100] and references therein). Combining dimensional analysis and similarity principles to laboratory models allow the modeller to unravel the fundamental physical laws and apply them to geological-scale volcanic plumbing systems [20].

Successful implementation of laboratory models requires the use of model materials with relevant properties. Classic rock analogues are gels [101, 102] and loose sand [103, 104] to simulate elastic rocks and cohesion-less Coulomb (i.e. frictional) rocks, respectively, which are two end-member behaviours of natural rocks. Recently, new materials of more complex rheology have been successfully used [105, 106]. Cohesive granular materials, some of which have variable cohesion, account for the complex elastoplastic properties of the brittle upper crust, and can simulate both mode I (tensile) and mode II (shear) fracturing [107]. Gels offer

http://dx.doi.org/10.5772/63959

the possibility to study the viscoelastic properties of the Earth's crust [108– 110]. On the other hand, many different fluids of diverse rheology and viscosity have been used as magma analogues [20]. Most noticeable is the implementation of two-phase fluids to model the dynamics of magma-bubble suspensions [111, 112]. These materials offer the possibility to model the natural complexity of geological systems, and hence, the physics of the complex processes in volcanic plumbing systems is studied.

Another recent enhancement of laboratory models has been the implementation of various monitoring methods that allow for more quantitative data acquisition and analysis [113]. The most commonly used methods are Particle Image Velocimetry (PIV) and Digital Image Correlation (DIC) [62, 114, 115] and stereo-photogrammetry [96] to monitor deformation of surfaces, as well as X-ray scanners to monitor *in situ* model interiors [116, 117]. The resulting quantitative data have become essential for (i) constraining the physical laws governing the modelled processes and (ii) integrating laboratory results with quantitative geological, geophysical and geodetic data.

The main limitations of laboratory models to be considered include the scale gap between the laboratory and geological systems, which is often critical and hard to fully constrain. The full characterization of model materials is not straightforward, even though it is essential, and requires a solid fundamental mechanics background. For example, cohesive and cohesion-less granular materials exhibit elastic properties that are difficult to measure, though they are crucial for the dynamics of the brittle crust [118, 119]. Another challenge is connected to recording the modelled processes, which often requires advanced techniques, such as laser or X-ray scanning, which are very costly and heavy to handle. Moreover, stress fields in granular material experiments cannot be measured, although stress distribution is a key factor on the dynamics and evolution of VPS. Finally, first-order assumptions need to be made due to technical limitations of model systems, neglecting for instance thermal effects [120] and chemical evolution of magmas.

3.5.2. Theoretical modelling

In order to assess first-order scaling laws governing a process in volcanic plumbing systems, theoretical (or analytical) models are employed. Theoretical models solve analytically or semianalytically the mathematical equations governing the studied processes (**Figure 4d**). During the mathematical derivations, the first-order scaling parameters commonly appear spontaneously [98, 121, 122], such that the first-order effect of the key physical parameters is obvious, and it is possible to identify whether distinct physical behaviours can be expected. Pioneering theoretical models of hydraulic fractures [123, 124], for example, are the foundation for most subsequent models of dyke or laccolith emplacement.

Although theoretical models are powerful, they require an advanced level of mathematical skill, which is often beyond the training level of most geoscientists. Moreover, theoretical models exhibit limitations, such that the solution of the equations requires a large number of simplifying assumptions. As a consequence, many geoscientists are not aware of the assumptions behind the mathematical models and extrapolate the model results beyond their domain of validity. Furthermore, geoscientists often accept the assumptions underlying the theoretical

models as rules, such that the assumptions are rarely questioned, in spite of contradicting evidence from nature. For example, it is commonly assumed that dykes and sills are hydraulic fractures emplaced in purely elastic host rocks, although clear field, geophysical, and laboratory evidence of first-order inelastic deformation accommodating their emplacement are frequently observed.

3.5.3. Numerical modelling

Numerical modelling uses mathematical equations to simulate a simple process or a combination of several processes (**Figure 4e**). Using numerical codes and software, which have often been developed for materials science applications, the studied system is subdivided into subsystems, so-called elements, and the equations solved for each element. Hence, numerical models can overcome some of the main limitations of theoretical models by accounting for boundaries of complex shapes [125], complex heterogeneities, etc. The models can take into account material properties, temperatures and pressures and calculate stresses and strains, as well as changes in temperature, pressure, and material properties. Furthermore, numerical models can account for static [86, 126], quasistatic, and transient processes [127, 128]. Therefore, in a transient model, it is possible to calculate at each time step, the stress field [129], flow field [130], and/or temperature field [131]. This represents a major advantage with respect to laboratory models, in which the material properties and processes within the model are challenging to measure and monitor. Another advantage is that the scales of numerical models can be directly set as the scale of geological systems. As computational power is the main constraint on how complex a numerical model may be, it is easy to systematically vary model parameters, such as the material properties, a major advantage compared to laboratory modelling.

There are two main types of numerical models with fundamentally different approaches, continuum models and discrete models. Continuum models solve the fundamental equations of continuum mechanics, such as Stokes and Navier-Stokes equations for fluid flow, Hook's law for elastic deformation, the heat equation calculating heat diffusion and/or advection, and Darcy's law for porous flow. Various solving methods exist, such as finite difference [132], finite element (e.g. [128]), and finite volume [97]. In volcanic plumbing system research, continuum models are commonly used to model the elastic deformation induced by magmatic intrusions [42, 86, 133], magma flow within intrusions [125], thermal impacts of intrusions on their host rock [131, 134], thermal convection within magma reservoirs [130], and recently magma emplacement [128, 132]. The main limitation of continuum models is that they cannot simulate the formation of new discontinuities, such as fractures or dykes, which is why the geometry of discontinuities has to be prescribed [42].

Discrete models calculate the behaviour of a pack of particles that interact with each other. Some main methods are discrete element models (DEM) and Lattice Boltzman (LBM). The particle interactions are represented by bounds with elastic, friction, or fluid-like properties and strengths [135]. Discrete models are very valuable to simulate processes that create discontinuities, such as fractures, and they appear very suitable to simulate caldera collapse [127], dyke, sill, and laccolith emplacement [129, 136]. The main limitation of discrete models

http://dx.doi.org/10.5772/63959

is to link the particle-scale interactions (e.g. bound stiffness, bound strength) with the bulk properties of the particle packing (Young's modulus, cohesion, internal friction), requiring heavy systematic calibration before running the models and interpreting the results.

4. Challenge: integrating the methods

Since our training and level of experience fundamentally influence how we interpret geological problems [137], different studies of volcanic plumbing systems that employ methods of different disciplines often lead to contradictory conclusions. For instance, shallow magma storage beneath Katla volcano has been suggested based on seismic and geodetic data [138, 139], whereas petrological studies so far found evidence for lower- to mid-crustal storage only [140]. Such contrasting results may lead to fundamentally different interpretations when it comes to volcanic risk and hazard assessment and may therefore have unforeseeable consequences (cf. [58]). However, these contrasting results may be due to the limitations of individual methods that commonly assess a fraction of the complex magmatic dynamics only, a discrepancy that is hardly possible to assess for decision makers.

The disciplinary boundaries in plumbing system research in part reflect the historical development of the Earth sciences in general (see Section 2). During the twentieth century, each of the disciplines involved in the study of magma transport and storage has become more specialised, and new disciplines, such as volcano geodesy, have emerged. Methods have become more and more sophisticated, revealing the complexity of individual, and the interplay between, physical and chemical processes at scales ranging from the size of the crystal lattice to the thickness of the lithosphere. While specialisation and methodological progress naturally continue, the true challenge of the twenty-first century is to overcome the boundaries of our disciplines in order to truly assess the complexity of volcanic plumbing system dynamics.

There are three key components required to foster multidisciplinary research in general, and VPS research in particular: communication, information, and education. The methodological specialisation of each discipline has been naturally accompanied by the development and evolution of specific terms, and in most cases even jargon, that are used within individual disciplines, but might not be accessible to researchers outside of the particular discipline. For instance, while structural geologists may refer to a magma body of a certain size as "pluton", the same intrusion may be a "magma reservoir" to igneous petrologists, a "shadow in s-wave attenuation" to geophysicists, and a "deformation source" to geodesists. On the other hand, different disciplines may use the same term but with different connotation. In order to overcome disciplinary boundaries, we need to be able to understand each other, which is preferentially achieved by developing a common language and avoiding jargon. In addition, it is key to learn to communicate one's research to a broad audience, for example, by explaining the essential message of a certain diagram or equation in terms of the research question or by summarising research results in the end of a publication in a way that is generally understandable.

	Field studies	**Petrology**	**Geophysics**	**Geodesy**	**Modelling**
Key questions	*How is magma transported, stored & erupted? Is there an interaction with the host rock?*	*How does magma form and evolve? When did the magma form? What triggers eruptions?*	*Where does the signal come from? What does it mean? Is the signal magmatic?*	*What does the deformation signal mean? Is the signal magmatic?*	*How does the magmatic plumbing system work? Are there general laws we can apply?*
Contribution from [below] towards [above]					
Field studies		Relative ages; structure; context & correlation; mechanical control	Lithology; types of structures; resolution	Shape & evolution of sources; complexity; response of rocks to deformation	Interpretation of kinematics; structural relationships; geometry; mechanics; properties
Petrology	Absolute ages; origin of magma; source evolution; eruption types; chemostratigraphy		Composition of samples; depths & rates; thermal evolution; rock properties	Depths of storage; time scales; sources	Time scales; composition; feedback
Geophysics	Depths & sizes; 4D imaging at depth	Rates; depths & sizes; 3D to 4D imaging at depth		3D to 4D imaging at depth; rock properties & geometries; rates	Rock properties; rates of processes
Geodesy	3D crustal structure; depths & sizes; rates	Rates; depths & sizes; temperature; density	Rates		Response signal of rocks due to processes
Modelling	Feedback on mechanisms & processes; interpretations of structures	Conceptual context; quantify conditions of magma evolution	Mechanisms & processes; state of stress	Mechanisms & processes	

Table 1. Overview of the main disciplines involved in studying volcanic plumbing systems, their main foci and the contribution each one of them can make to the other disciplines.

http://dx.doi.org/10.5772/63959

Another requirement to overcome disciplinary boundaries is to inform researchers from other disciplines about the capabilities and limitations of our own approaches, a process that requires clear communication. At the same time, we need to learn how other approaches can be used to complement our own methods. **Table 1** provides an overview of how approaches from each of the disciplines described earlier (Section 3) can complement research in other disciplines. The key questions and strengths of any of the disciplines can provide complementary data for research in other disciplines. For instance, quantitative constraints on the dimensions of sheet intrusions derived from field work in eroded volcanic systems [32, 141] can be used as input parameters for geodetic modelling of volcano deformation. Geobarometric calculations of the crystallisation depth of crystals in eruptive products of a volcano can be combined with seismic tomography to constrain the depth of magma storage [51]. 3D seismic imaging of intrusions in sedimentary basins can complement field studies on the shape and emplacement of sills [79, 129]. Geodetic monitoring data may help to quantify the amount of magma drained from the volcanic plumbing system during dyke intrusion [142]. Modelling of the emplacement of sheet intrusions can reveal the parameters that control what type of intrusion forms and why different sheet intrusion types are found in the same volcanic plumbing system [143]. These examples highlight only some of the benefits of combining different approaches.

Finally, we need to educate future generations of researchers to be open-minded and aware of the potential of other methods and to be able to communicate their research to a broad audience and collaborate beyond disciplinary boundaries. Multidisciplinary conferences, workshops, and research meetings should become common practice, as should multidisciplinary research projects and teams.

It is up to each one of us to try and understand the potential of other disciplines' methods, to communicate our research so that we can be understood beyond our own disciplines, and to educate our students to be open-minded and have a broad overview of the approaches in volcanic plumbing system research. Although this development may at first glance look like an about-face from the trend of specialisation in our disciplines, in reality, it implies the chance for a more thorough characterisation of the complexity of volcanic plumbing systems.

Acknowledgements

The authors are grateful for fruitful discussions with the participants, and in particular our coorganiser Valentin Troll, of the 2013 workshop "Mechanics of magma emplacement and volcanotectonics", which was funded by an ESF grant within the MeMoVolc scheme. Furthermore, we would like to thank Maria de los Angeles García Juanatey for discussions on geophysical methods and all our colleagues who provided photographs of plumbing system researchers at work through ResearchGate and other channels. The authors also acknowledge funding of their research from the Swedish Research Council (VR), the Swedish Royal Academy of Sciences (KVA), the Centre for Natural Disaster Science (CNDS), the Department of Earth Sciences, Uppsala University and the University in Oslo.

Author details

Steffi Burchardt[1] and Olivier Galland[2*]

*Address all correspondence to: olivier.galland@fys.uio.no

1 Department of Earth Sciences, Uppsala University, Uppsala, Sweden

2 Physics of Geological Processes (PGP), Department of Geosciences, University in Oslo, Blindern, Oslo, Norway

References

[1] Jerram DA, Bryan SE. Plumbing systems of shallow level intrusive complexes. In: Breitkreuz C, Rocchi E, editors. Physical Geology of Shallow Magmatic Systems. Advances in Volcanology. Springer. Edinburgh 2015.

[2] Hutton J. Abstract of a Dissertation read in the Royal Society of Edinburgh, upon the Seventh of March, and Fourth of April, MDCCLXXXV, concerning the System of the Earth, its Duration, and Stability, Royal Society of Edinburgh, Edinburgh 1785.

[3] Hall J. Experiments on whinstone and lava. Journal of Natural Philosophy, Chemistry, and the Arts. 1800;4:8–18, 56–65.

[4] Young DA. Mind over Magma: The Story of Igneous Petrology. Princeton University Press; Princeton University Press, Princeton. 2003. 686 p.

[5] Gilbert GK. Report on the Geology of the Henry Mountains. Washington, DC., Government Printing Office; 1877.

[6] Suess E. The Face of the Earth Germany. Freytag, Leipzig, Germany. 1885.

[7] Daly RA. The mechanics of igneous intrusions. American Journal of Science. 1903;15:269–298.

[8] Daly RA. Igneous Rocks and Their Origin. McGraw Hill; New York 1914.

[9] Clough CT, Maufe HB, Bailey EB. The cauldron subsidence of Glen Coe, and associated igneous phenomena. Quarterly Journal of the Geological Society of London. 1909;65:611–678.

[10] Bailey EB, Clough CT, Wright WB, Richey JE, Wilson GV. Tertiary and Post-Tertiary Geology of Mull, Loch Aline, and Oban. Geological Survey of Scotland Memoir. Edinburgh 1924.

[11] Bowen NL. Crystallisation-differentiation of silicate liquids. American Journal of Science. 1915;39:175–191.

[12] Grout FF. A type of igneous differentiation. Journal of Geology. 1918;26:626–658.

[13] Hall AL. The Bushveld Igneous Complex of the Central Transvaal. Geological Survey of South Africa Memoir. Pretoria Government Printer, Pretoria 1932;28.

[14] Wager LR, Deer WA. Geological investigations in East Greenland, part III. The petrology of the Skaergaard Intrusion, Kangerdluqssuad, East Greenland. Meddelelser om Grønland. 1939;105:1–352.

[15] Walker GPL. Zeolite zones and dyke distribution in relation to the structure of eastern Iceland. Journal of Geology. 1960;68:515–528.

[16] Sparks RSJ. The legacy of George Walker to volcanology. In: Thordarson T, Self S, Larsen G, Rowland SK, Höskuldsson A, editors. Studies in Volcanology. The Legacy of George Walker. Special Publications of IAVCEI. London 2009;2:pp. 1–15.

[17] Hubbert MK. Theory of scale models as applied to the study of geologic structures. Geological Society of America Bulletin. 1937;48:1459–1520.

[18] Ramberg H, editor. Model studies in relation to intrusion of plutonic bodies, Mechanism of igneous intrusion. Geological Journal Special Issue. 1970;2.

[19] Ramberg H. Gravity, Deformation and the Earth's Crust. Academic Press; Cambridge, Massachusetts 1981.

[20] Galland O, Holohan EP, van Wyk de Vries B, Burchardt S. Laboratory Modelling of Volcano Plumbing Systems: A Review. In: Breitkreuz C, Rocchi S, editors. Physical Geology of Shallow Magmatic Systems – Dykes, Sills and Laccoliths. Springer; Advances in Volcanology. Berlin 2015;pp. 1–68.

[21] Bott MHP, Tuson J. Deep structure beneath the Tertiary volcanic regions of Skye, Mull and Ardnamurchan, North-west Scotland. Nature Physical Science. 1973;242:114–116.

[22] Ameglio L, Vigneresse J-L. Geophysical imaging of the shape of granitic intrusions at depth: a review. In: Castro A, Fernández C, Vigneresse J-L, editors. Understanding Granites: Integrating New and Classical Techniques. Geological Society, London, Special Publications. 1999;168:pp. 39–54.

[23] Walker GPL. The Breiddalur central volcano, eastern Iceland. Quarterly Journal of the Geological Society. 1963;119:29–63.

[24] Mahan KH, Bartley JM, Coleman DS, Glazner AF, Carl BS. Sheeted intrusion of the synkinematic McDoogle pluton, Sierra Nevada, California. Geological Society of America Bulletin. 2003;115:1570–1582.

[25] Emeleus CH, Cheadle MJ, Hunter RH, Upton BGJ, Wadsworth WJ. The rum layered suite. Developments in Petrology. 1996;15:403–439.

[26] Cruden AR, McCaffrey KJW. Growth of plutons by floor subsidence: implications for rates of emplacement, intrusion spacing and melt-extraction mechanisms. Physics and Chemistry of the Earth, Part A: Solid Earth and Geodesy. 2001;26:303–315.

[27] Paterson SR, Fowler TK, Schmidt KL, Yoshinobu AS, Yuan ES, Miller RB. Interpreting magmatic fabric patterns in plutons. Lithos. 1998;44:53–82.

[28] O'Driscoll B, Troll VR, Reavy RJ, Turner P. The Great Eucrite intrusion of Ardnamurchan, Scotland: reevaluating the ring-dike concept. Geology. 2006;34:189–192.

[29] Stevenson CT, Owens WH, Hutton DH, Hood DN, Meighan IG. Laccolithic, as opposed to cauldron subsidence, emplacement of the Eastern Mourne pluton, N. Ireland: evidence from anisotropy of magnetic susceptibility. Journal of the Geological Society. 2007;164(1):99–110.

[30] Roni E, Westerman DS, Dini A, Stevenson C, Rocchi S. Feeding and growth of a dyke–laccolith system (Elba Island, Italy) from AMS and mineral fabric data. Journal of the Geological Society. 2014;171:413–424.

[31] Tibaldi A, Pasquarè AF, Rust D. New insights into the cone sheet structure of the Cuillin Complex, Isle of Skye, Scotland. Journal of the Geological Society. 2011;168:689–704.

[32] Krumbholz M, Hieronymus C, Burchardt S, Troll VR, Tanner D, Friese N. Weibull distributed dyke thickness reflects probalistic character of host-rock strength. Nature Communications. 2014;5:3272.

[33] Burchardt S, Tanner DC, Troll VR, Krumbholz M, Gustafsson LE. Three-dimensional geometry of concentric intrusive sheet swarms in the Geitafell and the Dyrfjöll Volcanoes, Eastern Iceland. Geochemistry Geophysics Geosystems. 2011;12:Q0AB09.

[34] Burchardt S, Troll VR, Mathieu L, Emeleus HC, Donaldson CH. Ardnamurchan 3D cone-sheet architecture explained by a single elongate magma chamber. Scientific Reports. 2013;3:2891.

[35] Mathieu L, Burchardt S, Troll VR, Krumbholz M, Delcamp A. Geological constraints on the dynamic emplacement f cone-sheets – the Ardnamurchan cone-sheet swarm, NW Scotland. Journal of Structural Geology. 2015;80:133–141.

[36] Buckley SJ, Enge HD, Carlsson C, Howell JA. Terrestrial laser scanning for use in virtual outcrop geology. The Photogrammetric Record. 2010;25:225–239. DOI: 10.1111/j.1477-9730.2010.00585.x.

[37] Senger K, Buckley SJ, Chevallier L, Fagreng Å, Galland O, Kurz TKO, Planke S, Tveranger J. Fracturing of doleritic intrusions and associated contact zones: insights from the Eastern Cape, South Africa. Journal of African Earth Sciences. 2015;102:70–85.

[38] Townsend M, Pollard DD, Johnson K, Culha C. Jointing around magmatic dikes as a precursor to the development of volcanic plugs. Bulletin of Volcanology. 2015;77:1–13. DOI: 10.1007/s00445-015-0978-z.

[39] Parcheta CE, Pavlov CA, Wiltsie N, Carpenter KC, Nash J, Parness A, Mitchell KL. A robotic approach to mapping post-eruptive volcanic fissure conduits. Journal of Volcanology and Geothermal Research. DOI: http://dx.doi.org/10.1016/j.jvolgeores.2016.03.006.

[40] Burchardt S, Tanner DC, Krumbholz M. Mode of emplacement of the Slaufrudalur Pluton, Southeast Iceland inferred from three-dimensional GPS mapping and model building. Tectonophysics. 2010;480(1):232–240. DOI: 10.1016/j.tecto.2009.10.010.

[41] Burchardt S, Tanner D, Krumbholz M. The Slaufrudalur pluton, southeast Iceland—an example of shallow magma emplacement by coupled cauldron subsidence and magmatic stoping. Geological Society of America Bulletin. 2012;124(1–2), 213–227.

[42] Burchardt S. New insights in the mechanics of sill emplacement provided by field observations of the Njardvik Sill, Northeast Iceland. Journal of Volcanology and Geothermal Research. 2008;173:280–288.

[43] Langmuir CH. Geochemical consequences of in situ crystallization. Nature. 1989;340:199–205.

[44] Rickwood PC. Boundary lines within petrologic diagrams which use oxides of major and minor elements. Lithos. 1989;22:247–263.

[45] Spera FJ, Bohrson WA. Energy-constrained open-system magmatic processes I: general model and energy-constrained assimilation and fractional crystallization (EC-AFC) formulation. Journal of Petrology. 2001;42(5):999–1018.

[46] Glazner AF, Bartley JM, Coleman DS, Gray W, Taylor RZ. Are plutons assembled over millions of years by amalgamation from small magma chambers? GSA Today. 2004;14:4–12.

[47] Ginibre C, Wörner G, Kronz A. Crystal zoning as an archive for magma evolution. Elements. 2007;3:261–266.

[48] Mock A, Jerram DA. Crystal size distributions (CSD) in three dimensions: insights from the 3D reconstruction of a highly porphyritic rhyolite. Journal of Petrology. 2005;46:1525–1541.

[49] Cashman K, Blundy J. Petrological cannibalism: the chemical and textural consequences of incremental magma body growth. Contributions to Mineralogy and Petrology. 2013;166:703–729.

[50] Saunders K, Buse B, Kilburn MR, Kearns S, Blundy J. Nanoscale characterisation of crystal zoning. Chemical Geology. 2014;364:20–32.

[51] Dahren B, Troll VR, Andersson UB, Chadwick JP, Gardner MF, Jaxybulatov K, Koulakov I. Magma plumbing beneath Anak Krakatau volcano, Indonesia: evidence for multiple magma storage regions. Contributions to Mineralogy and Petrology. 2012;163:631–651.

[52] Chadwick JP, Troll VR, Waight TE, van der Zwan FM, Schwarzkopf LM. Petrology and geochemistry of igneous inclusions in recent Merapi deposits: a window into the sub-volcanic plumbing system. Contributions to Mineralogy and Petrology. 2013;165:259–282.

[53] Muir DD, Blundy JD, Rust AC, Hickey J. Experimental constraints on dacite pre-eruptive magma storage conditions beneath Uturuncu volcano. Journal of Petrology. 2014;55:749–767.

[54] Deegan FM, Troll VR, Freda C, Misiti V, Chadwick JP, McLeod CL, Davidson JP. Magma–carbonate interaction processes and associated CO2 release at Merapi Volcano, Indonesia: insights from experimental petrology. Journal of Petrology. 2010;51:1027–1051.

[55] Jolis EM, Freda C, Troll VR, Deegan FM, Blythe LS, McLeod CL, Davidson JP. Experimental simulation of magma-carbonate interaction beneath Mt. Vesuvius, Italy. Contributions to Mineralogy and Petrology. 2013;166:1335–1353.

[56] Troll VR, Klügel A, Longpré M-A, Burchardt S, Deegan FM, Carracedo JC, Wiesmaier S, Kueppers U, Dahren B, Blythe LS, Hansteen T, Freda C, Budd D, Jolis EM, Jonsson E, Meade F, Berg S, Mancini L, Polacci M. Floating stones off El Hierro, Canary Islands: xenoliths of pre-island sedimentary origin in the early products of the October 2011 eruption. Solid Earth. 2012;3:97–100.

[57] Geiger H, Mattsson T, Deegan FM, Troll VR, Burchardt S, Gudmundsson O, Tryggvason A, Krumbholz M, Harris C. Magma plumbing for the 2014–2015 Holuhraun eruption Iceland. Geochemistry Geophysics Geosystems DOI: 10.1002/2016GC006317.

[58] Budd DA, Troll VR, Dahren B, Burchardt S. 2016. Persistent multitiered plumbing beneath Katla volcano, Iceland. Geochemistry Geophysics Geosystems. DOI: 10.1002/2015GC006118.

[59] Andrews-Hanna JC, Asmar SW, Head JW, Kiefer, WS, Konopliv AS, Lemoine FG et al. Ancient igneous intrusions and early expansion of the Moon revealed by GRAIL gravity gradiometry. Science. 2013;339(6120):675–678.

[60] Améglio L, Vigneresse J. L. Bouchez, D. H. W. Hutton, W. E. Stephens. Granite pluton geometry and emplacement mode inferred from combined fabric and gravity data. In: Granite: From Segregation of Melt to Emplacement Fabrics. Springer. Berlin 1997; pp. 199–214.

[61] Drenth BJ, Keller GR, Thompson RA. Geophysical study of the San Juan Mountains batholith complex, southwestern Colorado. Geosphere. 2012;8:669–684.

[62] Burchardt S, Walter TR. Propagation, linkage, and interaction of caldera ring-faults: comparison between analogue experiments and caldera collapse at Miyakejima, Japan, in 2001. Bulletin of Volcanology. 2010;72:297–308. DOI: 10.1007/s00445-009-0321-7.

[63] Hansen DM, Cartwright JA. Saucer-shaped sill with lobate morphology revealed by 3D seismic data: implications for resolving a shallow-level sill emplacement mechanism. Journal of the Geological Society. 2006;163(3):509–523.

[64] Jaxybulatov K, Shapiro NM, Koulakov I, Mordret A, Landès M, Sens-Schönfelder C. A large magmatic sill complex beneath the Toba caldera. Science. 2014;346(6209):617–619.

[65] Battaglia M, Gottsmann J, Carbone D, Fernández J. 4D volcano gravimetry. Geophysics. 2008;73:WA3–WA18.

[66] Zobin VM. Introduction to Volcanic Seismology. Elsevier; Amsterdam 2012.

[67] Sigmundsson F, Hooper A, Hreinsdóttir S, Vogfjörd KS, Ófeigsson BG, Heimisson ER., et al. Segmented lateral dyke growth in a rifting event at Bardarbunga volcanic system, Iceland. Nature. 2015;517:191–195.

[68] White RS, Drew J, Martens HR, Key J, Soosalu H, Jakobsdóttir SS. Dynamics of dyke intrusion in the mid-crust of Iceland. Earth and Planetary Science Letters. 2011;304:300–312.

[69] Einarsson P. S-wave shadows in the Krafla caldera in NE-Iceland, evidence for a magma chamber in the crust. Bulletin of Volcanology. 1978;41:187–195.

[70] Thomson K. Volcanic features of the North Rockall Trough: application of visualisation techniques on 3D seismic reflection data. Bulletin of Volcanology. 2004;67:116–128.

[71] Planke S, Rasmussen T, Rey SS, Myklebust R. Seismic characteristics and distribution of volcanic intrusions and hydrothermal vent complexes in the Vøring and Møre basins. In: Doré AG, Vining BA, editors. Proceedings of the 6th Petroleum Geology Conference of the Geological Society, London. 2005.

[72] Polteau S, Mazzini A, Galland O, Planke S, Malthe-Sørenssen A. Saucer-shaped intrusions: occurrences, emplacement and implications. Earth and Planetary Science Letters. 2008;266:195–204.

[73] Jackson CAL, Schofield N, Golenkov B. Geometry and controls on the development of igneous sill-related forced-folds: a 2D seismic reflection case study from offshore southern Australia. Geological Society of America Bulletin. 2013;125:1874–1890.

[74] Hansen DM, Cartwright JA, Thomas D. 3D seismic analysis of the geometry of igneous sills and sill junction relationships. In: Davies RJ, Cartwright J, Stewardt SA, Lappin M, Underhill JR, editors. 3D Seismic Technology: Application to the Exploration of Sedimentary Basins. Geological Society of London Memoir, London. 2004.

[75] Rateau R, Schofield N, Smith M. The potential role of igneous intrusions on hydrocarbon migration, West of Shetland. Petroleum Geoscience. 2013;19:259–272. DOI: 10.1144/petgeo2012-035.

[76] Schofield N, Heaton L, Holford SP, Archer, SG, Jackson CAL, Jolley DW. Seismic imaging of "broken bridges": linking seismic to outcrop-scale investigations of

intrusive magma lobes. Journal of the Geological Society. 2012;169:421–426. DOI: 10.1144/0016-76492011-150.

[77] Trude J, Cartwright J, Davies RJ, Smallwood J. New technique for dating igneous sills. Geology. 2003;31:813–816.

[78] Hansen DM, Cartwright JA. The three-dimensional geometry and growth of forced folds above saucer-shaped igneous sills. Journal of Structural Geology. 2006b;28:1520–1535.

[79] Jackson CAL, Schofield N. The influence of normal fault geometry on igneous sill emplacement and morphology. Geology. 2013;41:407–410. DOI: 10.1130/g33824.1.

[80] Dzurisin D. Volcano deformation: new geodetic monitoring techniques. Springer; Berlin 2007.

[81] Lagios E, Sakkas V, Novali F, Bellotti F, Ferretti A, Vlachou K, Dietrich V. SqueeSAR and GPS ground deformation monitoring of Santorini Volcano (1992–2012): tectonic implications. Tectonophysics. 2013;594:38–59.

[82] Chadwick Jr, WW, Jónsson S, Geist DJ, Poland M, Johnson DJ, Batt S, Harpp KS, Ruiz A. The May 2005 eruption of Fernandina volcano, Galápagos: the first circumferential dike intrusion observed by GPS and InSAR. Bulletin of Volcanology. 2011;73(6):679–697.

[83] Wauthier C, Cayol V, Smets B, d'Oreye N, Kervyn F. Magma pathways and their interactions inferred from InSAR and stress modeling at Nyamulagira Volcano, DR Congo. Remote Sensing. 2015;7(11):15179–15202.

[84] Lisowski M. Analytical volcano deformation source models. In: Dzurisin D, editor. Volcano Deformation: New Geodetic Monitoring Techniques. Springer. Berlin 2007.

[85] Pritchard ME, Simons M. A satellite geodetic survey of large-scale deformation of volcanic centres in the central Andes. Nature. 2002;418:167–171.

[86] Sigmundsson F, Hreinsdóttir S, Hooper A, Arnadottir, T, Pedersen R, Roberts MJ, Oskarsson N, Auriac A, Decriem J, Einarsson P, Geirsson H, Hensch M, Ofeigsson BG, Sturkell E, Sveinbjornsson H, Feigl KL. Intrusion triggering of the 2010 Eyjafjallajökull explosive eruption. Nature. 2010;468:426–430. DOI: 10.1038/nature09558.

[87] Sturkell E et al. New insights into volcanic activity from strain and other deformation data for the Hekla 2000 eruption. Journal of Volcanology and Geothermal Research. 2013;256:78–86.

[88] Klein FW. Eruption forecasting at Kilauea volcano, Hawaii. Journal of Geophysical Research: Solid Earth. 1984;89:3059–3073.

[89] Sparks RSJ. Forecasting volcanic eruptions. Earth and Planetary Science Letters. 2003;210:1–15.

[90] Cervelli PF, Fournier T, Freymueller J, Power JA. Ground deformation associated with the precursory unrest and early phases of the January 2006 eruption of Augustine Volcano, Alaska. Geophysical Research Letters. 2006;33:L18304.

[91] Dieterich JH, Decker RW. Finite element modeling of surface deformation associated with volcanism. Journal of Geophysical Research. 1975;80:4094–4102.

[92] Fialko Y, Khazan Y, Simons M. Deformation due to a pressurized horizontal circular crack in an elastic half-space, with applications to volcano geodesy. Geophysical Journal International. 2001;146:181–190.

[93] Murray MH, Marshall GA, Lisowski M, Stein RS. The 1992 M=7 Cape Mendocino, California earthquake: Coseismic deformation at the south end of the Cascadia megathrust. Journal of Geophysical Research. 1996;101:17707–17725.

[94] Cervelli PF, Murray MH, Segall P, Aoki Y, Kato T. Estimating source parameters from deformation data, with an application to the March 1997 earthquake swarm off the Izu Peninsula, Japan. Journal of Geophysical Research Solid Earth. 2001;106:11217–11237.

[95] Hreinsdóttir S, Sigmundsson F, Roberts MJ, Björnsson H, Grapenthin R, Arason P. Volcanic plume height correlated with magma-pressure change at Grimsvotn Volcano, Iceland. Nature Geoscience. 2014;7:214–218.

[96] Galland O, Bertelsen HS, Guldstrand F, Girod L, Johannessen RF, Bjugger F, Burchardt S, Mair K. Application of open-source photogrammetric software MicMac for monitoring surface deformation in laboratory models. Journal of Geophysical Research. 2016. DOI: 10.1002/2015JB012564

[97] Galland O, Gisler GR, Haug ØT. Morphology and dynamics of explosive vents through cohesive rock formations. Journal of Geophysical Research. 2014:119:LB011050, doi: 10.1002/2014JB011050.

[98] Galland O, Scheibert J. Analytical model of surface uplift above axisymmetric flat-lying magma intrusions: implications for sill emplacement and geodesy. Journal of Volcanology and Geothermal Research. 2013;253:114–130. DOI: http://dx.doi.org/10.1016/j.jvolgeores.2012.12.006.

[99] Daubrée A. Recherches expérimentales sur le rôle possible des gaz à hautes températures doués de très fortes pressions et animés d'un mouvement fort rapide dans divers phénomènes géologiques. Bulletin de la Société géologique de France. 1891;19:313–354.

[100] Barenblatt GI. Scaling. Cambridge University Press; Cambridge 2003.

[101] Hubbert MK, Willis DG. Mechanics of hydraulic fracturing. AIME Transactions. 1957;210:153–168.

[102] Takada A. Experimental study on propagation of liquid-filled crack in gelatin: shape and velocity in hydrostatic stress condition. Journal of Geophysical Research. 1990;95:8471–8481.

[103] Román-Berdiel T, Gapais D, Brun J-P. Analogue models of laccolith formation. Journal of Structural Geology. 1995;17:1337–1346.

[104] Corti G, Bonini M, Innocenti F, Manetti P, Mulugeta G. Centrifuge models simulating magma emplacement during oblique rifting. Journal of Geodynamics. 2001;31:557–576.

[105] Galland O, Cobbold PR, Hallot E, de Bremond d'Ars J, Delavaud G. Use of vegetable oil and silica powder for scale modelling of magmatic intrusion in a deforming brittle crust. Earth and Planetary Science Letters. 2006;243:786–804.

[106] Galland O. Experimental modelling of ground deformation associated with shallow magma intrusions. Earth and Planetary Science Letters. 2012;317–318:145–156. DOI: 10.1016/j.epsl.2011.10.017.

[107] Abdelamak MM, Bulois C, Mourgues R, Galland O, Legland JB, Gruber C. Description of new dry granular materials of variable cohesion and friction coefficient: implications for laboratory modelling of the brittle crust. Tectonophysics. 2016. in press: http://www.sciencedirect.com/science/article/pii/S0040195116001591.

[108] Hirata T. Fracturing due to fluid intrusion into viscoelastic materials. Physical Review E. 1998;57:1772–1779.

[109] Sumita I, Ota Y. Experiments on buoyancy-driven crack around the brittle–ductile transition. Earth and Planetary Science Letters. 2011;304:337–346. DOI: http://dx.doi.org/10.1016/j.epsl.2011.01.032.

[110] Di Giuseppe E, Corbi F, Funiciello F, Massmeyer A, Santimano TN, Rosenau M, Davaille A. Characterization of Carbopol® hydrogel rheology for experimental tectonics and geodynamics. Tectonophysics. 2015;642:29–45. DOI: tp://dx.doi.org/10.1016/j.tecto.2014.12.005.

[111] Vergniolle S, Jaupart C. Separated two-phase flow and basaltic eruptions. Journal of Geophysical Research: Solid Earth. 1986;91:12842–12860. DOI: 10.1029/JB091iB12p12842.

[112] Pioli L, Bonadonna C, Azzopardi BJ, Phillips JC, Ripepe M. Experimental constraints on the outgassing dynamics of basaltic magmas. Journal of Geophysical Research: Solid Earth. 2012;117. DOI: 10.1029/2011JB008392.

[113] Leever KA, Galland O, Acocella V. The science behind laboratory-scale models of the earth. Eos, Transactions American Geophysical Union. 2014;95:30. DOI: 10.1002/2014eo030008.

[114] Leever KA, Gabrielsen RH, Sokoutis D, Willingshofer E. The effect of convergence angle on the kinematic evolution of strain partitioning in transpressional brittle wedges: insight from analog modeling and high-resolution digital image analysis. Tectonics. 2011;30:TC2013. DOI: 10.1029/2010tc002823.

[115] Abdelmalak MM, Mourgues R, Galland O, Bureau D. Fracture mode analysis and related surface deformation during dyke intrusion: Results from 2D experimental

modelling. Earth and Planetary Science Letters. 2012;359–360:93–105. DOI: 10.1016/j.epsl.2012.10.008

[116] Adam J, Klinkmüller M, Schreurs G, Wieneke B. Quantitative 3D strain analysis in analogue experiments simulating tectonic deformation: integration of X-ray computed tomography and digital volume correlation techniques. Journal of Structural Geology. 2013;55:127–149. DOI: http://dx.doi.org/10.1016/j.jsg.2013.07.011.

[117] Poppe S, Holohan EP, Pauwels E, Cnudde V, Kervyn M. Sinkholes, pit craters, and small calderas: analog models of depletion-induced collapse analyzed by computed X-ray microtomography. Geological Society of America Bulletin. 2015;127:281–296, DOI: 10.1130/b30989.1.

[118] Lohrmann J, Kukowski N, Adam J, Onken O. The impact of analogue materials properties on the geometry, kinematics, and dynamics of convergent sand wedges. Journal of Structural Geology. 2003;25:1691–1711.

[119] Rosenau M, Nerlich R, Brune S, Oncken O. Experimental insights into the scaling and variability of local tsunamis triggered by giant subduction megathrust earthquakes. Journal of Geophysical Research. 2010;115:B09314. DOI: 10.1029/2009jb007100.

[120] Taisne B, Tait S. Effect of solidification on a propagating dike. Journal of Geophysical Research: Solid Earth. 2011;116:B01206, DOI: 10.1029/2009jb007058.

[121] Pollard DD. Derivation and evaluation of a mechanical model for sheet intrusions. Tectonophysics. 1973;19:233–269, DOI: http://dx.doi.org/10.1016/0040-1951(73)90021-8.

[122] Sparks RSJ, Huppert HE, Turner JS, Sakuyama M, O'Hara MJ. The fluid dynamics of evolving magma chambers [and discussion]. Philosophical Transactions of the Royal Society of London, Series A. 1984;310:511–534.

[123] Green AE. On Boussinesq's problem and penny-shaped cracks. Mathematical Proceedings of the Cambridge Philosophical Society. 1949;45:251–257.

[124] Weertman J. Theory of water-filled crevasses in glaciers applied to vertical magma transport beneath oceanic ridges. Journal of Geophysical Research. 1971;76:1171–1183.

[125] Petford N, Mirhadizadeh S. Eddy flow and associated particle dynamics during magma intrusion: the Basement Sill, Antarctica. EGU General Assembly Conference Abstracts. 2014;4182.

[126] Chestler SR, Grosfils EB. Using numerical modeling to explore the origin of intrusion patterns on Fernandina volcano, Galápagos Islands, Ecuador. Geophysical Research Letters. 2013;40:50833. DOI: 10.1002/grl.50833.

[127] Holohan EP, Schöpfer MPJ, Walsh JJ. Mechanical and geometric controls on the structural evolution of pit crater and caldera subsidence. Journal of Geophysical Research. 2011;116:B07202. DOI: 10.1029/2010jb008032.

[128] Keller T, May DA, Kaus BJP. Numerical modelling of magma dynamics coupled to tectonic deformation of lithosphere and crust. Geophysical Journal International. 2013;195:1406–1442, DOI: 10.1093/gji/ggt306.

[129] Malthe-Sørenssen A, Planke S, Svensen H, Jamtveit B. Formation of saucer-shaped sills. In: Breitkreuz C, Petford N, editors. Physical geology of high-level magmatic systems. Geological Society of London. Special Publication. London 2004;pp. 215–227.

[130] Longo A, Vassalli M, Papale P, Barsanti M. Numerical simulation of convection and mixing in magma chambers replenished with CO2-rich magma. Geophysical Research Letters. 2006;33:027760. DOI: 10.1029/2006GL027760.

[131] Aarnes I, Svensen H, Polteau S, Planke S. Contact metamorphic devolatilization of shales in the Karoo Basin, South Africa, and the effects of multiple sill intrusions. Chemical Geology. 2011;281:181–194. DOI: 10.1016/j.chemgeo.2010.12.007

[132] Gerya TV, Burg J-P. Intrusion of ultramafic magmatic bodies into the continental crust: numerical simulation. Physics of the Earth and Planetary Interiors. 2007;160:124–142.

[133] Amelung F, Jonsson S, Zebker H, Segall P. Widespread uplift and "trapdoor" faulting on Galápagos volcanoes observed with radar interferometry. Nature. 2000;407:993–996. DOI: 10.1038/35039604.

[134] Aarnes I, Podladchikov YY, Svensen,H. Devolatilization-induced pressure build-up: implications for reaction front movement and breccia pipe formation. Geofluids. 2012;12:265–279. DOI: 10.1111/j.1468-8123.2012.00368.x.

[135] Weatherley D, Hancock W, Abe S, Boros V. ESyS-Particle Tutorial and User's Guide Version 2.2. 2. 2013.

[136] Zhao C, Hobbs BE, Ord A, Peng S. Particle simulation of spontaneous crack generation associated with the laccolithic type of magma intrusion processes. International Journal for Numerical Methods in Engineering. 2008;75:1172–1193. DOI: 10.1002/nme.2287.

[137] Bond CE, Gibbs AD, Shipton ZK, Jones S. What do you think this is? "Conceptual uncertainty" in geoscience interpretation. GSA Today. 2007;17:4–10.

[138] Gudmundsson O, Brandsdottir B, Menke W, Sigvaldason GE. The crustal magma chamber of the Katla volcano in south Iceland revealed by 2-D seismic undershooting. Geophysical Journal International. 1994;119:277–296.

[139] Sturkell E, Sigmarsson F. Recent unrest and magma movements at Eyjafjallajökull and Katla volcanoes, Iceland. Journal of Geophysical Research. 2003;108:2369.

[140] Oladottir BA, Sigmarsson O, Larsen G, Thordarson T. Katla volcano, Iceland: magma composition, dynamics and ruption frequency as recorded by Holocene tephra layers. Bulletin of Volcanology. 2008;70:475–493.

[141] Kavanagh JL, Sparks RSJ. Insights of dyke emplacement mechanics from detailed 3D dyke thickness datasets. Journal of the Geological Society. 2011;168:965–978.

http://dx.doi.org/10.5772/63959

[142] Riel B, Milillo P, Simons M, Lundgren P, Kanamori H, Samsonov S. The collapse of Bárðarbunga caldera, Iceland. Geophysical Journal International. 2015;202:446–453.

[143] Galland O, Burchardt S, Hallot E, Mourgues R. Dynamics of dikes versus cone sheets in volcanic systems. Journal of Geophysical Research – Solid Earth. 2014;119:6178–6192.

Chapter 3

Photogrammetric Survey in Volcanology: A Case Study for Kamchatka Active Volcanoes

Viktor Dvigalo, Alina Shevchenko and Ilya Svirid

Additional information is available at the end of the chapter

http://dx.doi.org/10.5772/63577

Abstract

The photogrammetric method has been used to study active volcanoes in Kamchatka for more than 100 years. It is still the most effective method for consistently monitoring short-term changes in the morphology of volcanic structures and for obtaining accurate parameters of eruptions. This chapter shows the specific features of photogrammetry application in volcanological research and development of this method in the context of investigating Kamchatkan volcanoes. We also present the results of the study of volcanic objects with various morphologies, composition, and types of activity with regard to the specific features of the 2001–2012 growth of the dome at Molodoy Shiveluch Volcano, the effects of the 1975–1976 Great Tolbachik Fissure Eruption and of the 2012–2013 Tolbachik Fissure Eruption, the morphodynamics of Troitsky Crater on Maly Semyachik Volcano, and the morphological changes of Akademii Nauk Caldera after the catastrophic 1996 eruption. The chapter shows the way forward for the development of the photogrammetric method in volcanology.

Keywords: Kamchatkan active volcanoes, photogrammetry, lava dome, fissure eruption, volcanic lake, collapse caldera

1. Introduction

Photogrammetry is a branch of science at the junction of optics, mathematics, and photography, which is aimed at the identification of objects' shapes, sizes and locations using photographic images. Photogrammetric method is necessary in all branches of the natural sciences for obtaining objects' morphometric characteristics in cases when it is easier to take a photograph than to measure directly, e.g., in studying such complex and dangerous objects as volcanoes.

The photogrammetric method allows for the measurement of short-life or even moving objects and could be useful in determining geometric forms, sizes, and velocities of eruptive products, such as eruptive clouds, lava, and pyroclastic flows.

Photogrammetric investigations have been used in volcanology for more than a century. At the present time, there are many methods for remote sensing, such as airborne laser scanning or satellite radar and interferometry. Nevertheless, photogrammetry is still of great importance. It is cheaper and more universal than all other remote methods of measurement. In addition, the photogrammetric method could be used to process archival aerial photographs from conventional cameras as well as satellite stereoscopic images.

For a long time, the photogrammetric approach remained rare in volcanology, mainly due to the high cost of equipment and the complexity of the work. Lately, thanks to technological advances, photogrammetric studies have become more accessible. The increase in quality of conventional digital cameras makes it possible to use them for this purpose. The photogrammetric processing of images on the computer eliminates the need for expensive optical–mechanical equipment. Thus, the development of digital image processing caused the increase of interest in photogrammetry for volcanological investigations.

2. The sequence of photogrammetric works

A large number of special works refer to photogrammetric theory (see e.g. reference [1]). Therefore, we just briefly describe the method itself and some of the special characteristics of its application in volcanology. Concrete and practical recommendations depend on hardware and software, which is why we provide only the very general information necessary for understanding the essence and planning of photogrammetric investigations.

Photogrammetric work consists of four stages:

1. Geodetic preparatory work in situ;
2. Photo survey with all technological requirements;
3. Photogrammetric processing of images;
4. DTM plotting.

2.1. Geodetic preparatory work

During this stage of fieldwork, the ground control points are placed down on the surface of the object and their coordinates are defined for geodetic reference of further photogrammetric models. The ground control points are placed so that subsequently they can be easily identified in aerial photographs. This stage is the most laborious and expensive, but some tricks could be used to solve this problem. Thus, when a single object will be investigated over a number of years, this stage only needs to be performed once. After that, we can choose a georeferenced photogrammetric model with easily detected points that do not change their location over time

http://dx.doi.org/10.5772/63577

(e.g., rocks' tops, dykes, and large stones that are not on the slopes). We can then use their coordinates for the absolute orientation of all other models. This could be used not only to process images obtained after establishing the geodetic basement but also to process images that were made before. It can therefore be useful when working with archival images.

Though this method of orientation can result in the possible loss of absolute accuracy for the photogrammetric model, it has a rather high relative accuracy. Taking into account the alteration of the object's surface (e.g., when a crater is formed or filled with lava, pre- or posteruptive deformations of the earth's crust) is very essential for volcanological investigations, and so in most cases, in using the photogrammetric model one should choose relative rather than absolute accuracy. In the most difficult cases, for example, when the erupting volcano is investigated and geodetic work in the area is dangerous, absolute orientation could be made by points identified on topographic maps, if available.

2.2. Aerial photography

Stereophotogrammetric investigations provide the most accurate information about an object. To measure the parameters of the object, these investigations use stereoscopic photography. Stereoscopic images are obtained by shooting an object from different angles. The distance between the survey points is called a basis.

Volcanoes rise steeply above the surrounding terrain and also could pose a hazard during ground investigations, so the photography for photogrammetric purposes is better done from the air. Aerial photography using an analogue or digital camera usually requires a specially equipped air vehicle with a hatch in the floor of the cabin as well as an onboard operator. However, modern digital cameras meet the requirements for the photogrammetric investigation of volcanoes, and they are compact enough for both aerial camera mounting and handheld shooting.

Shooting for a photogrammetric survey can also be carried out using a nonindustrial professional camera. That camera must be equipped with a fixed-focus lens, and autofocus must be switched off. The camera can be calibrated either before or after shooting, but the focal length of the camera and the lens position should not be changed between calibration and shooting.

As a rule, for an aerial survey, the camera is directed vertically downward, and in this case, aerial images are called vertical. If the angle of deviation from the vertical is more than 5°, then this is an oblique aerial photographic survey.

Aerial photography for stereophotogrammetric processing has its own peculiarities. The same part of the object's surface should be shown on at least two frames. If the resolution of the camera or the flight altitude restriction does not allow for a stereo pair of images to be obtained with complete and detailed capturing of the object and the ground control points, then strip or block photography is used. For this type of survey, it is essential that some part of the object's surface (it does not matter which) should be captured in three images of the same strip; this is necessary for the creation of a continuous stereo model. Consequently, the overlap area of two adjacent frames in the strip should be at least 55% of the frame area. The block consists of

several strips with mutual side overlap of the object images. This overlap could be not so large and comprises 15–30% of the frame area.

It should be noted that the relative height of the volcanic edifice can be almost the same as the altitude of the aerial survey flight. As a result, there may be significantly less overlap for images of the object's higher-altitude surfaces than for its lower-altitude ones. To keep constant overlapping, we must correct the inter-frame time interval even in the process of surveying a single pass, reducing it when shooting the top part of the volcano, and increasing it when shooting the foot of the volcano.

2.3. Image processing

Regardless of the equipment and software used, the photogrammetric processing of images consists of the following stages:

1. Interior orientation of images;
2. Relative orientation of images;
3. Exterior orientation of the stereo model.

Interior orientation refers to the camera's geometric parameters: the exact focal length, frame size, main point position (i.e., point of the frame in front of the optical centre of the lens), and the lens radial distortion coefficients. All of these parameters can be obtained from the camera's calibration. In the case of analogue aerial cameras, one should also specify the position of fiducial marks or the distance between them in the frame. Fiducial marks are images of special elements in the film plane of analogue cameras, defining a system of rectangular coordinates for each image.

Relative orientation is made to combine the images into a free photogrammetric model (or stereo model), which is a set of images with the data on the relative camera location for each moment of photography. These include the data on angular position (i.e., angle of inclination and rotation) and spatial position (i.e., length and direction of the base) of the camera from frame to frame. They can either be received from sensors used for surveying (e.g., tiltmeters, gyroscopes, statoscope, GPS sensors) or calculated on the basis of the images. The last variant requires a set of corresponding points in six generally located zones in the overlapping areas of images in each stereo pair. Most photogrammetric software can find these points automatically. The accuracy of the detection of relative orientation parameters from images is generally higher than the data from sensors.

Exterior orientation establishes a correspondence of the photogrammetric model's spatial coordinates to the geodetic coordinates in the area of the object. The exterior orientation of photogrammetric models resulting from one stereo pair of images requires a minimum of three points with known geodetic coordinates that are not located on a one line. In the case of strip photo surveys, it is necessary to have two reference points at each end of the pass, and preferably at least one reference point in the middle. Block photo surveys require reference points at the corners of the shot area and a certain middle point. To exclude rough defects, one should have verification points with exact geodetic coordinates in addition to the minimum

http://dx.doi.org/10.5772/63577

number of reference points. It is good if quantity of verification points is equal to reference points. In the result of an association between the model calculated and the actual coordinates of the verification points, we can define horizontal and vertical errors.

Exterior orientation using GPS coordinates is possible, but it is not recommended to use only this method for aerial survey. The accuracy of surveying point coordinates obtained in flight is not high. Setting the coordinates in flight can result in their shifting along the flight line due to delays in their recording. Besides, all surveying points are on the flight line, which is usually nearly straight, and in such cases, it is practically impossible to make complete exterior orientation. The errors of such orientation may reach up to 10 m or more.

In case of the stereophotogrammetric processing of satellite images, the rational polynomial coefficient (RPC) model is typically used, the coefficients of which, accompanying the images, implicitly include all the necessary parameters of the interior, relative, and exterior orientation. Unfortunately, satellite stereo images often do not meet the requirements for the morphometric investigation of volcanoes. We need images with a spatial resolution of 1 m per pixel or higher to have good mapping of the topography changes associated with volcanic activity.

2.4. DTM plotting

After orientation, the photogrammetric model can easily provide the geodetic coordinates of any point on the object's surface. They can be plotted manually by adjusting marks on the image of the object's surface displayed on a stereo monitor (or by using a common monitor coupled with anaglyph glasses). However, a large number of points makes such processing difficult, thus the majority of photogrammetric processing software is capable of automatic point matching. The algorithms used in such software are based on scanning the images for unique objects with their subsequent matching in various images.

Unfortunately, the volcanic landscape has a set of features that complicates the algorithmic processes. These include steep slopes; texture zones that can easily be recognized in one image but can become faded in the next image; uniform surfaces, such as surfaces covered with scoria or snow with no unique objects; and steam and gas-and-ash emissions, which hide the surface from the camera lens. All of these peculiarities complicate automatic processing, which results in large errors during DTM plotting. Consequently, the software must support visual control to provide possibility of manual correction of automatically determined points within a stereo model.

The matching results in a point cloud, which is then transformed into DSM and subsequently into DTM. Fortunately, the active volcanoes on Kamchatka are barely covered with vegetation, thus the majority of DSM are equal to DTM.

The obtained DTM becomes a basis for the final materials. These may include maps, orthophotomaps, three-dimensional (3-D) pictures both in representative colours and, if available in the software, texturized from original photographs. Moreover, DTM allows for all necessary measurements to be taken, including volume measurements of solid deposits from eruptions, liquid lava, and negative landforms on the volcanic edifices. Such measurements require software that can compare the surfaces of two DTMs and measure the volume between them.

3. History of photogrammetric surveys in Kamchatka

3.1. The 1908–1910 Kamchatka expedition of the Russian Geographic Society

The photogrammetric method was used for the first time during the investigation of the Kamchatkan volcanoes in 1908–1910 by N. G. Kell and other members of the geological department of the Kamchatka expedition of the Russian Geographical Society [2–4]. One of the primary tasks set before the geological department was to study the forms, sizes, and locations of the volcanoes, so the scientists chose the theodolite triangulation method (**Figure 1**) and terrestrial photogrammetry. During the summer of 1908, the members of the expedition used conventional cameras. During the winter of 1908–1909, they constructed a "photogrammeter" using an Ernemann camera, parts from a surveyor's table, and an alidade. In spring 1910, the Laussedat phototheodolite was transported from St. Petersburg to Kamchatka and was used for a panoramic photogrammetric survey of the volcanoes.

Figure 1. N. G. Kell working with theodolite. Photo by S. A. Konradi, 1909.

http://dx.doi.org/10.5772/63577

The investigation resulted in about 2000 single photographs and stereo pairs of almost all of the active volcanoes and many of the dormant ones (**Figure 2**). Some of the stereo pairs, along with the results from the theodolite survey, were used by N. G. Kell for plotting the first map of the Kamchatkan volcanoes.

Figure 2. View of Avachinsky Volcano from the Southeast. Photo by S. A. Konradi, 1909.

3.2. The 1946 volcanological expedition

The head of the Laboratory of Volcanology at the USSR Academy of Sciences, academician A. N. Zavaritsky, launched the volcanological expedition in 1946. The expedition's goals included aerial photography of the most important volcanoes of the Soviet Union. Yu. S. Dobrokhotov, an employee of the Laboratory of Airborne Methods at the USSR Academy of Sciences, was responsible for planning and performing the aerial photography [5]. During the period from August 24 to October 2, 1946, the scientists conducted 10 aerial surveys covering about 9000 km in total and taking 6–7 h. The routes were traced in the way that photographs of each volcano were taken vertically, while the most interesting volcanoes were shot circlewise. Yu. S. Dobrokhotov tried to process the obtained materials photogrammetrically without the geodetic adjustment of the images because a ground geodetic survey had not been conducted before. The survey resulted in the maps of Avachinsky and Maly Semyachik volcanoes being plotted without ground control points, as well as topographic profiles of those volcanoes, also including Krasheninnikov Volcano. Besides, Yu. S. Dobrokhotov for the first time described the important role of photogrammetric investigation in volcanology and developed its basic principles.

3.3. Analogue instrumental stereophotogrammetry, 1973–2008

A new age of photogrammetric investigation of the Kamchatkan volcanoes started in 1973. The collaboration between the Institute of Volcanology and the Novosibirsk Institute of Engineers in Geodesy, Aerial Photography, and Cartography resulted in the establishment of reference geodetic networks on the most active Kamchatkan volcanoes, preliminary aerial photography of those objects, and the plotting of quality large-scale (between 1:2,000 and 1:20,000) topographic plans and maps. In doing so, the scientists formed the theoretical basis for the photogrammetric investigation of volcanoes [6].

For aerial photography, the scientists used USSR analogue aerial photogrammetric cameras and Carl Zeiss Jena phototheodolites. A Carl Zeiss Jena stereocomparator, a Romanovsky stereoprojector, and a coordinatograph were used for photogrammetric processing. In 1984, the Institute of Volcanology bought the most advanced equipment from Carl Zeiss Jena: a multipurpose processing device Stereometrograph-G, an automatic plotting table, a high-precision stereocomparator, a photogrammetric rectifier, a data logger, and a data storage unit, which allowed to accomplish nearly all the tasks related to the processing of aerial and ground-based images. This equipment was put into use in 1985 and was used for 23 years, until 2008.

The quantitative characteristics were mathematically calculated using the results from Stereometrograph-G and the stereocomparator with the help of software made by N. F. Dobrynin at the Institute of Volcanology [7].

The 1973–2008 photogrammetric investigations on Kamchatka allowed for detailed research on morphodynamics and for the calculation of the quantitative characteristics of the 1975–1976 Great Tolbachik Fissure Eruption (GTFE) [8]. They also helped to determine the formation of Novy Dome on Bezymianny Volcano in 1976–1981 and a dome on Molodoy Shiveluch Volcano in 1980–1981 and 1993–1995 [9, 10]. Large-scale topographic maps and plans for the majority of the active Kamchatkan volcanoes were plotted during that period. For the first time, the morphological precursors of activation were revealed for the most frequently surveyed volcanoes, including Klyuchevskoy, Shiveluch, Bezymianny, and Maly Semyachik Volcanoes [11]. In addition, the scientists conducted an assessment of volcanic hazard posed by the Klyuchevskoy group of volcanoes and Avachinsky Volcano.

3.4. Digital stereophotogrammetry from 2008 to the present

Digital techniques were gradually introduced for the photogrammetric investigation of Kamchatkan volcanoes from the late 1990s onward. However, the Laboratory of Geodesy and Remote Sensing at the Institute of Volcanology and Seismology entirely shifted to the digital methods of photogrammetric investigation in 2008 with the purchase of the stereophotogrammetric software Photomod 4.3 by Racurs Company. This software can be substituted for the above-described optomechanical instruments.

The processing of images using Photomod 4.3 results in vector DTMs based on a triangulated irregular network. Quality of stereo modelling is estimated automatically in Photomod 4.3 after the exterior orientation.

http://dx.doi.org/10.5772/63577

The calculation of quantitative characteristics of eruptions, mapping, and 3-D modelling are based on the results from digital photogrammetric processing using Photomod 4.3, followed by more processing with the Surfer 10 software. The volumes of the volcanic edifices and of their elements are determined by subtracting the base DTM of the pre-eruptive terrain from the DTM tied to the date of survey. The volume calculating error is usually less than 1%.

Digital photogrammetric techniques were used for the investigation of the 2001–2012 Shiveluch eruption [12], the 2010–2012 Kizimen eruption [13], the 2012–2013 Tolbachik Fissure Eruption [14], and for other Kamchatkan volcanic and hydrothermal objects [15, 16]. Thus, the investigations resulted in detailed topographic maps of the abovementioned objects, their precise morphometric characteristics and, in particular, the detailed description of the impact from the Kizimen eruption and an assessment of hazard posed by Molodoy Shiveluch [17].

4. Some examples of studied active volcanoes

This part contains data on several volcanoes in Kamchatka that have been studied using the photogrammetric method (**Figure 3**). Objects with various types of activity were chosen to demonstrate that this method is universal.

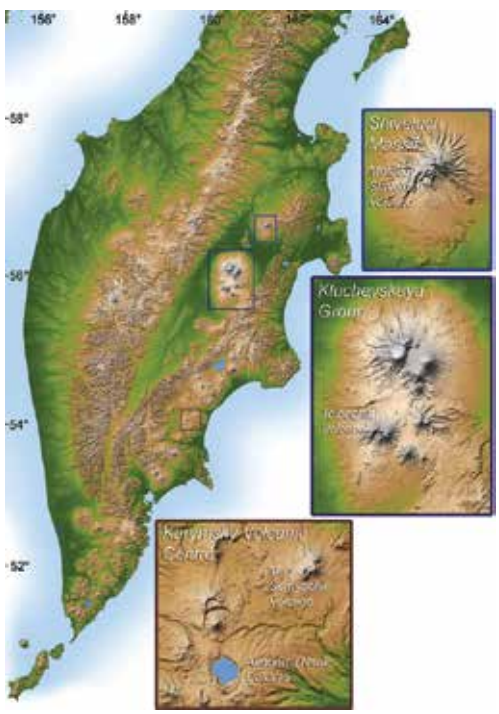

Figure 3. Map of the Kamchatka Peninsula showing the locations of the studied volcanic objects.

4.1. The growth of the Molodoy Shiveluch volcano dome

Molodoy Shiveluch volcano is located in the southwestern part of the Pleistocene Shiveluch massif (**Figure 4**) at a junction of the Aleutian and Kamchatkan volcanic arcs. The coordinates of the highest point of Molodoy Shiveluch are 56°38′10 N, 161°18′54 E, and its height is 2763 m. The volcanic edifice was comprised of several lava domes. The November 12, 1964, eruption resulted in their collapse and the 1.8 × 3.5 km double avalanche caldera formation [18]. The new lava dome has had three periods of steady growth: from 1980 to 1981, from 1993 to 1995, and now it has been growing since 2001.

Figure 4. View of the Shiveluch massif from the south in 2012.

Photogrammetric monitoring of the Molodoy Shiveluch caldera has been carried out since 1979. The investigation of the caldera surface using the 1980 models revealed that the 15-year hot lakes in the active crater on the caldera floor had already disappeared by July 3, 1980. Vertical deformations up to 3 m and a system of fractures were also revealed. The largest fracture was up to 2 × 55 m in size. The lakes' disappearance possibly resulted from the formation of fractures or from the heat flux increase in the area of the future dome formation. Hence, the disappearance of the lakes and the deformations of the caldera's active area surface were precursors to the lava dome's growth [11].

The investigation of the 1980–1981 and 1993–1995 periods, which was performed using instrumental photogrammetric survey, and of the 2001–2012 period, which was performed using a digital photogrammetric survey, allowed for the detailed monitoring of the dome's morphodynamics and revealed its quantitative characteristics.

During the 1980–1981 period, the lava dome reached the height of 185 m and became 0.02 km^3 in volume [9]. During the 1993–1995 eruption, the height of the dome reached 346 m, and its volume was estimated to be 0.2 km^3 [10]. The average lava output over the first two periods was estimated at 41,000 m^3/day and 280,000 m^3/day, respectively. In 1980–1981 and 1993–1995, the dome's growth was endogenous.

http://dx.doi.org/10.5772/63577

From 2001 to the present, the dome has mainly shown exogenous growth. In different parts of the dome, crease structures and lava lobes have formed and occasionally collapsed due to explosions and gravity.

In 2003, there was an inverse change in the type of the dome growth from exogenous to endogenous. Three lava plugs were formed in the western part of the dome (**Figure 5a**). The growth of the lava plugs resulted in the collapse of lava lobes that had covered the dome in 2002. There remained only a part of the northwestern lobe. Multiple avalanche chutes were formed on the southwestern flank of the dome. The relative height of the dome reached 499 m, and the volume reached 0.47 km^3.

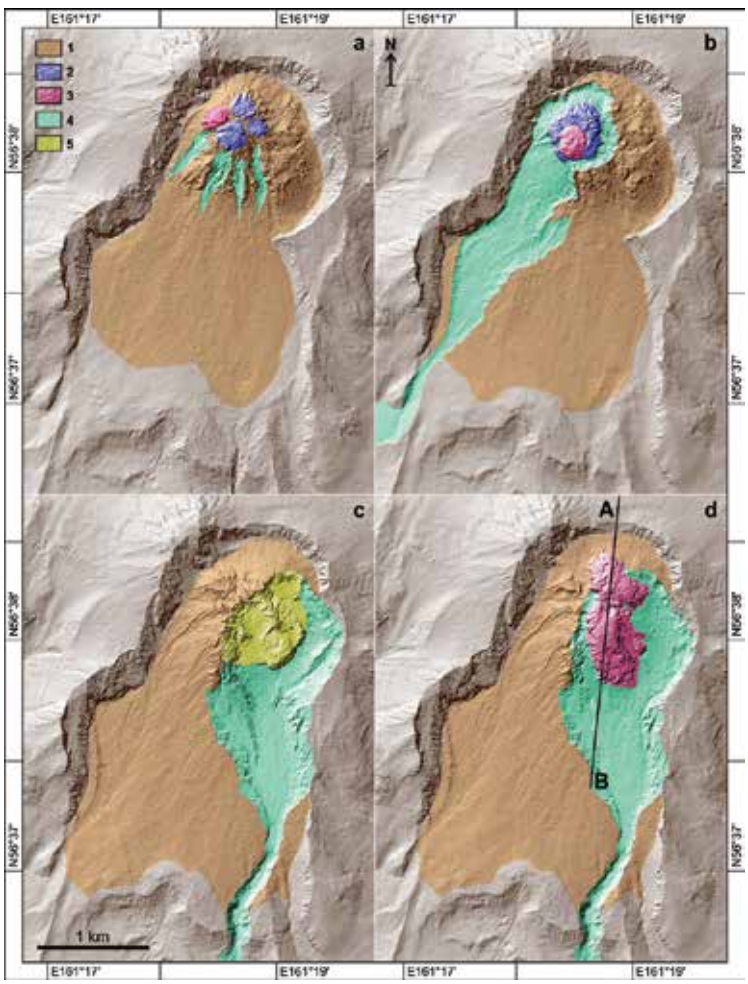

Figure 5. DTMs of the Molodoy Shiveluch caldera: a—October 7, 2003, b—August 21, 2005, c—November 22, 2010, d—July 12, 2012; 1—Dome with a talus mantle, 2—Endogenous lava units, 3—Exogenous lava units, 4—Negative landforms from collapses and explosions, 5—Inner part of the dome. The A–B line denotes the location of profiles shown in **Figure 6**.

We processed R. L. Wessels's images [19] using the photogrammetric method to reveal the state of the lava dome in 2005. It was found that the 2005 dome had been formed in several stages. The February 27, 2005, eruption resulted in a complex crater 730 m in diameter, a sector collapse of the dome, a Merapi-type pyroclastic flow, and the formation of an avalanche chute 620 × 2500 m in size (**Figure 5b**). The volume of the collapsed material was estimated at not less than 0.11 km^3. Then, a relatively small endogenous dome grew up inside the crater. An explosive funnel 280 m in diameter was formed in its southwestern sector. After that, round shape 55 m high and 270 m in diameter lava lobe with prominent crease structure on the surface was extruded from the funnel. The polygenetic dome's relative height was 484 m. Its volume was estimated at 0.48 km^3.

On October 27, 2010, another large sector collapse of the dome edifice occurred at Molodoy Shiveluch. It resulted in the outcrop of an inner part of the dome and the formation of an avalanche chute 1084 × 2455 m in maximum size (**Figure 5c**). The volume of the collapsed material was 0.28 km^3. After the collapse, the relative height of the dome was 557 m, and the volume was estimated to reach 0.54 km^3.

In 2012, the exogenous dome continued to grow (**Figure 5d**). A blocky lava lobe 385 × 755 m in maximum size was formed on its southern flank. A large explosive crater 60 m deep and 150 m in diameter was revealed at the top of the lobe. By July 12, 2012, the extrusive activity centre at Molodoy Shiveluch Volcano had moved to the northern flank of the dome. The new lava lobe of the northern centre was 450 × 590 m in size. Its scoriaceous surface was bisected by a 6 × 470 m fracture. In its uppermost part, the extrusion of ductile material formed a crease structure 160 × 210 m in maximum size. The relative height of the dome was 526 m, and the volume was 0.63 km^3. The average lava discharge in the 2001–2012 period exceeded 225,000 m^3/day [12].

Figure 6 shows profiles of the topographic alteration of the dome morphology during the 2001–2012 period as compared with the previous 1980–1981 and 1993–1995 periods. The July 12, 2012, cross-section of the dome shows that the migration of eruptive centres and the piling up of lava lobes on its surface caused its irregular shape. While the October 1, 1994, and October 22, 1980, cross-sections of the dome agree with its morphology of a classical endogenous type.

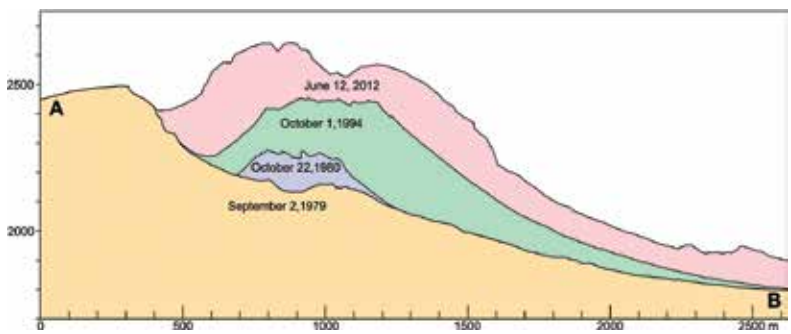

Figure 6. Profiles of the Molodoy Shiveluch lava dome. The A–B profile line location is shown in **Figure 5d**.

http://dx.doi.org/10.5772/63577

4.2. Tolbachik fissure eruptions

The doubled cone of the coalescing Ostry Tolbachik (55°49′50 N, 160°19′30 E) and Plosky Tolbachik volcanoes are located in the southwestern sector of the Klyuchevskaya group of volcanoes (**Figure 7**). Although these volcanoes' edifices were formed simultaneously in the Late Pleistocene [20], only Plosky Tolbachik Volcano was active in the Holocene. Additionally, not only were there summit eruptions, but there were also lateral eruptions from a large fissure zone that begins about 30 km to the south-southwest of the volcano, goes directly to its top, and continues about 10 km to the northeast of it. Historical eruptions occurred only in the south-southwestern part of the fissure zone in the territory known as Tolbachik Dale.

Figure 7. View of 2012–2013 Tolbachik Fissure Eruption from the north in 2012.

The largest and best-studied historical eruptions are the 1975–1976 Great Tolbachik Fissure Eruption (GTFE) and the 2012–2013 Tolbachik Fissure Eruption (TFE). Both eruptions were studied using aerial photogrammetric survey. From 1975 to 1977, aerial surveys of GTFE were carried out four times; archival aerial photographs from 1950 to 1974 were also used.

Photogrammetric processing resulted in the creation of maps and the obtaining of accurate data on the volume of terrain variations such as new lava fields, cinder cones, pyroclastic deposits, and subsidence effects in the summit pit crater of Plosky Tolbachik Volcano [8, 20].

From 2012 to 2013, the 2012–2013 TFE was investigated three times using aerial photography; we also used the 1987 archival aerial photos and the EO-1 satellite image from March 6, 2013. As the result of the 2012–2013 TFE images processing, we obtained DTMs, maps, and quantitative morphometric data. The analysis of the obtained data as well as the initial aerial images of the two eruptions allowed us to reveal their similarities and differences.

GTFE (**Figure 8**) consisted of two stages: Northern Breakthrough (from July 6 to September 15, 1975) and Southern Breakthrough (from September 15, 1975 to December 10, 1976). At that, eruptive centres appeared subsequently both in space and time and in rather short surface fissures (200–600 m), migrating first in the area of the Northern Breakthrough from the southwest to the northeast and then locally in the area of the Southern Breakthrough.

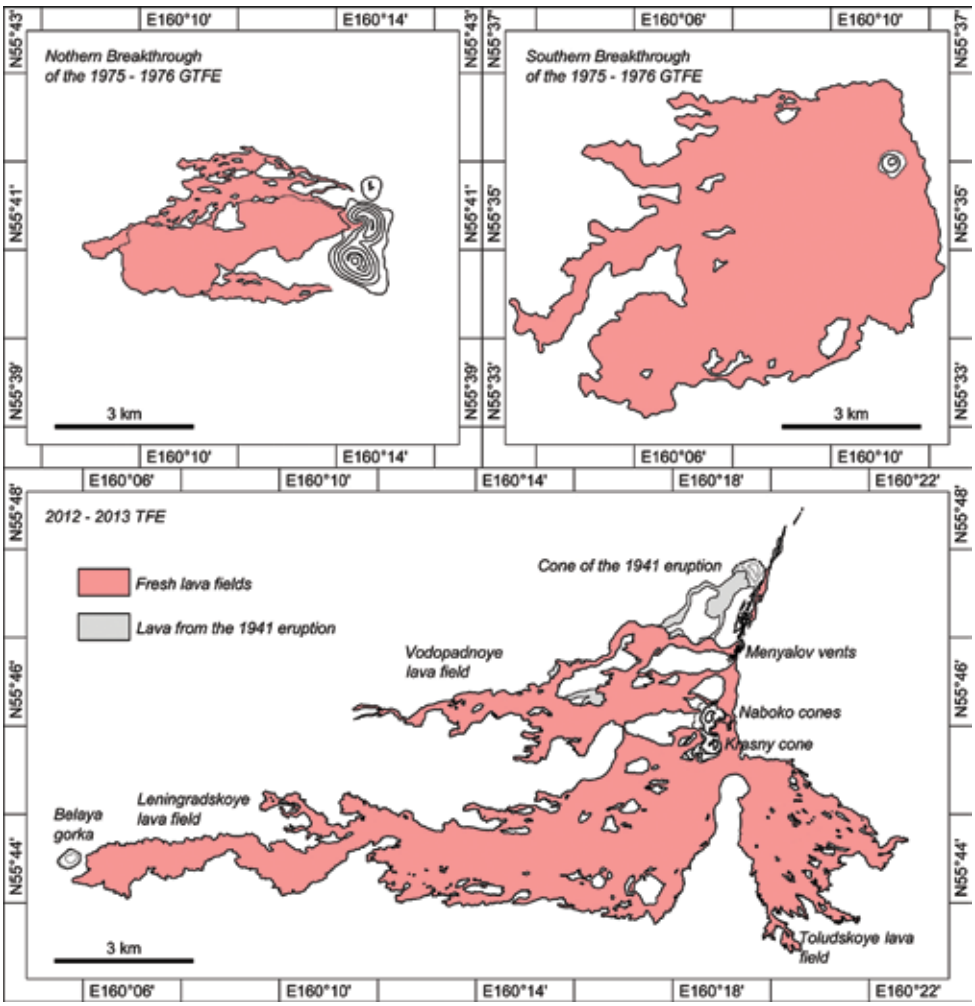

Figure 8. Maps of lava fields of the 1975–1976 Great Tolbachik Fissure Eruption and the 2012–2013 Tolbachik Fissure Eruption.

The eruption was preceded by a long build-up period and manifested in the activity of the summit pit crater of Plosky Tolbachik Volcano. During the period of 1967–1970 a lava lake, lava fountains, and the gas and steam emissions periodically appeared in it. After a 4-year period of repose from 1970 to 1974, the gas and steam emissions resumed and the ash and Pele's hair ejecta started 8 days prior to the eruption.

GTFE resulted in significant subsidence and collapses in the summit pit crater of Plosky Tolbachik volcano. In 1974, the volume of the well-shaped pit crater was estimated to be 0.02 km^3, and by the end of the eruption (1976), its volume increased to 0.35 km^3.

The eruption of Northern Breakthrough during GTFE was mainly explosive and resulted in the formation of cinder cones up to 300 m high. The volume of the cones and the adjacent area's pyroclastics was about 0.5 km^3. The volume of lava flows covering the 8.86 km^2 area reached 0.22 km^3. The eruption of Southern Breakthrough during GTFE was completely effusive and lasted 15 months. This resulted in the formation of lava flows 0.97 km^3 in volume that covered the 35.87 km^2 area and a small cinder cone that was 165 m high with a volume of 0.01 km^3 [8].

The 2012–2013 Tolbachik Fissure Eruption (**Figure 7**) started quite unexpectedly. Its fissure zone was over 5 km long and formed almost instantly. At first, a lot of explosive-effusive vents was erupting simultaneously within the whole fissure zone.

This eruption was mainly effusive. The rate of lava discharge to the surface during the first 2 days was 440 m^3/s, which was much greater than the rate of solid material discharge over the same period of time during the formation of the first GTFE's cinder cone in 1975.

However, by June 5, 2013, the area of the 2012–2013 TFE's lava fields, which was 35.23 km^2, nearly coincided with the area of GTFE's Southern Breakthrough, but the volume of lava was twice smaller and reached 0.52 km^3, which could be explained by the large slope angle of the underlying surface in the new eruption area. Furthermore, a lot of small cinder formations up to 15 m high and a group of Naboko cones up to 123 m high with a total volume of 0.02 km^3 were formed during the 2012–2013 TFE around the vents of the fissure zone [14].

The summit pit crater of Plosky Tolbachik Volcano was not involved during the 2012–2013 TFE. We only noted the very slight crumbling of the 1975–1976 pit crater's northwest walls. This crumbling was not associated with the eruptive activity and occurred under the influence of gravity.

4.3. Morphodynamics of Troitsky crater on Maly Semyachik volcano

Maly Semyachik volcano is a part of the Karymskaya group of volcanoes. It is located to the south of the central zone of the Eastern Kamchatkan volcanic belt. The coordinates of the active crater centre are 54°07′06″N and 159°39′20″ E. The volcano edifice is a 3-km-long ridge formed at the junction of three subsequently formed volcanic cones. Today, the active crater is Troitsky, which is located in the southwestern cone. One of the most acidic (pH varies from 0.5 to 0.75 [21]) volcanic lakes in the world Zelyonoe Lake is located in the crater.

Though Maly Semyachik was a common object of investigation, certain peculiarities were only revealed during systematic aerial photography, which has been conducted by the Institute of Volcanology since 1974.

For the first time, aerial photogrammetric surveys proved successful during the investigation of this volcano in 1986. The images from June 2, 1986, showed distinct concentric turbid spots on the surface of Zelyonoe Lake (**Figure 9**). The size of the spots varied from image to image within one aerial pass, which is evidence for the rapid movement of water masses in this part

of the lake [11]. This fact indicated an ongoing eruption, which was proven during the fieldwork in August–September 1986. Scientists detected increased water temperature as well as rapid gas emissions and other components of volcanic origin from the vent on the lake bed beneath the turbid spot [22].

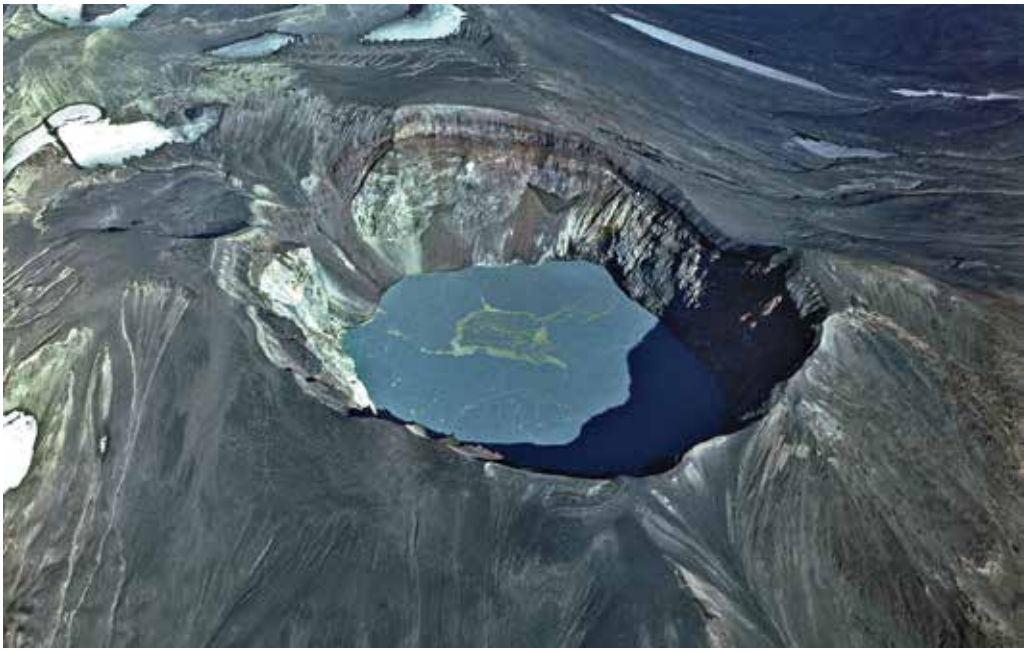

Figure 9. Zelyonoe Lake in Troitsky Crater of Maly Semyachik Volcano in 1986 from the southwest.

Further photogrammetric investigation of new and archival photos allowed for the detailed morphodynamic analysis of Troitsky Crater and Zelyonoe Lake during the 1946–2012 period, the estimation of the lake level and the crater shape, and these data relation to data from previous fieldwork.

Aerial photography revealed a considerable fall in water level over the 1946–1950 period. During that period of time, the morphology of the crater significantly changed: a negative landform appeared in the northeastern sector of the crater's lake shore. It was 200 m in diameter and had a gentle bottom profile. Its steep sides were as high as 50 m.

Though this negative landform was supposed to have an explosive nature [23], the 1950 images showed no traces of tsunami in the lake. Additionally, the appearance of this landform only caused a minor migration of fumarole gas emission near it and had no effect on the fumarole regime. Thus, this form most likely appeared due to gravity. The results from the photogrammetric measurements showed that the lake area increased by 8000 m^2 (for the 1138 m level). The crater reshaping and the fall in water level could have had a cause-and-effect relationship in the case of increased subsurface discharge within the newly formed lake bed, which is composed of permeable rocks that are unaltered by contact with thermal acid solution.

http://dx.doi.org/10.5772/63577

The analysis of the aerial photographs revealed constant landslides and crumbling on the inner walls of Troitsky Crater, the material that enters the lake, affecting its bed morphology and thus its surface level. The volumes of the above-water part of the crater for 1968 and 2012 toward one plane related to a higher level in 2012 were estimated to be 91,000,000 m^3 and 92,500,000 m^3, respectively. The difference in volumes is 1,500,000 m^3, which is the scree material deposited on the bottom of the crater during the last 44 years. Over the 1968–2012 period, the water level rose from 1139.1 to 1176.3 m, and thus increased by 37.2 m. The volume gain was estimated to be 9,000,000 m^3. Therefore, the bulk of scree material for 44 years accounts for 17% of the lake volume gain. With respect to the friability of the rocks that crumbled from the crater walls, the contribution of screes to the volume gain of water should be reduced to no less than 10%. Thus, when evaluating the dynamics of the lake depth, it is important to include the material that crumbled into the lake water over the entire period of investigation along with the feeding and discharge processes [16].

Based on the results of the photogrammetric processing of aerial photographs from various years, we plotted maps for 1950 and 2012 (**Figure 10**) and created crater profiles for 1950, 1968, and 2012 (**Figure 11**). Additionally, a graph of the lake water level for the period from 1946 to 2012 was plotted (**Figure 12**). The graph shows that the moderate increase of the water level —0.9 m per year—since 1950 has been accompanied by the rapid increase of the water level related to volcanic unrest. Over the 1968–1971 period, the water level rose by 13 m, and over the 1981–1986 period, it rose 8.7 m higher. According to the complex investigation [22, 24], the above periods were periods of high activity, which manifested in the maximum temperature of the lake water.

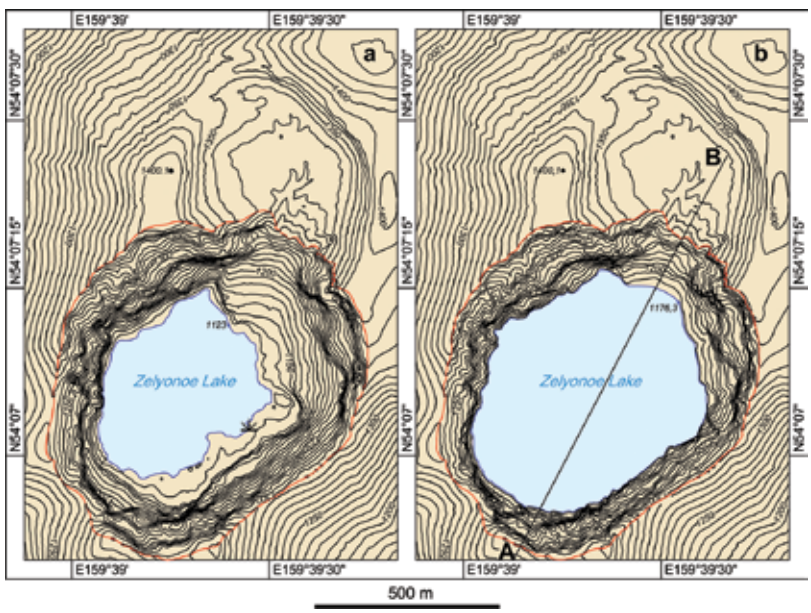

Figure 10. Maps of Troitsky Crater: a—1950, b—2012. The A–B line denotes the location of profiles shown in **Figure 11**.

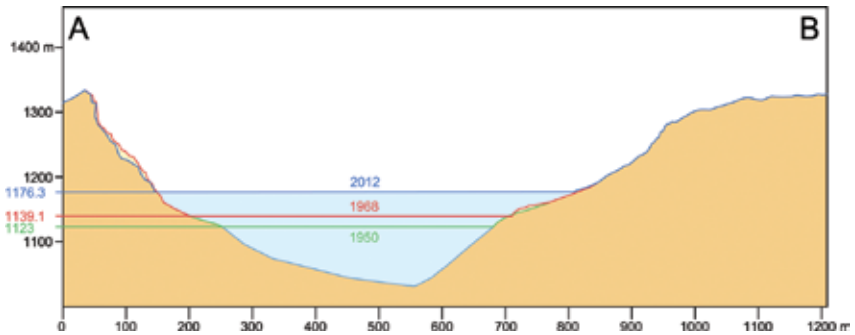

Figure 11. Profiles of Troitsky Crater in 1950, 1968, and 2012. The position of the A–B line is shown in **Figure 10b**.

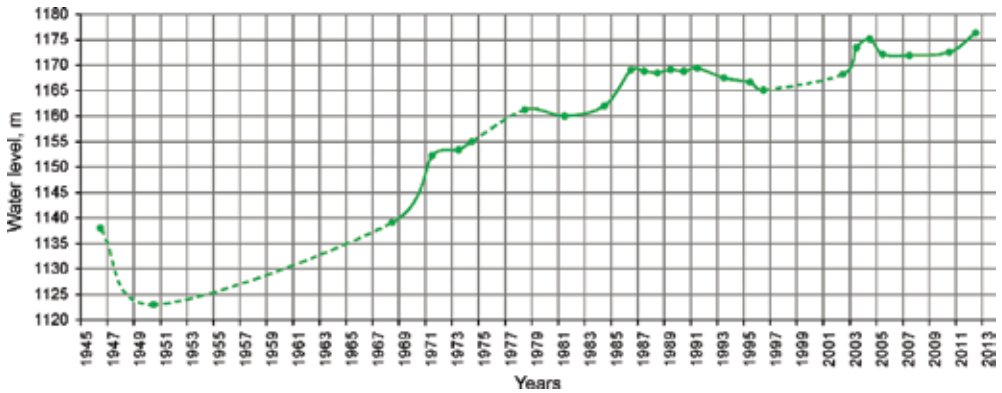

Figure 12. Graph of the Zelyonoe Lake water level over the period 1946–2012. The dotted line denotes the zones with at least 4-year-long pauses between monitoring.

4.4. Catastrophic eruption in Akademii Nauk Caldera

Akademii Nauk Caldera is located in the Karymsky Volcanic Centre 30 km from the eastern coast of Kamchatka. The coordinates of the caldera centre are 53°59′00″ N and 159°27′40″ E. The major part of the caldera contains Karymskoye Lake, which is one of the largest volcanic lakes in Kamchatka. The lake's middiameter is 3.7 km, and it is as deep as 70 m and occupies an area of 10.3 km^2. There are many thermal springs inside the lake and on its shore, including some geysers on its southeastern shore. The caldera had been supposed to be volcanically inactive until 1996.

On January 1, 1996, a swarm of shallow earthquakes with magnitudes up to 6.9 was detected within the Karymsky Volcanic Centre. That is the highest crust magnitude that has ever been detected in the history of seismological survey in Kamchatka [25]. The seismic event caused the simultaneous eruption of Karymsky Volcano and Akademii Nauk Caldera (**Figure 13**). The eruption in Akademii Nauk Caldera was short and lasted from 2 to 3 p.m. on January 2 to 11 a.m. on January 3 [26], yet it caused significant consequences:

http://dx.doi.org/10.5772/63577

1. A new crater called Tokarev appeared, resulting in the formation of the Novogodny Peninsula in the northern sector of Karymskoe Lake;
2. The lake shore and bed terrain was changed;
3. A tsunami washed out the once steep and overgrown shore;
4. The head of the Karymskaya River was blocked by erupted material, resulting in a lake dam, but on May 16, 1996, the dam was washed out and a flood rushed into Vulkanostantsiya Valley, deluging it for several hours.

Figure 13. The January 2, 1996, eruption in Akademii Nauk Caldera.

The events on January 1–3, 1996, caused ground cracks of submeridional trend and gaps within a 2×0.5 km area stretching from Tokarev Crater to a lava field near Lagerny Cone. Cracks and small maars were also formed on the surface of Novogodny Peninsula. The eruption caused new groups of thermal springs on the northern shore of Karymskoye Lake and on the rim of Tokarev Crater.

The changes caused by the events were studied using aerial photogrammetry. The Karymsky Volcanic Centre had been studied in detail before these events. There is a geodetic network with numerous ground control points within the volcanic centre that have been used since 1973 and have contributed greatly to the geodetic adjustment for photogrammetric models. The area of the events (the northern part of Karymskoye Lake) has been shot using aerial photography since 1978. In order to evaluate the impact of the events, we used images from the 1984 survey. The impact was investigated and mapped based on materials from several aerial surveys for certain years (1996, 2000, and 2003).

The aerial photographs and their photogrammetric processing contributed to detailed maps prior to and after the events of January 1–3, 1996 (**Figure 14**). The alterations were revealed in detail despite the lack of previous volcanological investigation in the northern part of Karymskoye Lake. Thus, the aerial photographs showed that there are both new and old ground cracks within the studied area.

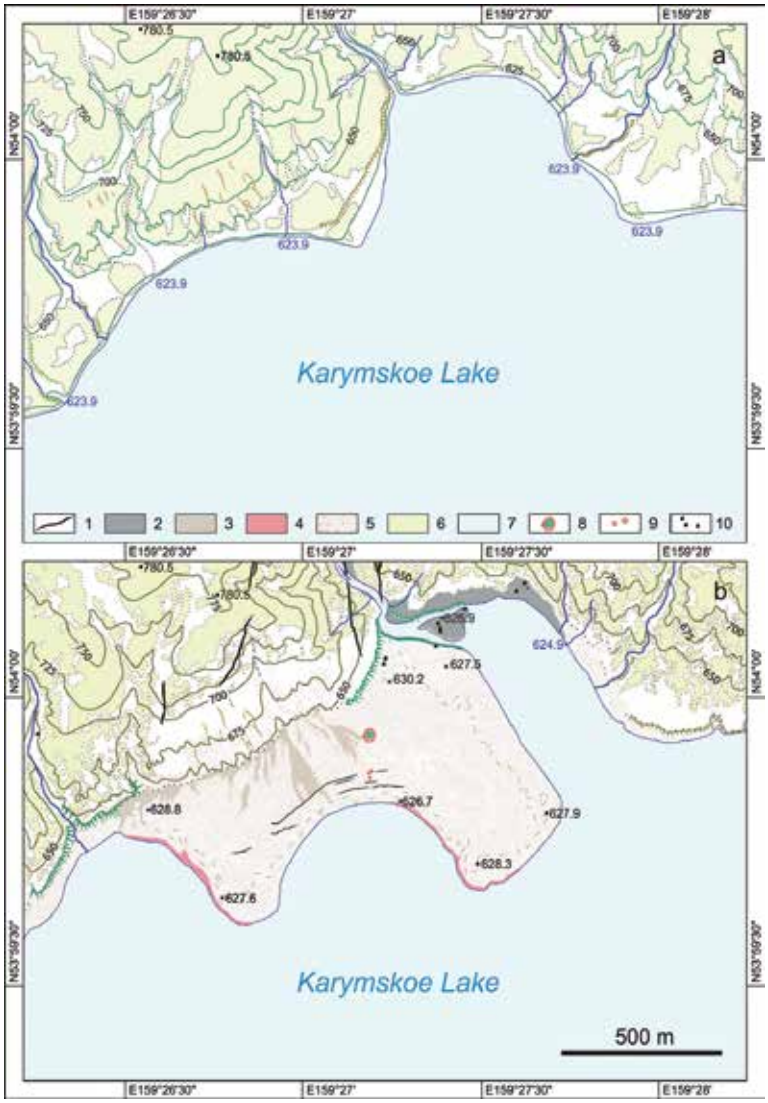

Figure 14. A map of northern sector of Akademii Nauk Caldera before (a) and after (b) the 1996 eruption: 1—Open-joint cracks caused by the 1996 event, 2—Deposits of the January–May 1996, mud flows, 3—Deposits of small mud flows in Novogodny Peninsula caused by the erosion of the shore cliff, 4—Heated zones, 5—Surface with destroyed vegetation or without it, 6—Forest cover, 7—Water surfaces, 8—Maar, 9—Explosion funnels and pit craters, 10—Large stones.

http://dx.doi.org/10.5772/63577

The stereo photogrammetric method helped to detect traces of tsunami waves on various sectors of the shore. The highest waves (50 m above water level) were detected in the northern sector of the lake, close to Novogodny Peninsula. The height of the waves on the outermost from Tokarev Crater southern sector of the lake was estimated to reach 10 m.

Mud deposits caused by the flood in Vulkanostantsiya Valley right after the dam washout covered the territory of 0.37 km^2 with an average thickness of 3 m.

Complex geodetic and photogrammetric investigation of Karymskoye Lake shore allowed for the creation of the first detailed topographic plans of thermal springs in Akademii Nauk Caldera. In addition to the coordinates of the springs, the tachymetry obtained the coordinates of the surface points where temperature was measured, which allowed for the precise definition of isotherms on those plans [27].

The investigation of the 1996 eruption in Akademii Nauk Caldera and of its impact showed that photogrammetry is an important, feasible, and universal method in volcanology and in the study of the local impacts of tsunamis and large seismic events. Materials from this work are not limited to the maps because the DTM plotted using these results may become the basis for the modelling of seismotectonic and tsunami-causing processes.

5. Conclusion

In the context of the investigation of active Kamchatkan volcanoes, we can trace over more than a century of evolution in the photogrammetric method from 1908 to the present. Until the middle of the last century, scientists had to expand their efforts to conduct ground-based photogrammetry. In 1946, aerial methods were introduced that provided more opportunities, yet photogrammetry was not used in full due to the lack of geodetic adjustment. Full-scale stereo photogrammetric investigations became available in the 1970s and 1980s with the introduction of advanced instruments and preparatory geodetic work at the studied objects. Later, digital technologies helped to facilitate image processing and reduced the time required to perform the operations. Additionally, the improvements in the software made it possible to obtain high-quality supporting materials (maps and 3-D models), which provided informative data on the studied volcanoes based on the results from photogrammetric processing.

It is necessary to notice that for the first time ever in volcanological research, the photogrammetric method was used in Kamchatka (1908–1910), and after that it was used in the 1940s for the study of the Paricutin Volcano eruption in Mexico [28]. Today, this method is used for the study of the morphology and morphodynamics of volcanoes all over the world, along with such remote sensing methods as interferometry and laser scanning.

The evolution of surveying instruments and computers makes the photogrammetric method ever more actual. Digital technology makes both surveying and photogrammetric processing much cheaper. New surveying instruments have been developed such as unmanned aerial vehicles and satellites equipped with high-resolution stereo cameras.

Algorithms for the photogrammetric processing of images have also been improved. One of the advanced developments is, we think, a pixel-to-pixel matching method that is capable of finding on stereo models a pair for each pixel of each image using a mathematical approach [29]. Computing capabilities of modern computers allow for detailed image analysis in order to reconstruct the shape of the studied object precisely (**Figure 15**).

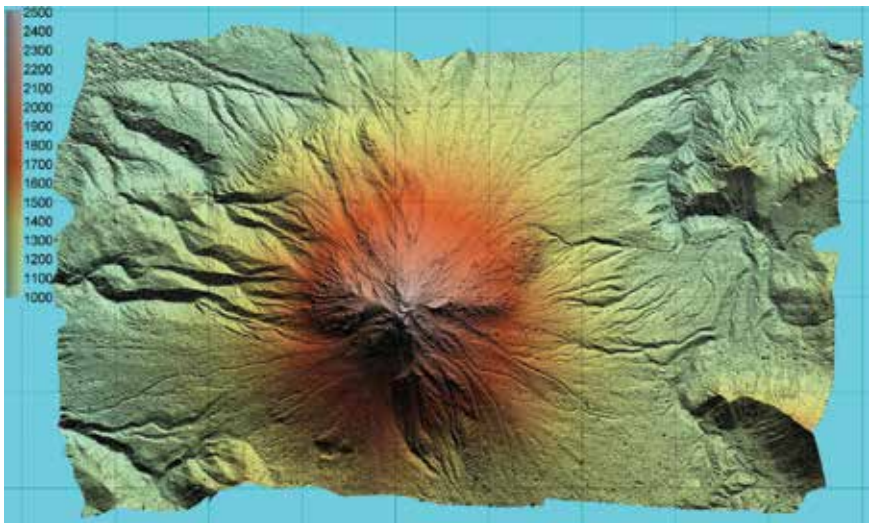

Figure 15. DTM of Kizimen Volcano made by independent programmer Andrey Matseevsky using the pixel-to-pixel matching method. Zones with weak correlation are smoothed.

We hope that the examples and information provided in this chapter will help to understand how to use the instrumental and scientific capabilities of images as well as how to advance photogrammetric investigation in volcanology.

Acknowledgements

The authors would like to express gratitude to Andrey Matseevsky for providing us with the DTM of Kizimen Volcano, and Dmitry Isaev and Ekaterina Minakova for assisting us with the translation.

Author details

Viktor Dvigalo*, Alina Shevchenko and Ilya Svirid

*Address all correspondence to: dvig@kscnet.ru

Institute of Volcanology and Seismology FEB RAS, Petropavlovsk-Kamchatsky, Russia

References

[1] Mikhail EM, Bethel JS, McGlone JC. Introduction to Modern Photogrammetry. New York: John Wiley & Sons Inc.; 2001. pp. 496.

[2] Dvigalo VN, Svirid IY, Shevchenko AV. The revival of the lost collection of photographic plates of the geological department of the F.P. Ryabushinsky's Expedition to Kamchatka, 1908–1910. Voprosy Geografii Kamchatki. 2008; 12: 87–98.

[3] Kell NG. Map of the Volcanoes of Kamchatka. Leningrad: Russian Geographical Society; 1928. 76 pp.

[4] Konrady SA, Kell NG. The geological department of the 1908–1910 expedition to Kamchatka. Izvestiya GRGO. 1925;57:3–32.

[5] Dobrokhotov YS. Aerial survey in volcanological expeditions of the USSR Academy of Sciences. Priroda. 1951;12:12–19.

[6] Gusev NA, Dobrynin NF. The theoretical grounds of the aerophotogrammetric method in volcanology. Vulkanologiya i Seismologiya. 1979;(5): 50–61.

[7] Fedotov SA, Dobrynin NF, Dvigalo VN. Analytical-photogrammetric system for quantitative evaluation of the volcanos activity. Geodeziya i Kartografiya. 1989;(1): 22–29.

[8] Fedotov SA, editor. Bol'shoe treshchinnoe Tolbachinskoe izverzhenie, 1975–1976 gg. [The 1975–1976 Great Fissure Tolbachik Eruption]. Kamchatka. Moscow: Nauka; 1984. pp. 640.

[9] Dvigalo VN. Growth of a dome in the crater of Shiveluch Volcano in 1980–1981 from photogrammetry data. Volcanol. Seismol. 1988;6:307–315.

[10] Melekestsev IV, Dvigalo VN, Kirsanova TP, Ponomareva VV, Pevzner MM. The 300 years of Kamchatka volcanoes: the Young Shiveluch. An analysis of the dynamics and impact of eruptive activity during the 17–20th centuries. Part II. 1965–2000. Vulkanologiya i seismologiya. 2004;(1):5–24.

[11] Dvigalo VN. Morphological precursors (first indications) of volcanic eruptions in Kamchatka. Volcanol. Seismol. 2000;22:351–369.

[12] Shevchenko AV, Dvigalo VN, Svirid IY. Airborne photogrammetry and geomorphological analysis of the 2001–2012 exogenous dome growth at Molodoy Shiveluch Volcano, Kamchatka. J. Volcanol. Geotherm. Res. 2015;304:94–107. DOI: 10.1016/j.jvolgeores.2015.08.013.

[13] Dvigalo VN, Melekestsev IV, Shevchenko AV, Svirid IY. The 2010–2012 eruption of Kizimen Volcano: the greatest output (from the data of remote sensing observations) for eruptions in Kamchatka in the early 21st century. Part I. The November 11, 2010 to

December 11, 2011 phase. J. Volcanol. Seismol. 2013;7:345–361. DOI: 10.1134/S074204631306002X.

[14] Dvigalo VN, Svirid IY, Shevchenko AV. The first quantitative estimates of parameters for the Tolbachik fissure eruption of 2012–2013 from Aerophotogrammetric observations. J. Volcanol. Seismol. 2014; 8: 261–268. DOI: 10.1134/S0742046314050029.

[15] Dvigalo VN, Melekestsev IV. The geological and geomorphic impact of catastrophic landslides in the Geyser valley of Kamchatka: Aerial photogrammetry. J. Volcanol. Seismol. 2009;3:314–325. DOI: 10.1134/S0742046309050029.

[16] Svirid IY, Shevchenko AV, Dvigalo VN. Investigation of Maly Semyachik Volcano (Kamchatka) activity using morphodynamic data from the Troitsky crater. Vestnik KRAUNTs. Nauki o Zemle. 2013;22:129–143.

[17] Shevchenko AV, Svirid IY. Hazard assessment for Molodoy Shiveluch Volcano from geomorphologic interpretation and photogrammetric processing of stereo photo- and satellite images. In: Proceedings of the VII Schukin conference on Geomorphological resources and geomorphological safety: from theory to practice; 18–21 May 2015; Moscow. Moscow: MSU; 2015. pp 206–209.

[18] Melekestsev IV, Volynets ON, Yermakov VA, Kirsanova TP, Masurenkov YP. Sheveluch Volcano. In: Fedotov SA, Masurenkov YP, editors. Active Volcanoes of Kamchatka. Vol. 1. Moscow: Nauka; 1991. pp. 82–103.

[19] Ramsey MS, Wessels RL, Anderson SW. Surface textures and dynamics of the 2005 lava dome at Shiveluch Volcano, Kamchatka. GSA Bull. 2012; 124: 678–689. DOI:10.1130/B30580.1.

[20] Dvigalo VN, Fedotov SA, Chirkov AM. Plosky Tolbachik. In: Fedotov SA, Masurenkov YP, editors. Active Volcanoes of Kamchatka. Vol. 1. Moscow: Nauka; 1991. pp. 198–211.

[21] Selyangin OB, Braitseva OA. Maly Semiachik Volcano. In: Fedotov SA, Masurenkov YP, editors. Active Volcanoes of Kamchatka. Vol. 2. Moscow: Nauka; 1991. pp. 160–179.

[22] Gavrilenko GM, Dvigalo VN, Fazlullin SM, Ivanov VV. The present-day state of Malyi Semyachik Volcano, Kamchatka. Volcanol. Seismol. 1993;15:129–135.

[23] Slezin YB, Kovalev GN, Grebzdy EI, Chegletsova EA. On activity of Maly Semiachic Volcano. Byulleten Vulkanologicheskih Stantsyi. 1971;47:37–39.

[24] Dvigalo VN, Andreev VI, Gavrilenko GM, Ovsyannikov AA, Razina AA, Chirkov AM. Activity of the southeast Kamchatka and north Kuriles volcanoes in 1985–1986. Volcanol. Seismol. 1990;10:347–359.

[25] Fedotov SA. Study and mechanism of the simultaneous 1996 Karymsky Volcano and Akademii Nauk Caldera eruptions in Kamchatka. Volcanol. Seismol. 1998;19:525–566.

[26] Fazlullin SM, Ushakov SV, Shuvalov RA, Aoki M, Nikolaeva AG, Lupikina EG. Underwater eruption in the Akademii Nauk Caldera, Kamchatka, and its consequences: Implications from hydrogeological, hydrochemical and hydrobiological studies. Volcanol. Seismol. 2001; 22:375–395.

[27] Karpov GA, Dvigalo VN. Thermal discharge in the caldera of Akademii Nauk: results of topographic and hydrologic surveys of thermal springs after the 1996 catastrophic submarine eruption. In: Proceedings of the Regional conference on Volcanism and associated processes; 30–31 March 2009; Petropavlovsk-Kamchatsky. Petropavlovsk-Kamchatsky: Institute of Volcanology and Seismology FEB RAS; 2009. pp. 101–114.

[28] Flores-Covarrubias L. Calculos para la determinacion de la altura del cono del volcan del Paricutin. [Calculations for determining the height of the Paricutin cone] In: Flores T, editor. El Paricutin. Estado de Michoacan. Mexico: Universidad Nacional Autonoma de Mexico. Instituto de Geologia; 1945. p. 19–20.

[29] Yaguchi Y, Iseki K, Oka R. Optimal pixel matching between images. In: Wada T, Huang F, Lin S, editors. Advances in Image and Video Technology. PSIVT 2009; 13–16 January 2009; Tokyo. Berlin: Springer-Verlag; 2009. pp. 597–610.

Chapter 4

Recent Developments and Trends in Volcano Gravimetry

Peter Vajda

Additional information is available at the end of the chapter

http://dx.doi.org/10.5772/63420

Abstract

The aim of this chapter is to take a look at some developments and new trends in volcano gravimetry. First, we will review the objectives of the research work within this subfield of geophysics, discuss the data and methods it uses, and outline the outputs it strives for. Then, we will turn our attention to three areas where innovative approaches possibly can forward this field of study. The first has to do with the coupling between vertical deformations of the topographic surface (elevation changes) and the observed gravity changes or, in other words, with the removal of the deformation-induced gravimetric signal from the observed gravity changes to obtain the net gravity changes caused by volcanic signals. The second and third areas regard the inversion of the observed gravity changes and deal with two recently or newly developed inversion approaches that both are characterized by the ability to produce a suite of diverse solutions that can be analyzed and discriminated based on additional independent constraints stemming from other earth science disciplines or from the cognition of the interpreter. With this in mind, the final goal is a better understanding of the mechanisms and processes of volcanic unrest or reawakening of a volcano and forecasting the threat of consequent activity and impacts.

Keywords: temporal gravity changes, deformation, surface displacements, inversion, interpretation, volcanic unrest

1. Introduction

Active and dormant volcanoes cover the face of the earth more plentifully than we usually percept. Their proximity is often richly inhabited by residents or visited by tourists, which gives rise to a tight link between the prosperity, wealth and health, and even the fate of those people and a volcano. As a natural consequence, the knowledge about the possible volcanic threat is of high demand. Our knowledge, however, of volcanic processes and behavior is far from

complete or ideal. There is a lot of room for earth science endeavors and research efforts to contribute to this knowledge. Here, we take a look at how much can a specific earth science discipline—gravimetry—contribute to this topic. Gravimetry is a discipline overlapping the fields of geophysics, geodesy, and geodynamics that deals with the geometry, properties, and changes of the earth gravity field by means of its observation, analysis, and interpretation.

When considering volcanic hazards, the knowledge of the following elements is essential: the geological past of a volcano, the geological structure of a volcano and its tectonic setting, and the subsurface processes taking place inside a restless or awakening volcano or deep underneath it within the crust and upper mantle. None of these three elements can be observed directly. The geological past of a volcano is inferred from its products left from the past eruptions and from the morphology of the volcano and its surroundings. The chemical and mechanical composition of the products testifies about the violence, size, and character (such as explosive versus effusive) of past eruptions. Geochemical, petrological, and morphological methods help recover such information. The geological structure of a volcano is not accessible to the naked eye either. Geophysical methods interpreting observations made on the surface, which are sensitive to the distribution of physical properties (parameters) of the volcano edifice, and the crust or uppermost mantle underneath, are applied to compile this knowledge. Seismic methods, gravimetry, magnetics, electrical soundings, induction, self- potential, and ground penetrating radar are examples of such exploration. Similar is the situation with acquiring knowledge on the subsurface volcanic processes linked with migration of magma and associated volatiles. From data monitored or observed on the surface, we aim at reconstructing the reality happening within the volcano. Subsurface physical and chemical (compositional) changes in the magma reservoirs (or changes in the volcano plumbing system in general), in hydrothermal systems, and within their surrounding rock environment, as well as underground mass movement, produce observable geophysical signals on the surface. In the sequel, we shall focus on two such observables: the temporal gravity changes and the vertical displacements (elevation changes) as the vertical component of the deformations of the earth surface.

2. Surface deformations and gravity changes

Processes associated with the physical and chemical changes in the magma storage system and intruding fresh magma both lead to changes in subsurface stress field producing strain that manifests itself on the surface in terms of surface deformations. The subsurface strain field and changes in the temperature field generate changes in the subsurface density distribution, which is sensed on the surface as microgravity changes. Moreover, the movement (migration) of masses such as magma within preexisting feeding or storage systems, as well as formation of new parts of the plumbing system in terms of dikes, sills, inclined or conical sheets, and rings [1], produces another component of changes in the subsurface density distribution. The same holds true for the movement of volcanic fluids (or volatiles in general) within the porous rock medium or along cracks and fractures or for any changes in hydrothermal systems as such. Any changes in the subsurface density distribution manifest themselves on the surface

as changes in the gravitational attraction vector. Typically, the vertical component is observed on the surface, referred to as temporal gravity changes. Naturally, both the stress field changes and the subsurface density distribution changes work in a concert, implying a simultaneous occurrence of both the surface displacements and the gravity changes. Therefore, it would be natural and advantageous to interpret surface deformations and gravity changes jointly. We must also mention that these two observables are coupled. This is due to the fact that any surface deformations lead to gravity changes caused by the vertical displacement of the topographic surface in the ambient gravity field regardless of the subsurface mass redistribution.

Volcanological experience has proven that the inflation (or deformation in general) of the volcano edifice is an essential precursor of volcanic eruptions [2–4]. Therefore, the monitoring of surface deformations plays an irreplaceable role in volcanic threat assessment. Surface deformations can be monitored using continuous or repeat survey terrestrial geodetic techniques as well as extraterrestrial techniques [3], such as differential interferometric synthetic aperture radar (DInSAR) or its permanent scatterer modification (PSInSAR). Gravity changes turned out to be also a valuable tool for predicting the reactivation of a volcano or for studying volcanic unrest [5, 6]. Cases have been reported when gravity changes were detected before seismic or other precursors at a reawakening volcano (e.g., [2, 7–9]). Gravity changes can be monitored continuously using tidal relative gravimeters or absolute gravimeters or in a repeat campaign (survey) mode at a network of gravity points (benchmarks, stations) covering a representative area over the volcano. While the repeat campaign (time-lapse) observations can better capture the spatial extent of the gravity changes, the continuous measurements at a station (or several stations) can pick up the fast changes to which the repeat survey mode is blind in the intracampaign period. The best, of course, appears to be the combination of the two modes [5]. Here, we shall focus on the time-lapse gravity changes and their interpretation. The continuous gravity changes and the benefits of their interpretation are well described in [5, 6].

Surface deformations are sensitive particularly to source pressure or volume changes [3, 4, 10]. Gravity changes help characterizing the source process by sensing mass changes along with volume changes, thus pointing at the source density changes [11–17]. Monitoring and interpreting temporal changes in 3D gravity data has been recently referred to as "4D (micro)gravity" or 4D gravimetry [5, 6]. A comprehensive overview of the purpose and benefits of the 4D gravity, both the discrete (time-lapse, repeat survey) and the continuous, illustrated on several cases at specific volcanoes, is given in [5]. A special case happens when gravity changes are observed without any significant surface deformations or vice versa [12, 15, 18]. By "significant" we mean within the accuracy threshold of the measuring technique. This strengthens the argument for concurrent monitoring of both the surface deformations and the gravity changes in volcanic areas.

Surface deformations and gravity changes can be interpreted either as stand-alone quantities or jointly. We have already indicated the pitfalls of monitoring and interpreting just one of them and the advantages of monitoring and interpreting them jointly. The (sole or joint) interpretation is based on either modeling or inversion. Modeling is based on assuming a

hypothesis about a source and its parameters, simplifying the structural rock environment, and solving the forward problem yielding the model surface deformations and model gravity changes. By iteratively changing the source parameters or the hypothesized model source, modeling is carried out until a reasonable fit ("match") is achieved between observed and modeled quantities (displacements and gravity changes). When a fit is reached, the model source with its parameters represents one of the possible solutions representing the volcanic process taking place at depth. Two approaches to modeling are at hand: analytical and numerical.

In analytical modeling, significant simplifications are applied to the source as such (its geometry) and to the structural environment: neglecting the topography and subsurface geologic structure (assuming the environment to be a homogenous isotropic elastic or viscoelastic half-space). Presuming simple geometries of the sources (such as magma chambers, dikes, and sills) leads to closed-form analytical expressions linking source parameters and the observable surficial quantities. Hence, analytical modeling can give quick results and first impressions about the nature and characteristics of the source process. On the contrary, the oversimplifications used in analytical modeling can lead to severe distortions of the obtained results with the risk of misleading the interpreter. A handy overview of analytical modeling approaches for pressurized source geometries given as spherical, ellipsoidal, cylindrical, sill-like, and dike-like are given in [6].

In numerical modeling, the simplifications of the analytical approach are remedied. The numerical approach takes into account the effect of topography, structural discontinuities and inhomogeneity, and even rheology. Such approach calls for applying finite element or boundary element methods (FEM, BEM). An instructive overview of the numerical modeling techniques in volcano geodesy is given again in [6].

Inversion works differently: a nonlinear inverse problem is solved by means of computing the source parameters directly from the observed surficial data. This gravimetric inverse problem is nonunique and ill-posed. The methods to solve it are the same as those in potential field inverse problems.

Some volcanic areas, especially calderas, display during their restlessness a special behavior —they produce systematic trends in their gravity/height ratios. By analogy, these ratios are typically referred to as gravity/height gradients. When the plots of gravity changes versus elevation changes show systematic trends clearly distinguished by two linear boundaries [free air gradients (FAGs) and Bouguer gradients], they are considered as signatures of the dominating typified subsurface processes [7, 8, 19–24]: magma rejuvenation or drainage, vesiculation or degassing, and water table rise or fall.

The mathematical source solutions (model solutions) obtained from either modeling or direct inversion must be associated with processes taking place in the volcano edifice or even deeper in the crust or lithospheric mantle and furthermore often with a volcanic threat or a prediction about an eruption. This is not a straightforward task. However, this topic is out-

side of the scope of our chapter here. We shall pay a particular attention only to inverting and interpreting temporal gravity changes.

There is an everlasting problem present with the monitoring and interpretation of geodetic (deformations) and gravimetric (gravity changes) data in volcanic areas: they are neither easy nor cheap to observe—their temporal as well as spatial resolution is never high enough to satisfy the inversion and interpretation demands. This will become particularly evident when we shall further below discuss the novel approaches to gravity inversion that require the input data given on an equidistant (regular) and dense enough grid. When the spatio-temporal gravity changes do not have a sufficient resolution and accuracy, it becomes hard, nay impossible, to discriminate among the possible sources of volcanic unrest and possibly draw reasonable conclusions about the threat of impending eruption.

3. Decomposition of superimposed gravity signals

Several natural (physical) phenomena produce a change in gravity observed at a point (benchmark) on the earth surface: changes in atmospheric attraction (due to mainly atmospheric pressure changes), tidal effects such as solid earth tides and ocean (loading) tides, hydrological effects such as groundwater table level changes, changes in snow or ice cover, soil moisture, volcanic effects associated with changes in magma storage (state of magma and magma transport), as well as magmatic volatiles/fluids. All of these signals (components)—gravitational effects of the individual contributions—are superimposed to form the gross observed gravity changes. When we aim at studying a particular geodynamic phenomenon, such as magma replenishment into an existing plumbing system of a volcano, a magma intrusion, or eventually magma vesiculation/degassing in a shallow chamber or vent, using gravimetry, we must be able to decompose the composite gravity signal. In other words, we need to remove (correct for) all unwanted signals. The net signal, stripped of any unwanted components, is typically referred to as "residual gravity changes".

First, we remove the contribution of the environment: gravity change components imposed by the atmosphere and tides. Then, we need to deal with the hydrological component due to pluvial water (precipitation). This turns out to be a cumbersome correction to handle in practice, the size of which often is at the level of the net signal chased after. Magma is associated with its volatiles and brines. Hydrothermal systems often reside above the magma storage systems. Physical changes (such as temperature and pressure) in both the magmatic and the hydrothermal systems have gravimetric signatures that may be difficult, nay impossible, to discern. Similar situation may arise with the gravimetric signatures associated with the transport (mobility) of magma and hydrothermal fluids.

This has become obvious in monitoring and interpreting unrest at calderas. Sometimes, researchers come to diverse conclusions interpreting the same data (gravity changes and surface deformations). Some interpretations favor a magma intrusion process (e.g., [2, 19, 25, 26]), whereas the opposing ones prefer a hydrothermal reasoning (e.g., [11, 14, 27–29]). Nat-

urally, these two source processes may act simultaneously complementing each other, being referred to as hybrid unrest (e.g., [15, 30, 31]).

For the purpose of inverting and interpreting the net signal, the residual gravity changes can be compiled using the following decomposition [32] (see also **Figure 1**):

$$\Delta g^{res} = \Delta g^{obs} - \Delta g^{ext} - \Delta g^{inst} - \Delta g^{w} - \Delta g^{def} - \Delta g^{surf}, \tag{1}$$

where the superscripts denote the following components of the gravity change: residual (res), observed (obs), external (ext), instrumental (inst), hydrological (w), deformation induced (def), and surficial (surf).

By external component, we mean environmental effects composed of tidal and atmospheric effects. Tidal effects comprise solid earth (body) tides and ocean loading effects. Atmospheric effects are gravity changes induced by pressure and temperature changes in the atmosphere (atmospheric attraction and loading effects). These effects are known and respective corrections have been published (e.g., [33–37]).

As instrument/survey effects, we consider the drift of gravimeters and adjustment of redundant measurements. We want to highlight one particular effect that must not be neglected in monitoring and interpreting time-lapse gravity change observations. Various gravimeters have various heights of the sensor, measured from the bottom of the instrument. In addition, various plates or tripods can be used, implying various heights of the bottom of the instrument above a benchmark (gravity station, gravity point). If various types of gravimeters or plates/tripods are used within an epoch survey or between epochs, observed gravity must be reduced to the elevation of the benchmark. Otherwise, significant systematic errors could be introduced to the residual gravity changes. To reduce the meter reading to the ground, actual vertical gradient of gravity (VGG) is needed. It may be either observed at each station, or estimated, as will be discussed further below (cf. also [38]).

Under hydrological effects, we mean the changes in the groundwater table level as well as in the soil/rock moisture (due to precipitation or drought). Strictly speaking to correct for this environmental signal, detailed 3D modeling needs to be performed, which is typically unachievable due to lack of required input data and/or knowledge about the near surface (or subsurface) geological structure (porosity, impermeable interfaces, etc.). Various approximations and estimates are used in practice; data on water table from wells are used wherever available. The simplest approximation is a planar Bouguer effect of a water table level change (e.g., Appendix in [14]). The hydrological correction is not the subject of our interest here, so we refer the reader to published works (e.g., [39–41]).

Deformation-induced topographic effects (DITEs) are of our high concern here. They are treated in Section 5.

http://dx.doi.org/10.5772/63420

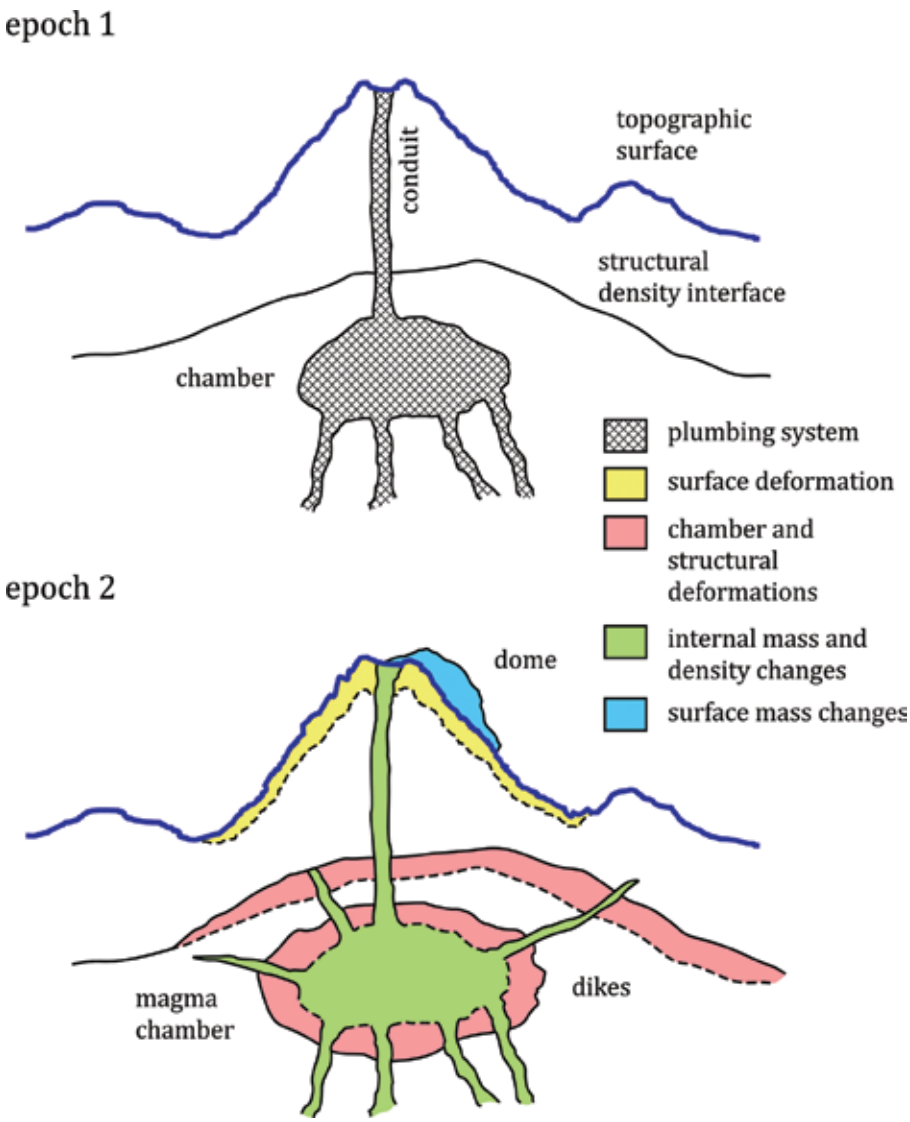

Figure 1. Schematic sketch of the sources contributing to the composite gravity changes.

Under the surface effects, we mean gravitational effects of mass changes taking place on the surface, but unrelated to surface deformation, such as magma extrusion, dome growth, dome collapse, lava flow, lahar, and flank collapse. These masses can be surveyed on the surface, their shapes and sizes can be digitized, and their gravitational effects can be computed by a numerical realization of the Newton volume integral for the vertical component of the attraction and subsequently subtracted (corrected for). This may be achieved with the help of photogrammetry, laser scanning, LIDAR, etc. These corrections are out of scope of our interest here. We refer the reader to published works (e.g., [16, 42]).

The residual gravity changes are consequently related to the subsurface volcanic processes associated with magma migration (rejuvenation or drainage of existing reservoirs and feeders, intrusions, and propagation along new paths, such as diking), hydrothermal fluid (volatile) migration, density changes due to physical and chemical (compositional) changes of the residing magma (cooling, heating, vesiculation, degassing, fractional crystallization, differentiation, mixing, partial melting, etc.), and density changes of the geological structure of the edifice due to stress-induced strain field (including the deformation of density interfaces) and due to temperature field changes via thermal expansivity. All of these changes represent the net sought signal, which in its nature is a fairly complex composite signal itself. This component of the gravity changes, the "residual gravity changes", is the subject of inversion or forward modeling and of subsequent interpretation of magma-related processes.

For decompositions analogical to our Eq. 1, see, e.g., Eq. 1 and **Figure 1** in [6], Eq. 1 and **Figure 1** in [16], and also [13, 19, 21, 43–47].

4. Recent developments and new trends

We want to take a look at some of the recent developments and contributions to the field of volcano gravimetry in the sequel. We will turn our attention to three topics:

1. Revisiting the DITEs on gravity changes dealing with the coupling between vertical displacements (elevation changes) and gravity changes, attempting to propose a more rigorous and accurate way of handling them (Section 5);
2. Taking a look at the benefits arising from applying a novel inversion methodology, as applied to time-lapse gravity changes, to which we shall briefly refer as the "Prutkin inversion methodology" (Section 6); and
3. Probing the possibilities of applying a novice inversion methodology, developed by Pohánka, based on n-harmonic (polyharmonic) functions, referred to as the "harmonic inversion method", to time-lapse gravity changes (Section 7).

For all the three above topics, we chose the Central Volcanic Complex (CVC) of Tenerife, Canary Islands, as our case study playground (**Figure 2**), on which we ran either synthetic simulations based on high-resolution digital elevation models and Mogi point sources or processed and inverted the gravity changes observed during the 2004 to 2005 volcanic unrest. The selected area has a suitable (significant and jaggy) topography for our simulations, as it comprises a caldera at the average elevation of roughly 2000 m asl, within which twin stratovolcanoes Teide and Pico Viejo are located reaching altitudes 3718 and 3135 m asl, respectively. Among other unrest indicators, spatiotemporal gravity changes were observed at the CVC at 14 benchmarks of a rapid reaction network between May 2004 and July 2005. No statistically significant areal surface deformation (either inflation or deflation) was observed accompanying these gravity changes. The observed gravity changes were corrected for tidal and hydrological effects. These point gravity data were taken as input data in both our inversion approaches (Sections 6 and 7). They were interpolated (extrapolated) onto a regular (equidistant) grid.

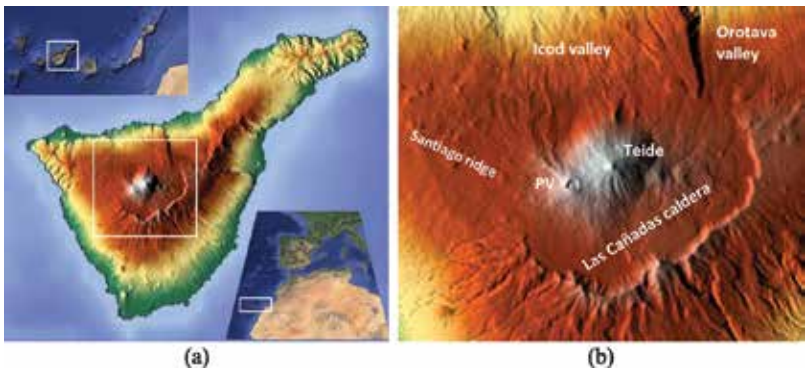

Figure 2. (**a**) Location of the Canary Islands and Tenerife and (**b**) the caldera and the twin stratovolcanoes Teide and Pico Viejo (PV).

5. Coupling between vertical deformations and gravity changes

Let us consider the gravitational effects imposed by the deformation of the topographic surface, i.e., by vertical displacements (elevation changes), illustrated (**Figure 3**), for instance, on inflation (uplift).

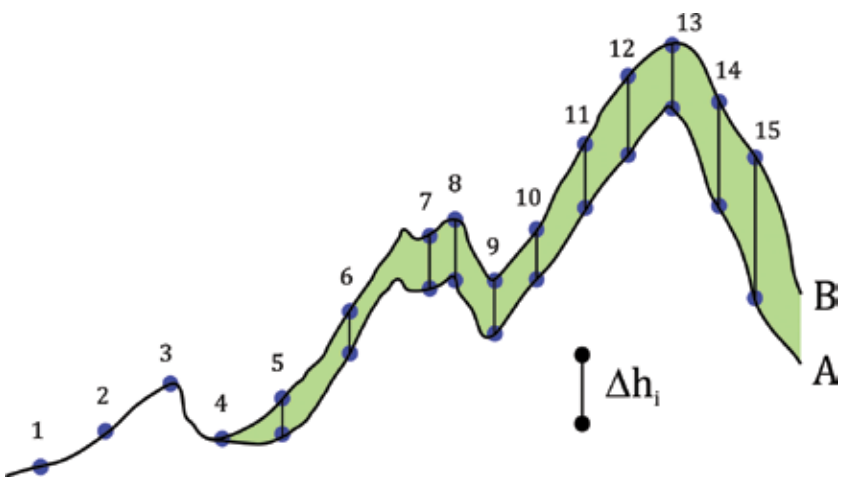

Figure 3. Schematic sketch of the DITEs on the gravity change. Benchmarks 5 to 15, unlike 1 to 4, experienced a significant uplift (Δ_{iii}). "A" denotes the predeformation topographic surface, whereas "B" denotes the postdeformation surface.

During the deformation (uplift), the gravity station (benchmark) is vertically displaced together with the topographic surface. We note that the subsurface density (geological) structure (including discontinuity interfaces) is deformed, too, but we treat this effect as part

of the residual gravity changes to be inverted and interpreted. The reason for this is that, unlike the topographic surface, which is known (described by a DEM), the geological structure is usually unknown or poorly known. We can hypothetically split the ground deformation effect into two subsequent stages (steps) with their respective effect components. In the first step, we move (lift up) the benchmark vertically from its original position (P) on the predeformation topographic surface to its new postdeformation position (P^*) in the ambient gravity field (in "free air") without deforming (inflating) the topographic surface (topographic masses) yet. In the second step, we move (deform, inflate) the topographic masses. Thus, we can write for these two separated components:

$$\Delta g^{\mathrm{def}}\left(P^*\right) = \Delta g^{\mathrm{FAE}}\left(P^*\right) + \Delta g^{\mathrm{TDE}}\left(P^*\right), \tag{2}$$

where Δg^{def} is the DITE; Δg^{FAE} is the gravity change due to the vertical displacement of the benchmark in ambient gravity field (in "free air"), in the sequel referred to as the "free air effect" (FAE); and Δg^{TDE} is the gravitational effect (vertical component of the attraction vector) of the topographic masses that were displaced into the volumetric domain between the predeformation and the postdeformation topographic surfaces (green domain in our schematic sketch of **Figure 3**). We have coined this effect the "topographic deformation effect" (TDE). Already from the sketch of **Figure 3**, we can intuitively deduce that, at benchmarks 1 to 4, which experienced no uplift (no significant elevation changes), the FAE will be zero, whereas the TDE will not be zero. The masses displaced into the topographic deformation rind (the green domain in our sketch) will impose gravitational effect not only on benchmarks 5 to 15, which have undergone nonzero elevation changes, but also on benchmarks 1 to 4, which experienced no uplift, zero elevation changes. This is an important insight. The size of the TDE at a specific benchmark will depend on its vertical position relative to, and horizontal distance from, the deformation shell (rind) and on the volume and shape of the deformation shell. Below, we shall examine the TDE by numerical simulations. As a consequence, the DITE might be nonzero even at benchmarks with zero elevation changes. This may hint on the possible insufficiency of expressions of the DITE that linearly depend on the vertical displacement, i.e., those being a product of some sort of a gradient (such as Bouguer or free air) and the vertical displacement. These issues associated with the DITE will be examined by numerical simulations further below.

5.1. FAE and its approximations

The FAE amounts to the vertical displacement of the benchmark ($\Delta h\,(P)$) times the true (in situ) VGG:

$$\Delta g^{\mathrm{FAE}}\left(P^*\right) = \left(\partial g/\partial h\right)^{o}\left(P\right) * \Delta h\left(P\right) \tag{3}$$

http://dx.doi.org/10.5772/63420

Inevitably, the VGG must be observed in situ at the benchmark (hence the superscript "o"). This can be practically achieved by relative gravimeters observing in a so-called tower mode, i.e., on the ground and at a certain height above the benchmark, such as 1 m, on a tripod (e.g., [38]).

If the VGG is not observed in situ, and its value remains unknown, it is usually (one could say habitually) approximated by the "theoretical FAG", also called the "normal FAG" (e.g., [43, 48]), which is the constant average vertical gradient of normal gravity at the surface of the normal reference ellipsoid. In the sequel, we shall abbreviate the normal FAG as NFAG (NFAG=-308.6 μGal/m). Observations indicate that the approximation of the true VGG by the NFAG can introduce a relative error of up to 88% in rugged terrain of alpine mountains, such as the High Tatras of Slovakia [38], or 77% at the CVC of Tenerife as shown below.

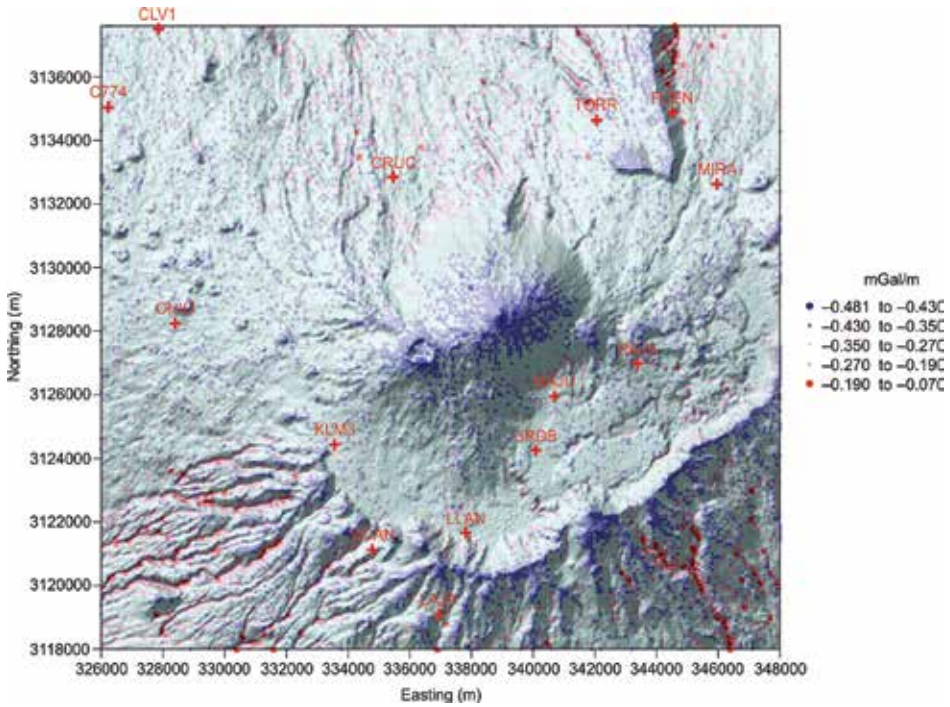

Figure 4. TNFAG values at the CVC of Tenerife. Minima (in absolute value) correspond with sharp concave topofeatures (valleys, gullies, drains), whereas maxima (in absolute sense) with sharp convex topofeatures (peaks, ridges, pillars, crests, and ribs). Max = −70, min = −481, mean = −315, SD = 34 (μGal/m).

Therefore, we propose a better approximation of the true VGG, in case it is not observed, than the NFAG [32]. In rugged terrain regions, the strongest (primary) contribution to the VGG comes from the terrain (topography and eventually also bathymetry for near shore points) from within the near vicinity of the benchmark. This contribution can be modeled (adopting a constant topodensity) using precise high-resolution digital terrain models (ibid). The NFAG can be refined (corrected for) using this topographic contribution to the VGG. In the sequel,

we shall abbreviate the "topocorrected NFAG" as "TNFAG". We show numerical values of the TNFAG for the CVC of Tenerife in **Figure 4**. The computational method and the used DEM are described in [32]. The topographic contribution (correction) amounts in the CVC area of Tenerife to 77% (in relative sense) of the NFAG itself, which is highly significant. This is the amount by which the true VGG may differ from the NFAG in a volcanic area of rugged topography.

The secondary contribution to the true VGG comes from the underground geological structure (density anomalies) of the earth. This contribution typically remains unmodeled, whereas the structure remains unknown. Alternatively, Rymer [21] and Berrino et al. [43] propose an approximation (of the VGG), a refinement to NFAG, based on the Bouguer anomaly map of the area. The contribution of geology to FAG in volcanic areas with significant (rugged) topography is expected to be smaller than that of topography, although, in flat areas (such as some calderas), the situation may be vice versa.

5.2. TDE and its approximations

The TDE is the gravitational effect (attraction) of the masses between the topographic surfaces before and after the deformation (within the topographic deformation shell) on the observed gravity change at each benchmark of the survey (see **Figure 3**). It must be computed by numerical evaluation of the Newton integral (for vertical component of the attraction vector) over this volumetric domain with assumed mean constant topographic density (ρ_0 representing the near surface rock environment).

The TDE is in volcanogravimetric applications commonly approximated by a Bouguer plate effect (e.g., [21, 43]), referred to as planar "Bouguer deformation effect" (BDE): $\Delta g^{TDE}(P^*) \approx \Delta g^{BDE}(P^*)$, where $\Delta g^{BDE}(P^*) = 2\pi G \rho_0 * \Delta h(P)$ G being the gravitational constant. Alternatively, the TDE is approximated by a spherical Bouguer term (e.g., [21, 49]), which is a combination of three dilation effects respective to a Mogi point source model [32]: $\Delta g^{TDE}(P^*) \approx (4/3)\pi G \rho_0 * \Delta h(P)$. For a detailed discussion about these approximations, as well as how the Bouguer gradients respective to these two Bouguer approximations relate to the gravity/height gradients, we refer the reader to [32]. In both (planar and spherical) Bouguer approximations of the TDE, the BDE depends linearly on the displacement of the benchmark. This fact alone is a clear indication that the BDE might not be a sufficient approximation of the TDE: for benchmarks with zero vertical displacement (such as benchmarks 1–4 in **Figure 3**), yet close enough to the deformed topographic masses to sense their attraction (at the order of 10 μGal), the BDE will be zero, whereas the TDE will not. This difference between the TDE and its BDE approximation (combined with the departure of the in situ VGG from the NFAG) explains the occurrence of observed data at many volcanoes that in terms of gravity/height plots often dramatically and erratically deviate from the linear trends of the FAG or Bouguer-corrected FAG (BCFAG).

To illustrate the size and spatial characteristics of the TDE—most of all that it significantly departs from its Bouguer approximation (BDE), we computed the TDE at the CVC of Tenerife for a synthetic deformation (surface displacement) field (shown in **Figure 4** of [32]) generated

by two (shallow and deep) Mogi sources and compared it to the planar BDE for the same displacement field by displaying the difference between the two in **Figure 5**. The shallow Mogi source was located at the depth of 500 m roughly below the Teide summit, scaled to have a displacement magnitude of 1 m, whereas the deep source was located at the depth of 6 km roughly 5 km to the northwest of the twin stratovolcanoes, scaled to have a displacement magnitude of 50 cm. For such significant surface deformations, the difference between the TDE and the BDE is also significant (see **Figure 5** and statistics given in the captions to the figure). In future simulations, we plan to compute the TDE also for smaller deformation fields to assess its deviation from the BDE approximation for smaller displacements.

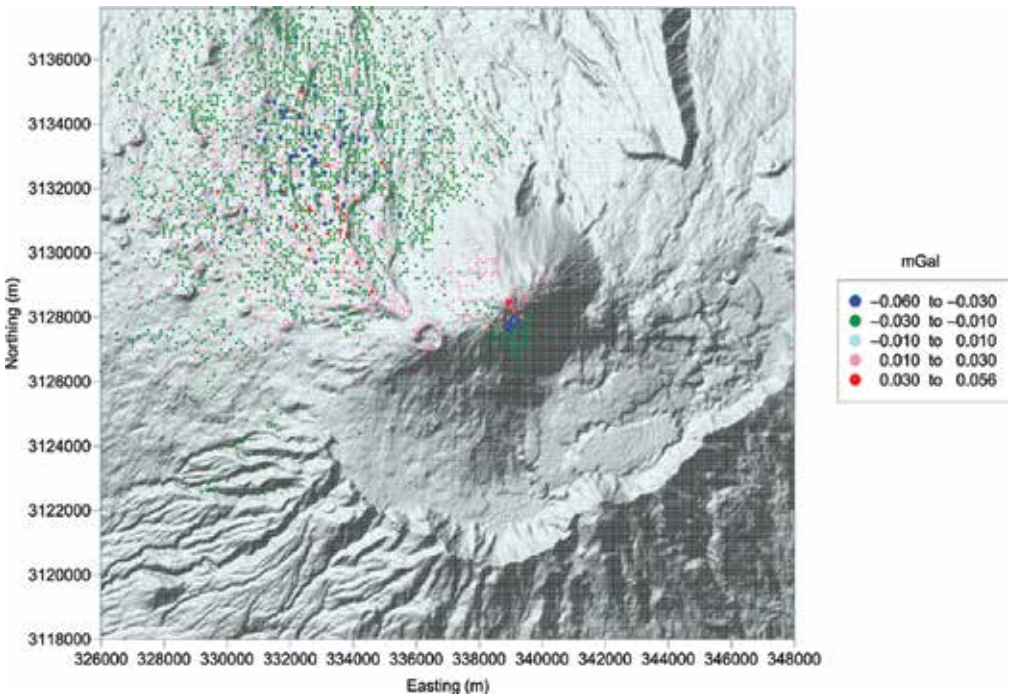

Figure 5. Difference between the TDE and its approximation by the planar BDE, both respective to a synthetic displacement field simulated at the CVC of Tenerife. Max = 56, min = −60, mean = −1, SD = 6 (μGal).

5.3. DITE and its approximations

The DITE on gravity change is the sum of the FAE and the TDE. Because we did not have observed values of the VGG available for our study area, we used the TNFAG values as an "allegedly sufficient" approximation of the VGG in the first (FAE) term of DITE. The second (TDE) term was computed numerically via the Newtonian integration. Next, we compared the DITE computed in this fashion (TN-DITE strictly speaking) to two of its commonly used approximations [32]: (a) the NFAG approximation of DITE ($\Delta g^{def}(P^*) \approx NFAG^*\Delta h(P)$) and (b) the BCFAG approximation of DITE ($\Delta g^{def}(P^*) \approx BCFAG(\rho_0)^*\Delta h(P)$). This comparison leads to

interesting findings: (1) the sharp short-wavelength spatial variability in the FAE term caused by the contribution of topographic masses to the VGG (the difference between NFAG and TNFAG) cancels out to some (if not great) extent with its counterpart in the TDE term (the difference between TDE and BDE) and (2) the NFAG approximation of DITE works better for narrow sharp displacement fields (generated by shallow point-like sources), whereas the BCFAG approximation of DITE works better for displacement fields of larger horizontal extents of several kilometers (generated by deeper sources). In other words, the situation with local (sharp/narrow) deformation is closer to "normal free air" situation, whereas the larger (more widespread) areal deformation is better approximated using the Bouguer plate effect in addition to the normal free air ("Bouguer situation").

6. Prutkin inversion methodology

The methodology under a brief working title "Prutkin inversion methodology" refers to a modular inversion methodology that consists of several modules or, in other words, several processing and inversion steps or algorithms. This modularity leads to producing several diverse inversion solutions that all equally well satisfy (mathematically) the input data (time-lapse gravity changes in the case of volcano gravimetry). The methodology was originally developed and applied to structural geophysical studies at global, regional, and even local scales [50–53]. We [31, 54] have applied it recently to temporal gravity changes and the results seem promising.

This methodology is used to be referred to as the "method of local corrections", which is not telling, as the name refers to the last algorithm of the methodology only. That is why we refer to it here loosely as the "Prutkin methodology". The methodology consists of the following blocks or algorithms: (a) trend removal (optional), where trend is defined as a 2D harmonic function and computed from the input data; (b) decomposition into shallow/deep (or more depth interval) field components (optional) using a triple harmonic continuation numerical procedure; (c) 3D line segments approximation of the sources, where the gravitational effect of these sources approximates the input gravity data; (d) field decomposition based on the individual or grouped line segment effects; and (e) solutions in terms of potato-shaped (closed compact star-convex) source bodies and/or contact surfaces (density discontinuity interfaces). All of these data processing and inversion steps are described mathematically in [31, 53]. When the methodology is applied to (time-lapse) gravity changes instead of gravity anomalies, the represent subsurface time-lapse (temporal) density changes instead of density anomalies. For instance, the potato-shaped bodies are volumetric domains of a homogenous density change.

A pilot study was carried out on gravity changes observed at Mayon Volcano, Philippines [54]. This study revealed that the methodology is applicable to time-lapse gravity changes observed during unrest or volcanic activity. The second study [31] was performed on gravity changes observed during the 2004/5 unrest on Tenerife [15]. This study manifested the true potential of the methodology. It produced a more revealing gravimetric picture of the unrest compared to the previous gravimetric interpretations. The decomposition of the observed gravity

changes into shallow and deep fields lead to the unveiling of the deeper source that was interpreted as magmatic [31]. This was possible only thanks to the unique feature of the methodology—the depth-wise decomposition of the signal based on the triple harmonic continuation. Previous interpretations were not capable of detecting this deeper source characterized as of magmatic origin. The sources pertinent to the shallow field were interpreted as hydrothermal fluids [31]. Consequently, the 2004/5 unrest on Tenerife was evaluated, based on the gravimetric interpretation, as hybrid (due to the presence of both magmatic and hydrothermal sources). Seismic constraints were adopted to assist and strengthen the gravimetric interpretation [31].

The great advantages of the Prutkin inversion methodology dwell in its modularity and versatility. Several combinations can be put together in processing the input data. Several combinations in decomposing the input signal can be introduced. This leans on whether trend removal is performed or not, whether the input signal is decomposed into shallow and deep fields (or even several depth components) or not, and what depth level is chosen for its decomposition. If the input data allow the approximation of sources by several line segments, additional decomposition of the input signal (field) is possible by separating the signal respective to the individual line segments or various groups of line segments. In addition, each field component can be inverted either in terms of a density contrast contact surface (interface) or in terms of 3D star convex compact homogenous ("potato-shaped") source body. Moreover, a priori density contrasts (differential densities), as well as a priori depths for the asymptotic planes of the interfaces, have to be selected, as they are free parameters. The choice of various density contrasts of various source bodies and/or interfaces creates additional variability in the sizes and shapes of the inversion solution sources. Consequently, the versatility and modularity of the methodology results in a possibly rich set of diverse inversion solutions. All of these solutions will equally well satisfy the input data (in terms of the forward problem). However, not all of them will be equally meaningful or reasonable in terms of geological, tectonic, geodynamic, or volcanological considerations. The great advantage of the presented methodology dwells in its ability to produce plentiful diverse solutions to the gravimetric inverse problem that can be at a later stage discriminated based on independent geophysical constraints (such as seismic) or cognition stemming from other earth science disciplines (such as geochemistry and petrology) or alternatively stemming from the experience of the interpreter. An illustration of such variability of gravimetrically acceptable diverse solutions can be found for the Kolarovo gravity anomaly in the Danube Basin presented in [53]. The same applies to gravimetric inversion of time-lapse gravity changes.

7. Harmonic inversion method

The harmonic inversion method was developed by Pohánka [55, 56]. It has been applied to gravity data in structural geophysical studies. We were curious about its applicability to temporal (time-lapse) gravity changes, so we stepped to testing it on the gravity changes observed during the 2004/5 unrest on Tenerife [57]. We used the same data set as in the Prutkin

inversion methodology (Section 6) to be able to compare inversion results of both methodologies.

The gravimetric inverse problem is nonunique. It has infinitely many solutions. Some special solutions can be sought, characterized by being smooth. This methodology searches for subsurface 3D solutions satisfying three conditions [55, 56]: (1) the solution is a n-harmonic function, where n is a small integer (n=3, n=4); (2) the solution has an extremum preservation property for a point source field, i.e., the main extremum of the solution coincides with the location of the point source generating the input gravitational field; and (3) the solution can be expressed as a linear integral transformation of the input gravity field. The tetraharmonic (n=4) solutions are called "characteristic density" or shortly "chi density". Such harmonic solutions are smooth and unrealistic, as they do not reflect subsurface geological settings. Therefore, in the subsequent step, these harmonic solutions are transformed to piece-wise homogenous density distributions by an automated iterative procedure, in which the harmonic solution (as a 3D subsurface function computed from the 2D surficial input data) serves as a mediator controlling the iterations in terms of the goodness of fit. The piece-wise homogenous solution consists of a set of homogenous closed-form source bodies of specific density contrasts with respect to an ambient constant density. Each source body can have its own density contrast.

The current version of the methodology works with a triharmonic function (n=3) called "quasi-gravitation", which serves the needs of the mediator in the iterative process resulting in the piece-wise constant subsurface density distribution, given as a set of homogenous source bodies. Density contrasts (differential densities) of these source bodies have to be selected a priori by the interpreter before running the iterative procedure. The iterative procedure, which modifies the shapes and sizes of the individual source bodies, runs until a satisfactory (preselected sufficient) fit is obtained between the quasi-gravitation of the found source bodies and the quasi-gravitation of the observed input gravity data. This fit guarantees also the fit between the surface gravity of the found source bodies and the observed input gravity. Regarding all the details about this inversion methodology based on n-harmonic functions, we refer the reader to [57]. When inverting gravity, the differential densities of the solution represent structural density anomalies. When inverting temporal (time-lapse) gravity changes, the differential densities represent time-lapse density changes.

The residual gravity changes of the 2004/5 Tenerife unrest (14 point data) were extrapolated onto a regular (equidistant) grid 60×60 km with a step of 200 m [57]. Quasi-gravitation (as a subsurface 3D function) was computed from the gravity changes in a domain 40×40 km to the depth of 12 km (2,424,060 cubic cells of the 200 m size). The computed quasi-gravitation had 11 local extrema (7 positive and 4 negative). These extrema served as seeds for growing the homogenous source bodies during the automated iterative process. For each extremum/body, the interpreter has to preselect the value of the differential density. The sizes and shapes of the obtained source bodies depend not only on the observed input data but partly also on the selection of the individual differential densities. Therefore, several different solutions, in terms of a set of source bodies (equal in number to the number of the extrema of the quasi-gravitation), can be obtained for various selections of the differential density of each body. In our pilot

http://dx.doi.org/10.5772/63420

study [57], in which we tested the applicability of the methodology to gravity changes, we focused on investigating the variability of the solutions depending on the choices of the individual differential densities. Several solutions originating from the harmonic inversion approach were presented for the gravity changes of the 2004/5 Tenerife unrest in [57]. We have learned the following lessons from the pilot study.

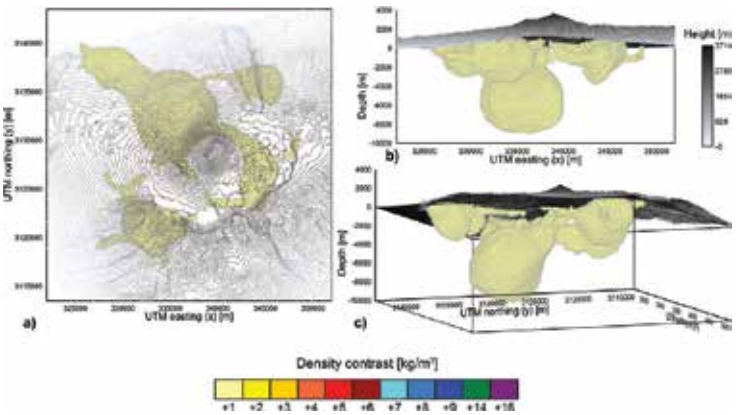

Figure 6. Harmonic inversion solution for the 2004/5 Teide unrest: source bodies with differential density 1 kg/m^3.

The smaller the differential density of a specific source body is, the larger is the source body and the more complex is its shape. The larger the differential density of a body is, the smaller and more spherical is the source body (tending towards a point mass). Interesting shapes and connections among the source bodies possibly indicating pathways of higher permeability were achieved for differential densities as low as 1 kg/m^3 (cf. **Figure 6**).

One of the admissible solutions obtained by the inversion approach based on harmonic functions is illustrated in **Figure 6**. For such small differential densities, the sizes of the source bodies might be unrealistically overgrown. We have yet to learn how to interpret (volcanologically) the source bodies found by the harmonic inversion approach. Some hints can be already grasped from our pilot study. One option is to view them as volumetric zones delineating the possible presence of magmatic sources of higher differential densities and lesser dimensions discretely distributed within the zones (such as dike/sill/sheet swarms or magma batches [1]) and/or zones of density changes due to migration of hydrothermal fluids through porous media. A follow-up work is needed to pursue this issue.

The case study based on the 2004/5 time-lapse gravity changes of the CVC on Tenerife indicates that the harmonic inversion methodology appears promising for inverting and interpreting gravity changes observed in volcanic areas during unrest or reactivation. In the follow-up work, we shall attempt to assign volcanological interpretation to the source bodies obtained by this inversion approach, such as the one presented in **Figure 6**. Additional case studies, in general, are needed to establish the link between the solutions obtained by the harmonic inversion method and their physical interpretation in terms of processes taking place inside the volcano edifice or deeper below.

8. Discussion and conclusions

The Achilles heel of the two presented inversion methodologies is that they need input data at an equidistant grid and, moreover, a fairly fine step to produce sources with reasonably detailed geometry. The data available in volcano gravimetry are typically sparse point data. Consequently, interpolation/extrapolation is inevitable. However, the extrapolation can easily introduce false signal features into the input, or artificially exaggerate the amplitude of highs and lows in the data, distorting the picture about the sources. There is no way around other than densifying the networks and acquiring more observations during the campaigns.

Both the inversion methods dealt with here require that the input data be given on the surface of a half-space (on a plane), which was not the case of the Tenerife gravity changes observed on and referred to the topographic surface. In our case studies reported here, this issue was neglected and the data were treated as if given on a plane at a level of roughly 2000 m asl. Strictly speaking, the data should have been harmonically continued from topography to a level surface, which in practice is numerically hardly achievable for sparse point data.

In potential field inverse problems, we often deal with composite signals, whereas the decomposition into multiple sources inherently remains an ambiguous task. Due to the nonuniqueness of the inverse gravimetric problem, also the solutions found by both the Prutkin inversion methodology and the harmonic inversion are again among many admissible solutions. Additional constraints from other earth science disciplines are required to validate physical (geological, volcanological) feasibility of any such solution. However, it is of great advantage when gravimetry alone provides several sets of admissible solutions that later on may be discriminated using available geologic or geoscientific constraints in the search for the most probable realistic scenario.

Acknowledgements

This work was supported by the Slovak Research and Development Agency (APVV) under Project No. APVV-0724-11 as well as by the VEGA grant agency under Project Nos. 2/0042/15 and 1/0141/15.

Author details

Peter Vajda

Address all correspondence to: Peter.Vajda@savba.sk

Earth Science Institute, Slovak Academy of Sciences, Bratislava, Slovakia

References

[1] Tibaldi A. Structure of volcano plumbing systems: A review of multi-parametric effects. J. Volcanol. Geotherm. Res. 2015;298:85–135.

[2] Dzurisin D. A comprehensive approach to monitoring volcano deformation. Rev. Geophys. 2003;49. DOI: 10.1029/2003RG000134

[3] Dzurisin D. Volcano Deformation: New Geodetic Monitoring Techniques. Springer, 2007. ISBN 978-3-540-49302-0

[4] Dvorak JJ, Dzurisin D. Volcano geodesy: The search for magma reservoirs and the formation of eruptive vents. Rev. Geophys. 1997;35:343–384.

[5] Williams-Jones G, Rymer H, Mauri G, Gottsmann J, Poland M, Carbone D. Towards continuous 4D microgravity monitoring of volcanoes. Geophysics. 2008;73:WA19–WA28. DOI: 10.1190/1.2981185

[6] Battaglia M, Gottsmann J, Carbone D, Fernández J. 4D volcano gravimetry. Geophysics. 2008;73:WA3–WA18. DOI: 10.1190/1.2977792

[7] Rymer H, Williams-Jones G. Volcanic eruption prediction: Magma chamber physics from gravity and deformation measurements. Geophys. Res. Lett. 2000;27:2389–2392.

[8] Gottsmann J, Rymer H. Deflation during caldera unrest: Constraints on subsurface processes and hazard prediction from gravity-height data. Bull. Volcanol. 2002;64:338–348.

[9] Sparks RSJ. Forecasting volcanic eruptions. Earth Planet. Sci. Lett. 2003;210:1–15.

[10] Mogi K. Relations between the eruptions of various volcanoes and the deformations of the ground surfaces around them. Bull. Earthquake Res Inst. 1958;36:99–134.

[11] Battaglia M, Troise C, Obrizzo F, Pingue F, De Natale G. Evidence for fluid migration as the source of deformation at Campi Flegrei caldera Italy. Geophys. Res. Lett. 2006;33:L01307. DOI: 10.1029/2005GL024904

[12] Carbone D, Budetta G, Greco F. Bulk processes some months before the start of the 2001 Mt. Etna eruption, highlighted through microgravity studies. J. Geophys. Res. 2003;108. DOI: 10.1029/2003JB002542

[13] Eggers AA. Residual gravity changes and eruption magnitudes. J. Volcanol. Geotherm. Res. 1987;33:201–216.

[14] Battaglia M, Segall P, Roberts C. The mechanics of unrest at Long Valley caldera, California: 2. Constraining the nature of the source using geodetic and micro-gravity data. J. Volcanol. Geotherm. Res. 2003;127:219–245.

[15] Gottsmann J, Wooller LK, Martí J, Fernández J, Camacho AG, Gonzalez PJ, Garcia A, Rymer H. New evidence for the reawakening of Teide volcano. Geophys. Res. Lett. 2006;33:L20311. DOI: 10.1029/2006GL027523

[16] Jousset P, Dwipa S, Beauducel F, Duquesnoy T, Diament M. Temporal gravity at Merapi during the 1993–1995 crisis: An insight into the dynamical behaviour of volcanoes. J. Volcanol. Geotherm. Res. 2000;100:289–320.

[17] Locke CA, Rymer H, Cassidy J. Magma transfer processes at persistently active volcanoes: Insights from gravity observations. J. Volcanol. Geotherm. Res. 2003;127:73–86.

[18] Rymer H, Murray JB, Brown GC, Ferrucci F, McGuire J. Mechanisms of magma eruption and emplacement at Mt. Etna between 1989 and 1992. Nature. 1993;361:439–441.

[19] Berrino G, Corrado G, Luongo G, Toro B. Ground deformation and gravity changes accompanying the 1982 Pozzuoli uplift. Bull. Volcanol. 1984;47:187–200.

[20] Berrino G. Gravity changes induced by height-mass variations at the Campi Flegrei caldera. J. Volcanol. Geotherm. Res. 1994;61:293–309.

[21] Rymer H. Microgravity change as a precursor to volcanic activity. J. Volcanol. Geotherm. Res. 1994;61:311–328.

[22] Gottsmann J, Berrino G, Rymer H, Williams-Jones G. Hazard assessment during caldera unrest at the Campi Flegrei, Italy: A contribution from gravity-height gradients. Earth Planet. Sci. Lett. 2003;211:295–309.

[23] Gottsmann J, Camacho A, Tiampo KF, Fernández J. Spatiotemporal variations in vertical gravity gradients at the Campi Flegrei caldera, Italy: A case for source multiplicity during unrest? Geophys. J. Int. 2006;167:1089–1096.

[24] Fernández J, Tiampo KF, Rundle JB, Jentzsch G. On the interpretation of vertical gravity gradients produced by magmatic intrusions. J. Geodyn. 2005;39:475–492. DOI: 10.1016/j.jog.2005.04.005

[25] Wicks CW, Thatcher W, Dzurisin D, Svarc J. Uplift, thermal unrest and magma intrusion at yellowstone caldera. Nature. 2006;440:72–75. DOI: 10.1038/nature04507

[26] Dvorak JJ, Berrino G. Recent ground movement and seismic activity in Campi Flegrei, southern Italy: Episodic growth of a resurgent dome. J. Geophys. Res. 1991;96:2309–2323.

[27] Bonafede M, Mazzanti M. Modelling gravity variations consistent with ground deformation in the Campi Flegrei caldera, Italy. J. Volcanol. Geotherm. Res. 1998;81:137–157.

[28] Gottsmann J, Folch A, Rymer H. Unrest at Campi Flegrei: A contribution to the magmatic versus hydrothermal debate from inverse and finite element modelling. J. Geophys. Res. 2006;111:7203. DOI: 10.1029/2005JB003745

[29] Gottsmann J, Carniel R, Coppo N, Wooller L, Hautmann S, Rymer H. Oscillations in hydrothermal systems as a source of periodic unrest at caldera volcanoes: Multiparameter insights from Nisyros, Greece. Geophys. Res. Lett. 2007;34:L07307. DOI: 10.1029/2007GL029594

[30] Jousset P, Mori H, Okada H. Elastic models for the magma intrusion associated with the 2000 eruption of Usu Volcano, Hokkaido, Japan. J. Volcanol. Geotherm. Res. 2003;125:81–106.

[31] Prutkin I, Vajda P, Gottsmann J. The gravimetric picture of magmatic and hydrothermal sources driving hybrid unrest on Tenerife in 2004/5. J. Volcanol. Geotherm. Res. 2014;282:9–18. DOI: 10.1016/j.jvolgeores.2014.06.003

[32] Vajda P, Zahorec P, Papčo J, Kubová A. Deformation induced topographic effects in inversion of temporal gravity changes: First look at free air and Bouguer terms. Contrib. Geophys. Geodes. 2015;45:149–171. DOI: 10.1515/congeo-2015-0018

[33] Wahr JM. Body tides on an elliptical, rotating, elastic and oceanless Earth. Geophys. J. R. Astron. Soc. 1981;64:677–703.

[34] Dehant V. Tidal parameters for an inelastic Earth. Phys. Earth Planet. Int. 1987;49:97–116.

[35] Merriam JB. Atmospheric pressure and gravity. Geophys. J. Int. 1992;109:488–500.

[36] Wenzel HG. The NanoGal Software: Earth tide data processing package ETERNA 3.30. Bull. Inf. Mare'es Terrestres. 1996:9425–9438.

[37] Boy JP, Gegout P, Hinderer J. Reduction of surface gravity data from global atmospheric pressure loading. Geophys. J. Int. 2002;149:534–545.

[38] Zahorec P, Papčo J, Mikolaj M, Pašteka R, Szalaiová V. Role of near topography and building effects in vertical gravity gradients approximation. First Break. 2014;32:65–71.

[39] Krause P, Naujoks M, Fink M, Kroner C. The impact of soil moisture changes on gravity residuals obtained with a superconducting gravimeter. J. Hydrol. 2009;373:151–163. DOI: 10.1016/j.jhydrol.2009.04.019

[40] Leirião S, He X, Christiansen L, Andersen OB, Bauer-Gottwein P. Calculation of the temporal gravity variation from spatially variable water storage change in soils and aquifers. J. Hydrol. 2009;365:302–309. DOI: 10.1016/j.jhydrol.2008.11.040

[41] Lampitelli C, Francis O. Hydrological effects on gravity and correlations between gravitational variations and level of the Alzette River at the station of Walferdange, Luxembourg. J. Geodyn. 2010;49:31–38. DOI: 10.1016/j.jog.2009.08.003

[42] Schiavone D, Capolongo D, Loddo M. Near-station topographic masses correction for high-accuracy gravimetric prospecting. Geophys. Prospect. 2009;57:739–752. DOI: 10.1111/j.1365-2478.2009.00799.x

[43] Berrino G, Rymer H, Brown GC, Corrado G. Gravity-height correlations for unrest at calderas. J. Volcanol. Geotherm. Res. 1992;53:11–26.

[44] Jousset P, Okada H. Post-eruptive volcanic dome evolution as revealed by deformation and microgravity observations at Usu Volcano (Hokkaido, Japan). J. Volcanol. Geotherm. Res. 1999;89:255–273.

[45] Currenti G, Del Negro C, Ganci G. Modeling of ground deformation and gravity fields using finite element method: An application to Etna Volcano. Geophys. J. Int. 2007;169:775–786.

[46] Trasatti E, Bonafede M. Gravity changes due to overpressure sources in 3D heterogeneous media: Application to Campi Flegrei caldera, Italy. Ann. Geophys. 2008;51:119–133.

[47] Battaglia M, Hill DP. Analytical modeling of gravity changes and crustal deformation at volcanoes: The Long Valley caldera, California, case study. Tectonophysics. 2009;471:45–57. DOI: 10.1016/j.tecto.2008.09.040

[48] Rymer H. Microgravity change as a precursor to volcanic activity. J. Volcanol. Geotherm. Res. 1994;61:311–328.

[49] Williams-Jones G, Rymer H. Detecting volcanic eruption precursors: A new method using gravity and deformation measurements. J. Volcanol. Geothermal Res. 2002;113:379–389.

[50] Prutkin I. Gravitational and magnetic models of the core-mantle boundary and their correlation. J. Geodyn. 2008;45:146–153.

[51] Prutkin I, Casten U. Efficient gravity data inversion for 3D topography of a contact surface with application to the Hellenic subduction zone. Comput. Geosci. 2009;35:225–233.

[52] Prutkin I, Saleh A. Gravity and magnetic data inversion for 3D topography of the Moho discontinuity in the northern Red Sea area, Egypt. J. Geodyn. 2009;47:237–245.

[53] Prutkin I, Vajda P, Tenzer R, Bielik M. 3D inversion of gravity data by separation of sources and the method of local corrections: Kolarovo gravity high case study. J. Appl. Geophys. 2011;75:472–478.

[54] Vajda P, Prutkin I, Tenzer R, Jentzsch G. Inversion of temporal gravity changes by the method of local corrections: A case study from Mayon Volcano, Philippines. J. Volcanol. Geotherm. Res. 2012;241–242:13–20. DOI: 10.1016/j.jvolgeores.2012.06.020

[55] Pohánka V. Application of the harmonic inversion method to the Kolárovo gravity anomaly. Contrib. Geophys. Geodes. 2001;31:603–620.

[56] Pohánka V. The harmonic inversion method: Calculation of the multi-domain density. Contrib. Geophys. Geodes. 2003;33:247–266.

[57] Pohánka V, Vajda P, Pánisová J. On inverting micro-gravimetric signals with the harmonic inversion method: Application to time-lapse gravity changes. Contrib. Geophys. Geodes. 2015;45:111–134. DOI: 10.1515/congeo-2015-0016

Chapter 5

Structural Analysis of Calderas by Semiautomatic Interpretation of the Gravity Gradient Tensor: A Case Study in Central Kyushu, Japan

Shigekazu Kusumoto

Additional information is available at the end of the chapter

http://dx.doi.org/10.5772/64557

Abstract

In order to understand the formation history and mechanism of volcanoes and their related structures, including calderas, their subsurface structures play an important role. In recent years, gravity gradiometry survey has been introduced, and new analyses techniques for gravity gradient tensors obtained by the survey have been developed. In this chapter, we first describe the gravity gradient tensor and its characteristics, and the method for obtaining the tensor from the gravity anomaly. Next, we review the semiautomatic interpretation methods for extracting information on subsurface structures, and apply some of the techniques to the volcanic zone of central Kyushu, Japan. The results showed that the horizontal and vertical gravity gradient methods, and the *CLP* method were useful for extracting outlines of important volcanic and tectonic structures in this region. Using the maximum eigenvector of the gravity gradient tensor, the caldera wall dip of the Aso caldera was successfully estimated to be in the range of 50–70°, and the dip of the Median Tectonic Line which was the largest tectonic line in the southwest Japan was consistent with seismic reflection surveys. In addition, a large circular structure surrounding the Shishimuta caldera with a diameter of 35 km was distinguished in some analyses.

Keywords: caldera, gravity gradient tensor, subsurface structure, semi-automatic interpretation method, edge emphasis, dip estimation, curvature of the potential field, Hohi Volcanic Zone, Shishimuta caldera, Aso caldera

1. Introduction

Subsurface structures reveal the current form of the static basement and crust and may also indicate the result of past crustal deformation. Consequently, subsurface structures are essentially fossil evidence of crustal movement, such as faulting, dyke emplacement, and/or volcanic activity, and the restoration of these subsurface structures provides important information on the tectonic and/or volcanic history of a region.

In volcanic areas, large eruptions produce widespread volcanic ejecta at the Earth's surface, such as ash and lava flows, as well as volcanic depressions in the Earth's crust. And, there are fossil magma chambers, that is, plutons. These are frequently recorded as gravity and magnetic anomalies, and especially collapse calderas formed by partial or total collapse of a magma chamber roof (e.g., [1–3]) have low gravity anomalies and it is a roughly concentric circular shape. Large eruption forming calderas occur with a very low frequency, however, since much smaller calderas such as the Miyake-jima caldera (e.g., [4]) form more frequently (e.g., [5]), understanding the mechanisms behind caldera formation is very important not only for advancing scientific knowledge but also for social purposes such as the construction of hazard maps.

Thus, studies on caldera formation have been conducted not only by geological surveys in the field but with analogue experiments, numerical simulations, and theoretical approaches (e.g., [6–21]). Although results obtained by these experiments have been compared with surface topography and ring-fault distributions, they have not been compared with subsurface structures or gravity anomalies reflecting subsurface structures. This is a result of the difficulty inherent in estimating caldera subsurface structures and in transforming analogue experiment results into gravity anomalies. Nevertheless, many researchers have recognized the importance of caldera subsurface structures and observed significant relationships between the dip of the caldera wall, the radius of the magma chamber, processes of caldera formation, and the type of caldera (e.g., [14, 19–21]).

Geoelectromagnetic and gravity surveys are popular geophysical techniques used in volcanic areas and have been employed frequently to estimate shallow to medium depth subsurface structures. In recent years, gravity gradiometry has been introduced. This measures the gravity gradient tensor generated by a source body, which consists of six components of three-dimensional (3D) gravity gradients. Gravity gradiometry survey has higher sensitivity than gravity surveys. Various analysis techniques for gravity gradient tensors have been developed and have given excellent results in subsurface structure estimation and edge detection, for example (e.g., [22–25]).

In this chapter, we first describe the gravity gradient tensor and its characteristics. Generally, the gravity gradient tensor is obtained by gravity gradiometry. However, surveys of this type have been made in only a few areas, so that tensor data are rarely available. Therefore, in Section 2.2, we present a method based on the work of Mickus and Hinojosa [26] that is used to obtain the tensor from the gravity anomaly. We then review the semiautomatic interpretation methods used to extract information on subsurface structures without additional geolog-

http://dx.doi.org/10.5772/64557

ical and geophysical information, and apply some of these techniques to the volcanic zone of central Kyushu in Japan.

2. Gravity gradient tensor

2.1. Characteristics of gravity gradient tensor

The gravity gradient tensor Γ is defined by the differential coefficients of the gravitational potential W (e.g., [27, 28]), as follows:

$$\Gamma = \begin{bmatrix} \frac{\partial^2 W}{\partial x^2} & \frac{\partial^2 W}{\partial x \partial y} & \frac{\partial^2 W}{\partial x \partial z} \\ \frac{\partial^2 W}{\partial y \partial x} & \frac{\partial^2 W}{\partial y^2} & \frac{\partial^2 W}{\partial y \partial z} \\ \frac{\partial^2 W}{\partial z \partial x} & \frac{\partial^2 W}{\partial z \partial y} & \frac{\partial^2 W}{\partial z^2} \end{bmatrix} \tag{1}$$

Defining g_x, g_y, and g_z, as the first derivative of W along the x, y, and z directions, we can rewrite Eq. (1) as follows:

$$\Gamma = \begin{bmatrix} \frac{\partial g_x}{\partial x} & \frac{\partial g_x}{\partial y} & \frac{\partial g_x}{\partial z} \\ \frac{\partial g_y}{\partial x} & \frac{\partial g_y}{\partial y} & \frac{\partial g_y}{\partial z} \\ \frac{\partial g_z}{\partial x} & \frac{\partial g_z}{\partial y} & \frac{\partial g_z}{\partial z} \end{bmatrix} = \begin{bmatrix} g_{xx} & g_{xy} & g_{xz} \\ g_{yx} & g_{yy} & g_{yz} \\ g_{zx} & g_{zy} & g_{zz} \end{bmatrix} \tag{2}$$

Here, g_z is the well-known gravity anomaly and g_{zz} is the vertical gradient of the gravity anomaly. The gravity gradient tensor is symmetric (e.g., [27]) and the sum of its diagonal components is zero since the gravitational potential satisfies Laplace's equation ($\Delta W = 0$).

Here, we set a point mass model under the surface (**Figure 1**). In this case, the gravitational potential W is:

$$W = -\frac{GM}{r} \tag{3}$$

where

$$r = \sqrt{(x - x')^2 + (y - y')^2 + (z - z')^2} \tag{4}$$

G is the gravitational constant and M is the mass. Taking the first derivative along the x-, y-, and z-directions gives

$$g_x = W_x = \frac{\partial W}{\partial x} = GM \frac{x - x'}{r^3} \tag{5}$$

$$g_y = W_y = \frac{\partial W}{\partial y} = GM \frac{y - y'}{r^3} \tag{6}$$

and

$$g_z = W_z = \frac{\partial W}{\partial z} = GM \frac{z - z'}{r^3} \tag{7}$$

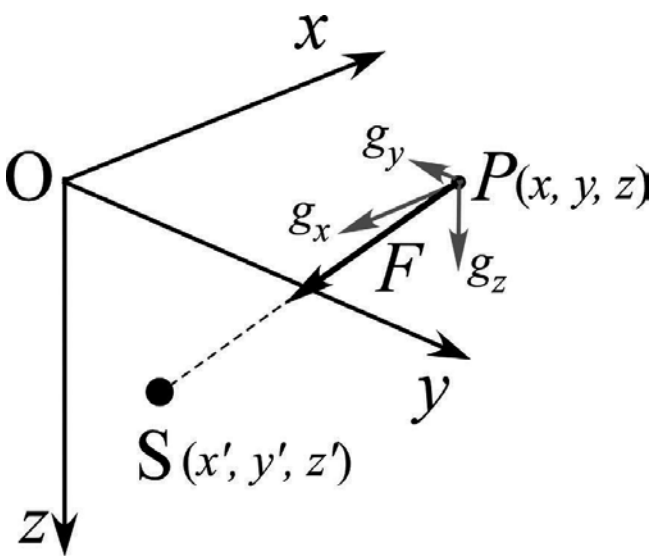

Figure 1. Point mass model. Schematic illustration of the gravitational vector due to a positive mass anomaly.

These are xyz components of the gravitation vector, F, due to the mass anomaly M.

Taking the second derivatives of the potential W along x, y, and z directions, six of the nine second derivatives are given by

http://dx.doi.org/10.5772/64557

$$g_{xx} = W_{xx} = \frac{\partial^2 W}{\partial x^2} = GM\frac{-3(x-x')^2 + r^2}{r^5} \tag{8}$$

$$g_{xy} = W_{xy} = \frac{\partial^2 W}{\partial x \partial y} = GM\frac{-3(x-x')(y-y')}{r^5} \tag{9}$$

$$g_{xz} = W_{xz} = \frac{\partial^2 W}{\partial x \partial z} = GM\frac{-3(x-x')(z-z')}{r^5} \tag{10}$$

$$g_{yy} = W_{yy} = \frac{\partial^2 W}{\partial y^2} = GM\frac{-3(y-y')^2 + r^2}{r^5} \tag{11}$$

$$g_{yz} = W_{yz} = \frac{\partial^2 W}{\partial y \partial z} = GM\frac{-3(y-y')(z-z')}{r^5} \tag{12}$$

and

$$g_{zz} = W_{zz} = \frac{\partial^2 W}{\partial z^2} = GM\frac{-3(z-z')^2 + r^2}{r^5} \tag{13}$$

These are six independent components of the gravity gradient tensor. The other three second derivatives can be obtained using the symmetry characteristics of the second derivative. And, since the sum of Eqs. (8), (11), and (13) is zero, namely

$$\begin{aligned} g_{xx} + g_{yy} + g_{zz} &= GM\left[\frac{-3(x-x')^2 + r^2}{r^5} + \frac{-3(y-y')^2 + r^2}{r^5} + \frac{-3(z-z')^2 + r^2}{r^5}\right] \\ &= GM\left\{\frac{-3\left[(x-x')^2 + (y-y')^2 + (z-z')^2\right] + 3r^2}{r^5}\right\} = 0 \end{aligned}$$

diagonal components satisfy Laplace's equation ($\Delta W = 0$).

We show a numerical example for the point mass model in **Figure 2**. In the numerical example, we set the point mass model with a depth of 4 km and a mass anomaly of -5.7×10^4 kg. Here, negative mass anomaly means lack of mass caused by negative density contrast such as hole in the crust, and the mass anomaly of -5.7×10^4 kg is equivalent to a sphere having radius of 3 km and density contrast of –500 kg/m^3. The vertical component, g_z, of the gravitational vector

is negative because of a negative mass anomaly (**Figure 2(i)**). The horizontal components of the gravitational vector, g_x (**Figure 2(a)**) and g_y (**Figure 2(e)**), are positive in the area where the terms $(x - x')$ or $(y - y')$ in Eqs. (5) and (6) are positive, and negative in the area where the terms are negative, because material surrounding the point mass is denser and gravitation vectors point to dense area, that is, the outside of the point mass.

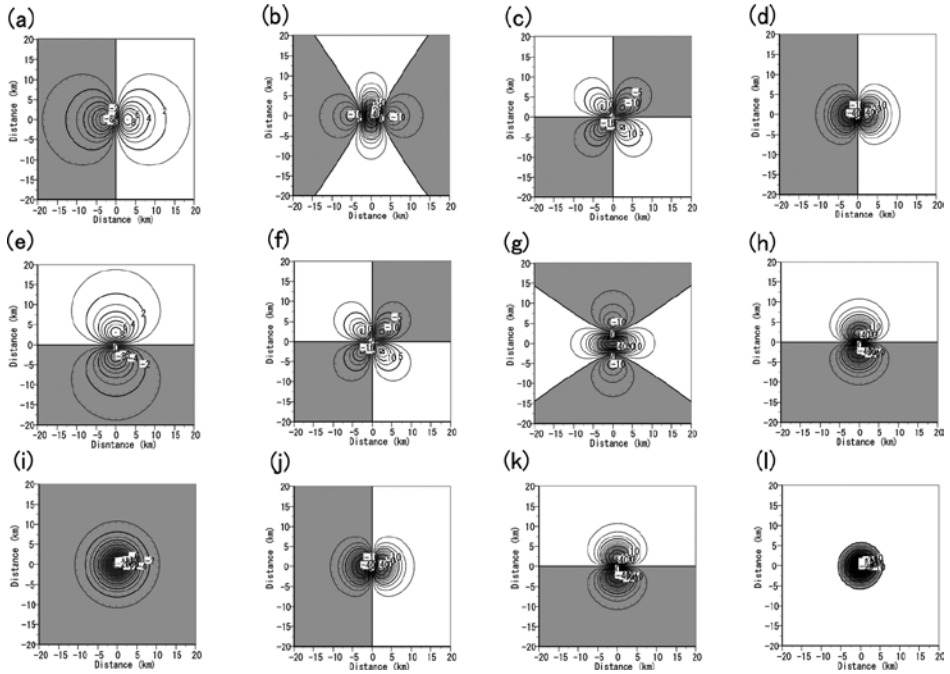

Figure 2. Components of the gravitational vector and gravity gradient tensor caused by a point mass with a depth of 4 km and a mass anomaly of -5.7×10^4 kg. Negative mass anomaly means lack of mass caused by negative density contrast such as hole in the crust. Negative areas are colored gray. The gravitational vector unit is given in mGal, and mGal = 10^{-5} m/s^2. The unit of the gravity gradient tensor is given in E (Eötvös), and 1 E = 0.1 mGal/km. (a) g_x component of gravitational vector, (b) g_{xx} component of gravity gradient tensor, (c) g_{xy} component, (d) g_{xz} component, (e) g_y component, (f) g_{yx} component, which is equal to g_{xy}, (g) g_{yy} component, (h) g_{yz} component, (i) $g_z$component; gravity anomaly, (j) g_{zx} component, which is equal to g_{xz}, (k) g_{zy} component, which is equal to g_{yz}, and (l) g_{zz} component.

In the gravity gradient tensor, Γ, we first find the triplet pattern, negative-positive-negative, in the g_{xx} component (**Figure 2(b)**). This pattern can be understood by examining the slopes of the anomalies of g_x as we proceed from left to right along the x-axis. We notice that the steepest slope is at the center of the map of g_x and it is positive; the zero slopes are at the trough and peak of g_x, and the gentle negative slopes are to the left and right of the trough and peak, respectively. In a similar manner, we can explain the triplet pattern of the g_{yy} component (**Figure 2(g)**). In the g_{xy} component (**Figure 2(c)**), we find the quadruplet pattern, negative-positive-negative-positive. This pattern can be understood by examining the slopes of the anomalies of g_y as we proceed from left to right along the x-axis, or by examining the slopes

http://dx.doi.org/10.5772/64557

of the anomalies of g_x as we proceed from left to right along the y-axis. The components g_{xz} (**Figure 2(d)**), g_{yz} (**Figure 2(h)**), and g_{zz} (**Figure 2(l)**) are differential coefficients of g_x, g_y, and g_z in the z direction and emphasize the high frequencies of each gravitational component without any changes in the location or shape of the anomalies.

2.2. Derivation of gravity gradient tensor from gravity anomaly

In general, the gravity gradient tensor is measured with gravity gradiometry (e.g., [29–31]). However, we can obtain the tensor from gravity anomaly data using calculations shown in [26], even if the gravity gradiometry surveys have not yet been undertaken.

As a technique for calculating the gravity gradient tensor from the gravity anomaly data, Mickus and Hinojosa [26] used the following procedure: (1) application of a Fourier transformation to the gravity anomaly, (2) estimation of the gravitational potential by integration of the gravity anomaly in the Fourier domain, (3) calculation of the gravity gradient components from second-order derivatives of the potential in each direction, and (4) application of a Fourier inverse transformation to finally obtain all components of the tensor in the spatial domain.

When the Fourier transformation of a function $f(x, y)$ is denoted by the shorthand notation $\mathcal{F}[f]$, that is,

$$\mathcal{F}[f] = F(k_x, k_y) = \int_{-\infty}^{\infty}\int_{-\infty}^{\infty} f(x, y) e^{-i(k_x x + k_y y)} dx dy \,, \tag{14}$$

The Fourier inverse transformation of the function $F(k_x, k_y)$ in the Fourier domain is denoted by the shorthand notation $\mathcal{F}^{-1}[F]$ (e.g., [32]), that is,

$$\mathcal{F}^{-1}[F] = f(x, y) = \frac{1}{4\pi^2}\int_{-\infty}^{\infty}\int_{-\infty}^{\infty} F(k_x, k_y) e^{i(k_x x + k_y y)} dk_x dk_y \,, \tag{15}$$

where k_x and k_y are wave numbers and are inversely related to wavelengths λ_x and λ_y in the x and y directions, respectively: $k_x = 2\pi/\lambda_x$ and $k_y = 2\pi/\lambda_y$. If G_z is the Fourier transform of the gravity anomaly g_z, the relationships between g_z and G_z are as follows:

$$G_z = \mathcal{F}[g_z] \tag{16}$$

$$g_z = \mathcal{F}^{-1}[G_z] \tag{17}$$

and we use the notation $g_z \leftrightarrow G_z$ for this relationship. Differentiation of a function in the space domain is equivalent to multiplication by a power of the wavenumber in the Fourier domain (e.g., [32]). If $f(x, y) \leftrightarrow F(k_x, k_y)$, then,

$$\frac{\partial^m}{\partial x^m}\frac{\partial^n}{\partial y^n} f(x,y) \leftrightarrow (ik_x)^m (ik_y)^n F(k_x, k_y) \tag{18}$$

Integration of the function in the Fourier domain is given by division of the wavenumber. From these and relationships between gravity and gravitational potential, we derive the following equations on gravitational vector components:

$$G_x = ik_x U \tag{19}$$

$$G_y = ik_y U \tag{20}$$

$$G_z = |\mathbf{k}| U \tag{21}$$

where U is the Fourier transform of the gravitational potential, W, and $|\mathbf{k}| = (k_x^2 + k_y^2)^{1/2}$. From Eq. (21), we can obtain the gravitational potential U from the gravity anomaly by

$$U = \frac{G_z}{|\mathbf{k}|} \tag{22}$$

and Eqs. (19) and (20) are rewritten as follows:

$$G_x = \frac{ik_x}{|\mathbf{k}|} G_z \tag{23}$$

$$G_y = \frac{ik_y}{|\mathbf{k}|} G_z \tag{24}$$

Therefore, we can obtain g_x and g_y from g_z by the Fourier inverse transformation of G_x and G_y.

In a similar manner, we derive equations to obtain each component of the gravity gradient tensor:

$$G_{xx} = -k_x^2 U = \frac{-k_x^2}{|\mathbf{k}|} G_z \tag{25}$$

http://dx.doi.org/10.5772/64557

$$G_{yy} = -k_y^2 U = \frac{-k_y^2}{|\mathbf{k}|} G_z \tag{26}$$

$$G_{zz} = |\mathbf{k}| G_z \tag{27}$$

$$G_{xy} = ik_x ik_y U = \frac{-k_x k_y}{|\mathbf{k}|} G_z \tag{28}$$

$$G_{zx} = ik_x G_z \tag{29}$$

and

$$G_{zy} = ik_y G_z \tag{30}$$

From these equations, as summarized in [26], we can obtain all components of the gravity gradient tensor from the gravity anomaly as follows:

$$\begin{bmatrix} g_{xx} & g_{xy} & g_{xz} \\ g_{yx} & g_{yy} & g_{yz} \\ g_{zx} & g_{zy} & g_{zz} \end{bmatrix} = \mathcal{F}^{-1}\left\{ \begin{bmatrix} \frac{-k_x^2}{|\mathbf{k}|} & \frac{-k_x k_y}{|\mathbf{k}|} & ik_x \\ \frac{-k_x k_y}{|\mathbf{k}|} & \frac{-k_y^2}{|\mathbf{k}|} & ik_y \\ ik_x & ik_y & |\mathbf{k}| \end{bmatrix} G_z(\mathbf{k}) \right\}. \tag{31}$$

3. Semiautomatic interpretation techniques

3.1. Edge emphasis

Edge emphasis techniques are extraction techniques used to find locations (namely, edge) where the gravity anomaly changes abruptly due to density variations, and these techniques play an important role in interpretation of potential field data (e.g., [33–35]).

In these techniques, the horizontal and vertical gravity gradient methods have frequently been employed to find structural boundaries such as faults or contacts between different materials (e.g., [36–39]). The vertical gravity gradient (*VG*) is the g_{zz} component of the gravity gradient tensor, and the horizontal gravity gradient (*HG*) is given using the components of the gravity gradient tensor shown in Eq. (2) as follows:

$$HG = \sqrt{g_{zx}^2 + g_{zy}^2} \tag{32}$$

In addition to these gravity gradients, the second vertical derivative, $\partial^2 g_z/\partial z^2$, is well known and is a classical edge emphasis technique for edge detection (e.g., [40–43]).

Miller and Singh [44] proposed the *TDR* (tilt derivative), defined by the arctangent of the ratio of the vertical gravity gradient to the *HG*:

$$TDR = \arctan\left(\frac{g_{zz}}{\sqrt{g_{zx}^2 + g_{zy}^2}}\right) \tag{33}$$

This emphasis technique does not extract extremely large amplitude signals in the short wavelength range and is known as a balanced method. However, it is noted that the *TDR* extracts a phantom boundary at the zero line if positive and negative anomalies exist side by side (e.g., [45, 46]).

Wijns et al. [47] proposed the *THETA* map that could be used to obtain the structural boundaries,

$$THETA = \arccos\left(\frac{\sqrt{g_{zx}^2 + g_{zy}^2}}{\sqrt{g_{zx}^2 + g_{zy}^2 + g_{zz}^2}}\right) \tag{34}$$

and Cooper and Cowan [44] proposed the *TDX* defined by the following equation:

$$TDX = \arctan\left(\frac{\sqrt{g_{zx}^2 + g_{zy}^2}}{|g_{zz}|}\right) \tag{35}$$

Li et al. [48] conducted a numerical test of these emphasis techniques for structural boundary extraction. As a result, they found that (1) the *HG* method can determine structural boundaries of the causative body but its ability decreases with depth, (2) the *TDR* and *THETA* methods

http://dx.doi.org/10.5772/64557

are also able to retrieve the structural boundaries but their extracted shapes are not clear and, as mentioned above, these methods introduce a phantom boundary at the zero line in case of side by side positive and negative anomalies, and (3) the *TDX* has the same phantom boundary limitation but the method can give clearer boundary location than both *TDR* and *THETA*.

Based on these discussions, Li et al. [48] suggested the *CLP* method, which extracts the outlines of subsurface structures without the phantom boundary. The *CLP* is defined as follows:

$$CLP = \arctan\left[\frac{\sqrt{\left(\frac{\partial g_z}{\partial x}\right)^2 + \left(\frac{\partial g_z}{\partial y}\right)^2}}{p + k \times \left|\frac{\partial g_z}{\partial z}\right|}\right] \tag{36}$$

where p is a previously determined constant, typically 1/10 of the maximum value of the horizontal gravity gradient. And k is defined as follows:

$$k = \frac{mean\left|\frac{\partial g_z}{\partial z}\right|}{mean\left|\frac{\partial^2 g_z}{\partial z^2}\right|} \tag{37}$$

In recent years, specialized edge emphasis techniques have been developed to find the edges of potential field data related to multi subsurface structures. For example, Ma [46] suggested the Improved Local Phase method (*ILP*):

$$ILP = \arcsin\left[\frac{\sqrt{\left(\frac{\partial g_z}{\partial x}\right)^2 + \left(\frac{\partial g_z}{\partial y}\right)^2}}{\sqrt{\left(\frac{\partial g_z}{\partial x}\right)^2 + \left(\frac{\partial g_z}{\partial y}\right)^2 + \left(\frac{\partial^2 g_z}{\partial x^2} + \frac{\partial^2 g_z}{\partial y^2}\right)^2}}\right] \tag{38}$$

And, Ferreira et al. [49] have suggested the *TAHG*:

$$TAHG = \arctan\left[\frac{\frac{\partial HG}{\partial z}}{\sqrt{\left(\frac{\partial HG}{\partial x}\right)^2 + \left(\frac{\partial HG}{\partial y}\right)^2}}\right] \tag{39}$$

Using numerical tests, Zhang et al. [50] showed that the *ILP* and the *TAHG* successfully extract the edges of potential field data relating to multi subsurface structures, and they also suggested a more sensitive edge detection method, *THVH*. The *THVH* is defined as follows:

$$THVH = \arctan\left[\frac{\frac{\partial^2 HG}{\partial z^2}}{\sqrt{\left(\frac{\partial}{\partial x}\frac{\partial HG}{\partial z}\right)^2 + \left(\frac{\partial}{\partial y}\frac{\partial HG}{\partial z}\right)^2}}\right] \tag{40}$$

Kusumoto [51] pointed out that because the *CLP*, *ILP*, *TAHG*, and *THVH* are all very sensitive high pass filters, which respond to very small signals (perhaps also including noise), other geological or geophysical data of the region would be required in order to fully understand the results obtained by these techniques.

3.2. Curvature of the potential field

Curvatures of potential field data vary in response to density changes in the subsurface structure, and these curvatures are described by the g_{xx}, g_{yy}, and g_{xy} components (e.g., [27, 28]).

Pedersen and Rasmussen [52] defined the invariant ratio, *I*, of the gravity gradient tensor as follows:

$$I = \frac{-27I_2^2}{4I_1^3} \tag{41}$$

Here, I_1 and I_2 are invariants of the tensor. Each invariant is given by three eigenvalues (λ_1, λ_2, λ_3) of the gravity gradient tensors, as follows:

$$\begin{aligned} I_1 &= \lambda_1\lambda_2 + \lambda_2\lambda_3 + \lambda_1\lambda_3 \\ I_2 &= \lambda_1\lambda_2\lambda_3 \end{aligned} \tag{42}$$

The invariant ratio *I* varies between 0 and +1. If the body causing a gravity anomaly is a 2D structure, *I* is 0. If the causative body is 3D, *I* is +1. Beiki and Pedersen [53] named this ratio the dimensionality index and suggested $I = 0.5$ as the threshold between a 2D and 3D causative structure. In addition, for the case of a 2D causative structure such as a dike, the maximum eigenvector of the gravity gradient tensor points to the causative body and the minimum eigenvector is parallel to the strike direction of the structure.

Cevallos et al. [54] and Cevallos [55] pointed out that the shape index (e.g., [56, 57]) is useful for determining the characteristics of potential fields and is defined by

http://dx.doi.org/10.5772/64557

$$Si = \frac{2}{\pi}\arctan\left[\frac{g_{zz}}{\sqrt{\left(g_{xx}-g_{yy}\right)^2+4g_{xy}^2}}\right] \tag{43}$$

The shape index, *Si*, varies from –1 to +1, and it is suggested that values of –1, –0.5, 0, +0.5, and +1 correspond to bowl, valley, flat, ridge, and dome structures, respectively. Cevallos [55] found that a map of the shape index at depth was consistent with deep structures integrated by geophysical and geological data in the King Sound area of the Canning Basin, Western Australia.

Studies on the curvature of the potential field have recently been developed as new interpretation techniques because they use a lot of the characteristics of the gravity gradient tensor (e.g., [58–62]). However, some problems relating to its practical usage remain unsolved. In fact, Li [63] conducted numerical tests for 13 well-known semiautomatic interpretation methods based on the curvature of the potential field and concluded that the shape of the potential does not always correspond to the subsurface structure, and therefore care should be taken when interpreting these results.

3.3. Euler deconvolution

Euler deconvolution is a semiautomatic interpretation method based on Euler's homogeneity equation and is often employed to estimate locations and/or outlines of causative bodies. Because the Euler deconvolution technique can provide rapid interpretations of any potential field data in terms of depth and geological structures, it has been used by several researchers for analyzing both magnetic anomalies (e.g., [64–66]) and gravity anomalies (e.g., [67]).

The Euler deconvolution based on the three orthogonal gradient components of the potential field is simply called Euler deconvolution or conventional Euler deconvolution. For the gravity anomaly g_z, it uses the following equation:

$$(x-x_0)g_{zx}+(y-y_0)g_{zy}+(z-z_0)g_{zz}=N(B_z-g_z) \tag{44}$$

In Eq. (44), x_0, y_0, and z_0 are unknown location parameters of the causative body center or edge that have to be estimated, and x, y, and z are known location parameters of the observation point of the gravity and its gradients. N is the structural index and B_z is the regional component of the gravity anomaly that has to be estimated.

Rewriting Eq. (44), we obtain the following equation in which we can separate unknown parameters from known parameters:

$$x_0 g_{zx} + y_0 g_{zy} + z_0 g_{zz} + NB_z = x g_{zx} + y g_{zy} + z g_{zz} + N g_z \tag{45}$$

There are four unknown parameters in Eq. (45). If we have enough data, namely $n \geq 4$, to solve for these unknowns within a selected window, we can estimate these four parameters using the least-squares method.

Zhang et al. [68] suggested the Tensor Euler deconvolution, designed to consider the full gravity gradient tensor (Eq. (2)) and all components (g_x, g_y, g_z) of the gravitational vector. The Tensor Euler deconvolution is defined by the following simultaneous equations:

$$\begin{aligned}
(x - x_0) g_{xx} + (y - y_0) g_{xy} + (z - z_0) g_{xz} &= N(B_x - g_x) \\
(x - x_0) g_{yx} + (y - y_0) g_{yy} + (z - z_0) g_{yz} &= N(B_y - g_y) \\
(x - x_0) g_{zx} + (y - y_0) g_{zy} + (z - z_0) g_{zz} &= N(B_z - g_z)
\end{aligned} \tag{46}$$

Here, B_x and B_y are the regional components of the gravity anomaly that have to be estimated. Thus, there are six unknown parameters in this equation, and if we have enough data to solve for these six unknowns within a selected window, namely $n \geq 6$, these parameters can be estimated using the least squares method. Using a numerical study and applying it to field data, Zhang et al. [68] showed that the Tensor Euler deconvolution produces a significantly improved resolution compared to the conventional Euler deconvolution.

3.4. Dip estimation of a fault or structural boundary

In recent years, a technique estimating the dip of structures such as dikes, faults, or other geological structure boundaries has been developed and produced good results as a semiautomatic interpretation method using the gravity gradient tensor.

Beiki [69] suggested that the dip, α, of the causative body could be estimated from the three components (x, y, z) of the maximum eigenvector (v_1) of the gradient tensor of the potential field (**Figure 3**) as follows:

$$\alpha = \arctan\left(\frac{v_{1z}}{\sqrt{(v_{1x})^2 + (v_{1y})^2}} \right) \tag{47}$$

where v_{1x}, v_{1y}, and v_{1z} are the x, y, and z components of the maximum eigenvector, v_1. Beiki [69] applied this method to an aeromagnetic data set of the Åsele area in Sweden, and provided

http://dx.doi.org/10.5772/64557

useful information on the dip of dike swarms. Kusumoto [70] applied this technique to estimate the dip of the Median Tectonic Line located in southwest Japan, and obtained a dip distribution compatible with results from other geophysical surveys, including a reflection survey. Since gravity gradient tensor consists of differential coefficients of gravitation caused by causative body the tensor has higher accuracy than gravity anomaly. In addition, since analysis using eigenvalues and eigenvectors of the tensor considers all components of the tensor, this technique would give good results. In this technique, we do not need to know or assume density contrast between layers or structures.

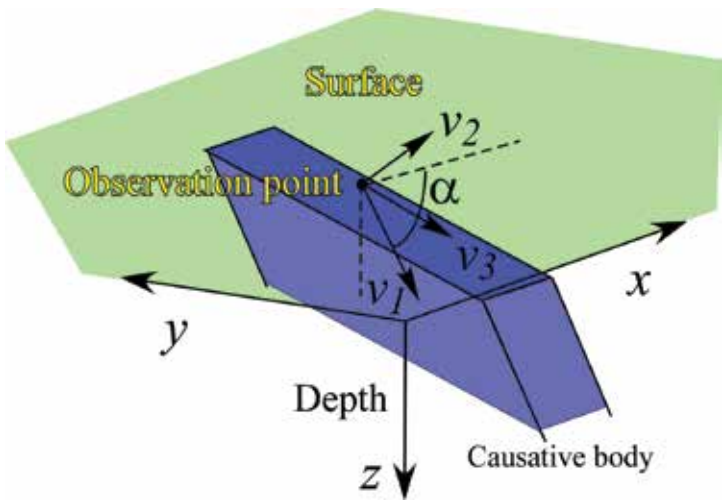

Figure 3. Schematic illustration of the eigenvectors for a 2D structure such as dike. In this figure, v_1, v_2, and v_3 are the maximum, intermediate, and minimum eigenvectors of the gravity gradient tensor, respectively. The maximum eigenvector points to the causative body and the minimum eigenvector is parallel to the strike direction of the body. The angle α between the surface and maximum eigenvector is the angle of the structural boundary and/or fault.

4. Application of semiautomatic interpretation method

Here, we apply the semiautomatic interpretation methods shown in the previous section to a volcanic area located in central Kyushu, Japan. This area consists of the Aso caldera and the Hohi Volcanic Zone containing a buried caldera, the Shishimuta caldera, where many previous geological and geophysical studies have been conducted. In addition, a database of the Bouguer gravity anomaly is available for use (e.g., [71]), although a gravity gradiometory survey covering this area has not yet been carried out. Since this gravity anomaly database employed in this study gives users 1 km × 1 km mesh data, we discussed structures larger than several kilometers in this study. If we would like to discuss fine structures, it would be possible by employing denser mesh data.

4.1. Background of Hohi Volcanic Zone and Aso caldera

4.1.1. Hohi Volcanic Zone and Shishimuta caldera

The Hohi Volcanic Zone (e.g., [73]) is located in the eastern part of central Kyushu (**Figure 4**) and is characterized by a wedge-shaped low gravity anomaly area, which becomes narrow toward the east (**Figure 5**). In the Hohi Volcanic Zone, there are four conspicuous low anomaly areas toward the west-southwest from Beppu Bay, which correspond to the Beppu Bay, Shonai Basin, Shishimuta caldera, and Kuju basin, respectively. The Beppu Bay has the lowest gravity anomaly, which reaches –50 mGal.

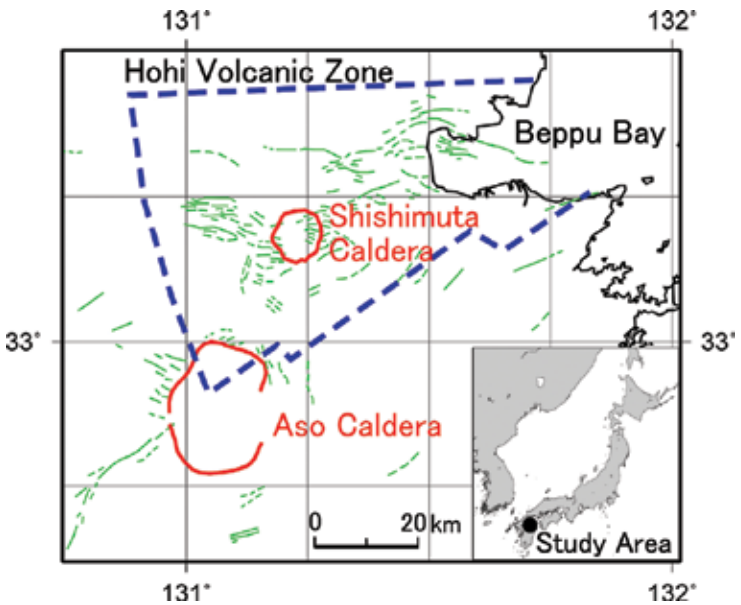

Figure 4. Location map of study area. Blue dashed line indicates the outline of the Hohi volcanic zone. Red lines indicate the caldera. Green lines are active faults (e.g., [72]).

Subsurface structures in this region have been estimated by gravity anomaly data, drill core data, reflection survey, and surface geology data (e.g., [74, 75]). Kusumoto et al. [75] showed that, although the average depth of the basement was estimated to be approximately 1.2 km in the Hohi Volcanic Zone, the small basins (the Shonai basin and the Kuju basin) along the Oita-Kumamoto Tectonic Line (the tectonic line suggested by a steep gravity gradient (e.g., [76])) are deeper than 2 km. In addition, it was shown that the basement depth in Beppu Bay reaches to approximately 4 km. Detailed geological surveys have shown that this volcanic zone consists of half-grabens detailing volcanic activity that began 6 Ma (e.g., [73]) and pull-apart basins that formed after the half-graben formation (e.g., [77]).

During formation of the Hohi Volcanic Zone, it is known that eruption of more than 5000 km^3 of material occurred in the last six million years, and that eruption rate gradually de-

http://dx.doi.org/10.5772/64557

creased. The volcanic zone erupted 2900 km^3/Ma in its initial stage of activity from 5 to 4 Ma. After that, the zone erupted approximately 1300, 900, 400, and 200 km^3 between 4–3, 3–2, 2–1, and 1–0 Ma, respectively [73]. The formation of the pull-apart basin began 1.5 Ma; this tectonic change occurred due to a counter-clockwise shift of the subducting Philippine Sea Plate (e.g., [77]).

Kusumoto et al. [78] attempted to restore the tectonic structures by numerical simulations based on the dislocation theory (e.g., [79]). They showed that tectonic structures such as half-grabens and pull-apart basins can be restored by obeying the tectonics suggested by Itoh et al. [77]. Kusumoto et al. [80] assumed a simple two-layer structure model, which consisted of the basement and the sediment, and estimated the gravity anomaly field from the vertical displacement field of the basement obtained by tectonic modeling [78]. As a result, it was shown that a gravity anomaly of volcanic origin cannot be restored. In this model, the unrestored gravity anomaly was that relating to the Shishimuta caldera.

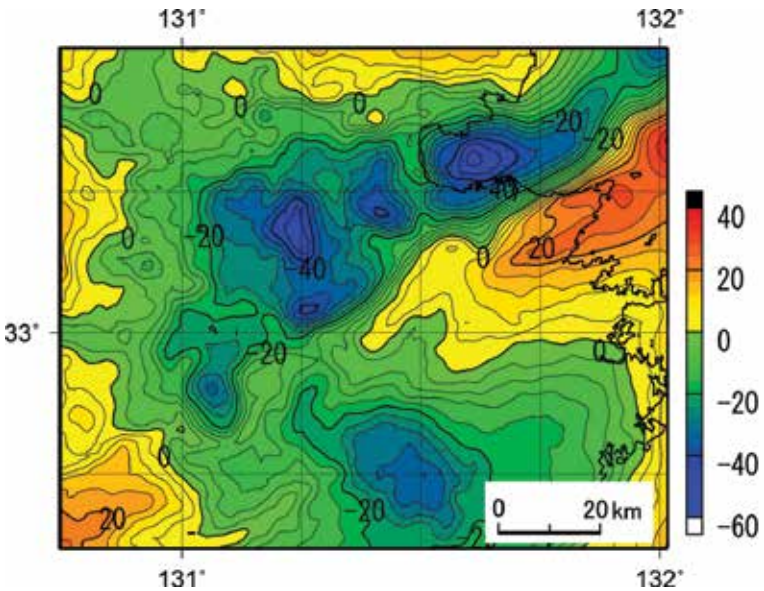

Figure 5. Residual Bouguer gravity anomaly map of the study area and surroundings. The contour interval is 4 mGal. In the residual Bouguer gravity anomaly map, the regional linear trend of the Bouguer gravity anomalies, such as the effect of the subducting plate, is estimated and removed by the least squares method from the Bouguer gravity anomalies. The Bouguer gravity anomaly used here is based on the gravity anomaly database (1 km × 1 km mesh data) by Komazawa [71], and a Bouguer density of 2670 kg/m^3 is employed.

The Shishimuta caldera is a buried caldera and is the origin of the Yabakei and Imaichi pyroclastic flows that are widely distributed throughout central Kyushu (e.g., [81, 82]). The volumes of these flows have been estimated as 40 km^3 (e.g., [81]) and 90 km^3 (e.g., [82]), respectively, based on detailed surface geological surveys. The red circle shown in **Figure 4** indicates the caldera wall at 1 km depth with a diameter of approximately 8–10 km, estimated from drilling core data and gravity anomalies (e.g., [81]). Density contrast between basement

and sedimentary layers is estimated to be in the range of 300–700 kg/m^3 by Kusumoto et al. [75]. As shown in **Figure 5**, this Shishimuta caldera does not have the concentrically circular low gravity anomaly found in many calderas; rather, this caldera has a triangular low gravity anomaly.

The subsurface structure of the Shishimuta caldera was estimated from a geological perspective, and the structure shallower than 3 km depth was revealed by drill core data and gravity anomalies. On the basis of drill core data, gravity anomalies, active fault distribution, microearthquake activity, and geological surveys in and near the Shishimuta caldera, Kamata [81] estimated that the shape of this caldera is a funnel type. In addition, Kamata [81] estimated a magma chamber depth of the Shishimuta caldera would be 7–12 km depth. This was estimated by assuming that the original depth of the Yabakei pyroclastic flow is equal to the source depth of the Ito pyroclastic flow of Aira caldera, Kagoshima (e.g., [83]).

4.1.2. Aso caldera

The Aso caldera, like the Shishimuta caldera, is located in central Kyushu (**Figure 4**). However, it extends approximately 25 km in the south-north direction and about 18 km in the east-west direction and is thus elliptical in plan view, and is one of the largest calderas in the world.

It is known that the Aso caldera was formed by four eruptions with large-scale pyroclastic flows. The first large pyroclastic flow is called Aso-1 and flowed out from the present Aso caldera prior to 0.27 Ma. The second is called Aso-2 and was erupted before 0.14 Ma. The Aso-2 was the smallest pyroclastic flow and its volume is estimated at approximately 25 km^3. The third pyroclastic flow is called Aso-3 and is dated at 0.12 Ma. The fourth pyroclastic flow is called Aso-4 and is the largest pyroclastic flow with a volume of more than 80 km^3. From detailed geological surveys, it has been found that Aso-4 would have flown over the sea (the Seto inland sea and Tachibana Bay) and reached Yamaguchi Prefecture and Shimabara Peninsula. In the Aso caldera, there is also a central group of volcanic cones, which are currently active (e.g., [84]).

Gravity surveys of this region have been initiated by Tsuboi et al. [76] and Kubotera et al. [85]. Yokoyama [86] estimated that the subterranean caldera structure is similar to a funnel-shape. Komazawa [87] accumulated gravity data and conducted high accuracy, high-resolution analyses for the compiled gravity data. As a result, they found that the Aso caldera has a piston-cylinder type structure rather than a funnel-shaped structure with a single low anomaly. In addition, five minor local gravity lows exist in the caldera, which make up the major low gravity zone of the Aso caldera. The major gravity low has a steep gradient inside the caldera rim, and the central area of the minor gravity anomalies has a relatively flat bottom.

4.2. Gravity gradient tensor in central Kyushu

In **Figure 6**, we show all components of the gravitation vector and gravity gradient tensor. Since the gravity gradiometry survey covering this region has not been conducted, the gravitation vector and gravity gradient tensor were calculated from the Bouguer gravity anomaly data shown in **Figure 5**.

http://dx.doi.org/10.5772/64557

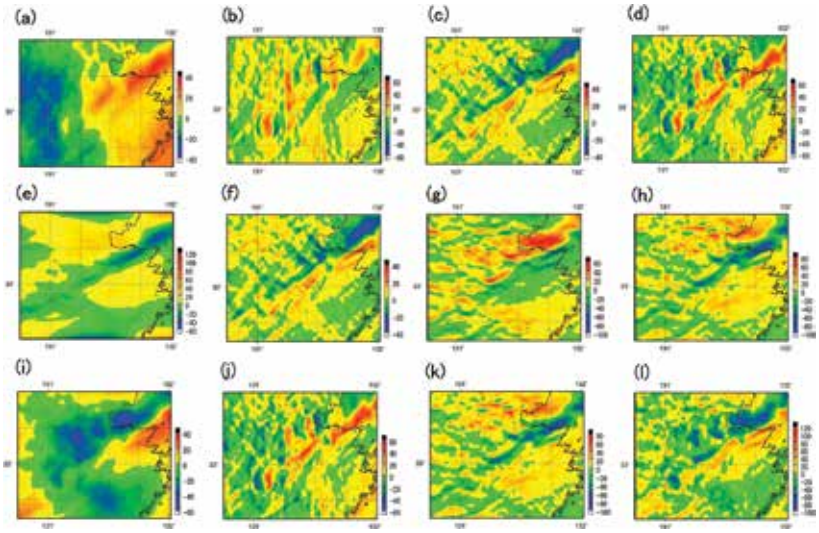

Figure 6. Components of gravitational vector and gravity gradient tensor calculated from g_z data shown in **Figure 5**, using the method of Mickus and Hinojosa [24]. The gravitational vector unit is given in mGal, and mGal = 10^{-5} m/s^2. The unit of the gravity gradient tensor is given in E (Eötvös), and 1 E = 0.1 mGal/km. (a) g_x component of gravitational vector, (b) g_{xx} component of gravity gradient tensor, (c) g_{xy} component, (d) g_{xz} component, (e) g_y component, (f) g_{yx} component, which is equal to g_{xy}, (g) g_{yy} component, (h) g_{yz} component, (i) $g_z$component; gravity anomaly, (j) g_{zx} component, which is equal to g_{xz}, (k) g_{zy} component, which is equal to g_{yz}, and (l) g_{zz} component.

Although all components of the gravity gradient tensor were theoretically estimated by the method of Mickus and Hinojosa [26], we also obtained components of the gravity gradient tensor by numerical differentiation of g_x, g_y, and g_z in the space domain, since short wavelength noise due to differentiation in the Fourier domain can sometimes be generated. The gravitation vector was, however, calculated using the method of Mickus and Hinojosa [26].

5. Results and discussion

5.1. Edge emphasis

In this section, we applied the 10 edge emphasis techniques shown in Section 3.1 to the field data. The results obtained by each method are shown in **Figures 7–16**.

The maps of the horizontal gravity gradient (*HG*: Eq. (32)), the vertical gravity gradient (*VG:* g_{zz}), and the second vertical derivative ($\partial^2 g_z/\partial z^2$, or g_{zzz}) are shown in **Figures 7–9**, respectively. The horizontal gravity gradient map extracts the outlines of the Hohi Volcanic Zone, the Shishimuta caldera, and the Aso caldera. In addition to these caldera or volcanic depressions, tectonic lines such as the Median Tectonic Line and Oita-Kumamoto Tectonic Line, which are important structures in this region, are also extracted (**Figure 7**). These lineaments were extracted as a high gravity gradient belt with an NE-SW trend crossing the Aso caldera. The land area of the belt corresponds to the Oita-Kumamoto Tectonic Line, and the sea area of the

belt corresponds to the Median Tectonic Line. The Median Tectonic Line is the largest tectonic line in the southwest Japan, and it is known that the tectonic line has moved as a right lateral fault with normal faulting in the Quaternary. Furthermore, we also detect a large circular belt with a high gravity gradient outside of the high gradient belt that represents the Shishimuta caldera.

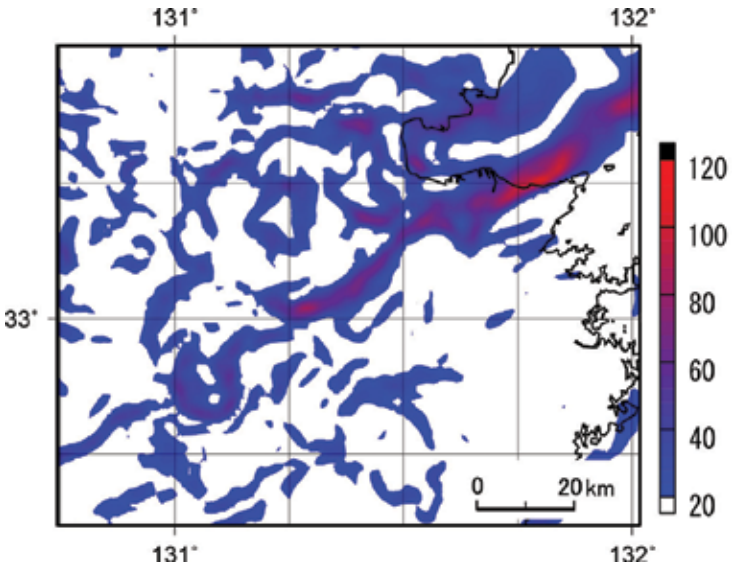

Figure 7. Horizontal gravity gradient map for values over 20 E. Units are given in E (Eötvös). Colored areas indicate locations of structural boundaries such as faults or contacts between different materials.

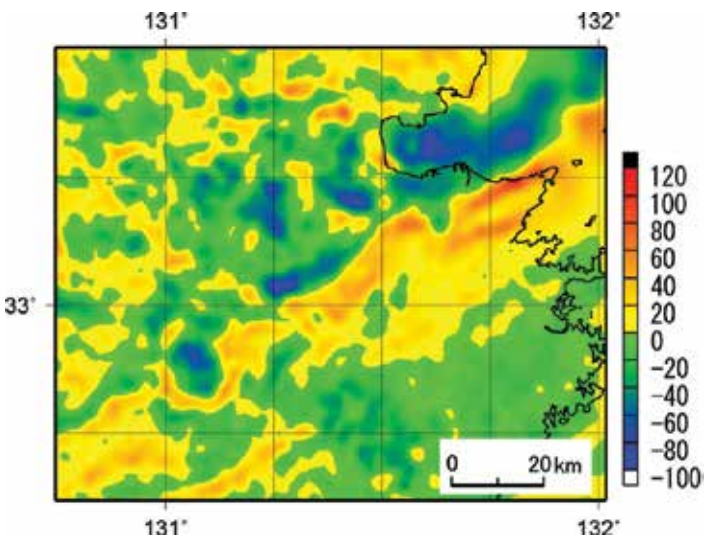

Figure 8. Vertical gravity gradient (g_{zz}) map. Units are given in E (Eötvös). Vertical gravity gradient evaluates vertical gradient of the Bouguer gravity anomaly, and estimates geological or structure boundary by line $g_{zz} = 0$.

http://dx.doi.org/10.5772/64557

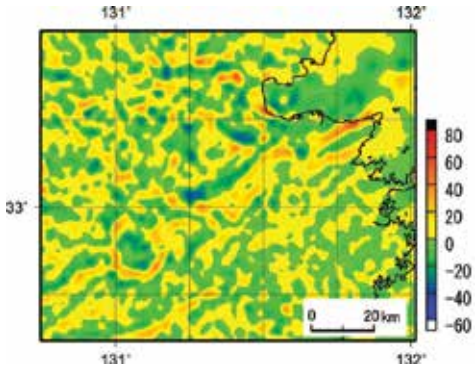

Figure 9. Vertical gravity gradient (second differential coefficient: $\partial^2 g_z/\partial z^2$, g_{zzz}) map. Units are given in E/km. E (Eötvös) is unit of the gravity gradient tensor, and 1 E = 0.1 mGal/km. This map indicates geological or structure boundary more sharply than g_{zz}.

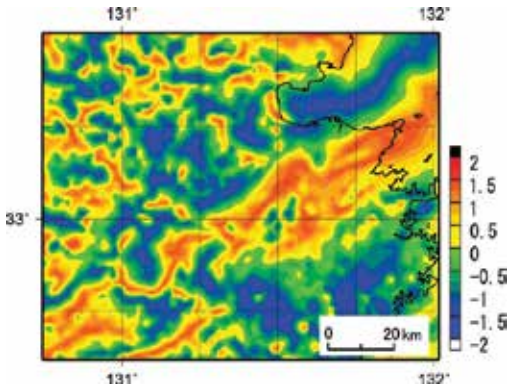

Figure 10. *TDR* map. Units are radians. This map indicates geological or structure boundary by line *TDR* = 0.

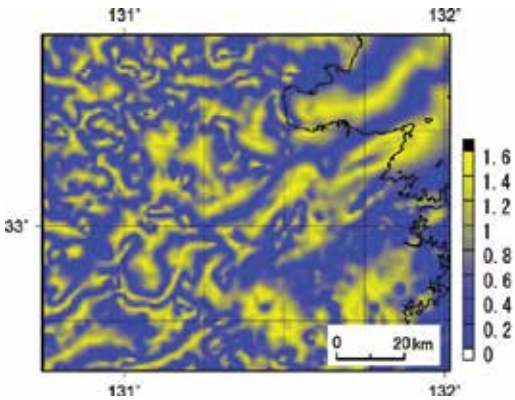

Figure 11. *THETA* map. Units are radians. This map indicates geological or structure boundary by line *THETA* = 0.

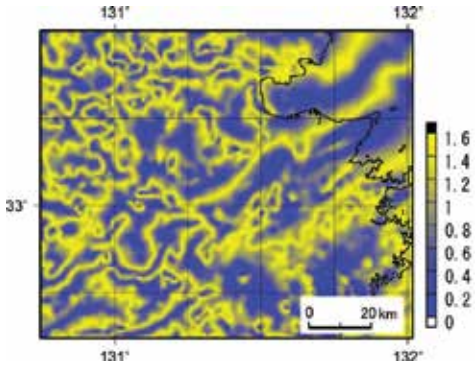

Figure 12. *TDX* map. Units are radians. This map indicates geological or structure boundary by line *TDX* = max (here, *TDX* = 1.6).

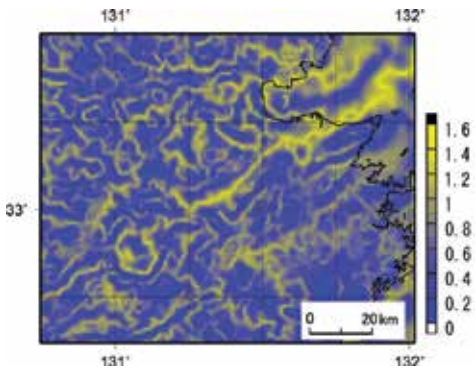

Figure 13. *CLP* map. Units are radians. This map indicates geological or structure boundary by line *CLP* = max (here, *CLP* = 1.6).

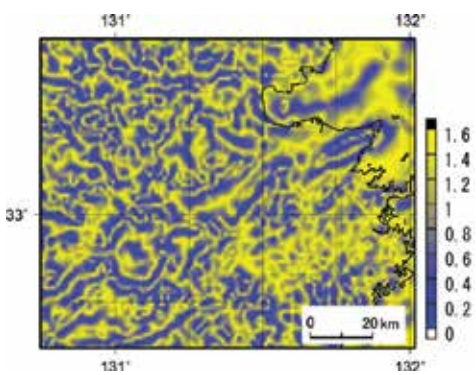

Figure 14. *ILP* map. Units are radians. This map extracts the edge of the gravity anomaly related to multi subsurface structures.

http://dx.doi.org/10.5772/64557

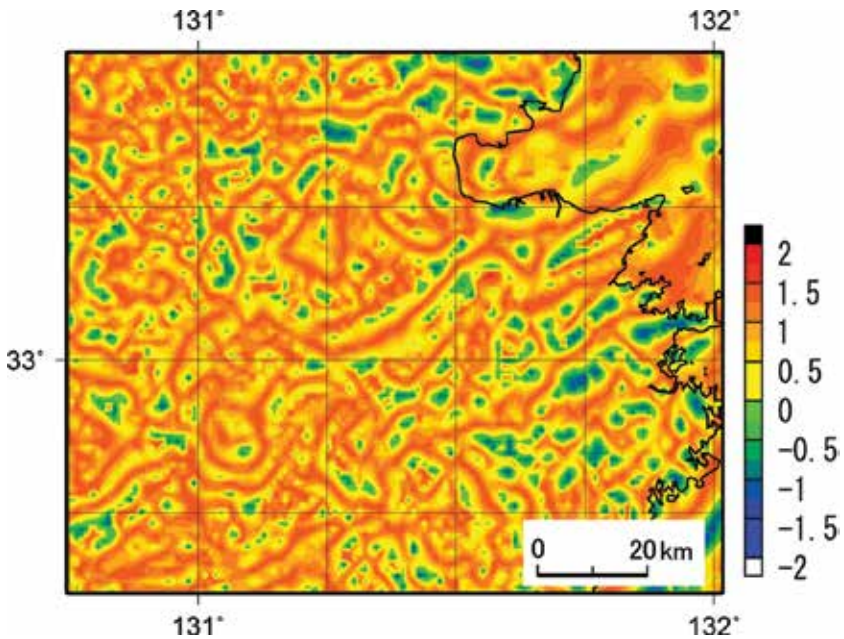

Figure 15. *TAHG* map. Units are radians. This map extracts the edge of the gravity anomaly related to multi subsurface structures.

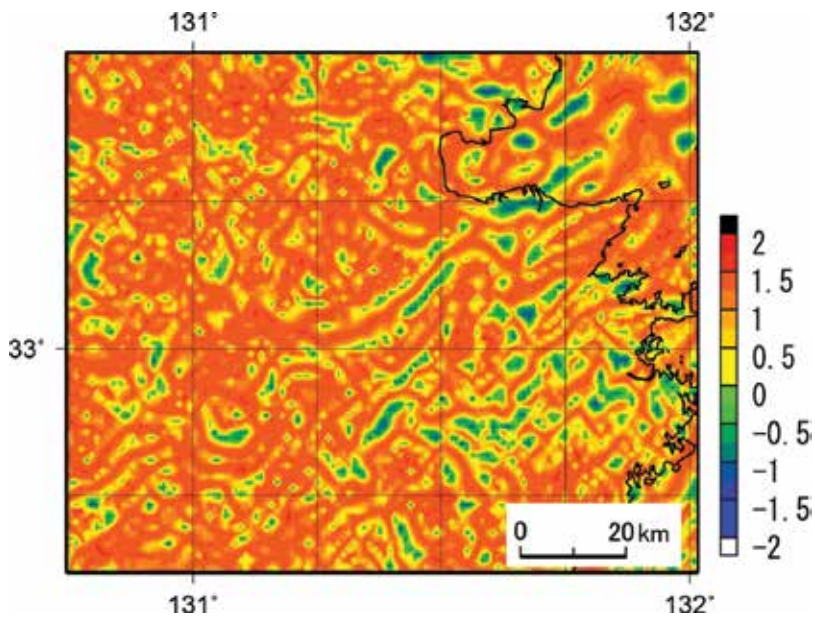

Figure 16. *THVH* map. Units are radians. This map extracts the edge of the gravity anomaly related to multi subsurface structures.

The vertical gravity gradient extracts the boundaries of the low gravity and high gravity areas, and emphasizes areas of low density (**Figure 8**). In particular, the caldera rim of the Aso caldera and boundaries of the tectonic lines and sedimentary basins are clearly extracted. In addition, areas of low-density material such as ash, pyroclastic flows, and sediments are accurately predicted and emphasized, and correspond to the inner areas of the Aso caldera, Shishimuta caldera, Kuju basin, Shonai basin, and Beppu Bay. The g_{zzz} map (**Figure 9**) shows each rim of the Aso caldera and Shishimuta caldera more clearly and emphasizes shorter wavelength signals. However, it seems that this technique does not highlight the density structures as effectively as the vertical gravity gradient, g_{zz}.

The maps of the *TDR* (Eq. (33)), the *THETA* (Eq. (34)), the *TDX* (Eq. (35)), and the *CLP* (Eq. (36)) are shown in **Figures 10–13**, respectively. The *TDR* shows the original structural boundaries at zero lines [44]. If we obeyed this judgment criterion, the boundaries of the green and yellow areas would be the structural boundaries such as lineaments, faults, and caldera rims. And, if we did not persist in the criterion, from this *TDR* we can derive information on both the structural boundaries and the density structures extracted by *HG* and *VG*. In fact, the *TDR* shows local low gravity areas more clearly or in greater detail than the vertical gravity gradient map.

The *THETA* map, the *TDX* map, and the *CLP* map extract structural boundaries by lines. In particular, it appears that the *CLP* technique is an excellent boundary extraction technique as it extracts very distinctly the caldera rims of the Aso caldera and the Shishimuta caldera, as well as locations of the Median Tectonic Line and the Oita-Kumamoto Tectonic Line (**Figure 13**). In addition, we also observe the larger circular lines outside the yellow lines indicating the Shishimuta caldera rim and the Aso caldera rim. The larger circular line outside of the Shishimuta caldera was also shown in the horizontal gravity gradient (*HG*) map (**Figure 7**).

The maps of the *ILP* (Eq. (38)), *TAHG* (Eq. (39)), and *THVH* (Eq. (40)) are shown in **Figures 14–16**, respectively. These techniques have been developed for finding the edges of the potential field related to multi subsurface structures, and generally they emphasize very small signals caused by the deep structures. The *ILP* map extracts the Aso caldera rim, but it is difficult to interpret what the other strong short wavelength lines represent. The *TAHG* and *THVH* maps are similar to the *ILP* map and have similar interpretation difficulties.

5.2. Curvature analysis

Figures 17 and **18** are the dimensionality index map and the shape index map. The dimensionality index map indicates whether the subsurface structure in the region is 2D, such as a vertical or subvertical dike or fault, or 3D, such as a dome structure. If the subsurface structure is 2D, the dimensionality index, $I < 0.5$. Since areas of $I \leq 0.5$ are widely distributed in **Figure 17**, we can conclude that the subsurface structures in the study area predominantly consist of 2D structures. However, in the inner area of the Shishimuta caldera rim, the dimensionality index is more than 0.7, and 3D structures are therefore predicted (**Figure 17**). In addition, the dimensionality index is also more than 0.7 in part of the inner area of the Aso caldera rim. This area corresponds to the volcanic cone group in the Aso caldera.

http://dx.doi.org/10.5772/64557

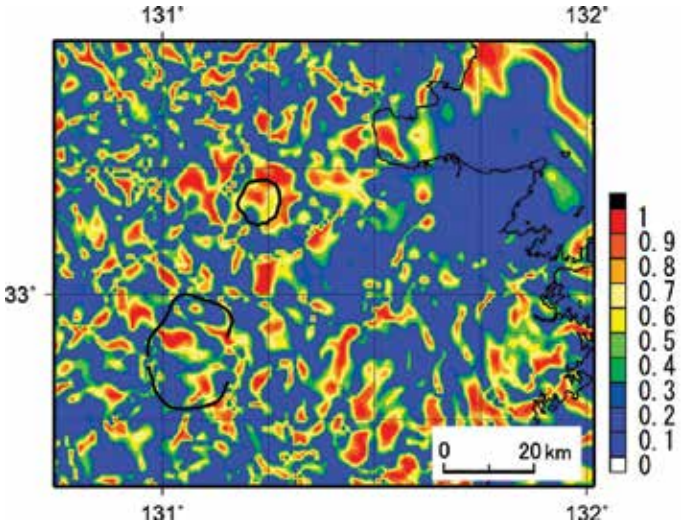

Figure 17. Map of dimensionality index, *I*. 2D structures are predicted in areas where $I < 0.5$. Locations of the caldera rim are shown by black lines. The northern small caldera is the Shishimuta caldera and its diameter is 8–10 km. The southern large caldera is the Aso caldera and its diameter is approximately 25 km in the south-north direction and about 18 km in the east-west direction.

The shape index in the Shishimuta caldera rim reaches –1 (**Figure 18**). This indicates that the potential shape of the low-density material is either bowl-like, a downward convex structure, or both. In fact, since Kamata [81] predicted that the Shishimuta caldera would be a funnel type caldera, the obtained results are considered suitable. Furthermore, these results are compatible with the result shown in **Figure 17**; the inner structure of the Shishimuta caldera would be 3D. In addition, locally low shape index areas are distributed around the Shishimuta caldera.

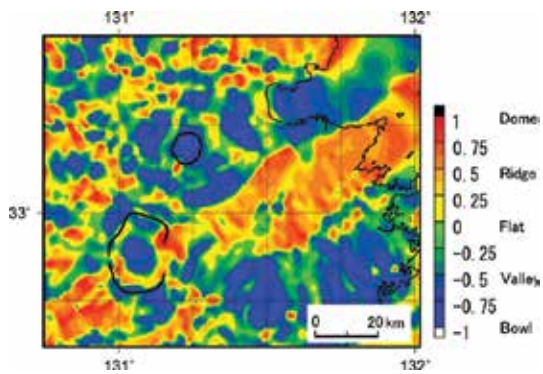

Figure 18. Shape index map. Values of –1, –0.5, 0, +0.5, and +1 indicate bowl, valley, flat, ridge, and dome structures, respectively. Locations of the caldera rim are shown by black lines. The northern small caldera is the Shishimuta caldera and its diameter is 8–10 km. The southern large caldera is the Aso caldera and its diameter is approximately 25 km in the south-north direction and about 18 km in the east-west direction.

In the Aso caldera, the shape index is in the range of –1 to +1. This indicates that the subsurface structures would be complex since the Aso caldera has experienced four caldera formations. Moreover, areas of locally low shape index less than –0.75 correspond to the five local minor gravity lows found by Komazawa [87].

5.3. Euler deconvolution

We employed here the Tensor Euler deconvolution [68] to obtain information on the subsurface structures. In the calculation, we set a 24 km width window (the required amount of data to solve Eq. (9) is 576) with a structure index of 0.001. Generally, a structure index of 0 is employed for sills, dikes, and faults (e.g., [88]), but calculations with this value did not give solutions in our study field. The value of 0.001 was obtained through trail and error.

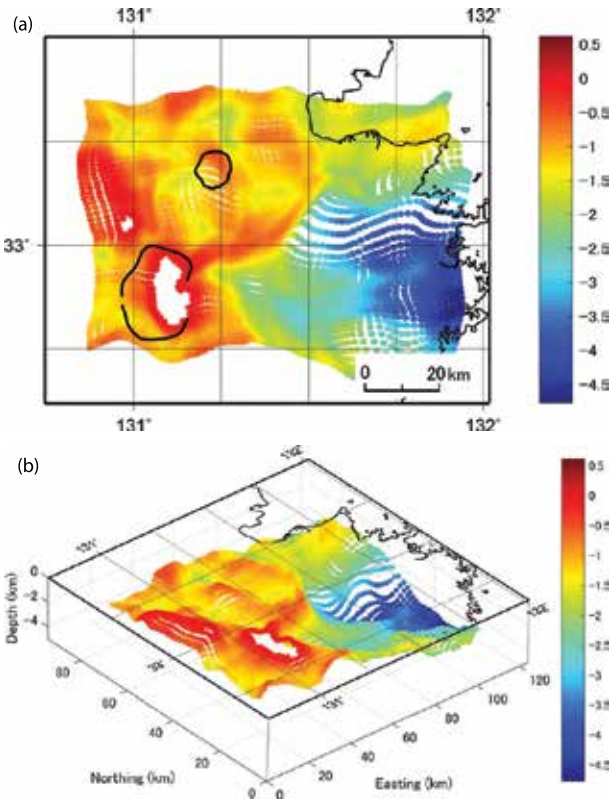

Figure 19. Solution clouds given by the Tensor Euler deconvolution. In the calculation, a 14km width window and a structure index of 0.5 are assumed. (a) Distribution of the solutions in map view. Units are km. Locations of the caldera rim are shown by black lines. The northern small caldera is the Shishimuta caldera and its diameter is 8–10 km. The southern large caldera is the Aso caldera and its diameter is approximately 25 km in the south-north direction and about 18 km in the east-west direction. (b) Distribution of the solutions in bird's-eye view. Units are km.

In **Figure 19**, we show the solution clouds given by the Tensor Euler deconvolution. We identify a deep and flat structure like a sedimentary basin at the east of the Aso caldera. There

http://dx.doi.org/10.5772/64557

are large structural gaps between this structure and the Hohi Volcanic Zone, and the gaps appear to resemble a cliff (**Figure 19b**). In the Aso caldera, structural boundaries within the caldera are extracted as a void area of the solutions. However, these inner boundaries were not extracted in the Shishimuta caldera. In addition, we detect a large circular wall structure surrounding the Shishimuta caldera. Although partially observable in map view (**Figure 19a**), the structure is more clearly distinguished in bird's-eye view (**Figure 19b**).

5.4. Dip estimation

Dips of faults and/or structural boundaries were estimated in the areas that satisfied the conditions I (dimensionality index) < 0.5 and HG (horizontal gravity gradient) ≥ 20 E (**Figure 20**). From **Figure 20**, we found that dip of the Median Tectonic Line and Oita-Kumamoto Tectonic Line are in the range of 40–70°, and are interpreted as high angle faults. In part of the Median Tectonic Line, the dip is very high, exceeding 70°. Since it is known that the Median Tectonic Line moved as a right lateral fault with normal faulting in the Quaternary, it is reasonable that this tectonic line has a high dip reaching 70° or 80°. The dip of the Median Tectonic Line becomes gradually lower to the north, toward Beppu Bay area. Seismic reflection surveys (e.g., [89]) confirm that dip of normal faults distributed in the Beppu Bay are <45°. Consequently, the obtained dip distribution is consistent with the observed data, suggesting that this technique is a useful semiautomatic interpretation method. In our results, the dip of the Oita-Kumamoto Tectonic Line is estimated to be approximately 60°, but its actual dip is unknown. Since, for many numerical simulations evaluating deformation fields by fault motions, the dip of the fault plays an important role, this technique will give us useful information on fault shape even if the result is a first approximation solution.

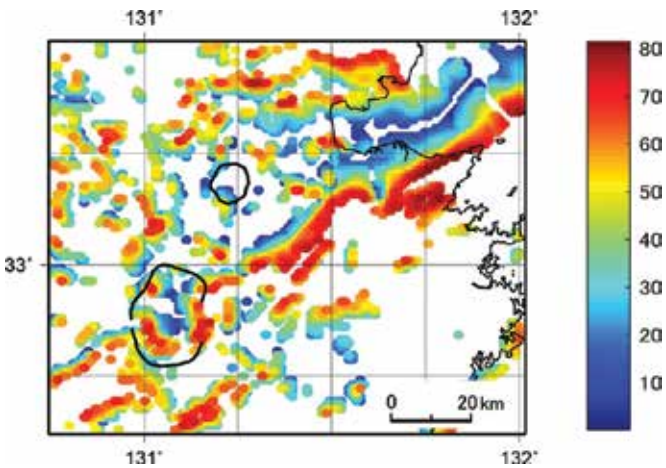

Figure 20. Distribution of estimated dip of faults and/or structural boundaries. Locations of the caldera rim are shown by black lines. The northern small caldera is the Shishimuta caldera and its diameter is 8–10 km. The southern large caldera is the Aso caldera and its diameter is approximately 25 km in the south-north direction and about 18 km in the east-west direction. Dip estimation was conducted for the areas that satisfied the conditions I < 0.5 and HG (horizontal gravity gradient) ≥ 20 E.

In the Aso caldera, dip of its caldera wall are in the range of 50–70° (inward dipping), as shown in **Figure 20**. Dips become gradually lower toward the caldera center, which is almost flat. These subsurface structural characteristics in the inner area of the Aso caldera have already been observed by detailed gravity analysis [87], and our results and Komazawa's results support to each other. However, this is the first time that caldera wall dips have been explicitly determined. In the Shishimuta caldera, because the condition of the dimensionality index was not satisfied, the distribution of caldera wall dips could not be estimated. Since the dip of the caldera wall leads to a discussion of the radius of the magma chamber, the process of caldera formation, and the type of caldera (e.g., [9, 14, 19–20]), the dip of the wall is thought to be as important as the fault dip.

The dips of the large circular wall structure surrounding the Shishimuta caldera are in the range of approximately 45–60° (inward dipping). This large structure appears in *HG* (**Figure 7**), *VG* (**Figure 8**), *TDR* (**Figure 10**), *CLP* (**Figure 13**), shape index (**Figure 18**), and Tensor Euler deconvolution (**Figure 19**) data, and it has a diameter of approximately 35 km. Since the Hohi Volcanic Zone was formed by eruption of more than 5000 km^3 or material during six million years (e.g., [73]), it is suggested that this structure represents a depression or group of depressions resulting from these eruptions. However, because the obvious sedimentary basins such as the Kuju basin and the Shonai basin are included within this area, more detailed surveys and studies would be required to discuss this large structure surrounding the Shishimuta caldera.

6. Conclusions

By obtaining the gravity gradient tensor from the gravity anomaly, we can use a variety of techniques to extract subsurface structures. In this study, we reviewed semiautomatic interpretation methods using the gravity gradient tensor, and applied some of the techniques to the volcanic zone of central Kyushu, Japan. This area consists of the Aso caldera and the Hohi Volcanic Zone containing a buried caldera, the Shishimuta caldera, and has large tectonic lines such as the Median Tectonic Line and the Oita-Kumamoto Tectonic Line, and tectonic sedimentary basins such as the Beppu Bay, the Kuju basin, and the Shonai basin.

Most edge detection methods extracted the outlines of these structures, and some of them indicated density structures. In spite of classical methods, the horizontal gravity gradient method and the vertical gravity gradient method were excellent edge detection methods. As for recent methods, the *CLP* method clearly extracted structural boundaries such as the caldera rim and tectonic lines as lines.

In the curvature analysis, we obtained useful information from the shape index and the dimensionality index that indicated caldera shape. In the estimation of the dip of structural boundaries using the eigenvector of the gravity gradient tensor, we obtained the fault dip of the Median Tectonic Line, which is consistent with seismic reflection surveys, and estimated the caldera wall dip of the Aso caldera, which corresponds to that obtained by detailed gravity analysis.

http://dx.doi.org/10.5772/64557

Through these data analyses, we distinguished a large circular structure with a diameter of 35 km surrounding the Shishimuta caldera. This structure appeared also in solution clouds obtained by the Tensor Euler deconvolution. However, we cannot confidently judge what this structure represents using only the gravity gradient tensor. More detailed surveys and studies are required to further discuss this issue.

Acknowledgements

This work was supported partially by JSPS (Japan Society for the Promotion of Science) KAKENHI Grant Number 15K14274. The author is grateful to the agency. The author is also most grateful to Agust Gudmundsson for very useful comments that have considerably improved the manuscript. In addition, the author is most grateful to Karoly Nemeth and Dajana Pemac for their editorial advices and cooperation.

Author details

Shigekazu Kusumoto

Address all correspondence to: kusu@sci.u-toyama.ac.jp

Graduate School of Science and Technology for Research, University of Toyama, Toyama, Japan

References

[1] Smith R L, Bailey R A. Resurgent calderas. Geological Society of America Memoirs 1968; 116: 613–662.

[2] Druitt T H, Sparks R S. On the formation of calderas during ignimbrite eruptions. Nature 1984; 310: 679–681.

[3] Lipman P W. Subsidence of ash-flow calderas: relation to caldera size and magma-chamber geometry. Bulletin of Volcanology 1997; 59: 198–218.

[4] Geshi N, Shimano T, Chiba T, Nakada S. Caldera collapse during the 2000 eruption of Miyakejima Volcano, Japan. Bulletin of Volcanology 2002; 64: 55–68. doi:10.1007/s00445-001-0184-z.

[5] Gudmundsson, A. Magma-chamber geometry, fluid transport, local stress and rock behavior during collapse caldera formation. In: Gottsmann J, Marti J, editors. Caldera

volcanism – analysis, modelling and response. Amsterdam: Elsevier; 2008. p. 313–349. doi:10.1016/S1871-644X(07)00008-3.

[6] Komuro, H. Experiments on caldron formation: a polygonal cauldron and ring fractures. Journal of Volcanology and Geothermal Research 1987; 31: 139–149.

[7] Marti J, Ablay G J, Redshaw L T, Sparks R S J. Experimental studies of collapse calderas. Journal of the Geological Society, London 1994; 151: 919–929.

[8] Acocella V, Cifelli F, Funiciello R. Analogue models of collapse calderas and resurgent domes. Journal of Volcanology and Geothermal Research 2000; 104: 81–96.

[9] Roche O, Druitt T H, Merle O. Experimental study of caldera formation. Journal of Geophysical Research 2000; 105: 395–416.

[10] Walter T R, Troll V R. Formation of caldera periphery faults: an experimental study. Bulletin of Volcanology 2001; 63: 191–203.

[11] Troll V R, Walter T R, Schmincke H U. Cycle caldera collapse: piston or piecemeal subsidence ? Field and experimental evidence. Geology 2002; 30: 135–138.

[12] Ruch J, Acocella V, Geshi N, Nobile A, Corbi F. Kinematic analysis of vertical collapse on volcanoes using experimental models time series. Journal of Geophysical Research 2012; 117: B07301. doi:10.1029/2012JB009229.

[13] Gudmundsson A. Formation and development of normal fault calderas and the initiation of large explosive eruptions. Bulletin of Volcanology 1998; 60: 160–170.

[14] Roche O, Druitt T H. Onset of caldera collapse during ignimbrite eruptions. Earth and Planetary Science Letters 2001; 191: 191–202.

[15] Folch A, Marti J. Geometrical and mechanical constraints on the formation of ring-fault calderas. Earth and Planetary Science Letters 2004; 221: 215–225.

[16] Hardy S. Structural evolution of calderas: insights from two-dimensional discrete element simulations. Geology 2008; 36: 927–930. doi:10.1130/G25133A.1.

[17] Holohan E P, Schôpfer M P J, Walsh J J. Mechanical and geometric controls on the structural evolution of pit crater and caldera subsidence. Journal of Geophysical Research 2011; 116: B07202. doi:10.1029/2010JB008032.

[18] Kusumoto S, Takemura K. Numerical simulation of caldera formation due to collapse of a magma chamber. Geophysical Research Letters 2003; 30: 2278, doi10.1029/2003GL018380.

[19] Kusumoto S, Takemura K. Caldera geometry determined by the depth of the magma chamber. Earth Planets and Space 2005; 57: e17–e20.

[20] Kusumoto S, Gudmundsson A. Magma-chamber volume changes associated with ring-fault initiation using a finite-sphere model: application to the Aira caldera, Japan. Tectonophysics 2009; 471: 58–66. doi:10.1016/jtecto.2008.09.001.

http://dx.doi.org/10.5772/64557

[21] Browning J, Gudmundsson A. Caldera faults capture and deflect inclined sheets: an alternative mechanism of ring dike formation. Bulletin of Volcanology 2015; 77: 1–13. doi:10.1007/s00445-014-0889-4.

[22] Barnes G, Barraud J. Imaging geologic surfaces by inverting gravity gradient data with depth horizons. Geophysics 2012; 77: G1–G11.

[23] Uieda L, Barbosa V C F, Robust 3D gravity gradient inversion by planting anomalous densities. Geophysics 2012; 77: G55–G66.

[24] Lu W, Qian J. A local level-set method for 3D inversion of gravity-gradient data. Geophysics 2015; 80: G35–G51.

[25] Martinetz C, Li Y, Krahenbuhl R, Braga M A. 3D inversion of airborne gravity gradiometry data in mineral exploration: a case study in the Quadrilatero Ferrifero, Brazil. Geophysics 2013; 78: B1–B11.

[26] Mickus K L, Hinojosa J H. The complete gravity gradient tensor derived from the vertical component of gravity: a Fourier transform technique. Journal of Applied Geophysics 2001; 46: 159–174.

[27] Torge W. Gravimetry. Berlin: Walter de Gruyter; 1989. 465 p.

[28] Hofmann-wellenhof B, Moritz H. Physical Geodesy. Berlin: Springer; 2005. 403 p.

[29] Lee J B. Falcon gravity gradiometer technology. Exploration Geophysics 2001; 32: 247–250.

[30] Barnes G, Lumley J. Processing gravity gradient data. Geophysics 2011; 76: I33–I47.

[31] Dransfield M H, Christensen A N. Performance of airborne gravity gradiometers. The Leading Edge 2013; 32: 908–922. doi:10.1190/tle32080908.1.

[32] Blakely R J. Potential theory in gravity and magnetic applications. Cambridge: Cambridge University Press; 1996. 441 p.

[33] Nabighian M N. The analytic signal of two-dimensional magnetic bodies with polygonal cross-section: its properties and use for automated anomaly interpretation. Geophysics 1972; 37: 507–517.

[34] Cordell L, McCafferty A E. A terracing operator for physical property mapping with potential field data. Geophysics 1989; 54: 621–634.

[35] Cooper G R J. The removal of unwanted edge contours from gravity datasets. Exploration Geophysics 2012; 44: 42–47.

[36] Blakely R, Simpson R W. Approximating edges of source bodies from magnetic or gravity anomalies. Geophysics 1986; 51: 1494–1498.

[37] Shichi R, Yamamoto A, Kimura A, Aoki H. Gravimetric evidences for active faults around Mt. Ontake, central Japan: specifically for the hidden faulting of the 1984

Western Nagano Prefecture Earthquake. Journal of Physics of the Earth 1992; 40: 459–478.

[38] Kudo T, Kono Y. Relationship between distributions of shallow earthquakes and gradient of gravity anomaly field in southwest Japan. Zishin 2 1999; 52: 341–350 (in Japanese with English abstract).

[39] Yamamoto A. Gravity anomaly atlas of the Ishikari Plain and its vicinity, Hokkaido, Japan. Geophysical Bulletin of Hokkaido 2003; 66: 33–62 (in Japanese with English abstract).

[40] Elkins T A. The second derivative method of gravity interpretation. Geophysics 1951; 16: 29–50.

[41] Tsuboi C, Kato M. The first and second vertical derivatives of gravity. Journal of Physics of the Earth 1952; 1: 95–96.

[42] Bott M H P. A simple criterion for interpreting negative gravity anomalies. Geophysics 1962; 27: 376–381.

[43] ten Brink U S, Ben-Avarham Z, Bell R E, Hassouneh M, Coleman D F, Andreasen F, Tibor G, Coakley, B. Structure of the Dead Sea pull-apart basin from gravity analyses. Journal of Geophysical Research 1993; 98: 21877–21894.

[44] Miller H G, Singh V. Potential field tilt – a new concept for location of potential field sources. Journal of Applied Geophysics 1994; 32: 213–217.

[45] Cooper G R J, Cowan D R. Enhancing potential field data using filters based on the local phase. Computers and Geosciences 2006; 32: 1585–1591.

[46] Ma G. Edge detection of potential field data using improved local phase filter. Exploration Geophysics 2013; 44: 36–41.

[47] Wijns C, Perez C, Kowalezyk P. Theta map: edge detection in magnetic data. Geophysics 2005; 70: L39–L43.

[48] Li L, Huang D, Han L, Ma G. Optimized detection filters in the interpretation of potential field data. Exploration Geophysics 2014; 45: 171–176. doi:10.1071/EG13059.

[49] Ferreira F J F, de Souza J, de B e S Bongiolo A, de Castro L G. Enhancement of the total horizontal gradient of magnetic anomalies using the tilt angle. Geophysics 2013; 78: J33–J41.

[50] Zhang X, Yu P, Tang R, Xiang Y, Zhao C-J. Edge enhancement of potential field data using an enhanced tilt angle. Exploration Geophysics 2014; 46: 276–283. doi:10.1071/EG13104.

[51] Kusumoto S. Semi-automatic interpretation methods for extracting structural boundaries using gravity gradient tensors. Butsuri-Tansa 2016; 69: 53–64 (in Japanese with English abstract).

http://dx.doi.org/10.5772/64557

[52] Perdersen L B, Rasmussen T M. The gradient tensor of potential field anomalies: some implications on data collection and data processing of maps. Geophysics 1990; 55: 1558–1566.

[53] Beiki M, Pedersen L B. Eigenvector analysis of gravity gradient tensor to locate geologic bodies. Geophysics 2010; 75, I37–I49.

[54] Cevallos C, Kovac P, Lowe S J. Application of curvatures to airborne gravity gradient data in oil exploration. Geophysics 2013; 78: G81–G88.

[55] Cevallos C. Automatic generation of 3D geophysical models using curvatures derived from airborne gravity gradient data. Geophysics 2014; 79: G49–G58.

[56] Koenderink J J, van Doorn A J. Surface shape and curvature scales. Image and Vision Computing 1992; 10: 557–564.

[57] Robert A. Curvature attributes and their application to 3D interpreted horizons. First Break 2001; 19: 85–99.

[58] Beiki M, Analytic signals of gravity gradient tensor and their application to estimate source location. Geophysics 2010; 75: I59–I74.

[59] Sertcelik I, Kafadar O. Application of edge detection to potential field data using eigenvalue analysis of structure tensor. Journal of Applied Geophysics 2012; 84: 86–94.

[60] Zhou W, Du X, Li J. The limitation of curvature gravity gradient tensor for edge detection and a method for overcoming it. Journal of Applied Geophysics 2013; 98: 237–242.

[61] Orç B, Sertçelik I, Kafadar Ö, Selim H H. Structural interpretation of the Erzurum Basin, eastern Turkey, using curvature gravity gradient tensor and gravity inversion of basement relief. Journal of Applied Geophysics 2013; 88: 105–113.

[62] Yuan Y, Huang D, Yu Q, Li P. Edge detection of potential field data with improved structure tensor methods. Journal of Applied Geophysics 2014; 108: 35–42.

[63] Li X. Curvature of a geometric surface and curvature of gravity and magnetic anomalies. Geophysics 2015; 80: G15–G26.

[64] Thompson D T. EULDPH – a new technique for making computer assisted depth estimates from magnetic data. Geophysics 1982; 47: 31–37.

[65] Barongo J O. Euler's differential equation and the identification of the magnetic point-pole and point-dipole sources. Geophysics 1984; 49: 1549–1553.

[66] Reid A B, Allsop J M, Granser H, Millett A J, Somerton I W. Magnetic interpretation in three dimensions using Euler deconvolution. Geophysics 1990; 55: 80–91.

[67] Marson I, Klingele E E. Advantages of using the vertical gradient of gravity for 3-D interpretation. Geophysics 1993; 58: 1588–1595.

[68] Zhang C, Mushayandebvu M F, Reid A B, Fairhead J D, Odegrad M E. Euler deconvolution of gravity tensor gradient data. Geophysics 2000; 65: 512–520.

[69] Beiki M. TSVD analysis of Euler deconvolution to improve estimating magnetic source parameters: an example from the Asele area, Sweden. Journal of Applied Geophysics 2013; 90: 82–91.

[70] Kusumoto S. Estimation of dip angle of fault or structural boundary by eigenvectors of gravity gradient tensors. Butsuri-Tansa 2015; 68: 277–287 (in Japanese with English abstract).

[71] Komazawa M. Gravity grid database of Japan. ver. 2, Digital Geoscience Map P-2 [CD-ROM]. Tsukuba: Geological Survey of Japan; 2004.

[72] Research Group for Active Faults. The Active Faults in Japan: Sheet Maps and Inventories. Rev. ed. Tokyo: University of Tokyo Press; 1991. 437 p (in Japanese with English abstract).

[73] Kamata H. Volcanic and structural history of the Hohi volcanic zone, central Kyushu, Japan. Bulletin of Volcanology 1989; 51: 315–332.

[74] Komazawa M, Kamata H. The basement structure of the Hohi geothermal area obtained by gravimetric analysis in central-north Kyushu, Japan. Reports, Geological Survey of Japan 1985; 264: 305–333 (in Japanese).

[75] Kusumoto S, Fukuda Y, Takemoto S, Yusa Y. Three-dimensional subsurface structure in the eastern part of the Beppu-Shimabara Graben, Kyushu, Japan, as revealed by Gravimetric Data. Journal of the Geodetic Society of Japan 1996; 42: 167–181.

[76] Tsuboi C, Jitsukawa A, Tajima H. Gravity survey along the lines of precise levels throughout Japan by means of a Worden gravimeter. Bulletin of the Earthquake Research Institute, University of Tokyo 1956; Supplementary Volume IV, Part 8: 476–552.

[77] Itoh Y, Takemura K, Kamata H. History of basin formation and tectonic evolution at the termination of a large transcurrent fault system: deformation mode of central Kyushu, Japan. Tectonophysics 1998; 284: 135–150.

[78] Kusumoto S, Takemura K, Fukuda Y, Takemoto S. Restoration of the depression structure at the eastern part of central Kyushu, Japan, by means of the dislocation modeling. Tectonophysics 1999; 302: 287–296.

[79] Okada Y. Surface deformation due to shear and tensile faults in a half-space. Bulletin of Seismological Society of America 1985; 75: 1135–1154.

[80] Kusumoto S, Fukuda Y, Takemura K. A distinction technique between volcanic and tectonic depression structures based on the restoration modeling of gravity anomaly: a case study of the Hohi Volcanic Zone, central Kyushu, Japan. Journal of Volcanology and Geothermal Research 1999; 90: 183–189.

[81] Kamata H. Shishimuta caldera, the buried source of the Yabakei pyroclastic flow in the Hohi volcanic zone, Japan. Bulletin of Volcanology 1989; 51: 41–50.

[82] Kamata H, Danhara T, Yamashita T, Hoshizumi H, Hayashida A, Takemura K. Correlation of the Azuki Volcanic Ash of the Osaka Group and the Ku6C Volcanic Ash of the Kazusa Group to the Imaichi pyroclastic flow deposit in central Kyushu, Japan – a co-ignimbrite ash erupted from Shishimuta caldera. The Journal of the Geological Society of Japan 1994; 100: 848–866.

[83] Aramaki S. Hydrothermal determination of temperature and water pressure on the magma of Aira caldera, Japan. American Mineralogist 1971; 56: 1760–1768.

[84] Watanabe, K., 2010, Aso volcanoes, In: Sano, H. editor. Regional Geology of Japan, 8. Kyushu and Okinawa. Tokyo: Asakura; 2010. p. 267–271 (in Japanese).

[85] Kubotera A, Tajima H, Sumitomo N, Doi H, Izutsuya S. Gravity surveys on Aso and Kuju volcanic region, Kyushu district, Japan. Bulletin of the Earthquake Research Institute, University of Tokyo 1969; 47: 215–225.

[86] Yokoyama I. Volcanic caldera and meteorite craters with the special relation to their gravity anomalies. Journal of the Faculty of Science, Hokkaido University Ser. 7 1963; 2: 37–47.

[87] Komazawa M. Gravimetric analysis of Aso volcanoes and its interpretation, Journal of the Geodetic Society of Japan 1995; 41: 17–45.

[88] Rodrigues R S, de Castro D L, dos Reis J A Jr. Characterization of the Potiguar rift structure based on Euler deconvolution. Revista Brasileira de Geofisica 2014; 32: 109–121.

[89] Itoh Y, Kusumoto S, Takemura K. Evolutionary process of the Beppu Bay in central Kyushu, Japan: a quantitative study of basin-forming process under the control of plate convergence modes. Earth, Planets and Space 2014; 66: 74. doi:10.1186/1880-5981-66-74.

Chapter 6

Investigating Source Conditions and Controlling Parameters of Explosive Eruptions: Some Experimental-Observational-Modelling Case Studies

Fabio Dioguardi, Tobias Dürig,
Samantha L. Engwell, Magnus T. Gudmundsson and
Susan C. Loughlin

Additional information is available at the end of the chapter

http://dx.doi.org/10.5772/63422

Abstract

Explosive volcanic eruptions are complex systems that can generate a variety of hazardous phenomena, for example, the injection of volcanic ash into the atmosphere or the generation of pyroclastic density currents. Explosive eruptions occur when a turbulent multiphase mixture, initially predominantly composedf of fragmented magma and gases, is injected from the volcanic vent into the atmosphere. For plume modelling purposes, a specific volcanic eruption scenario based on eruption type, style or magnitude is strictly linked to magmatic and vent conditions, despite the subsequent evolution of the plume being influenced by the interaction of the erupted material with the atmosphere. In this chapter, different methodologies for investigating eruptive source conditions and the subsequent evolution of the eruptive plumes are presented. The methodologies range from observational techniques to large-scale experiments and numerical models. Results confirm the relevance of measuring and observing source conditions, as such studies can improve predictions of the hazards of eruptive columns. The results also demonstrate the need for fundamental future research specifically tailored to answer some of the still open questions: the effect of unsteady flow conditions at the source on the eruptive column dynamics and the interaction between a convective plume and wind.

Keywords: explosive volcanic eruptions, convective plumes, eruption monitoring, large-scale experiments, numerical models

1. Introduction

The disruptive eruption of Eyjafjallajökull volcano in 2010 was a catalyst that has driven research agendas across disciplines from aeronautical engineering and satellite earth observation to social science and volcanology. In particular, there has been considerable focus on better observing and constraining the parameters of the 'volcanic source', which are used to initialise the flow field solution of most ash dispersal models used by Volcanic Ash Advisory Centres (e.g. [1, 2]). The volcanic source for ash dispersal models is generally a volcanic plume that is simulated with simplified models for obtaining plume properties (solid particles' mass/volumetric concentration, plume height and width, etc.). The plume evolution depends both on flow properties at the vent ('mass eruption rate' MER, which is the mass of ejected material per unit time and particles' properties like grain size distribution, density, shape and mass/volumetric concentration) and atmospheric conditions (e.g. wind and moisture vertical profile). Because of the considerable challenges inherent in measuring MER, it is usually indirectly inferred by applying empirical relationships or simplified models to measurements of plume height (e.g. [3, 4]). Such empirical models make a number of assumptions and are intended to simplify the system to support operational ash cloud forecasting. For example, for any given plume height, the mass eruption rate will vary depending on eruption type and meteorology [5, 6] giving rise to errors of up to a factor of 4 [3]). In some meteorological circumstances errors may be even larger if, for example, deep moist convection resulting in much larger plume heights than expected (e.g. [6–8]). In addition, there is an urgent need to better understand the controls on eruption column collapse that can generate pyroclastic density currents.

Developments in modern technology allow both qualitative and quantitative time-series observation of volcanic plumes (e.g. plume height, temperature, etc.), enabling variation with time to be observed in detail (e.g. [9–12]). Due to the non-steady nature of the process, monitoring dynamic source conditions (e.g. MER) at vent remains a difficult task. Here we use the recent innovations of Dürig et al. [13, 14] to highlight ways in which emerging techniques can be used to better understand source processes. Dürig et al. [13, 14] established a means of quantifying the mass eruption rate of individual explosive pulses at the vent based on high-resolution imagery (optical and thermal) of the Eyjafjallajökull eruption. Their technique can be applied in near real-time to monitor the changing mass eruption rate. They embraced the complexity of the eruption by studying the pulsatory explosive source in detail Interestingly, they found that simple 1D models predict similar plume heights, even for a pulsatory eruption.

Experimental studies are a means of controlling conditions to isolate and investigate particular parameters and/or processes. We summarise a series of large-scale experiments of explosive eruptions, which have enabled identification of new parameters and have quantified controlling factors in changing regimes between eruption types (e.g. collapsing columns and convective plume). We propose the next steps in experimental volcanology including the representation of a pulsatory source and interaction with wind.

Finally, we summarise recent advances in plume rise modelling, in particular the recent model intercomparison study. These studies show that a key weakness in modelling volcanic plumes, is the treatment of the effects of the wind on the rising plume. Finally, we highlight how such

http://dx.doi.org/10.5772/63422

weaknesses may be addressed using a combination of numerical modelling and experimental studies.

Better understanding of the source conditions and how these affect the development and evolution of eruptive plumes is essential to reduce uncertainties in ash dispersion modelling and facilitates forecasting of ash fall and pyroclastic density current hazards. In this chapter, we propose that a combination of improved observations, experiments and modelling will initiate a step change in the way scientists can contribute to risk reduction in near real-time. We present three case studies and their results to demonstrate both the outstanding issues and potential solutions.

2. Insights from observations: case study 1—determination of the mass eruption rate of a pulsating eruption (Eyjafjallajökull 2010)

In May 2010, Martin Rietze, a bold German photographer climbed to the top of the Icelandic volcano Eyjafjallajökull on three subsequent days and managed to mount his camera a mere 850 m from the vent, before taking cover behind a large rock, which Icelanders call "Goðasteinn" (God's rock). Fortunately, he and his camera survived these risky missions, providing the volcanological community with close-up footage of explosive activity at the vent. The Eyjafjallajökull eruption 2010, which received broad international attention because of the disruptive consequences on aviation in large parts of Europe, initiated with "wet" phreatomagmatic explosive activity from 14th to 18th April [15]. After a short period of significantly decreased discharge rate and mixed effusive-explosive activity, on 5th May the eruption entered a second explosive stage, which was "dry" and purely magmatic [15, 16]. This stage was characterised by repetitive closely timed explosions, each resulting in the release of discrete ash pulses [10, 17]. The repetitive explosions continued for over 2 weeks with a decline in eruptive activity between 17 and 21 May and the end of continuous eruptive activity recorded on 22nd May [15]. From a distance, and particularly downwind, the rising plume appeared quasi-steady and sustained throughout this stage of the eruption. Measurements made by a thermal camera mounted at a distance of 8.3 km from the vent on 4th May revealed average initial pulse velocities of 45 m s^{-1} and average pulsation intervals t_{pulse} of ~20 s (see **Table 1** for Notation), meaning that on average three pulses occurred every minute [17]. However, the ash pulses within the footage taken 4, 5 and 6 days later showed an increase in the average initial vertical velocities to 65 m s^{-1} and—even more prominent—a significant drop of the average pulsation interval t_{pulse} to 4.2 s, coinciding with the significantly increased overall mass flux [13]. Furthermore, these video analyses revealed that two types of explosive pulses could be discriminated by their observed diameter at the vent exit: 'strong' pulses, featuring diameter at a vent of greater than 50 m and 'weaker' pulses, characterised by a diameter at the vent exit of less than 50 m [13]. The two types also significantly differed in their rate of occurrence: the time between weaker pulses (t_{pulse}) was on average 4.7 s and between strong pulses on average of 37.5 s [13]. Studies of ejecta trajectories enabled characterization of the vent as a funnel with a depth of 51±7 m, an inner diameter of 8–15 m and an outer diameter (8–10 May) of 65±2 m [14]. The inner vent is the surface from which the column starts to expand

(intersection point of ballistic profiles) but is not the same as the site of magma fragmentation, which is probably deeper. These studies indicated that the "weaker" pulses can be seen as punctuating jets that are sourced from areas of only ~8 m diameter in the 'inner vent', whereas the 'stronger' pulses occupy a greater area of the inner vent [14].

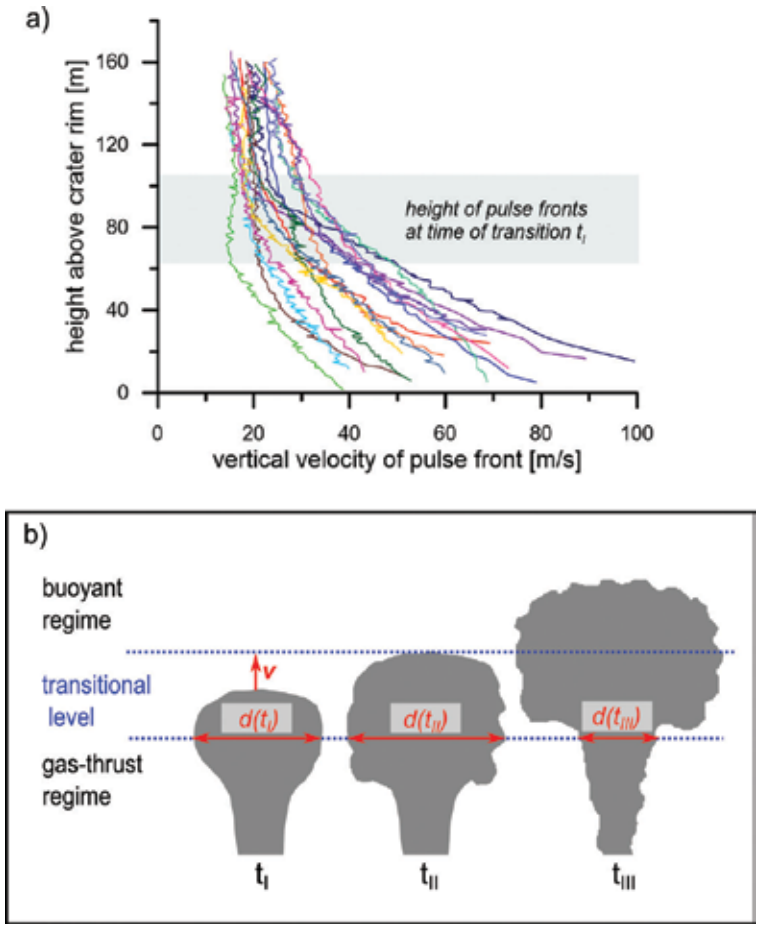

Figure 1. Temporal evolution of an ash pulse. (**a**) Vertical velocities of 16 pulses of the Eyjafjallajökull 2010 eruption. When entering the transitional level between gas-thrust and buoyant regime, many velocity curves show a clear "kink," a phenomenon that has previously been reported for other eruptions, e.g. Patrick et al. [19] and Marchetti et al. [20]. The moment of change in dynamic behaviour is defined as t_I. (**b**) The elevation of the maximum pulse width $d(t_I)$ determines the position of the lower boundary of the transitional level, which is used as a reference plane for estimating the mass flux by the pulse velocity-derived model (PVDM). The upper boundary is defined by the elevation of the pulse front at the moment t_{II}, when the pulse width $d(t)$ shows its maximum extension. After that, moment $d(t)$ decreases. As a cut-off criterion, the end of the ash transport through the reference plane is defined by the moment t_{III}, when the width has dropped to $d(t_{III}) = d(t_I)/e^{0.5}$. Copyright Dürig et al. [13], published by SpringerOpen.

Based on these findings, a pulse velocity-derived model (PVDM) was developed [13]. This model determines the mass flux contribution of individual ash pulses analysed in the videos in order to estimate the overall MER. The starting point of the PVDM is the temporal evolution

http://dx.doi.org/10.5772/63422

of individual ash bursts, which can be summarised as follows: a pulse exits the vent as a momentum-driven negatively buoyant jet, which expands during its rise due to entrainment of ambient air, before finally reaching a transitional level. At this level, buoyancy takes over as the dominant uplift mechanism, generating a convecting plume as the bulk density of the gas-particle mixture making up the pulse approximates the density of ambient air (e.g. Sparks [18]). As reported for other eruptions [19, 20], the videos of the Eyjafjallajökull eruption showed that the vertical velocities of the pulse fronts dropped with height until entering the level of transition. At this point, the vertical velocity curves are characterised by a distinct kink (see **Figure 1a**), showing a constant uplift velocity within the subsequent buoyancy-driven stage.

Change in the vertical velocity profile can be used to identify the moment of transition into the buoyant stage, t_I. The maximum pulse width $d(t_I)$ defines the lower boundary of the transitional level (see **Figure 1b**). With ongoing pulse evolution, $d(t)$ increases until it reaches a maximum $d(t_{II})$. The upper boundary of the transitional level is defined by the elevation of the pulse tip at t_{II}. Following this key assumption, the density of the gas-solid mixture ρ in the zone of transition can be approximated to be equal to that of the surrounding air. With this parameter known, the volume fraction C of solids within a pulse made of a mixture of gas (density ρ_g) and tephra (density ρ_t) can be computed by:

$$C = \frac{\rho - \rho_g}{\rho_t - \rho_g} \tag{1}$$

The mass flux $Q(t_I)$ of a pulse can be approximated as that of a homogenous gas-particle mixture with a velocity v through a cylindrical cross-section of the diameter $d(t_I)$.

$$Q(t_I) = \rho_t \cdot C \cdot \left(\frac{d(t_I)}{2} \right)^2 \cdot \pi \cdot v \tag{2}$$

while the vertical velocity v can be estimated by tracking the pulse tip between t_I and t_{II}, the temporal change in diameter $d(t)$ complicates the calculation of the time-dependent mass flux $Q(t)$. Dürig et al. [13] suggested bracketing the mass flux by calculating two end-members, representing the range of possible values. Therefore, they specified the duration τ for which the mass flux has decreased by a factor of $1/e$, with $\tau = t_I - t_{III}$, where t_{III} is the moment when the pulse diameter at the lower transitional boundary has decreased to $d(t_I)/e^{0.5}$ (see **Figure 1b**). The lower and the upper limit of the mass flux of tephra, Q_{min} and Q_{max}, can then be estimated by:

$$Q_{min} = \frac{\tau}{t_{pulse}} \cdot Q(t_I) \cdot (1 - 1/e) \tag{3}$$

$$Q_{max} = \frac{\tau}{t_{pulse}} \cdot Q(t_I) \tag{4}$$

The PVDM provided MER estimates of 2.2–3.5·10^4 kg s^{-1} for the period studied [13]. These values have been shown to be in good agreement to those resulting from simple 1D plume models and empirical relationships fed by plume height data observed for 8–10 May (2.9–3.3 km above vent). For example, the model of Wilson and Walker [21] suggests 2.3–3.8·10^4 kg s^{-1}, Sparks et al. [5] estimates 2.2–3.5·10^4 kg s^{-1} and Mastin et al. [3] predicts 1.2–2.1·10^4 kg s^{-1}. Gudmundsson et al. [15], who calibrated the Mastin model for Eyjafjallajökull 2010 using a scaling factor adjusted to mapped fallout, suggest MER values of 1.9–3.3·10^4 kg s^{-1} for 8–10 May.

Interestingly, according to the results of the PVDM, the greater part (78%) of the total mass flux on 8–10 May was provided by the frequent pulses of the "weaker" type, despite the fact that the less frequent "strong" pulses each transported, on average, 2.3 times more mass of tephra than a 'weak' pulse. These findings underline the need to consider the whole spectrum of explosive pulses when applying the PVDM. The good agreement between the models can be seen as an indication that the "simple" 1D models and empirical relations work also for pulsating eruptions—and that near-field observation based models, such as the PVDM, provide a possibility to quickly estimate the overall mass flux in near real-time.

The application of this new observational technique helped researchers to better constrain source conditions, in particular to better estimate the mass of ejected particles and MER even in unsteady conditions. The next challenge is to apply this method in near-real-time.

Due to the innate complexity of the phenomena taking place during explosive eruptions, it is hard both to monitor all the aspects of the multiphase flow at the source (e.g. particle concentration) and to relate these flow field variables to the observable dynamics. For this reason, large-scale experiments aimed at reproducing constrained eruptive regimes and defining scaling laws between source conditions and the erupted plume represent a powerful tool towards a better and more comprehensive understanding of explosive eruptions.

3. Insights from large-scale experiments on eruptive columns: case study 2—source conditions (single pulse of variable duration) and eruptive regime

3.1. Overview of experimental apparatus and runs

The highly complex nature of the phenomena that occur during explosive eruptions means that prior to early 2000 experimental research in volcanology was limited to small laboratory scale experiments that did not reach a scale comparable to natural phenomena [22]. In this section, the results of the first large-scale experiments carried out between 2005 and 2009 by researchers from the University of Bari (Italy) and the University of Würzburg (Germany) are summarized [23–26]. In particular, relationships between eruptive regimes and source

http://dx.doi.org/10.5772/63422

conditions obtained by experiments and their application to hypothetical natural-scale eruptions are presented. In the following years, the importance of achieving large-scale conditions when reproducing the processes that take place during explosive has been realised. Following the pioneering results described here, new large-scale experimental facilities were developed [27, 28]. One of the reasons for this large scale is that, as gas-particle coupling is influenced by the shape and size of volcanic particles [23], the dimension of the experimental facility needs to be sufficiently large to allow the use of real volcanic particles sampled from tephra deposits. The other reason is that, in order for the reproduced volcanic flows (conduit, eruptive column, pyroclastic flow) to be comparable to natural phenomena from a fluid dynamic point of view, their Reynolds number (*Re*) needs to be of a similar order of magnitude or at least scalable. In turn, *Re* depends directly on a characteristic dimension and velocity of the flow, thus the larger the setup and the faster the generated flow, the closer *Re* is to that of natural flows.

The experimental apparatus used in the modelling is fully described in recent papers [23–26] and schematized in **Figure 2**.

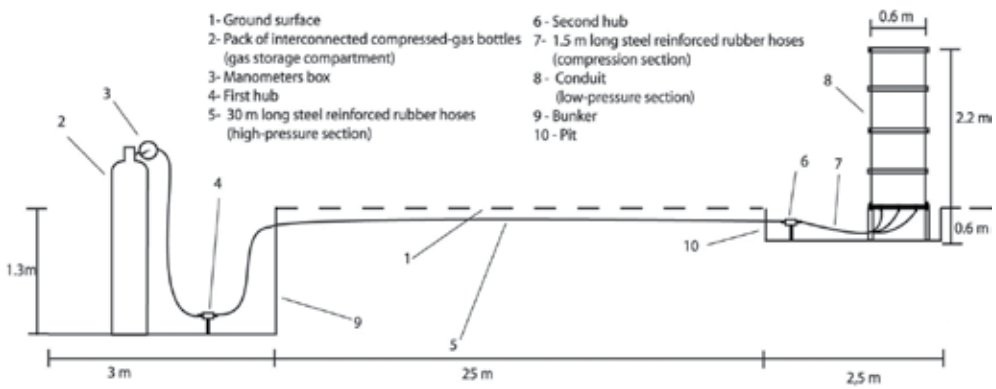

Figure 2. Schematic representation of the experimental apparatus. Copyright 2007 by the American Geophysical Union. Reprinted by permission of John Wiley & Sons, Inc.

Briefly, the model setup was designed to achieve coupling between an applied mechanical energy and ash and lapilli particles in a vertical conduit. Both cold and hot (up to 300 °C) ash and lapilli were used to investigate the role of temperature in plume dynamics. Mechanical energy was provided by expanding overpressured gases in rubber tubes connected to the conduit; when expanding, the gas coupled with the particles in the conduit, generating a multiphase flow. The time scale of mechanical energy release was forced to be similar to that of the mechanical energy release during magma fragmentation experiments [29, 30]. Accounting for the link between gas and particle acceleration with magma fragmentation in the conduit in real eruptions [24]. Depending on experimental conditions, this multiphase flow produced different eruptive regimes: collapsing columns (generating pyroclastic density currents), convective plumes, radially expanding jets and transitional regimes between these extremes

(**Figure 3**). The experimental facility allowed complete control of eruptive regime. Specifically, the ratio between the total expansion energy E_{tot} (given by the product of the driving pressure ΔP and the gas volume W) and the particle mass load m, known as specific mechanical energy (SME) [23], was crucial in determining eruptive regime. After the first experimental runs, threshold values for this parameter were obtained: when SME > 2.6 kJ kg^{-1} a dilute column evolving as a convective plume was generated (**Figure 3a**); in comparison, when SME < 1.5 kJ kg^{-1} a dense column was reproduced which, depending on conduit exit overpressure, could evolve either as a collapsing column or an overpressured radially expanding jet (**Figure 3b** and **c**). Transitional behaviours were reproduced for intermediate values of SME (**Figure 3d**).

Figure 3. The four different eruptive styles reproduced in the experiments. (**a**) Convective plume. (**b**) Collapsing fountain generating a pyroclastic density current. (**c**) Overpressured radially expanding jet. (**d**) Transitional style between convective plume and collapsing column.

3.2. Source conditions controlling the evolution of eruptive columns

While SME is a fundamental parameter controlling the eruptive regime of the experiments, due to its functional form it does not have a practical use for forecasting or even describing real eruptive regimes. For this purpose, parameters strictly linked to source conditions at vent (conduit exit) that can be reasonably hypothesised for future eruptions and/or measured during ongoing eruptions (e.g. exit velocity) are of fundamental importance.

http://dx.doi.org/10.5772/63422

Discriminating between different eruptive regimes is not merely a scientific exercise but has important implications in hazard assessment of explosive eruptions, as each style is responsible for particular hazards (e.g. the injection of fine ash into the atmosphere by plumes or the formation of pyroclastic density currents from collapsing columns). Thus, source parameters have been investigated using measured experimental data.

From data recorded during the experiments, both new parameters and those that are already used in fluid dynamics and volcanological literature have been measured. In particular, three parameters were identified as being crucial for describing the activity observed during an eruption. The first parameter was newly defined for discriminating between dilute (**Figure 3a**) and dense collapsing columns (**Figure 3b–d**). It is well established that the formation of convective plumes is favoured by high exit velocities U_0, low particle concentration C_0 and small vent radius r_0 and vice versa for collapsing columns [24, 31]. These variables have been combined to obtain the following parameter:

$$\Omega = \frac{2U_0}{r_0 C_0} \tag{5}$$

Where 2 derives from the ratio between column surface area and volume, which is $2/r_0$ for a cylinder. This ratio is fundamental for the entrainment of external air into the column. In the experiments, U_0 was measured by video analysis, whereas C_0 was inferred assuming a complete dilution of the volume of ash in the conduit. Ω is dimensionally analogous to vorticity (s^{-1}), thus it can be seen as a measure of turbulence intensity in the column. In its functional form, the higher Ω (the more intense the turbulence), the more likely a convective plume will be generated. This is not surprising, as turbulence enhances air entrainment into the column, the main process leading to the formation of a convective plume [32].

The second parameter was defined for discriminating between vertically evolving columns (both plumes and collapsing columns) and radially expanding jets. Radially expanding jets are typical of phreatomagmatic eruptions, where magma fragmentation occurs on interaction with groundwater at shallow levels in the crust [33]. The short distance between the location at which wet fragmentation typically occurs and conduit exit causes the eruptive mixture to exit from the vent with a static overpressure in respect to atmosphere [34, 35]. Thus, the eruptive mixture expands in all directions as it equilibrates to atmospheric pressure and dilutes pyroclastic density currents form. This process has been reproduced in experiments by shortening the conduit. From these considerations, a regime parameter Γ designed for discriminating between over-pressured and pressure-balanced eruptive columns should combine static exit overpressure $P_{over,0}$ and dynamic pressure $P_{dyn,0}$ (which favours vertical columns) at the source:

$$\Gamma = \frac{P_{,0}}{P_{dyn,0}} = \frac{P_{st,0} - P_{atm}}{P_{dyn,0}} \tag{6}$$

where $P_{st,0}$ is the static pressure at conduit exit, which is extrapolated from the static pressure measured by the pressure sensor positioned close to the experimental conduit exit; $P_{dyn,0}$ is half of the product between mixture density (a function of C_0) and the squared exit velocity. By its definition, the higher Γ, the more likely a radially expanding jet is generated.

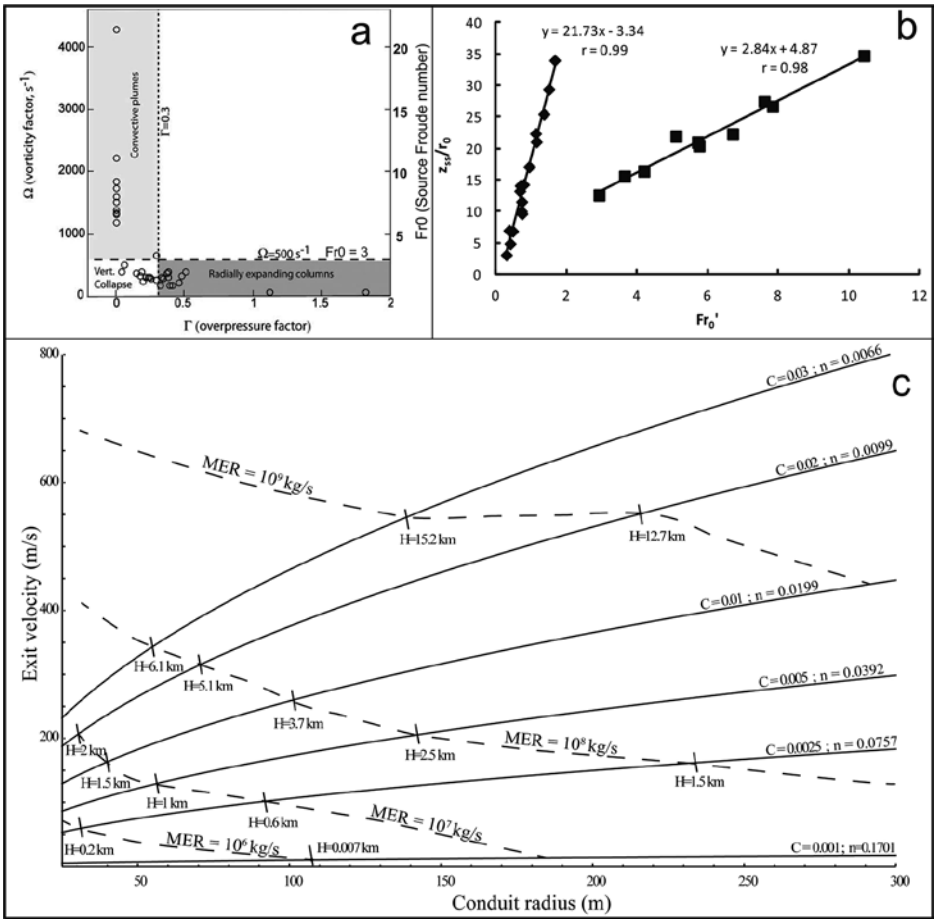

Figure 4. (**a**) Regime stability field of experiments as a function of Fr_0', Γ and Ω. Small white area corresponds to the field of vertical collapse; light grey area is the convective plume stability field, whereas dark grey area corresponds to radial expanding columns (**b**) z_{ss} vs. Fr_0' diagram; diamonds and square represent dense-collapsing columns and dilute convective plumes, respectively. Fitting lines are also traced. Note that data points here are less numerous than in **Figure 4a**, as it was not possible to measure z_{ss} for all the experiments. (**c**) Regime diagram showing exit velocity (U_0) vs. conduit radius (r_0) for real-scale eruptions. Solid lines represent different values of particle volumetric concentration C_0 (or the corresponding mass fraction n) at source; dashed lines represent different values of mass eruption rate (MER). "Bulletin of Volcanology, Volcanic jets, plumes, and collapsing fountains: evidence from large-scale experiments, with particular emphasis on the entrainment rate, 76, 2014, 834, Dellino P., et al., © Springer-Verlag Berlin Heidelberg 2014. With permission of Springer"

The third parameter, the densimetric Froude number Fr_0', originates from published literature on the fluid dynamics of jets and fountains:

http://dx.doi.org/10.5772/63422

$$Fr_0' = \frac{U_0}{\sqrt{g_0' r_0}} = \frac{1}{\sqrt{Ri}} \quad (7)$$

Where g_0' is the reduced gravity, a function of gravitational acceleration and density contrast between the flow and air at the source; Ri is the Richardson number. Fr_0' has been used in fluid dynamic literature as the parameter controlling the regime of flows issuing from circular nozzles [36, 37] and, later, in volcanology for similar purposes [38, 39]. Fr_0' was also found to influence the entrainment rate in the jet [40].

Ω, Γ and Fr_0' have been evaluated from data recorded during the experimental runs and their threshold values discriminating different eruptive regimes were inferred by plotting their values on charts. In **Figure 4a**, an experimental regime diagram is displayed: the two y-axes represent Ω and Fr_0', whereas Γ is on the x-axis. Lines representing the threshold values are also traced. In particular, the experiments showed that when $\Omega > 500$ s^{-1} a convective plume forms, otherwise a collapsing column or radially expanding jets develops. The stability fields of these last two eruptive regimes are divided by the line $\Gamma = 0.3$, with radially expanding jets lying in the area $\Gamma > 0.3$. Finally, the threshold value for Fr_0' is also reported (3), which acts similarly to $\Omega = 500$ s^{-1}, with convective plumes forming when $Fr_0' > 3$. This last threshold value has been obtained in a slightly different way. In **Figure 4b**, experimental results are plotted in a diagram z_{ss}/r_0 vs. Fr_0', where z_{ss} is the steady state height of the column [26, 41]; squares and diamonds represent convective plumes and collapsing columns, respectively. In agreement with the fluid dynamics literature of jets [37, 42], the two types of experiments follow very different linear trends, and a threshold value of $Fr_0' = 3$ can be identified.

These findings allowed the production of regime diagrams for hypothetical real eruptions [26]. One example is shown in **Figure 4c**, in which solid lines represent different values of particle volumetric concentration C_0 (or the equivalent solids' mass fractions n) at the threshold condition $Fr_0' = 3$. For each line, the area above it is the plume stability field, while the area below it represents the collapsing column stability field. The dashed lines represent different values of source mass eruption rate (MER).

The regime diagram agrees well with volcanological theory and observations. Given a conduit radius and fixed a source particle volume fraction, the higher the exit velocity, the more likely the formation of a convective plume [43]. The collapsing column stability field expands as source particle volumetric concentration and conduit radius increase. Furthermore, this regime diagram is in very good agreement with other diagrams obtained from numerical simulations [26, 38–40], proving that both experiments and models are valuable tools for gaining insights into the dynamics of these complex phenomena.

Results show how eruptive regimes are strongly controlled by source conditions. This is not surprising: in particular, the influence of the source Froude number on eruptive column conditions agrees very well with classical fluid dynamic theory of jet and plumes issuing from circular nozzles. Large-scale experiments confirm that applying such concepts to eruptive columns (for example, for computing the trajectory of a convective plume) is a good approximation and that experiments scale well with real eruptions.

3.3. The role of air entrainment in eruptive dynamics

The generation, regime and evolution of an eruptive column are not only controlled by source conditions but also by other fundamental processes (gas condensation, entrainment, particle segregation, etc.). Among these, entrainment of external air into the eruptive column by the action of turbulent eddies plays a crucial role [32, 44]. Once entrained air is in contact with hot gases and volcanic particles in the eruptive mixture, it heats and expands, reducing the column's bulk density and contributing to its radial expansion and ascent. This process is particularly important in the dynamics of convective plumes. The concept of entrainment was been formalised by Morton et al. [32], who introduced entrainment velocity in their simplified steady 1D model of buoyant plumes. Entrainment is a process linked to turbulence and is thus inherently three-dimensional (3D) and unsteady. For this reason, entrainment has to be parametrized in order for it to be taken into account in simplified steady 1D models. Entrainment velocity is defined as the volume flow rate per unit area of external air entering into the plume and is directly proportional to plume vertical velocity. The constant of proportionality is the so-called entrainment coefficient α.

The entrainment coefficient appears explicitly in the mass and energy conservation equations of 1D plume models. These models are widely employed in volcanology, in particular for initializing ash dispersal simulations [2, 45] or, by inversion, for estimating source conditions from observations (e.g. [4]). The importance of an accurate estimate of α is therefore evident. Fortunately, there is substantial agreement on the value of α, with values of about 0.09–0.1 usually considered to be reliable [37, 40, 44]. Recently, some authors introduced variable entrainment coefficient laws, with entrainment being a function of Froude number (thus of density contrast between plume and atmosphere) and complex height-dependent coefficients [39, 40]. The dependency of α on density contrast is not surprising: it is well established that the higher the density contrast, the lower the entrainment [46]. Thus, the use of variable entrainment coefficients allows more realistic simulations of convective plumes.

This is confirmed by large-scale experiments. A method has been devised that, from analysis of the spreading rate of experimental eruptive columns, allows the quantification of entrainment velocity [26] and, from measurements of plume vertical velocity, α. For hot dilute convective plumes (**Figure 3a**), an average value of 0.11 was determined, in agreement with values reported in the volcanological literature. Interestingly, α has been found to vary with experimental eruptive regime: average values of 0.06 for cold plumes and transitional columns (**Figure 3d**) were calculated (which agree with the values of pure jets in fluid dynamics [36, 37, 40]), whereas for collapsing columns (**Figure 3b**) α was always negligible. A collapsing column can thus be considered as an incompressible fluid, whose trajectory is completely described by the Bernoulli equation. This approximation enables the maximum height reached by a collapsing column to be obtained from source conditions (bulk density and velocity) and is a measure of potential energy that is converted to kinetic energy at collapse. From these considerations, it is possible to infer initial and boundary conditions of pyroclastic flows, starting from source conditions of collapsing columns.

Large-scale experiments confirmed the importance of entrainment coefficient not only in the dynamics of convective plumes but also in the generation of a specific type of explosive

eruption. As aforementioned, a number of other parameters play a role, especially in convective plume dynamics. The relative importance of different parameters, particularly when applying 1D numerical model to simulate volcanic plumes, is further discussed in Section 4.

3.4. Future perspectives

While these experiments provided key insights into important parameters controlling the eruptive regime, their design did not allow to investigate other fundamental processes controlling the evolution of eruptive columns. In particular, the experiments were characterised by a single pulse, although of variable duration, of ejected eruptive mixture. Section 2 has stressed the importance of taking into account other possible flow patterns at the source, like pulsating mass flux, and a new method for quantifying the mass eruption rates of eruptions characterised by a pulsating source has been presented. A verification of this model using large-scale experiments would represent a further necessary step, also in the view of finding empirical relationships between eruptive column characteristics (e.g. height) and pulsating source properties.

Furthermore, these experiments were not designed for studying the interaction between convective plumes and wind. Wind plays a major role in controlling the convective plume trajectory [4, 39, 47–51] for two reasons: (1) it enhances air entrainment, by the addition of a wind-induced tangential component to the already mentioned radial one and (2) it bends the plume trajectory (hence affecting plume height), especially of weak plumes. As plume height is influenced by the presence of wind and is used for inferring the source MER, it is evident how wind effects should not be neglected, in particular for weak plumes. New experiments specifically designed for investigating plume-wind interactions would be of fundamental importance, especially for assessing the wind entrainment rate, which is currently the most uncertain parameter in simplified models of bent-over plumes.

4. Insights from modelling: case study 3—results from sensitivity analyses of numerical plume models

As with many other physical phenomena, numerical models have been employed to understand the processes that occur during explosive volcanic eruptions (a range of models can be found on the open access platform VHuB [52]). Specifically, a number of models have been developed to simulate plume rise into the atmosphere, with such models commonly used to determine appropriate input parameters for ash dispersion models. Two types of model exist, one-dimensional integral models, which evaluate plume rise along a centre line, solving equations for conservation of mass, momentum and thermal energy along that line (e.g. Plumeria: Mastin [6]; PlumeRise: Woodhouse et al. [49]; PlumeMom: de' Michieli Vitturi [53]), and 3D models, which account for more complex interactions between the rising plume and the atmosphere (e.g. ATHAM: Herzog et al. [54]; ASHEE: Cerminara et al. [55]). One-dimensional models are often used in an operational sense in the event of an eruption because they are quick to employ and, due to the simplicity of the models they require less detailed

knowledge of, for example, atmospheric conditions. However, the simplicity of these models means that establishing important plume dynamics, and characteristics, for example the neutral buoyancy height, and the behaviour of the plume above the height of neutral buoyancy is not possible.

As mentioned above, one-dimensional numerical models are commonly used to estimate the maximum plume height and the mass flux at this height. Inputs for these models include atmospheric conditions (temperature, density and pressure with height), initial vent radius, eruption velocity and temperature (which together describe eruption mass flux), and particle characteristics (grain size, particle density and drag coefficient and the settling law to be employed). Further key parameters are those that describe entrainment of ambient air into the plume, both by simple turbulent entrainment and by interaction with wind as mentioned above in Section 3.3.

Following the ash dispersion model intercomparison study [2], Costa et al. [45] led a plume model intercomparison study to identify key differences between plume models. The intercomparison study involved 13 models: 9 one-dimensional and 4 three-dimensional models. Each model was applied to a bent-over plume (based on the Shinmoedake eruption of 2011) and a vertical plume (based on the climatic eruption of Pinatubo 1991) example. The aim of the exercise was to determine the cases in which the different models perform best and to highlight areas for future research. Results from the one-dimensional models were consistent, unsurprising given that all of the models are based on the mathematical description of turbulent buoyant plumes by Morton et al. [32], and were also largely consistent with results from three-dimensional models. While there are discrepancies on a local scale between 1D and 3D models for the vertical plume example, predicted plume heights are similar, highlighting the utility of 1D models for operational means [45]. The greatest discrepancy in results occurred when weak plumes erupting into a crosswind were modelled, with a 20% difference in modelled plume height results.

A key result from the exercise concerned the treatment of entrainment by the models. As described above, interaction between a volcanic plume and ambient wind leads to enhanced entrainment of air, and horizontal momentum, plume bending and a decrease in the maximum plume height for a given mass eruption rate [47]. Within the models, the effect of wind on entrainment is described by:

$$U_{\epsilon} = \alpha \left| U - V cos\vartheta \right| + \beta \left| V sin\vartheta \right| \tag{8}$$

Where ϑ is the angle between plume centreline and the horizon, $\alpha \left| U - V\, cos\vartheta \right|$ describes the radial entrainment minus the amount swept tangentially along the plume margins, $\beta \left| V\, sin\vartheta \right|$; describes the entrainment due to wind, α describes the radial entrainment coefficient and β is the wind entrainment coefficient [47, 56]. There is substantial agreement among the different bent-over plume models on combining radial and tangential entrainment components in this linear way, but other nonlinear combination have also been proposed [57]. As mentioned above, the radial entrainment coefficient is well defined in the literature. Laboratory experi-

http://dx.doi.org/10.5772/63422

ments [56] have shown the wind entrainment coefficient to be near unity, but this value is much less well constrained than for radial entrainment; in fact, its value varies from about 0.5 to 1 in the literature [4, 39, 47–51]. Results from the intercomparison exercise indicate that 1D models fail to reproduce entrainment for large plumes, despite providing reasonable estimates of column height. Results from a number of recent studies highlight the importance of entrainment, and particularly that associated with wind, in controlling behaviour of volcanic plumes, for example whether plume collapse occurs or not [26, 39, 48, 49, 51, 57]. Modelling studies have also shown that in some cases, increase in entrainment associated with eruption into wind leads to a plume that would otherwise collapse to become buoyant.

A number of the studies that contributed to the intercomparison exercise used formal sensitivity techniques to evaluate the performance of the models, and specifically the manner by which uncertainties in input parameters affect model output uncertainties. Sensitivity analysis is used to show how variation in model output can be attributed to different sources of uncertainty in model inputs. Such analysis enables key model parameters to be identified, such that they can be studied with greater depth than those parameters that have little influence on model results. Application of this technique requires identification of an appropriate probability density distribution for each input parameter. The model is run a number of times, with each simulation sampling the input distributions such that the entire parameter space is sampled, and model response to varying input parameters can be statistically evaluated. Application of sensitivity analysis by de' Michieli Vitturi et al. [58] and Woodhouse et al. [50] to one-dimensional plume models highlight the dependence of model results not only on source mass flow rate (described by exit velocity, temperature and water fraction), but also the input entrainment assumptions, and in particular the entrainment associated with wind.

5. Conclusive remarks

Results from experiments, observations and models highlight the fundamental role played by source conditions at the vent in the dynamics of explosive eruptions and dispersion of ash clouds. Large-scale experiment results demonstrate a quantitative link between eruptive characteristics and source conditions, by means of new (e.g. vorticity and overpressure factor) and well-established parameters in the fluid dynamics of jets and fountains (Froude number). Recent visual observations of the Eyjafjallajökull eruption, on the other hand, revealed the potential for pulsating behaviour of mass flux at the source of weak sustained eruptions. A new model for measuring MER in real time based on video analysis has been developed. Outcomes from the application of this model confirm that unsteadiness significantly influences the mass eruption rate, and in particular, the evaluation of the total mass of particles injected into the atmosphere. In fact, it has been shown that measurement of the MER considering the most intense pulse as representative of the whole eruption would have resulted in an overestimate by about 50 %. [13]. This has important implications for monitoring of explosive eruptions: monitoring tools should be able to provide accurate time-dependent measurements of source condition, in order to produce reliable estimates of MER.

In the case of the Eyjafjallajökull eruption (that is, for the specific eruption magnitude and range of pulsation frequency), there is a substantial agreement between measured and computed MER values with simplified 1D plume models. However, this was verified only on the specific case here presented; further tests on eruptions with different properties (e.g. magnitude, pulsation frequency, etc.) should be carried out in the future. It is also not clear to what extent this pulsating behavior plays a role in large eruptions (MER > 10^7 kg s^{-1}).

Finally, results from sensitivity analysis carried out on simplified 1D numerical models further confirm the dependence of plume dynamics on source mass flux and, hence, the importance of reliable estimates of MER for accurate characterisation of plume height and trajectory, which are in turn used for initializing ash dispersion models. Numerical models are not only sensitive to uncertainties in source conditions, but also to the air entrainment parameterization. While there is a substantial agreement for the radial entrainment component, this is not the case for the tangential wind-induced one, for which a wide range of values are still used. This is reflected in the 1D plume model outputs, as wind plays a major role in affecting plume maximum height and trajectory, which in turn has an influence on MER estimates and on the initialization of ash dispersion models, for which 1D numerical models provide the initial distribution of ash in the atmosphere. We believe that scientific research on convective plumes should be specifically aimed at better constraining the parameterization of the wind entrainment coefficient, with both complex numerical simulations and new large-scale experiments (**Table 1**).

Symbol	Description	Units
C	Particle volumetric concentration	-
C_0	Particle volumetric concentration at the source	-
d	Plume width	m
Fr_0'	Source densimetric Froude number	-
g_0'	Source reduced gravity	m s^{-2}
m	Particle mass load	kg
MER	Mass eruption rate	kg s^{-1}
n	Solids mass fraction	-
P_{atm}	Atmospheric pressure	Pa
$P_{dyn,0}$	Dynamic pressure at the source	Pa
$P_{over,0}$	Static overpressure at the source	Pa
$P_{st,0}$	Static pressure at the source	Pa
Q	Mass flux of a pulse	kg s^{-1}
r_0	Vent radius	m
Re	Reynolds number	-
Ri	Richardson number	-
SME	Specific mechanical energy	kJ kg^{-1}
t	Time	s
t_{pulse}	Average pulsation interval time	s

http://dx.doi.org/10.5772/63422

Symbol	Description	Units
U	Axial plume velocity	m s^{-1}
U_0	Exit velocity	m s^{-1}
U_ε	Entrainment velocity	m s^{-1}
v	Vertical velocity of a pulse	m s^{-1}
V	Wind speed	m s^{-1}
W	Gas volume	m^3
α	Radial entrainment coefficient	-
β	Tangential (wind) entrainment coefficient	-
Γ	Overpressure factor	-
ΔP	Gas overpressure	Pa
θ	Inclination of the plume centreline to the horizon	°
ρ	Eruptive mixture density	kg s^{-1}
ρ_g	Gas density	kg s^{-1}
ρ_t	Tephra density	kg s^{-1}
τ	Time for which the mass flux has decreased by a factor $1/e$	s
Ω	Vorticity factor	s^{-1}

Table 1. Notation.

Acknowledgements

Published with permission of the Executive Director of British Geological Survey (NERC). The research of Dr. Tobias Dürig presented in this chapter (Section 2) was supported by the EU FP7 supersite project Futurevolc and used photos and infrared (FLIR) images that were acquired by Björn Oddsson and Thordís Högnadóttir. The research of Dr. Fabio Dioguardi presented in this chapter (Section 3) was partially funded by DPC-INGV agreement 07–09 and MIUR PRIN 06. We like to thank Dr. Jacopo Taddeucci for his valuable suggestions that helped to improve the manuscript.

Author details

Fabio Dioguardi[1*], Tobias Dürig[2], Samantha L. Engwell[1], Magnus T. Gudmundsson[2] and Susan C. Loughlin[1]

*Address all correspondence to: fabiod@bgs.ac.uk

1 British Geological Survey, The Lyell Centre, Edinburgh, United Kingdom

2 Nordvulk, Institute of Earth Sciences, University of Iceland, Reykjavík, Iceland

References

[1] Dacre H.F., Grant A.L.M., Hogan R.J., Belcher S.E., Thomson D.J., Devenish B.J., et al. Evaluating the structure and magnitude of the ash plume during the initial phase of the 2010 Eyjafjallajökull eruption using lidar observations and NAME simulations. J. Geophys. Res. 2011;116:D00U03. DOI: 10.1029/2011JD015608.

[2] Bonadonna C., Folch A., Loughlin S., Puempel H. Future developments in modelling and monitoring of volcanic ash clouds: outcomes from the first IAVCEI-WMO workshop on Ash Dispersal Forecast and Civil Aviation. Bull. Volcanol. 2012;74(1):1–10. DOI: 10.1007/s00445-011-0508-6.

[3] Mastin L.G., Guffanti M., Servranckx R., Webley P., Barsotti S., Dean K., et al. A multidisciplinary effort to assign realistic source parameters to models of volcanic ash-cloud transport and dispersion during eruptions. J. Volcanol. Geotherm. Res. 2009;186:10–21. DOI: 10.1016/j.jvolgeores.2009.01.008.

[4] Degruyter W., Bonadonna C. Improving on mass flow rate estimates of volcanic eruptions. Geophys. Res. Lett. 2012;39:L16308. DOI: 10.1029/2012GL052566.

[5] Sparks R.S.J., Bursik M.I., Carey S.N., Gilbert J.S., Glaze L.S., Sigurdsson H., et al. Volcanic Plumes. Chichester: Wiley & Sons; 1997.

[6] Mastin L.G. A user-friendly one-dimensional model for wet volcanic plumes. Geochem. Geophys. Geosyst. 2007;8:Q03014. DOI: 10.1029/2006GC001455.

[7] Tupper A., Oswalt J.S., Rosenfeld D. Satellite and radar analysis of the volcanic-cumulonimbi at Mount Pinatubo, Philippines, 1991. J. Geophys. Res. 2005;110:D09204. DOI: 10.1029/2004JD005499.

[8] Tupper A., Davey J., Stewart P., Stunder B., Servranckx R., Prata F. Aircraft encounters with volcanic clouds over Micronesia, Oceania, 2002–03. Aust. Met. Mag. 2006;55:289–299.

[9] Marzano F.S., Lamantea M., Montopoli M., Di Fabio S., Picciotti E. The Eyjafjöll explosive volcanic eruption from a microwave weather radar perspective. Atmos. Chem. Phys. 2011;11:9503–9518. DOI: 10.5194/acp-11-9503-2011.

[10] Björnsson H., Magnusson S., Arason P., Petersen G.N. Velocities in the plume of the 2010 Eyjafjallajökull eruption. J. Geophys. Res. Atmos. 2013;118:1–14. DOI: 10.1002/jgrd.50876.

[11] Scharff L., Hort M., Varley N.R. Pulsed Vulcanian eruptions: a characterization of eruption dynamics using Doppler radar. Geology. 2015;43(11):993. DOI: 10.1130/G36705.1.

[12] Gaudin D., Taddeucci J., Scarlato G., Moroni M., Freda C., Gaeta M., et al. Pyroclast Tracking velocimetry illuminates bomb ejection and explosion dynamics at Stromboli

(Italy) and Yasur (Vanuatu) volcanoes. J. Geophys. Res.. 2014;119(7):5384–5397. DOI: 10.1002/2014JB011096.

[13] Dürig T., Gudmundsson M.T., Karmann S., Zimanowski B., Dellino P., Rietze M., et al. Mass eruption rates in pulsating eruptions estimated from video analysis of the gas thrust-buoyancy transition – a case study of the 2010 eruption of Eyjafjallajökull, Iceland. Earth Planet Space 2015;67:180. DOI: 10.1186/s40623-015-0351-7.

[14] Dürig T., Gudmundsson M.T., Dellino P. Reconstruction of the geometry of volcanic vents by trajectory tracking of fast ejecta – the case of the Eyjafjallajökull 2010 eruption (Iceland). Earth Planet Space 2015;67:64. DOI: 10.1186/s40623-015-0243-x.

[15] Gudmundsson M.T., Thordarson Th., Höskuldsson A., Larsen G., Björnsson H., Prata F.J., et al. Ash generation and distribution from the April-May 2010 eruption of Eyjafjallajökull, Iceland. Sci. Rep. 2012;2:572. DOI: 10.1038/srep00572.

[16] Dellino P., Gudmundsson M.T., Larsen G., Mele D., Stevenson J.A., Thordarson Th., et al. Ash from the Eyjafjallajökull eruption (Iceland): fragmentation processes and aerodynamic behavior. J. Geophys. Res. 2012;117:B00C04. DOI: 10.1029/2011JB008726.

[17] Ripepe M., Bonadonna C., Folch A., Delle Donne D., Lacanna G., Marchetti E., et al. Ash-plume dynamics and eruption source parameters by infrasound and thermal imagery: the 2010 Eyjafjallajökull eruption. Earth Planet. Sci. Lett. 2013;366:112–121. DOI: 10.1016/j.epsl.2013.02.005.

[18] Sparks R.S.J. The dimensions and dynamics of volcanic eruption columns. Bull. Volcanol. 1986;48:3–15.

[19] Patrick M.R., Harris A.J.L., Ripepe M., Dehn J., Rothery D.A., Calvari S. Strombolian eruptive styles and source conditions: insights from thermal (FLIR) video. Earth Planet. Sci. Lett. 2007;69:769–784. DOI: 10.1007/s00445-006-0107-0.

[20] Marchetti E., Ripepe M., Harris A.J.L., Delle Donne D. Tracing the differences between Vulcanian and Strombolian explosions using infrasonic and thermal radiation energy. Earth Planet. Sci. Lett. 2009;279:273–281. DOI: 10.1016/j.epsl.2009.01.004.

[21] Wilson L., Walker G.P.L. Explosive volcanic eruptions—VI. Ejecta dispersal in Plinian eruptions: the control of eruption conditions and atmospheric properties. Geophys. J. R. Astron. Soc. 1987;89:657-679.

[22] Burgisser A., Bergantz G.W., Breidenthal R.E. Addressing complexity in laboratory experiments: the scaling of dilute multiphase flows in magmatic systems. J. Volcanol. Geotherm. Res. 2005;141:245–265. DOI: 10.1016/j.jvolgeores.2004.011.001.

[23] Dellino P., Zimanowski B., Büttner R., La Volpe L., Mele D., Sulpizio R. Large-scale experiments on the mechanics of pyroclastic flows: design, engineering and first results. J. Geophys. Res. 2007;112:B04202. DOI: 10.1029/2006JB004313.

[24] Dellino P., Dioguardi F., Zimanowski B., Büttner R., Mele D., La Volpe L., et al. Conduit flow experiments help constraining the regime of explosive eruptions. J. Geophys. Res. 2010;115:B04204. DOI: 10.1029/2009JB006781.

[25] Dellino P., Büttner R., Dioguardi F., Doronzo D.M., La Volpe L., Mele D., et al. Experimental evidence links volcanic particle characteristics to pyroclastic flow hazard. Earth Planet. Sci. Lett. 2010;295:314–320. DOI: 10.1016/j.epsl.2010.04.022.

[26] Dellino P., Dioguardi F., Mele D., D'Addabbo M., Zimanowski B., Büttner R., et al. Volcanic jets, plumes and collapsing fountains: evidence from large-scale experiments, with particular emphasis on the entrainment rate. Bull. Volcanol. 2014;76:834. DOI: 10.1007/s00445-014-0834-6.

[27] Graettinger A.H., Valentine G.A., Sonder I., Ross P.S., White J.D.L. Facies distribution of ejecta in analog tephra rings from experiments with single and multiple subsurface explosions. Bull. Volcanol. 2015;77:66. DOI: 10.1007/s00445-015-0951-x.

[28] Lube G., Breard E.C.P., Cronin S.J., Jones J. Synthesizing large-scale pyroclastic flows: experimental design, scaling, and first results from PELE. J. Geophys. Res.: Solid Earth 2015;120(3):1487–1502. DOI: 10.1002/2014JB011666.

[29] Büttner R., Dellino P., Raue H., Sonder I., Zimanowski B. Stress-induced brittle fragmentation of magmatic melts: theory and experiments. J. Geophys. Res. 2006;111:B08204. DOI: 10.1029/2005JB003958.

[30] Dürig T., Dioguardi F., Buttner R., Dellino P., Mele D., Zimanowski B. A new method for the determination of the Specific Kinetic Energy (SKE) released to pyroclastic particles at magmatic fragmentation: theory and first experimental results. Bull. Volcanol. 2012;74:895-902. DOI: 10.1007/s00445-011-0574-9.

[31] Valentine G.A. Eruption column physics. In: Freundt A., Rosi M., editors. From Magma to Tephra: modelling physical processes of explosive volcanic eruptions. New York: Elsevier Science; 1998. p. 91-138.

[32] Morton B.R., Taylor G., Turner J.S. Turbulent gravitational convection from maintained and instantaneous sources. Proc. R. Soc. A. 1956;234(1196):1-23.

[33] Zimanowski B. Phreatomagmatic explosions. In: Freundt A., Rosi M., editors. From Magma to Tephra: modelling physical processes of explosive volcanic eruptions. New York: Elsevier Science; 1998. p. 25–53.

[34] Papale P. Dynamics of magma flow in volcanic conduits with variable fragmentation efficiency and non-equilibrium pumice degassing. J. Geophys. Res.. 2001;106(B6): 11043-11065.

[35] Dioguardi F., Dellino P., de Lorenzo S. Integration of large-scale experiments and numerical simulations for the calibration of friction laws in volcanic conduit flows. J. Volcanol. Geotherm. Res. 2013;250:75-90. DOI: 10.1016/j.jvolgeores.2012.09.011.

[36] Bloomfield L.J., Kerr R.C. A theoretical model of a turbulent fountain. J. Fluid Mech. 2000;424:197-216. DOI: 10.1017/S0022112000001907.

[37] Kaye N.B., Hunt G.R. Weak fountains. J. Fluid Mech. 2006;558:319-328. DOI: 10.1017/S0022112006000383.

[38] Suzuki Y.J., Koyaguchi T. 3-D numerical simulations of eruption column collapse: effect of vent size on pressure-balanced jet/plumes. J. Volcanol. Geotherm. Res. 2012;221-222:1-12. DOI: 10.1016/j.jvolgeores.2012.01.013.

[39] Degruyter W., Bonadonna C. Impact of wind on the condition for column collapse of volcanic plumes. Earth Planet. Sci. Lett. 2013;377:218-226. DOI: 10.1016/j.epsl.2013.06.041.

[40] Carazzo G., Kaminski E., Tait S. On the dynamics of volcanic columns: a comparison of field data with a new model of negatively buoyant jets. J. Volcanol. Geotherm. Res. 2008;178(1):94-103. DOI: 10.1016/j.jvolgeores.2008.01.002.

[41] Turner J.S. Jets and plumes with negative or reversing buoyancy. J. Fluid Mech. 1966;26:779-792. DOI: 10.1017/S0022112066001526.

[42] Lin W., Armfield S.W. Direct simulation of weak axisymmetric fountains in a homogeneous fluid. J. Fluid Mech. 2000;403:67-88. DOI: 10.1017/S0022112099006953.

[43] Wilson L., Sparks R.S.J., Walker G.P.L. Explosive volcanic eruptions – IV. The control of magma properties and conduit geometry on eruption column behaviour. Geophys. J. Roy. Astron. Soc. 1980;63:117-148.

[44] Woods A.W. The fluid dynamics and thermodynamics of eruption columns. Bull. Volcanol. 1988;50:169-193. DOI: 10.1007/BF01079681.

[45] Costa A., Suzuki Y.J., Cerminara M., Devenish B.J., Esposti Ongaro T., Herzog M., et al. Results of the eruptive column model inter-comparison study. J. Volcanol. Geotherm. Res. In press. DOI: 10.1016/j.jvolgeores.2016.01.017.

[46] Kaminski E., Tait S., Carazzo G. Turbulent entrainment in jets with arbitrary buoyancy. J. Fluid Mech. 2005;526:361-376. DOI: 10.1017/S0022112004003209.

[47] Bursik M. Effect of wind on the rise height of volcanic plumes. Geophys. Res. Lett. 2001;28(18):3621-3624.

[48] Devenish B.J. Using simple plume models to refine the source mass flux of volcanic eruptions according to atmospheric conditions. J. Volcanol. Geotherm. Res. 2013;256:118-127. DOI: 10.1016/j.jvolgeores.2013.02.015.

[49] Woodhouse M.J., Hogg A.J., Phillips J.C., Sparks R.S.J. Interaction between volcanic plumes and wind during the 2010 Eyjafjallajökull eruption, Iceland. J. Geophys. Res.: Solid Earth 2013;118(1):92-109. DOI: 10.1029/2012JB009592.

[50] Woodhouse M.J., Hogg A.J., Phillips J.C. A global sensitivity analysis of the PlumeRise model of volcanic plumes. J. Volcanol. Geotherm. Res. In press. DOI: 10.1016/j.jvolgeores.2016.02.019.

[51] Suzuki Y.J., Koyaguchi T. Effects of wind on entrainment efficiency in volcanic plumes. J. Geophys. Res.: Solid Earth 2015;120(9):6122–6140. DOI: 10.1002/2015JB012208.

[52] National Science Foundation. Vhub.org. Collaborative volcano research and risk mitigation [Internet]. Available from: https://vhub.org.

[53] de' Michieli Vitturi M., Neri A., Barsotti S. PLUME-MoM 1.0: a new integral model of volcanic plumes based on the method of moments. Geosci. Model Dev. 2015;8(8): 2447-2463. DOI: 10.5194/gmd-8-2447-2015.

[54] Herzog M., Graf H.F., Textor C., Oberhuber J.M. The effect of phase changes of water on the development of volcanic plumes. J. Volcanol. Geotherm. Res. 1998;87(1):55-74. DOI: 10.1016/S0377-0273(98)00100-0.

[55] Cerminara M., Esposti Ongaro T., Berselli L.C. ASHEE-1.0: a compressible, equilibrium-Eulerian model for volcanic ash plumes. Geosci. Model Dev.. 2016;9(2):697-730. DOI: 10.5194/gmd-9-697-2016.

[56] Hewett T.A., Fay J.A., Hoult D.P. Laboratory experiments of smokestack plumes in a stable atmosphere. Atmos. Environ. 1971;5:767-789.

[57] Devenish B.J., Rooney G.C., Webster H.N., Thomson D.J. The entrainment rate for buoyant plumes in a crossflow. Boundary-layer Meteorol. 2010;134:411-439. DOI: 10.1007/s10546-009-9464-5.

[58] de' Michieli Vitturi M., Engwell S.L., Neri A., Barsotti S. Uncertainty quantification and sensitivity analysis of volcanic columns models: Results from integral model PLUME-MoM. J. Volcanol. Geotherm. Res. In press. DOI: 10.1016/j.jvolgeores.2016.03.014.

Section 3

Volcanic Eruptions and their Impact to the Environment

Chapter 7

Pyroclastic Density Current Hazards at the Baekdusan Volcano, Korea: Analyses of Several Scenarios from a Small-Case to the Worst-Case Colossal Eruption

Angelo Paone and Sung-Hyo Yun

Additional information is available at the end of the chapter

http://dx.doi.org/10.5772/62340

Abstract

The Baekdusan volcano was formed through three stages of activity: (a) a basalt shield (aging between 22.6 and 1.48 Ma), (b) a trachytic comendite stratocone (aging between 1.19 and 0.02 Ma), (c) a trachyte-comendite ignimbrite deposits (aging from 20 ka till date). Volcanic seismicity, ground deformation, and volcanic gas geochemistry yield new evidence for magmatic unrest of the volcano between 2002 and 2006. The monitoring data suggest that Mt. Baekdusan is a potentially active volcano and that its close monitoring is needed. One of the possible volcanic hazards from this volcano is the pyroclastic density currents. In order to evaluate the small-scale pyroclastic flow emplacement scenario of the 1903 AD eruption, Titan2d mass-flow model is used. The 1668–1702 AD and the Millennium eruption are characterized by 4–5 and ~7 VEI, respectively. The Millennium eruption can be considered as the last colossal super-eruption like Tambora, and so Baekdusan volcano could have even a global effect. The parameters used are as follows: volume (5–10 × 10^7, 1 × 10^9, 2 × 10^{10} m^3), the vents of the 1903, 1668–1702, and Millennium eruptions; the pyroclastic flow runout calculated in the field are small (3,000 m : 1903 eruption), intermediate (5,000 m :1668–1702 eruptions), and large (7–80,000 m, Millennium eruption). The initial velocities (m/s) range from 50 (1903 eruption) to as high as 300 (Millennium eruption). The input parameters have constructed three scenarios (1903, 1668–1702, and Millennium eruptions) following the recent volcanic history of Baekdusan volcano. These eruptions embrace all the possibly explosive eruptive scenarios that can occur at Baekdusan volcano in the future. The 1903 type scenario has been performed; according to the vent location, the flow moves in diverse directions (NE, SE) with a thickness of 3 m, and if the vent is the center of the caldera the flow fills the caldera with a thickness of 5 m. The emplacement of the 1668–1702 AD scenarios will involve at least two populated cities nearest to Baekdusan volcano. The scenario of the Millennium eruption will be much more severe and it will hit all the cities and towns within a range of 80 km. The impact will be from regional to global. This, however, is an underestimation of the runout for the diluted pyroclastic density currents.

Keywords: Baekdusan volcano, pyroclastic density currents, hazard, eruptive scenario, super-eruption, Titan2d

1. Introduction

When active volcanoes are located in strategic and controversial territory with a history of political and military conflicts [1, 2], their studies and the better understanding of how those volcanoes work are much more difficult, especially when the earth scientists have to deal with mitigation measures to protect the population living around [3–6]. This is surely the case of an active volcano known by a few until 15 years ago, situated between the China and North Korea borders, called by different names by the countries that surround it. The name of the volcanic field surrounding Tianchi(=Cheonji) caldera lake is 白頭山 in Chinese characters which means "White Head Mountain" These characters are Romanized as Baegdu-san, Baekdu-san, or Paektu-san in Korea, Hakuto-san in Japan, and Changbaishan(長白山) in China [7, and references therein]. From now on, we will use the Korean name, Baekdusan, to avoid confusion. Baekdusan volcano has recently become of greater interest to volcanologists after the sign of unrest during the period 2002–2009, with several volcanic precursors such as volcanic earthquake, surface inflation, specific volcanic gas emission, higher temperatures of hot springs [8–10], which have prompted the Eastern Asian Volcanological Community to pay major attention to this volcano by establishing a Volcanological Observatory (the Chinese Tianchi Volcanological Observatory has collected data since 1999 [11]) and by setting up an improved monitoring network around the volcano [12, 13]. Since 2012, the South Korean scientists have also taken steps in this direction, and the National Emergency Management Agency of Korea (Ministry of Public Safety and Security of Korea) has sponsored a vast research project on Baekdusan volcano (NEMA-BAEKDUSAN-2012-1-2), granted from the Volcanic Disaster Preparedness Centre (MPSS-NH-2015-81), and through the Natural Hazard Mitigation Research Group. Under the auspices of these groups, we analyzed the hazards from pyroclastic density currents and their impact on the population and infrastructures around Baekdusan volcano [14]. Further, we present arguments as to why this volcano has many characteristics as a potential site for the development of the conditions that can cause a super-eruption. Thus, we must also consider this extreme event if we do have to prepare for the next eruption, as it would have a global impact [15].

2. Regional tectonic of Baekdusan volcano and an outline of the plumbing system

Baekdusan volcano is an intraplate stratovolcano included in the larger Changbaishain area, where we can list a series of intraplate volcanoes (Wangtiane volcano, Bukpotaesan volcano, Zhenfengshan volcano, [7], **Figure 1**). Cenozoic intraplate basalts are widely distributed around the Changbaishan volcanic area. Beneath the Baekdusan volcano, a prominent low-

http://dx.doi.org/10.5772/62340

velocity anomaly with a plume-like shape has been imaged in the upper mantle by P-wave tomography [16, 17]. This suggests an upwelling of hot and wet material from the mantle transition zone (410–670 km [18]), where a stagnant subducted Pacific slab produces fluids and deep earthquakes through faults preserved in the stagnant slab. Hence, fluids and magmas may be supplied to the upper mantle under Baekdusan volcano, unlike beneath other volcanic and nonvolcanic areas in NE Asia, because large deep earthquakes occur frequently in the vicinity (a distance of about 200 km) of the Baekdusan volcano. At least some of these earthquakes are caused by the reactivation of faults which were produced within the plate, even after plate subduction. Further, the fluids could be released to the overlying mantle wedge from the preserved faults in the slab when large deep earthquakes occur. As a result, the Baekdusan volcano has to be considered much more active and prominent than other intraplate volcanoes in NE Asia [9, 10], because more magmas are produced from the fluids released from the slab by the deep earthquakes [19]. Further, Kuritani et al. [20] use the trace element and Pb isotope data to demonstrate the intense hydration of the big mantle wedge beneath the Baekdusan volcano, through two different dehydration events of an ancient stagnant slab (~1.5 Gyr) and the most recent subducted Pacific slab (**Figure 2A** and **B** show the most recent setting). The wet mantle wedge is likely to result in more frequent rise of diapiric wet melts, as shown from the tomography [17, references therein], and develop a deep hot zone intruded by mafic sills repeatedly at the MOHO depth or/and scattered in the lower crust [21, and references therein]. Enrichment in fluid-mobile elements (e.g. Cs, Ba, K, Sr, U, Pb), a lack of enrichment in nonfluid-mobile elements (e.g. Nb, Ta, Ti, etc), together with specific isotopic signatures (e.g. $^{87}Sr/^{86}Sr$, $^{206}Pb/^{204}Pb$) in island-arc basalt or subduction- related magmatism are interpreted as a result of metasomatism of the magma source by slab-derived fluids or melts. Their detailed

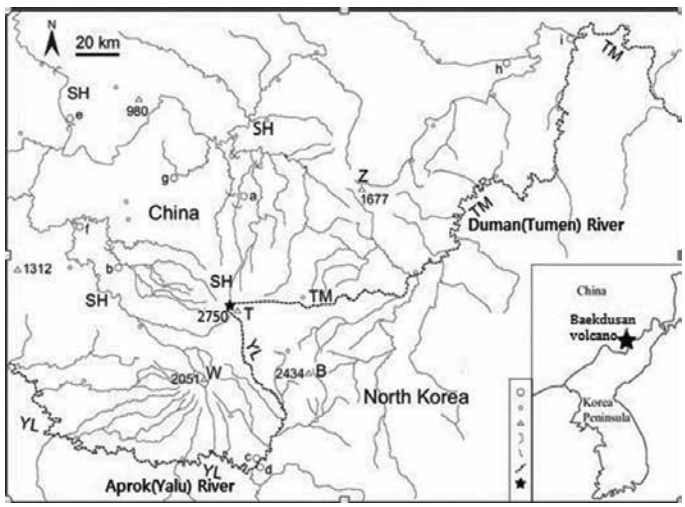

Figure 1. Regional setting of Baekdusan (Tianchi) volcano. Symbols mean the following. ○ Densely populated city or town: (a) Erdaobaihe; (b) Songjianghe; (c) Changbai; (d) Hyesan; (e) Baishan; (f) Fusong; (g) Lushuihe; (h) Yanji, and (i) Tumen. ° Populated village. Δ Mountain tops with the elevation asl. ★ Baekdusan (Tianchi) volcano. Capital letters indicate places referred to in text: T, Baekdusan (Tianchi) volcano; W, Wangtiane volcano; B, Bukpotaesan volcano; Z, Zhenfengshan volcano; SH, Songhua River; YL, Yalu(Aprok) River; and TM, Tumen (Duman) River.

investigation has helped to establish the current, rather empirical, model of slab dehydration and subduction-related melting processes. But, according to petrochemical characteristics and magma genesis of Holocene volcanic rocks at Mt. Baekdusan [22], trace elements from the Baekdusan volcano do not indicate significant contributions from a subduction slab of the Pacific plate. Volcanic activity in Mt. Baekdusan summit during Holocene resulted from intraplate magmatism [after 23, 24], caused by upwelling of asthenospheric mantle under extensional tectonic conditions (**Figure 3** [24]). Hot zone melts are H_2O-rich as in Baekdusan volcano (e.g., Millennium eruption [25]). Consequently, they have low viscosity and density, and can readily detach from their source and ascend rapidly. Crystallization begins only when the ascending magma intersects its H_2O-saturated liquidus at shallow depths. Decompression and degassing are the driving forces behind crystallization, which take place at shallow depths

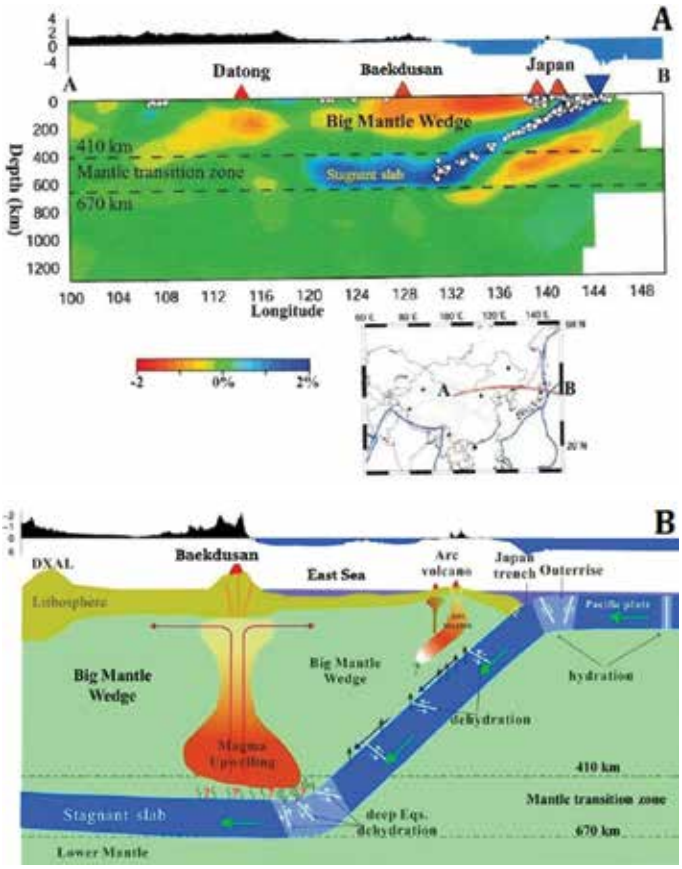

Figure 2. A. Regional tomography from the surface down to 1,300 km depth along a cross-section line shown on the inset map. The velocity perturbation scale is shown below the cross section. White dots denote earthquakes. The two dashed lines show the 410 and 670 km discontinuities. The red and black triangles show the active volcanoes. The surface topography along the profile is shown at the top of the tomographic image. The blue lines on the inset map denote the major plate boundaries (modified from [17]). **B**. A sketch showing the main features of the upper-mantle structure around Baekdusan volcano in East Asia, emphasizing the possible relationship between the intraplate volcanism and deep earthquakes in the Pacific slab [17], DXAL, Daxing-Anling (modified from [17]).

http://dx.doi.org/10.5772/62340

on timescales of decades or less. Degassing and crystallization at shallow depths lead to large increases in viscosity and stalling of the magma to form volcano-feeding magma chambers [26, 27]. The above model is well confirmed from the study of Wei [24] at the Baekdusan volcano. The heating of the deep crust was inefficient in early times, because much of the basalts erupted out directly, and much of the heat from magma was not used to heat the wall rocks. Annan and Sparks [27] state that there is an initial incubation period in which the basalt intrusions solidify. Generation of silicic melts initiates when the solidus temperature of either the basalt magma or the surrounding crust is reached. At an intrusion rate of 50 m per 10,000 years, incubation periods in the range 10^5–10^6 years are estimated, consistent with geochronology and stratigraphy at Baekdusan volcano, with its evolution from mafic to silicic volcanism (the stratigraphy and geochronology will be treated in the next section). Once a zone of residual partial melt develops in the deep hot zone and starts to prevent the basalt from eruption, the temperature rises more efficiently, and the production of residual melt is accelerated. Large amounts of evolved residual silicic melt have been formed in the last 10,000 years and then intruded into the upper crust to form magma chambers large enough to result in the caldera-forming explosive eruptions. The repose time between eruptions of size similar to the Millennium eruption was about thousands of years, one order greater than less-explosive parasitic eruptions of hundreds of years [7].

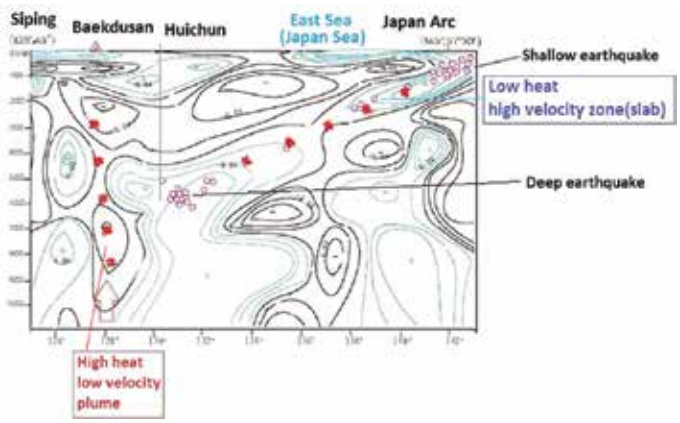

Figure 3. Siping–Changbaishan–Japan seismic profile of the structure of Changbaishan area [24].

3. Summary of stratigraphy and geochronology of Baekdusan volcano

The volcanic activity at the Baekdusan volcano goes back as far as nearly 25 Ma B.P [7, 28, 29]. Wei et al. [7] describe the volcanic activity in three stages: early shield-forming; middle cone-construction; and late ignimbrite-forming eruptions. The volcanic rocks were alkaline and tholeiitic basalts during the shield stage, trachyte and comendite lavas, and their pyroclastic equivalents during the cone-construction stage, and mostly comenditic pyroclastic rocks in the

final stage (**Table 1**, **Figure 4**). However, Yang et al. [30] affirm on the basis of a large amount of age and stratigraphic data ($^{40}Ar/^{39}Ar$, U-series disequilibria) that Baekdusan volcano has been more active in the last 20 ka (~19, 16, 11 ka) than that was previously thought. From historical records, several authors [31, 32] affirm the high frequency of eruptive events, and since the Millennium eruption, more than 31 eruptive events have been documented, most of which are the Plinian eruptions with volcanic ash that dispersed into the regions in the vicinity of the volcano. Many authors concord that the last explosive eruptions are in chronological order, 1668 AD (**Figure 5**), 1702 AD (**Figure 6**), and 1903 AD (**Figure 7**) [32–34]. In **Figure 4** is shown the Baekdusan volcano's geological map with all the terrains outcropping (see the legend of **Figure 4** for more major details). The shield-forming stage lasted from the Miocene into the early Pleistocene. Alkali olivine and tholeiite basalt form the main part of a shield-like lava plateau that covers an area of 7,200 km^2 centered at Cheonji. In addition to the eruptions from central vents, there also were fissure eruptions, as evidenced by feeder dikes along the headwaters of the Tumen (Duman) and Heishihe Rivers. The youngest shield basalts are located near Cheonji cone and are overlain by the alkaline trachytes of the cone, except in the northwestern part of the shield. The shield basalts are ~150 m thick near the Baishan Forestry Center in the headwaters of the Yalu River (Aprok River). The cone-construction stage lasted from ~1.0 Ma to perhaps as young as ~20 ka. The latter is about the age of the youngest trachyte lava on the caldera rim near Tianwenfeng (K–Ar, 19 ± 5 ka) and one of the youngest comendite lavas, Qixiangzhan, which was dated recently at 17 ± 1 ka. This stage was characterized by eruption of trachyte and comendite lavas and pyroclastic rocks, and dominated by trachyte lava effusion from the center of Cheonji volcano. The cone-construction stage has been subdivided into four stratigraphic formations for the main cone and the Laofangzixiaoshan

Stages	Formation and age	Lithologies
	Liuhaojiie Tuff Ring (1903 AD)	Comendite phreatomagmatic eruption
Late:	Wuhaojie (1702 AD)	White gray comentite fine glass
Igninbrite-forming	Baguamiao (1668 AD)	Dark gray trachyte ignimbrite and pumice
	Millennium eruption (~936–1200 AD)	White gray comentite ignimbrite and Air fall pumice with minor trachyte Ignimbrite and air fall pumice
	Qixiangzhan (17 ka)	Comentite lava and pyroclasts
Middle: Cone construction	Baitoushan III (0.02–0.22 Ma)	Trachyte and comendite lava
	Baitoushan II (0.25–0.44 Ma)	Trachyte with Laohudong basalt
	Baitoushan I (0.53–0.61 Ma)	Trachyte
	Laofangzixiaoshan (0.75–1.17 Ma)	Basalt
	Xiaobaishan (0.75–1.17 Ma)	Trachyandesite and trachyte
	Baishan (1.48–1.66 Ma)	Basalt
Early: Shield-forming	Toudao (2.35–5.02 Ma)	Basalt
	Naitoushan (15.6–22.6 Ma)	Basanite, Basalt

Table 1. Baekdusan volcano stratigraphy and petrography of the volcanic products simplified after Wei et al. [7, 28, 29].

http://dx.doi.org/10.5772/62340

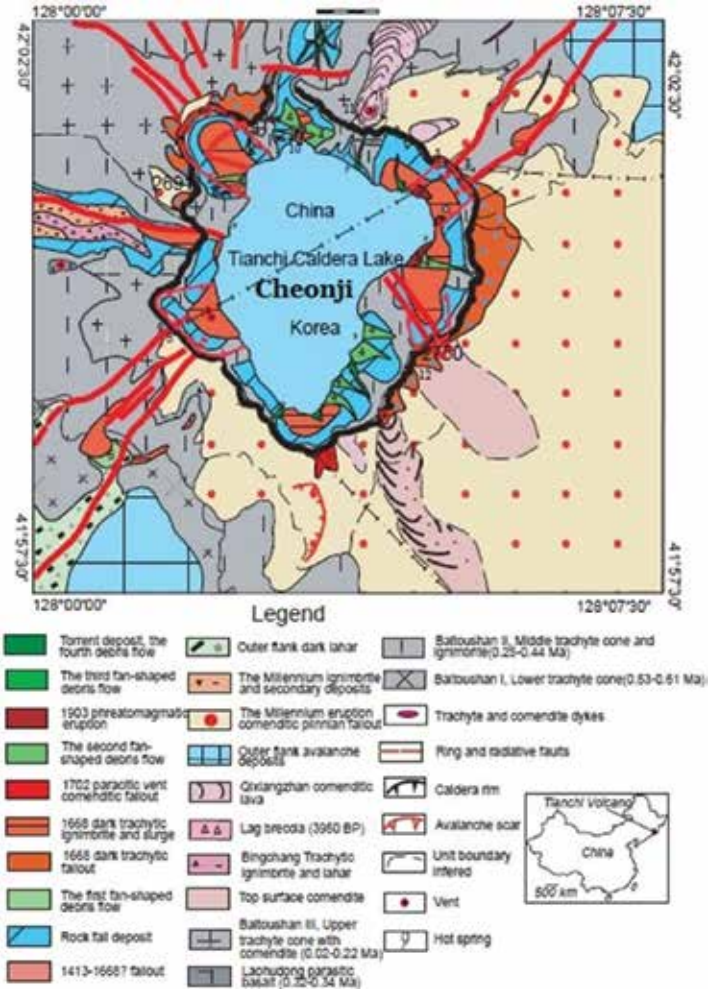

Figure 4. Geological map of the summit area of Baekdusan volcano. Northeast distribution of the basaltic shield, trachytic composite cone, and the comenditic ignimbrite sheet of the Baekdusan volcano. 1, Torrent deposit, the fourth debris flow (1994); 2, The third fan-shaped debris flow; 3, 1903 phreatomagmatic eruption; 4, The second fan-shaped debris flow; 5, Dark trachytic ignimbrite and surge (1668); 6, Dark trachytic fallout (1668); 7, The first fan-shaped debris flow; 8, Rock fall deposit; 9, Fallout (?1413–1668); 10, Outer flank dark lahar; 11, The Millennium ignimbrite and secondary deposits; 12, The Millennium valley and pond ignimbrite; 13, The Millennium eruption comenditic Plinian fallout; 14, Outer flank avalanche deposits; 15, Qixiangzhan distal comenditic lava; 16, Qixiangzhan middle comenditic lava; 17, Qixiangzhan proximal comenditic lava; 18, Qixiangzhan calstogenic lava, comendite, and obsidian; 19, Ice ground brown and gray trachytic ignimbrite, lahar; 20, Heifengkou Lag breccias (3950 ±120 a); 21, Upper trachyte and comendite cone (0.04–0.2 Ma); 22, Middle trachyte cone (0.25–0.44 Ma); 23, Lower trachyte cone (0.53–0.61 Ma); 24, Xiaobaishan trachyandesite and trachyte (1–1.49 Ma); 25, Laohudong parasitic basalt and scoria (0.32–0.34 Ma); 26, Laofangzixiaoshan basalt (0.31–0.58 Ma); 27, Baishan basalt (0.93–1.39 Ma); 28, Toudao basalt (1.91–2.77 Ma); 29, Comendite dyke; 30, Trachytic welded tuff dyke; 31, Trachyte dyke; 32, Ring and radioactive faults; 33, Caldera rim; 34,Avalanche scar; 35,Vent; 36, Hot spring; 37, Inferred geologic boundary; 38, Flow units boundary; 39, Facies boundary; 40, National boundary. β, Basalt; τ, Trachyte; λ, Comendite; π, Porphyry dyke (modified from [7]; Yun, unpublished data).

part of the shield (**Table 1**). In general, outcrops of lava decrease image with elevation on the cone. In plane view, the eastern sector of the cone consists of younger trachytes, whereas older lavas are distributed more widely. However, all the rocks share similar geochemical compositions and appear to be genetically related. The young Laohudong basalts are sparsely distributed as monogenetic vents around the caldera. Its largest and most explosive Plinian eruption occurred around 946–947 AD and is known as the "Millennium eruption."

Figure 5. The Buguamiao welded ignimbrite of the 1668 AD pyroclastic flow eruption is shown in all the pictures. The outcrops are in the vicinity of the Tianchi caldera**.** In the Baguamiao ignimbrite is also apparent its welded character.

Figure 6. The 1702 AD pyroclastic flow eruption on the summit of the cliff.

http://dx.doi.org/10.5772/62340

Figure 7. The 1903 AD pyroclastic flow deposits. The outcrop is separated by levels. The 1° level belongs to the 1702 AD eruption, and the others belong to the 1903 pyroclastic flow eruption. It is clear that the thickness of the 1903 deposit is near the caldera.

This eruption has a volcanic explosivity index (VEI) of 7, comparable to the 1815 eruption of Tambora in Indonesia. Horn and Schmincke [25] have suggested that the Cheonji eruption column reached ca 25 km in height, injecting about 9 $\times 10^{10}$ kg of volatile halogens into the atmosphere, with an estimated volume of pyroclastic material on the order of ~100 km^3. Volcanic ash from the eruption has been found 1,000 km away from the site of the eruption. A 5 cm thick deposit was observed in southern Hokkaido, Japan [38]. Accordingly, the Millennium eruption of the Baekdusan Cheonji volcano has been considered as one of the greatest volcanic eruptions of the past 2000 years.

3.1. An outline of the Millennium eruption

One of the most largest destructive eruptions from the Baekdusan volcano occurred on Earth in the last millennium, about 1,000 years ago, and it is named the Millennium eruption [25, 29, 34, 35]. It involved more than ~100 km^3 of magma erupted [10], and the Plinian column was

estimated to have had a height of 25 km. A widespread ash-fall deposit has been traced across the Sea of Japan to Hokkaido, and it is several centimeters thick, at more than 1,000 km from the source [35, 37]. Unwelded pyroclastic flows associated with collapse events of the Plinian eruption column extended to more than 70 km from the crater rim (**Figure 8**). The Millennium eruption formed a large caldera with a diameter of about 5 km and an area of 20 km^2, forming the Cheonji (Tianchi = Sky) lake. Currently, the lake has a maximum depth of 374 m and an area of ~ 9.8 km^2, with a water surface elevation of 2,189 m. It has a volume of 2 km^3. A composite stratigraphic section of the Millennium eruption is given by Machida et al. ([35]; **Figure 9**). According to Machida et al. [35], the section is broadly composed of five levels (A, B, C, E, F; for major details, see **Figure 9**). **Figure 10** shows some unwelded Millennium pyroclastic flow outcrops with relative thicknesses and sites. However, there is a controversy if the complete volcanological section of the Millennium eruption has to be interpreted as a single continuous eruption rather than one with two distinct pulses, with the initial phase anticipating the major phases of tens or hundreds of years [39]. The scientific literature reports a large range of ages for the Millennium eruption [40]. The results show a variety of periods ranging from approximately AD eighth to fourteenth centuries, which are the dates of the Balhae(= Bohai) and Goryeo dynasties [40, and references therein]. The last geochronological data (radiocarbon wiggle-match dating) on the Millennium eruption show a much more restricted range, respectively, of 938–939 AD [41], 946–947 AD [42], and 1024 AD [28].

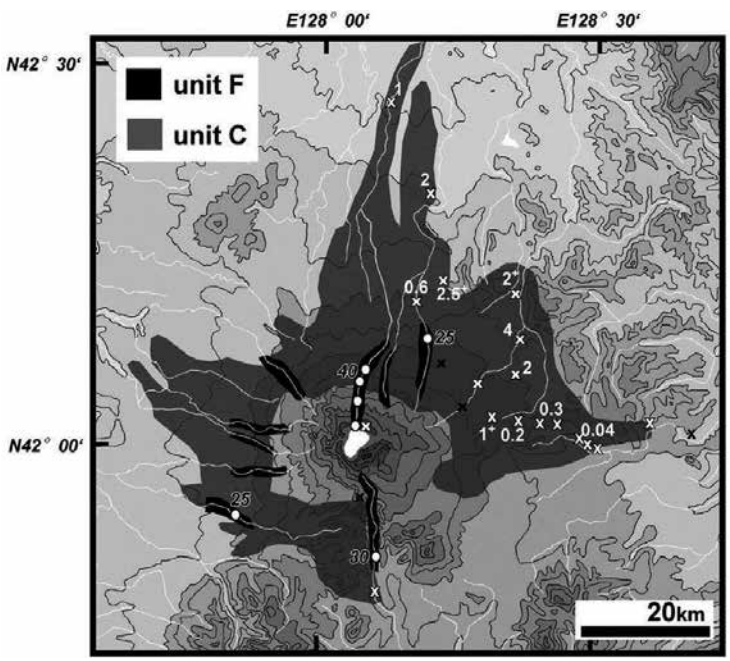

Figure 8. Distribution of pyroclastic density currents of the Millennium eruption in China side. Numbers are thickness (m). Units C and F are the two pyroclastic flow levels.

http://dx.doi.org/10.5772/62340

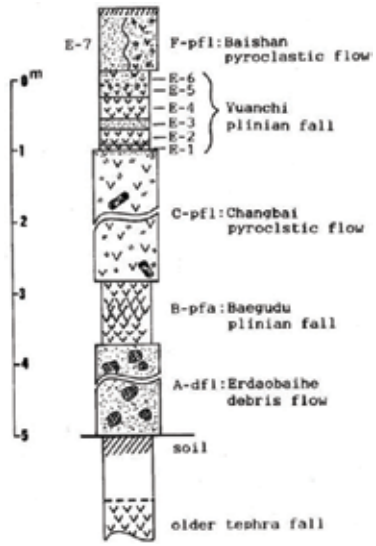

Figure 9. Stratigraphy of the Millennium eruption on the eastern slope of Baekdusan volcano (modified from [35]). pfa, pyroclastyc fall deposit; pfl, pyroclastic flow deposits; dfl, debris flow deposits.

Figure 10. Millennium unwelded pyroclastic flow outcrops at the north and south flanks of the caldera with the respective thicknesses. (**A**) Millennium eruption pyroclastic flow deposits, northern slope: 20 m thickness. (**B**) Millennium eruption pyroclastic flow deposits, southern slope: 60 m thickness.

4. Scenarios of the 1903 AD, 1668–1702 AD, and the Millennium eruptions

The scenarios envisaged here are based on the large amount of data that have been collected by the Korean research project, CATER2011-5210 [36], and by the new literature produced [25, 32–34, among others] in order to assign a selected VEI (Volcanic Explosivity Index [43]). The main parameters are summarized in **Table 2** (VEI, maximum volume erupted, and column height) for each eruption. The volumes considered for just the pyroclastic density currents are obviously less than the total volume and are listed in **Table 3**. **Figure 11** shows that between several volcanic-related disasters, the pyroclastic density currents have to be considered the most dangerous, given the number of fatalites in the last 2,000 years.

Eruption date	VEI	Volume (m^3)	Column height (km)
1903 AD eruption	**2**	**10^6–10^8**	**1–5**
	3		**3–15**
1668–1702 AD eruption	**4**	**10^8–10^{10}**	**10–25**
	5		**>25**
Millennium eruption	**7**	**10^{11}–10^{12}**	**>25**

Table 2. Summary of the main parameters for the 1093 AD, 1702 AD, 1668 AD, and the Millennium eruptions. Volumes are taken from Newhall and Self [43] compared with the VEI for each eruption.

Eruption type	Runout length (m)	Volume (m^3)	Initial velocity (m/s)	Time duration (s)
1903-type	**~3000**	**10^7–10^8**	**30**	**3600**
1668–1702 type	**~4000–5000**	**10^9**	**50**	**>3600**
Millennium eruption	**7–80,000**	**10^{10}**	**80–300**	**>3600**

Table 3. Main parameters used to analyze the impact of the pyroclastic density currents and to show small-scale simulations [34, 61].

Branney and Kokelaar [44] illustrate in detail how different types of pyroclastic density currents originate (**Figure 12**). From **Figure 12**, the pyroclastic density currents most likely to occur at Beakdusan volcano are the following: A, B, C, depending on the size and the amount of interaction with external water. For laterally moving systems, the pyroclastic density currents can be identified as two end-member types: (A) Concentrated currents or pyroclastic flows, (B) Dilute currents or pyroclastic surges (Note that these are often a spectrum, with gradations in between). The end-member A has the following main characteristics:

1. It has solids in concentrations of tens of volume percentage, and so they have higher densities than surges.
2. They have a free surface, above which solids' concentration decreases sharply.
3. Transport of material is by fluidization, and most flows are considered to be laminar.

http://dx.doi.org/10.5772/62340

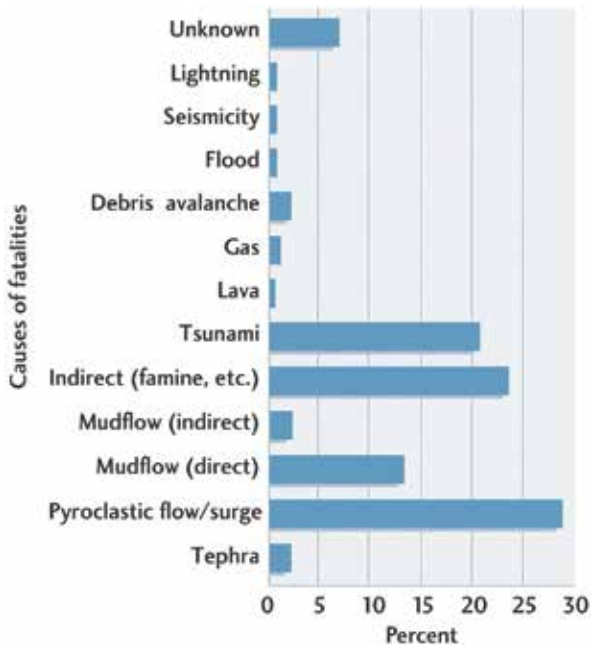

Figure 11. Statistical percentage of fatalities for volcanic-related phenomena in last 2000 years. Pyroclastic density current is the most deadly phenomena in the last 2,000 years (Figure taken from the web and modified).

4. Velocities vary, typically by 10s of meters per second up to several hundred meters per second, inferred from the heights of obstacles overcome by flows.

The end-member B has the following main characteristics:

1. It contains less than 0.1–1.0% by volume of solids, even near ground surface, and so they are relatively of low density.

2. They are density-stratified, with the highest particle concentration near the ground surface.

3. Material is transported primarily by turbulent suspension.

4. Transport system is modeled as one that loses particles by sedimentation, which depletes the system of mass. Eventually, the system may become buoyant, in which case it becomes a plume.

5. Velocities vary, typically by 10s of meters per second, but they can also be much faster [44–48].

In fluid dynamics, the equations that govern the concentrated current are well known [49, 50], and the mathematics based on this volcanic phenomena is broadly used to model pyroclastic flows, along with other gravity currents: avalanches, seafloor turbidity currents, lahars, and lava flows. Two numerical codes apply these equations with small differences: Titan2D [51] and Volcflow [52, 53], but so far they have not produced any modeling for diluted currents.

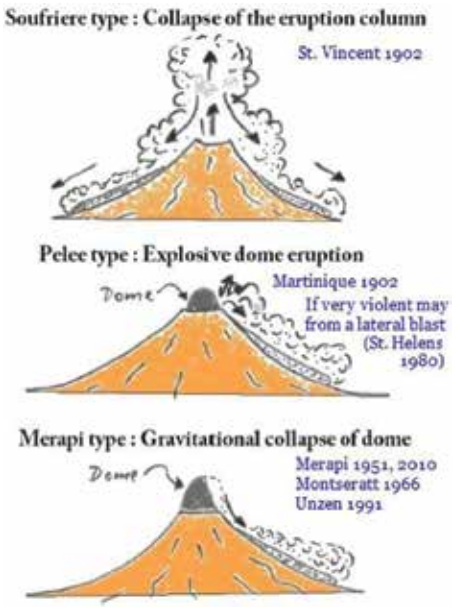

Figure 12. Origins of pyroclastic density currents. (A) Short single-surge current derived by momentary collapse from a Plinian eruption column. (B) Sustained current derived from prolonged pyroclastic fountaining. The height of the jet (gas thrust) that feeds the current may vary and is transitional into (C). (C) A sustained current derived from a prolonged low pyroclastic fountaining explosive eruption. (D) Current with a single (or multiple) surge derived from lateral blasts initiated by catastrophic decompression of a magmatic and/or hydrothermal system. (E) Single-surge current derived from a collapsing lava dome or flow front. Hot rock avalanches generate turbulent density currents. (F) Deposit-derived pyroclastic density current caused by gravitational collapse and avalanching of unstable loose ignimbrite. The current may be a single-surge or more sustained where the collapse is retrogressive. Most large-volume ignimbrites derive from current types (B) and (C), which may involve periods of quasi-steady flow. Many may include significant components derived from currents of type (F) [44, 45]. For Baekdusan, we chose the following three types: Soufriere, Pelee, and Merapi types (modified from [62]).

The only numerical code that models the diluted currents is called PDAC [54]. An application is shown for Somma-Vesuvius volcano, where pyroclastic density currents are modeled on the data of the 1631 AD sub-Plinian eruption ([55]; **Figure 13**). Kelfourn [53] tried to model two-fluid model block-ash flows and cloud-ash surge at Merapi volcano, developing new equations, but there is not yet an agreement (Kelfourn, personal communication). The importance of modeling diluted currents together with dense currents for the hazard of an explosive active volcano is commonly witnessed from the volcanological history, as seen in the work of Mastrolorenzo [56] who demonstrate the causes of mortality in PDCs at Pompeii and surroundings, on the basis of a multidisciplinary volcanological and bioanthropological study. Field and laboratory studies of the eruption products and victims, merged with numerical simulations and experiments, indicate that heat was the main cause of death. Their results show that exposure to at least 250°C hot surges at a distance of 10 km from the vent was sufficient to cause instant death, even if people were sheltered within buildings. Despite the fact that impact force and exposure time to dusty gas declined toward PDCs' periphery up to the survival conditions, lethal temperatures were maintained up to the PDCs' extreme depositional limits. This study suggests that diluted currents are very dangerous, and if the

http://dx.doi.org/10.5772/62340

runout of the pyroclastic flow must be chosen, it is always underestimated when considering diluted currents, especially for large eruption.

Figure 13. 4D immersive visualization of the simulated partial column collapse scenario at Vesuvius. The collapse of the volcanic eruption column and the propagation of pyroclastic density currents (PDCs), for selected medium-scale (sub-Plinian) eruptive scenarios at Vesuvius, Italy (modified from [55]).

5. Relationship between the Baekdusan eruptions: 1903 AD, 1668–1702 AD, and Millennium eruptions, and the most devastating eruptions in the recent history of the earth

As indicated in **Table 1**, the 1903 AD, 1668–1702 AD, and the Millennium eruptions are characterized by the following VEI, respectively: 2–3, 4–5, and ~7. From the classification of Newhall and Self [43], the magnitude of each eruption with all the volcanological parameters can be deduced. If we compare the total volume ejected from Baekdusan volcano in the last Millennium activity with the most devastating eruptions in the recent history of volcanology, it appears that the two most recent eruptions shown, from Mount St. Helens and Mount Pinatubo, each caused extensive damage and received intense media interest. Ejected volumes, however, were only about 1/10,000 (St. Helens) and 1/500 (Pinatubo) of the volumes associated with either the 74 ka Toba or the 2 Ma Yellowstone super-eruptions. Even the 1883 Krakatau eruption, which accounted for over 35,000 deaths, was smaller than the Toba and Yellowstone eruptions by two orders of magnitude. The 1815 Tambora eruption, which had an ejected volume of less than 5% of those of Toba or Yellowstone and was distinctly less than "super," affected global climate and was responsible for over 50,000 deaths (**Figure 14A** and **B** [57]).

(A)

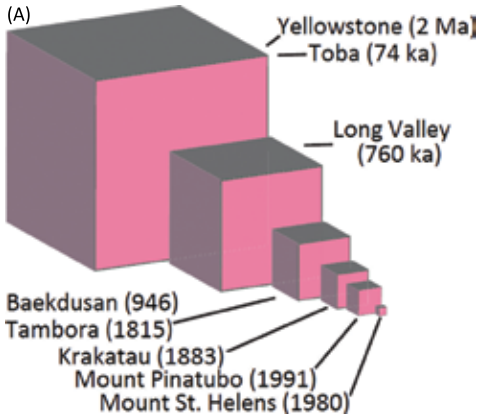

(B)

VEI	Plume height (km)	Ejected volume (km^3)	Frequency on Earth	Example
0	<0.1	>~10^{-6}	daily	Kilauea, Hawai'i
1	0.1–1	>~10^{-5}	daily	Stromboli, Italy
2	1–5	>~10^{-3}	weekly	Galeras, Colombia, 1993
3	3–15	>~10^{-2}	yearly	Nevado del Ruiz, Colombia, 1985
4	10–25	>~10^{-1}	~every 10 y	Soufrière Hills, West Indies, 1995
5	>25	>~1	~every 50 y	Mount St. Helens, USA, 1980
6	>25	>~10	~every 100 y	Pinatubo, Philippines, 1991
7	>25	>~100	~every 1000 y	Tambora, Indonesia, 1815
8	>25	>~1000	~every 10,000–100,000 y	*Supereruptions:* Toba, 74 ka

Figure 14. A. Relative volumes of pyroclastic material erupted from the large eruption in the 2 Ma [57]. **B**. Classification of the VEI modified after [4] (modified from [57]).

The 1903 AD eruption can be compared to two recent eruptions: (A) Nevado del Ruiz, Colombia, 1985, (B) Soufrière Hills, West Indies, 1995 (**Figure 14B**). The two eruptions of 1668–1702 AD of similar size can be compared to the following eruptions: (A) Soufrière Hills, West Indies, 1995, (B) Mount St. Helens, USA, 1980 (**Figure 14B**). The Millennium eruption may have been slightly larger than the 1815 Tambora eruption, Indonesia. Millennium eruption can be considered a super-eruption alike other eruptions (e.g., Campanian Ignimbrite, Campi Flegrei, Napoli [58]; **Figure 15**). This assumption is confirmed from some South Korean scientists that during the 2nd International Workshop for Volcanic Disaster Preparedness at Chungbuk National University, Korea affirmed that the Millennium eruption could have been as high as **7** VEI. Further, Xu et al. [42, 59] suggest that the Millennium eruption was a Toba-like "ash giant/sulfur dwarf" and had much smaller global climatic impacts. Sun et al. [60] confirm that the eruption most probably occurred around AD 940s, 7 years after the Eldgjá eruption on Iceland, and examining the eruption's potential for climate-forcing using the sulfate records

http://dx.doi.org/10.5772/62340

from the ice cores, they conclude that it was unlikely to have had a global impact. Zircons U–Th data of Millennium eruption indicate that magma resided only ~8 ka prior to eruption. Therefore, Baekdusan volcano can produce catastrophic, explosive eruptions in the foreseeable future [36]. Thus, Baekdusan is the most active volcano in China [14], and it is a high-risk volcano because more than 100,000 people live on or near the slopes, with the addition of many tourists.

Eruption magnitude or VEI (Volcanic Explosivity Index)	Minimum erupted mass (kg)	Minimum volume of magma erupted (km^3)	Minimum volume of ash (km^3)	Example of typical eruption	Frequency (average number of eruptions per 100 years)	Minimum probability of one or more eruptions of this size during 21st century
7 (low)	1×10^{14}	40	100	An event a little larger than Tambora, 1815	0.1 – 0.5	10 – 50%
7 (moderate)	2.5×10^{14}	100	250	Possibly Kikai, Japan, 6000 years ago	0.01 – 0.06	1 – 6%
7 (high)	8×10^{14}	300	750	Campanian, Italy, 35,000 years ago	0.001 – 0.01	0.1 – 1%
8 (low)	1×10^{15}	400	1000	Taupo caldera, New Zealand, 26,000 years ago	<0.001	0.1%
8 (high)	8×10^{15}	3200	>5000	A Toba-size event	0.0001	Approximately 0%

Figure 15. The Volcanic Explosivity Index (VEI) is calculated with a logarithmic-based scale of erupted mass, as well as past examples, estimated frequency, and probability. It includes large eruptions from 40 km^3 in magma volume up to the largest super-eruptions known (modified from [15]).

5.1. An example of Titan2D simulation with the size of 1903 AD eruption

The size of the 1903 AD eruption has been evaluated, and consequently some Titan2D simulations are presented, taking into account where the vents of the 1903 AD, 1668 AD, and 1702 AD were located. Five vent locations are considered: three inside the caldera lake and two outside the caldera, as illustrated in **Figure 16**. The simulations start with an initial column (or pile) that collapses. The column is a vertical cylinder with a diameter 250 m and the height Hcol (**Table 4**). In **Figure 17** we report the thickness of the deposit when the flow is stopped. We consider 1 h (3,600s) after the initial collapse of the eruption column which can be formed by the Plinian eruption. The scenario performed shows, according to the vent locations, that the flow moves in diverse directions (NE, SE) with a thickness of 3 m, and that if the vent is located inside the caldera the flow fills the caldera with a thickness of 5 m. If the vent is on the border of the caldera, the flow will deposit thickly, mostly in the northern valley, the upper stream region of Erdaobaihe (**Figure 17** [34, 61]).

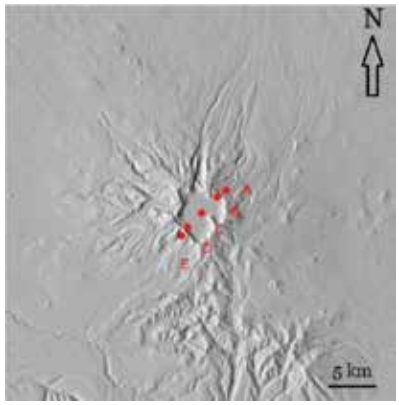

Figure 16. Location of the considered vents for the Titan2D simulation of the small-scale 1903 AD eruption.

Number	Vent	Int. frict.	Bed. Frict	Hcol (m)	Diameter (m)	Volume (m^3)
1	A	30	25	1000	250	4.9×10^7
2	A	30	16	1000	250	4.9×10^7
3	A	25	16	1000	250	4.9×10^7
4	A	25	16	2000	250	9.8×10^7
5	B	25	16	2000	250	9.8×10^7
6	C	25	16	2000	250	9.8×10^7
7	D	25	16	2000	250	9.8×10^7
8	E	25	16	2000	250	9.8×10^7

Table 4. Parameters used to simulate the pyroclastic flow of 1903 AD eruption needed by Titan2D code.

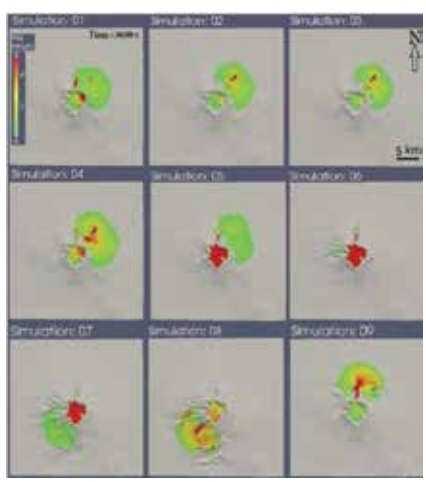

Figure 17. Results of the Titan2D simulation for a small-scale scenario (VEI 3) similar to the 1903 AD eruption [34, 61].

http://dx.doi.org/10.5772/62340

6. The impact of 1668–1702 AD and Millennium eruption around Baekdusan volcano

From the pyroclastic density currents scenario of the 1668–1702 AD eruptions with a runout around 5,000 m (**Figure 18**), two densely populated cities which are nearest to Baekdusan volcano would suffer significant damage: Erdaobaihe and Songjianghe. Possibly, the pyroclastic density currents could also affect two other cities located slightly further away, such as Fusong and Lushuihe. In the case of the Millennium eruption, considering only the direct impact, without considering the indirect effect which in the case of such eruption could be severe, and considering an underestimation of the runout, the following cities will be hit: Erdaobaihe, Songjianghe, Changbai, Huishan, Baishan, Fusong, Lushuihe, and Tumer (**Figure 19**).

Figure 18. Possible area covered by a pyroclastic density current of the size of the 1668–1702 AD eruption. The runout chosen could have been underestimated so that the impact would be more severe than expected.

Figure 19. Possible area covered by a pyroclastic density current of the size of the Millennium eruption. The runout chosen could have been underestimated so that the impact would be more severe than expected and surely of regional scale, if not global.

7. Concluding remarks on the worst-case scenario

The worst-case scenario is surely an eruption of a colossal size (Millennium eruption), but it has to be excluded from the scenario of the 1668–1702 AD eruption. In this case, the hazard and the risk must be evaluated carefully, and the population around Baekdusan volcano must be informed in detail. We think in this case, the population at risk is not aware of the possible hazard of the volcano. In all sorts of circumstances, the population has to be alerted. Every sign of unrest has to be monitored and communicated to everybody involved in the decision-making to the people. As far as we are concerned there is not a robust monitoring system around Baekdusan volcano, especially on North Korea side. An emergency plan must be created for Baekdusan volcano.

8. Future research prospectives

In the near future, there are several points in research direction that the Asian scientists could undertake, if they have not done yet: (A) Evolution of the Baekdusan volcano plumbing system in the least 20,000 years. (B) Developing an open source numerical code to model diluted density currents (surge) for the worst-case scenario, (C) Making an event tree study of Baekdusan volcano like that of Somma-Vesuvius volcano, Napoli, Italy.

Acknowledgements

This research was supported by a grant [MPSS-NH-2015-81] through the Natural Hazard Mitigation Research Group funded by Ministry of Public Safety and Security of Korean government. Thanks to Dr. Giovanni Macedonio for helping in making the simulation of **Figure 17** at Osservatorio Vesuviano, INGV, Napoli, Italy. Thanks to Chris Hawkesworth for an early review of the manuscript. Thanks to Steve Sparks to critically looking at the manuscript and addressing the journal for the content of the manuscript.

Author details

Angelo Paone[1,2] and Sung-Hyo Yun[1*]

*Address all correspondence to: yunsh@pusan.ac.kr

1 Pusan National University, Department of Earth Science Education, Busan, Republic of Korea

2 Liceo Scientifico Meucci, Aprilia, Latina, Italy

http://dx.doi.org/10.5772/62340

References

[1] Gomà Daniel, 2004. Border Disputes between China and North Korea. China Perspectives, 52 Online since 23 April 2007. URL: http://chinaperspectives.revues.org/806

[2] Gomà Daniel, 2006. The Chinese-Korean border issue: an analysis of a contested frontier. Asian Survey, Vol. 46, No. 6, pp. 867–880. URL: http://www.jstor.org/stable/10.1525/as.2006.46.6.867

[3] Cashman K. V., Sparks R. S. J., 2013.How volcanoes work: a 25 year perspective. Geological Society of America Bulletin, Vol. 125, No. 5–6, pp. 664–690.

[4] Sparks R. S. J., Biggs J., Neuberg J. W., 2012. Monitoring volcanoes. Science, Vol. 335, pp. 1310–1311.

[5] Sparks R.S.J., 2003. Forecasting volcanic eruptions. Earth and Planetary Science Letters, Vol. 210, pp. 1–15.

[6] Newhall C., Andreastuti S., Lara L., Rosi M., Woo G., 2014. (3.I.F) Managing Worst-Case Scenarios (with Reference to Merapi 2010, St. Helens 1980, Pinatubo 1991, and The Next VEI 7 Eruption) Cities on Volcanoes 8, Living in Harmony with Volcano: Bridging the will of nature to society, Yogyakarta, 9–13 September 2014

[7] Wei H., Liu G., Gill J., 2013. Review of eruptive activity at Tianchi volcano, Changbaishan, northeast China: implications for possible future eruptions. Bulletin of Volcanology, Vol. 75, pp. 1–14.

[8] Yun S. H., Lee J. H., 2012. Analysis of unrest signs of activity at the Baegdusan volcano. Journal of Petrological Society of Korea, Vol. 21, pp. 1–12.

[9] Yun S. H., Lee J. H., Chang C., 2013. A study on the change of magma activity from 2002 to 2009 at Mt. Baekdusan using surface displacement. Journal of Korean Earth Science Society, Vol. 34, No. 6, pp. 470–478 (in Korean with English abstract).

[10] Xu J., Liu G., Wu J., Ming Y., Wang Q., 2012. Recent unrest of Changbaishan volcano, northeast China: a precursor of a future eruption? Geophysical Research Letters, Vol. 39, p. L16305, doi: 10.1029/2012GL052600

[11] Liu G., Liu G. R., Zhang H. R., Kong Q. J., Wu C. Z., Guo F., Zhang C. F., 2004. Elementary analysis of data from Tianchi volcano. Journal of Geoscience Research NE Asia, Vol. 7, No. 2, pp. 156–16.

[12] Gun U. Y., Ok J. U., Song K. M., Song R. G., Nam R. K., Hammond J. O., Oppenheimer C., Whaler K., Park S., Dawes G., Iacovino K., 2013.The Mt. Paektu geoscientific experiment. IAVCEI 2013 Scientific Assembly, July 20–24, Kagoshima, Japan.

[13] Liu G., 2013.Changbaishan seismic mornitoring network and recent unrest of the volcano. IAVCEI 2013 Scientific Assembly, July 20–24, Kagoshima, Japan.

[14] Wei H., Sparks R. S. J., Liu R., Fan Q., Wang Y., Hong H., Zhang H., Chen H., Jiang C., Dong J., Zheng Y., Pan Y., 2003. Three active volcanoes in China and their hazards, Journal of Asian Earth Sciences, Vol. 21, pp. 515–526.

[15] Sparks S., Self S., Grattan J., Oppenheimer C., Pyle D., Rymer H., 2005. Super-eruptions: Global Effects and Future Threats. Report of a Geological Society of London Working Group (2nd (print) Edn.). Original (Web) edition available at www.geolsoc.org.uk/supereruptions.

[16] Lei J., Zhao D., 2005. P-wave tomography and origin of the Changbai intraplate volcano in Northeast Asia. Tectonophysics, Vol. 397, pp. 281–295.

[17] Zhao D., 2012.Tomography and dynamics of western-Pacific subduction zones. Monographs on Environment, Earth and Planets, Vol. 1, No. 1, 1–70.

[18] Zhao D., Liu L., 2010. Deep structure and origin of active volcanoes in China. Geoscience Frontiers, Vol. 1, pp. 31–44.

[19] Zhao D., Tian Y., 2013. Changbai intraplate volcanism and deep earthquakes in East Asia: a possible link? Geophysics Journal International, Vol. 195, pp. 706–724.

[20] Kuritani T., Ohtani E., Kimura J.-I., 2011.Intensive hydration of the mantle transition zone beneath China caused by ancient slab stagnation. Nature Geoscience, Vol. 4, pp. 713–716.

[21] Annen C., Blundy J.D., Sparks R. S. J., 2006. The genesis of intermediate and silicic magmas in deep crustal hot zones. Journal of Petrology, Vol. 47, pp. 505–539.

[22] Yun S. H., Koh J. S., Chang C. W., 2015. Magma genesis of Holocene volcanism at Mt. Baekdusan. Abstract Book, 2015 Fall Joint Conference of Geological Science of Korea (2015. 10. 28-31), Jeju, Korea, pp. 518, 39.

[23] Yun S. H., Won C. K., Lee M. W., 1993. Cenozoic volcanic activity and petrochemistry of volcanic rocks in the Mt. Paektu area. Journal of Geological Society of Korea, Vol. 29, pp. 291–307 (in Korean with English abstract).

[24] Wei H., 2010. Magma up-moving process within the magma prism beneath the Changbaishan volcanoes. Earth Science Frontiers, Vol. 17, No. 1, pp. 11–23 (in Chinese with English abstract).

[25] Horn S., Schmincke H.U., 2000. Volatile emission during the eruption of Baitoushan Volcano (China/North Korea) ca. 969 AD. Bulletin of Volcanology, Vol. 61, pp. 537–555.

[26] Annen C., Blundy J. D., Sparks R. S. J., 2006. The sources of granitic melt in deep hot zones. Transactions of the Royal Society of Edinburgh: Earth Sciences, Vol. 97, pp. 297–309, doi: 10.1017/S0263593300001462

[27] Annen C., Sparks R. S. J., 2002. Effects of repetitive emplacement of basaltic intrusions on thermal evolution and melt generation in the deep crust. Earth and Planetary Science Letters, Vol. 203, pp. 937–955.

http://dx.doi.org/10.5772/62340

[28] Wei H., Wang Y., Jin J., Gao L., Yun S.H., Jin B., 2007.Timescale and evolution of the intracontinental Tianchi volcanic shield and ignimbrite-formation eruption, Changbaishan, Northeast China. Lithos, Vol. 96, pp. 315–324.

[29] Wei H., Taniguchi H., Myamoto T., Jin B., 2007. Stratigraphic sequences and magmatic cycles of the Tianchi volcano, Changbaishan. Northeast Asian studies Vol. 11, pp. 173–193.

[30] Yang L., Wang F., Feng H., Wu L., Shi W., 2014.$^{40}Ar/^{39}Ar$ geochronology of Holocene volcanic activity at Changbaishan Tianchi volcano, Northeast China. Quaternary Geochronology, Vol. 21, pp. 106–114.

[31] Yun S. H., 2013.Volcanological interpretation of historical eruptions of Mt. Baekdusan volcano. Journal Korean Earth Science Society, Vol. 34, No. 6, pp. 456–469.

[32] Yun S. H., Cui Z. X., 1996. Historical eruption records on the Cheonji caldera volcano in the Mt. Peaktu. Journal of Korean Earth Science Society, Vol. 17, No. 5, pp. 376–382 (in Korean with English abstract).

[33] Yun S. H., Lee J. H., 2011. Volcanological interpretation of historic record of 1702 fallout-ash from the Mt. Baekdusan. Journal of Petrological Society of Korea, Vol. 20, No. 4, pp. 243–250 (in Korean with English abstract).

[34] Yun S. H., Lee J. H., Kim S., Chang C., Cho E., Yang I., Kim Y., Kim S., Lee K., Kim S., Macedonio G., 2013. TITAN2D simulations of pyroclastic flows from small scale eruption at Mt. Baekdusan. Journal of Korean Earth Science Society, Vol. 34, No. 7, pp. 615–625 (in Korean with English abstract).

[35] Machida H., Hiroshi M., Zhao D. C., 1990, The recent major eruption of Changbai eruption and its environmental effects. Geophysical Reports of Tokyo Metropolitan University, Vol. 25, pp. 1–20.

[36] Yun et al., 2012. A study on the cooperative diagnosis on eruption possibility of Baegdusan volcano. Pusan National University Project. CATER 2011–5210 pp. 1–131 (in Korean with the references in English).

[37] Zou H., Fan Q., Zhang H., 2010. Rapid development of the great Millennium eruption of Changbaishan (Tianchi) volcano, China/North Korea: evidence from U–Th zircon dating. Lithos, Vol. 119, pp. 289–296.

[38] Machida H., Arai F., 1992, Atlas of Tephra in and around Japan. University of Tokyo Press, Tokyo. 276 p (in Japanese).

[39] Nakagawa M., Nishimoto J., Miyamoto T., Taniguchi H., 2013. Magma system and its eruption processes of the caldera-forming 10th century eruption of Changbaishan (Baitoushan) Volcano: inferred from petrological and geochemical characteristics. IAVCEI 2013 Scientific Assembly, July 20–24, Kagoshima, Japan.

[40] Chu K. S., Tsuji Y., Baag C. E., Kang T. S., 2011.Volcanic eruptions of Mt. Baekdu Changbai occurring in historical times. Bulletin of Earthquake Research Institute, University of Tokyo, Vol. 20, pp. 11–27 (in Japanese with English abstract).

[41] Yin J., Jull T., Burr G. S., Zheng Y., 2012. A wiggle-match age for the Millennium eruption of Tianchi volcano at Changbaishan, Northeastern China. Quaternary Science Reviews, Vol. 47, pp. 150–159.

[42] Xu J., Pan B., Liu T., Hajdas I., Zhao B., Yu H., Liu R., Zhao P., 2013. Climatic impact of the Millennium eruption of Changbaishan volcano in China: new insights from high-precision radiocarbon wiggle-match dating. Geophysical Research Letters, Vol. 40, pp. 1–6, doi: 10.1029/2012GL054246

[43] Newhall C., Self S., 1982.The volcanic explosivity index (VEI): an estimate of explosive magnitude for historical volcanism. Journal of Geophysical Research, Vol. 87, pp. 1231–1238.

[44] Branney M. J., Kokelaar P., 2002. *Pyroclastic Density Currents and the Sedimentation of Ignimbrites.* Geological Society, London, Memoirs, 27, pp. 152.

[45] Sparks R. S. J., Bursik M. I., Carey S. M., Gilbert J. S., Glaze L. S. Sigurdsson H., Woods A. W., 1997.Volcanic Plumes. Wiley, Chichester.

[46] Gilbert J. S., Sparks R. S. J. (eds), 1998. The Physics of Explosive Volcanic Eruptions. Geological Society, London, Special Publications, Vol. 145, pp. 193.

[47] Parfitt E. A., Wilson L., 2008. Fundamentals of Physical Volcanology. Blackwell Publishing Ltd., pp. 256.

[48] Fagents S. A., Gregg T. K. P., Lopes R. M. C., 2012. Modeling Volcanic Processes. The Physics and Mathematics of Volcanism. Cambridge University Press, pp. 448.

[49] Savage S. B., Hutter H., 1989. The motion of a finite mass of granular material down a rough incline. Journal of Fluid Mechanics, Vol. 199, pp. 177-215

[50] Iverson Denlinger, 2001. Flow of variably fluidized granular masses across three-dimensional terrain 1. Coulomb mixture theory. Journal of Geophysical Research, Vol. 106, p. 537.

[51] Patra A. K., Bauer A. C., Nichita C., Pitman E. B., Sheridan M. F., Bursik M. I., 2005.Parallel adaptive simulation of dry avalanches over natural terrain. Journal of Volcanology and Geothermal Research, Vol. 139, pp. 1–21.

[52] Kelfoun K., 2011.Suitability of simple rheological laws for the numerical simulation of dense pyroclastic flows and long-runout volcanic avalanches. Journal of Geophisical Research, Vol. 116, p. B08209, doi: 10.1029/2010JB007622

[53] Kelfourn K., 2011. A two-fluid model for block-and-ash flows and ash-cloud surge confronted with the 1994 eruption of Merapi volcano (Indonesia). European Geosciences Union. General Assembly, Vienna, Austria, Poster.

http://dx.doi.org/10.5772/62340

[54] Esposti O. T., Cavazzoni C., Erbacci G., Neri A., Salvetti M. V., 2007. A parallel multiphase flow code for the 3D simulation of explosive volcanic eruptions. Parallel Computer. doi: 10.1016/j.parco.2007.04.003

[55] Neri A., Esposti Ongaro T., Menconi G., De' Michieli Vitturi M., Cavazzoni C., Erbacci G., Baxter P.J., 2007. 4D simulation of explosive eruption dynamics at Vesuvius. Geophysical Research Letters, Vol. 34, p. L04309.

[56] Mastrolorenzo G., Petrone P., Pappalardo L., Guarino F.M., 2010. Lethal thermal impact at periphery of pyroclastic surges: evidences at Pompeii. PLoS ONE, Vol. 5, No. 6, pp. 1–12.

[57] Miller C. F., Wark D. A., 2008. Supervolcanoes and their explosive supereruptions. Elements, Vol. 4, pp. 11–16.

[58] Costa A., Folch A., Macedonio G., Giaccio B., Isaia R., Smith V. C., 2012. Quantifying volcanic ash dispersal and impact of the Campanian Ignimbrite super-eruption. Geophysical Research Letters, Vol. 39, p. L10310, doi: 10.1029/2012GL051605

[59] Xu J., Pan B., Liu T., Hajdas I., Zhao B., Yu H., Liu R., 2013.The millennium eruption of Changbaishan volcano in northeast China: high-precision wiggle-match radiocarbon chronology and implications. IAVCEI 2013 Scientific Assembly, July 20–24, Kagoshima, Japan.

[60] Sun C., Plunkett G., Liu J., Zhao H., Sigl M., McConnell J. R., Pilcher J. R., Vinther B., Steffensen J. P., and ValerieHall, 2014. Ash from Changbaishan Millennium eruption recorded in Greenland ice: implications for determining the eruption's timing and impact. Geophysical Research Letters, Vol. 41, pp. 694–701, doi: 10.1002/2013GL058642.

[61] Yun S. H., Paone A., Macedonio G., Jeong Lee H., Kim S. K., Cho E., Kim Y. J., 2013. A preliminary evaluation of the impact of pyroclastic flows using Titan 2D at the Baegdusan volcano according to three different scenarios. 2nd International Workshop for Volcanic Disaster Preparedness. Chungbuk National University. Abstract and Oral communication.

[62] Francis P., 1993, Volcanoes: A planetary perspective. Oxford University Press, Walton Street, New York, 249, 443 p.

Chapter 8

Magnitude-Frequency Distribution of Slope Failures in Japan: Statistical Approach to a True Perspective on Volcanic Mega-Collapses

Hidetsugu Yoshida

Additional information is available at the end of the chapter

http://dx.doi.org/10.5772/63131

Abstract

The relationship between magnitude and frequency of mega-collapses (i.e., sector collapses), mainly of volcanic edifices, in Japan is examined by using existing datasets for volcanic mega-collapses and smaller but more frequent events. Statistical analysis of these datasets showed that the magnitude-frequency distribution of slope failures with volumes greater than or equal to 10^7 m^3 can be expressed by a simple exponential function: $\log N(x) = a - bx$, where $N(x)$ is the cumulative number of mass-movement events with magnitude $\geq x$. When this function was fitted to the datasets, the slope coefficient, b, was 0.7 or 0.8. The frequency distribution of mega-collapses was similar to that of smaller (volume $>10^{5-6}$ m^3) events. Records from the past millennium in Japan suggest that this magnitude-frequency relationship may be applicable to the last several tens of thousands of years. Therefore, it is possible to predict event probability and the recurrence interval of events of a certain magnitude. In this way, mega-collapses with a volume of over 10^9 m^3 may be estimated to occur at least every 1000–2000 years somewhere in Japan. Therefore, mega-collapses in Japan should not be considered "rare"; rather, they are "normal" events on a geomorphological timescale.

Keywords: exponential regression, probability, recurrence interval, sector collapse, debris avalanche

1. Introduction

In recent years, terrestrial slope failure and rapid mass movement have been attracting increasing attention as disastrous geomorphic processes [1–3]. Rapid mass movements range

from maximal events, such as the gigantic sector collapse of a volcanic edifice, to much smaller but more frequently observed slope failures. In a geomorphological context, it is important to critically examine the relationship between the magnitude and frequency of rapid mass-movement events to determine the relative contributions of large and small events to the denudation processes of mountains (including volcanoes) in an area of active uplift and denudation such as Japan (**Figure 1**) [4, 5].

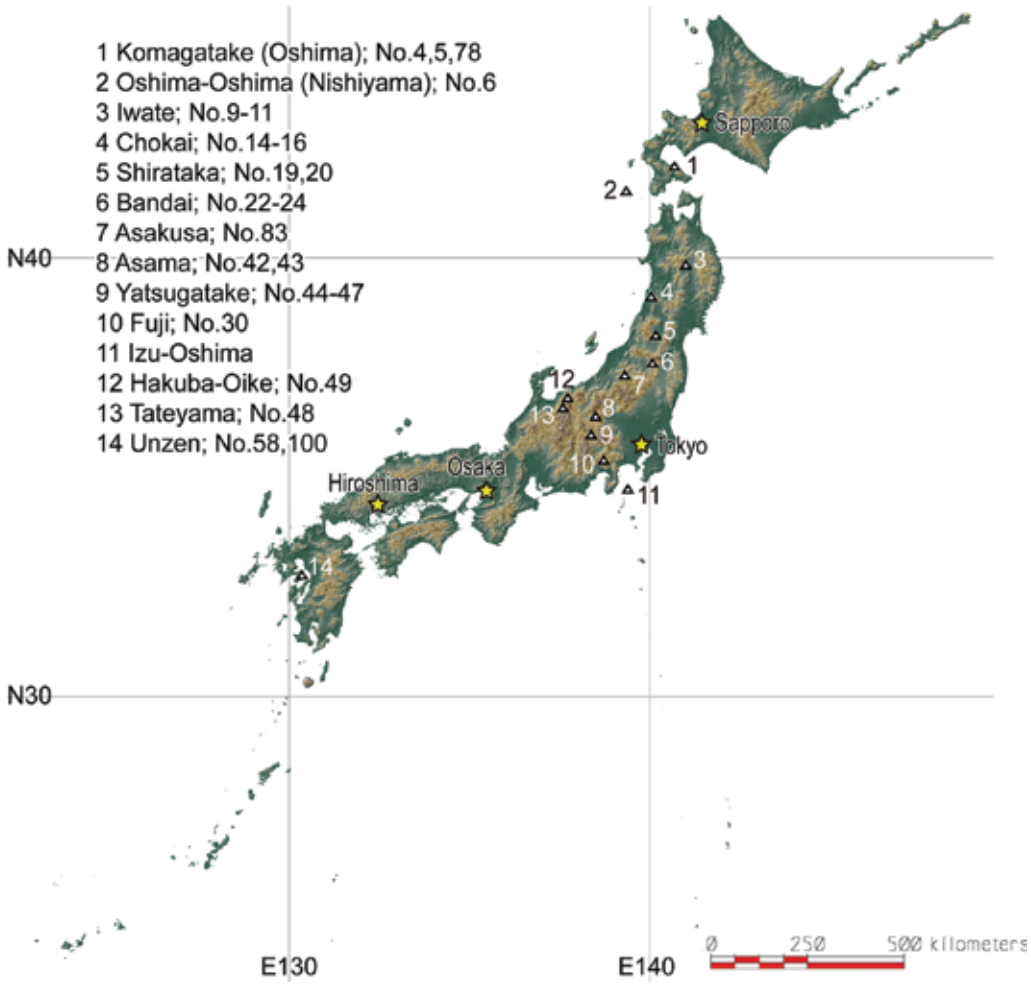

Figure 1. Topographic map of the Japanese islands, produced from DEMs of the Geospatial Information Authority of Japan, showing the locations of the volcanoes referred to in the text.

Many studies have investigated magnitude-frequency relationships of earth surface processes and landforms [6–10], the best-known example of which is possibly the Gutenberg-Richter equation in seismology. In geomorphology, the frequency distribution of landslides has often been analyzed because landslides can have significant impacts on human activities. In

http://dx.doi.org/10.5772/63131

particular, studies have focused on the relationship between landsliding potential and geologic [8] or climatic conditions and changes [9]. In general, the frequency distributions of landslides and other mass movements are similar [10], and they can be simply expressed by the following exponential equation:

$$\log \mathrm{N}(x) = \mathrm{a} - \mathrm{b}x \tag{1}$$

where $N(x)$ is the cumulative number of landsliding or mass-movement events with magnitude ≥ x and a and b are constants. Here, x is equal to log$A$, where A is the landform area (e.g., landslide area).

By contrast, very few attempts have been made to investigate statistically the magnitude-frequency distribution of gigantic sector collapses of volcanic edifices [11], although Yoshida [12] has analyzed the magnitude-frequency distribution of hummocks on rockslide-debris avalanche deposits associated with volcanoes. Thus, the question of whether the relationship between magnitude and frequency of mega-collapses shows a similar trend to that observed for much smaller events remains unanswered.

One reason for this situation, of course, is the paucity of examples, because gigantic sector collapses occur much less frequently than small slope failures. Although mega-collapses have been qualitatively characterized as relatively low-frequency events [13, 14], it is important to assess the impact of mega-collapses (which are mainly volcanic) from a more rigorous geostatistical viewpoint. Because the impact of an event is the product of its magnitude and frequency [10], despite their low frequency, mega-collapses can contribute substantially to long-term geomorphic changes and sediment transport to alluvial plains [14], and they also have the potential to cause greater disasters than smaller-scale events [1–3]. The accumulation of research results, particularly in the field of volcanology, has made it possible to analyze the relationship between magnitude and frequency of mega-scale mass movements by combining published datasets of magnitude-frequency distributions.

The aim of this chapter is to explore the characteristics of the magnitude-frequency distribution of mega-scale slope failures in Japan, which typically occur on the flanks of mature volcanoes [15]. These huge events (generally >10^8 m^3 in volume) are significant in terms of the geomorphic development of volcanic edifices and other mountains and the regions surrounding them, as shown by the catastrophic rockslide-debris avalanche event associated with the 1980 eruption of Mt. St. Helens [16, 17]. Here, to deepen our understanding of volcanic mega-collapses in Japan several datasets of mega-scale and smaller slope failures are examined statistically, and event probabilities and recurrence intervals are also discussed.

2. Data and methods

First, it is necessary to define "rapid mass movement" as used in this research. Mass movements include a variety of phenomena, which have been characterized by terms such as

"creep," "fall," "topple," "slip," "avalanche," "slide," "flow," "heave," "sink," and "subsidence" [18–20]. Among these terms, slip, avalanche, and flow may denote rapid (e.g., 10^0–10^2 m/s or even faster if expressed as speed) mass movements in which the collapsed materials are transported relatively far from the source region in short time. Because in particular "slide" (landslides) can in fact describe both rapid and slow events, this study excludes selectively slow slides (landslides) (e.g., 10^0–10^5 cm/y) from rapid mass movements, unless the landslide mass is well segregated and the depositional area shows a hummocky terrain [21–24] as in the case of a debris avalanche. Mega-collapses of volcanic edifices can be considered slips or avalanches.

Given this criterion, three datasets were prepared as follows (**Table 1**):

In this chapter	Target	Original reference	No. of events analyzed in this study	Magnitude expression	Magnitude range	Notes
Table 2	Mega-collapses of Quaternary volcanoes	Yoshida (2010)	67	Volume	$59 \geqq 10^8$ m^3, $8 \geqq 10^7$ m^3	
-	Large-scale collapses	Machida et al. (1987)	332	Depositional area	10^5–10^7 m^2	Of 333 recorded events
-	Rapid mass-movements during 1975–1983	Ohmori and Hirano (1988)	2083	Depositional area	10^3–10^7 m^2	1739 rocky mudflows, 344 steep slope collapses
Table 3	Estimates based on the empirical relationship between caldera area and (partly depositional) volume	-	36	Volume	>10^7 m^3	

Table 1. Datasets of rapid mass movements in Japan used in this study.

1. Mega-collapses of volcanic edifices in Japan reported by Yoshida [25], together with additional data retrieved by a literature search.

In 2010, Yoshida [25] identified 58 mega-collapses in Japan with an estimated debris (or partly scar) volume greater than or equal to 10^8 m^3. Most of these events occurred in the Middle Pleistocene or later. The volume data of some of these events have been corrected on the basis of new data in this chapter. In addition, for the Kurumizaka debris avalanche (Oshima-Komagatake volcano; **Figure 1**), the author considered here as two events, the Shikabe and Onuma lobes. In addition, eight large collapses with a volume greater than or equal to 10^7 m^3 identified by an additional literature search have been integrated into the dataset. Thus, a total of 67 events were included in the dataset analyzed in this study

http://dx.doi.org/10.5772/63131

(**Table 2**). Note that reference [25] includes only a very rough discussion of the magnitude-frequency relationship of mega-collapses.

2. Large-scale collapses in Japan compiled by Machida et al. [26]

Machida et al. [26] identified 333 large-scale collapses in Japan by examining aerial photographs and maps. For each event, they described the area of the collapse scar, the depositional area (i.e., the area covered by the collapse deposit), and the equivalent coefficient of friction. They did not report volumes, except for a few representative cases. The reported deformed (i.e., depositional) areas ranged from 10^5 to 10^7 m^2. They estimated that most of the identified events (74%) were associated with a volcanic edifice or a volcanic terrain. They also noted that the compiled events represented rapid mass movements, not slow sliding or creep events. In this chapter, the depositional area of each event is used as the measure of its magnitude.

3. Rocky mudflow and steep slope collapse data reported by Ohmori and Hirano [10], based on data for 9 years (1975–1983) originally compiled by the former Construction Ministry of Japan.

Ohmori and Hirano [10] aggregated the depositional area of three types of mass-movement events, which they called "landcreep" (1428 events), "rocky mudflows" (1739 events), and "steep slope collapses" (344 events), and examined the magnitude-frequency relationship of each type. In this chapter, only the rocky mudflow and steep slope collapse events are interpreted as rapid mass movements. Thus, the dataset analyzed in this study consisted of 2083 events that occurred in Japan during 1975–1983.

No.	Volcano	Debris avalanche	Age		Averaged Volume age	Volume	Averaged volume	Caldera area	Caldera area to the three-halves power	References (for corrected and additional data; asterisks)
			×10⁴ yBP	Recent event	×10⁴ yBP	×10⁸m³	×10⁸m³	(×10⁸m²)	(×10⁸m³)	
1	Shiribetsu	Rusutsu	10–5		7.5	20	20	0.0228	34.50	
2	Yotei	Old-Yotei	4		4	13*	13			[27]
3	Usu	Zenkoji	0.8–0.7		0.75	10–20	15			
4	Komagatake (Oshima)	Kurumizaka (Shikabe)		AD 1640	0.0369	14.2-17.0	15.6	0.0551	129.23	
5	Komagatake (Oshima)	Kurumizaka (Onuma)		AD 1640	0.0369	3	3	0.0231	35.19	
6	Oshima-Oshima	Nishiyama		AD 1741	0.0268	24	24	0.0119	13.05	
7	Iwaki	Tokoshinai	65		65	13	13			

No.	Volcano	Debris avalanche	Age		Averaged age	Volume	Averaged volume	Caldera area	Caldera area to the three-halves power	References (for corrected and additional data; asterisks)
			×10⁴ yBP	Recent event	×10⁴ yBP	×10⁸m³	×10⁸m³	(×10⁸m²)	(×10⁸m³)	
8	Tashirodake	Iwasegawa	>2.5		2.5	1	1	0.0106	10.98	
9	Iwate	Aoyamacho	15		15	7.6	7.6			
10	Iwate	Oishiwatari-Koiwai	12		12	25	25			
11	Iwate	Hirakasa	0.6		5	2	2	0.0135	15.76	
12	Hachimantai	Matsuo	5		0.6	20–30	25			
13	Komagatake (Akita)	Sendatsugawa	2.2		2.2	>1	1			
14	Chokai	Kisakata	0.26		0.26	28.5	28.5	0.1393	519.98	
15	Chokai	West Chokai	9		9	14	14	0.0761	209.75	
16	Chokai	Yurihara	1.978		1.978	52	52			
17	Kurikoma	Sukawa	1.8–1.7		1.75	3.7	3.7			
18	Gassan	Sasagawa	<40–30		30	50 ± 30	50	0.1057	343.52	
19	Shirataka	Hataya	80		80	20	20			
20	Shirataka	Hariu	90		90	13	13	0.0687	180.21	
21	Zao	Sukawa	7		7	30	30	0.0341	62.88	
22	Bandai	Ura-Bandai		AD 1888	0.0121	4.9*	4.9	0.0262	42.34	[28]
23	Bandai	Biwasawa	0.25		0.25	1	1	0.0188	25.70	
24	Bandai	Okinajima	4.6–3.0		3.8	22.5*	22.5	0.0642	162.60	[29]
25	Nasu	Kannongawa	1.74		1.74	3	3	0.0050	3.55	
26	Nasu	Ofujisan	4–3		3.5	>10	10	0.0682	178.13	
27	Nyoho-Akanagi	Namekawa	15–12		13.5	7.9	7.9	0.0109	11.39	
28	Akagi	Nashigi	22		22	40–80	60			
29	Onoko	Hirasawa	>55		55	14	14			
30	Fuji	Gotemba	0.29		0.29	17.6	17.6	0.1005	318.45	
31	Myoko	Suginosawa	0.27		0.27	1	1	0.0081	7.23	
32	Myoko	Taguchi	0.9		0.9	2	2			
33	Myoko	Yashirogawa	1		1	5	5			

http://dx.doi.org/10.5772/63131

No.	Volcano	Debris avalanche	Age		Averaged age	Volume	Averaged volume	Caldera area	Caldera area to the three-halves power	References (for corrected and additional data; asterisks)
			×10⁴ yBP	Recent event	×10⁴ yBP	×10⁸m³	×10⁸m³	(×10⁸m²)	(×10⁸m³)	
34	Myoko	Sekikawa	1.9		1.9	14	14	0.1154	392.17	
35	Myoko	Nihongi	4.5		4.5	3	3			
36	Myoko	Tagiri	9		9	3	3			
37	Kurohime	Nabewarigawa	4.3		4.3	8–10	9	0.0327	59.00	
38	Kurohime	Terao	25–15		20	50	50			
39	Iizuna	Koshimizu	20		20	5	5	0.0124	13.80	
40	Iizuna	Mure	23–22		22.5	30–50	40			
41	Yakeyama (Niigata)	Nishi-Onogawa	0.18		0.18	1	1	0.0154	19.17	
42	Asama	Kambara		AD 1783		1.38	1.38			
43	Asama	Okuwa-Maebashi	2.4		2.4	40	40	0.0336	61.59	
44	Yatsugatake	Otsukigawa		AD 888	0.1121	3.5	3.5	0.0283	47.68	
45	Yatsugatake	Nirasaki	24–20		22	90	90			
46	Yatsugatake	Aikigawa	80–100		90	1	1			
47	Yatsugatake	Kannonji	80–130		105	60	60			
48	Tateyama	O-Tombi		AD 1858	0.0151	1.3–2.7	2			
49	Hakuba-Oike	Hiedayama		AD 1911	0.0098	1.5	1.5			
50	Ontake	Kaida-Kisogawa	5		5	16–27	21.5			
51	Hakusan	Oshirakawa	0.44		0.44	1.2	1.2	0.0054	3.95	
52	Kyogatake	Karatanigawa	3–4		3.5	3	3	0.0075	6.45	
53	Takahiradake	Matsuzuka	13–80		46.5	1	1			
54	Takahiradake	Kannawa	13–80		46.5	5	5	0.0163	20.73	
55	Tobidake	Wakasugi	<7		7	1	1	0.0041	2.59	
56	Ojikayama	Higashiyama	<50		50	2	2			

No.	Volcano	Debris avalanche	Age		Averaged age	Volume	Averaged volume	Caldera area	Caldera area to the three-halves power	References (for corrected and additional data; asterisks)
			×10⁴ yBP	Recent event	×10⁴ yBP	×10⁸m³	×10⁸m³	(×10⁸m²)	(×10⁸m³)	
57	Noine-Hanamure	Tashiro	40	40	9	9				
58	Unzen	Mayuyama		AD 1792	0.0217	4.4	4.4	0.0140	16.63	
59	Kujyu	Matsunodai	1		1	1.5	1.5			
60	Tokachidake	Taisho		AD 1926		0.02–0.004*	0.012			[30]
61	Yakeyama (Akita)	—				0.051*	0.051			[30]
62	Nasu	Miyama	0.08–0.07			>0.1*	0.100			[30]
63	Hiuchigatake	Numajiri	0.8			0.3*	0.300			[30]
64	Kurohime	Komazume	1			0.2*	0.200	0.0037	2.22	[31]
65	Ontake	Denjo		AD 1984		0.34*	0.340	0.0058	4.37	[30]
66	Yufu	Tsukahara	0.2			0.4*	0.400			[32]
67	Mizuguchi-Kuraki	Tsue		AD 1596		0.3*	0.300	0.0012	0.40	[32]

Asterisks indicate corrected and additional data with the source (reference) of each of these collapses. See "References" of the last column.

Table 2. Mega-collapses of volcanic edifices in Japan.

To increase the number of mega-collapses (volume >$10^{7–8}$ m^3) in the dataset 1 as above, three procedures were used as follows:

a. In Japan, Inokuchi [13] recognized more than 100 mega-collapses, and Yoshida [25] identified 58 (reinterpreted here as 59) events with a volume greater than or equal to 10^8 m^3 by surveying the volcanic, geologic, and geomorphologic literature, including the catalog in reference [13]. Therefore, that leaves several tens of mega-collapses whose volume is unknown, even roughly.

b. Thus, to estimate the magnitudes of additional mega-collapses, topographic collapse features such as horseshoe calderas (amphitheaters) associated with these mega-collapse

http://dx.doi.org/10.5772/63131

events were investigated. In some cases, the collapse landforms are almost completely preserved and in other cases, they are partly preserved. The relationship between the areal extent of the collapse feature to the three-halves power, based on the geometry, and the mega-collapse volume was examined for 33 events for which both the caldera area and collapse volume were known (**Figure 2**). As a result, the following positive empirical relationship was found:

$$V = 0.5299(A^{1.5})^{0.6805} \tag{2}$$

where V is the volume and A is the caldera area. The correlation coefficient (R) is 0.78, which is quite high, indicating the applicability of Eq. (2) as a predictive one to estimate volumes from the caldera area.

c. Then, 36 events whose topographic characteristics suggest formation as a result of a catastrophic mega-collapse were identified, and their volumes were estimated by substituting caldera area for A into Eq. (2). For example, the caldera of Asakusadake volcano (No. 83) in northern Honshu (**Figure 1**) has an area of 0.0396×10^8 m^2; the caldera opens to the northwest, and a partly dissected hummocky terrain exists below the caldera opening (**Figure 3**). The event volume estimated with Eq. (2) is 10.33×10^8 m^3. The estimated volumes of all 36 events are given in **Table 3**, and these 36 events were added to the mega-collapse dataset compiled in reference [25]. Thus, the expanded dataset, including the eight events added above (see Eq. (1)) by a literature search, comprises 103 mega-collapses, most with a volume greater than 10^8 m^3.

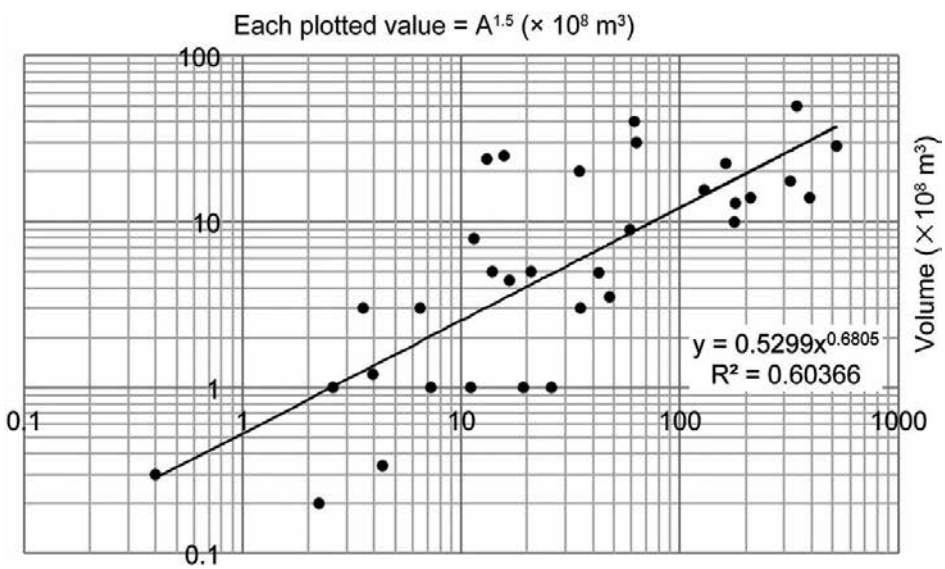

Figure 2. Relationship between event volume and caldera area to the three-halves power for 33 events.

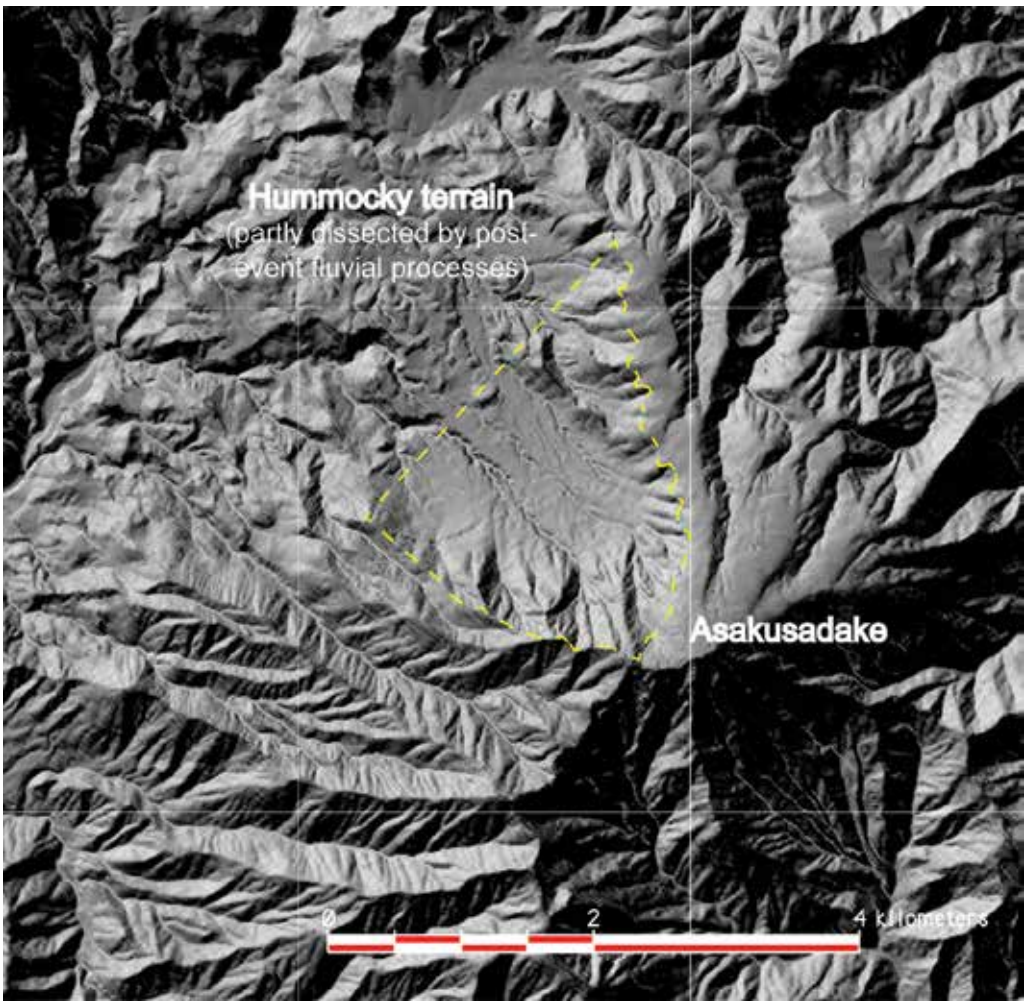

Figure 3. Topography around Asakusadake volcano, northeast Japan. The caldera scar, which opens to the northwest, is outlined by the dashed line. The base map is from 10-m-mesh data provided by the Geospatial Information Authority of Japan.

No.	Volcano		Caldera area ($\times 10^8 m^2$)	Caldera area to the three-halves power ($\times 10^8 m^3$)	Estimated volume ($\times 10^8 m^3$)
68	Shiretoko		0.0090	8.56	2.28
69	Shiretoko-Chinishidake	(landslide?)	0.0295	50.73	7.67
70	Shiretoko-Onnebetsu	NW (landslide?)	0.0129	14.63	3.29
71	Shiretoko-Onnebetsu	E (landslide?)	0.0112	11.81	2.84

http://dx.doi.org/10.5772/63131

No.	Volcano		Caldera area ($\times 10^8 m^2$)	Caldera area to the three-halves power ($\times 10^8 m^3$)	Estimated volume ($\times 10^8 m^3$)
72	Shiretoko-Iou		0.0189	26.06	4.87
73	Mashu		0.0096	9.37	2.43
74	Oakan		0.0192	26.57	4.94
75	Muine	West	0.0193	26.73	4.96
76	Muine	East	0.0075	6.55	1.90
77	Eniwa	NE	0.0033	1.90	0.82
78	Komagadake (Oshima)	Oshirogawa	0.0094	9.17	2.39
79	Esan	Es-3	0.0038	2.34	0.95
80	Mutsu-Hiuchigadake		0.0452	95.99	11.83
81	Zao	Kanno	0.0295	50.56	7.65
82	Hayama		0.1213	422.43	32.44
83	Asakusadake		0.0396	78.66	10.33
84	Nikko-Nantai		0.0110	11.53	2.80
85	Haruna	Miyukida	0.0167	21.52	4.28
86	Haruna	Jimba	0.0136	15.83	3.47
87	Hakone	Kamiyama	0.0069	5.77	1.75
88	Toshima		0.0050	3.52	1.25
89	Mikurajima		0.0223	33.24	5.75
90	Torishima		0.0034	2.01	0.85
91	Kurikoma	Tsurugidake A	0.0027	1.43	0.67
92	Madarao		0.0065	5.26	1.64
93	Tomuro		0.0043	2.82	1.07
94	Okinoshima	West (landslide?)	0.0049	3.45	1.23
95	Okinoshima	South (landslide?)	0.0013	0.46	0.31
96	Okinoshima	(landslide?)	0.0093	8.92	2.35
97	Sambe		0.0021	0.98	0.52
98	Yufu-Garandake		0.0018	0.75	0.44
99	Yufu-Kuehiranoyama		0.0029	1.56	0.72
100	Unzen	Shimabara	0.0057	4.26	1.42
101	Kirishima-Hinamoridake	Kobayashi	0.0508	114.40	13.33

No.	Volcano	Caldera area ($\times 10^8 m^2$)	Caldera area to the three-halves power ($\times 10^8 m^3$)	Estimated volume ($\times 10^8 m^3$)
102	Suwanosejima	0.0406	81.91	10.62
103	Akusekijima	0.0064	5.07	1.60

Table 3. Mega-collapse events whose volumes were estimated using Eq. (2).

3. Magnitude-frequency distribution of volcanic edifice mega-collapses

The magnitude-frequency distribution of 103 mega-collapses (dataset 1) was investigated. First, the event volumes were transformed to their common logarithm values (log$V$). Then, the magnitudes (log$V$ values) were grouped into bins of 0.4 (**Figure 4**). The resulting unimodal distribution resembles a log-normal distribution, especially if the smaller bins are ignored. In fact, the cumulative frequencies of events in the lower (smaller magnitude) bins are likely to be too low, a phenomenon known as rollover, which is often observed in, for example, landslide magnitude-frequency curves [33–35]. Thus, the magnitude-frequency distribution represented by the larger bins may be closer to the true distribution. However, the maximum magnitude of slope failures is necessarily limited by the slope length; thus, it is logically inappropriate to apply a log-normal distribution, which implies a maximum collapse of infinite volume [7]. Therefore, an exponential distribution (Eq. (1)) with constant b fitted to the distribution after excluding the five smallest bins affected by rollover. As a result, the fitted values of a and b were 7.14 and 0.64, respectively, and the correlation was high (R = -0.985) (**Figure 5**). Thus, the magnitude-frequency distribution of the mega-collapse dataset with log$V$ ≥8.0 can be explained by an exponential distribution with constants described above.

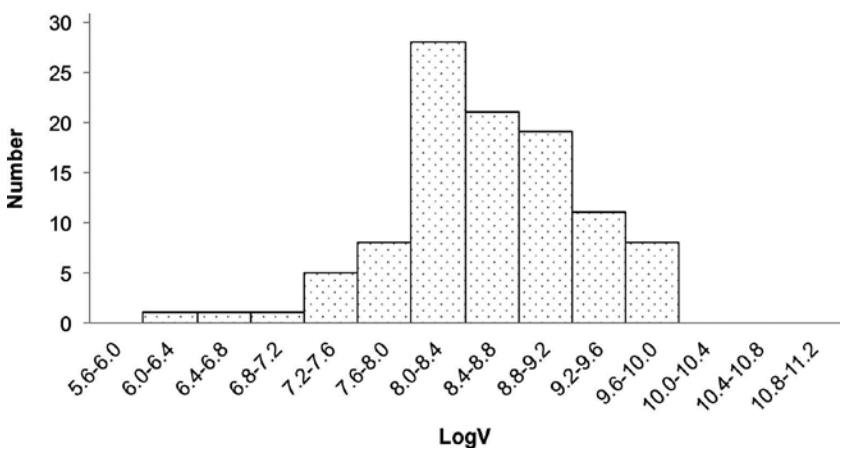

Figure 4. Magnitude (log$V$)-frequency histogram of 103 mega-collapses in Japan. The bin size is 0.4.

http://dx.doi.org/10.5772/63131

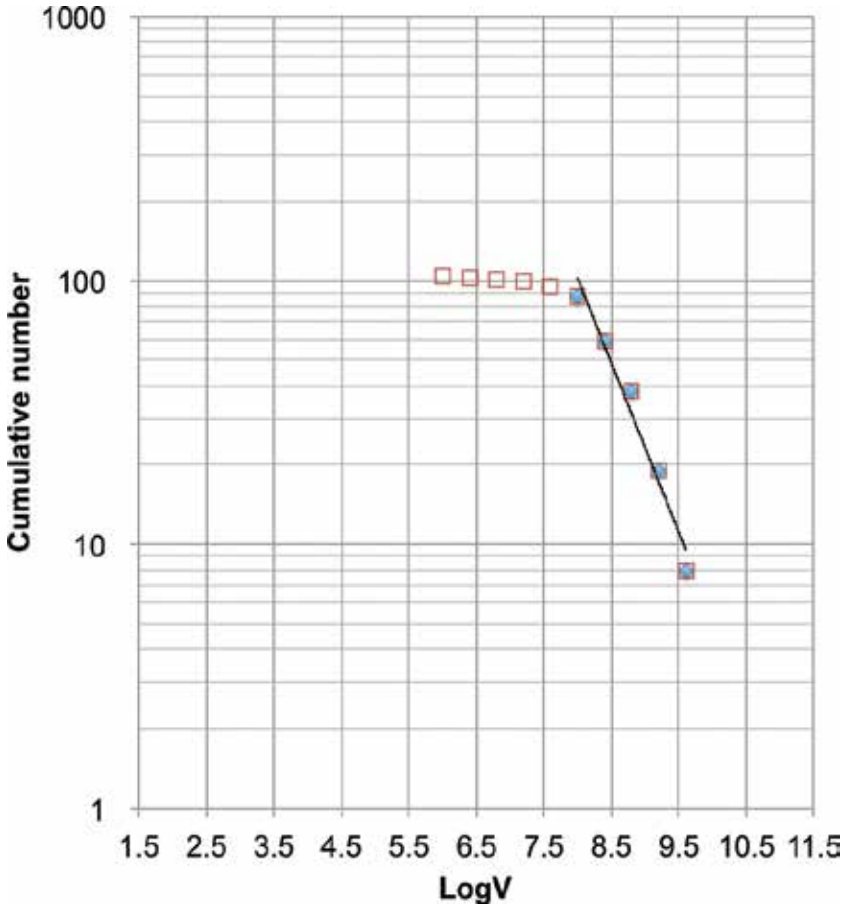

Figure 5. Regression analysis result of 103 mega-collapses in Japan, obtained by fitting Eq. (1) to the filled data points.

4. Magnitude-frequency distribution of large-scale collapses

Similarly, the magnitude-frequency distribution of large-scale collapses (but smaller than mega-collapses) in Japan compiled in reference [26] (dataset 2) was investigated. Because this dataset does not include individual volume data, the depositional area of each event ($10^{5–7}$ m^2) was used as its magnitude. Among the 333 events, the depositional area of one event was recorded as "0"; therefore, 332 events were used in this analysis. First, each depositional area was transformed to its common logarithm (log$A$). Then, the magnitudes (log$A$ values) were grouped into bins of 0.2 (**Figure 6**). The resulting magnitude-frequency distribution is quite similar to that for the mega-collapse dataset (**Figure 4**). In a similar manner, Eq. (1) was fitted the distribution (after excluding the four smallest bins as affected by rollover; see Section 3). The resulting fitted values of a and b were 13.54 and 1.84, respectively, with a high correlation (R = -0.981) (**Figure 7**).

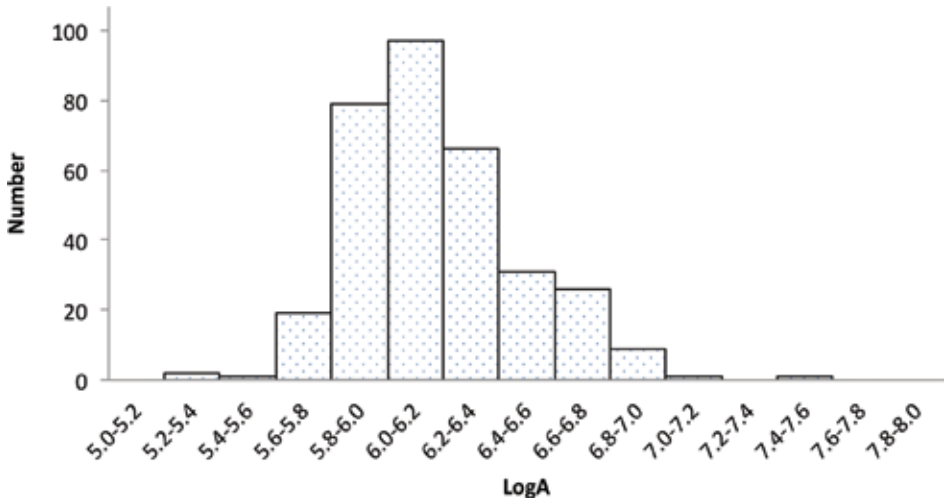

Figure 6. Magnitude (log*A*)-frequency histogram of 332 large-scale collapses in Japan. The bin size is 0.2.

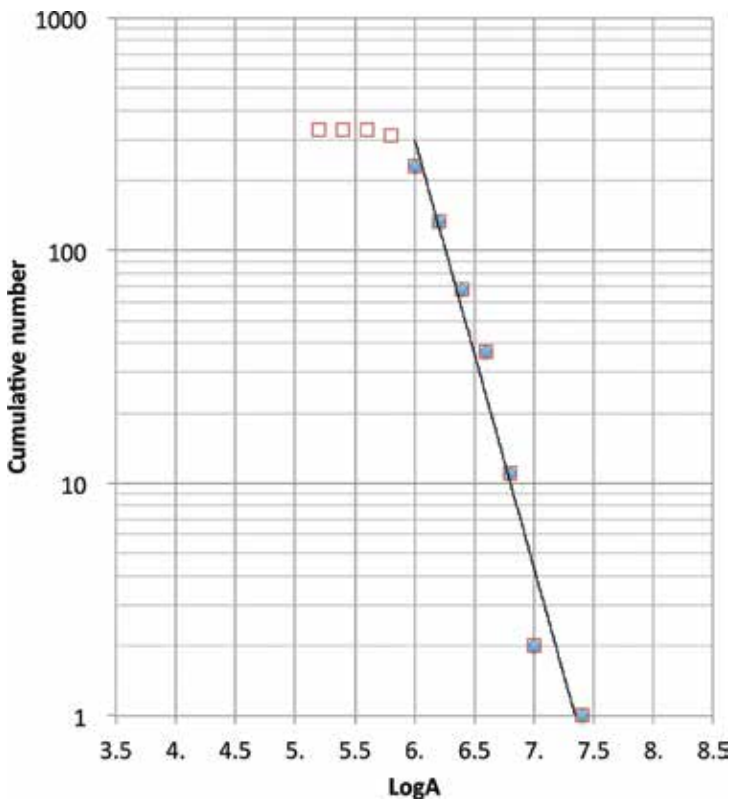

Figure 7. Regression analysis result for the 332 large-scale collapses obtained by fitting Eq. (1) to the filled data points.

http://dx.doi.org/10.5772/63131

5. Combined analysis of the large-scale collapse and mega-collapse datasets

The magnitude-frequency distributions of both the mega-collapse and large-scale collapse datasets are similar: the distribution is exponential even though magnitude is expressed as event volume in the former dataset and as event area in the latter. Therefore, it can be anticipated that if the two datasets are merged into a single combined dataset, then in the resulting dataset, magnitude and frequency should also show an exponential relationship. To determine whether this view is valid, the depositional area of each event was converted to its equivalent volume.

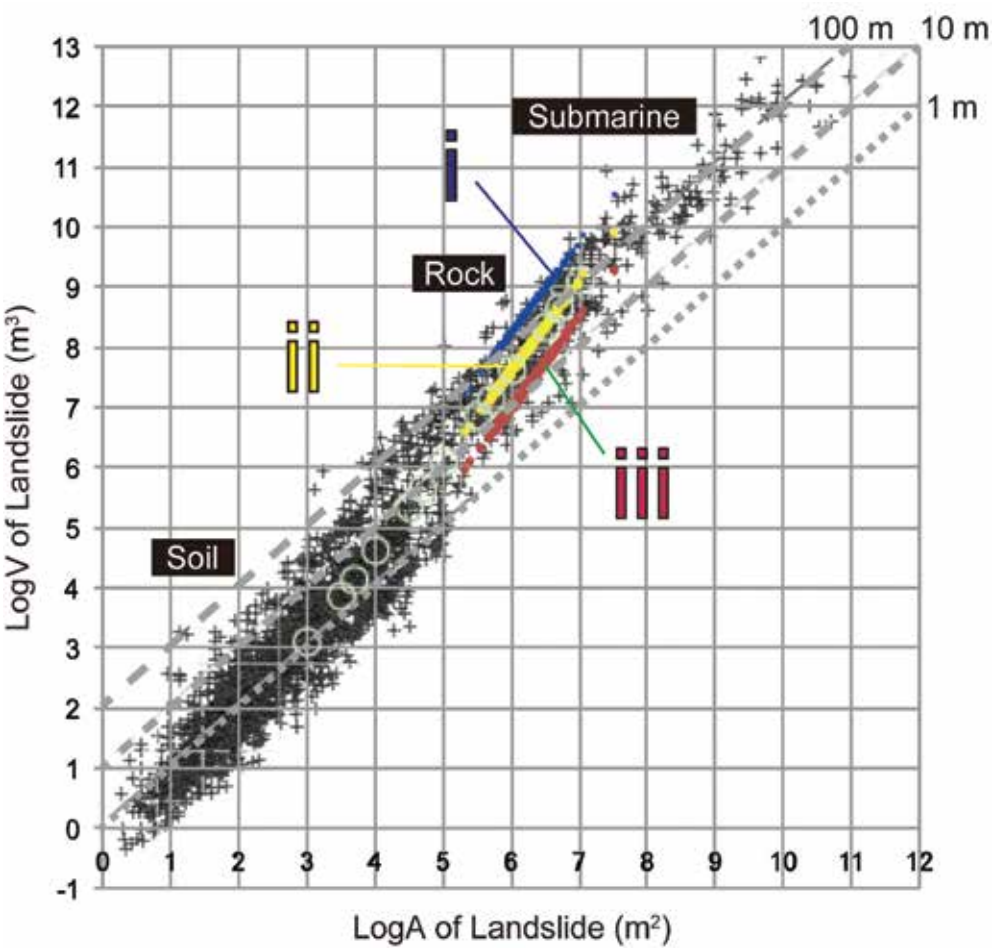

Figure 8. Relationship between log*A* and log*V* for about 4200 globally observed soil, bedrock, and submarine landslides [35, 36]. The two dashed lines and dotted lines shown in the figure indicate the average thicknesses of 100 m, 10 m, and 1 m, respectively. The colored data points were obtained by using relationships i, ii, and iii to estimate the areas of the 332 large-scale collapses of dataset 2. The 13 large circles show the relationship for events with areas of 10^3–10^7 m^2 (calculated by applying thickness-area relationship ii).

Korup [35], following Larsen et al. [36], performed volume-area scaling of about 4200 soil, bedrock, and submarine landslides (**Figure 8**). Here, the term "landslide" encompasses a wide variety of mass-movement types. Korup [35] reported that "more than half of ca. 4200 landslides with field-verified volume and area data have an average thickness of 1 m, a value largely controlled by local soil depth," and Larsen et al. [36] noted that large bedrock landslides produce much thicker deposits (10–100 m) than smaller ones. In the current author's experience, too, an increase in the areal magnitude of an event is associated with an increase in the average thickness of the collapsed landmass: the thickness of smaller mass movements is <10 m, whereas the thickness of the largest ones can be more than 100 m. Therefore, in this study, the average thickness of each of 332 events described in reference [26] was estimated as described below to produce a volume-based dataset that could be merged with mega-collapse dataset 1. Three possible thickness-area relationships were tested:

i. Average thickness is equivalent to the square root of the depositional area divided by 100.

ii. Average thickness is equivalent to the square root of the depositional area divided by 25.

iii. Average thickness is equivalent to the square root of the depositional area divided by 6.

Equivalent volumes of 332 events were calculated using each of the three relationships (i, ii, iii), and relationship ii was selected as the most appropriate because the resulting data points aligned in the central part of the larger global dataset (N = ca. 4200) (**Figure 8**). Therefore, the volumes of the 332 events of dataset 2 were calculated by multiplying the square root of the depositional area divided by 25. The calculated volumes ranged from 10^7 to 10^9 m^3, which agree well with the range of suggested volumes noted in reference [26].

Thus, the large-scale collapse and mega-collapse datasets were combined after converting the areal magnitudes to volume magnitudes as described above. Twelve events were included in both datasets, including Ura-Bandai, Bandai volcano (No. 22 in **Figure 1**, **Table 2**); Otsukigawa, Yatsugatake volcano (No. 44); and Mayuyama, Unzen volcano (No. 58). For these 12 events, the volume data reported in **Table 2** (dataset 1) were used in the analysis because they were based on geological and topographical evidence. Therefore, a total of 423 events, 103 from dataset 1 and 320 events from dataset 2, were analyzed to determine the magnitude (volume)-frequency distribution of collapses with volumes of 10^7–10^9 m^3 or larger.

The resulting distribution (**Figure 9**) was interpreted as exponential. The fitted values of a and b (Eq. (1)) were 8.67 and 0.80, respectively, and the correlation was extremely strong (R = -0.995), when the four smallest bins were excluded from the regression analysis (**Figure 10**). This exponential distribution thus represents the combined large-scale and mega-scale collapse dataset, which includes collapses with volumes of 10^7–10^9 m^3 or more in Japan.

http://dx.doi.org/10.5772/63131

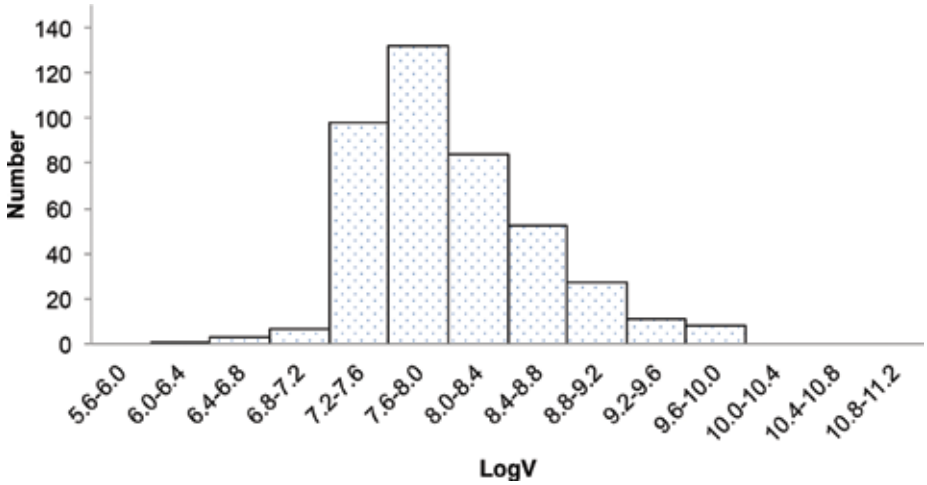

Figure 9. Magnitude (log*V*)-frequency histogram for 423 collapses with volumes greater than 10^7 m^3 (datasets 1 and 2 combined). The bin size is 0.4.

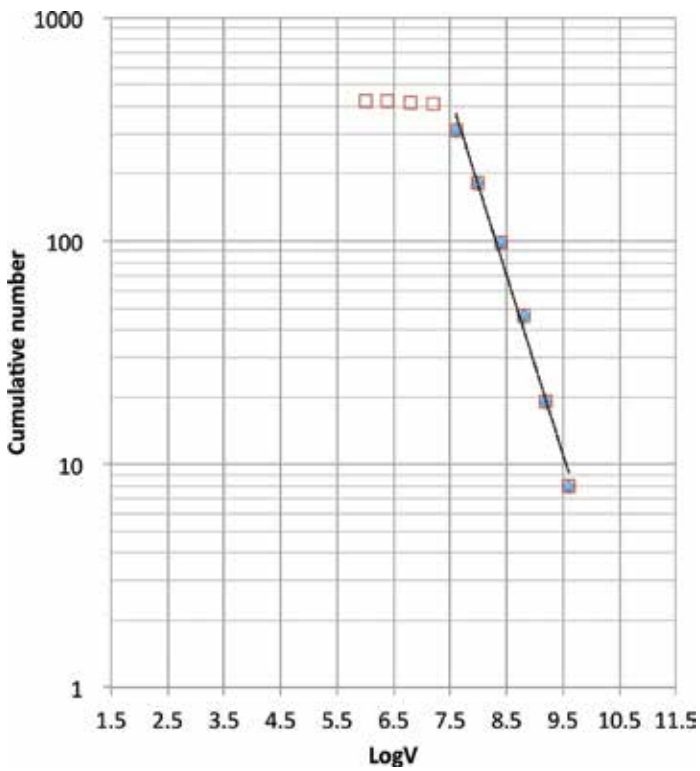

Figure 10. Regression analysis result for the 423 large-volume collapses in Japan, obtained by fitting Eq. (1) to the filled data points.

In Japan, most of slope failures with a volume of more than 10^9 m^3 occur on volcanic edifices, and the largest one known is the Middle Pleistocene sector collapse of Yatsugatake volcano, central Japan. This collapse produced the Nirasaki debris avalanche, whose volume has been estimated to be about 9×10^9 m^3 [37]. Drilling surveys in the Kofu depositional basin [38] have suggested that the actual volume was probably even larger, perhaps more than 10×10^9 m^3. On the other hand, by using the magnitude-frequency distribution determined above for collapses with volumes of $10^{7–9}$ m^3 or more in Japan, the maximum volume can be estimated as $10^{10.8}$ m^3 (=6.3×10^{10} m^3) (**Figure 10**). Thus, this volume estimate is of the same order of magnitude as well as with those of the largest known sector collapse volumes in other parts of the world, such as Shasta volcano, the United States (estimated volume, 4.6×10^{10} m^3); Avachinsky volcano, Kamchatka, Russia ($1.6–2.0 \times 10^{10}$ m^3); and Popocatépetl volcano, Mexico (2.8×10^{10} m^3) [11, 39].

In Japan, future mega-collapses with a comparable magnitude are most likely to occur on large stratovolcanoes with steep slopes. A prime candidate is Fuji volcano, the highest mountain in Japan (summit altitude ~3800 m, central Japan) (**Figures 1** and **11B**). The following discussion examines the likely magnitude of a mega-collapse on Fuji volcano by considering its geometry and comparing it with that of Bandai volcano, still another candidate volcano for a future mega-collapse event even though multiple slope failures occurred there previously.

Bandai volcano (**Figure 11A**) was the site of the Ura-Bandai event in AD 1888 (No. 22), which attracted attention globally [40]. The largest sector collapse in the history of Bandai volcano occurred in the Late Pleistocene, ca. 40 ka, and affected 30% of the volcano by area; this collapse created a horseshoe-shaped caldera on the southwestern side of the summit and produced the Okinajima debris avalanche deposits, which are distributed on the slope below the caldera [29]. If a similar proportion of Fuji volcano were to collapse, the maximum volume of the resulting mega-collapse would exceed 5×10^{10} m^3; this estimate is consistent with the maximum collapse volume of 6.3×10^{10} m^3 computed above from the magnitude-frequency distribution determined in this study. For a more realistic estimate, however, the difference in magma type between the Bandai and Fuji volcanoes should be taken into account. Bandai volcano is andesitic, and as a result the slopes of the volcanic edifice are relatively steep. By contrast, Fuji volcano, somewhat rare for Quaternary Japan, mainly produces basaltic lavas. As a result, the slopes, especially the lower slopes, of the Fuji volcanic edifice are gentler than those of Bandai volcano. Fundamentally, volcanic mega-collapses are triggered by gravitational instability in connection with the growth of the volcanic edifice [15]. Therefore, because the slopes of Fuji volcano are less steep, the area of the volcanic edifice that is susceptible to topographical instability should be smaller than the susceptible area of Bandai volcano. Note that in **Figure 11**, Bandai and Fuji volcanoes are shown at different map scales (the scale of the Bandai map is three times that of the Fuji map). The white circles on the maps are centered on the present summit of each volcano, and the area of Fuji volcano that is encircled is nine times the encircled area of Bandai volcano. In addition, the contour interval is 100 m on the Bandai map and 300 m on the Fuji map. Thus, the relative steepness of the two volcanic edifices can be visually compared. The source area of a possible mega-collapse of Fuji volcano may be roughly within the area defined by the white circle, which was determined by the reference to the case

http://dx.doi.org/10.5772/63131

of Bandai volcano. If 30% of the area enclosed by the circle collapsed, the estimated volume of the Fuji volcanic edifice that would be involved in the collapse is 2×10^{10} m^3; this volume is equivalent to the second or third largest event in the magnitude-frequency distribution.

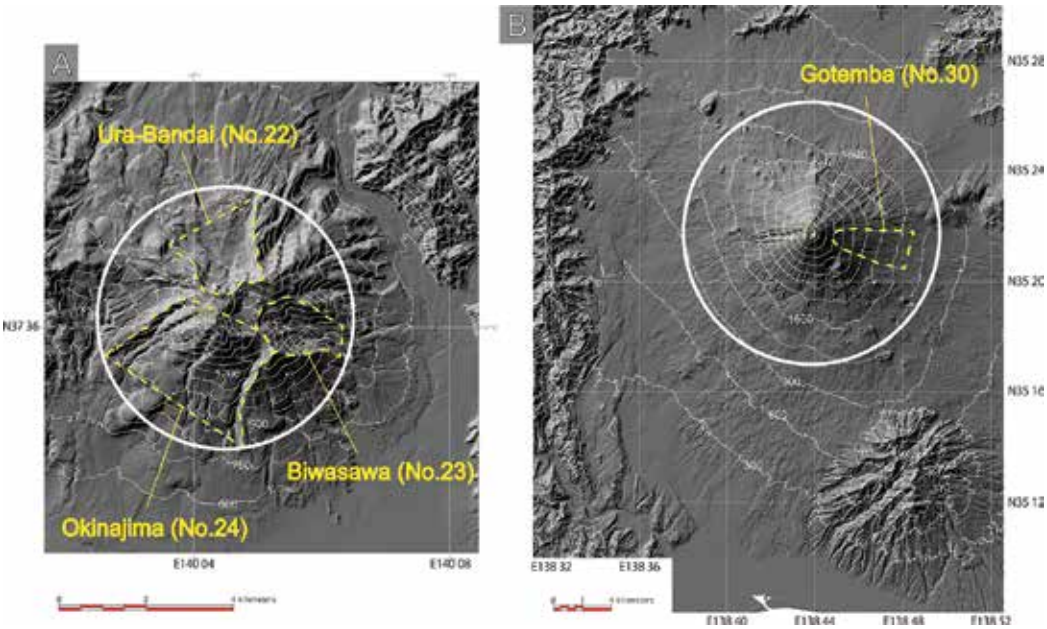

Figure 11. Topography of Bandai (A) and Fuji (B) volcanoes, both on Honshu Island. The dashed yellow lines outline collapse calderas. The white circle on Bandai volcano is drawn to enclose the three collapse scars (A). A white circle of the same relative size is centered on the summit of Fuji volcano (B).

6. Examination of smaller-scale rapid mass movements

The volume range ($10^{7–9}$ m^3) of the very large events discussed so far is equivalent to a depositional area of more than $10^{5.5–6}$ m^2. The question arises of whether the relationship between magnitude and frequency of these very large collapses, including catastrophic volcano sector collapses, is similar to the relationship for much smaller, more frequently observed events. To answer this question, rapid mass movements recorded in Japan during 1975–1983 [10] (dataset 3) were examined. These slope failure events have an areal range from 10^3 to 10^7 m^2; thus, their magnitudes in terms of area are smaller than those of the larger collapses examined in the previous sections of this chapter.

In this analysis, rapid mass-movement data for rocky mudflows and steep slope collapses [10], a total of 2083 events, were considered (see Section 2). Although a few of these events might not fit the criterion of this study for a rapid mass movement, the number would be sufficiently small that they would not significantly affect the results of the following statistical analysis.

First, the depositional areas were converted into equivalent volumes. Each event was identified on 1:25,000 or 1:50,000 topographic maps, and the depositional area was measured in hectares. Then, Ohmori and Hirano [10] divided their log$A$ values from 3.0 to 7.0 into 13 bins. Here, these areas were converted to volumes (by multiplying the depositional area by the twenty-fifth part of its square root), and the resulting log$V$ values ranged from 3.12 to 9.10 (13 plotted circles in **Figure 8**).

These equivalent volume data show an exponential relationship between magnitude and cumulative frequency, and Eq. (1) can be fitted to the entire dataset (R = -0.975). Nonetheless, it is also possible to fit two regression lines to the magnitude-frequency data (**Figure 12**), using as a cutoff value log$V$ around 5.0–5.5. Therefore, the five smallest (log$V$ <5.5; **Figure 12A**), or the four smallest bins (log$V$ <5.0; **Figure 12B**), were analyzed separately from the larger bins. In the former case, the correlation coefficients are -0.990 and -0.985 (**Figure 12A**), and in the latter case, they are -0.980 and -0.986 (**Figure 12B**), for the smaller and larger bins, respectively. Thus, the correlation coefficients for the larger events are almost the same between the two cutoff values, whereas those for the smaller events are somewhat different. Here, the regression function for events with log$V$ greater than ~5.5 is considered to effectively represent the trend of the combined rocky mudflow and steep slope collapse data. When Eq. (1) was fitted to the events with log$V$ >5.5, the fitted values of a and b were 6.90 and 0.77, respectively.

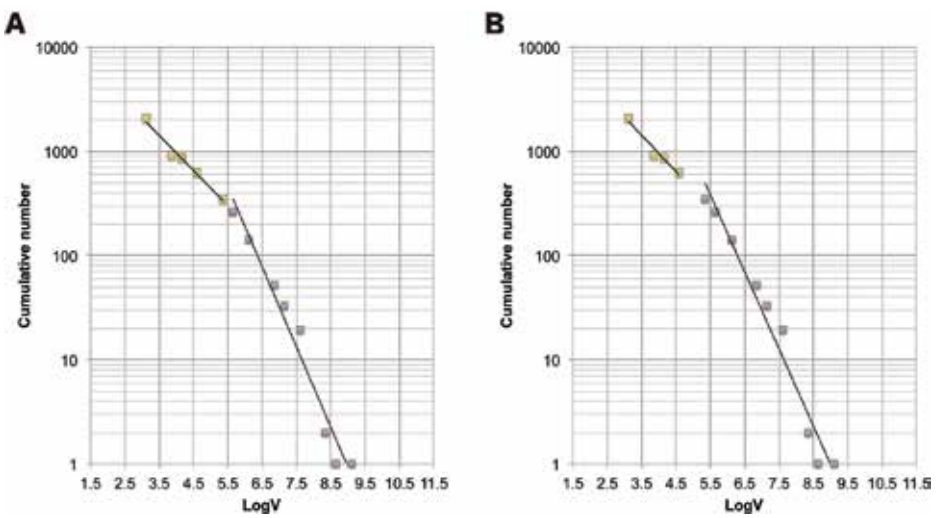

Figure 12. Results of regression analyses of 2083 smaller events in Japan, obtained by fitting Eq. (1) separately to the green and blue data points with a cutoff value of log$V$ = 5.5 (A) or 5.0 (B).

The value of b, 0.77, is surprisingly close to the value (0.80) obtained for the combined dataset of very large (>10^7 m^3) collapses, as described in Section 5, although they were obtained from two completely independent datasets. Basically, b is the slope coefficient, and when b is positive, it shows the rate of decrease in the cumulative number of events as the magnitude increases. Thus, its value can potentially vary over a wide range. Nevertheless, these data for

http://dx.doi.org/10.5772/63131

Japan show that for slope failure events with volumes of more than $10^{5.5}$ m^3, b is uniformly in the range of 0.7–0.8. The value of b may depend on the geological or geomorphological setting, and various b values have been recognized for different local study areas [7, 10]. However, the present result suggests that in an analysis targeting all of Japan, it is unnecessary to take into account the local setting and that a single regression formula with a constant b value can be unambiguously derived.

7. How frequently do mega-collapses of volcanic edifices occur in Japan?

By using the results of the regression analysis of very large collapses (V>10^7 m^3) in Japan, based on the combined dataset of large-scale and mega-collapses, and taking into account the results obtained in Section 6 for events with V>$10^{5.5}$ m^3, some statistical values respecting slope failures with volumes of more than $10^{5.5}$ m^3 can be calculated. The magnitude-frequency relationship of slope failures of this magnitude can be expressed as follows:

$$\log N(x) = 8.67 - 0.80x \tag{3}$$

By using Eq. (3) with a minimum value of x of 5.6, the cumulative number of events can be calculated to be 14,941. Because all of the analyzed events occurred after the Middle Pleistocene, the empirical relationship expressed by Eq. (3) reflects the situation during the last 800,000 years in Japan. Thus, the recurrence interval of events of a certain magnitude (more than $10^{5.5}$ m^3) can be calculated as follows [7, 10]. First, Eq. (1) is rewritten as

$$F(x) = N(x) = 10^{a} 10^{-bx}. \tag{4}$$

Then, the probability (p(x)) that an event with a magnitude equal to or greater than a certain magnitude (x) has a cumulative frequency $F(x)$ which is calculated as

$$p(x) = F(x) / F(x_0) = 10^{-b(x-x_0)}, \tag{5}$$

where x_0 is the recorded minimum magnitude (5.6 in this study). Further, if the total number of recorded events occurred during a certain time span, then the recurrence interval (y) between events with a magnitude greater than or equal to a certain value x is calculated as

$$r(x) = 1 / p(x) / n \tag{6}$$

where n is the total number of events. Thus, probabilities and recurrence intervals were calculated using Eqs. (5) and (6) for various values of x and three time spans by way of experiment (**Table 4**). For example, if a time span of 0.8 My is assumed, then the calculated

recurrence interval of events with a magnitude (log*V*) of 8.0 is ~4500 years. However, a large number of mega-collapses (i.e., volume ≥10^8 m^3) may have occurred in the last 100,000 years (**Figure 13**) [25], which suggest that the recurrence interval of 4500 years might be too long. Further, although the occurrence date of some events in dataset 2 is not clear [25], most of them probably occurred since the Late Pleistocene. This assumption is reasonable because many landforms in Japan older than the Late Pleistocene are no longer identifiable, owing to rapid crustal movements and the humid climatic conditions, which cause topographical changes to be extremely rapid [4, 5]. More specifically, although a few of the oldest (and largest) events occurred around a million years ago, it is probably impossible to recognize every event that occurred during the last million years.

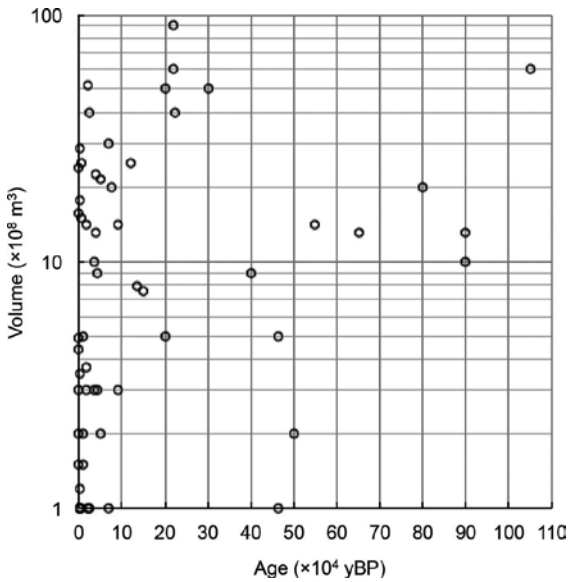

Figure 13. Occurrence ages of mega-collapses with volume ≥10^8 m^3 in Japan.

Therefore, it is necessary to select a realistic and suitable time span to which the magnitude-frequency relationship obtained in this study can be applied. Thus, the recurrence interval of events with a volume of 10^8 m^3 for time spans of 40,000 or 20,000 years, for an experiment, was computed to be about 230 and 110 years, respectively (**Table 4**). These computed values were then compared with such events occurring in the last thousand years (**Table 2**). During the past millennium, nine events with volumes of more than 10^8 m^3 occurred (**Table 5**), for a recurrence interval of 110 years. This corresponds well with the recurrence interval computed for a time span of 20,000 years. Among the nine events, the volume of the two largest, the Shikabe lobe of the Kurumizaka debris avalanche, Oshima Komagatake volcano, and the Nishiyama debris avalanche of Oshima-Oshima, both in Hokkaido (see **Figure 1**), each exceeds 10^9 m^3. More strictly, their volumes are $10^{9.2–9.3}$ m^3 (one has a volume of $10^{9.2}$ and the other a volume of $10^{9.3}$ m^3). For time spans of 20,000–40,000 years, the computed recurrence interval of events of such magnitude is 1000–2000 years. Among events with magnitude 10^9 m^3, the

http://dx.doi.org/10.5772/63131

Kisakata debris avalanche of Chokai volcano and the Gotemba debris avalanche of Fuji volcano occurred 2600 and 2900 years ago, respectively (**Table 2**, locations shown in **Figure 1**). Thus, in the last 3000 years, four mega-collapses (volume >10^9 m^3) have occurred. This result concords well with the recurrence interval of 700–1400 years computed under the assumption that the magnitude-frequency distribution determined in this study is applicable over a time span of 20,000–40,000 years for events with their volumes of 10^9 m^3.

Log *V*	Cumulative frequency among 423 events	Estimated frequency	Probability p(*x*)	Recurrence interval (*y*)		
				0.8 My	40 ky	20 ky
9.6	8	9	0.0006	87217.1	4360.7	2180.3
9.2	19	19	0.0013	41630.6	2081.4	1040.7
8.8	46	40	0.0027	19871.2	993.5	496.8
8.4	98	84	0.0056	9484.9	474.2	237.1
8.0	182	177	0.0118	4527.4	226.4	113.2
7.6	314	370	0.0248	2161.0	108.0	54.0
7.2	412	776	0.0519	1031.5	51.6	25.8
6.8	419	1625	0.1088	492.4	24.6	12.3
6.4	422	3404	0.2278	235.0	11.8	5.9
6.0	423	7132	0.4773	112.2	5.6	2.8
5.6	-	14941	1.0000	53.5	2.7	1.3

Estimated collapses (N = 14941; log$V$ ≥5.6); a' = 468854337.7, b = 0.802972851

Table 4. Statistical results of estimated frequency, probability of occurrence, and recurrence intervals of the events with volume ≥$10^{5.6}$ m^3 in Japan.

No. (from Table 2)	Volcano	Debris avalanche	Date	Volume
			(AD)	×$10^8$$m^3$
49	Hakuba-Oike	Hiedayama	1911	1.5
22	Bandai	Ura-Bandai	1888	4.9
48	Tateyama	O-Tombi	1858	1.3-2.7
58	Unzen	Mayuyama	1792	4.4
42	Asama	Kambara	1783	1.38
6	Oshima-Oshima	Nishiyama	1741	24
5	Komagatake (Oshima)	Kurumizaka (Onuma)	1640	3
4	Komagatake (Oshima)	Kurumizaka (Shikabe)	1640	14.2–17.0
44	Yatsugatake	Otsukigawa	888	3.5

Table 5. Collapse events with volume ≥10^8 m^3 during the past millennium in Japan .

Even when much smaller events are considered, the findings are still reasonable. The smallest events with magnitudes of $10^{5.6–6.0}$ m^3 have recurrence intervals of 1.3–2.7 or 2.8–5.6 years. Because many such relatively small slope failures have obviously occurred in recent years in Japan, these results should be close to reality. For example, the magnitude of a slope failure on Izu-Oshima Island (location shown in **Figure 1**) in 2013 corresponds to an event that should recur every several years (debris flow volume estimated to be $>10^6$ m^3). Similarly, slope failures (non-volcanic) such as those that occurred in Hiroshima City in 2014 might be expected to recur once every 1–3 years (numerous slope failures with an estimated maximum sediment volume of several tens of thousands of cubic meters occurred approximately simultaneously as a result of heavy rainfall). Thus, when records for the past millennium in Japan are considered, the magnitude-frequency relationship proposed in this study substantially reflects the real situation during the last several tens of thousands of years.

Finally, how often is a given volcano likely to experience an extremely large collapse (volume $>10^9$ m^3)? Certainly, the answer will differ depending on the volcano. Therefore, the question should be phrased in another way: in all of Japan today, how often can such a huge-scale collapse be expected to occur? This question can be answered by referring to some well-known examples. Some volcanoes in Japan have experienced collapses of this magnitude more than once. Multiple huge-scale collapses have been recorded during the last 0.10–0.15 My for Iwate, Chokai, Shirataka, and Bandai volcanoes (locations shown in **Figure 1**). This information suggests that a similar volcanic body will experience a huge slope failure ($>10^9$ m^3) about every 50,000 years. If at any given time, 25–50 candidate volcanoes for such a huge collapse exist, then one should occur at least every 1000–2000 years somewhere in Japan. This recurrence interval range is of the same order as that calculated by using Eq. (6) as shown above.

8. Concluding remarks

This study aimed to explore the characteristics of the magnitude-frequency distribution of mega-scale slope failures in Japan, which often occur on the flanks of mature volcanoes. Despite the importance of this topic for possible mitigation of disasters caused by huge and rapid mass movements, few studies have addressed it, mainly because relatively few such gigantic events occur within a short time period, though large amounts of data on much smaller collapses are available for statistical analysis. Such huge events (e.g., with volume $>10^8$ m^3) have been recognized as not only "usual" in a geological context but also significant in terms of the geomorphic development of volcanic (or mountain) bodies and surrounding areas, as shown by the catastrophic event associated with the eruption of Mt. Saint Helens. However, to date, knowledge of such events has been mainly qualitative. To deepen our understanding of volcanic mega-collapses in Japan, this study used a statistical approach.

Three datasets were used for statistical analysis as follows:

1. Volcanic mega-collapses in Japan, comprising 59 events with a volume of more than 10^8 m^3 and eight with a volume of more than 10^7 m^3.

http://dx.doi.org/10.5772/63131

2. Large-scale slope failures in Japan, comprising 332 events with an estimated volume on the order of $10^{7–9}$ m^3 (from the original data of area with $10^{5–7}$ m^3). More than 74% of these originated on volcanic bodies and in volcanic terrains.

3. Smaller rapid mass movements in Japan (rocky mudflows and steep slope collapses) recorded between 1975 and 1983 by the former Ministry of Construction of Japan. The estimated volume range of these events is $10^{3–9}$ m^3 (from the original data of area with $10^{3–7}$ m^3).

Datasets (1) and (2) were used to show that the magnitude-frequency distribution of slope failures with volumes greater than or equal to 10^7 m^3 can be fitted by an exponential equation. For these events, the slope coefficient (b in Eq. (1)), which represents the rate of decrease in the cumulative frequency with increasing magnitude, was about 0.7 or 0.8; thus, smaller events occur more frequently. In addition, a reanalysis of dataset (3) showed that a comparable constant b value could be obtained for events with volumes greater than or equal to $10^{5–6}$ m^3. These results show that the frequency-magnitude relationship of mega-collapses is similar to that of such smaller events. This finding leads to the conclusion that b may be 0.7–0.8 for all Japanese slope failures with volumes from about 10^5 m^3 (not necessarily volcanic) to 10^{10} m^3 (generally volcanic). Recent records for the past millennium or so in Japan show that the obtained magnitude-frequency relationship substantially reflects the situation during the past several tens of thousands of years. This finding allows the probability and recurrence interval of an event with a certain magnitude to be estimated. For example, mega-collapses with a volume more than 10^9 m^3 should recur at least every 1000–2000 years somewhere in Japan, from a probabilistic viewpoint. This geo-statistical investigation indicates that mega-collapses are not so much "rare" events as "millennial" events in Japan.

Acknowledgements

The author expresses his cordial gratitude to Dr. Karoly Nemeth, chief editor of this book, for inviting this contribution. Financial support from Meiji University is also acknowledged.

Author details

Hidetsugu Yoshida

Address all correspondence to: yoshidah@meiji.ac.jp

Department of Geography, School of Arts and Letters, Meiji University, Chiyoda, Tokyo, Japan

References

[1] Siebert L. Threats from debris avalanches. Nature. 1992; 356: 658–659.

[2] Ui T, Takarada S, Yoshimoto M. Debris avalanches. In: Sigurdsson H, Houghton B, McNutt SR, Rymer H, Stix J, editors. Encyclopedia of Volcanoes. San Diego: Academic Press; 2000. p. 617–626.

[3] van Wyk de Vries B, Davies T. Landslides, debris avalanches and volcanic gravitational deformation. In: Sigurdsson H, Houghton B, McNutt SR, Rymer H, Stix J, editors. The Encyclopedia of Volcanoes Second Edition. San Diego: Academic Press; 2015. p. 665–685.

[4] Yoshikawa T, Kaizuka S, Ota Y. The Landforms of Japan. Tokyo: University of Tokyo Press; 1981. 222 p.

[5] Yoshikawa T. Denudation and tectonic movement in contemporary Japan. Bulletin of the Department of Geography, University of Tokyo. 1974; 6: 1–14.

[6] Wolman MG, Miller JP. Magnitude and frequency of forces in geomorphic processes. Journal of Geology. 1960; 68: 54–74.

[7] Hirano M, Ohmori H. Magnitude-frequency distribution for rapid mass movements and its geomorphological implication. Transactions, Japanese Geomorphological Union. 1989; 10: 95–111 [in Japanese with English abstract].

[8] Sugai T, Ohmori H, Hirano M. Rock control on magnitude-frequency distribution of landslides. Transactions, Japanese Geomorphological Union. 1994; 15: 233–251.

[9] Korup O, Görüm T, Hayakawa Y. Without power? Landslide inventories in the face of climatic change. Earth Surface Processes and Landforms. 2012; 37: 92–99.

[10] Ohmori H, Hirano M. Magnitude, frequency and geomorphological significance of rocky mud flows, landcreep and the collapse of steep slopes. Zeitschrift für Geomorphologie, Suppl. Bd. 1988; 67: 55–65.

[11] Siebert L, Glicken H, Ui T. Volcanic hazards from Bezymianny- and Bandai-type eruptions. Bulletin of Volcanology. 1987; 49: 435–459.

[12] Yoshida H. Magnitude-frequency distribution of hummocks on rockslide-debris avalanche deposits and its geomorphological significance. Geosciences. 2016; 6: 5; doi: 10.3390/geosciences6010005

[13] Inokuchi T. Properties of sector-collapse and debris avalanches on Quaternary volcanoes in Japan. Journal of the Japan Landslide Society. 2006; 42: fr.1–fr.1, 409–420 [in Japanese with English abstract].

http://dx.doi.org/10.5772/63131

[14] Yoshida H, Sugai T, Ohmori H. Quantitative study on catastrophic sector collapses of Quaternary volcanoes compared with steady denudation in non-volcanic mountains in Japan. Transactions, Japanese Geomorphological Union. 2008; 29: 377–385.

[15] Moriya I. Volcanic Landforms in Japan. Tokyo: University Tokyo Press; 1983. 135 p. [in Japanese].

[16] Glicken H. Rockslide-debris avalanche of May 18, 1980, Mount St. Helens volcano, Washington. USGS Open-file Report. 1996; 96–677: 1–90.

[17] Voight B, Janda RJ, Glicken H, Douglass PM. Nature and mechanism of the Mount St. Helens rockslide-avalanche of May 1980. Geotechnique. 1983; 33: 243–273.

[18] Summerfield MA. Global Geomorphology: An Introduction to the Study of Landforms. Harlow, England: Longman; 1991. 537 p.

[19] Suzuki T. Introduction to Map Reading for Civil Engineers, Volume 3 Terraces, Hills and Mountains. Tokyo, Japan: Kokon-Shoin; 2000. 388 p. [in Japanese].

[20] Highland LM, Bobrowsky P. The Landslide Handbook – A Guide to Understanding Landslides. Reston, VA: U.S. Geological Survey Circular, 1325; 2008. 129 p.

[21] Clavero JE, Sparks RSJ, Huppert HE. Geological constraints on the emplacement mechanism of the Parinacota debris avalanche, northern Chile. Bulletin of Volcanology. 2002; 64: 40–54.

[22] Paguican EMR, van Wyk de Vries B, Lagmay AMF. Hummocks: how they form and how they evolve in rockslide-debris avalanches. Landslides. 2012; 11: 67–80.

[23] Dufresne A, Davies TR. Longitudinal ridges in mass movement deposits. Geomorphology. 2009; 105: 171–181.

[24] Yoshida H, Sugai T, Ohmori H. Size-distance relationship for hummocks on volcanic rockslide-debris avalanche deposits in Japan. Geomorphology. 2012; 136: 76–87.

[25] Yoshida H. Catastrophic sector collapses of Quaternary volcanoes as significant sediment sources in Japan. Journal of Geography. 2010; 119: 568–578 [in Japanese with English abstract].

[26] Machida H, Furuya T, Nakamura S, Moriya I. Large-scale slope failures in Japan. In: Shindo S, editor. Scientific Research Fund by The Ministry of Education, Science, Sports and Culture of Japan, Special research for Natural disaster (1), Magnitude, Manner, Frequency of Slope Failures and Related Dynamics of Groundwater under the Mountains [English translations by the present author]; 1987. p. 165–187, 254–262 [in Japanese].

[27] Yoshida H. Restored image of volcanic sector collapse at "Old" Yotei volcano, southwestern Hokkaido of Japan, by the geomorphological interpretation of hummocks' distribution. Journal of Geography. 2015; 124: 575–586 [in Japanese with English abstract].

[28] Yonechi F, Chiba N, Ozawa A, Ishimaru S. Large scale slope failure caused by Mt. Bandai's eruption in 1888. Abstracts of the 27th Annual Meeting of the Japan Landslide Society, 1989: 20–21 [in Japanese].

[29] Yoshida H. Reexamination of volume loss due to the catastrophic sector-collapse causing the Okinajima debris avalanche of Bandai volcano, Japan. Transactions, Japanese Geomorphological Union. 2013; 34: 1–19 [in Japanese with English abstract].

[30] Geological Survey of Japan. Catalog of eruptive events during the last 10,000 years in Japan, version 2.2. https://gbank.gsj.jp/volcano/eruption/index.html (last sited in 2016/03/10) [in Japanese].

[31] Hayatsu K. Myoko Volcanic Group [English translations by the present author]. Tokyo, Japan: Jitsugyo-Kouhousha; 2008. 424 p. [in Japanese].

[32] Hoshizumi H, Mimura K. Debris avalanche deposits in Beppu district, Kyushu, Japan. Programme and abstracts the Volcanological Society of Japan, 1988: 90 [in Japanese].

[33] Hovius N, Stark CP, Allen PA. Sediment flux from a mountain belt derived from landslide mapping. Geology. 1997; 25: 231–234.

[34] Malamud BD, Turcotte DL, Guzzetti F, Reichenbach P. Landslide inventories and their statistical properties. Earth Surface Processes and Landforms. 2004; 29: 687–711.

[35] Korup O. Landslides in the earth system. In: Clague, Stead, editors. Landslides: Types, Mechanisms and Modeling. Cambridge, UK: Cambridge University Press; 2012. p. 10–23.

[36] Larsen IJ, Montgomery DM, Korup O. Landslide erosion controlled by hillslope material. Nature Geoscience. 2010; 3: 247–251.

[37] Kofu Basin Quaternary Research Group. Geology of the southern foot of the Yatsugatake Volcanic Chain, Central Japan. Journal of the Geological Society of Japan. 1969; 75: 401–416 [in Japanese with English abstract].

[38] Umino Y. Sedimentation processes of the Kofu Basin, Yamanashi Prefecture - The feature after Tertiary age. Monograph, the Association for the Geological Collaboration in Japan - Uplifting of the Fossa Magna. 1991; 38: 19–25 [in Japanese with English abstract].

[39] Siebert, L. Landslides resulting from structural failure of volcanoes. In: Evans SG, DeGraff JV. editors. Catastrophic Landslides: Effects, Occurrence, and Mechanisms. Geological Society of America, Reviews in Engineering Geology. 2002. p. 209–235.

[40] Sekiya S, Kikuchi Y. The eruption of Bandaisan. The Journal of the College of Science, Imperial University, Japan. 1889; 3: 91–172.

Chapter 9

Radiative Impacts of Volcanic Aerosol in the Arctic

Cindy L. Young and Jennifer W. Telling

Additional information is available at the end of the chapter

http://dx.doi.org/10.5772/63421

Abstract

High latitude volcanic eruptions are high-frequency and intensity events capable of releasing large amounts of aerosols into the environment. Studies have shown that the Arctic is particularly sensitive to radiative perturbations due to aerosols, and a high sensitivity to volcanic aerosols would be expected. Despite the potential for volcanic aerosols to significantly perturb the Arctic radiation balance, the radiative impacts of volcanic aerosols in the Arctic are poorly understood and have received less attention than the effects of other aerosol types that are often present in the region, both natural and anthropogenic. A novel review of this topic is presented in detail in this chapter, focusing on the current state of the knowledge and the natural complexities involved with the problem, the important research tools, and the improvements that can be made over the status quo. The Arctic environment is both unique and complicated, and the perturbations caused by volcanic aerosol need to be examined in a regional context. An introduction to remote sensing and data collection in the Arctic is provided because there are often specific challenges, including high surface reflectivities, persistent meteorological clouds, the lack of winter daylight, and harsh conditions that hamper both in situ and remote data collection. Methods for tracking both aerosol and gas plumes in the Arctic that can help mitigate these issues are introduced. In addition to the physical constraints of data collection presented by the Arctic environment, volcanic aerosol is a complex mixture of varying aerosol compositions and sizes. Dealing with the nature of volcanic aerosol for optical calculations is further described, leading into a detailed discussion of the radiative impacts of volcanic plumes in the atmosphere. Radiative forcing comparisons of other aerosol types with comparable plume characteristics (e.g., thicknesses and optical depths) suggest that aerosol layers composed of significant proportions of volcanic ash can dominate the aerosol forcing in the region. Similar comparisons for ash deposits with other types of deposits that can be present in the region emphasize the ability of volcanic ash to produce large, and in some cases extreme, loadings that reduce albedo, which can have profound impacts on the Arctic radiation balance and hydrological cycle. The strengths and shortcomings of volcanic ash transport and dispersion models are reviewed and recommendations are made for future research that would strengthen the use of these models in Arctic environments. In particular, ash aggregation (or the sticking together of ash particles) is often not

considered fully in transport modeling, and the consequences of this are discussed. Finally, we present a review of secondary volcanic impacts to oceans and ecosystems that have not been constrained in an Arctic context but are potentially important to the Arctic environment and the global CO_2 cycle.

Keywords: Arctic, volcanic eruptions, ash, sulfate, remote sensing, transport modeling

1. Introduction

There is a strong need to understand the role natural aerosols play in modulating Arctic climate. The radiative impacts of smoke [1] and dust [2] have been considered. However, volcanic aerosols continue to be largely overlooked in the Arctic environment. The Arctic environment has a high sensitivity to radiative perturbations, as demonstrated by many previous studies of other types of aerosols (i.e., smoke, dust, and haze), and may be strongly sensitive to volcanic aerosols. This chapter defines the "Arctic region" to include the true Arctic (north of 66.5°N) and the sub-Arctic (50–66.5°N), because both areas are more sensitive to radiative perturbations than lower latitudes and aerosol can be easily transported between regions.

Volcanic eruptions are capable of producing a huge, sporadic aerosol signal, lasting from minutes to years [3], and high northern latitude eruptions can distribute aerosols over large areas, as evidenced by the 2010 eruption of Eyjafjallajökull in Iceland, which halted air transportation in much of Europe. The Alaska Volcano Observatory (AVO) reports that Alaskan volcanoes alone have had an average eruption frequency of two per year over the past 40 years. Depending on the time of year, volcanic aerosol may be present along with other aerosol types. Despite the high frequencies and intensities of volcanic eruptions, volcanic aerosols in the Arctic are relatively neglected in assessments of Arctic aerosol.

Volcanoes in the Arctic have been the source of many climatically important eruptions in the last several centuries. The June 1783 eruption of Laki, a volcanic fissure in Iceland, caused a drop in global temperatures [4], drought, and famine [5]. The June 1912 Novaerupta-Katmai eruption near Kodiak, Alaska, was the most powerful eruption of the 20th century, causing surface cooling in the Northern Hemisphere throughout the summers of 1912 and 1913 and a maximum surface cooling of −0.9°C for September 1912 [6]. Recent volcanic eruptions in the region include Redoubt (Alaska, USA) in March to April 2009, Sarychev (Russia) in June 2009, Shiveluch (Russia) in September 2009, Eyjafjallajökull (Iceland) in April to May 2010, and Plosky Tolbachik (Russia) in 2012 to 2013. Recent and ongoing eruptions in the Arctic have fortunately been small to medium-sized events. Although small to mid-sized volcanic eruptions are less extreme events, they occur more frequently and provide a more regular stream of ash and gases to the environment than larger eruptions.

Volcanic aerosols can be external mixtures of ash, sulfates, and hydrometeors and/or internal mixtures of ash coated with sulfates, water, and/or ice [7]. Ash and sulfates are considered the dominant aerosol components of most eruptive plumes (e.g., [8]). In volcanic eruptions,

http://dx.doi.org/10.5772/63421

sulfates are formed from a reaction between emitted volcanic sulfur dioxide (SO_2) and water and can remain in the stratosphere for up to 3 years [9], causing cooling at the surface and warming in the stratosphere [10]. The lifetime of fine ash (aerodynamic diameter <2.5 μm) in the stratosphere is on the order of a few weeks [11]. Consequently, sulfates are usually the only aerosol included in global climate perturbation estimates from a particular eruption [12]. However, volcanic ash and sulfate aerosols in the troposphere are important on a regional level and have comparable lifetimes (approximately days to weeks). Therefore, both ash and sulfate must be included in assessing the regional radiative impact of volcanic aerosol.

Volcanic aerosols can reflect and absorb shortwave (SW) radiation, and they scatter, absorb, and emit radiation in the longwave (LW) part of the spectrum. The interaction of volcanic aerosols with electromagnetic radiation can cause warming or cooling of the surface and atmosphere depending on the reflectivity of the underlying surface, the solar zenith angle (SZA), the optical properties of the aerosol layer, the vertical structure of temperature and humidity, and cloud characteristics. Ash deposits can lower the albedo of highly reflective snow and ice surfaces and may perturb the Arctic radiation budget and cause early snowmelt, analogous to dust deposits [13] and soot deposits [14]. Little consideration has been given to the radiative impacts due to volcanic ash deposits in snow (e.g., [15, 16]), and even fewer studies focus on the surface radiative impacts of volcanic ash deposits from Arctic eruptions or map the entire extent of the deposit area (e.g., [17, 18]). Additionally, ash [19, 20] and sulfates [21] can serve as cloud condensation nuclei and ice nuclei. **Figure 1** illustrates the broad impacts volcanic aerosols can have on the Arctic environment.

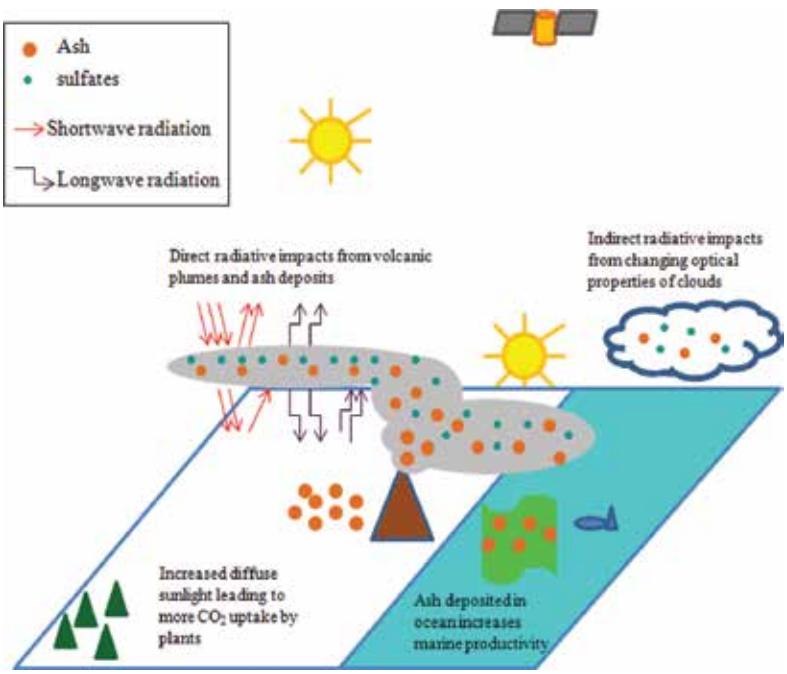

Figure 1. Broad impacts of volcanic aerosols on the Arctic environment.

This chapter will review the current state of the science behind the radiative impacts of volcanic aerosol in the Arctic and what remains to be explored. The work will touch on techniques involving satellite remote sensing, field measurements, and different types of modeling (radiative transfer, ash dispersion and transport, and atmospheric chemistry and circulation) that are used to help constrain the complexities of this problem. This chapter will focus mainly on the direct radiative impacts and then will briefly touch on other effects volcanic aerosols can have on the Arctic environment.

2. Radiative impacts of volcanic aerosol plumes

Determining the radiative influence volcanic aerosols have on the Arctic environment is a challenging problem because of the complexities of volcanic aerosols and the few measurements of their physical, optical, and chemical properties, which must be known to calculate radiative transfer and spectral refractive index. Particle counters on balloons and aircrafts have measured size distributions of stratospheric sulfate aerosol several weeks to months after an eruption (e.g., [22]), but these measurements are not helpful in determining the size distributions of less aged plumes of sulfate and/or ash. Models have been developed that include the sulfate formation and aging process [23] and have been added into general circulation models (GCMs) [11]. Size distributions for volcanic ash are dangerous to measure in situ and are usually measured on ash fall samples, which are not representative of atmospheric size distributions because of sorting that takes place during transport [24]. The role of plume aging on altering the composition and size distribution of volcanic aerosol is important to consider and is expected to substantially influence the radiative impacts.

In addition to SZA, surface albedo, and optical properties of aerosol, there are more aerosol layer-specific characteristics that must be known for radiative calculations. For an aerosol plume, these include aerosol optical depth (AOD), physical thickness, and vertical placement of the layer in the atmosphere. Sun photometers and ground-based lidars can help determine AOD, and ground-based lidars can also be used to obtain thickness and vertical placement. However, the coverage of ground-based sensors is limited. Due to the limitations of ground-based sensors and field measurements as well as the remote locations of Arctic volcanoes, satellite remote sensing is essential for monitoring aerosol from volcanic eruptions. The NASA afternoon satellite constellation A-Train provides a unique opportunity to examine eruptions and the evolution of volcanic plumes. The A-Train consists of six polar orbiting satellites [Aqua, Aura, Cloud-Aerosol Lidar and Infrared Pathfinder Satellite Observations (CALIPSO), CloudSat, GCOM-W1, and OCO-2] flying in close configuration, each equipped with different sensors measuring in wavelength ranges from the ultraviolet (UV) to radio. Combining the data retrieved from several sensors allows for an unprecedented view of volcanic eruptive plumes.

The Moderate Resolution Imaging Spectroradiometer (MODIS) instrument flying aboard Aqua and Terra satellites, the Ozone Monitoring Instrument (OMI) on the Aura spacecraft, and the Cloud-Aerosol with Orthogonal Polarization (CALIOP) aboard the CALIPSO platform are sensors capable of detecting volcanic aerosols. The MODIS instrument provides true color

http://dx.doi.org/10.5772/63421

images of ash plumes and deposits and AOD of volcanic plumes. The OMI provides a UV aerosol index (AI) that can detect the presence of UV-absorbing aerosols, such as ash, dust, smoke, and SO_2 emissions. CALIPSO provides the vertical plume structure, which is useful in determining the placement of the plume in the atmosphere, the plume top height, and the plume thickness. In addition to these platforms, the Atmospheric Infrared Sounder (AIRS) aboard the NASA Aqua satellite views the Earth in the infrared (IR) and is sensitive to the SO_2 absorption band at ~7.3 μm [25]. AIRS and OMI observations can often complement each other, as AIRS is not dependent on solar UV and OMI is less sensitive to water vapor, which hinders AIRS observations near the tropopause. However, in the Arctic, environmental conditions, such as meteorological clouds, little to no winter daylight, and high surface reflectivities, often hamper retrievals for passive instruments measuring in the visible and UV, such as MODIS and OMI, as well as space-based lidars, such as CALIPSO. It is because of these challenging environmental conditions that modeling of the eruptive plume transport, dynamics, and dispersion is essential to accompany, and sometimes supplement, satellite data retrievals in the Arctic region.

2.1. Tracking volcanic plumes

Tracking the movement, areal extent, and evolution of volcanic plumes is not only relevant for radiative purposes but also from an aviation safety and public health standpoint. It is possible to track both gaseous and particulate species in the volcanic plume using satellite remote sensing and transport modeling. Two of the most common volcanic gases, H_2O and CO_2, are also major atmospheric constituents, making them hard to distinguish from the background. Volcanic SO_2, however, has a relatively low background concentration, making it an ideal trace gas for many volcanic eruptions. SO_2 is observable in both the UV and thermal IR (TIR). For use as a tracer in Arctic environments, the absorption bands in both the UV and TIR are critical. During the Arctic winter, the lack of daylight hinders UV observations, as solar radiation is the dominant source of UV, whereas TIR measurements can still be collected. Conversely, low thermal contrast between the volcanic plume and the ambient environment makes observations in the TIR difficult, diminishing the potential for TIR instruments to observer older, cooler plumes. Due to the strong absorption of water in the TIR, high water vapor content in the lower troposphere can also limit TIR observations of SO_2 [25]. In most of the world, this means that TIR instruments are best used to observe plumes above 3 km [25]; however, the generally low relative humidity in the Arctic can mitigate this issue.

A combination of plume observations from both UV and TIR observations can allow plumes to be tracked for days or even weeks depending on the size of the eruption. As a volcanic plume matures and moves away from its source, dilution from atmospheric mixing and conversion of SO_2 to sulfate aerosol make plumes more difficult to separate from the surrounding atmosphere. Atmospheric models, such as NOAA HYSPLIT [26, 27], which predict the direction and altitude of the plume movement, can complement the use of AIRS, CALIPSO, MODIS, and OMI data to improve and prolong plume tracking metrics.

Tracking both Arctic and sub-Arctic plumes is crucial, as even plumes in the sub-Arctic region can be easily transported into the Arctic, possibly amplifying their environmental impacts in

this sensitive region. SO_2 from the initial activity from the 2012 to 2013 eruption of Plosky Tolbachik Volcano, in the Kamchatka Peninsula, could be observed for a week as it moved northwest from the source and then across the Siberian Sea before heading south again [28]. Despite its longevity, the Plosky Tolbachik plume had remarkably little influence on the Arctic environment because it was predominately transported in the troposphere, over water, during the winter, and had significantly more SO_2 than ash [28, 29].

Due to the lower neutral buoyancy height of particles versus that of gases and the possibility of wind shears, particles may be concentrated at lower levels in the atmosphere and can move in different directions than the gases. Tracking ash in volcanic plumes can be accomplished with the use of UV and visible satellite remote sensing (e.g., OMI AI and MODIS AOD) as well as using IR brightness temperature difference (BTD) techniques (e.g., [30, 31]), employing instruments such as AIRS, Geostationary Operational Environment Satellite (GOES), Advanced Very High Resolution Radiometer (AVHRR), and MODIS. Often called the "split window technique," this method takes advantage of the distinctive negative BTDs that result from volcanic ash/sulfates in bands centered at 11 and 12 μm and can be used to estimate optical depth, particle sizes, and masses of ash/sulfate that match the observed BTD from varying these parameters in a radiative transfer model [30]. This method assumes spherical particle shapes, a thin plume parallel to a homogenous surface, and a predetermined range of particle sizes. Fixed refractive indices are often used (selection of these are described further in Section 2.2), but the sensitivity as demonstrated by Wen and Rose [30] is higher for the assumed size distribution than the refractive indices. Meteorological clouds can give similar BTD values to ash and sulfate, and the BTD must be used along with other information (e.g., true color images) to support a definitive particle detection. Dense eruptive plumes can cause issues for the retrieval algorithm, since it was developed for a semitransparent plume, and are better suited for single-band studies. Positive BTDs have been used to infer the presence of ice in the eruptive plume, and similar radiative transfer calculations were done to estimate the size distributions and masses of ice [31]. However, ice is often not the dominant particle in eruptions that occur above 40°latitude, in contrast to those that occur closer to the tropics, because the entrained tropospheric air has a lower water vapor content at higher latitudes [7]. Particle depolarization ratios from CALIPSO may also be used to confirm the presence of nonspherical particles within the plume, but lidars are more suited to studying plume profiles than areal extents. Ash transport models are another tool for understanding plume transport and ash deposition and are discussed later in this chapter (Section 3.1).

2.2. Constraining the optical properties of volcanic plumes

To develop a microphysical model, the compositional types of volcanic aerosols present in the eruptive plume and their refractive indices, size distributions, and relative abundances with respect to other aerosol types present must be ascertained. Refractive indices can be measured in a laboratory for a variety of aerosol types and compositions. The Optical Properties of Aerosols and Clouds (OPAC) data set [32] compiles refractive indices for several typical aerosols under different atmospheric humidity conditions. To represent volcanic sulfate, sulfuric acid solutions of ~70% are often used (e.g., [12]), but at Arctic ambient air temperature

http://dx.doi.org/10.5772/63421

and relative humidity these concentrations tend to be lower (~40–50%) [33]. Because the temperature and relative humidity in a fresh volcanic plume are higher than that of the surrounding air, sulfuric acid solutions closer to 70% are a more realistic estimate for a fresh volcanic plume than the ambient air mixtures. The refractive indices of ashes with varying silica content have also been measured (e.g., [34]) and are commonly used to represent an ash component in microphysical models.

Other quantities that must be included in the microphysical model (i.e., size distributions and relative abundances) cannot be measured directly, especially in the case of "fresh" plumes. Most microphysical models treat volcanic aerosols with a lognormal size distribution, similar to the form from Kearney and Watson [35]:

$$n_c(r) = \frac{1}{\sqrt{2\pi\sigma}} e^{-\frac{(\ln(r)-\mu)^2}{2\sigma^2}} \tag{1}$$

where n_c is the particle number concentration, r is the particle radius, and σ is the variance of the size distribution or the log of the standard deviation:

$$\mu = (\ln \mathrm{Reff}) - 2.5\sigma^2 \tag{2}$$

where Reff is the effective radius [35].

Sulfates are typically nanometer-scale particles and occur only in the fine-mode fraction (aerodynamic diameter <2.5 μm), but ash sizes can vary greatly from coarse to fine. As the plume ages, sulfate aerosols grow larger in size and more numerous, as the effective radius for ash becomes smaller and larger grain sizes are scavenged. A more sophisticated model, such as a GCM, may be able to estimate and track the evolution of size distributions and the relative abundances of the aerosol types given a set of initial conditions and may even treat sulfate formation from SO_2 [11]. However, these estimates are difficult to validate and initial conditions may add uncertainty, especially in the Arctic. When available, satellite data may be used to deduce size distributions (e.g., [30]), and ratios of fine- and coarse-mode aerosols can be constrained to determine the proper proportions to externally mix aerosol types (e.g., using MODIS fine-mode fraction retrievals). Literature investigations of size distributions for representative eruptions can be used to study end-member cases of fresh and aged plumes under Arctic conditions [29, 35].

An additional consideration when determining the optical properties of volcanic aerosol is whether to consider particle nonsphericity of ash and ice in the calculations. This can be done employing the T-matrix method. However, because the relative errors in radiative flux calculations for using the single scattering properties of spherical particles to approximate those of nonspherical dust particles are low [36], optical properties calculated with the Mie theory are often still used.

2.3. Comparing the radiative impacts of Arctic aerosol plumes

The direct aerosol radiative forcing (DARF) of two moderately thin volcanic layers from a mid-sized volcanic eruption have been compared to those for other aerosol types [29]. Two volcanic layers were chosen to represent a young, ash-rich/sulfate-poor plume and an older, sulfate-rich/ash-poor plume. Radiative modeling was used to obtain upward and downward fluxes. Net fluxes (Fnet) for both the SW and LW components at the top of the atmosphere (TOA) and at the surface were computed by subtracting the upward flux from the downward flux. The total net flux at TOA and at the surface were then calculated by adding the respective SW and LW net fluxes. DARF efficiency (DARFE), defined as the change in the net flux with respect to the change in AOD (550 nm), was computed as

$$DARFE = \frac{\Delta F_{net}}{\Delta AOD_{550\ \mathrm{nm}}} \tag{3}$$

To calculate DARFE for an aerosol layer, the surface DARFE was subtracted from the DARFE at TOA. The units of DARFE are W m^{-2} AOD^{-1}, and a similar definition of DARFE to that of Stone et al. [1] was selected to consistently compare radiative impacts for all aerosol types. Calculations of DARF were done by multiplying DARFE by the layer AOD, resulting in units of W m^{-2}.

Volcanic eruptions are special events because of their ability to create aerosol layers many times thicker and more optically opaque than sources of other aerosol types frequently found in the region. In considering the nature of volcanic eruptions, it is expected that they could produce larger vertical loadings and dominate over the radiative impacts of other aerosols. Although many factors influence the regional radiative impacts, similar surface albedo, AOD, SZA, and plume thickness for each aerosol type were chosen to study the effects of different aerosol compositions and size distributions alone (for more information, see Table 4 in Young et al. [29]). A comparison of DARFs for two volcanic aerosol compositions [29], mineral dust

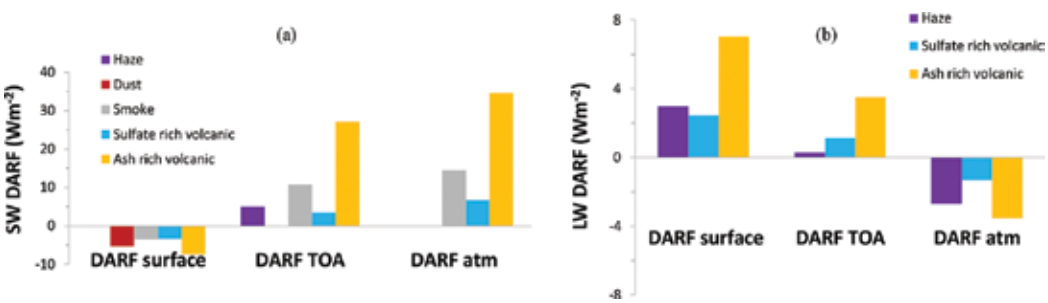

Figure 2. (a) SW DARFs [37], dust [2], smoke [1], and ash- and sulfate-rich volcanic aerosols [29]. Values of forcing for dust were only available at the surface. (b) LW DARFs for haze [38] and ash- and sulfate-rich volcanic aerosols (taken from Young et al. [29]).

[2], wildfire smoke [1], and haze [37, 38] is presented in **Figure 2** (taken from Young et al. [29]).

The ash-rich volcanic mixture, followed by mineral dust, attenuates the most incoming solar radiation at the surface and also absorbs more solar radiation in the layer than the other aerosol types (**Figure 2a**). The ash-rich mixture is the most important aerosol type with regards to the LW radiative impacts (**Figure 2b**). It should be noted that the LW forcing for smoke is negligible due to small particle sizes [39] and is not shown in **Figure 2b**. LW forcings of dust and volcanic aerosols are important because those particles are of sufficient size to interact with LW radiation. In the Arctic, LW radiation can dominate the forcing during seasons when the sun is low and can change the sign of the total forcing, but the LW component is rarely considered in radiative assessments of Arctic aerosols. Comparisons of both SW and LW components suggest that a thin ash-rich volcanic layer can dominate the aerosol radiative impacts in the Arctic.

3. Radiative impacts of volcanic deposits

Similar information to plume radiative modeling is needed to calculate the radiative impacts of ash deposited onto ice and snow, but knowledge on ash deposit loadings and areal extents also must be ascertained. Ground measurements are helpful but usually do not map out the entire extent of deposits or provide an adequate spatial resolution of samples. Volcanic ash transport models can assist in characterizing ash plumes and deposits. Past research has employed GCMs to simulate the dispersion and deposition of volcanic ash by assigning an initial flux amount of ash into the atmosphere (e.g., [11]) without treating the source conditions of the eruption (e.g., the initial distribution of ash in the eruptive column). Failing to consider the dynamics of the eruption and initial eruptive column will impact the regional transport and deposition of ash. In efforts to account for previously neglected eruption dynamics, a preprocessing tool was developed to determine the initial ash fields from source conditions for input into mesoscale atmospheric chemistry models [40]. As an alternative to GCMs, volcanic ash transport and dispersion models (VATDMs) compute initial ash fields directly from eruption source condition input parameters, consider a full-sized spectrum of ash, and can include nonspherical ash particles.

3.1. Constraining VATDMs

VATDMs can be presented in either Eulerian (e.g., Fall3D and TEPHRA) or Lagrangian (e.g., Puff and HYSPLIT for volcanic ash) reference frames. Volcanic advection-diffusion models (e.g., [41]) are Eulerian models that can predict atmospheric ash concentrations and ground deposit loadings by considering advection, turbulent diffusion, and gravitational settling, making them useful tools in assessments of the radiative impacts of ash deposits. In general, advection-diffusion models require input of source conditions [mass flow rate (MFR), source type, and plume temperature], ash properties (initial size distribution, particle density, and shape), and transport conditions (meteorological data and diffusion coefficients).

Commonly, MFR is estimated by comparing eruption plume heights to those predicted with simple plume theory for a particular eruption rate (e.g., [42]), assuming there are no variations in plume height during the eruptive activity. Error can be introduced when determining the height of the plume, which is often deduced from seismic data or reported by pilots in the area. Another technique that is often used involves erupted masses determined from mapped deposits and the seismic durations of eruptive events [43, 44], but this technique relies on the assumption that MFR is constant over the entire duration of the eruptive episode. The success of this method hinges upon a thorough and timely sampling of the eruptive deposits, including only ash deposited from the relevant eruptive event. Because of the large uncertainties that go into any MFR calculation, independent estimates of MFR for a given eruptive event can vary over orders of magnitude [43–45]. There are not many good estimates of MFR for Arctic eruptions due to the remote locations of many volcanoes, making MFR a poorly constrained parameter to which advection-diffusion models can exhibit a high degree of sensitivity [46].

The volcanic column source type determines how ash concentrations will be initially allocated within the atmosphere. For example, the Fall3D model [41] handles three different source types: plume, point, and Suzuki. The plume source describes the distribution of ash within a rising, hot, buoyant plume in which ash concentrations increase with height, up to a height of neutral buoyancy with the atmosphere. The point source dispenses all ash from a single point and height within the atmosphere. The Suzuki source allows for the height of the largest ash concentration and how the total mass is distributed around it to be chosen based on the strength of the eruption (i.e., more violent eruptions distribute the highest concentration of ash more closely to the maximum column height).

Due to the dangers involved with measuring the size distributions of ash in plumes in situ, the initial size distributions used in VATDMs are measured from deposits in the field. These measurements are often depleted in fine ash because fine particles can be swept to great distances from the volcano, where they cannot be collected and measured [47]. Particle densities and shapes are also typically measured from field deposits and, along with the size, also affect the settling rate of ash. Particle density varies with vesicularity, which can be a function of particle size, and particle shapes can range widely from spherical to nonspherical [48]. Advection-diffusion models, such as Fall3D, can exhibit high sensitivity to particle shape [46], which is a parameter that eruption-specific and extensive field deposit sampling could better constrain relatively easily.

Transport-related parameters (i.e., wind fields and diffusion coefficients) govern the advection and diffusion portions of the model. The diffusion coefficients represent the dispersion of ash due to small-scale turbulent motion without directly modeling the scale of this process and impact the width of ash plumes and deposits [41, 49]. The values of diffusion coefficients can be challenging to determine and are often tuned to match model results with observations, thereby accounting for some turbulent processes that are not directly modeled. Most of the transport processes for large eruptive columns occur outside the boundary layer, causing the vertical diffusion coefficient to be negligible compared to the horizontal diffusion coefficient [49]. Despite the uncertainty and wide range of possible horizontal diffusion coefficients, the

model is typically not as sensitive to this parameter as it is MFR, some source types, and particle shape [46].

To constrain VATDMs in the Arctic, where data are sparse, Young et al. [46] developed a methodology to use the most data-rich event and obtain the best-fit model parameters by solving the inverse problem [46]. These best-fit parameters were then used to extrapolate those for other less studied eruptive episodes. This methodology was applied by Young et al. [46] to the 2009 eruption of Redoubt Volcano in Alaska, USA, and would be applicable to other eruptions for which a small period of the explosive activity was better characterized than most of the explosive events. Although this technique resulted in good to moderate model agreement with the available satellite and field data, the model had particular difficulty reproducing ash deposit loadings measured by Schaefer and Wallace (2012) in the far field (200–300 km from the vent) for even the most studied eruptive episode [50]. Other works employing Eulerian models to simulate ash deposition from the same eruptive event had similar issues for many model runs in the far field using a similar model set-up [44, 51]. Potential sources of error for all studies include distinguishing between ash layers from different eruptive events in the field [43], issues with wind field resolution through high elevation regions, and ash aggregation effects (discussed below in detail) that are not currently treated by any volcanic transport model.

Aggregation models, such as the one developed by Telling et al. [52], should be incorporated in VATDMs. Additionally, the process of comminution, which is the break-up of particles due to collisions, is not considered. Comminution is likely important in the initial conduit, where particle densities and energies are high and more bounce events between particles occur than aggregation events [53] and also, potentially, in the lowest region of the volcanic column, where particle densities are highest. Aggregation is more critical to consider when attempting to reconcile deposition and long-range atmospheric transport models with field and satellite data.

3.2. Ash aggregation studies for future VATDM improvements

Aggregation, or sticking, between volcanic particulate is a key source of error in any volcanic transport model. Volcanic ash is defined as any solid particulate with a diameter less than 2 mm in size [24]. Depending on the eruption type, size, and duration, fine ash (1–10 μm) typically has a lifetime on the order of days [11, 54], whereas fine ash (0.1–1 μm) can remain in the atmosphere for months to years in the case of stratospheric eruptions [11]. This can be a particular concern for Arctic eruptions because the boundary between the troposphere and stratosphere is lower in the Arctic environment. Typically, the Arctic tropopause occurs between 8 and 10 km, depending on season, whereas the tropopause occurs between 12 and 16 km over the tropics.

Marzano et al. [55] cited the lack of information regarding particle aggregation as a key source of error in their efforts to model the 2004 eruption of Grimsvötn. More recently, the 2010 eruption of Eyjafjallajökull, Iceland, produced an abundance of both fine ash (raising concerns for aircraft travel and respiratory health impacts) and coarse ash [54]. However, aggregation processes ultimately removed much of the fine ash close to Eyjafjallajökull, dampening the

regional hazards [56] and demonstrating the importance of these processes on both regional and global scales [19, 56].

Gilbert and Lane [57] provided a number of classifications for aggregates, but the two broadest categorizations are simply dry and wet. Dry aggregates are bound by particle charging [57], which can be a result of either triboelectric charging, resulting from particle-particle interactions in the flow, or fractoemission, which occurs in the conduit during fragmentation [58]. Wet aggregation arises from the presence of water in a volcanic flow, forming when liquid-coated particles collide and stick together or when dry aggregates are scavenged by a water droplet [57]. In general, the Arctic environment is drier than that in the mid-latitudes and tropics, and this is particularly true in the winter over land. Consequently, electrostatic aggregation is a particularly important consideration in the Arctic, although wet aggregation is still likely dominant in a fresh eruptive plume because water is abundant and atmospheric mixing has not yet cooled the plume.

Numerous models have been proposed to treat aggregation in volcanic and atmospheric simulations. The most simplistic of these typically assume that a certain percentage of ash will aggregate, that only wet or dry aggregation processes are important but not both [19], or that particle aggregation will mimic water droplet coalescence. More complex formulations treat aggregation as a function of Stokes number, with aggregation efficiency decreasing as the Stokes number increases [59]; however, this accounts only for wet aggregation. This is a serious shortcoming for any model used in an Arctic setting because the environment over land is typically dry, especially in winter, and aggregation processes would be poorly modeled as soon as the volcanic plume began to dilute. Research has also been done to experimentally determine how much water is needed to promote wet, over dry, aggregation [52, 57] and to determine the degree of charging required to form electrostatic aggregates [52, 58]. The delineation between wet and dry aggregation zones occurs at ~71% relative humidity [20, 52] and the wet and dry aggregation zones, which each have different behavioral characteristics, can be defined accordingly. Telling et al. [52] developed these experimental relationships into a series of equations that define aggregation efficiency as a function of the collisional energy of two particles for the wet and dry cases separately.

Considering aggregation in radiative calculations would call for an updated microphysical model of ash, which is discussed by Textor et al. [19]. In both dry and wet cases, aggregation would influence how the size distribution evolves with time. The formation of heavier aggregates from smaller particles would lead to aggregates with different shapes than the individual particles and change the gravitational settling rates of ash. Wet aggregation involves the addition of a water layer, which could also be frozen into an ice layer and would modify the refractive index of the ash.

3.3. Constraining a radiative model for volcanic ash deposits

Radiative modeling of volcanic ash deposits on snow and ice requires some similar knowledge to that of plume modeling (i.e., SZA, underlying surface reflectance, ash effective radius, and refractive index) but also must include additional snow layer properties (i.e., snow layer thickness, snow density for each layer, and snow effective radius) and particle mass mixing

http://dx.doi.org/10.5772/63421

ratios of ash in snow. A spectral or monochromatic underlying surface reflectivity can be used, but the model would not be sensitive to this parameter if the snow depth is large.

Even the most detailed depositional maps are often not resolved enough to study the radiative impacts due to the entire extent of the deposit, especially in the aerosol size range (radius ≤50 μm), because the measured area typically includes only deposits proximal to the vent. Modeled depositional loading fields can be converted into mixing ratios using the density of snow and the mixing depth of ash in the snowpack. As reported by Young et al. [46], the shape of the ash particles is important in advection-diffusion modeling, with spherical particles having better agreement with field measurements in most areas, whereas nonspherical particles produce loadings that agree better with field data for locations ≥210 km from the vent [46]. Advection-diffusion models can also do fairly well at reproducing deposited ash median radius compared to field data (except in areas ≤12 km from the vent, where aerosol-sized particles are less abundant), which is useful for optics calculations [18].

Assuming only aerosol-sized ash particles are being considered, the optical properties of the ash may be calculated with the Mie theory for a lognormal size distribution and deposited ash mean effective radii and standard deviation fields determined from transport modeling. This assumption can be made because the larger particles are relatively low in abundance and are concentrated in regions close to the vent [43]. Ash refractive indices for a given composition can be taken from previous laboratory studies, where available (e.g., [34]). Although the inclusion of nonspherical particles is important for transport modeling [46], spherical particles and the Mie theory may be used in calculating the optical properties of ash because relatively little error arises from approximating particles as equal volume to projected area spheres in the radiative flux calculations [17, 36].

The snow properties required by the radiative model can be measured in the field, but in the absence of field data and adequate spatial/temporal coverage data sets, such as the Natural Resources Conservation Service (NRCS) Snow Telemetry (SNOTEL), may be used to estimate snow layer thickness and density. The refractive indices of ice are often taken from the literature (e.g., [60]). Snow effective grain size radius can vary between 50 and 1100 μm (e.g., [61]), with new snow having smaller grains. If snow effective radius profiles are unknown for the time and region of interest, smaller grain sizes may be used to represent fresher snow and larger sizes for older snow.

At the time of eruption, ash would be deposited on top of the snowpack, which could be blanketed by snowfall or another ash layer [62]. The covering of ash deposits with new snow may substantially increase the surface albedo, and the layering structure of snow and ash should be considered. It is likely that measurements of this kind have not been made throughout the entire extent of the ash deposits, and a representative layering scheme may need to be constructed from what is known. However, new snowfall onto ash may not have a long-lived effect on albedo because, as the snow melts, water will flow downward through pore spaces in the snow, and ash will become concentrated at the top of the snowpack. A concern might also be blowing winds spreading freshly fallen ash, but after melting starts wet ash particles will stick to the snow.

3.4. Radiative impacts of aerosol deposits in the Arctic

The radiative impacts of several types of aerosol deposits (i.e., black carbon, volcanic ash, and dust) in snow measured in the field are compared to those for volcanic ash deposits from the mid-sized 2009 eruption of Redoubt Volcano, modeled by Young et al. [18]. High surface reflectivity and cloudy conditions prevented the retrieval of satellite albedos for this eruption, and there were also no known measurements of albedo in the field, both of which are typical issues surrounding Arctic eruptions. In keeping with isolated observations of complete ash cover in many regions, significant albedo reductions were modeled for these areas [18]. **Table 1** breaks down the particulate species and the quantities compared by Young et al. [18].

Aerosol species	Reference	Loadings (ppb)	Percent surface albedo reduction	SW surface forcing (W m^{-2})	Percent increase in melt rate compared to pure snow
Ash[a]	Young et al. [18]	7×10^{4}–1×10^{8}	0–85	0–96	220–330
Ash[b]	Young et al. [18]	≤1.6×10^{7}	X	X	140–160
Black carbon	Clarke and Noone [62]	5–50	1–3	X	X
Dust	Skiles et al. [64]	2×10^{5}–4×10^{6}	X	35–70	X
Ash	Dadic et al. [16]	1×10^{0}–1×10^{6}	0–37	X	X
Ash	Driedger [15]	X	X	X	≥90

Please note that due to the nature of the measured deposits not all of the quantities are directly comparable (as will be discussed in the text) but are presented here to illustrate the extents of impacts possible from various particles. Calculations were done for a layer deposited on both new and old snow, and the ranges reported for albedo reduction and forcing include both cases from the edges of the deposits to the vent [18]. Melt rate increases were calculated at the maximum loadings only to report an upper bound. Information that was not reported is denoted by an X.
a Ash layer covering loadings from the vent to the edges of the deposits.
b Ash layer calculations only considering low to intermediate loadings.

Table 1. Measured radiative impacts of black carbon, volcanic ash, and dust deposits on snow compared to those modeled by Young et al. [18] for volcanic ash.

For a similar particle size and concentration, black carbon is far more absorbing than ash [63], but at the large loadings that may be produced by a mid-sized eruption ash would cause the most significant albedo reductions. To compare volcanic eruptions, it is important to look at albedo changes from similar loadings. The greatest deposit loading used in Young et al. [18] is two orders of magnitude larger than that measured by Dadic et al. [16] in Antarctica. It is

possible that the deposits measured by Dadic et al. [16] were from a smaller eruption (or a mid-sized to large eruption under windier conditions), the study had only measured ash in more distal locations, or greater mixing of ash and snow had taken place. Young et al. [18] reported an albedo reduction of ~37% for ash deposited on new snow when considering only loadings at more distal locations (~200 km from the vent) and concentrations of ~2.8×10^7 ppb [18]. This albedo reduction is comparable to that of Dadic et al. [16] for the area of the largest ash concentration measured. These studies may not be directly comparable, however, due to potentially different size distributions in deposits at the locations of interest.

The SW surface net fluxes calculated by Young et al. [18] were made at a daily mean SZA for late March and can be viewed as 12-hour daily averages [18]. Skiles et al. [64] also computed springtime daily mean forcings for dust deposits on snow in Colorado. The SW imaginary part of the refractive index for ash [34] is similar to that of dust [65], but the mean daily forcings from dust would be much smaller in the Arctic than in Colorado. This is because the average Arctic dust concentrations are about two to three orders of magnitude lower (i.e., [66]), and the incident solar radiation is lessened at higher latitudes. Using the method of Skiles et al. [64] to calculate minimum forcings due to the direct effects of ash deposition onto snow alone, Young et al. [18] computed a range from the edges of the deposit to the vent of ~0 to 96 W m^{-2}.

The restricted degree-day radiation balance approach described in Melloh [67] was used by Young et al. [18] to estimate a range of melt rates from SW surface net fluxes. Although no significant increases in melt rate were found for the edges of the deposits, regions with larger ash loadings had daily melt rates that were substantially greater than pure snow (~220–320%). However, these areas included ash layer thicknesses exceeding 0.3 cm, which will start to insulate the snow at this thickness [15], making these estimates of snowmelt an upper bound. Considering only intermediate loadings ≤1.6×10^7 ppb with layer thicknesses <0.3 cm achieved more conservative maximum melt rates ~140% to 160% larger than ash-free snow. These estimates are generally in agreement with conservative maximum snowmelt increases of at least 90% measured for snow plots manually covered with ash by Driedger [15]. Melting in regions where snow is present year-round can lead to an increase in albedo that results in further snowmelt. In areas that typically melt in the summer, early or accelerated snowmelts have the capacity to reduce runoff in later months and deplete water resources [68].

4. Other impacts

4.1. Indirect radiative effects

The indirect aerosol effect refers to the ability of aerosols to cause radiative perturbations by altering the microphysical properties (e.g., changing the refractive index, particle number, and/or size distribution), lifetime, and coverage of meteorological clouds, thereby also influencing the hydrological cycle [69]. The Intergovernmental Panel on Climate Change (IPCC) reports that the current understanding of the indirect effects of aerosols on clouds is low [70]. Studies have shown that sulfate from the eruption of Mount Pinatubo in the Philippines produced a global impact on cirrus formation and evolution [21] through increases in aerosol number,

homogeneous ice nucleation rate and ice crystal number, and ice water path [21, 71]. Additionally, it was found that ash can uptake water efficiently and can serve as cloud condensation nuclei [20] and ice nuclei [19]. The indirect effects in the Arctic may be different than in other regions because of the special properties of the surface and atmosphere, and the Arctic is more sensitive to aerosol effects [69]. The aerosol indirect effects due to volcanic eruptions may be particularly significant, as eruptions supply a large number of particles (i.e., ash, ice, and sulfates) compared to the low particle levels in the ambient Arctic atmosphere. More research is needed on the subject of the indirect radiative effects of volcanic aerosols in the Arctic.

4.2. Effects on ecosystems

The effect that volcanic eruptions have on ecosystems has been well documented. Forests [72], oceans [73–75], and even large global cycles, such as CO_2 variability typically controlled by the El Niño-Southern Oscillation (ENSO) [76, 77], can be influenced by volcanic eruptions. This section examines a few of these effects in further detail.

4.2.1. Increased diffuse radiation to plants

Beyond the direct radiative impacts of volcanic eruptions, volcanic ash and aerosol can have long-lasting secondary effects. The ash-rich eruption of Tambora Volcano, Indonesia, in 1815, resulted in the well-known "year without summer" in 1816 [78]. Stratospheric ash loading reduced direct solar radiation globally, leading to widespread cooling, crop failure, and slowed forest growth [72, 78]. However, Gu et al. [79] found that large aerosol-rich eruptions, such as Mount Pinatubo, can have a quite different effect. Although the 1991 eruption of Mount Pinatubo did decrease the direct solar radiation as expected, it also increased the diffuse solar radiation [79]. Gu et al. [79] showed that this increase in diffuse solar radiation led to an increase in forest photosynthesis, which, in turn, led to a temporary decline in the amount of atmospheric CO_2 [76]. Although neither of these eruptions occurred in the Arctic, both the Tambora and Mount Pinatubo events were felt globally for years afterward [69, 79] and potentially had a disproportionate effect on the Arctic environment either by promoting additional growth of vegetation in the tundra or by reducing the already short Arctic growing season. Further study is needed to better understand the effects of large volcanic eruptions on the Arctic environment, which is home to thousands of plant species.

4.2.2. Increased ocean productivity

Plate tectonics dictate that many of Earth's explosive volcanism sources are located near oceans and the effects of volcanic eruptions on ocean ecosystems have only been examined in a few studies. Olgun et al. [80] found that eruptions from Mount Etna, Italy, have contributed appreciable amounts of nitrogen, phosphorus, silicon, iron, and zinc to the Mediterranean Ocean between 2001 and 2007. Durant et al. [75] found enhanced amounts of calcium, sodium, and iron in lakes following the 2008 eruption of Chaitén Volcano, Chile. The iron contribution, in particular, made by volcanic deposits, has been particularly interesting to studies of ocean chemistry. Much of the ocean away from continental boundary regions is iron poor [73]. Deposits of volcanic ash, which becomes coated in minerals, deliver iron, a necessary nutrient

http://dx.doi.org/10.5772/63421

for phytoplankton [73, 74], to otherwise iron-poor regions of the ocean. Phytoplankton blooms were noted after the 2008 eruption of Kasatochi Volcano (Alaska) [74], Mount Spurr (Alaska), Arenal Volcano (Costa Rica), and Sakurajima Volcano (Japan) [73]. The phytoplankton blooms were large enough to be seen by MODIS from space [73, 74].

The effect on Earth's ecosystem does not end with increased phytoplankton growth, though. Similar to the effect seen in forests, the large phytoplankton blooms cause a temporary but significant decrease in atmospheric CO_2 [73, 81]. The decrease in CO_2 caused by moderate to large volcanic eruptions is on par with that caused by ENSO and can mitigate or exacerbate the effects of ENSO depending on when during the ENSO cycle an eruption occurs [76, 77]. Modeling studies by Rothenberg et al. [81] and Frölicher et al. [77] both showed that the additional CO_2 uptake results in further global cooling that is particularly strong in the Arctic region.

5. Conclusions

Volcanic aerosol, although sporadically present, can have a profound influence on the Arctic environment. There is a potential for volcanic aerosol to provide a sizeable contribution to the radiative effects and even exceed the impacts of other types of aerosol when significant amounts of volcanic ash are present, as in young volcanic plumes and volcanic ash deposits. The composition, thickness, and AOD of volcanic plumes vary greatly and are, in many cases, difficult to constrain. Meteorological clouds also often hamper satellite retrievals, making transport modeling necessary for plume tracking.

The development of multiphase models (e.g., [82]) to study eruption dynamics may assist in creating better microphysical models for volcanic ash and have the capacity to be modified to treat the formation and transport of other volcanic aerosols, such as sulfates and ice. The deployment of balloons with particle counters attached would also further our understanding of the evolution of aerosol size distributions in plumes, which are hazardous to fly through and difficult to fully characterize with deposit measurements. There is a need for better constrained eruption-specific model input parameters (i.e., MFR, source type, and nonsphericity of ash particles). Discrepancies in modeled and measured loadings tend to be larger farther from the vent, which could indicate issues with wind field resolution or aggregation and comminution processes. Existing aggregation models, such as the one developed by Telling et al. [52], should be incorporated in volcanic ash dispersion and transport models. Additionally, the process of comminution, which typically only occurs in the volcanic conduit, is not considered. These improvements to eruption source and dispersion parameters will provide more accurate ash deposition estimates, which are critical for understanding how volcanic plumes and deposits interact with the Arctic environment. Other plume-related simplifications, which are often made in radiative transfer modeling and which need to be addressed, include the partitioning of volcanic aerosol types at different altitudes and sulfate, water, and ice coatings on ash.

Loadings of ash and the optical properties of ash and snow are important to radiative calculations. Future studies should consider improving ash loading estimates and the acquisition of eruption-specific snow and ash properties for radiative modeling. The calculation of global radiative effects could be made possible by a more intimate coupling of volcanic eruption source conditions, transport, and deposition with radiative transfer and global circulation models. Improvements that could be made through fieldwork include measurements of albedo change and snow ablation rates, which could be done through coordination with local volcano observatories. Alternatively, laboratory simulations on a smaller scale could be conducted when fieldwork is not possible.

Additionally, volcanic aerosols may have strong impacts on ecosystems and the carbon cycle. Because of the important radiative effects of volcanic aerosols in the Arctic, it is recommended that volcanic aerosols be included in future assessments of the Arctic regional radiation budget to facilitate efforts in understanding the radiative impacts of natural aerosols on the Arctic environment. Because of the persistence of cloud cover in this region, the radiative impacts of meteorological clouds in the presence of volcanic plumes and deposits should be considered. The effects of volcanic aerosol on other permanently and seasonally snow-covered environments might also be considered; these include glaciers at lower latitudes (e.g., in the Andes) and in Antarctica.

Author details

Cindy L. Young[1*] and Jennifer W. Telling[2]

*Address all correspondence to: cindy.young@eas.gatech.edu

1 School of Earth and Atmospheric Sciences, Georgia Institute of Technology, Atlanta, GA, USA

2 National Center for Airborne Laser Mapping (NCALM), University of Houston, Houston, TX, USA

References

[1] Stone, R.S., Anderson, G.P., Shettle, E.P., Andrews, E., Loukachine, K., Dutton, E.G., Schaaf, C., Roman, M.O. Radiative impact of boreal smoke in the Arctic: Observed and modelled. J. Geophys. Res. Atmos. 2008;113(D14) pp. 1–17 . DOI: 10.1029/2007JD009657

[2] Stone, R.S., Anderson, G.P., Andrews, E., Dutton, E.G., Shettle, E.P. Incursions and radiative impact of Asian dust in northern Alaska. Geophys. Res. Lett. 2007;34:L14815. DOI: 10.1029/2007gl029878

[3] Simkin, T., Siebert, L. Volcanoes of the World. 2nd ed. Tucson: Geoscience Press; 1994. 369 pp.

[4] Thordarson, T., Self, S. Atmospheric and environmental effects of the 1783–1784 Laki eruption: A review and reassessment. J. Geophys. Res. 2003;108(D1):4011.

[5] Frogner-Kockum, P.C., Herbert, R.B., Gislason, S.R. A diverse ecosystem response to volcanic aerosols. Chem. Geol. 2006;231(1):57–66.

[6] Hildreth, W., Fierstein, J. The Novarupta-Katmai eruption of 1912: Largest eruption of the twentieth century. In: Centennial Perspectives. U.S. Department of the Interior, U.S. Geological Survey; 2012. Reston, Virginia USA, 259 pp.

[7] Rose, W.I., Bluth, G.J.S., Watson, I.M. Ice in volcanic clouds: When and where? In: Proceedings of the 2nd International Conference on Volcanic Ash and Aviation Safety. Washington, DC: OFCM, 2004.

[8] Andersson, S.M., Martinsson, B.G., Friberg, J., Brenninkmeijer, C.A.M., Rauthe-Schöch, A., Hermann, M., van Velthoven, P.F.J., Zahn, A. Composition and evolution of volcanic aerosol from eruptions of Kasatochi, Sarychev and Eyjafallajokull in 2008–2010 based on CARIBIC observations. Atmos. Chem. Phys. 2013;13(4):1781–1796.

[9] Carslaw, K.S., Boucher, O., Spracklen, D.V., Mann, G.W., Rae, J.G.L., Woodward, S., Kulmala, M. Atmospheric aerosols in the earth system: A review of interactions and feedbacks. Atmos. Chem. Phys. 2009;9:10087–11183.

[10] Robock, A. Volcanic eruptions and climate. Rev. Geophys. 2000;38:191–219.

[11] Niemeier, U., Timmreck, C., Graf, H.F., Kinne, S., Rast, S., Self, S. Initial fate of fine ash and sulphur from large volcanic eruptions. Atmos. Chem. Phys. 2009;9(22):9043–9057. DOI: 10.5194/acp-9-9043-2009

[12] Stenchikov, G.L., Kirchner, I., Robock, A., Graf, H.F., Antuna, J.C., Grainger, R.G., Lambert, A., Thomason, L. Radiative forcing from the 1991 Mount Pinatubo volcanic eruption. J. Geophys. Res. Atmos. 1998;103:13837–13857.

[13] Painter, T.H., Deems, J.S., Belnap, J., Hamlet, A.F., Landry, C.C., Udall, B. Response of Colorado River runoff to dust radiative forcing in snow. Proc. Natl. Acad. Sci. U. S. A. 2010;107(40):17125–17130. DOI: 10.1073/pnas.0913139107

[14] Flanner, M.G., Zender, C.S., Randerson, J.T., Rasch, P.J. Present-day climate forcing and response from black carbon in snow. J. Geophys. Res. Atmos. 2007; pp. 1–17 112(D11). DOI: 10.1029/2006JD008003

[15] Driedger, C. Effect of ash thickness on snow ablation. In: Lipman, P.W., Christiansen, R.L., editors. The 1980 Eruptions of Mount St. Helens. Washington, DC, 1981. pp. 757–760.

[16] Dadic, R., Mullen, P.C., Schneebeli, M., Brandt, R.E., Warren, S.G. Effects of bubbles, cracks, and volcanic tephra on the spectral albedo of bare ice near the Transantarctic

Mountains: Implications for sea glaciers on Snowball Earth. J. Geophys. Res.: Earth Surface. 2013;118(3):1658–1676.

[17] Flanner, M.G., Gardner, A.S., Eckhardt, S., Stohl, A., Perket, J. Aerosol radiative forcing from the 2010 Eyjafjallajökull volcanic eruptions. J. Geophys. Res. Atmos. 2014. pp. 9481–9491, Vol. 119 DOI: 10.1002/2014JD021977

[18] Young, C.L., Sokolik, I.N., Flanner, M.G., Dufek, J. Surface radiative impacts of ash deposits from the 2009 eruption of Redoubt Volcano. J. Geophys. Res. Atmos. 2014;119(19) pp. 11387–11397 .

[19] Textor, C., Graf, H.F., Herzog, M., Oberhuber, J.M., Rose, W.I., Ernst, G.G.J. Volcanic particle aggregation in explosive eruption columns. Part I: Parameterization of the microphysics of hydrometeors and ash. J. Volcanol. Geotherm. Res. 2006;150:359–377. DOI: 10.1016/j.jvolgeores.2005.09.007

[20] Lathem, T.L., Kumar, P., Nenes, A., Dufek, J., Sokolik, I.N., Trail, M., Russell, A. Hygroscopic properties of volcanic ash. Geophys. Res. Lett. 2011;38(L11802) pp. 1–4 . DOI: 10.1029/2011GL047298

[21] Liu, X., Penner, J.E. Effect of Mt. Pinatubo H_2SO_4/H_2O aerosol on ice nucleation in the upper troposphere using a global chemistry and transport model (IMPACT). J. Geophys. Res. 2002;107(4141) pp. 1–18 . DOI: 10.1029/2001JD000455

[22] Jager, H., Deshler, T. Lidar backscatter to extinction, mass and area conversions for stratospheric aerosols based on midlatitude balloonborne size distribution measurements. Geophys. Res. Lett. 2002;29 pp. 1–4 . DOI: 10.1029/2002gl015609

[23] Stier, P., Feichter, J., Kinne, S., Kloster, S., Vignati, E., Wilson, J., Ganzeveld, L., Tegen, I., Werner, M., Balkanski, Y., Schulz, M., Boucher, O., Minikin, A., Petzold, A. The aerosol-climate model echam5-ham. Atmos. Chem. Phys. 205;5:1125–1156.

[24] Rose, W.I., Durant, A.J. Fine ash content of explosive eruptions. J. Volcanol. Geotherm. Res. 2009;186(1–2):32–39. DOI: 10.1016/j.jvolgeores.2009.01.010

[25] Prata, A.J., Bernardo, C. Retrieval of volcanic SO_2 column abundance from atmospheric infrared sounder data. J. Geophys. Res. Atmos. 2007;112 pp. 1–17 . DOI: 10.1029/2006JD007955

[26] Draxler, R.R., Rolph, G.D. NOAA Air Resources Laboratory, College Park, MD. HYSPLIT (Hybrid Single-Particle Lagrangian Integrated Trajectory) Model access via NOAA ARL READY Website [Internet]. Available at: http://www.arl.noaa.gov/HYSPLIT.php

[27] Rolph, G.D. Real-time Environmental Applications and Display System (READY) Website. NOAA Air Resources Laboratory, College Park, MD. [Internet]. Available at: http://www.ready.noaa.gov

[28] Telling, J., Flower, V.J.B., Carn, S.A. A multi-sensor satellite assessment of SO_2 emissions from the 2012–13 eruption of Plosky Tolbachik Volcano, Kamchatka. J. Volcanol. Geotherm. Res. 2015;307:98–106. DOI: 10.1016/j.volgeores.2015.07.010

[29] Young, C.L., Sokolik, I.N., Dufek, J. Regional radiative impact of volcanic aerosol from the 2009 eruption of Mt. Redoubt. Atmos. Chem. Phys. 2012;12(8):3699–3715. DOI: 10.5194/acp-12-3699-20.

[30] Wen, S., Rose, W.I. Retrieval of sizes and total masses of particles in volcanic clouds using AVHRR bands 4 and 5. J. Geophys. Res. Atmos. 1994;99(D3):5421–5431.

[31] Rose, W.I., Delene, D.J., Schneider, D.J., Bluth, G.J.S., Krueger, A.J., Sprod, I., McKee, C., Davies, H.L., Ernst, G.G.J. Ice in the 1994 Rabaul eruption cloud: Implications for volcano hazard and atmospheric effects. Nature. 1995;375(477–479).

[32] Hess, M., Koepke, P., Schult, I. Optical properties of aerosols and clouds: The software package OPAC. B. Am. Meteorol. Soc. 1998;79:831–844.

[33] Yue, G.K., Poole, L.R., Wang, P.H., Chiou, E.W. Stratospheric aerosol acidity, density, and refractive-index deduced from SAGE-II and NMC temperature data. J. Geophys. Res. Atmos. 1994;99:3727–3738.

[34] Pollack, J.B., Toon, O.B., Khare, B.N. Optical properties of terrestrial rocks and glasses. Icarus. 1973;19:372–389.

[35] Kearney, C.S., Watson, I.M. Correcting satellite-based infrared sulphur dioxide retrievals for the presence of silicate ash. J. Geophys. Res. Atmos. 2009;114(D22208) pp. 1–12 . DOI: 10.1029/2008jd011407

[36] Fu, Q., Thorsen, T.J., Su, J., Ge, J.M., Huang, J.P. Test of Mie-based single-scattering properties of non-spherical dust aerosols in radiative flux calculations. J. Quant. Spectrosc. Radiat. Transfer. 2009;110(14):1640–1653. DOI: 10.1016/j.jqsrt.2009.03.010

[37] Quinn, P.K., Shaw, G., Andrews, E., Dutton, E.G., Ruoho-Airola, T., Gong, S.L. Arctic haze: Current trends and knowledge gaps. Tellus B. 2007;59:99–114. DOI: 10.1111/j.1600-0889.2006.00238.x

[38] Ritter, C., Notholt, J., Fischer, J., Rathke, C. Direct thermal radiative forcing of tropospheric aerosol in the arctic measured by ground based infrared spectrometry. Geophys. Res. Lett. 2005;32:L23816. DOI: 10.1029/2005gl024331

[39] Myhre, C.L., Toledano, C., Myhre, G., Stebel, K., Yttri, K.E., Aaltonen, V., Johnsrud, M., Frioud, M., Cachorro, V., De Frutos, A., Lihavainen, H., Campbell, J.R., Chaikovsky, A.P., Shiobara, M., Welton, E.J., Torseth, K. Regional aerosol optical properties and radiative impact of the extreme smoke event in the European Arctic in spring 2006. Atmos. Chem. Phys. 2007;(7):5899–5915.

[40] Stuefer, M., Freitas, S.R., Grell, G., Webley, P., Peckham, S., McKeen, S.A., Egan, S.D. Inclusion of ash and SO_2 emissions from volcanic eruptions in WRF-Chem: Develop-

ment and some applications. Geosci. Model Dev. 2013;6(2):457–468. DOI: 10.5194/gmd-6-457-2013

[41] Costa, A., Macedonio, G., Folch, A. A three-dimensional Eulerian model for transport and deposition of volcanic ashes. Earth Planetary Sci. Lett. 2006;241(3–4):634–647. DOI: 10.1016/j.epsl.2005.11.019

[42] Wilson, L., Sparks, R.S.J., Huang, T.C., Watkins, N.D. Control of volcanic column heights by eruption energetic and dynamics. J. Geophys. Res. 1978;83(NB4):1829–1836.

[43] Wallace, K.L, Schaefer, J.R., Coombs, M.L. Character, mass, distribution, and origin of tephra-fall deposits from the 2009 eruption of Redoubt Volcano, Alaska—Highlighting the significance of particle aggregation. J. Volcanol. Geotherm. Res. 2013;259:145–169. DOI: 10.1016/j.jvolgeores.2012.09.015

[44] Mastin, L.G., Schwaiger, H., Schneider, D.J., Wallace, K.L., Schaefer, J., Denlinger, R.P. Injection, transport, and deposition of tephra during event 5 at Redoubt Volcano, 23 March, 2009. J. Volcanol. Geotherm. Res. 2013;259:201–213. DOI: 10.1016/j.jvolgeores.2012.04.025

[45] Schmehl, K.J., Haupt, S.E., Pavolonis, M.J. A genetic algorithm variational approach to data assimilation and application to volcanic emissions. Pure Appl. Geophys. 2012;169(3):519–537. DOI: 10.1007/s00024-011-0385-0

[46] Young, C.L., Dufek, J., Sokolik, I.N. Assessment of depositional ash loading from the 2009 eruption of Mt. Redoubt. J. Volcanol. Geotherm. 2014;274:122–138.

[47] Rose, W.I., Chesner, C.A. Dispersal of ash in the great Toba eruption, 75 ka. Geology. 1987;15(10):913–917. DOI: 10.1130/0091-7613(1987)15<913:DOAITG>2.0.CO;2

[48] Bonadonna, C., Genco, R., Gouhier, M., Pistolesi, M., Cioni, R., Alfano, F., Hoskuldsson, A., Ripepe, M. Tephra sedimentation during the 2010 Eyjafallajokull eruption (Iceland) from deposit, radar, and satellite observations. J. Geophys. Res. Sol. Ea. 2011;116 pp. 1–20. DOI: 10.1029/2011JB008462

[49] Bonadonna, C., Connor, C.B., Houghton, B.F., Connor, L., Byrne, M., Laing, A., Hincks, T.K. Probabilistic modelling of tephra dispersal: Hazard assessment of a multiphase rhyolitic eruption at Tarawera, New Zealand. J. Geophys. Res. Sol. Ea. 2005;110(B3) pp. 1–21 . DOI: 10.1029/2003/JB002896

[50] Schaefer, J.R. The 2009 eruption of Redoubt Volcano, Alaska, with contributions by Bull, K.P., Cameron, C.E., Coombs, M.L., Diefenbach, A.K., Lopez, T., McNutt, S.R., Neal, C.A., Payne, A.L., Power, J.A., Schneider, D.J., Scott, W.E., Snedigar, S.F., Thompson, G., Wallace, K.L., Waythomas, C.F., Webley, P.W., Werner, C.A. Report of Investigations RI 2011-5, State of Alaska, Department of Natural Resources, Division of Geological and Geophysical Surveys, Fairbanks, Alaska. 2011;5:45.

[51] Steensen, T., Stuefer, M., Webley, P., Grell, G., Freitas, S. Qualitative comparison of Mount Redoubt 2009 volcanic clouds using the PUFF and WRF-Chem dispersion

models and satellite remote sensing data. J. Volcanol. Geotherm. Res. 2013;259:235–247. DOI: 10.1016/j.jvolgeores.2012.02.018

[52] Telling, J.W., Dufek, J., Shaikh, A. Ash aggregation in explosive volcanic eruptions. Geophys. Res. Lett. 2013;40(10):2355–2360. DOI: 10.1002/grl.50376

[53] Dufek, J., Manga, M., Patel, A. Granular disruption during explosive volcanic eruptions. Nat. Geosci. 2012;5:561–564.

[54] Gislason, S.R., Hassenkam, T., Nedel, S., Bovet, N., Eiriksdottir, E.S., Alfredsson, H.A., Hem, C.P., Balogh, Z.I., Dideriksen, K., Oskarsson, N., Sigfusson, B., Larsen, G., Stipp, S.L.S. Characterization of Eyjafjallajokull volcanic ash particles and a protocol for rapid risk assessment. Proc. Natl. Acad. Sci. U. S. A. 2011;108:7307–7312. DOI: 10.1073/pnas.1015053108

[55] Marzano, F., Barbieri, S., Picciotti, E., Karlsdóttir, S. Monitoring subglacial volcanic eruption using ground-based C-band radar imagery. IEEE Trans. Geosci. Remote Sensing. 2010;48:403–414.

[56] Taddeucci, J., Scarlato, P., Montanaro, C., Cimarelli, C., Del Bello, E., Freda, C., Andronico, D., Gudmundsson, M.T., Dingwell, D.B. Aggregation-dominated ash settling from the Eyjafjallajkull volcanic cloud illuminated by field and laboratory high-speed imaging. Geology. 2011;39(9):891–894. DOI: 10.1130/G32016.1

[57] Gilbert, J.S., Lane, S.J. The origin of accretionary lapilli. Bull. Volcanol. 1994;56:398–411. DOI: 10.1007/BF00326465

[58] Gilbert, J.S., Lane, S.J., Sparks, R.S.J., Koyaguchi, T. Charge measurements on particle fallout from volcanic plume. Nature. 1991;349:598–600. DOI: 10.1038/349598a0

[59] Costa, A., Folch, A., Macedonio, G. A model for wet aggregation of ash particles in volcanic plumes and clouds: 1. Theoretical formulation. J. Geophys. Res. 2010;115 pp. 1–14. DOI: 10.1029/2009JB007175

[60] Warren, S.G., Brandt, R.E., Grenfell, T.C. Visible and near-ultraviolet absorption spectrum of ice from transmission of solar radiation into snow. Appl. Opt. 2006;45(21):5320–5334.

[61] Painter, T.H., Dozier, J., Roberts, D.A., Davis, R.E., Green, R.O. Retrieval of subpixel snow-covered area and grain size from imaging spectrometer data. Remote Sensing Environ. 2003;85(1):64–77.

[62] Clarke, A.D., Noone, K.J. Soot in the Arctic snowpack: A cause for perturbations in radiative transfer. Atmos. Environ. 1985;19(12):2045–2053.

[63] Wang, L., Li, Z., Tian, Q., Ma, Y., Zhang, F., Zhang, Y., Li, D., Li, K., Li, L. Estimate of aerosol absorbing components of black carbon, brown carbon, and dust from ground-based remote sensing data of sun-sky radiometers. J. Geophys. Res. Atmos. 2013;118:6534–6543. DOI: 10.1002/jgrd.50356

[64] Skiles, S.M., Painter, T.H., Deems, J.S., Bryant, A.C., Landry, C.C. Dust radiative forcing in snow of the Upper Colorado River Basin: 2. Interannual variability in radiative forcing and snowmelt rates. Water Resources Res. 2012;48(7) pp. 1–11 .

[65] Smith, A.J.A., Grainger, R.G. Does variation in mineral composition alter the short-wave light scattering properties of desert dust aerosol? J. Quant. Spectrosc. Radiat. Transfer. 2014;133:235–243. DOI: 10.1016/j.jqsrt.2013.08.005

[66] Zdanowicz, C.M., Zielinski, G.A., Wake, C.P. Characteristics of modern atmospheric dust deposition in snow on the Penny Ice Cap, Baffin Island, Arctic Canada. Tellus B. 1998;50(5):506–520. DOI: 10.1034/j.1600-0889.1998.t01-1-00008.x

[67] Melloh, R.A. A synopsis and comparison of selected snowmelt algorithms. Hanover, NH: Cold Regions Research and Engineering Lab; 1999. No. CRREL-99-8.

[68] Qian, Y., Gustafson, W.I., Leung, L.R., Ghan, S.J. Effects of soot-induced snow albedo change on snowpack and hydrological cycle in western United States based on Weather Research and Forecasting chemistry and regional climate simulations. J. Geophys. Res. Atmos. 2009;114(D3) pp. 1–19 . DOI: 1029/2008JD011039

[69] Sokolik, I.N., Curry, J.A., Radionov, V. Interactions of Arctic aerosols with land-cover and land-use changes in northern Eurasia and their role in the Arctic climate system. In: Gutman, G., Reissell, A., editors. Arctic Land-Cover and Land-Use in a Changing Climate: Focus on Eurasia. Springer; New York, USA, 2011.

[70] Anisimov, O.A., Vaughan, D.G., Callaghan, T.V., Furgal, C., Marchant, H., Prowse, T.D., Vilhjálmsson, H., Walsh, J.E. Polar regions (Arctic and Antarctic). In: Parry, M.L., Canziani, O.F., Palutikof, J.P., Van der Linden, P.J., Hanson, C.E., editors. Climate Change 2007: Impacts, Adaptation and Vulnerability. Contribution of Working Group II to the Fourth Assessment Report of the Intergovernmental Panel on Climate Change. Cambridge University Press; Cambridge, England, 2007. pp. 653–685.

[71] Lohmann, U., Karcher, B., Timmreck, C. Impact of the Mount Pinatubo eruption on cirrus clouds formed by homogeneous freezing in the ECHAM4 GCM. J. Geophys. Res. Atmos. 2003;108(4568) pp. 1–13 . DOI: 10.1029/2002jd003185

[72] Yadav, R. Basin specificity of climate change in western Himalaya, India: Tree-ring evidences. Curr. Sci. 2007;92(10):1424–1429.

[73] Duggen, S., Croot, P., Schacht, U., Hoffmann, L. Subduction zone volcanic ash can fertilize the surface ocean and stimulate phytoplankton growth: Evidence from biogeochemical experiments and satellite data. Geophys. Res. Lett. 2007;34(L01612) pp. 1–5 . DOI: 10.1029/2006GL027522

[74] Langmann, B., Zaksek, K., Hort, M., Duggen, S. Volcanic ash as fertilizer for the surface ocean. Atmos. Chem. Phys. 2010;10:3891–3899.

[75] Durant, A.J., Villarosa, G., Rose, W.I., Delmelle, P., Prata, A.J., Viramonte, J.G. Long-range volcanic ash transport and fallout during the 2008 eruption of Chaitén Volcano, Chile. Phys. Chem. Earth. 2012;45–46:50–64. DOI: 10.1016/j.pce.2011.09.004

[76] Jones, C.D., Cox, P.M. Modeling of the volcanic signal in the atmospheric CO_2 record. Global Biogeochem. Cycles 2001;15(2):453–465. DOI: 10.1029/2000GB001281

[77] Frölicher, T.L., Joos, F., Raible, C.C., Sarmiento, J.L. Atmospheric CO_2 response to volcanic eruptions: The role of ENSO, season, and variability. Global Biogeochem. Cycles 2013;27:239–251. DOI: 10.1002/gbc.20028

[78] Oppenheimer, C. Climatic, environmental and human consequences of the largest known historic eruption: Tambora Volcano (Indonesia) 1815. Prog. Phys. Geog. 2003;27(2):230–259. DOI: 10.1191/0309133303pp379ra

[79] Gu, L., Baldocchi, D.D., Wofsy, S.C., Munger, J.W., Michalsky, J.J., Urbanski, S.P., Boden, T.A. Response of a deciduous forest to the Mount Pinatubo eruption: Enhanced photosynthesis. Science. 2003;299(5615):2035–2038.

[80] Olgun, N., Duggen, S., Andronico, D., Kutterolf, S., Croot, P.L., Giammanco, S., Censi, P., Randazzo, L. Possible impacts of volcanic ash emissions of Mount Etna on the primary productivity in the oligotrophic Mediterranean Sea: Results from nutrient-release experiments in seawater. Mar. Chem. 2013;152:32–42. DOI: 10.106/j.marchem. 2013.04.004

[81] Rothenberg, D., Mahowald, N., Lindsay, K., Doney, S.C., Moore, J.K., Thornton, P. Volcano impacts on climate and biogeochemistry in a coupled carbon-climate model. Earth Syst. Dyn. 2012;3:121–136. DOI: 10.5194/esd-3-121-2012

[82] Dufek, J., Bergantz, G.W. Suspended load and bed-load transport of particle-laden gravity currents: The role of particle-bed interaction. Theor. Comp. Fluid Dyn. 2007;21:119–145. DOI: 10.1007/s00162-007-0041-6

Chapter 10

Effect of Volcano-Polluted Seawater on the Corrosion Behaviour of Different Alloys

Rita Sánchez-Tovar, Ramón Fernández-Domene,
Rafael Leiva-García, Clara Escrivà-Cerdán,
Bianca Lucas-Granados and José García-Antón

Additional information is available at the end of the chapter

http://dx.doi.org/10.5772/63523

Abstract

During a subsea volcano eruption, gases and thermal water emissions are released. This might change the behaviour of the materials that are in contact with the seawater caused by the decrease of the pH value. For this reason, the materials for marine applications are selected to maintain the integrity of the structure and to be corrosion resistant. In spite of this, corrosion can cause great damage to marine steel infrastructures such as bridges, wharfs, platforms and pipeline systems. These corrosion problems could be aggravated if the medium is altered, due to volcano emissions, since the resistance of the surface film is influenced by the environmental conditions.

Electrochemical techniques are useful to evaluate the corrosion behaviour of different metals and alloys. However, literature regarding the influence of underwater-volcano-polluted seawater on the passivation/corrosion behaviour of stainless steels is scarce. According to this, the objective of the chapter is the evaluation of the influence of an underwater volcano eruption on the corrosion behaviour of different materials that might be used in seawater environments. Electrochemical techniques are applied to evaluate the performance of the different materials when they are immersed in polluted volcano seawater. The results are relevant in the evaluation of natural hazard risk assessments involving critical infrastructures.

Keywords: submarine volcano, corrosion, water chemistry, electrochemistry, stainless steels

1. Introduction

The aim of natural hazard risk assessment is the evaluation of the extent and nature of risk in a particular area by evaluating potential hazards that together could harm people, property and services. Therefore, an effective natural hazard risk assessment requires the characterisation of both hazards and vulnerabilities of exposed elements [1]. Disasters such as the Eyjafjallajökull eruption in Iceland (2010), or the Tōhoku earthquake and tsunami in Japan (2011), suggest the need for effective natural hazard risk management and sustainable development.

Threats and issues with volcanoes are important, around 600 million people are living in areas that could be affected by volcano eruptions [2]. Therefore, the assessment of the volcano impacts on the different areas together with volcanic monitoring can help to prevent and minimise losses associated with these natural disasters [3]. Among the issues related with volcanoes that can be assessed the effects on critical infrastructures are important. Critical infrastructure is defined as a network of man-made systems and processes that function collaboratively to produce and distribute essential goods and services [4] which are heavily relied upon by society for daily function. Critical infrastructures include electrical supply networks, water and wastewater distribution systems or terrestrial transportation systems. Changes in the chemistry of water sources in the area, tephra falls, lars and lava flows are some of the volcano hazards that can affect to the critical infrastructures. One of the hazards that can affect the critical infrastructures in both short and long term is the corrosion of structural materials.

According to the American Society for Testing and Materials, corrosion can be defined as 'The chemical or electrochemical reaction between a material, usually a metal, and its environment that produces a deterioration of the material and its properties [5]'. Corrosion has serious economical, technological and safety consequences to society. From the economical point of view, it has to be taken into consideration all the costs related with over dimensioning during the design, inspection, maintenance and replacement of the equipment. Several studies performed in different countries have tried to determine the cost of corrosion [6, 7]. The most throughout of these studies was the one conducted in the United States in 1976 which found that the overall annual cost of metallic corrosion to the U.S. economy was $70 billion, or 4.2% of the gross national product [8]. Besides, any loss of mechanical properties in the metallic materials may lead to an accident with human or environmental consequences. Therefore, any risk-based inspection methodology has to consider the effect of corrosion on infrastructures, and if facilities are installed in areas with volcanic activity, the hazard effects of volcanoes have to be taken into account.

Corrosion is a well-established phenomenon in volcanically active areas [9, 10]. Hydrogen sulphide, gas, SO_2, CO_2 and other pollutants such as selenium, mercury and arsenic react with oxygen and the atmospheric moisture to produce volcanic smog and acid rain. Thus, those changes in the environment related with volcano eruptions can accelerate the corrosion of the surrounding infrastructures [11]. Specifically, widely distributed volcanic ash derived from explosive volcanic eruption creates short- and long-term hazards to infrastructures including exposed building materials such as metal roofing [12, 13]. The metal corrosion related with

http://dx.doi.org/10.5772/63523

volcanoes has been attributed to volcanic ashes in several studies [14]. In order to study the effect of volcanoes on corrosion, Hawthorn et al. [10] installed a corrosion test site at the Kilauea volcano in Volcanoes National park of the island of Hawai in 2006. They monitored during 1 year the atmospheric conditions, rainwater chemistry and chlorides deposition. They also exposed some aluminium coupons to the volcano environment. After 1 year of experiments, they observed that the corrosion rate was seven times higher in the volcanic environment than in an industrial site in Oahu [10]. Oze and collaborators also checked the effect of the volcanic ashes on the corrosion of metal roof materials [15]. Increased corrosion of metal roofing from chemically reactive volcanic ash following ash deposition post eruption is a major concern due to the decreasing on the functionality and stability of roofs. They tried to obtain some quantitative information about corrosion rates by coating different materials with volcanic ashes; they could not observe clear trends in the corrosion rates with the performed experiments; however, they observed that in field situations, the corrosion was increased by the presence of volcanic ashes. Therefore, they concluded that volcanic corrosion could be a major problem and the experiments performed had to be improved in order to have into account all the circumstances that can be found in volcanic environments [15]. Therefore, the corrosion induced by the presence of volcanic activity is a problem that has to be taken into consideration during the natural hazards assessments.

However, not too much data have been published on the effect of subaquatic volcanoes on the corrosion of offshore structural materials [16, 17]. Subaquatic volcanoes are normal features on certain regions of the ocean floor. Some may be currently active and, in shallow water, show their actions by blasting steam and debris over the surface of the sea. Many others form at great depths where the weight of the water above them results in confining pressure preventing the violent release of steam and gases. They are estimated to account for 75% of annual magma output. The majority are located near areas of tectonic plate movement (ocean ridges). Submarine volcanoes inject large amounts of material of variable size, texture and chemical composition into the oceans [18]. The state of a submarine eruption evolves from ongoing magmatic activity to highly evolved hydrothermal systems. Some of the features observed during submarine volcanic eruptions are as follows: lava flows, bubbles of lava, lava debris, ash, pumice, steam-blast eruptions, hydrothermal vents, plumes of fine materials and dissolved gas, explosions and discolouration of seawater to light blue and reddish brown. Subaerial volcanos are well characterised; however, there is a lack of study of those in submarine settling [19, 20]. Direct observations of submarine eruptions have been scarce, as they normally occur in remote locations. The first registered underwater eruption was that of the NW Rota in the Southwest Pacific Ocean [21] in 2006. More recently, the dynamic of the Monowai underwater volcano has been described [22]. In all the cases, the carbonate system is modified and the pH reduced as a consequence of the emission of magmatic gas and other compounds [23].

Santiana-Casiano et al. [24] studied the eruption of the island of El Hierro (Canary Islands, Spain) in 2011. This was the first submarine eruption to be monitored from the initial unrest. The eruption started in October 11, 2011, first evidence of eruption was observed in the form of a discolouration of the surface water in the area, going from light green to pale blue to a

brown colour [24]. Those changes may be related to the discharge of high-temperature hydrothermal fluids as well as gases and volcanic particles [25]. Bubbling took place, and the presence of rock fragments was observed floating on the surface of the ocean during the initial steps of the eruption. During the strongest episodes of the eruption, an elevated quantity of dissolved inorganic carbon and a large decrease in the pH value of the surrounding water were observed. The lowest values of pH were concentrated in a layer of 75–100 m of depth; however, due to the intensity of the ejected gases, low values of pH reached the surface water. They also observed at some point during the eruption that the water chemistry of the entire southeast of the island was affected by the presence of the volcano. In April 2012, when the eruption stopped, the system evolved to a hydrothermal system and the pH of the area got to normal values and only some peaks of pH were observed around the area of the volcano [24]. Regarding the dissolved CO_2, the concentration in the southeast of the island reached levels of 11,000–19,000 πatm, which was an important change in the chemistry of the water. The same rise was observed for sulphur species and oxidants. Therefore, in the event of the eruption of a submarine volcano and the subsequent hydrothermal activity, a change in the chemistry and properties of the seawater in the area should be expected (presence of CO_2, H_2S, SO_2, Fe^{2+} and drop in the local pH). Not only submarine eruptions can change the local chemical-physical properties of the water but also passive emissions of gasses and acidic compounds to the environment in islands with volcanic activity can modify the water chemistry. Oceans are a significant store of CO_2. They exchange it with the atmosphere and provide a reservoir for CO_2. Therefore, the emissions of CO_2 and other gasses to the environment due to the volcanic activity can decrease the local pH in harbours of volcanic islands.

Those changes can strongly affect the corrosion activity of seawater, raising the probability of corrosion of the metallic materials of the shore and offshore facilities. This corrosion could be generalised, in the case of non-passive materials or localised (pit formation) in the case of passive materials (stainless steels). Corrosion can cause great damage to marine steel infrastructures such as bridges, wharfs, platforms, ships and pipeline systems [26]. These corrosion problems will be aggravated due to the alteration on the chemistry of the water as a consequence of the volcano emissions [27]. Therefore, an adequate selection of the materials and a proper hazard assessment of the volcano effects are very important to predict how some of the critical infrastructures will be affected. Austenitic stainless steel grades 1.4401 (AISI 316) and its derivatives are suitable for shore and offshore service, splash zone applications and temporary immersion in seawater. Duplex stainless steels (e.g. 1.4462/ASTM S31803) may be used in estuaries where the chloride content of the water is lower than that of the open sea. Additionally, superduplex stainless steels (e.g. 1.4410/ASTM S32750) may also be used in direct and continuous contact with seawater (e.g. in offshore oil platforms or desalination plants).

There are some studies dealing with the passivation/corrosion processes of stainless steels in natural seawater [28, 29]. Corrosion studies can be performed in different ways; there are direct measurements (weight loss) and indirect measurements (electrochemical techniques). Electrochemical techniques are useful to evaluate the corrosion behaviour of different metals and alloys in a short period of time providing useful information about the corrosion mechanisms taking place.

http://dx.doi.org/10.5772/63523

According to this, the objective of this chapter will be to evaluate the influence of an underwater volcano eruption on the corrosion behaviour of different materials that might be used in seawater environments. In this way, the electrochemical behaviour of different stainless steels, that is AISI 316 SS and duplex SS, when immersed in solutions which have been polluted by volcano-seawater (collected from the volcano that erupted in the Atlantic Ocean near the island of El Hierro) have been studied. To achieve this objective, different electrochemical techniques have been used, notably open-circuit potential (OCP) measurements, polarization tests and electrochemical impedance spectroscopy (EIS). All these techniques would make possible to achieve a comprehensive view of the corrosion behaviour of stainless steels in volcano seawater. These results may provide and insight in the corrosion effects of volcanic eruptions that could be used in the preparation of natural hazard risk assessments related with volcanoes. This approach has been presented for submarine volcanoes, but the same methodology could be applied to the assessment of corrosion risks due to subaerial volcanoes. In this book chapter, a whole section describing in detail the electrochemical techniques used in the characterisation of the studied stainless steels, has been included, so the readership could better understand the obtained results. These results are used to demonstrate, using electrochemical techniques, that volcano eruptions can negatively affect the lifetime of very important metallic infrastructures, such as harbours, and to establish a link between electrochemistry of materials and volcanology.

2. Electrochemical techniques

Since corrosion occurs via electrochemical reactions, electrochemical techniques are useful for the study of the corrosion processes. In these electrochemical techniques, a metal sample is used to model the metal in a corroding environment. The metal sample is immersed in a solution similar to the corroding environment of the metal that is being studied. Additional electrodes are introduced to the system to make an electrochemical cell, which allows measuring the different parameters to study the system. In order to evaluate the effect of volcano-polluted seawater on the corrosion behaviour of different alloys, several electrochemical techniques have been used and they are explained in this section. These techniques are open-circuit potential (OCP), polarization tests and electrochemical impedance spectroscopy (EIS).

2.1. Open-Circuit Potential (OCP)

The open-circuit potential (OCP) or corrosion potential is a parameter that indicates the thermodynamically tendency of a material to the electrochemical oxidation in a corrosive medium. According to the ASTM G-15 Standard [5], the OCP is the measured potential between the working electrode and the reference electrode at which there is no current in the circuit. In order to measure the OCP value of a metal, the studied material must be immersed in the solution and after a certain period it stabilizes around a stationary value. When the metal is immersed in the solution, the corrosion starts to occur and electrochemical reactions characteristic of the metal-solution interface take place at the surface of the metal (oxidation

formation of a passive layer or immunity), which can produce variations of the OCP value during the stabilization [5, 30, 31].

2.2. Polarization tests

Polarization tests of a metal-electrolyte solution are used in order to characterize the metal by its current-potential relationship. Experimentally, the polarization tests involve changing the potential of the working electrode and register the current as a function of the potential obtaining potentiodynamic curves. Since the current density (the current divided into the area) can experiment high variations, the potentiodynamic curves represent the logarithm of the current density vs the potential [32]. The potential starts at a value lower than the corrosion potential (cathodic region) and increases in the anodic direction. In order to study the repassivation behaviour of a material, the direction of the cyclic potentiodynamic curve can be changed backward to cathodic potentials after achieving a certain current value (once the pitting potential was reached). **Figure 1** shows as an example, a cyclic potentiodynamic curve, with the corresponding corrosion parameters that can be obtained from the curve.

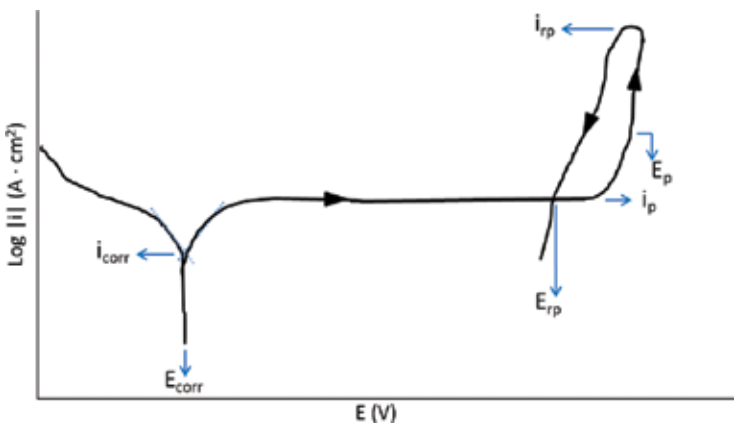

Figure 1. Cyclic potentiodynamic curve with the corrosion parameters. i_{corr}: corrosion current density, E_{corr}: corrosion potential, i_p: current density of passivation, E_p: pitting potential, i_{rp}: repassivation current density, E_{rp}: repassivation potential.

When the metal is immersed in the corrosive medium, reduction and oxidation processes occur in its surface. Generally, the metal oxidizes (corrodes) and the medium is reduced both anodic and cathodic currents occur in its surface. If the anodic and cathodic currents are equals in magnitude (i.e. the rate of oxidation and reduction are the same), there is no net current to be measured. The potential at which the current is non-measurable is called corrosion potential (E_{corr}).

At potentials more negative than the corrosion potential ($E < E_{corr}$), the cathodic current predominates whereas the anodic current is insignificant, so the curve is in the cathodic region. In contrast, if the potential is more positive than the corrosion potential ($E > E_{corr}$), the predominant current is the anodic one and the curve is in the anodic region [32, 33].

http://dx.doi.org/10.5772/63523

In order to calculate the current density (i), the Butler-Volmer equation [Eq. (1)] can be useful as it considers the corrosion of a system with cathodic and anodic reaction.

$$i = i_{corr} \cdot [\exp(\frac{2.303 \cdot (E - E_{corr})}{b_a})] - \exp(-\frac{2.303 \cdot (E - E_{corr})}{b_c}) \quad (1)$$

In Eq. (1), i is the external current density, i_{corr} is the corrosion current density, E is the applied potential to polarize the system, E_{corr} is the corrosion potential, b_a is the anodic Tafel slope and b_c is the cathodic Tafel slope. If the applied potential is equal to the corrosion potential then, $i = i_{corr}$, but if E is different from E_{corr}, Eq. (1) gives the Tafel law [Eq. (2)]:

$$E = a \pm b \cdot \log |i| \quad (2)$$

where a is a constant and b is b_a or b_c according to the region of the curve (anodic or cathodic, respectively) [32–34].

In the potentiodynamic curves, for applied potentials more positive than the ones of the cathodic region, in the materials that can be passivated, there is a region where the current density becomes constant (passivation current density, i_p). This region is called passivation region, and it is characterized because a passive layer (metal oxide) is formed on the surface of the metal and its chemical reactivity is reduced.

As the applied potential continues increasing, the current density could experiment an abrupt increase and the passive layer could locally breaks by pitting corrosion if the medium contains aggressive ions. The potential at which the pitting corrosion starts is called pitting potential (E_p, when the current density reaches 100 μA/cm^2). Finally, if the potential scan is reversed, the current density decreases and eventually the backward curve intersects the forward one: this final region is called repassivation region because the metal recovers the passive state (the potential and current density of the repassivation regions are E_{rp} and i_{rp}, respectively).

2.3. Electrochemical impedance spectroscopy

Electrochemical impedance spectroscopy is a non-destructive technique that is used to study the metal/electrolyte interface. It consists of applying an electrical disturbance (potential) to an electrical circuit in a range of frequencies and measure the current response of the system to each frequency. The applied disturbance of potential can be expressed as a sinusoidal signal as Eq. (3) shows.

$$E = E_0 \cdot \sin(\omega \cdot t) \quad (3)$$

where ω is the angular frequency (2π times the conventional frequency in Hz). On the other hand, the current response can also be expressed as a sinusoidal signal that is desphased certain angle (ϕ), as Eq. (4) shows.

$$I = I_0 \cdot \sin(\omega \cdot t + \phi) \tag{4}$$

The impedance is the quotient of the applied potential and the measured current and it follows the Ohm law; therefore, it can be expressed as Eq. (5) shows.

$$Z = \frac{E}{I} = \frac{E_0 \cdot \sin(\omega \cdot t)}{I_0 \cdot \sin(\omega \cdot t + \phi)} = Z_0 \cdot \frac{\sin(\omega \cdot t)}{\sin(\omega \cdot t + \phi)} \tag{5}$$

where Z is the complex impedance (which in some electrochemical systems depends on applied potential frequency). The complex impedance can be expressed in terms of a real (Z') and an imaginary component (jZ'') as Eq. (6) shows.

$$Z(\omega) = Z_{\mathrm{Re}} - jZ_{Im} \equiv Z' - jZ'' \tag{6}$$

Plotting the results of the impedances in a correct frequency range, it is possible to extract conclusions about the physical and chemical properties of the materials and the electrochemical systems. Two diagrams are typically extracted from the EIS measurements: Nyquist and Bode diagrams. In the Nyquist diagrams, the real and imaginary components of the impedance at different frequencies are represented. The Bode diagrams represent the log $|Z|$ vs log f (Bode-modulus), and ϕ vs log f (Bode-phase). **Figure 2** shows an example of a Nyquist diagram with the equivalent circuit and an example of a Bode diagram [35, 36].

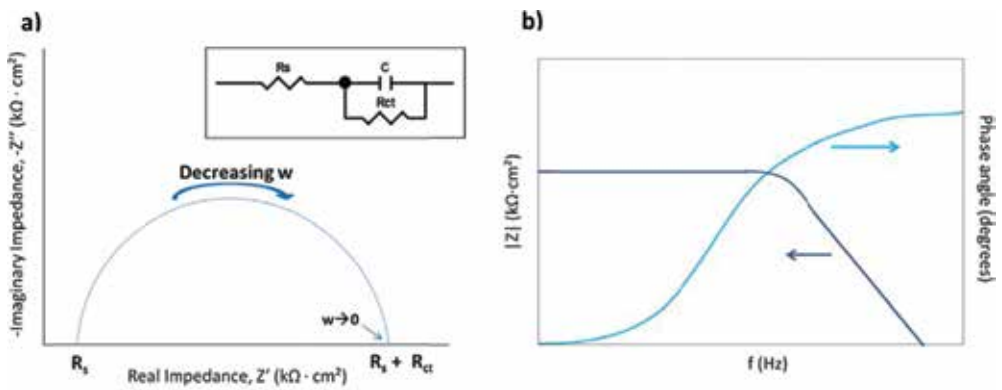

Figure 2. Nyquist diagram with the equivalent circuit (**a**) and Bode-modulus and Bode-phase plots (**b**). R_S is the solution resistance and R_{ct} the charge transfer resistance.

In order to solve the mathematical difficulties in the data treatment of the EIS, the results can be adjusted to an equivalent electrical circuit (**Figure 2**). These circuits try to represent the electrical characteristics of the model and are composed by basic elements such as resistances, capacitances and inductances.

http://dx.doi.org/10.5772/63523

3. Experimental procedure

In order to evaluate the influence of an underwater volcano eruption on the corrosion behaviour of different materials, a practical example is detailed in this chapter. In this way, the electrochemical behaviour of different stainless steels, that is AISI 316 stainless steel (SS) and duplex SS, immersed in volcano-seawater (collected from a volcano that erupted in the Atlantic Ocean near the island of El Hierro, Canary Islands, Spain) have been studied. To achieve this objective, different electrochemical techniques have been used. That is OCP measurements, polarization tests and electrochemical impedance spectroscopy (EIS). All these techniques would make possible to achieve a comprehensive view of the corrosion behaviour of stainless steels in volcano seawater.

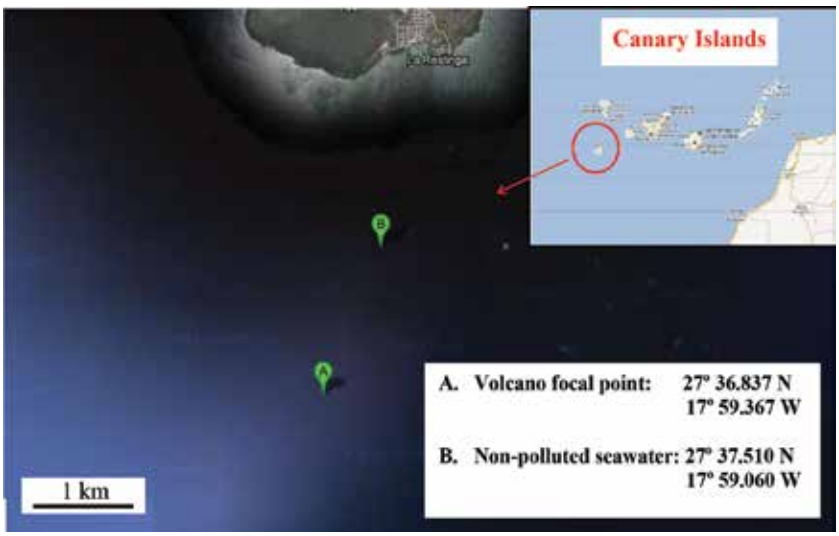

Figure 3. Map showing the zones near the island of El Hierro where the non-polluted and polluted seawater samples were taken.

3.1. Materials, solution and electrochemical cell

Experiments were performed in non-polluted (NPS) and polluted seawater (PS). **Figure 3** shows the coordinates where the seawater samples were taken on December 19, 2011. The polluted water was obtained on the focus of the volcano. The non-polluted samples were taken at enough distance to avoid the influence of the pollutants spread by the volcano, following the suggestions of the Spanish National Geographic Institute. Additionally, **Table 1** presents the main parameters of the non-polluted and polluted by the "El Hierro" volcano eruption seawaters. Prior to each experiment the pH and conductivity of the non-polluted and polluted seawater was measured. As shown in **Table 1**, the most substantial difference between both seawaters is pH.

Value	Unpolluted seawater	Polluted seawater
pH	8.02	6.23
Conductivity (μS cm^{-1})	65,850	66,400
Sodium (mg l^{-1})	11,080	11,868
Potassium (mg l^{-1})	438	447
Calcium (mg l^{-1})	558	400
Magnesium (mg l^{-1})	1486	1320
Sulphates (mg l^{-1})	2400	2600
Chlorides (mg l^{-1})	20,926	21,200
Bicarbonates (mg l^{-1})	159	220
Carbonates (mg l^{-1})	5.53	0.00

Table 1. Composition of both non-polluted and polluted seawater samples, given by the Spanish Institute of Geodesy.

The composition in weight percent of the AISI 316 SS and duplex SS (Alloy 900) used in this work is presented in **Table 2**. The shape of the electrodes was cylindrical, and they have a diameter of 8 mm and a length of 5 mm. They were coated in polytetrafluoroethylene, having an exposed area to the solution of 0.5 cm^2. The samples were wet abraded with different silicon carbide papers (from 500 to 4000), and they were finally cleaned with ethanol, distilled water and dried in air.

	Cr	Ni	Mn	Mo	S	Si	P	C	Fe	Cu	N	Ti
AISI 316	16.96	10.17	1.34	2.30	0.00	0.37	0.03	0.08	Bal.	–	–	–
Alloy 900	22.34	4.85	1.59	2.69	–	0.35	0.02	0.03	67.80	0.13	0.20	0.01

Table 2. Chemical composition in weight % of AISI 316 and Alloy 900 stainless steels.

An electrochemical vertical cell made of glass was used to carry out the tests. A configuration of three electrodes was used to perform the electrochemical measurements, that is the stainless steel was the working electrode, a platinum wire was the counter electrode and a silver/silver chloride (Ag/AgCl 3M KCl) was used as reference electrode. All these electrodes were connected to a pontentiostat (Autolab PGSTAT302N). The electrochemical tests were repeated at least three times to verify reproducibility of the data obtained in the non-polluted and polluted seawater. The tests were carried out at 25°C.

3.2. OCP measurement and polarization tests

Before each polarization measurement, the open-circuit potential (OCP) was measured for 1 h in the test solution. The average value of the potentials recorded during the last 300 s was the value of the OCP. Afterwards, the potential was shifted to −0.25 $V_{Ag/AgCl}$ with respect to the OCP, in order to start the polarization measurements. Then, the potential was scanned in the

anodic direction until a value of current density of 10 mA/cm^2 was obtained. In this moment, the potential scan was reversed. The scan rate used to perform the polarization measurements was 0.5 mV s^{-1}.

3.3. EIS and capacitance measurements

EIS measurements were performed after forming a stable passive film on the surface of the samples at a constant applied potential (−0.1 $V_{Ag/AgCl}$) for 1 h. EIS measurements were conducted at that formation potential in the frequency range of 100 kHz–10 mHz, with a signal amplitude of 10 mV.

4. Results and discussion

4.1. OCP

The OCP value was calculated as the mean value of the last 5 min of the complete OCP register, which lasted 1 h. The OCP values obtained for the SSs in the different media (polluted and non-polluted seawater) are shown in **Table 3**. In relation to **Table 3**, it can be pointed out that there is no significant influence of the composition of the seawater on the OCP values. On the other hand, the OCP values obtained for Alloy 900 in the non-polluted and polluted seawaters are slightly more negative than those determined for the AISI 316 SS.

Seawater	AISI 316	Alloy 900
Non-polluted	−90 ± 7	−161 ± 2
Polluted	−116 ± 4	−155 ± 8

Table 3. Open-circuit potential values for AISI 316 SS and Alloy 900 in both non-polluted and polluted seawater.

4.2. Polarization tests

One of the reproducible cyclic polarization curves obtained for the SS in non-polluted and polluted seawater are presented in **Figure 4**. From the polarization curves shown in **Figure 4**, several corrosion and repassivation parameters can be calculated. These parameters, all presented in **Table 4**, are the corrosion potential (E_{corr}), the corrosion current density (i_{corr}), the passivation current density (i_p), pitting potential (E_p) and the repassivation potential (E_{rp}). The magnitude order of the corrosion potential is the same regardless of the studied media; however, there is an important influence of the seawater on the passivation current densities, which were obtained when the current was stable within the passivation range. Corrosion resistance of these stainless steels is directly associated with a passive film mainly formed by chromium III oxide [37]. It is important to point out that **Table 4** only shows the i_p values as a measure of the corrosion rates of passive alloys (this parameter has been selected to quantify the corrosion rate instead of i_{corr} since the SSs used in this work are passivable in the studied media). In relation to the passivation current densities, they importantly increase in polluted

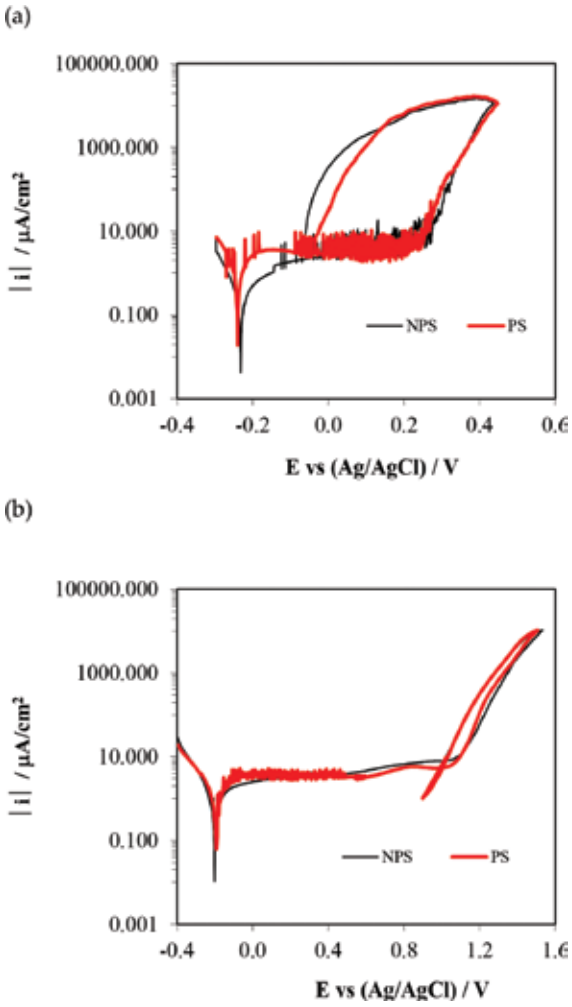

Figure 4. Potentiodynamic polarization cyclic curves for AISI 316 SS (**a**) and Alloy 900 (**b**) in both non-polluted (NPS) and polluted seawater (PS) solutions at 25°C.

seawater. This fact could be associated to the lower pH which presented this kind of medium. Besides, Alloy 900 SS has higher i_p values in comparison with the ones obtained for the AISI 316 SS. However, several oscillations in the current density register of the AISI 316 SS in both seawaters and in the register of the Alloy 900 in polluted seawater can be clearly observed in **Figure 4**. These current oscillations indicate that polluted seawater increase the susceptibility of the stainless steels to metastable pitting [38]. In order to evaluate the susceptibility to pitting corrosion of the SS the pitting potential value was evaluated. This parameter is the potential at which the current density reaches 100 µA cm^{-2} and refers to the susceptibility to local breakdown and stable pit initiation [39]. The stainless steels are susceptible to pitting corrosion in both media since chlorides (present in the seawater) are very aggressive ions which are

responsible for the breakdown of the passive films formed on these SSs [39, 40]. **Table 4** shows that the E_p values for the Alloy 900 are more positive in comparison to AISI 316. This is due to the fact that Duplex SSs, such as Alloy 900, possess a very high resistance to localized corrosion due to their high nitrogen, chromium and molybdenum contents (see **Table 2**). On the other hand, **Table 4** also shows that the values of the pitting potential are similar despite the studied media, but they are to some extent more positive in the non-polluted seawater.

	E_{corr} vs (Ag/AgCl)/mV	i_p/μA cm^{-2}	E_p vs (Ag/AgCl)/mV	E_{rp} vs (Ag/AgCl)/mV
Seawater	AISI 316			
Non-polluted	−230 ± 8	3.89 ± 0.32	309 ± 10	−69 ± 11
Polluted	−239 ± 5	4.66 ± 0.11	302 ± 7	−55 ± 15
	Alloy 900			
Non-polluted	−203 ± 11	4.35 ± 0.44	1220 ± 47	990 ± 22
Polluted	−197 ± 6	5.02 ± 0.09	1200 ± 29	990 ± 30

Table 4. Electrochemical parameters for AISI 316 SS and Alloy 900 in both non-polluted and polluted seawater, obtained from cyclic polarization curves.

The repassivation potentials were obtained at the crossing point between the backward and forward scans of the polarization curves. This parameter refers to the limit below which the material remains passive and active pits can repassivate. According to this, an E_{rp} value which is more negative than the corresponding E_{corr} indicates that the SS is not able to repassivate the pits. Contrary to this, an E_{rp} value which is more positive than the corrosion potential indicates that the SSs can regenerate an eventual breakdown of the passive film. **Table 4** shows that the repassivation potentials for the studied SS are, in all the studied media, more positive than the corresponding corrosion potential; therefore, the SSs can repassivate the pits.

4.3. EIS measurements at an applied anodic potential

In order to characterise the electrochemical behaviour of the passive film/electrolyte interface for the two stainless steels under study, EIS measurements were performed at an applied potential of −0.1 $V_{Ag/AgCl}$ in both non-polluted and polluted seawater, after a passive film was formed on the electrodes' surface at the same potential. **Figure 5** shows the EIS spectra of AISI 316 and Alloy 900 in the form of Nyquist and Bode plots. In all cases, EIS diagrams exhibit a typical passive state shape characterized by a semicircular shape and high impedance values in Nyquist plots, and by phase angle values close to 90° in Bode-phase plots, suggesting that a stable passive film is formed on all the electrodes [41, 42]. In general, higher impedance values are observed for passive films formed in non-polluted seawater (NPS). The highest impedances are obtained for the duplex stainless steel.

The equivalent electric circuit used to interpret EIS spectra of anodically formed passive films is shown in **Figure 6**. In this equivalent circuit, R_S represents the electrolyte resistance, CPE_1 is

related to the capacitance of the passive film/electrolyte interface, R_1 corresponds to the charge transfer resistance at that interface and Z_{WS} is a Warburg impedance, which has been used to interpret the transport of vacancies within the passive film, in the frame of the Point Defect Model [42–44]. The Warburg impedance used here models dimensional diffusion through a layer of finite thickness with absorbing boundary condition [45, 46]:

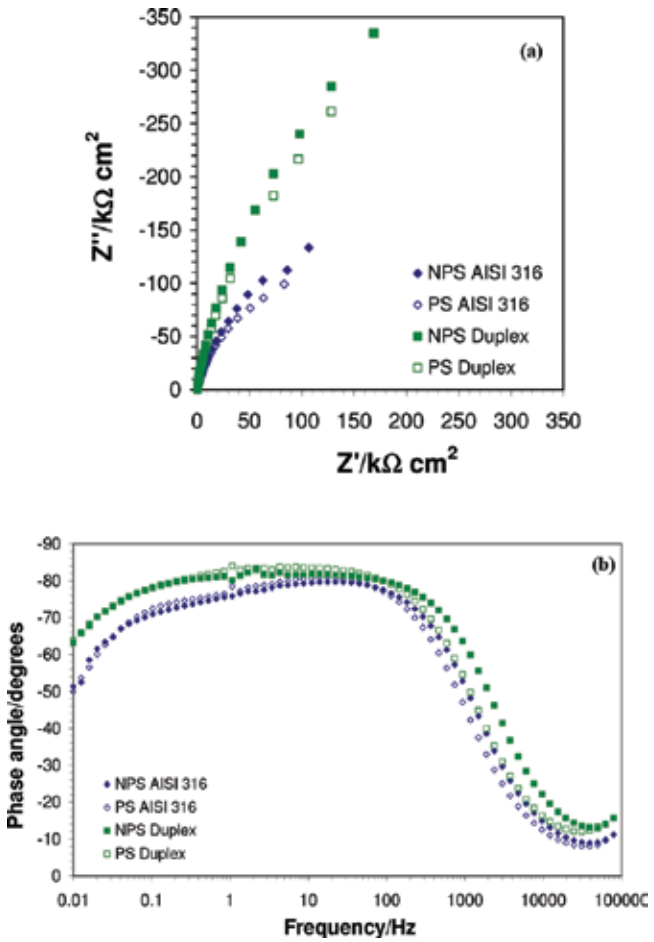

Figure 5. Nyquist (**a**) and Bode-phase (**b**) plots for AISI 316 and Alloy 900 in both non-polluted (NPS) and polluted seawater (PS) at 25°C, at a film formation potential of −0.1 $V_{Ag/AgCl}$.

$$Z_{WS} = \frac{R_W \tanh(B\sqrt{j\omega})}{B\sqrt{j\omega}} \tag{7}$$

where $B = \delta/(D)^{1/2}$, δ is the diffusion layer thickness, D is the diffusion coefficient of the diffusing species, R_W is the Warburg resistance, ω is the angular frequency, and j is the imaginary unit.

http://dx.doi.org/10.5772/63523

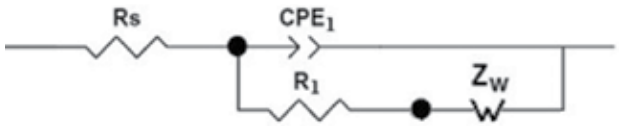

Figure 6. Equivalent circuit used to interpret the EIS data.

A constant-phase element (CPE) representing a shift from the ideal capacitor has been used instead of the capacitance itself. The impedance of a constant-phase element is defined as:

$$Q = Z_{CPE} = [C(j\omega)^n]^{-1} \tag{8}$$

where n, defined as a CPE power, is an adjustable parameter that lies between −1 and 1. For $n = 1$ the CPE describes an ideal capacitor, and for $0.5 < n < 1$ the CPE describes a frequency dispersion of time constants due to local heterogeneities in the dielectric material.

The CPE used in the equivalent electric circuit of **Figure 6** has been converted into a pure capacitance (C) through the following equation [47, 48]:

$$C = Q^{1/n}(R_S^{-1} + R_1^{-1})^{(n-1)/n} \tag{9}$$

where $Q = Z_{CPE}$ [Eq. (9)].

The parameters of the equivalent circuit obtained from the fitting procedure are shown in **Table 5**. The values of χ^2 are of the order of 10^{-3}, indicating that the fittings are good from a mathematical point of view.

		R_S/Ω cm²	R_1/k Ω cm²	C_1/μF cm⁻²	n_1	R_W/k Ω cm²	χ^2 (×10⁻³)
AISI 316	Non-polluted seawater	5.4 ± 0.1	26 ± 4	16.2 ± 1.1	0.90 ± 0.01	295 ± 14	3.8
	Polluted seawater	4.8 ± 0.2	26 ± 3	24.8 ± 1.7	0.90 ± 0.01	207 ± 18	3.7
Alloy 900	Non-polluted seawater	4.7 ± 0.3	535 ± 30	12.4 ± 1.3	0.91 ± 0.01	753 ± 53	3.0
	Polluted seawater	4.9 ± 0.3	320 ± 11	18.3 ± 1.2	0.92 ± 0.01	544 ± 18	2.7

Table 5. Equivalent circuit parameters obtained by fitting the experimental results of EIS, for AISI 316 and Alloy 900 in both non-polluted and polluted seawater, at −0.1 $V_{Ag/AgCl}$.

It can be observed from **Table 5** that the charge transfer resistance at the interface, R_1, is equal or lower, in general, for passive films formed in the polluted seawater. The Warburg resistance, R_W, follows the same tendency, decreasing in the polluted electrolyte. These results indicate an enhancement of charge transfer processes at the passive film/electrolyte interface and of point defects transport through the passive film for the samples immersed in the polluted seawater, reflecting the poorer protective properties of passive films formed in this electrolyte.

On the other hand, the capacitance of the passive film/electrolyte interface, C_1, is higher in the polluted seawater. The interfacial capacitance has a strong influence on electrochemical processes in passive systems. This is due to the fact that its characteristics establish the potential drop at the semiconducting passive film/electrolyte interface [42, 49, 50]. Therefore, an increase in C_1 suggests, along with the decrease observed in R_1 and R_W, that passive films formed in polluted seawater are less protective. The values of the exponent n_1 (lower than unity in all the cases) support the introduction of CPEs in the equivalent circuit rather than pure capacitors.

Concerning the comparison between the protective properties of passive films formed on the two stainless steels under study, R_1 values are significantly lower in the case of AISI 316 (more than 10 times lower than in Alloy 900), and R_W is the lowest for this stainless steel, as well. Besides, C_1 values for AISI 316 are the highest, regardless of the type of seawater (**Table 5**). On the other hand, the highest resistances (R_1 and R_W) and the lowest interfacial capacitance values (C_1) are obtained for the duplex stainless steel (Alloy 900), denoting that passive films formed on Alloy 900 are the most resistant to corrosion in both seawater media.

5. Conclusion

The electrochemical techniques used in this work have been proved to be useful in order to study the corrosion behaviour of stainless steels in volcano polluted seawater. From polarization curves, it has been demonstrated that Alloy 900 is more resistant to pitting corrosion than AISI 316. Moreover, the decrease of the charge transfer resistance, R_1, and the Warburg resistance, R_W, along with the increase of the interfacial capacitance, C_1, indicate worse protective properties of passive films formed in the polluted seawater, especially for AISI 316 SS.

Comparing both stainless steels, it can be concluded that passive films formed on Alloy 900 present better protective properties than those of AISI 316 SS.

Acknowledgements

We wish to express our gratitude to the Ministerio de Ciencia e Innovación (Project CTQ2009-07518), to Prof. Dr. Aurora Santos López, Dr. Rosario Lunar Hernández and Dr. Jose Arnoso Sampedro (Instituto de Geociencias (CSIC, UCM)), Dr. Carmen López Moreno (Head of the Volcano Monitoring Unit, Spanish National Geographic Institute), Humberto Gutiérrez García (Head of the Civil Protection and Emergency Management Service of the General Directorate of Security and Emergencies of the Canary Islands) and Alejandro Ramos Fernández (Coordinador Multisectorial del Centro Coordinador de Emergencias 1-1-2 del Gobierno de Canarias) for their help in supplying both non-polluted and polluted seawater samples.

Author details

Rita Sánchez-Tovar[1], Ramón Fernández-Domene[1], Rafael Leiva-García[2], Clara Escrivà-Cerdán[1], Bianca Lucas-Granados[1] and José García-Antón[1*]

*Address all correspondence to: jgarciaa@iqn.upv.es

1 Chemical and Nuclear Engineering Department, Polytechnic University of Valencia, Electrochemical Engineering and Corrosion (IEC), Valencia, Spain

2 School of Materials, University of Manchester, Manchester, UK

References

[1] UNISDR 2009. *UNISDR Terminology on Disaster Risk reduction*, United Nations, Geneva, Switzerland (2009).

[2] M.R. Auker, R.S.J. Sparks, L. Siebert, H.C. Crossweller, J. Ewert. *A statistical analysis of the global volcanic fatalities record*. Journal of Applied Volcanology 2013, 2: 1–24. doi: 10.1186/s13617-014-0014-6

[3] R.S.J. Sparks, W.P. Aspinall, H.S. Crossweller, T.K. Hincks. *Risk and uncertainty assessment of volcanic hazards*. In: J. Rougier. R.S.J. Sparks, L. Hill (Eds). *Risk and uncertainty assessment of for natural hazards*. Cambridge University Press, Cambridge (2013), p. 588.

[4] S.M. Rinaldi, J.P. Peerenboom, T.K. Kelly. *Identifying understanding and analyzing critical infrastructure interdependencies*. IEEE Control Systems 2001, 21: 11–25. doi: 10.1109/37.969131

[5] ASTM G15-89A, Standard Terminology Relating to Corrosion and Corrosion testing. ASTM, Philadelphia (1990).

[6] T.P. Hoar. *Report of the Committee on Corrosion and Protection—A Survey of Corrosion Protection in the United Kingdom*. HMSO, London (1971).

[7] C.G. Okamoto *Report of the Committee on Corrosion and Protection—A Survey of the Cost of Corrosion to Japan*, Japan Society of Corrosion Engineering and Japan Association of Corrosion Control (1977).

[8] *Research Needs Report Energy Convention Research Task force on Energy Conversion Research*, Am. Society of Mechanical Engineering, New York (1976).

[9] M. Watanabe, A. Hokazono, T. Handa, T. Ichino, N. Kuwani. *Corrosion of copper and silver plates by volcanic gases*. Corrosion Science 2006, 48: 3759–3776. doi: 10.1016/j.corsci.2005.12.009

[10] G.A. Hawthorn, N. Mullet, R. Srinivasan, L.H. Hihara. *Corrosion testing and atmospheric monitoring in an active volcanic environment*. Proceedings of the 2007 Tri-service conference, US Department of Defence (2007).

[11] R.J. Blong. *Volcanic hazards: a sourcebook on the effects of eruptions*. Academic Press, North Ryde, NSW (1984). p. 424.

[12] S. Izumo, H. Sueyoshi, K. Kitamura, Y Ohzono. *Corrosion of metal in volcanic environments*. Corrosion Engineering 1990, 39: 271–281.

[13] R.J. Blong. *Building damage in Rabaul, Papua, New Guinea*. Bulletin of Volcanology 2003, 65: 43–54. doi: 10.1007/s00445-002-0238-x

[14] J. Becker, R. Smith, D. Johnston, A. Munro. *Effects of the 1995–1996 Ruapehu eruptions on communities in central North Island, New Zealand, and people's perceptions of volcanic hazards after the event*. Australian Journal of Disaster Trauma Studies 2001, 1: 23.

[15] C. Oze, J. Cole, A. Scott, T. Wilson, G. Wilson, S. Gaw, S. Hampton, C. Doyle, Z. Li. *Corrosion of metal roof materials related to volcanic ash interactions*. Natural Hazards 2014, 71: 785–802. doi: 10.1007/s11069-013-0943-0

[16] R.M. Fernández-Domene, R. Sánchez-Tovar, C. Escrivà-Cerdán, R. Leiva-García, J. García-Antón. *Study of passive films formed on AISI 316L stainless steel in non-polluted and underwater-volcano-polluted seawater*. Corrosion 2014, 70: 390–401. doi: 10.5006/0934

[17] R.M. Fernández-Domene, R. Sánchez-Tovar, C. Escrivá-Cerdán, R. Leiva-García, J. García-Antón. *Comparison of the effect of non-polluted and underwater-volcano-polluted seawater on the corrosion resistance of different stainless steels*. Materials and Corrosion. 2015, 66: 1279–1289. doi: 10.1002/maco.201408172

[18] V.M. Mantas, A.J.S.C. Pereira, P.V. Morais. *Plumes of discolored water of volcanic origin and possible implications for algal communities. The case of the Home Reef eruption of 2006 ga, Southwest Pacific Ocean)*. Remote Sensing of Environmental 2011, 115: 1341–1352.

[19] J.A. Resing, E.T. Baker, J.E. Lupton, K. Nakamura. *Chemistry of hydrothermal plumes above submarine volcanoes of the Mariana Arc*. Geochemistry Geophysics Geosystems 2009, 10: Q02009. doi: 0.1029/2008GC002141

[20] C.E.J. de Ronde, E.T. Baker, G.J. Massoth, J.E. Lupton, I.C. Wright, R.J. Sparks, S.C. Bannister, M.E. Reyners, S.L. Walker, R.R. Greene, J. Ishibashi, K. Faure, J.A. Resing, G.T. Lebon. *Submarine hydrothermal activity along the mid-Kermadec Arc, New Zealand: large-scale effects on venting*. Geochemistry Geophysics Geosystems 2007, 8: Q07007.

[21] R.W. Embley. *Extensive and diverse submarine volcanism and hydrothermal activity in the NE Lau Basin*. Eos, Transactions, AGU (Fall Meeting Supplement) 90, abstr. V51D–1719 (2009).

[22] A.B. Watts. *Rapid rates of growth and collapse of Monowai submarine volcano in the Kermadec Arc*. Nature Geoscience 2012, 5: 510–515. doi: 10.1038/ngeo1473

[23] H. Guillou, J.C. Carracedo, F. Pérez Torrado, E. Rodriguez Badiol. *K-Ar ages and magnetic stratigraphy of a hotspot-induced, fast grown oceanic island: El Hierro, Canary Islands*. Journal of Volcanology and Geothermal Research 1996, 73: 141–155. doi: 10.1016/0377-0273(96)00021-2

[24] J.M. Santana-Casiano, M. Gonzalez-Davila, E. Fraile-Nuez, D. de Armas, A.G. Gonzalez, J.F. Domınguez-Yanes, J. Escanez. *The natural ocean acidification and fertilization event caused by the submarine eruption of El Hierro*. Scientific Reports Nature 2013, 3: Article number: 1140. doi: 10.1038/srep01140

[25] K. Nogami, M. Yoshida, J. Osaka. *Chemical composition of discolored seawater around Satsuma-Iwojima, Kagoshima, Japan.* Bulletin Volcanology Society of Japan 1993, 38: 71–77.

[26] J. Duan, S. Wu, X. Zhang, G. Huang, M. Du, B. Hou. *Corrosion of carbon steel influenced by anaerobic biofilm in natural seawater*. Electrochimica Acta 2008, 54: 22–28. doi: 10.1016/j.electacta.2008.04.085

[27] L. Freire, M.J. Carmezim, M.G.S. Ferreira, M.F. Montemor. *The passive behaviour of AISI 316 in alkaline media and the effect of pH: a combined electrochemical and analytical study*. Electrochimica Acta 2010, 55: 6174–6181. doi: 10.1016/j.electacta.2009.10.026.

[28] A. Al Odwani, M. Al-Tabtabaei, A. Abdel-Nabi. *Performance of high chromium stainless steels and titanium alloys in Arabian Gulf seawater.* Desalination 1998, 120: 73–81. doi: 10.1016/S0011-9164(98)00203-3

[29] S.A. Al-Fozan, A.U. Malik. *Effect of seawater level on corrosion behavior of different alloys.* Desalination 2008, 228: 61–67. doi: 10.1016/j.desal.2007.08.007

[30] C.J. Brabec, A. Cravino, D. Meissner, N. Serdar Sariciftci, T. Fromherz, M.T. Rispens, L. Sanchez, J.C. Hummelen. *Origin of the open circuit voltage of plastic solar cells.* Advanced Functional Materials 2001, 11: 374–380. doi: 10.1002/1616-3028(200110)11

[31] G. Berthomé, B. Malki, B. Baroux. *Pitting transients analysis of stainless steels at the open circuit potential.* Corrosion Science 2006, 48: 2432–2441. doi: 10.1016/j.corsci.2005.09.012.

[32] X.L. Zhang, Zh.H. Jiang, Zh. P. Yao, Y. Song, Zh. D. Wu. *Effects of scan rate on the potentiodynamic polarization curve obtained to determine the Tafel slopes and corrosion current density.* Corrosion Science 2009, 51: 581–587. doi: 10.1016/j.corsci.2008.12.005.

[33] E. McCafferty. *Validation of corrosion rates measured by the Tafel extrapolation method.* Corrosion Science 2005, 47: 3202–3215. doi: 10.1016/j.corsci.2005.05.046.

[34] O.A. Petrii, R.R. Nazmutdinov, M.D. Bronshtein, G.A. Tsirlina. *Life of the Tafel equation: current understanding and prospects for the second century*. Electrochimica Acta 2007, 52: 3493–3504. doi: 10.1016/j.electacta.2006.10.014.

[35] D.V. Ribeiro, J.C.C. Abrantes. *Application of electrochemical impedance spectrosopy (EIS) to monitor the corrosion of reinforced concrete: a new approach.* Construction and Building Materials 2016, 111: 98–104. doi:10.1016/j.conbuildmat.2016.02.047.

[36] R.L.C. Naumann. Functional Polymer Films: 2 Volume Set. Chapter 25. *Electrochemical Impedance Spectroscopy (EIS).* Wiley Online Library, Germany. doi: 10.1002/9783527638482.ch25.

[37] N.E. Hakiki, S. Boudin, B. Rondot, M. Da Cunha Belo. *The electronic structure of passive films formed on stainless steels*. Corrosion Science 1995, 37:1809–1822. doi: 10.1016/0010-938X(95)00084-W

[38] R.C. Newman. *Understanding the corrosion of stainless steel*. Corrosion 2001, 57: 1030–1041. doi: doi: 10.5006/1.3281676

[39] M. Kaneko, H.S. Isaacs. *Pitting of stainless steel in bromide, chloride and bromide/chloride solutions*. Corrosion Science 2000, 42: 67–78. doi: 10.1016/S0010-938X(99)00056-6

[40] M. Kaneko, H.S. Isaacs. *Effects of molybdenum on the pitting of ferritic- and austenitic-stainless steels in bromide and chloride solutions*. Corrosion Science 2002, 44: 1825–1834. doi: 10.1016/S0010-938X(02)00003-3.

[41] J. Pan, D. Thierry, C. Leygraf. *Electrochemical impedance spectroscopy study of the passive oxide film on titanium for implant application*. Electrochimica Acta. 1996, 41: 1143–1153. doi: 10.1016/0013-4686(95)00465-3.

[42] R.M. Fernández-Domene, E. Blasco-Tamarit, D.M. García-García, J. García-Antón. *Passive and transpassive behaviour of alloy 31 in a heavy brine libr solution.* Electrochimica Acta 2013, 95: 1–11. doi: 10.1016/j.electacta.2013.02.024.

[43] D.D. Macdonald, R.Y. Liang, B.G. Pound. *An electrochemical impedance study of the passive film on single crystal Ni(111) in phosphate solutions*. Journal of Electrochemical Society 1987, 134: 2981–2986. doi: 10.1149/1.2100326

[44] M. Sánchez, J. Gregori, M.C. Alonso, J.J. García-Jareño, F. Vicente, *Anodic growth of passive layers on steel rebars in an alkaline medium simulating the concrete pores*. Electrochimica Acta 2006, 52: 47–53. doi: 10.1016/j.electacta.2006.03.071.

[45] J. Bisquert, G. Garcia-Belmonte, F. Fabregat-Santiago, P.R. Bueno. *Theoretical models for ac impedance of finite diffusion layers exhibiting low frequency dispersion*. Journal of Electroanalytical Chemistry 1999, 475: 152–163. doi: 10.1016/S0022-0728(99)00346-0

[46] Z. Grubac, Z. Petrovic, J. Katic, M. Metikos-Hukovic, R. Babic. *The electrochemical behaviour of nanocrystalline nickel: a comparison with polycrystalline nickel under the same experimental condition*. Journal of Electroanalytical Chemistry 2010, 645: 87–93. doi: 10.1016/j.jelechem.2010.04.018.

[47] G.J. Brug, A.L.G. van den Eeden, M. Sluyters-Rehbach, J.H. Sluyters. *The analysis of electrode impedances complicated by the presence of a constant phase element*. Journal of Electroanalytical Chemistry 1984, 176: 275–295. doi: 10.1016/S0022-0728(84)80324-1.

[48] B. Hirschorn, M.E. Orazem, B. Tribollet, V. Vivier, I. Frateur, M. Musiani. *Determination of effective capacitance and film thickness from constant-phase-element parameters*. Electrochimica Acta 2010, 55: 6218–6227. doi: 10.1016/j.electacta.2009.10.065.

[49] J.O. Bockris, K. Uosaki, H. Kita. *Interfacial electron transfer as a significant step in photoelectrochemical reactions on some semiconductors*. Journal of Applied Physics 1981, 52: 808–810. doi: 10.1063/1.328847

[50] K. Uosaki, H. Kita. *Effects of the Helmholtz Layer capacitance on the potential distribution at semiconductor/electrolyte interface and the linearity of the Mott-Schottky plot*. Journal of Electrochemical Society 1983, 130: 895–897. doi:10.1149/1.211985

Chapter 11

Fumarolic Minerals: An Overview of Active European Volcanoes

Tonči Balić-Žunić, Anna Garavelli,
Sveinn Peter Jakobsson, Kristjan Jonasson,
Athanasios Katerinopoulos,
Konstantinos Kyriakopoulos and
Pasquale Acquafredda

Additional information is available at the end of the chapter

http://dx.doi.org/10.5772/64129

Abstract

The fumarolic mineralogy of the Icelandic active volcanoes, the Tyrrhenian volcanic belt (Italy) and the Aegean active arc (Greece) is investigated, and literature data surveyed in order to define the characteristics of the European fumarolic systems. They show broad diversity of mineral associations, with Vesuvius and Vulcano being also among the world localities richest in mineral species. Volcanic systems, which show recession over a longer period, show fumarolic development from the high-temperature alkaline halide/sulphate, calcic sulphate or sulphidic parageneses, synchronous with or immediately following the eruptions, through medium-temperature ammonium minerals, metal chlorides, or fluoride associations to the late low-temperature paragenesis dominated by sulphur, gypsum, alunogen, and other hydrous sulphates. The situation can be different in the systems that are not recessing but show fluctuations in activity, illustrated by the example of Vulcano where the high-temperature association appears intermittently. A full survey of the mineral groups and species is given in respect to their importance and appearance in fumarolic associations.

Keywords: fumarolic minerals, Iceland fumaroles, Tyrrhenian volcanic belt fumaroles, Aegean active arc fumaroles, mineral sublimates

1. Introduction

At present, there are three active volcanic provinces in Europe (**Figure 1**). The first one is situated in NW corner, on the spreading Mid-Atlantic Ridge, nurtured by the Iceland hot spot and causing intermittent activation of numerous volcanoes. The second is the Tyrrhenian volcanic belt with a very active volcanism. It comprises the Roman comagmatic province, which is related to the extension of the Tyrrhenian basin and the rollback of the Apennine chain, and the Aeolian Arc, the genesis of which is generally ascribed to the subduction of the Ionian microplate under Calabria. The third one is the Aegean Active Volcanic Arc, related to the eastern Mediterranean lithosphere subduction under the Aegean-Anatolian microplate. It is characterized by a dormant or recessing volcanism. Is this remarkable variety in causes of volcanism and its activity reflected in the products of volcanic emanations, and in which way? This chapter tries to summarize the mineralogical evidence and give the answer to this question.

Figure 1. Europe from the space with locations of the three volcanic provinces described in this chapter.

There is no process in geology that, on closer inspection, can be called simple. Compared to the processes on the similar scale, the mineralization of a fumarole or a fumarolic field might well be the most complex one. It happens in an open system with high kinetic energy, high mass transport rate, and subject to constantly fluctuating conditions. It involves reactions of gases, fluids, and solids at the boundary between the atmosphere, volcanic gases, meteoric water, hydrothermal solutions, lava, and country rock. Minerals in fumaroles form either as direct sublimates due to changes in temperature or composition of gases, as accumulations of aerosols carried by gas, through gas-solid reactions either by the assimilation of gas components or by leaching of solid, through temperature-induced reactions (mineral reactions, phase transitions, dehydration), through the action of water or vapour (hydration or dissolution) or

http://dx.doi.org/10.5772/64129

by crystallization from solution. Inspection of the literature about fumaroles reveals that authors use the following two distinct attributions: sublimates and encrustations. The term sublimate is used for the minerals formed by deposition from gases, and encrustations are formed from fumarolic fluids, but the study reveals many inconsistencies. The reason is that the processes mentioned earlier happen simultaneously at the same place and are entangled. Moreover, most of the minerals can be formed through more than one process. Here, we will consider all minerals in fumaroles that are formed under whatsoever influence of volcanic gases as fumarolic minerals and avoid making classifications that would have too many exemptions and in many cases be misleading. Another question is the definition of a fumarole itself. In their work on Icelandic fumaroles, Jakobsson et al. [1] distinguished the following two types of fumarolic associations: volcanogenic, which are formed by short-lived, shallow-rooted thermal systems and characterized by no discharge of water and by encrustations that are primarily product of magmatic degassing; and solfataric hydrothermal systems, which are long-lived with a deep-rooted source and surface exposures of high-temperature hydrothermal activity with extensive water-rock interaction. We keep our choice of the European localities as close as possible to the former type (volcanogenic), although it, in the context broader than specific Icelandic conditions, becomes more arbitrary because the fumaroles of a quiescent volcano closely resemble solfataras in their process of formation and mineralogy. The fumaroles on the Solfatara crater, which gave the name to the second category, are not identical in all their characteristics to those encountered on Iceland and illustrate how difficult it is to draw a border line. We are aware that our choice of what to include and what to exclude among the European places with gas emanations can be disputed, but we think that it illustrates well all stages of surface pneumatic processes connected to volcanism from its birth to its old stage and the last breaths of a volcano.

Measured with geological scales, fumaroles are short-lived phenomena. They are a surface or close to the surface feature of a volcano and much more sensitive to weathering than surrounding lava. The formation and dissolution and erosion of fumarolic minerals are contemporary processes, and when the gas emanations ultimately stop, the mineral content in the vents of fumaroles disappears in a short time and just the roots of a fumarolic system can be found in a fossilized form. Besides high chemical reactivity and instability, the fumarolic minerals often appear in microcrystalline aggregates and in the mixtures of many phases. The methods of research therefore require specific approaches and strategies.

2. Methods

2.1. Sample collection and preparation

In this work, the samples from 12 European volcanoes and other fumarolic systems have been investigated (Krafla, Askja, Hekla, Fimmvörðuháls, Eldfell, Surtsey, Vulcano, Etna, Soussaki, Milos, Santorini, and Nisyros). The data for Campi Flegrei and Vesuvius, plus additional data for investigated volcanoes, have been taken from the literature.

The samples have been left to cool down at atmospheric conditions after extraction. The fragile samples were mounted in plastic boxes fixed to avoid the physical damage. The less sensitive ones or those that were extracted in crushed form were sealed in plastic bags. After separating the chosen parts under the microscope, the samples for the X-ray diffraction (XRD) were crushed in agate mortar, and the samples for the scanning electron microscope with energy-dispersive spectrometer (SEM-EDS) analyses were sputtered with a 30-nm-thick carbon film using an Edwards Auto 306 thermal evaporator. The fumarolic samples are mostly composed of intimate mixtures of several minerals with micrometer-sized crystals. Even the most painstaking separation work is many times not in stand to produce a pure one-phase sample for powder X-ray diffraction (PXRD), and hence, the separation of multiple seemingly different portions of a sample was almost always performed in order to get the best overview of the phase composition.

2.2. X-ray diffraction

PXRD is the method of choice for the identification of minerals, alone or in mixtures, and for the quantitative phase analysis. Essential for handling complex mixtures is a diffractometer with high resolution, and therefore, the D8ADVANCE Bruker-AXS powder diffractometer with the primary Ge_{111} monochromator and the LinxEye silicon strip detector in reflection geometry was used for the measurement of bulk samples (at the Department of Geosciences, University of Copenhagen). The wavelength of X-ray used for measurement was 1.54059 Å. The separated portions of samples for PXRD were usually in very small quantities (≤20 mm^3). They were therefore mounted as thin layers on specially cut single-crystal quartz plates that produce no scattering inside the instrument's measuring range that was 5° to 70° or 90° 2θ, with measurement steps of 0.02° and sufficient measuring time for producing good diffraction patterns (usually 4 s per step). The identification of minerals was done with the help of the JCPDS powder diffraction database (ICDD product) and the own set of calculated patterns from the ICSD database (FIZ Karlsruhe product) plus use of the Rietveld method (Topas 4.1 program, Bruker-AXS product). Modern single-crystal diffractometers enable fast analyses of small grains (only several tens of micrometer in diameter). The full crystal structure characterisation they offer is essential in the definition of new mineral species encountered in fumaroles and builds the basis for many of results reported here.

2.3. SEM-EDS

The use of a SEM equipped with EDS (Si(Li), Ge or silicon drift) gives a possibility to obtain very good images by secondary and backscattered electrons together with a chemical micro-analysis. The ED detector has the advantage of providing a full spectrum in a very short time that can be very helpful for quick, preliminary identification of minerals. The high counting efficiency of the solid-state ED detectors allows a complete analysis of a mineral in very short time (50 s or less) and with very low probe currents of the beam (about 500 pA). The low probe current involves the generation of a small X-ray escape volume and therefore accurate analysis of minerals even in the case of crystals of extremely small size and in the co-presence of other mineral phases, without the risk of evaporating the sample. Moreover, an ED detector that

http://dx.doi.org/10.5772/64129

does not require critical positioning of the sample [2, 3] can give good quantitative chemical data analysing directly the natural faces of the crystals without a need of polished surfaces required for microprobe, but mostly impossible for fumarolic samples, which as a rule consist of loose aggregates of tiny crystals. The last generation of solid-state silicon drift detectors (SSD), normally equipped with a very thin polymeric SuperAtmosphere Thin Window©, gives an output signal with much higher count rates that guarantee also a better sensitivity for light elements even at very low probe currents. Their use in conjunction with the newest software for the correction of the matrix effects [4] is highly recommended for the samples of fumarolic minerals.

Our investigations were carried out with two SEM instruments: the Stereoscan 360 of Cambridge Instruments and the EVO-50XVP of Zeiss-Cambridge. Microanalyses were carried out with Oxford-Link Ge ISIS energy dispersive spectrometer or Oxford X-max (80 mm^2) silicon drift detector, both equipped with a SuperAtmosphere Thin Window©. The operating conditions were as follows: 15 kV accelerating potential, 500 pA probe current, counting time 100 s. The software used was Z AF4/FLS and eXtended Pouchou and Pichoir (XPP) correction scheme, respectively, both Oxford-Link Analytical products.

3. The minerals

More than 200 different minerals have been described from European fumaroles. With the rest of the world, the number might be over 300. Most of them are rare or extremely rare but can be important as indicators of specific conditions in the fumarole where they have been found. **Table 1** gives the chemical and crystallographic parameters of the scientifically confirmed European fumarolic minerals. In the following text, we describe the main features of the mineral groups and individual minerals in fumaroles. The exposition of species follows the mineral classification of Strunz [5] with small modifications. Jakobsson et al. [1] listed in their work a number of supposed new minerals and labelled them each with a two-letter symbol. For those that still do not have mineral names, we used the same notation. The labels for the localities are as follows: A (Askja), CF (Campi Flegrei), El (Eldfell), Et (Etna), F (Fimmvörðuháls), H (Hekla), Kr (Krafla), M (Milos), N (Nisyros), Sa (Santorini), So (Soussaki), Su (Surtsey), Ve (Vesuvius), and Vu (Vulcano).

Minerals	Formula	Sp.gr.	Unit cell parameters (Å, °)	ICSD
Sulphur-α*	S_8	Fddd	10.465 12.866 24.49	63082
Sulphur-β	S_8	$P2_1/c$	10.926 10.855 10.790 95.9	870
rosickýite	S_8	P2/c	8.455 13.052 9.267 124.9	66517
sulphurite*	S+As,Se	amorph		amorph
Selenium-α	Se_8	$P2_1/n$	9.054 9.083 11.601 90.8	2718

Minerals	Formula	Sp.gr.	Unit cell parameters (Å, °)	ICSD
siderazot	Fe_3N	$P6_322$	4.698 4.379	79983
Gold	Au	Fm-3m	4.079	52700
tellurium	Te	$P3_12$	4.456 5.921	65692
covellite	CuS	$P6_3/mmc$	3.796 16.36	41975
sphalerite	ZnS	F-43m	5.409	77082
wurtzite	ZnS	$P6_3mc$	3.823 6.261	67453
chalcopyrite	$CuFeS_2$	I-42d	5.289 10.423	2518
pyrrhotite	$Fe_{11}S_{12}$	Cc	6.897 11.954 17.702 101.3	166063
millerite	NiS	R3m	9.611 3.151	151599
galena*	PbS	Fm-3m	5.934	38293
pyrite*	FeS_2	Pa-3	5.416	109377
realgar*	As_4S_4	$P2_1/n$	9.325 13.571 6.587 106.4	15238
pararealgar	As_4S_4	$P2_1/c$	9.909 9.655 8.502 97.29	80125
alacranite1	As_8S_9	P2/c	9.942 9.601 9.178 101.9	98792
alacranite2	As_4S_4	C2/c	9.943 9.366 8.908 102.0	95290
dimorphite-α (HT)	As_4S_3	Pnma	9.158 8.033 10.200	188058
dimorphite-β (LT)	As_4S_3	Pnma	11.217 9.922 6.607	188059
demicheleite	BiS(Br,Cl,I)	Pnam	8.042 9.851 4.033	161637
bismuthinite*	Bi_2S_3	Pnma	11.269 3.972 11.129	153946
mozgovaite	$PbBi_4(S,Se)_7$	Bbmm?	13.18 37.4 4.05?	[28]
galenobismutite*	$PbBi_2S_4$	Pnam	11.802 14.569 4.076	158392
cannizzarite*	$Pb_{48}Bi_{56}(S_{1-x}Se_x)_{132}$	$P2_1/m$	38.87 4.090 39.84 102.3	169960
cosalite	$Pb_2Bi_2S_5$	Pnma	23.89 4.062 19.143	169944
lillianite	$Pb_3Bi_2S_6$	Bbmm	13.540 20.64 4.110	246062
heyrovskyite	$Pb_6Bi_2S_9$	Bbmm	13.719 31.39 4.132	180078
kirkiite	$Pb_{10}Bi_3As_3S_{19}$	$P2_1/m$	8.700 26.24 8.774 119.7	156249
vurroite	$Pb_8(Pb,Bi)_2(Sn,Bi)(As,Bi,Pb)(Bi,As)_{10}S_{27}Cl_3$	C2/c	8.371 45.50 27.27 98.8	160401
sylvite*	KCl	Fm-3m	6.285	165593
halite*	NaCl	Fm-3m	5.620	18189
salammoniac*	NH_4Cl	Pm-3m	3.877	22141
lafossaite	TlCl	Pm-3m	3.901	5253
sellaite	MgF_2	$P4_2/mnm$	4.621 3.052	394
chloromagnesite	$MgCl_2$	R-3m	3.636 17.666	86439

http://dx.doi.org/10.5772/64129

Minerals	Formula	Sp.gr.	Unit cell parameters (Å, °)	ICSD
scacchite	$MnCl_2$	R-3m	3.711 17.59	33752
fluorite*	CaF_2	Fm-3m	5.463	41413
oskarssonite*	$Al(F,OH)_3$	R-3c	4.982 12.387	5243
parascandolaite	$KMgF_3$	Pm-3m	4.003	192409
molysite*	$FeCl_3$	R-3	6.056 17.407	39764
carnallite	$KMgCl_3(H_2O)_6$	Pnna	16.119 22.47 9.551	64691
eriochalcite	$CuCl_2(H_2O)_2$	Pbmn	7.414 8.089 3.746	40290
ammineite	$CuCl_2(NH_3)_2$	Cmcm	7.688 10.645 5.736	180189
chloraluminite	$AlCl_3(H_2O)_6$	R-3c	11.827 11.895	22071
ferruccite	$NaBF_4$	Cmcm	6.837 6.262 6.792	36067
avogadrite	KBF_4	Pnma	8.659 5.480 7.030	9875
barberiite	NH_4BF_4	Pnma	9.077 5.679 7.279	9918
rosenbergite	$AlF_3(H_2O)_3$	P4/n	7.715 3.648	66691
HI	$FeF_3(H_2O)_3$	P4/n	7.846 3.877	14134
HU	$FeF_3(H_2O)_3$	R-3	9.253 4.675	unp
pachnolite	$NaCaAlF_6H_2O$	Fd	12.117 10.414 15.680 90.4	40132
gearksutite	$CaAlF_4(OH)H_2O$	P-1	4.94 6.81 6.978 101.1 94.9 110.1	89800
jakobssonite*	$CaAlF_5$	C2/c	8.601 6.290 7.219 114.6	188924
leonardsenite*	$MgAlF_5(H_2O)_2$	Imma	7.064 10.131 6.774	411650
HG	$Na_2Ca_3Al_2F_{14}$	$I2_13$	10.257	202657
coulsellite	$CaNa_3AlMg_3F_{14}$	R-3m	7.161 17.594	168054
thermessaite	$K_2AlF_3SO_4$	Pbcn	10.810 8.336 6.822	161272
thermessaite-(NH_4)	$(NH_4)_2AlF_3SO_4$	Pbcn	11.301 8.612 6.850	[45]
ralstonite*	$Na_xMg_xAl_{2-x}(F,OH)_6(H_2O)_y$	Fd-3m	9.91	31345
HH	$Ca_3Al_2F_{10}(OH)_2(H_2O)_3$?	C2/m?	6.257 22.19 6.311 115.5 (?)	unp
HB	Na-Ca-Al-F?	?	?	[1]
HD*	$(NH_4)_xFe_2F_6$	Fd-3m	10.325	202047
meniaylovite	$Ca_4AlSi(SO_4)F_{13}(H_2O)_{12}$	Fd-3	16.71	100728
cossaite	$Mg_{0.5}Al_6H(SO_4)_7F_6(H_2O)_{33}$	R-3	22.01 9.238	188928
malladrite*	Na_2SiF_6	P1	8.859 8.859 5.038 90 90 120	40917
hieratite	K_2SiF_6	Fm-3m	8.134	29407
demartinite	K_2SiF_6	$P6_3mc$	5.646 9.232	158483
heklaite*	$KNaSiF_6$	Pnma	9.339 5.503 9.796	183232

Minerals	Formula	Sp.gr.	Unit cell parameters (Å, °)	ICSD
cryptohalite*	$(NH_4)_2SiF_6$	Fm-3m	8.395	18033
bararite	$(NH_4)_2SiF_6$	P-3m	5.784 4.796	18027
HT	$FeSiF_6(H_2O)_6$	R-3m	9.616 9.675	41535
knasibfite	$K_3Na_4(SiF_6)_3BF_4$	Imm2	5.522 17.106 9.175	160430
chlormanganokalite	K_4MnCl_6	R-3c	11.926 14.787	24475
erythrosiderite	$K_2FeCl_5H_2O$	Pnma	13.75 9.92 6.93	30321
kremersite	$(NH_4)_2FeCl_5H_2O$	Pnma	13.706 9.924 7.024	200322
mitscherlichite	$K_2CuCl_4(H_2O)_2$	$P4_2/mnm$	7.477 7.935	16052
melanothallite	Cu_2OCl_2	Fddd	7.469 9.597 9.700	96610
atacamite*	$Cu_2Cl(OH)_3$	Pnma	6.030 6.865 9.120	61252
paratacamite*	$Cu_2Cl(OH)_3$	R-3	13.654 14.041	1810
connellite	$Cu_{36}Cl_{7.86}(SO_4)_{0.67}(NO_3)_{0.5}(OH)_{62.3}(H_2O)_{5.6}$	$P6_3/mmc$	15.787 9.101	415129
cumengeite	$Pb_{21}Cu_{20}Cl_{42}(OH)_{40}(H_2O)_6$	I4/mmm	15.101 24.49	157067
bismoclite	BiOCl	P4/nmm	3.887 7.354	74502
lucabindiite	$(K,NH_4)As_4O_6((Cl,Br)$	P6/mmm	5.239 9.014	289996
cotunnite	$PbCl_2$	Pnam	7.619 9.043 4.534	202130
pseudocotunnite	K_2PbCl_4	?	?	[10]
challacolloite*	KPb_2Cl_5	$P2_1/c$	8.849 7.918 12.472 90.1	416430
hephaistosite	$TlPb_2Cl_5$	$P2_1/c$	9.003 7.972 12.569 90.05	166293
brontesite	$(NH_4)_3PbCl_5$	Pnma	8.435 15.773 8.445	166092
panichiite	$[NH_4)_2SnCl_6$	Fm-3m	10.064	163660
steropesite	Tl_3BiCl_6	Cc	26.69 15.127 13.014 108.1	163661
argesite	$[NH_4)_7Bi_3Cl_{16}$	R-3c	13.093 102.68	5283
tenorite	CuO	C2/c	4.684 3.423 5.129 99.5	16025
spinel	$MgAl_2O_4$	Fd-3m	8.089	40030
magnesioferrite	$MgFe_2O_4$	Fd-3m	8.394	158402
magnetite	Fe_3O_4	Fd-3m	8.396	30860
hausmannite	Mn_3O_4	$I4_1/amd$	5.765 9.442	68174
minium	Pb_3O_4	$P4_2/mbc$	8.811 6.563	4106
corundum	Al_2O_3	R-3c	4.761 12.995	9770
hematite*	Fe_2O_3	R-3c	5.035 13.749	82904
ilmenite	$FeTiO_3$	R-3	5.088 14.085	30664
pseudobrookite	Fe_2TiO_5	Ccmm	9.793 3.730 9.976	51225

http://dx.doi.org/10.5772/64129

Minerals	Formula	Sp.gr.	Unit cell parameters (Å, °)	ICSD
opal*	$SiO_2(H_2O)_x$	amorph		amorph
cristobalite*	SiO_2	$P4_12_12$	4.978 6.948	9327
tridymite	SiO_2	Cc	18.494 4.991 23.76 105.8	1109
quartz*	SiO_2	$P3_22$	4.913 5.405	174
anatase	TiO_2	$I4_1/amd$	3.784 9.515	9852
rutile	TiO_2	$P4_2/mnm$	4.592 2.957	33837
akaganeite	$FeOOHCl_x$	I2/m	10.600 3.034 10.513 90.2	69606
portlandite	$Ca(OH)_2$	P-3m	3.585 4.895	15471
gibbsite	$Al(OH)_3$	$P2_1/n$	8.684 5.078 9.736 94.5	6162
doyleite	$Al(OH)_3$	P-1	5.00 5.168 4.983 97.4 118.7 104.7	50581
calcite*	$CaCO_3$	R-3c	4.988 17.061	40107
magnesite	$MgCO_3$	R-3c	4.635 15.019	40117
dolomite*	$CaMg(CO_3)_2$	R-3	4.806 16.006	66333
hydromagnesite	$Mg_5(CO_3)_4(OH)_2(H_2O)_4$	$P2_1/c$	10.105 8.954 8.378 114.4	920
aragonite	$CaCO_3$	Pmcn	4.961 7.970 5.742	166085
cerussite	$PbCO_3$	Pmcn	5.180 8.492 6.134	6178
azurite	$Cu_3(CO_3)_2(OH)_2$	$P2_1/c$	5.011 5.850 10.353 92.4	158577
thermonatrite	$Na_2CO_3H_2O$	$P2_1ab$	6.472 10.724 5.259	1852
natron	$Na_2CO_3(H_2O)_{10+x}$	Cc	12.750 9.001 12.590 115.8	97924
trona	$Na_3H(CO_3)_2(H_2O)_2$	C2/c	20.41 3.493 10.333 106.5	192710
sassolite*	H_3BO_3	P-1	7.039 7.053 6.578 92.6 101.2 119.8	24711
metaborite	HBO_2 (HT>140°C)	P-43n	8.886	34639
clinometaborite	HBO_2 (LT)	$P2_1/a$	7.127 8.842 6.773 93.2	183581
ameghinite	$NaB_3O_3(OH)_4$	C2/c	18.428 9.882 6.326 104.4	4219
chalcocyanite	$CuSO_4$	Pnma	8.409 6.709 4.833	71017
vanthoffite	$Na_6Mg(SO_4)_4$	$P2_1/c$	9.797 9.217 8.199 113.5	16607
EN	$Na_3Al(SO_4)_3$	R-3	13.376 8.933	unp
EA	$NaMgAl(SO_4)_3$	R-3	8.303 21.87	unp
EI	$Na_2Mg_2(SO_4)_3$	?	?	unp
langbeinite*	$K_2Mg_2(SO_4)_3$	$P2_13$	9.921	40986
manganolangbeinite	$K_2Mn_2(SO_4)_3$	$P2_13$	10.114	200897
steklite	$KAl(SO_4)_2$	P321	4.728 8.001	[75]
pyracmonite	$(NH_4)_3Fe(SO_4)_3$	R3c	15.217 8.932	169964

Minerals	Formula	Sp.gr.	Unit cell parameters (Å, °)	ICSD
aluminopyracmonite	$(NH_4)_3Al(SO_4)_3$	R-3	15.032 8.878	190666
eldfellite	$NaFe(SO_4)_2$	C2/m	8.043 5.139 7.115 92.1	166768
yavapaiite	$KFe(SO_4)_2$	C2/m	8.150 5.162 7.855 94.9	26004
thenardite*	Na_2SO_4	Fddd	5.860 12.304 9.817	2895
metathenardite*	Na_2SO_4 (HT)	$P6_3/mmc$	5.326 7.126	63077
aphthitalite*	$KNaSO_4$	P3m	5.607 7.177	26014
glaserite	$K_3Na(SO_4)_2$	P-3m	5.680 7.309	26018
palmierite	$K_2Pb(SO_4)_2$	R-3m	5.497 20.86	94234
mascagnite	$(NH_4)_2SO_4$	Pnam	7.782 10.636 5.993	34257
mercallite	$KHSO_4$	Pbca	8.415 9.796 18.967	249738
FB	$Na_3H(SO_4)_2$	$P2_1/c$	8.644 9.641 9.139 108.8	249553
therasiaite	$(NH_4)_3KNa_2Fe_2(SO_4)_3Cl_5$	Cc	18.284 12.073 9.535 108.1	5296
anhydrite*	$CaSO_4$	Amma	6.991 6.996 6.238	15876
gypsum*	$CaSO_4(H_2O)_2$	C2/c	6.277 15.181 5.672 114.1	161622
bassanite	$CaSO_4(H_2O)_{0.5}$	C2	17.559 6.962 12.070 133.4	380286
omongwaite	$Na_2Ca_5(SO_4)_6(H_2O)_3$	C2	12.089 6.903 6.354 90.1	88942
glauberite	$CaNa_2(SO_4)_2$	C2/c	10.129 8.306 8.533 112.2	16901
barite	$BaSO_4$	Pbnm	7.154 8.879 5.454	76926
celestite	$SrSO_4$	Pbnm	6.867 8.354 5.346	92608
anglesite	$PbSO_4$	Pbnm	6.955 8.472 5.397	92609
dolerophanite	Cu_2OSO_4	C2/m	9.370 6.319 7.639 122.3	61513
antlerite	$Cu_3SO_4(OH)_4$	Pnma	8.289 6.079 12.057	96348
d'ansite	$Na_{21}Mg(SO_4)_{10}Cl_3$	I-43d	15.90	[86]
d'ansite-(Mn)	$Na_{21}Mn(SO_4)_{10}Cl_3$	I-43d	15.929	190535
d'ansite-(Fe)	$Na_{21}Fe(SO_4)_{10}Cl_3$	I-43d	15.882	190536
aiolosite	$Na_4Bi(SO_4)_3Cl$	$P6_3/m$	9.626 6.880	166960
natroalunite*	$(Na,K)Al_3(SO_4)_2(OH)_6$	R-3m	6.973 16.877	166305
alunite*	$KAl_3(SO_4)_2(OH)_6$	R-3m	7.020 17.223	12106
natrojarosite	$NaFe_3(SO_4)_2(OH)_6$	R-3m	/.315 16.587	160409
jarosite*	$KFe_3(SO_4)_2(OH)_6$	R-3m	7.315 17.224	12107
adranosite	$(NH_4)_4NaAl_2(SO_4)_4Cl(OH)_2$	$I4_1/acd$	18.118 11.320	169963
adranosite-(Fe)	$(NH_4)_4NaFe_2(SO_4)_4Cl(OH)_2$	$I4_1/acd$	18.261 11.562	[90]
euchlorine*	$KNaCu_3O(SO_4)_3$	C2/c	18.41 9.43 14.21 113.7	69451

http://dx.doi.org/10.5772/64129

Minerals	Formula	Sp.gr.	Unit cell parameters (Å, °)	ICSD
chlorothionite	$K_2CuSO_4Cl_2$	Pnma	7.732 6.078 16.292	22364
linarite	$PbCuSO_4(OH)_2$	$P2_1/m$	9.701 5.650 4.690 102.6	68173
baliczunicite	$Bi_2O(SO_4)_2$	P-1	6.739 11.184 14.175 80.1 88.5 89.5	[13]
leguernite	$Bi_{38}O_{42}(SO_4)_{15}$	P2	11.249 5.657 11.914 99.2	[91]
kieserite	$MgSO_4H_2O$	C2/c	6.891 7.624 7.645 117.7	68345
rozenite*	$FeSO_4(H_2O)_4$	$P2_1/n$	5.979 13.648 7.977 90.4	23912
chalcanthite	$CuSO_4(H_2O)_5$	P-1	6.116 10.716 5.961 82.4 107.3 102.6	20657
pentahydrite	$MgSO_4(H_2O)_5$	P-1	6.314 10.565 6.030 81.1 109.8 105.1	2776
hexahydrite*	$MgSO_4(H_2O)_6$	C2/c	10.110 7.212 24.41 98.3	16546
nickelhexahydrite	$NiSO_4(H_2O)_6$	C2/c	9.880 7.228 24.13 98.4	65018
römerite*	$Fe_3(SO_4)_4(H_2O)_{14}$	P-1	6.463 15.309 6.341 90.5 101.1 85.7	15207
coquimbite	$(Fe,Al)_2(SO_4)_3(H_2O)_9$	P-31c	10.937 17.081	169956
halotrichite*	$FeAl_2(SO_4)_4(H_2O)_{22}$	$P2_1/c$	6.195 24.26 21.26 100.3	96598
pickeringite	$MgAl_2(SO_4)_4(H_2O)_{22}$	$P2_1/c$	6.184 24.27 21.23 100.3	90028
meta-alunogen	$Al_2(SO_4)_3(H_2O)_{14}$	?	?	[43]
alunogen*	$Al_2(SO_4)_3(H_2O)_{17}$	P-1	7.42 26.97 6.062 89.6 97.3 91.5	12129
mirabilite	$Na_2SO_4(H_2O)_{10}$	$P2_1/c$	11.474 10.356 12.788 107.8	411348
campostriniite	$(NH_4,K)_2Bi_{2.5}Na_{2.5}(SO_4)_6{\cdot}H_2O$	C2/c	17.748 6.982 18.221 114.0	[92]
rhomboclase*	$FeH(SO_4)_2(H_2O)_4$	Pnma	9.742 18.333 5.421	183662
voltaite*	$K_2Fe_8Al(SO_4)_{12}(H_2O)_{18}$	Fd-3c	27.25	9254
löweite	$Na_{12}Mg_7(SO_4)_{13}(H_2O)_{15}$	R-3	18.924 13.538	15209
eugsterite	$Na_4Ca(SO_4)_3(H_2O)_2$	?	?	[93]
hydroglauberite	$Ca_3Na_{10}(SO_4)_8(H_2O)_6$	?	?	[94]
syngenite	$K_2Ca(SO_4)_2H_2O$	$P2_1/m$	9.771 7.145 6.247 104.0	157072
kröhnkite	$Na_2Cu(SO_4)_2(H_2O)_2$	$P2_1/c$	5.518 12.666 5.808 108.4	422593
ferrinatrite	$Na_3Fe(SO_4)_3(H_2O)_3$	P-3	15.560 8.666	14003
cyanochroite	$K_2Cu(SO_4)_2(H_2O)_6$	$P2_1/a$	9.066 12.13 6.149 104.4	2925
bloedite	$Na_2Mg(SO_4)_2(H_2O)_4$	$P2_1/a$	11.135 8.248 5.542 100.8	151453
polyhalite	$K_2Ca_2Mg(SO_4)_4(H_2O)_2$	F-1	11.690 16.330 7.600 91.6 90 91.9	6304
tamarugite*	$NaAl(SO_4)_2(H_2O)_6$	$P2_1/a$	7.353 25.22 6.097 95.2	15187
picromerite	$MgK_2(SO_4)_2(H_2O)_6$	$P2_1/a$	9.072 12.212 6.113 104.8	26772

Minerals	Formula	Sp.gr.	Unit cell parameters (Å, °)	ICSD
metavoltine	$K_2Na_6Fe^{2+}Fe_6^{3+}O_2(SO_4)_{12}(H_2O)_{18}$	P3	9.575 18.17	8270
kalinite	$KAl(SO_4)_2(H_2O)_{11}$	C2/c	19.92 9.27 8.304 98.8	[95]
alum-(K)	$KAl(SO_4)_2(H_2O)_{12}$	Pa-3	12.164	280548
kainite	$KMgSO_4Cl(H_2O)_{2.75}$	C2/m	19.72 16.23 9.53 94.9	26003
SH	$Na_2Mg_3(SO_4)_2(OH)_2(H_2O)_4$	$Cmc2_1$	19.735 7.223 10.028	425875
chessexite	$Na_4Ca_2Mg_3Al_8(SiO_4)_2(SO_4)_{10}(OH)_{10}(H_2O)_{40}$	?	?	[96]
chlorapatite	$Ca_5(PO_4)_3(Cl,OH)$	$P6_3/m$	9.564 6.816	1706
mimetite	$Pb_5(AsO_4)_3Cl$	$P6_3/m$	10.240 7.440	188080
phoenicochroite	Pb_2OCrO_4	C2/m	14.001 5.675 7.137 115.2	34831

Chemical formula, space group, unique unit cell parameters and the ICSD identification number (ICSD = Inorganic Crystal Structure Database, Fachinformationszentrum Karlsruhe, Germany). For the species that still lack ICSD entry, the reference is given as a citation, as unp = unpublished data, or amorph = amorphous compound. Minerals common in fumaroles are marked with a star.

Table 1. Minerals from European fumaroles.

3.1. Elements

Sulphur is the most abundant native element in fumaroles and generally one of the most common minerals in this environment. It appears in the following various forms: as thick yellow blocky crystalline masses, well-formed crystals (in cavities or on surfaces), granular crusts and acicular spear-like dendritic crystals (at vents of fumaroles, **Figure 2**) or as an admixture to earthy altered rock material, giving it grey colour. Sulphur forms through oxidation of H_2S. It is typically accompanied by alunite, gypsum or salammoniac, but it is also found in other associations. The molecules in the crystal structure consist of puckered eight-member rings of atoms in all three polymorphs found in nature. Native sulphur or α-sulphur is orthorhombic and at atmospheric pressures stable up to 95°C when it transforms reversibly to the monoclinic β-form with the melting temperature of 119°C. It can therefore be supposed that a significant part of sulphur found in fumaroles was formed as the high-temperature form and on cooling transformed to the alpha form observed typically on XRD diagrams. As solid unstable over 120°C, sulphur can be found only in the low-temperature fumaroles or at the outer rims of the hotter ones. It was found on all localities except F.

Rare: **Rosickýite or γ-sulphur**: observed once in a small transparent green-yellow crust made of platy crystals (Vu [6]). Metastable at all temperatures [7]. Conditions of formation still not completely understood. **Sulphurite**, amorphous S with As and Se, Vu [8]. **Selenium**: observed as red crusts (Ve [9], Vu [10]) and so it seems that it was the metastable form, which contains ring molecules similar to that of sulphur and not the stable polymorph with infinite spiral molecules, which is metallic in appearance. Melts at 217°C. **Siderazote**, Ve [9]: iridiscent cover

http://dx.doi.org/10.5772/64129

on lavas. **Gold** and **tellurium**, Vu [11], observed as several micrometer-sized grains in the silicic alteration zone of the crater.

Figure 2. Spear-like crystals of sulphur. Fumarole on Nisyros.

3.2. Sulphides

Metallic sulphides are confined to deeper parts of a volcanic system with its high-temperature hydrothermal conditions and rarely appear as sublimates and then in small amounts on the surface of the fumaroles. Here, their formation depends on the persistence of reducing conditions in parts of these largely fluctuating systems. These were especially characteristic for Vesuvius in the periods immediately following the eruptions and for Vulcano during the thermal "crisis" (temperature increase in the fumaroles). Semimetals form stronger covalent bonds with sulphur and are more volatile, and therefore, they can appear in fumaroles in significant quantities either as simple sulphides or, when combining with metals, as sulphosalts (see below). Observed in the investigated localities are As and Bi, whereas Sb did not appear in quantities sufficient to form its minerals. Arsenic forms discrete molecules with sulphur and its simple sulphides are confined to low-temperature hydrothermal deposits and low-temperature fumaroles where they can appear in important quantities (CF). On Vulcano, however, it is mostly a constituent of sulphosalts together with Bi. The transport of the latter is supposed to occur as Bi-Cl complexes, so the abundance of its sulphides, sulphosalts and other minerals in the fumaroles of Vulcano is interpreted as a combined action of both elements [12].

Rare: **Covellite**, Ve [9]: deep-blue thin crusts. **Sphalerite**, Vu [13]: Cd-rich, in HT association of sulphides and sulphosalts. **Wurtzite**, Vu [13]: Metastable under 1020°C, accompanies sphalerite. **Chalcopyrite**, Ve [9]: metallic thin crusts composed of minute crystals. **Pyrrhotite**, Ve [14], Vu [13]: metallic hexagonal lamellae. **Millerite**, Ve [9]: observed once in capillary

crystals. **Galena**, Ve [9]: with Fe-sulphides and oxides; Vu [12]: Se-rich, in company of Bi-Pb sulphosalts of the similar silver colour and metallic lustre. **Pyrite**, Vu [13], Ve [9]: with other sulphides; CF [15]: minute crystals dispersed in altered tuffs; So: in opalized rock; M: in microcrystals with rhomboclase and voltaite.

As-sulphides realgar, pararealgar, alacranite and **dimorphite** have molecular crystal structures with As_4S_n cage molecules. The commonest of them is **realgar (Figure 3)**. As_4S_4 melts at 309°C [16] and is therefore confined to low-to-intermediate *T* fumaroles. CF [17]: the main constituent in a fumarole on Solfatara in grainy or crusty aggregates of sub-mm prismatic light red lustrous crystals associated with salammoniac; Ve [9]: rare small red crystals associated with sulphur and selenium. Realgar transforms under the influence of visible or UV light into the orange-yellow **pararealgar** [18], earlier often mistaken for orpiment. CF: it is the alteration product of realgar. The synthetic HT polymorph β-As_4S_4 is stable over 267°C [16]. In natural occurrences, this type of molecule is partly substituted by As_4S_5 until the 1:1 proportion as in the type specimen of **alacranite (As_8S_9)** that has the ordered arrangement of the two types of molecules and different symmetry than β-As_4S_4 [19]; CF [20]: orange small crystals with realgar and dimorphite. **Dimorphite** has two polymorphs. LT β-form transforms to HT α-form at 130°C [21], which melts at 211°C [16]. CF, Ve [17]: tiny orange or yellow crystals with adamantine lustre. **Demicheleite** (Vu [22–24]) is a solid solution with three end-members containing different halogene elements (Cl, Br, I). Very rare prismatic red to black sub-mm crystals associated with other Bi minerals.

Figure 3. Realgar, Solfatara. Sample from the Natural History Museum in Copenhagen.

3.3. Sulphosalts

Sulphosalts, sulphides containing thioarsenide, thioantimonide, or thiobismuthite group(s), are relatively rare constituents of fumaroles. Among the fumaroles reported here, they appear

http://dx.doi.org/10.5772/64129

only on Vulcano where they were abundant during the "thermal crises" when the fumarolic temperatures exceeded approximately 450°C. Recent analysis of the roots of paleofumarole at El Indio, Chile, revealed subsurface formation of sulphosalts crystallized from a melt condensing from hot fumarolic gases [25]. We could expect the same situation in the roots of the fumaroles on Vulcano during the periods of lower gas dynamics. When it increased during the thermal crisis, the hot front of the sulphosalt formation reached the surface and this established the new thermodynamical conditions where their crystals formed as sublimates at fumarole vents through a quenching process, producing generally very small crystals, homogeneous and lacking traces of decomposition [26]. They are silver-grey in colour, with metallic lustre and acicular (the latter with the exceptions of kirkiite and cannizzarite). A simple sulphide bismuthinite is here described together with sulphosalts because of its close structural and genetic relation to these minerals.

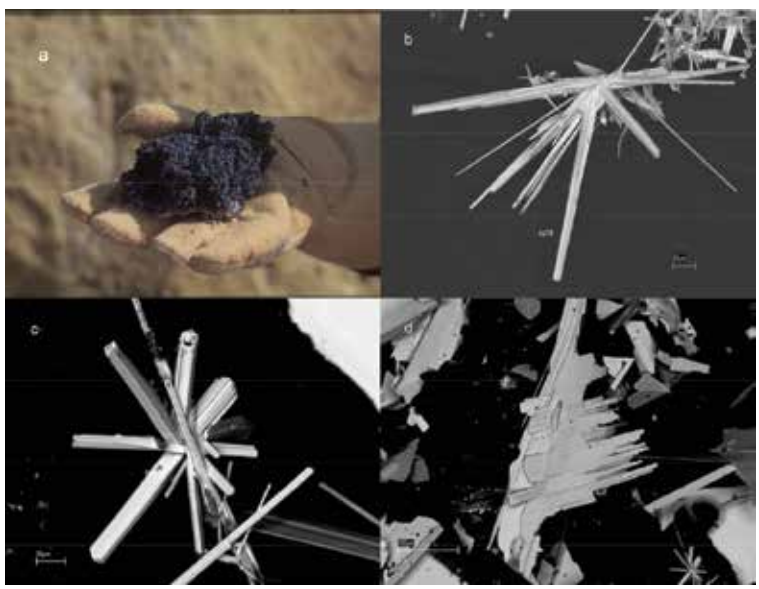

Figure 4. (a) A sample with sulphosalts, Vulcano; (b) SEM photograph of vurroite; (c) SEM photograph of bismuthinite and (d) SEM photograph of cannizzarite.

Sulphosalts belonging to the PbS-Bi_2S_3 system predominate on Vulcano due to high concentration of Pb and Bi in the gases, transported as volatile chlorides or chlorosulphide complexes [12]. **Bismuthinite** is relatively common and with galena mixed with Pb-Bi sulphosalts [27]. **Mozgovaite** [28] is known only from Vulcano and very rare. **Galenobismutite** is fairly common [12]. **Cannizzarite** [27] is a mineral with an incommensurate structure, which gives it a complex stoichiometry, large unit cell and specific crystal form (thin long leaves reaching sometimes mm diameters but only tens of microns thick). It is relatively abundant. **Cosalite** is rare [12] like **lillianite** [29]. The crystal structure of the latter typifies a homologous series [30] where also the rare **heyrovskyite** [31] with a higher Pb/Bi proportion belongs. Some new or very rare minerals were formed by the admixture of other elements to the Bi-Pb sulphosalts.

Kirkiite [32] and **vurroite** [33] are characterized by a partial substitution of Bi by As in the crystal structure, a feature rare in hydrothermal sulphosalt minerals. The former appears in short prismatic crystals and the latter in slender needle-like crystals, both among the smallest crystals in this sulphosalt association. The sulphosalts from Vulcano are specific in having small amounts of Se substituting for S. Another unusual feature is that some of them have also Cl substituting for S (galenobismutite, lillianite) [26] or playing a distinct role in the crystal structure (vurroite) [34] (**Figure 4**).

3.4. Halides

Halides are abundant in some fumaroles and some of them appear commonly in fumaroles (e.g. halite and salammoniac). Where the halides are abundant, they usually appear with a number of species many of which are unique for the fumarolic environment or have it as the main mode of occurrence. As compounds with predominately ionic bonding, they mostly are colourless or light colour and are relatively soft. Characteristic for fluorides in fumaroles is the partial substitution of F by OH. In chlorides, the substitution of OH for Cl is rare or non-existing due to the difference in ionic sizes. When present together, Cl, OH, and O play distinct structural roles and form oxy- or hydroxychlorides. Br and I often partly substitute Cl. Among complex fluorides, the groups of borofluorides, aluminofluorides, and silicofluorides can be defined. Finally, halides in combination with other anions, usually of complex type (like $[SO_4]^{2-}$) also exist in fumaroles. Degassing dynamics of Cl, F and other halogens is a complex function of physical and chemical magma conditions [35] and can vary largely between different volcanoes. Cl generally degasses faster than F [36] and the abundance of H_2O enhances it further [37], which can produce a temporal segregation of the major amounts of chlorides and fluorides in the fumaroles after volcanic eruptions. This, however, can be modified if other sources than magma contribute to gas production. Significant amounts of fluorides appear in most of the Icelandic volcanoes. They are less abundant, but still in important quantities on Vulcano, whereas they are rarer on Vesuvius and Etna. Alumino-fluorides are characteristic for all Icelandic volcanoes (except Askja that does not have registered fluorides). Fumaroles on Hekla contain also significant silicofluorides. They are found on Vulcano as well, but here more characteristic are borofluorides. Contrary to fluorides, chlorides are more important in Italian fumaroles (especially Vesuvius and Vulcano) than in Icelandic ones. On Icelandic volcanoes, they were present in important quantities in the first fumaroles after the eruptions, but a decrease with time is also observed while fumaroles still were producing significant amounts of fluorides (El, H). An important thermodynamic distinction exists between the most abundant chlorides in fumaroles, where those of alkali elements represent the high-temperature product, whereas salammoniac characterizes the low-temperature fumaroles. The border line is approximately at 300°C.

Sylvite and **halite** form a complete solid solution at temperatures higher than approximately 480°C and limited solid solution at lower temperatures with higher solubility of Na in sylvine than K in halite. This is often observed in fumaroles and can be deduced from the shift of the powder diffraction maxima. Halite is much more abundant than sylvite. Su [1]: in crusts and stalactites with Ca and Na sulphates. F: crusts or powdery covers of sub-mm cubic crystals

http://dx.doi.org/10.5772/64129

with anhydrite, gypsum and other sulphates. Ve [9]: halite and sylvite are present in high-temperature "dry fumaroles" as earthy or dendritic crusts, rarely as crystals. Et [38]: Halite appears in stalactites and concretions in volcanic tubes accompanied by sylvite; El, H, A, Kr: halite is common in crusts on lava [39].

Figure 5. Salammoniac, Etna. Sample from the Natural History Museum in Copenhagen.

Salammoniac (CsCl structure type) (**Figure 5**) is one of the characteristic minerals in low-temperature fumaroles. Its sublimation temperature is 338°C. El [1]: the main constituent of white and yellowish crusts on lava shortly after eruption, but 15 years later no more present. H [1]: one of the main first fumarolic minerals, but already after one year disappeared from the fumaroles. Ve [14]: the representative main mineral of a type of fumaroles mostly on lower lava flows and rarely close to the crater with the temperature around 300°C. Vu [40]: the enrichment in Br follows the enrichment in the magmatic component of the gases. Crusts and aggregates of colourless soft isometric crystals sometimes reaching mm size. Also A, Kr, CF, Et. Typical accompanying minerals are cryptohalite (El, H) sassolite and sulphur (Vu), mascagnite and As sulphides (CF). Isostructural is **lafossaite** [41]; Vu: small grey-brown crystals (<100 μm) covering sulphosalts and pyrite or as opaque crusts; Ve [42]: <100 μm colourless cubic crystals, very rare.

Sellaite, El: in a brown crust with ralstonite and fluorite covering white microcrystalline anhydrite; Ve [43]: in ejected blocks with anhydrite; Et [43]: with fluorite. Very rare. **Chloro-magnesite** and isostructural **scacchite**: very rare, with halite and sylvite (Ve [9]). **Fluorite** is common in fumaroles. Su [1]: the main fluoride in a lava tube and the only fluoride on the

inner wall of a nearly closed crater, but not on the surface of lava where ralstonite is the dominating fluoride. H [1]: it is fairly common but subordinate to ralstonite and jakobssonite. Ve [44]: it is observed on pre-existing tenorite and rare. El: in a brownish crust with ralstonite and sellaite. Very rare. **Oskarssonite** [45] is the stable trigonal low-temperature form of AlF_3 with a perovskite-type framework of AlF_6 octahedra. El: in thick white microcrystalline crusts with other fluorides, opal, and anatase, more abundant than ralstonite in late fumaroles due to decreased amounts of Na and Mg in the gases and rock. Chemical analysis reveals partial replacement of F by OH, consistent with observations by Rosenberg on synthetic material [46]. **Parascandolaite**, Ve [47]: in colourless transparent sub-mm cubic crystals. Very rare.

Molysite Ve [9]: in yellow and red covers of the altered rocks near the crater. **Carnallite**, Su [1]: in a yellow-brown stalactite together with K-enriched halite. **Eriochalcite**, Ve [9]: rare blue wool-like aggregates together with other Cu minerals. **Ammineite**, Ve [48]: bluish crusts on altered tenorite together with opal and artroeite. Very rare. **Chloraluminite**, Ve [14]: small rhombohedral or prismatic crystals in high-temperature fumaroles. Very rare.

Ferruccite and **avogadrite** (Ve [43]) are very rare fumarolic borofluorides. **Barberiite**, Vu [49]: globular aggregates of colourless platy sub-mm crystals. With sulphur, salammoniac, sassolite, malladrite, and realgar.

Rosenbergite, H ([1]: mineral HM): in yellow to brown crusts with other fluorides. Rare. El: secondary hydration phase on oskarssonite. Very rare. **Mineral HI**, isostructural to rosenbergite. H [1]: in yellow to brown crusts together with its polymorph **mineral HU** [1] and other fluorides. Both rare. **Pachnolite**, H [1]: in a yellow/brown/green crust with ralstonite. **Gearksutite**, Vu [50]: in veins, impregnations, pockets, and concretions as alteration product of plagioclase under influence of F-rich solutions; Ve [48]: on post-1944 eruption fumaroles.

Jakobssonite [51] (mineral HA [1]) H, El, F, Kr: white crusts or thin overgrowths of sub-100 μm acicular crystals together with leonardsenite, ralstonite and other alumino- and silicofluorides. Common. Less abundant are **leonardsenite** [52] in orthorhombic-prismatic colourless crystals, and the presumed new mineral **HG** [1] in rhombic-dodecahedral crystals, both sub-100 μm. In similar associations as jakobssonite (H, El). The latter is identical to the synthetic compound of the same composition [53]. **Coulsellite**, Ve [47]: accompanies parascandolaite. **Thermessaite** [54] and **thermessaite-(NH_4)** [55] Vu: in medium temperature fumaroles (around 300°C) in sub-mm colourless prismatic crystals associated with alunite, sassolite, anhydrite, and metavoltine. Very rare.

Ralstonite has a crystal structure consisting of a pyrochlore-type framework of AlF_6 octahedra, with Al partly substituted by Mg, and Na and H_2O in framework cavities [56]. Common, dominating among fluorides in microcrystalline yellow crusts on Iceland (**Figure 6**) (H, El, Su [1]; F, Kr). The presumably new mineral HS [1] (H) shows the same diffraction characteristics as Rosenberg's AHF phase [46] with the composition $Al(F,OH)_3(H_2O)_n$ isostructural to ralstonite. The compositional range of ralstonite is still not sufficiently investigated and it is not clear if HS is a new mineral or a variant of ralstonite. The presumed new mineral **HH** (El, H [1]): thin platy colourless crystals of hexagonal habit up to over 100 μm in diameter in the surface part of the fumaroles. The composition and crystallography are preliminary deter-

http://dx.doi.org/10.5772/64129

mined. Rare. The presumed new mineral **HB** (H, El [1]): in white to yellowish crusts typically with ralstonite. Composition and crystallography unknown. Fairly common. The presumed new mineral **HD** (H, El, Su [1]) is probably an ammonium-free variant [57] of the zeolitic $NH_4Fe^{2+}Fe^{3+}F_6$ with a pyrochlore framework of FeF_6 octahedra [58]. In yellow to brownish crusts mixed with alumino- and silicofluorides. Fairly common. **Meniaylovite**, [59] is a minor constituent in yellow to brownish crusts in association with various other fluorides (Su, El, F, Kr). **Cossaite**, [60] Vu: only two 100 μm crystals found in a medium-T (~350°C) fumarole.

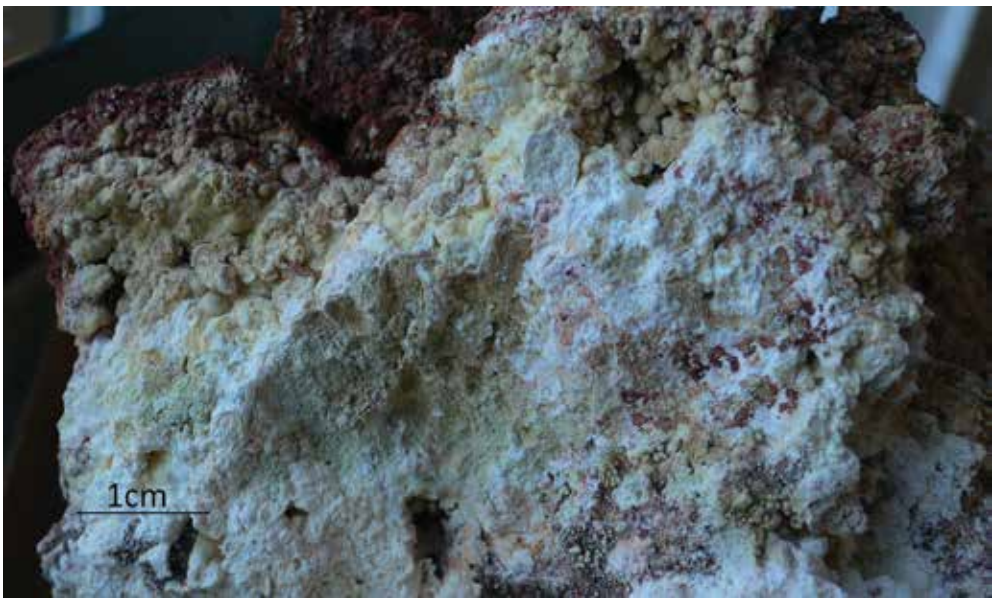

Figure 6. Fluoride crust from Eldfell. Mixture of ralstonite, jakobssonite, oskarssonite and other minor fluorides.

Malladrite, H [1]: fairly common in yellow crusts with ralstonite and jakobssonite; El [1], Kr: rare, in a yellow-brown crust with ralstonite; Vu [49]: rare, in association with barberiite. **Hieratite**, Vu [61]: in small colourless crystals with hexahedral habit associated with sulphur, realgar, sassolite, and several sulphates. Also Ve [43], H [1]. Rare. **Demartinite**, Vu [62] polymorph of hieratite, probably metastable. In colourless hexagonal pyramidal sub-mm crystals. **Heklaite**, H [63]: fairly common with malladrite and sometimes hieratite, because crystal structure differences prevent miscibility of Na and K silicofluorides. **Cryptohalite**, Ve [14]: in colourless cubic or octahedral crystals. Typically follows salammoniac, like on H and El in the first fumaroles [1]. **Bararite** is the low-temperature polymorph of the former, stable under 5°C. Found with salammoniac and cryptohalite (H). Probably a climatic influence. Also Ve [43]. Very rare. Presumed new mineral **HT** [1] is identical with synthetic $FeSiF_6(H_2O)_6$. H: very rare aggregates of micron-sized granular crystals overgrown with aggregates of HU crystals. **Knasibfite**, Vu [64]: with hieratite, avogradite and demartinite in low temperature fumaroles. Very rare.

Chlormanganokalite, Ve [14]: rare yellow crystals in high-temperature fumaroles. **Erythrosiderite**, Ve [14]: rare, in stalactites and crusts of tabular and pseudooctahedral red-orange deliquescent crystals in medium- and high-temperature fumaroles. **Kremersite**, Ve, Vu, Et [43]: rare small orange crusts. **Mitscherlichite**, Ve [43]: very rare in greenish-blue thin crusts. **Melanothallite**, Ve [9]: in rare thin black scales. **Atacamite**, Ve [14]: fairly common in thin green crusts or small prismatic crystals on lava. **Paratacamite**, Ve [9]: fairly common green alteration of tenorite. **Connellite**, Ve [65]: very rare, in post-1994 eruption fumaroles. **Cumengéite**, Ve [44]: very rare small transparent crystals of deep blue colour, adamantine lustre and pseudocuboctahedral habit, with tenorite, gypsum, and cotunnite. **Bismoclite**, Vu [22]: very rare sub-mm brilliant dipyramidal or tabular anatase-like orange crystals. **Lucabindiite**, Vu [8]: rare μm-size platy colourless transparent crystals with samammoniac, sulphur, and arsenolite. **Cotunnite**, Ve [9, 14]: rare colourless lustrous acicular crystals, scales, arborescent aggregates and fused masses, sometimes as pseudomorphs after galena in the high-temperature fumaroles. Vu [66]: variously coloured, fairly common in association with challacolloite. **Pseudocotunnite**, Ve [9]: very rare thin crusts and needles. Not fully crystallographically characterized species. **Challacolloite**, Ve [14]: rare colourless acicular crystals with adamantine lustre in HT fumaroles; Vu [66]: colourless to yellow, red, and brown, fairly common. **Hephaistosite**, Vu [67]: rare aggregates of pale yellow-green tabular crystals associated with Bi and Pb sulphides and chlorides. **Brontesite**, Vu [68]: very rare minute white tabular crystals. **Panichiite**, Vu [69]: very rare minute colourless to pale yellow octahedral crystals with adranosite, alunite, anhydrite. **Steropesite**, Vu [70]: very rare yellow-green minute crystals or crusts covering lafossaite. **Argesite**, [71] Vu: in sub-mm pale yellow very rare crystals in association with bismuthinite.

3.5. Oxides and hydroxides

Oxides are mostly products of reaction of gases with scoria, lava or other rocks in which fumaroles form and in lesser amount form as sublimates. The leaching of lava by aggressive fumarolic gases can lead to material consisting exclusively of oxides of Si, Al, Fe, and Ti, opal-cristobalite, corundum, hematite, and anatase, respectively, mixed with anhydrite (in Icelandic fumaroles) or alunite (in Greek fumaroles).

Tenorite, CuO, Ve [14]: lamellar, leaf-like or fan-like aggregates of crystals of a black metallic appearance in the HT fumaroles (T > 400°C [72]); Et [38]: thin scales with hematite and polyhalite in volcanic tubes. Rare. **Spinel, $MgAl_2O_4$**, El: very rare, in a cellular brown crust consisting mainly of hematite, also accompanied by corundum, anhydrite and steklite. **Magnesioferrite, $MgFe_2O_4$**, and **magnetite, Mg_3O_4**, Ve [9]: minute iron-grey crystals. Rare. **Hausmannite, Mn_3O_4**, Ve [9]: rare thin brown coatings on lavas. **Minium** Ve [9]: very rare dusty red layers cementing volcanic conglomerate. **Corundum**, El: one of the main constituents of the wall rock (with cristobalite, hematite, and anhydrite) of a fumarole (**Figure 7**). **Hematite:** abundant (Su, El, H, F, Ve, Et, M, Sa) and the main reason for the red colour of scoria- and lava-bearing fumaroles. Mostly a decomposition product; also a sublimate in small black crystals with metallic lustre (El). **Ilmenite**, H [1]: in a brownish crust with hematite and

http://dx.doi.org/10.5772/64129

fluorides. **Pseudobrookite**, El: very rare, admixture in a sample of white to grey granular to earthy crust of cristobalite and anhydrite on a substrate of hematite.

Figure 7. Hematite (red) and corundum (white) with opal in the altered lava on Eldfell.

Opal is common in all fumaroles. Primarily a product of decomposition of silicate minerals, but observed amorphous material could also be a primary glassy part of lava. In a sample from El, opal-CT forms the compact part of the leached lava, whereas opal-A fills holes as hydrothermal deposit. Opal is often associated with **cristobalite** (El, CF, Et, So, M, Sa, N) or **tridymite** (Et, Sa, N). They could also be products of fumarolic reactions or just unaltered remnant of lava. **Quartz** is absent in the majority of fumaroles but abundant in some (M, N, El). Mostly remnant of the primary rock, but appearance as granular crust suggests also secondary origin (M). **Anatase:** fairly common in late fumaroles with other oxides (El); rare in the altered rock with quartz, sericite and alunogen (M). Analyses of partly to fully leached lava on Eldfell show that TiO_2 remained as the only other component besides SiO_2 in the opalized rock, which shows it to be relatively immobile [1]. **Rutile**, high-temperature polymorph of TiO_2, stable over 600°C at atmospheric pressures, is rarely observed (M, N) probably primary from lava.

Portlandite, Et [38]: coralloid concretions with calcite in a volcanic tube. **Gibbsite**, Ve [9]: with basanite in hexagonal scales. Its polymorph **doyleite** was confirmed by XRD in one sample from Surtsey, in association with hematite [1].

3.6. Carbonates

Carbonates are rare constituents in fumaroles. It might look strange considering how abundant CO_2 is in volcanic gases, but the scarcity of solid products is due to the typical high acidity of

the fumarolic environments making most carbonates unstable. Where they appear in significant quantities, specific conditions are present, for example, low acidic or even basic environments and high water activity, like in the case of occurrences of Na carbonates on Vesuvius or calcite on Surtsey and Etna.

Calcite is the most frequent carbonate in fumaroles. Common in caves and cavities of lava where steam emanations were vigorous (Su [1]). Fairly common in stalactites and concretions in volcanic tubes (Et [38]). Fairly common in altered rock with **magnesite** and **dolomite** (So [73]). **Hydromagnesite**, Su [1]: in a white botryoidal crust with calcite and fluorite in a lava tube. **Aragonite**, So [73]: rare, with anhydrite and Fe-Mg hydrous sulphates. **Cerussite** accompanies parascandolaite (Ve [47]). **Azurite**, Ve [9]: blue covers on older lavas. **Sodium carbonate hydrates** appear in the high-temperature fumaroles on Vesuvius dominated by potassium and sodium salts [9, 14]; **thermonatrite** in white crusts, sometimes stalactites, **natron** in transparent granules and small translucent crusts as efflorescence in the interior of lavas, and **trona** in small tabular pseudohexagonal crystals or whitish crusts. The latter was also found with halite in concretions in a lava cave on Etna [38].

3.7. Borates

Over 210 boron minerals are known. Among them only three borofluorides mentioned earlier and four borates are observed in fumaroles. The boric acid, **sassolite**, melts at 171°C and is therefore constrained to the low-temperature fumarole. Ve [9]: rare thin colourless scales together with gypsum or sulphur or realgar; Vu [10]: common in colourless plates, up to 5 mm or white covers with sulphur and salammoniac in low-temperature fumaroles. Exploited in the past as the raw material. **Metaborite** and **clinometaborite**, Vu [74]: with sassolite and andranosite in a medium-temperature fumarole (~250°C). **Ameghinite**, Et [38]: very rare, in macrocrystalline crusts with thenardite.

3.8. Sulphates

Together with halides sulphates are the group of minerals with the largest number of various species in fumaroles. Calcium sulphates, such as gypsum and in lesser grade anhydrite, are common and in many fumaroles very abundant. Sodium sulphate, thenardite, and K-Al sulphate, alunite, can also appear in large quantities in some types of fumaroles. Specific for sulphates is existence of often several hydrous forms related to the anhydrous ones. They possess different stability fields that depend on the humidity and temperature, and can, therefore, appear in various zones of the same fumarole. The anhydrous sulphates of fumarolic origin are generally instable and readily hydrate under atmospheric conditions (anhydrite and barite group minerals are exemptions).

Chalcocyanite, Ve [9]: fairly common in greenish to sky-blue crusts, rapidly changing to chalcanthite. **Vanthoffite**, F: main phase in a white "snow-like" compact crust on lava with thenardite, löweite, and glauberite; El: in white to greyish crusts with thenardite, anhydrite, glauberite, and other sulphates. Presumed new **mineral EN**, F: in orange spongy crust together with halite, gypsum, and a mineral from voltaite group; El: in paragenesis with presumed new

http://dx.doi.org/10.5772/64129

mineral EA, anhydrite, langbeinite, tamarugite, and hexahydrite. The composition and crystallography of **EN** and **EA** is confirmed by SEM-EDS and XRD. They form crusts of intermixed < 10 μm isometric grains and leaves, respectively. Presumed new **mineral EI**, El [1]: in saussage-like thin fragile hollow white or red (coloured by hematite) crusts, which easily hydrate to löweite and hexahydrite when exposed to the humid atmosphere. Composition confirmed, but crystal structure unknown. **Langbeinite**, El ([1]: mineral EB): in white crusts on scoria together with sulphates or with fluorides at temperatures from 80 to 230°C; F: With anhydrite in a glassy vesicular crust covering lava. **Manganolangbeinite**, Ve [9]: in microscopic pink tetrahedra and stalactites with thenardite and Na-K chlorides. **Steklite**, [75] El: accompanying hematite with corundum, spinel and anhydrite. Very rare. **Pyracmonite**, [76] Vu: aggregates of sub-mm colourless elongated hexagonal prismatic crystals with salammoniac and kremersite in a medium-temperature fumarole (~250°C). **Aluminopyracmonite**, Vu [77]: very rare globular aggregates of prismatic colourless crystals. **Eldfellite**, [78] El: in a frothy yellow to brown crust together with tamarugite, EN and anhydrite. Very rare. Isostructural **yavapaiite**, Vu [79]: very rare minute pink crystals in association with other Fe sulphates.

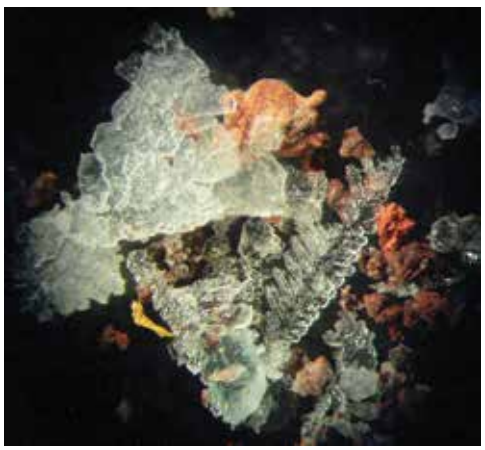

Figure 8. Dendritic aphthitalite crystals with hematite and bluish granular Cu-enriched metathenardite. Field of view 1 cm.

Thenardite is a frequent mineral in fumaroles. In Iceland, four different parageneses were observed: with gypsum, glauberite, and minor hydrous sulphates (Su, H); with metathenardite, aphthitalite, and glaserite (F, Kr, Su) with vanthoffite, anhydrite, and halite (El); with halite and minor other sulphates (A). In stalactites (Su, Ve, Et), white to lightly coloured friable microcrystalline crusts or in glass-like crusts and visible crystals when in association with aphthitalite and glaserite. The latter association includes its high-temperature polymorph **metathenardite**, stable over 271°C. Green due to Cu content, rare (F, Kr). **Aphthitalite (Figure 8)**, Ve [9], F, Kr: fairly common in millimetre size dendritic "snow flake" crystals on lava variously coloured from white to yellowish and greenish or bluish due to Cu content; Et [38]: in macrocrystalline crusts and stalactites in volcanic caves. **Glaserite**, F, Kr: in platy crystals mixed with aphthitalite. Rare. The crystal name was abandoned [80], although it is a

distinct LT phase (<150°C) in the phase system [81] with a distinct crystal structure [82]. **Palmierite**, Ve [9]: in minute hexagonal scales together with aphthitalite, ferronatrite, jarosite, and euchlorine in the "dry" fumaroles. **Mascagnite**, Ve [9]: in white crystalline crusts mixed with salammoniac, halite, and sylvite in the high-temperature fumaroles; Vu [10]: rare sub-mm colourless platy crystals with adranosite and sassolite.

Mercallite, Et [83]: in a lava tunnel; F: in fine-grained colourless crystalline aggregates on the bluish dendritic thenardite with Kröhnkite. Rare. Presumed new **mineral FB** appears with the former (F). **Therasiaite**, Vu [84]: in very rare brown equant sub-mm crystals with salammoniac. Instable.

Figure 9. Gypsum crystals. Soussaki.

Anhydrite, Su, F, El, Vu, So: common, with hematite the main constituent of the altered wall-rock, in compact to earthy materials mixed with other minerals or as separate acicular crystals; Ve [14]: rare in tabular colourless or whitish crystals. **Gypsum (Figure 9)** is one of the main fumarolic minerals in general. It forms at lower temperatures because it dehydrates already at 120–130°C. In various forms: large (> cm) crystals (So), crusts of various thicknesses from thin colourless and glassy to white or lightly coloured massive, also as efflorescence and in various associations (Su, El, CF, Ve, Et, Sa, F, N, Vu). Rare on H and M, not observed on A. **Bassanite** is stable to about 200°C. Ve [14]: in altered volcanic bombs as acicular white crystals; Su [1]: in crusts with anhydrite and gypsum; El: mixed with oskarssonite in a yellowish earthy material. Rare. Isostructural **omongwaite** [85] Su ([1]: mineral SA): in a solid white to colourless

http://dx.doi.org/10.5772/64129

crust on lava together with halite, anhydrite, glauberite, and other sulphates. **Glauberite**, Su,H [1] F: in small quantities accompanying thenardite and/or anhydrite. Very rare. **Barite**, M: mixed with alunite in a yellowish-white earthy crust that covers quartz crystals. Rare. **Celestite**, Et [38]: rare, in concretions in the lava caves. **Anglesite**, Ve [9]: rare, in small pale violet crystals with acicular and pseudooctahedral habit; Vu [13]: very rare in association with Bi oxy-sulphates.

Dolerophanite, Ve [9]: very rare dark brown crystals. **Antlerite**, Ve [9]: very rare, in grass-green aggregates of minute crystals as the alteration product of dolerophanite. **D'ansite** [86], A [1]: in a stalactite together with thenardite, halite, löweite, and blödite; Et [38]: in a macro-crystalline crust accompanying thenardite in a lava cave. Very rare. **D'ansite-(Mn)** [87] Ve: very rare colourless tris-tetrahedral crystals, with halite and aphthitalite. **D'ansite-(Fe)** [87] Vu: very rare aggregates of minute isometric colourless crystals with sassolite. **Aiolosite**, Vu [88]: very rare colourless acicular crystals in a medium-temperature (250°C) fumarole. **Natroalunite**, Su [1] Sa: in white-greyish crust on the inner wall of a crater, with opal, gypsum, and fluorite. **Alunite** is one of the main fumarolic minerals on Greek islands. In granular aggregates, dendritic crystals, flakes, white powdery to compact cover on lava, colourless, orange and red glassy crusts, white and yellowish botryoidal crusts, and grey cauliflower-like crusts accompanied by sulphur and alunogen and rarely by jarosite or barite, rhomboclase, and voltaite (M); constituent of the altered rock and around the fumaroles on the crater floor (N); in alteration with natroalunite accompanies sulphur in different fumaroles (Sa); in a yellow crust on lava block with halite, sylvite, gypsum, and erythrosiderite in the low-temperature fumarole (Ve [9, 14]); rare, in concretions in lava caves (Et [38]). **Natrojarosite**, El: rare in altered scoria with hematite, anhydrite, and opal with ralstonite, fluorite, and oskarssonite. **Jarosite**, El [1]: in yellow crusts together with gypsum, anhydrite, and fluorides; Ve [9]: in thin crusts with aphthitalite, euchlorine, and some chlorides; M: mixed with alunite. Rare. **Adranosite** and **adranosite-(Fe)**, Vu [89, 90]: very rare aggregates of colourless or pale yellow, respectively, acicular sub-mm crystals in medium-temperature (~250°C) fumaroles. **Euchlorine**, Ve [9]: fairly common in grass-green to emerald-green encrustations and tabular crystals together with chalcocyanite and with metavoltine. **Chlorothionite**, Ve [9]: rare greenish blue to green crusts. **Linarite**, Ve [9]: rare microscopic crystals in gypsum. **Balićžunićite** [13] and **leguernite** [91]: in cavities of a sample taken from the high-temperature fumarole (T = 600°C) in minute transparent prismatic crystals in association with anglesite and in the vicinity of sulphosalt formation. Very rare.

Kieserite, Su [1]: very rare, in association with halite, kainite, löweite, and pentahydrite in stalactites in a lava tube; Et [38]: very rare in stalactites in a lava cave. **Rozenite**, So [73]: the main mineral in white efflorescences. **Chalcanthite**, Ve [9, 14]: rare sky-blue granular masses or crusts, a product of alteration of primary fumarolic Cu minerals. **Pentahydrite**, F: very rare white sublimate on volcanic ash together with halite and **hexahydrite**: in a spongy yellowish crust with tamarugite and kainite (F); a hydration product of mineral EI and in a white crust with löweite and anhydrite (El); rare constituent of concretions in association with thenardite in lava caves (Et [38]); among sublimates at the exhausts of fumarolic vents (So). **Nickelhexahydrite**, So [73]: trace amount in a sample with römerite. **Römerite**, So [73]: the main mineral

in green efflorescences. **Coquimbite**, So: rare in a grey earthy mass mixed with gypsum, anhydrite rhomboclase, and voltaite; Sa: with rhomboclase and tamarugite accompanying alunogen. **Halotrichite:** fairly common silky white needles (CF [PSCF], N). Characteristic is the "daisy" form: halotrichite "petals" growing on the core of globular yellow core of rhomboclase (N) or presumably coquimbite [15](**Figure 10**). **Pickeringite**, CF [15]: in thick wool-like aggregates of needle-like white crystals on the wall of a cave; Et (ferroan) [83]: in an eruptive fracture (*T* around 100°C) and on the rim of the NE crater (*T* 300–400°C). **Meta-alunogen**, Et [38]: with thenardite in stalactites in a lava cave; N: in colourless platy dendritic crystals together with alunogen, tamarugite, and voltaite on the floor of the crater. **Alunogen**, Ve [9, 14]: with kalinite and as silky fibrous masses in low-temperature fumaroles; M: accompanying alunite; Sa: alternating with alunite and natroalunite as the main mineral in crusts covered by sulphur crystals; N: around the fumaroles on the crater floor. **Mirabilite**, Su [1]: in a colourless crust with thenardite in a lava tube; Ve [9]: forming from solutions and by recrystallization of fumarolic salts; Et [38]: stalagmites in a lava cave. **Campostriniite**, [92] Vu: very rare white prismatic micrometre crystals, with adranosite, sassolite, and other Bi minerals.

Figure 10. Yellow globules of rhomboclase with acicular halotrichite, Nisyros.

Rhomboclase, So: rare constituent of the earthy mass with gypsum, anhydrite, coquimbite, and voltaite; M: accompanying alunite; Sa: accompanying alunogen together with coquimbite and tamarugite; N: microscopic yellow globular aggregates associated with silky needles and plates of halotrichite. **Voltaite** is of a dark-green or blue to black colour due to its content of mixed-valence iron. Ve [9, 14]: rare granular aggregates of cubic crystals in the low-temperature fumarole; CF [15]: rare black lustrous crystals mixed with halotrichite; So: rare part of a grey earthy mass; M: very rare together with alunite, alunogen, rhomboclase, and pyrite; N: in granular aggregates on the crater floor with tamarugite, alunogen, and meta-alunogen. A light-coloured mineral from the voltaite group is observed in H and F samples but not

characterized in detail. **Löweite**, Su [1]: rare, in stalactites together with halite and mineral SH or Mg sulphates; A [11]: with other Na-Mg sulphates in a stalactite; El: a hydration product of mineral EI. **Eugsterite** [93] Su [1]: rare, in a soft white-to-yellow crust containing also glauberite, anhydrite, gypsum, thenardite, and Blödite. **Hydroglauberite** [94] H [1]: component of a yellow-whitish crust on lava together with thenardite and glauberite. **Syngenite**, Ve [14]: rare transparent minute tabular crystals; Et [38]: very rare, with thenardite in stalactites in a lava cave. **Kröhnkite**, F,Kr: rare, in bluish dendritic crystalline crusts with aphthitalite, glaserite, metathenardite, and thenardite. **Ferrinatrite**, Ve [9]: very rare thin fibres with adamantine lustre with aphthitalite and palmierite. **Cyanochroite**, Ve [9]: rare pale blue crystalline crusts.

Blödite, Su [1]: rare, mixed with Na-Ca sulphates and halite in stalactites and soft white-yellowish crusts; A [1]: rare, in a stalactite together with other Na-Mg sulphates; El: very rare hydration product of mineral EI; Et [38]: rare in concretions, stalactites, and macrocrystalline crusts, primarily with thenardite in lava caves. **Polyhalite**, Su [1]: very rare, in a solid white to colourless crust made of halite, anhydrite, and other sulphates; Et [38]: very rare in polycrystalline aggregates with hematite and tenorite in a lava cave. **Tamarugite**, El [1]: rare, accompanies minerals EN and EA, most probably as their hydration product and also accompanying eldfellite; F: very rare in a yellowish spongy crust with a smooth glassy surface together with hexahydrite and kainite; Sa: rare, together with alunite, alunogen, rhomboclase, and coquimbite; N: on the crater floor together with voltaite, alunogen, and meta-alunogen. **Picromerite**, Ve [9, 14]: in white to colourless crusts of elongated minute crystals; Et [38]: very rare, in concretional crusts in a lava cave. **Metavoltine**, Ve [9, 14]: in thin yellow crusts of tabular hexagonal crystals associated with euchlorine. **Kalinite** [95] Ve [9]: rare white crusts in the sulfurous fumaroles. **Alum-(K)**, Ve [14]: rare whitish crusts or octahedral to cuboctahedral crystals in medium-temperature fumarole. **Kainite**, Su [1]: rare white to colourless crusts and stalactites in mixture with other Mg, Ca, and Na sulphates; A [11]: rare, in a stalactite with thenardite and halite; F: rare, in a spongy crust with tamarugite and hexahydrite. Presumed new **mineral SH**, Su [1]: rare, in a colourless to white crust with halite, anhydrite, glauberite, kainite, omongwaite, and polyhalite and in stalactites with halite and löweite. **Chessexite** [96] El [1]: rare, in white crusts with gypsum and ralstonite at 80–100°C.

3.9. Other minerals

Chlorapatite and **mimetite** are isostructural. The former was identified in a stalactite accompanying thenardite in a lava cave (Et [38]). The latter and **phoenicochroite** accompany parascandolaite (Ve [47]).

4. European fumaroles

4.1. Icelandic volcanoes

Iceland is one of the most active terrestrial volcanic regions, with eruption frequencies of ≥20 events per century. It is also one of the most productive with magma output rates of ~8 km^3

per century in historic time [97]. Volcanism in Iceland is caused by the interaction of the Mid-Atlantic Ridge and the Iceland mantle plume. This volcanism can be traced back to the opening of the North Atlantic at 61 Ma as evidenced by massive volcanism in East Greenland, Ireland, Scotland, and the Faroe Islands. The oldest volcanic rocks exposed in Iceland are about 16 Ma [98]. During Late-Pleistocene and Holocene times, some 41 volcanic systems have been active in Iceland and its insular shelf. They are confined to volcanic zones, which are either rift zones or non-rifting flank zones. Volcanic systems in the rift zones produce rocks belonging to the tholeiitic series, while rocks of the mildly alkalic and transitional alkalic series are confined to the flank zones [99]. The majority of volcanic rocks are basalts, but significant amounts of silicic and intermediate rocks have also been produced. Encrustations have been studied from the products of seven eruptions in five volcanic systems in Iceland (**Figure 11**).

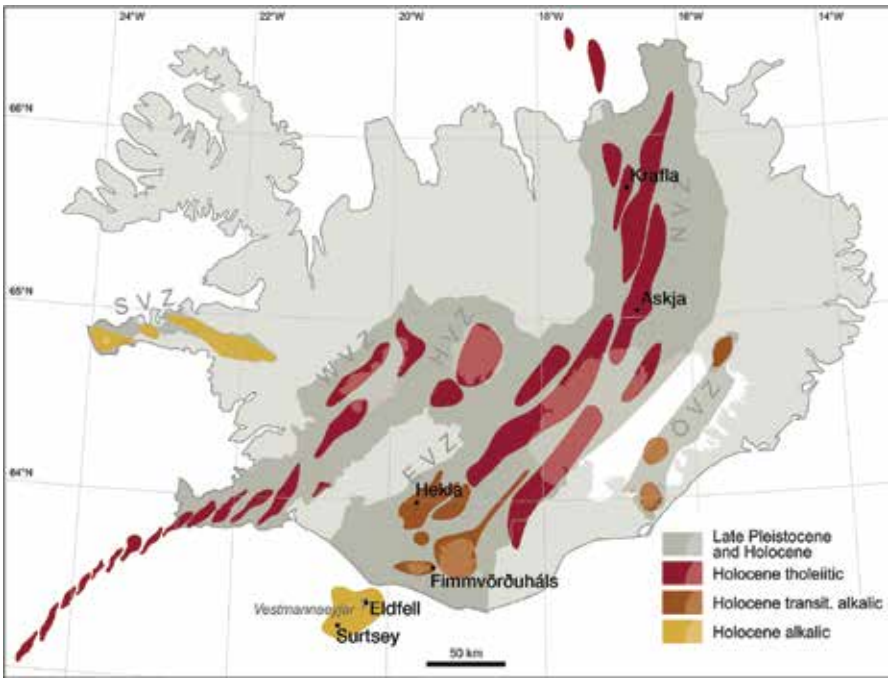

Figure 11. The volcanic systems of Iceland with the locations of investigated volcanoes.

4.1.1. The Vestmannaeyjar volcanic system

The Vestmannaeyjar archipelago represents the southernmost volcanic system in the eastern volcanic zone of Iceland. It is a partly submarine system-producing basaltic to intermediate rocks of the alkalic series. Encrustation samples from two separate eruptions were examined, the 1963–1967 Surtsey eruption and the 1973 Eldfell eruption.

The 1963–1967 Surtsey eruption. Surtsey is the south-westernmost island of the Vestmannaeyjar archipelago. It was constructed from the sea floor in a volcanic eruption occurring from

http://dx.doi.org/10.5772/64129

1963 to 1967 [100–102]. During the hydromagmatic explosive submarine phase of the eruption, from November 14, 1963 to April 4, 1964, alkali basalt tephra formed two crescent-shaped cones which merged. The eruption then evolved into an effusive alkali basalt lava phase which lasted until June 5, 1967. Two lava shields were formed with a thickness of 70–100 m. However, individual lava flow units are thin, usually only a few metres thick. The eruptive temperature of the lava was about 1140–1180°C. It is estimated that the total output of the 1963–1967 Surtsey eruption was 1.1 km^3 of basalt tephra and lava [102].

The surface encrustations on Surtsey were mainly deposited in two types of environments, as sublimates deposited directly from a gaseous state on lava and scoria at relatively high temperatures, and in a vapour-dominated system in lava craters and shallow lava caves, where steam emanation was vigorous [103]. Encrustation samples were collected in 13 expeditions from 1965 to 1998 [1]. One can recognize the following main mineral associations: 1. gypsum with thenardite, calcite, and fluorite; 2. halite with anhydrite, glauberite, thenardite, and Na-K-Mg hydrous sulphates; 3. ralstonite with other fluorides (**Figure 12**).

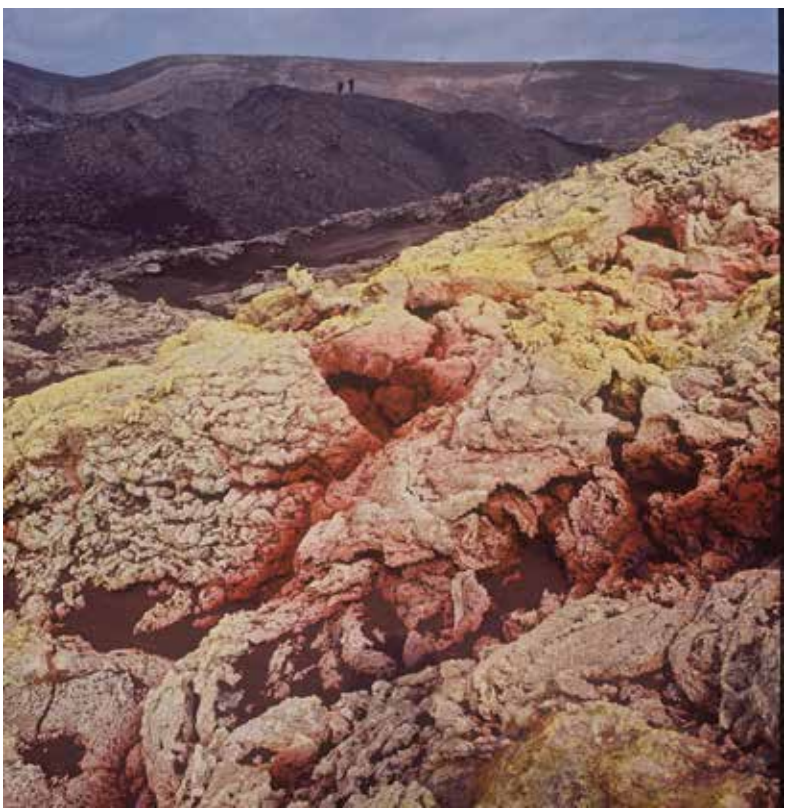

Figure 12. Surface encrustations on Surtsey in 1967. Photograph by H Bárðarson.

The 1973 Eldfell eruption. The Eldfell volcano is situated on Heimaey, the largest and the only inhabited island of the Vestmannaeyjar archipelago. The Eldfell eruption started on January

23, 1973, on a 1.5-km-long fissure, producing lava along its entire length. Eruptive activity quickly concentrated at the central part of the fissure and a scoria cone, Eldfell, was built up, reaching a height of 245 m asl. [104]. The Eldfell eruption ended on June 26, 1973. The magma was of hawaiite-mugearite composition [105]. At the end of the eruption, the lava covered 3.2 km^2, and the total output of lava and scoria was estimated to be 0.25 km^3 [106]. The Eldfell lava reaches a thickness of about 110 m at the eastern side of Eldfell, and large sections of the lava are 40–60 m thick. The eruptive temperature of the lava was 1030°C.

The Eldfell magma was more evolved than the magma erupted at Surtsey and as a result released a larger amount of volatiles. After the cessation of the Eldfell eruption, the extrusives and the feeder dikes have continued to release a considerable amount of gases, especially at the Eldfell scoria cone. The Eldfell lava is blocky, although large parts of it are covered with an apron of scoria. Early on, volcanic gases formed extensive encrustations on the surface of the lava and the first encrustations were already collected in February 1973 [39]. The lava encrustations on Eldfell were deposited directly as sublimates from a gaseous phase discharged from the cooling lava at a range of temperatures. Due to its thickness, the lava has been cooling down at a considerably slower rate than on Surtsey. The Eldfell crater is made up of coarse scoria mixed with volcanic bombs and lava fragments. When the crater was visited in June 2012, a narrow section of the crater rim was still very hot, reaching maximum temperatures of 290°C at 15 cm depth. Encrustation specimens were collected on the lava in 1973 and 1975, and at Eldfell crater between 1988 and 1995, and in 2009, all from the areas that were not affected by the cooling operations undertaken on the island during the eruption. The observed mineral associations are as follows: (1) (early) salammoniac, cryptohalite, gypsum, jarosite; (2) anhydrite, bassanite, gypsum; (3) anhydrite with ralstonite (later oskarssonite), jakobssonite and other fluorides; (4) anhydrite with Na-K-Al-Mg anhydrous and hydrous sulphates and (5) (late) anhydrite, hematite, corundum, anatase, opal/cristobalite.

4.1.2. The Eyjafjallajökull volcanic system

The Eyjafjallajökull volcanic system is located in the southern part of the eastern volcanic zone. It produces rocks belonging to the transitional alkalic series and consists of a ridge-shaped central volcano elongated E-W, reaching an altitude of 1651 m. It has a large summit crater flanked by mainly E-W-oriented eruptive fissures.

The 2010 Fimmvörðuháls eruption. Two connected eruptions occurred at Eyjafjallajökull in 2010. First, a basaltic fissure eruption occurred at Fimmvörðuháls on the eastern flank of the volcano. It started on March 20 and ended on April 12. Two days later, on April 14, an explosive eruption started in the summit crater of Eyjafjallajökull, which lasted until May 22nd [107]. The magma erupted at Fimmvörðuháls was a porphyritic transitional basalt, the majority of which solidified as aa-type lava, in addition to two scoria cones. The same type of basalt was involved in the explosive eruption at Eyjafjallajökull, where it was mixed with rhyolite, forming benmoreite and trachyte [108], much of which was dispersed as very fine-grained ash.

Encrustations were sampled at Fimmvörðuháls during the eruption, and at three separate times in the following months of 2010, and once in 2011. Very high gas temperatures (up to 800°C) were recorded during sampling. Volcanic ash from the Eyjafjallajökull eruption was

http://dx.doi.org/10.5772/64129

cemented into a crust on the hot surfaces of craters and lava. This provided favourable conditions for the formation and preservation of volcanogenic encrustations beneath the crust. During the eruption, thin white coatings were observed on the fresh lava. Such coatings also appeared on samples collected while hot. The coatings were found to be thenardite, a readily soluble mineral that is quickly washed away [109]. The mineral associations determined through the analysis of samples are as follows: (1) halite and sulphates (Na-K-Mg-Ca-Al) and (2) ralstonite with other fluorides (**Figure 13**).

Figure 13. Formation of fumarolic minerals at 575°C in a fissure on the main scoria crater on Fimmvörðuháls about 2 months after the eruption.

4.1.3. The Hekla volcanic system

The Hekla central volcano is one of the most active volcanoes in Iceland, with more than 18 eruptions recorded in historical time. It is the production centre of the Hekla volcanic system in south Iceland. It produces basaltic to intermediate rocks of the transitional alkalic series and intermediate to silicic rocks belonging to the tholeiitic series.

The 1947–1948 Hekla eruption occurred solely within the top fissure (Heklugjá) of the volcano. The eruption started on March 29, 1947 and lasted until April 21, 1948. About 0.2 km^3 of tephra was produced during the plinian phase of the eruption. Lava covered 40 km^2 and its volume was about 0.8 km^3 [110]. The chemical composition of the extrusives changed from transitional mugearite at the beginning of the eruption, to transitional hawaiite at the end. A large amount of gas and vapour emanated from the craters, especially Axlargígur at the SW shoulder of the volcano. The encrustation samples from the 1947–1948 Hekla eruption were collected from five localities during 1947–1952. Encrustations have been observed in many of the eruptions of Hekla. For example, Schythe reports large deposits of encrustations at the craters which erupted in 1845–1846 [111].

The 1991 Hekla eruption started on January 17 with a short-lived plinian phase that was accompanied with an effusive lava phase [112]. After two days of eruption, the volcanic activity was mainly restricted to a single fissure trending east-southeast from the top of the mountain. The eruption came to an end on March 11, 1991. The 1991 Hekla extrusives are transitional

mugearite [99]. On flat ground, the lava is of a block lava type; however, on the slopes of the mountain, it is mainly of an aa type. The lava has commonly a thickness of only 4-8 m on flat ground and covers about 23 km^2. The main crater is made up of coarse scoria mixed with volcanic bombs [112]. The total amount of tephra and lava produced is estimated to be 0.15 km^3. A considerable amount of volcanic gases and vapour was released during the eruption. Pollution of groundwater and rivers around the volcano was observed already a few days after the onset of the eruption, by the rise of concentration of fluorine, carbonate, sulphate, and other dissolved solids. The average content of soluble fluorine from tephra formed on January 17 was 1600 ppm [112]. Two lava surface localities and one lava cave were visited in January and March 1991. The most prolific area with respect to encrustations was on the eruption fissure above the main crater at 1105 m asl. The lavas, the main crater and the linear eruption fissure of the 1991 Hekla eruption cooled down to ambient temperatures at the surface in less than 10 years. The surface encrustations at Hekla were mainly deposited in two types of environments, as sublimates deposited directly from a gaseous state at relatively high temperatures on lava and scoria at the linear eruption fissure, and in a vapour-dominated system in the shallow lava cave where steam emanation was vigorous.

The observed mineral associations in fumaroles are as follows: (1) (early) salammoniac, cryptohalite, gypsum, sulphur; (2) ralstonite with jakobssonite and other alumino- and silicofluorides and (3) thenardite, anhydrite or gypsum, glauberite.

4.1.4. The Askja volcanic system

The Askja volcanic system is located in the Northern Volcanic Zone in the central highland of Iceland. It consists of a central volcano with nested calderas bisected by a volcanic fissure swarm. The youngest caldera was formed following a plinian eruption in 1875. The system produces mainly tholeiitic basalts, with minor rhyolite, dacite and hybrid intermediate rocks.

The 1961 Askja eruption occurred within the large Askja caldera. It was preceded by the formation of big solfataras on a N-S line along the eastern caldera wall of Askja, about 10 days before the eruption [113]. The volcanic eruption started along a fissure northwest of the solfatara area on October 26 and lasted until November 28 [114]. It was a small eruption, only producing about 0.1 km^3 of tholeiitic basalt lava. The lava, Vikrahraun, covered 11 km^2 and large parts of it are estimated to be only few meters in thickness.

Temperatures of 420°C were still measured at a depth of 20 cm at the crater in June 1962 [113]; however, in August 1962, all soluble salts had been washed away and, apparently, no new encrustations were being formed. Encrustations formed both at the lava surface and in caves but were apparently not widespread [115]. Óskarsson [39] studied samples collected in June 1962 and found encrustations of sulfur, sal ammoniac and an NH-Fe-Cl-compound at surface, and stalactites of metathenardite in lava caves. The 1961 Askja samples available to us, all of which were presumably collected during the summer of 1962, derive from two shallow lava caves. The observed mineral associations are as follows: (1) thenardite with halite and Na-Mg-K (chloro)sulphates and (2) salammoniac.

http://dx.doi.org/10.5772/64129

4.1.5. The Krafla volcanic system

The Krafla volcanic system is located in the northern part of the northern volcanic zone. It consists of a central volcano with rhyolite formations around the rim of a caldera. A volcanic fissure swarm bisects the central volcano. The rocks belong to the tholeiitic series ranging from olivine tholeiites to rhyolites.

The 1980 Krafla eruption. The Krafla fires were a major episode of rifting and volcanism in 1975–1984 [116]. The first years were dominated by rifting, dike injections, and minor eruptions. Five larger eruptions occurred in 1980–1984. The 1980 Krafla eruption started on July 11 on several discontinuous fissures on a 4 km long line. After the first day, it concentrated on the northernmost crater where the eruption continued until July 18. The tholeiitic basalt lava covered 5.3 km^2 and the volume is estimated to be 0.02 km^3. Encrustations were collected from lava surfaces on July 30, 1980. The observed mineral associations are as follows: (1) sulphur, salammoniac; (2) thenardite with aphthitalite and (3) ralstonite with other fluorides.

4.2. Italian volcanoes

Italy is one of the most volcanically active countries in Europe. Its recent and active volcanism is mainly connected with the convergence of the Eurasian and the African plate and the extension induced by the formation of the Tyrrhenian basin, which produced volcanism along the Tyrrhenian Sea, in Sicily and Sicily Channel, and on the Tyrrhenian Sea floor. This Plio-Quaternary magmatism exhibits an extremely variable composition and permits to distinguish various magmatic provinces, which differ in major and/or trace elements and/or isotopic compositions. The most important Italian localities showing a fumarolic activity belong to the Neapolitan area (Mt.Vesuvius and Campi Flegrei), to the Aeolian Arc (La Fossa Crater at Vulcano) and to the Sicily Province (Mt. Etna). In addition to these, a number of interesting areas with actual hydrothermal activity are present in Italy, but they have not been considered in this paper because nowadays they do not produce sublimates (**Figure 14**).

Figure 14. Map of the SE Tyrrhenian Sea with locations of volcanoes and fumarolic fields.

4.2.1. The Campanian Plain

The Neapolitan Province is located in the Campania Region, along the Tyrrhenian coastline, in one of the most densely populated active volcanic areas of the Earth. The geology of the area is prevalently represented by volcanics erupted from the Upper Pleistocene to present by Mt. Somma-Vesuvius on the east, by Ischia and Campi Flegrei volcanic fields on the west and by different ignimbrite eruptions (Campanian Ignimbrites) connected to fissural volcanism along fractures activated in the Campanian Plain. Campanian Plain is a waste graben bordered by Mesozoic carbonate platforms, which began to form in Late Pliocene but largely developed in Quaternary times. Its origin is related to the counter-clockwise rotation of the Italian Peninsula and the contemporaneous opening of the Tyrrhenian Sea, which generated a stretching and thinning of the continental crust accompanied by the consequent subsidence of the carbonate platform along most of the Tyrrhenian coast. The formation of the Campanian Plain was accompanied by the uplift of the central part of the Southern Appennines, in a regional stress regime generating NW-SE and NE-SW-trending faults and establishing the ideal conditions for magma to form and rise to the surface. With the exception of oldest volcanic rocks with calc-alkaline composition, erupted magmas younger than 400 ka are alkaline, with high potassium compositions erupted only at Vesuvius [117].

4.2.2. The Phlegrean Fields

Figure 15. As-sulphide fumarole at Pozzuoli, Campi Flegrei. Photograph by courtesy of Fabrizio Reale.

The Phlegrean Fields (Campi Flegrei: "The Burning Plain") are an area of active volcanism located about 25 km west of Vesuvius and 5 km west-southwest of Naples and consists of a large caldera formed about 35,000 years ago with the eruption of 80 km^3 of ash (the Campanian Tuff). The caldera is about 12 km in diameter and includes a series of mostly monogenetic pyroclastic vents. After the caldera formation, with a progressive decrease in volume of the emitted products, the eruptive centres migrated towards the centre of the caldera. There were two historic eruptions in the area. The 1198 phreatic eruption was at Solfatara, a pyroclastic cone formed about 4000 years ago and still in a fumarolic stage. The last one in 1538 produced

http://dx.doi.org/10.5772/64129

the new pyroclastic cone of Monte Nuovo. It was explosive and generated pyroclastic flows, but also produced a lava lake and lava flows. After that, the Phlegrean area is characterized by fumarolic activity and periodic episodes of unrest involving seismic activity and slow ground motion (bradyseism) with uplifts. Spectacular fumaroles, with temperatures rising to 160°C, are mainly located at the Solfatara cone, but occur also along active fractures throughout the area both on land and in the Gulf of Pozzuoli. They belong to a widespread geothermal system, which is characterized by a geothermal gradient of up to 170°/km, numerous superimposed aquifers, and a zoning typical of hydrothermal mineral deposition [118]. The predominance of magmatic volatiles over the meteoric water in the volcanic fluids is suggested by isotopic compositions, as well as by the modelling of the fluxes of CO_2 and S. The mineralogy of Solfatara is generally characterized by sulphur and a sulphate paragenesis (alunite and alunogen with other sulphates) [119]. At La Bocca Grande vent, where the vent temperature reaches 160°C, arsenic sulfides (realgar and pararealgar) are deposited [120] (**Figure 15**).

4.2.3. Mt. Somma-Vesuvius

The present Somma-Vesuvius is a moderate size composite central volcano rising more than 1200 m asl. The activity of Monte Somma has been characterized by a series of sub-Plinian and Plinian eruptions alternating with long quiescent periods lasting from centuries to millennia, followed by periods of semipersistent activity characterized by lava effusions and low-energy explosive eruptions in the past 4 kyr. The Plinian AD 79 eruption [121] broke a long period of quiescence and represented one of better-known devastating events in the Mt. Vesuvius history. The recent Vesuvius cone has grown within the oldest Mt. Somma caldera possibly after this eruption. After it, the volcano featured two sub-plinian events in AD 472 and 1631 [121]. Throughout the following centuries, Vesuvius activity was characterized by periods of open-conduit activity with the alternating strombolian activity with violent eruptions. The eruption of 1906 is the largest explosive eruption of the twentieth century. The climax of the eruption was reached on the April 7th, when impressive lava fountains, accompanied by earthquakes, rose from the crater. At the end of the eruption, the top of the cone was truncated to form a vast crater. After this explosive event, the Vesuvius area was characterized by quiescent periods alternated by prolonged volcanic activity, effusions of lava and low energy explosions. The last eruption occurred in March 1944.

Mt. Vesuvius is presently affected by relatively low level volcanic-hydrothermal activity, which is mainly characterized by the following: (a) widespread fumarolic emissions that are accompanied by diffuse soil CO_2 degassing in the crater area [122]; (b) CO_2-rich groundwaters along the southern flank of Vesuvius and in the adjacent plain and (c) seismic activity with epicentres clustered inside the crater [123]. Fumarolic fluids discharging by the crater rim fumaroles are of relatively low temperatures (<75°C) and are mainly composed of atmospheric components. Fumaroles from the crater bottom have H_2O and CO_2 as the major components, followed by H_2, H_2S, N_2, CH_4, CO, and He (in order of decreasing content), and discharge temperature of about 95°C [123]. CH_4 and NH_3 contents suggest that the origin of these fluids could be from a high-temperature hydrothermal system located below the Vesuvius' crater [122]. Lacroix classified older Vesuvian fumaroles in four different types [9]: (1) HT (>300°C)

with halite, sylvite, thenardite, Na-K carbonates, aphthitalite, sulphides, Cu-oxide and chlorides (alteration); (2) ("acid", *T*=300–100°C) with Mg-Fe-Al chlorides, sulphur, and realgar; (3) (around 300°C) containing salammoniac with ammonium sulphate and fluoride and (4) (sulphurous, LT around 100°C) with sulphur, gypsum, sassolite, K-Al-Fe sulphates, opal.

4.2.4. Vulcano Island

Vulcano is the southernmost of the seven islands that form the Aeolian archipelago. Its activity dates back about 120 Ka. The four main eruptive centres of the island (Vulcano Primordiale, Lentia, La Fossa cone, and Vulcanello) are formed by a progressive migration of the volcanic activity from SSE to NNW. In the middle of La Fossa caldera sits La Fossa cone, the active volcanic centre of the island, which formed during the last 5.5 ka through recurrent hydro-magmatic to volcanic explosive phases [124]. Since its last eruption in 1888–1890, Vulcano has remained in a fumarolic stage of varying intensity with shallow seismicity. Presently, active fumarole fields are concentrated in the northern section of the La Fossa crater and in the neighbourhood of the coast at Baia di Levante. The former show high variability in temperature and fluid compositions as a function of the volcanic activity, the latter are typical hydrothermal emissions.

Figure 16. Fumaroles on La Fossa Crater, Vulcano.

Over the last two decades, several models were proposed to explain the genesis of the Vulcano fumarole fluids, each of them involving the presence of a deep and a shallow component in the gas phase. Compositionally, the crater fumaroles are rich in CO_2 as the main component and have significant concentrations of HCl, SO_2, H_2S, HF, and CO [125]. The diffuse emissions at Baia di Levante are more typical of hydrothermal fluids, with higher CH_4 and H_2S contents than the crater fumaroles, lower CO concentrations, and no measurable amount of SO_2 [126]. Strong variations of the chemicophysical features of the gas output at the crater have been observed periodically. During these so-called "crisis", the crater fumaroles demonstrated a substantial increase in temperature from the usual range between 330 and 400°C and in the magmatic component of the total gas flux. The interest in the collection and analysis of the

http://dx.doi.org/10.5772/64129

fumarolic minerals especially increased during the last thermal crisis, which started in 1988 and reached a maximum in 1993. A systematic research was started, supported by the Italian National Group of Volcanology. This led to the discovery of a large variety of rare phases and new minerals [8, 12, 13, 26–29, 31–34, 40, 49, 55, 66, 90, 91]. La Fossa crater became a mineralogical attraction and the large number of already described minerals from the locality [10] increases constantly making it one of the most prolific type locality in the world. The fumarolic mineral association observed on La Fossa Crater are (1) (LT + MT) sulphur, borates, borosilicates, sulphates (mainly hydrous, only in oxidizing conditions), halogenides and sulfohalogenides and (2) (HT >400–450°C) sulphides, sulphosalts, sulfochlorides (reducing conditions); anhydrous sulfates (oxidizing conditions) (**Figure 16**).

4.2.5. Mt. Etna

Mount Etna is one of the largest European volcanoes, world famous for its spectacular and frequent eruptions. Its main feature is the voluminous lava emission, occasionally associated with explosive activity from its four summit craters. Mt. Etna is a basaltic composite apparatus, with a basal diameter of 40 km and 3350 m of altitude, situated on the eastern border of Sicily. The Etnean volcanism is still not definitely understood in its geological context. Mt Etna is situated on the crossing of important regional fault systems trending NW-SE, NE-SW, and WSW-ESE and this probably facilitates the uprise of magma in this place. There is some evidence that Etna is but the most recent manifestation of volcanism fed from a very long-lived mantle source, having caused numerous earlier phases of mafic volcanism in the Monti Iblei, SE Sicily, from the late Triassic to the early Pleistocene. Mt. Etna has erupted many times in historical time and presently is constantly active with spectacular summit and flank eruptions, interspersed by periods of intermittent activity. The recent volcanic activity has been characterized by almost continuous summit eruptions of effusive and moderate explosive activity. Its most powerful historical eruption occurred in 122 BC [127]. This plinian summit eruption produced a large volume of pyroclastics (ash and lapilli), which fell in a sector on the southeast flank of the volcano, causing devastation in the city of Catania. Presently, the frequent eruptive activity heavily affects the morphology of the summit area that consists of a central crater (Voragine) surrounded by three active cones (Bocca Nuova, NE Crater, and SE Crater) and is cut by N-S-oriented fracture system, mainly related to the extensional stress produced by magma ascent [128]. From the four active craters in historical times, a large number of summit and flank eruptions have occurred [129] producing numerous composite lava fields and more than 300 scoria and spatter cones. The chemical composition of magmas produced in historical times is rather uniform, ranging from alkali basalt to basic mugearite.

The fumarolic activity at the crater area of Mt. Etna is variable and largely influenced by the activity of the volcano, which is continuous and changes frequently. Consequently, as the morphology of the summit area undergoes significant variations over time, also the localization and amplitude of gas discharging and temperature of fumaroles change. Generally, the fumaroles are aligned along dynamic fractures produced by extensional stress phenomena, but also around hornitos. Intense fumarolic activity is often present due to residual degassing during the cooling of erupted lava. The most of the gas discharging is from the surface of lava

flows, but it also happens in the inner parts of volcanic lava tubes and caves in which the cooling of the gases often produces interesting deposition of sublimates and encrustations. After exsolving from magmas, the gases ascend along rock fractures sometimes reaching directly the surface (high-temperature fumarole). In other cases (low-temperature fumarole), they interact with peripheral hydrothermal systems and surficial acquifers, undergo contamination and change their pristine composition [130]. The observed main mineral associations are as follows: (1) (surface, HT) thenardite, halite and sylvine; (2) (surface, LT) sulphur, salammoniac, hydrous sulphates and (3) (in caves) halite, sylvite with thenardite, and hydrous sulphates.

4.3. Greek volcanoes

4.3.1. The Aegean (Hellenic) active volcanic arc

The Aegean volcanic arc is one of the tectonically most active regions of the Mediterranean area, extending from the mainland of Greece through the volcanic centers of Soussaki, Aegina, Methana, Poros, Milos, Santorini, Kos, Yali, and Nisyros, to the Bodrum peninsula in Turkey. In that area, the eastern Mediteranian lithosphere subducts under the Aegean and the Aegean microplate overrides the eastern Mediterranean [131]. The volcanism started 3.5 Ma ago and is still continued up today in the form of post-magmatic activity [132–135]. The Pliocene-Quaternary volcanic arc of the Aegean arose from the subduction of the African plate beneath the microplate of the Aegean-Anatolian [136] with simultaneous destruction of intermediate-Tethys oceanic crust. The Pliocene-Pleistocene volcanism in the arc of the Aegean Sea is

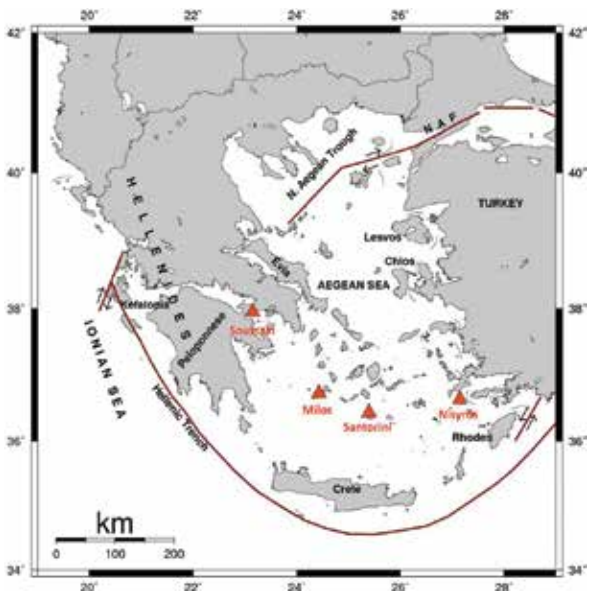

Figure 17. Map of Greece with the locations of the investigated volcanoes and fumarolic fields.

dominated by andesites and dacites, while in the central and eastern parts of the arc, the lower Quaternary volcanism is characterized by dacitic or rhyolitic composition (**Figure 17**).

4.3.2. Soussaki volcano

The Soussaki area represents the NW end of the active Aegean volcanic arc. The volcanic activity took place between 4.0 and 2.3 Ma ago. The lithological types occurring in the area are rocks of the dacitic and rhyolitic composition, remnants of the late Pliocene to Quaternary volcanic activity [132–135, 137]. Gas manifestations display typical geothermal compositions with CO_2 and water vapour as the main components and CH_4 and H_2S as minor species. The volcanic activity observed today manifests itself by emanation of warm fluids, while widespread fumarolic alteration, vapours, and warm (35–45°C) gas emissions are still observed. Reaction between the fluids and pre-existing rocks, consisting mainly of serpentinite, chert, marlstone, limestone, and subordinate rhyodacitic lava, has resulted in the formation of gypsum, sulphur, silica polymorphs, and Fe and Mg sulphates. Kaolinite, anhydrite, carbonates, and Ni, and K-Al sulfates are also present in some cases ([73], this work). The observed main mineral associations can be summarized as follows: (1) gypsum with quartz and carbonates and (2) Fe-Mg hydrous sulphates.

4.3.3. Milos Island

The Milos volcanic district is a wide volcanic archipelago comprising the islands of Milos, Kimolos, Antimilos, and Poliegos. The volcanic activity started about 5 million years ago and is now considered to be extinct. Milos Island is located at the western end of the Aegean Volcanic Arc. It is built mainly of calcalkaline volcanic rocks (tuffs, pumice flows, ignimbrites, pyroclastic flows, domes, and lava flows of andesitic-dacitic, and rhyolitic composition). The volcanic sequence is built on Miocene-Pliocene clastic and carbonate platform sediments, which unconformably overly a metamorphic basement. Following their emplacement, volcanic rocks were involved in an intense hydrothermal activity. The volcanism in the area developed with submarine activity character and was followed by a sub-aerial effusive phase. The distribution of the hydrothermal minerals derived basing on cores and cuttings from the two drill sites to a depth of about 1100 m [138] indicates the dilution of the K-, Na-, Cl-rich hydrothermal fluid of the deep reservoir by a Ca-, Mg-rich cold water at a shallower level. In some places, the hydrothermal activity is expressed by the occurrence of many hot springs (30–85°C), fumaroles (98–102°C), hot grounds (100°C at a depth of 30–40 cm) and submarine gas emissions, widespread on and around the island. Fyriplaka volcano is the expression of the most recent volcanic activity on the island and includes fumaroles, solfataras, and hot grounds. Where gas emanations are very high, the soils are altered and covered with thin layers of secondary minerals as alunite, magnesite, and sulphur.

We examined samples from the area of Amygdales and in the neighbourhood of Paleochori. The substrate rock is argillaceous, composed of SiO_2 polymorphs and kaolinite mixed with alunite, which is the dominating fumarolic mineral. The main fumarolic associations are as follows: (1) alunite with sulphur (plus quartz, opal, kaolinite) and (2) alunite and alunogen with Fe-hydrous sulphates and barite (plus sulphur, pyrite, quartz, opal, muscovite).

4.3.4. Santorini volcano

The volcanic field of Santorini consists of various islands (Thera, Therasia, Aspronisi, Palea Kameni, and Nea Kameni), the Christiania islands around 20 km to the southwest and the submerged Columbus volcano 7 km to the northeast. It is the most active part of the Aegean Volcanic Arc. Between Thera, Therasia, and Aspronisi, exists a sea-flooded caldera of about 13 km diameter. According to various geochronological data, the volcanic activity in the Santorini volcano started about 2 Ma ago. The field has had 12 major (1–10 km^3 or more of lava), and numerous minor, explosive eruptions over the last ~200 ka. A hypothesis the eruption mechanism [139] supposes a large water-filled crater, an extensional environment to facilitate downward penetration of water, and a hot silicic magma.

Figure 18. Fumarole on Nea Kameni, Santorini.

Nea Kameni fumaroles have a distinct hydrothermal nature with compositions dominated by H_2O, CO_2 and H_2 with minor H_2S, and SO_2 typically absent [140]. We investigated samples from the fumaroles at the Nea Kameni central crater. The altered rock consists of cristobalite, opal, plagioclase (around An50), gypsum, alunite or natroalunite and sporadic quartz, trydimite, hematite, and kaolinite. The sublimate is mostly sulphur that makes yellowish crusts, aggregates of isometric crystals or spear-like dendritic crystals. Hydrated sulphates are alunogen (mixed with the substrate or as thin platy crystals), rhomboclase, coquimbite, and tamarugite. Jarosite is also found in small quantities (**Figure 18**).

4.3.5. Nisyros volcano

Nisyros is the newest of the major active volcanoes of Greece, composed almost exclusively of volcanic rocks, with the oldest of them being little less than 160,000 years and the youngest

http://dx.doi.org/10.5772/64129

reaching the limits of prehistory, about 20,000 years ago. In the wider area of Nisyros at the eastern margin of the volcanic arc, the first eruptions date 3.4 million years. Since then, small or large eruptions built up Nisyros and the islets Pirgousa, Pachia, Strogyli, and Giali. None of the eruptions of the volcano recorded in historical sources produced molten rock, as they are hydrothermal and originate from the overheated steam in the underground of the island. Seawater and rainwater penetrate the rocks of the island, are heated by magma and converted to superheated steam, which exerts tremendous pressure and causes a hydrothermal explosion when overcomes the weight and consistency of the caprock. Such explosions were recorded in Nisyros in historical times. In the southern part of the caldera floor, there are traces of 20 craters, 10 of them being well preserved. The largest and most striking crater is Stephanos. The latest hydrothermal craters are concentrated in the area of Lofos (=hill), a small post-dome that largely has been destroyed by hydrothermal explosions. Here are situated six well-preserved craters, the creation of three of them being recorded in historical sources. In October or November 1871, a powerful earthquake caused the beginning of a series of hydrothermal explosions, which until 1873 created two small craters: Polyvotis and Alexandos (or Flegethron). The last recorded hydrothermal explosion in Nisyros is the one of 1887, which created the crater of Small Polyvotis. Various amounts of volcanic gases come out from the intracaldera soil area including also the main fumarolic craters of Kaminakia, Ramos, Stefanos, Lofos, and Flegethron. The gas species are H_2S, CO_2, CH_4, and CO [141–143](**Figure 19**).

Figure 19. Fumaroles in the Stephanos crater, Nisyros.

The only sublimate mineral observed at the vents at the edges of the Stefanos and Polyvotis craters is sulphur. It develops as granular aggregates or acicular spear-like crystals. On the floor of the Stefanos crater, numerous circular formations surround the "hot spots" of the fluid, vapour, and gas emanations. The central part of these formations consists of the reddish to yellowish sand formed by grains of quartz, labradoritic plagioclase, alunite, alunogen, and gypsum. They are surrounded by white rims containing dendritic crystals of alunogen and

metaalunogen. On their outer part is a blackish zone with additional voltaite and tamarugite. The outermost rim consists of aggregates of microscopic yellowish globules of rhomboclase overgrown by silky needles of halotrichite.

5. Discussion

The list of the minerals found in European fumaroles impresses by the number of different species, especially taking in account that some prolific mineral groups (like silicates and phosphates) do not contribute to the list or contribute very little. Among the European fumarole localities, Vesuvius and Vulcano stand as the two volcanoes with the richest mineralogy. This status is due to the exceptional abundance of otherwise rare elements in their emanations: Cr, Mn, Ni, Cu, B, Tl, Pb, As, Se on Vesuvius, Ba, Au, Zn, B, Tl, Sn, Pb, As, Bi, Se, Te, Br, I on Vulcano. The presence of the rare elements that form rare minerals is, however, not the only reason for the diversity of fumarole mineralogy. Although they do not contain minerals of rare elements, the three Icelandic volcanoes Surtsey, Eldfell, and Hekla each have around 30 different minerals in their fumaroles. Moreover, their dominating mineral associations are different from the main associations of both Vesuvius and Vulcano, and are differing among themselves, although all five fumarolic systems are formed by the same combination of main gaseous species (H_2O, CO_2, HCl, HF, SO_2, and H_2S). This illustrates the importance of various factors that can influence the processes and through that the mineral world of fumaroles mentioned in the introduction. The intensive parameters, composition and temperature of volcanic gases and lava, can decisively be supplemented by other factors in forming or modifying the minerals in fumaroles. We will try to examine them in the following comparison of different fumarolic systems.

In general, the fumaroles can be classified according to their temperature of formation and mineral stability. Already in the nineteenth century, Lacroix made a classification of Vesuvius fumaroles [9] after their mineralogy, reflecting the temperature of formation. He distinguished the high-temperature "dry" fumaroles characterized by the K and Na salts and also some sulphides and oxides, the medium-temperature "acid" fumaroles characterized by the chlorides of Fe, Mg, Al, and Mn, fumaroles of even lower temperature characterized by salammoniac and other ammonium minerals, and the low-temperature fumarole producing sulphuric acid and steam with sulphur and gypsum as typical minerals. We shall try to classify the fumaroles investigated in this work in three categories: (1) HT, the high temperature (>400°C), (2) MT, medium temperature (200–400°C) and (3) LT, low temperature (<200°C). The given temperature ranges are approximate. HT fumaroles appear with the eruption of the volcano and are short living after its finish. Alternatively, they can be products of temperature increase in the volcanic system not leading to eruption, but again short-lived (Vulcano). MT and LT fumaroles might be active at the same time as the HT fumaroles, but at different places in the system where fumarolic gases travelled longer and got cooled and/or diluted by the atmosphere before they come to the surface. MT fumaroles prevail in the period of recession after the paroxysm and last roughly for decades, maybe centuries, while the shallow intruded magma cools down, or the degassing surface of the magma retreats to greater depths. LT

http://dx.doi.org/10.5772/64129

fumaroles are the only ones present in the quiescence period with a deep thermal source and may transform eventually to a solfatara (mofeta), if the volcanic cycle is finished or very much prolonged.

Inspecting the mineralogy of European fumaroles, we can see that specific three (or four) minerals are typical in most cases for the HT fumaroles. These are halite, (meta) thenardite (with or without aphthitalite), and anhydrite. The mentioned four minerals are all stable to over 800°C. The fumarolic systems can be classified according to relative abundances of these minerals reflecting the Na(+K)/Ca and Cl/S proportions in the fumarolic paragenesis. In this classification, the alcalic fumaroles are those of Vesuvius (dominantly chloridic), Fimmvörðuháls and Askja (chloridic-sulphatic) and Krafla (sulphatic). The mixed alcalic-calcic are Surtsey and Etna (chloridic-sulphatic) and Hekla (sulphatic), the calcic is Eldfell (sulphatic). Outside the classification stands Vulcano, with a high-temperature association composed of sulphides/sulphosalts in combination with sulphochlorides. It can be locally expanded with an association of anhydrous sulphates where and when the atmospheric influence is large and the general reducing conditions change to oxidative.

The MT fumaroles reflect more the individual nature of each fumarolic system. First of all, the range of temperature, the relatively slow flux rates and the chemistry of fumarolic systems permit the deposition and the growth of a larger number of mineral phases, including products of reaction between gas, steam, or liquid and minerals previously formed. In addition, the often longer time of their existence and the longer and slower ascent of the fluid phase allows for a larger contribution of other influences on magmatic exhalations, that is, interaction with the wall rock and surficial fluids. Here, we can recognize the following associations: A, salammoniac in association with other ammonium minerals; B, metal chlorides (Fe-Al-Mg plus others); C, fluoride association with ralstonite as the dominating mineral, typically mixed with other aluminofluorides. Type A was registered on all recently active volcanoes except Surtsey and Fimmvörðuháls. On Eldfell and Hekla, it was forming only early following the eruption. On Vesuvius and especially Vulcano, it is a persistent feature, where the latter also demonstrates a rich variety of ammonium minerals not found on other places. The situation on Icelandic volcanoes suggests that nitrogen in the volcanic gases is one of the first species to be exhausted upon an eruptive episode. If it is true, it would mean that the shallow-degassing magmas of Vesuvius and Vulcano are constantly replenished in nitrogen or that it is there supplied from some other sources. Type B is found on Vesuvius and Vulcano. On the former, the chlorides are mixed with fluorides, on the latter with fluorides (boro- and silicofluorides), bromides and even an iodate. The type C is characteristic for a number of Icelandic volcanoes (Surtsey, Eldfell, Fimmvörðuháls, Hekla, Krafla). In Hekla fumaroles, silicofluorides appear together with aluminofluorides.

The dominating minerals in the LT fumaroles are sassolite, gypsum, alunogen, and sulphur (listed with decreasing thermal stability). The differences in thermal stability are practically of no importance in this group because all minerals form at temperatures that are around 100°C or even lower in this type of fumaroles. Here, also alunite can be named as an abundant component. It is a product of feldspar decomposition through action of sulphuric gases and solutions in solfataras and low-temperature fumaroles, together with opal, and in this respect

does not represent a simple sublimate. It is stable to around 500°C and could be a component of high-temperature fumarole as well, but the process of formation makes it a typical representative of the low-temperature one. The LT fumaroles can be categorized by the contents of the above-mentioned minerals. The sulphur dominated fumaroles are found on Nisyros, Etna, Campi Flegrei, Vesuvius, Vulcano, and Krafla. Gypsum dominated are those of Soussaki, Surtsey, Eldfell, and Hekla. Vulcano and Vesuvius have low-temperature fumaroles that contain also abundant sassolite together with sulphur and gypsum. The second type of fumaroles on Nisyros and fumaroles on Milos are dominated by alunogen, and finally, the fumaroles on Santorini have comparable amounts of sulphur, gypsum and alunogen. In all of them, various kinds of hydrous sulphates appear, which can be used as fine-tuning indicators of temperature and humidity conditions.

The classifications given above can serve a general orientation purpose and understanding of the actual conditions in the fumarolic system under investigation. They are in no way clearly delimited categories and mixing of associations is a frequent phenomenon. It can be produced as a consequence of the gradual lowering of temperature and the flux rate, but often also a simultaneous formation of closely separated minerals at quite different temperatures occurs due to the high fluctuation of conditions on a small scale at the border between the volcanic gases and the atmosphere. On Vulcano, the high-temperature anhydrous sulphates that form under the locally oxidizing conditions are found in close association with sulphides and sulphosalts formed under the reducing conditions. Our detailed investigation of fumarolic profiles on Eldfell shows that within less than 20 cm the low-temperature mineral association of fluorides changed to the high-temperature association of anhydrous sulphates. The mixed associations can also be an artefact produced by the mineral instability at atmospheric conditions, and laboratory analyses taken alone can give misleading results. Our analyses of Eldfell material showed always hydrous Mg-Al sulphates accompanying the anhydrous ones taken from the levels featuring temperatures over their stability ranges. Their formation as atmospheric hydration products was confirmed by the field observations of the deliquescent behaviour of exposed excavated samples and through laboratory analyses of freshly crushed massive ones. The caveat about the above classification is that it presents a general picture from which numerous important details have been removed in order to give as clear as possible an overview. For a full characterization of individual fumarolic systems, the details are indispensable, and this emphasizes the importance of detailed studies.

The realm of fumarolic mineralogy presents us with interesting and important still unanswered questions. For example, the seeming contradiction of the experimental results that show sulphuric species to be the ones with the fastest and earliest devolatilization from silicic melts, and the observation that sulphates and elemental sulphur are the most persistent parts of fumaroles, leads to important enquiries into the sub-surface volcanogenic sulphuric cycle (see e.g. [144]). Another interesting largely unsolved problem is the understanding of reasons why sometimes large differences in mineral compositions of seemingly similar fumarolic systems exist. During the last century, the appearance of powerful methods of research on microscale has revealed a great number of new mineral species from fumarolic samples, typically rare and exotic, and contributed to the solid state science and the general minera-

logical knowledge. We believe that the application of these methods to investigation of both minor and main components of fumaroles and integrated with research in other fields (like gas evolution and composition and gas-magma-rock interactions) can also bring answers to the most intriguing questions of the genesis and origins of particular fumaroles. Accomplishing this, they can become another important tool in the surveillance of active volcanic systems.

Acknowledgements

The authors are grateful to researchers and students with whom they collaborated in the investigations of European fumaroles: Filippo Vurro, Daniela Pinto, Donatella Mitolo, Eric Leonardsen, Sigurður S. Jónsson, Níels Óskarsson, Sigmundur Einarsson, Anna Katerinopoulou and Morten J. Jacobsen. We thank Helene Almind for the technical assistance during XRD measurements and Dora Balić Žunić for technical support during the field work and manuscript preparation. Parts of the research work were financially supported by the Danish Agency for Science Technology and Innovation and the National Group for Volcanology, Italy.

Author details

Tonči Balić-Žunić[1*], Anna Garavelli[2], Sveinn Peter Jakobsson[3], Kristjan Jonasson[3], Athanasios Katerinopoulos[4], Konstantinos Kyriakopoulos[4] and Pasquale Acquafredda[2]

*Address all correspondence to: toncib@snm.ku.dk

1 University of Copenhagen, Copenhagen, Denmark

2 University of Bari, Bari, Italy

3 Icelandic Institute of Natural History, Gardabaer, Iceland

4 University of Athens, Athens, Greece

References

[1] Jakobsson SP, Leonardsen ES, Balic-Zunic T, Jónsson SS. Encrustations from three recent volcanic eruptions in Iceland: the 1963–1967 Surtsey, the 1973 Eldfell and the 1991 Hekla eruptions. Fjölrit Náttúrufræðistofnunar (Special Publication of the Icelandic Institute of Natural History).2008;52:65 p.

[2] Ruste J. X-ray spectrometry. In: Maurice F, Meny L, Tixier R, editors. Microanalysis and Scanning Electron Microscopy. Orsay: Les Editions de Physique; 1979. pp. 215–267.

[3] Acquafredda P, Paglionico A. SEM-EDS microanalyses of microphenocrysts of Mediterranean obsidians: a preliminary approach to source discrimination. European Journal of Mineralogy. 2004;16:419–429.

[4] Pouchou JL, Pichoir F. Quantitative analysis of homogeneous or stratified microvolumes applying the model "PAP". In: Heinrich KFJ, Newbury DE, editors. Electron Probe Quantitation. New York: Plenum Press; 1991. pp. 31–75.

[5] Strunz H, Nickel EH. Strunz Mineralogical Tables. 9th ed. Stuttgart: E. Schweizerbart'sche Verlagsbuchhandlung (Nägele u. Obermiller); 2001. 870 p.

[6] Panichi U. Muthmann'scher Schwefel, auf der Insel Vulcano beobachtet. Zeitschrift für Krystallographie. 1915;54:393–394.

[7] Steudel R, editor. Elemental Sulphur and Sulphur-Rich Compounds I, Topics in Current Chemistry 230. 1st ed. Berlin, Heidelberg, New York: Springer; 2003. 166 p.

[8] Garavelli A, Mitolo D, Pinto D, Vurro F. Lucabindiite, $(K,NH_4)As_4O_6(Cl,Br)$, a new fumarole mineral from the "La Fossa" crater at Vulcano, Aeolian Islands, Italy. American Mineralogist. 2013; 98;470–477.

[9] Pelloux A. The minerals of Vesuvius. American Mineralogist. 1927;12:14–21.

[10] Campostrini I, Demartin F, Gramaccioli CM, Russo M. Vulcano: tre secoli di (Vulcano: three centuries of its mineralogy). Cremona: Ami Associazione Micromineralogica Italiana; 2011. 343 p.

[11] Fulignati P, Sbrana A. Presence of native gold and tellurium in the active high-sulfidation system of the La Fossa volcano (Vulcano, Italy). Journal of Volcanology and Geothermal Research. 1998;86:187–198.

[12] Garavelli A, Laviano R, Vurro F. Sublimate deposition from hydrothermal fluids at the Fossa crater – Vulcano, Italy. European Journal of Mineralogy. 1997;9:423–432.

[13] Pinto D, Garavelli A, Mitolo D. Balićžunićite, $Bi_2O(SO_4)_2$, a new fumarole mineral from La Fossa crater, Vulcano, Aeolian Islands, Italy. Mineralogical Magazine. 2014;78:1043–1055.

[14] Russo M. I minerali di formazione fumarolica della grande eruzione Vesuviana del 1906 (Minerals of fumarolic origin from the large 1906 eruption of Vesuvius). Istituto Nazionale di Geofisica e Vulcanologia, sezione Napoli – Osservatorio Vesuviano. Open File Report; 2006. 39 p.

[15] Parascandola A. Contributo alla mineralogia Flegrea (A contribution to the Phlegrean mineralogy). Bolletino della Società Geologica Italiana (Bulletin of the Italian Geological Society). 1951;70(3):527–532.

[16] Emelina AL, Alikhanian AS, Steblevskii AV, Kolosov EN. Phase diagram of the As-S system. Inorganic Materials. 2007;43(2):95–104.

[17] Gavezzotti A, Demartin F, Castellano C, Campostrini I. Polymorphism of As_4S_3 (tris-(μ_2-sulfido)-tetra-arsenic): accurate structure refinement on natural α- and β-dimorphites and inferred room temperature thermodynamic properties. Physics and Chemistry of Minerals. 2013;40:175–182.

[18] Roberts AC, Ansell HG, Bonardi M. Pararealgar, a new polymorph of AsS, from British Columbia. Canadian Mineralogist. 1980;18:525–527.

[19] Bonazzi P, Bindi L, Popova V, Pratesi G, Menchetti S. Alacranite, As_8S_9: structural study of the holotype and re-assignment of the original chemical formula. American Mineralogist. 2003;88:1796–1800.

[20] Campostrini I, Demartin F, Russo M. A new ammonium arsenite chloride from the Solfatara di Pozzuoli, Napoli, Italy. Rendiconit della Società Geologica (Statements of the Italian Geological Society). 2014;31(Suppl.1):309.

[21] Whitfield HJ. Crystal structure of the β-form of tetra-arsenic trisulphide. Journal of the Chemical Society Dalton Transactions. 1973;17:1737–1738.

[22] Demartin F, Gramaccioli CM, Campostrini I, Orlandi P. Demicheleite, BiSBr, a new mineral from La Fossa crater, Vulcano, Aeolian Islands, Italy. American Mineralogist. 2008;93:1603–1607.

[23] Demartin F, Gramaccioli CM, Campostrini I. Demicheleite-(Cl), BiSCl, a new mineral from La Fossa crater, Vulcano, Aeolian Islands, Italy. American Mineralogist. 2009;94:1045–1048.

[24] Demartin F, Gramaccioli CM, Campostrini I. Demicheleite-(I), BiS(I,Br,Cl), a new mineral from La Fossa crater, Vulcano, Aeolian Islands, Italy. Mineralogical Magazine. 2010;74(1):141–145.

[25] Henley RW, Mavrogenes J, Tanner D. Sulfosalt melts and heavy metal (As-Sb-Bi-Sn-Pb-Tl) fractionation during volcanic gas expansion: the El Indio (Chile) paleo-fumarole. Geofluids. 2012;12:199–215.

[26] Pinto D, Balić-Žunić T, Garavelli A, Makovicky E, Vurro F. Comparative crystal-structure study of Ag-free lillianite and galenobismutite from Vulcano, Aeolian Islands, Italy. The Canadian Mineralogist. 2006;44:159–175.

[27] Borodaev YS, Garavelli A, Garbarino C, Grillo SM, Mozgova NN, Organova NI et al. Rare sulfosalts from Vulcano, Aeolian Islands, Italy. III. Wittite and cannizzarite. The Canadian Mineralogist. 2000;38:23–34.

[28] Vurro F, Garavelli A, Garbardino C, Moëlo Y, Borodaev YS. Rare sulfosalts from Vulcano,Aeolian Islands, Italy. ll. Mozgovaite, $PbBi_4(S,Se)_7$, a new mineral species. The Canadian Mineralogist. 1999;37:1499–1506.

[29] Borodaev YS, Garavelli A, Garbardino C, Grillo SM, Mozgova NN, Uspenskaya TY, et al. Rare sulfosalts from Vulcano, Aeolian Islands, Italy. IV. Lillianite. The Canadian Mineralogist. 2001;39:1383–1396.

[30] Moëlo Y, Makovicky E, Mozgova NN, Jambor JL, Cook N, Pring A, et al. Sulfosalt systematics: a review. Report of the sulpfosalt sub-committee of the IMA Commission on Ore Mineralogy. European Journal of Mineralogy. 2008;20:7–46.

[31] Borodaev YS, Garavelli A, Garbarino C, Grillo SM, Mozgova NN, Paar WH, et al. Rare sulfosalts from Vulcano, Aeolian Islands, Italy. V. Selenian Heyrovskýite. The Canadian Mineralogist. 2003;41:429–440.

[32] Borodaev YS, Garavelli A, Kuzmina O, Mozgova NN, Organova NI, Trubkin NV, et al. Rare sulfosalts from Vulcano, Aeolian Islands, Italy. I. Se-bearing kirkiite, $Pb_{10}(Bi,As)_6(S,Se)_{19}$. The Canadian Mineralogist. 1998;36:1105–1114.

[33] Garavelli A, Mozgova NN, Orlandi P, Bonaccorsi E, Pinto D, Moëlo Y, et al. Rare sulfosalts from Vulcano, Aeolian Islands, Italy. VI. Vurroite, $Pb_{20}Sn_2(Bi,As)_{22}S_{54}Cl_6$, a new mineral species. The Canadian Mineralogist. 2005;43:703–711.

[34] Pinto D, Bonaccorsi E, Balić-Žunić T, Makovicky E. The crystal structure of vurroite, $Pb_{20}Sn_2(Bi,As)_{22}S_{54}Cl_6$: OD-character, polytypism, twinning, and modular description. American Mineralogist. 2008;93:713–727.

[35] Métrich N, Wallace PJ. Volatile abundances in basaltic magmas and their degassing paths tracked by melt inclusions. Reviews in Mineralogy and Geochemistry. 2008;69:363–402.

[36] Ustunisik G, Nekvasil H, Lindsley DH, McCubbin FM. Degassing pathways of Cl^-, F^-, H^-, and S-bearing magmas near the lunar surface: implications for the composition and Cl isotopic values of lunar apatite. American Mineralogist. 2015;100:1717–1727.

[37] Villemant B, Boudon G. H_2O and halogen (F, Cl, Br) behaviour during shallow magma degassing processes. Earth and Planetary Science Letters. 1999;168: 271–286.

[38] Barone G, Mazzoleni P, Priolo G. Catalogo delle mineralizzazioni secondarie riscontrate all'interno di alcune grotte vulcaniche etnee (A catalogue of the secondary mineralizations in some Etnean volcanic caves). In: Proceedings of XXII Congresso Nazionale di Speleologia "Condividere i dati", Sessione Documentatione – a1; 30 May – 2 June 2015; Pertosa-Auletta (SA). pp. 99–109.

[39] Oskarsson N. The chemistry of Icelandic lava incrustations and the latest stages of degassing. Journal of Volcanology and Geothermal Research. 1981;10:93–111.

[40] Coradossi N, Garavelli A, Salamida M, Vurro F. Evolution of Br/Cl ratios in fumarolic salammoniac from Vulcano (Aeolian Islands, Italy). Bulletin of Volcanology. 1996;58:310–316.

[41] Roberts AC, Venance KE, Seward TM, Grice JD, Paar WH. Lafossaite, a new mineral from the La Fossa Crater, Vulcano, Italy. Mineralogical Record. 2006;37:165–168.

[42] Campostrini I, Russo M. Lafossaite e dimorphite: due nuove specie per il Vesuvio (Lafossaite and dimorphite: two new mineral species from Vesuvius). Micro. 2012;3/2012:136–141.

[43] Palache C, Berman H, Frondel C. The System of Mineralogy of James Dwight Dana and Edward Salisbury Dana Yale University 1837–1892, Volume II. 7th ed. New York: John Wiley and Sons, Inc.; 1951. 1124 p.

[44] Cruciani G, Orlandi P, Pasero M, Russo M. First Italian occurrence of cumengeite from Vesuvius: crystal-structure refinement and revision of the chemical formula. Mineralogical Magazine. 2005;69(6):1037–1045.

[45] Jacobsen MJ, Balić-Žunić T, Mitolo D, Katerinopoulou A, Garavelli A, Jakobsson SP. Oskarssonite, AlF_3, a new fumarolic mineral from Eldfell volcano, Heimaey, Iceland. Mineralogical Magazine. 2014;78(1):215–222.

[46] Rosenberg PE. Stability relations of aluminium hydroxyl-fluoride hydrate, a ralstonite-like mineral, in the system AlF_3-Al_2O_3-H_2O-HF. The Canadian Mineralogist. 2006;44;125–134.

[47] Demartin F, Campostrini I, Castellano C, Russo M. Parascandolaite, $KMgF_3$, a new perovskite-type fluoride from Vesuvius. Physics and Chemistry of Minerals. 2014;41:403–407.

[48] Russo M, Campostrini I. Ammineite, matlockite and post 1944 eruption fumarolic minerals at Vesuvius. Plinius. 2011;37:312.

[49] Garavelli A, Vurro F. Barberiite, NH_4BF_4, a new mineral from Vulcano, Aeolian Islands, Italy. American Mineralogist. 1994;79:381–384.

[50] Bernauer F. Eine Gearksutit-Lagerstätte auf der Insel Vulcano (A gearksutite-deposit on the island Vulcano). Zeitschrift der Deutschen Gesellschaft für Geowissenschaften (Journal of the German Geoscientific Society). 1941;93:65–80.

[51] Balić-Žunić T, Garavelli A, Mitolo D, Acquafredda P, Leonardsen E. Jakobssonite, $CaAlF_5$, a new mineral from fumaroles at the Eldfell and Hekla volcanoes, Iceland. Mineralogical Magazine. 2012;76(3):751–760.

[52] Mitolo D, Garavelli A, Balić-Žunić T, Acquafredda P, Jakobsson SP. Leonardsenite, $MgAlF_5(H_2O)_2$, a new mineral species from Eldfell volcano, Heimaey Island, Iceland. The Canadian Mineralogist. 2013;51:377–386.

[53] Courbion G, Ferrey G. $Na_2Ca_3Al_2F_{14}$: a new example of a structure with "independent F" – a new method of comparison between fluorides and oxides of different formula. Journal of Solid State Chemistry. 1988;76:426–431.

[54] Demartin F, Gramaccioli CM, Campostrini I. Thermessaite, $K_2[AlF_3|SO_4]$, a new ino-aluminofluoride-sulfate from La Fossa crater, Vulcano, Aeolian Islands, Italy. The Canadian Mineralogist. 2008;46:693–700.

[55] Garavelli A, Mitolo D, Pinto D. Thermessaite-(NH_4), IMA 2011-077. CNMNC Newsletter No. 12, February 2012; page 152; Mineralogical Magazine. 2012;76:151–155.

[56] Effenberger H, Kluger F. Ralstonit: ein Beitrag zur Kenntnis von Zusammensetzung und Kristallstruktur (Ralstonite: a contribution to the knowledge of its composition and crystal structure). Neues Jahrbuch fuer Mineralogie. Monatshefte. 1984;1984:97–108.

[57] de Pape R, Ferey G. A new form of FeF_3 with the pyrochlore structure: soft chemistry synthesis, crystal structure, thermal transitions and structural correlations with the other forms of FeF_3. Materials Research Bulletin. 1986;21(8):971–978.

[58] Ferey G, Leblanc M, de Pape R. Crystal structure of the ordered pyrochlore $NH_4Fe^{(II)}Fe^{(III)}F_6$ structural correlations with $Fe_2F_5(H_2O)_2$ and its dehydration product $Fe_2F_5H_2O$. Journal of Solid State Chemistry. 1981;40:1–7.

[59] Vergasova LP, Semyonova TF, Epifanova VB, Filatov SK, Chubarov VM. Meniaylovite, $Ca_4AlSi(SO_4)F_{13}{\cdot}12H_2O$, a new mineral of volcanic exhalations. Vulkanologiya i Seismologiya (Volcanology and Seismology). 2004;2:3–5.

[60] Demartin F, Gramaccioli CM, Campostrini I, Castellano C. Cossaite, $(Mg_{0.5},\square)Al_6(SO_4)_6(HSO_4)F_6{\cdot}36H_2O$, a new mineral from La Fossa crater, Vulcano, Aeolian Islands, Italy. Mineralogical Magazine. 2011;75(6):2847–2855.

[61] Cossa A. Sulla hieratite, nuova specie mineralogica (About hieratite, new mineral species). Transunti dell'Accademia dei Lincei (Summaries of the Lincei Academy). 1881–1882;3(6):141–142.

[62] Gramaccioli CM, Campostrini I. Demartinite, a new polymorph of K_2SiF_6 from La Fossa crater, Vulcano, Aeolian Islands, Italy. The Canadian Mineralogist. 2007;45:1275–1280.

[63] Garavelli A, Balić-Žunić T, Mitolo D, Acquafredda P, Leonadsen E, Jakobsson SP. Heklaite, $KNaSiF_6$, a new fumarolic mineral from Hekla volcano, Iceland. Mineralogical Magazine. 2010;74:147–157.

[64] Demartin F, Gramaccioli CM, Campostrini I. Knasibfite, $K_3Na_4[SiF_6]_3[BF_4]$, a new hexafluorosilicate-tetrafluoroborate from La Fossa crater, Vulcano, Aeolian Islands, Italy. The Canadian Mineralogist. 2008;46:447–453.

[65] Russo M, Campostrini I, Demartin F. Fumarolic minerals after the 1944 Vesuvius eruption. In: Abstracts, Congresso SGI-SIMP; 10–12 September 2014; Milan. Rendiconti Societa Geologica Italiana. 2014;31(Suppl. 1):315.

[66] Mitolo D, Pinto D, Garavelli A, Bindi L, Vurro F. The role of the minor substitutions in the crystal structure of natural challacolloite, KPb_2Cl_5, and hephaistosite, $TlPb_2Cl_5$, from Vulcano (Aeolian Archipelago, Italy). Mineralogy and Petrology. 2009;96:121–128.

[67] Campostrini I, Demartin F, Gramaccioli CM. Hephaistosite, $TlPb_2Cl_5$, a new mineral species from La Fossa crater, Vulcano, Aeolian Islands, Italy. The Canadian Mineralogist. 2008;46:701–708.

[68] Demartin F, Gramaccioli CM, Campostrini I. Brontesite, $(NH_4)_3PbCl_5$, a new product of fumarolic activity from La Fossa Crater, Vulcano, Aeolian Islands, Italy. The Canadian Mineralogist. 2009;47:1237–1243.

[69] Demartin F, Campostrini I, Gramaccioli CM. Panichiite, natural ammonium hexachlorostannate(IV), $(NH_4)_2SnCl_6$, from La Fossa Crater, Vulcano, Aeolian Islands, Italy. The Canadian Mineralogist. 2009;47:367–372.

[70] Demartin F, Gramaccioli CM, Campostrini I. Steropesite, Tl_3BiCl_6, a new thallium bismuth chloride from La Fossa Crater, Vulcano, Aeolian Islands, Italy. The Canadian Mineralogist. 2009;47:373–380.

[71] Demartin F, Campostrini I, Castellano C, Gramaccioli CM. Argesite, $(NH_4)_7Bi_3Cl_{16}$, a new mineral from La Fossa Crater, Vulcano, Aeolian Islands, Italy: A first example of the $[Bi_2Cl_{10}]^{4-}$ anion. American Mineralogist. 2012;97:1446–1451.

[72] Parascandola A. I minerali di Vesuvio nella eruzione del marzo 1944 e quelli formati durante l'attuale periodo di riposo (Vesuviam minerals from the March 1944 eruption, and those formed during the present quiescent period). Bollettino della Società Geologica Italiana (Bulletin of the Italian Geological Society). 1952;70:523–526.

[73] Kyriakopoulos K, Kanakis Sotiriou R, Stamatakis M. The authigenic minerals formed from volcanic emanations at Soussaki, West Attica peninsula, Greece. The Canadian Mineralogist. 1990;28:363–368.

[74] Demartin F, Gramaccioli CM, Campostrini I. Clinometaborite, natural beta-metaboric acid from La Fossa Crater, Vulcano, Aeolian Islands, Italy. The Canadian Mineralogist. 2011;49:1273–1279.

[75] Murashko MN, Pekov IV, Krivovichev SV, Chernyateva AP, Yapaskurt VO, Zadov AE, et al. Steklite, $KAl(SO_4)_2$: a finding at the Tolbachik Volcano, Kamchatka, Russia, validating its status as a mineral species and crystal structure. Geology of Ore Deposits. 2013;55(7):594–600.

[76] Demartin F, Gramaccioli CM, Campostrini I. Pyracmonite, $(NH_4)_3Fe(SO_4)_3$, a new ammonium iron sulfate from La Fossa Crater, Vulcano, Aeolian Islands, Italy. The Canadian Mineralogist. 2010;48:307–313.

[77] Demartin F, Campostrini I, Castellano C. Aluminopyracmonite, IMA 2012-075. CNMNC Newsletter No. 15, February 2013, page 9. Mineralogical Magazine, 2013;77:1–12.

[78] Balić-Žunić T, Garavelli A, Acquafredda P, Leonardsen E, Jakobsson SP. Eldfellite, $NaFe(SO_4)_2$, a new fumarolic mineral from Eldfell volcano, Iceland. Mineralogical Magazine. 2009;73:51–57.

[79] Campostrini I, Demartin F, Gramaccioli CM. Vulcano: ein aussergewohnlicher Fundpunkt von neuen und seltenen Mineralien. MineralienWelt. 2010;21(3):40–57.

[80] Burke EAJ. A mass discreditation of GQN minerals. The Canadian Mineralogist. 2006;44:1557–1560.

[81] Mofaddel N, Bouaziz R, Mayer M. Le polymorphisme du sulfate de sodium anhydre et les phases intermediaires, glaserite et aphtitalite, dans le binaire Na_2SO_4-K_2SO_4. Thermochimica Acta. 1991;185:141–153.

[82] Okada K, Ossaka J. Structures of potassium sodium sulphate and tripotassium sodium disulphate. Acta Crystallographica. 1980;B36:919–921.

[83] Garavelli A, Grasso MF, Vurro F. Sublimates and fumarolic incrustations at Mt. Etna from 1993 to 1996. Acta Vulcanologica. 1997;9:87–89.

[84] Demartin F, Castellano C, Campostrini I. Therasiaite, $(NH_4)_3KNa_2Fe^{2+}Fe^{3+}(SO_4)_3Cl_5$, a new sulphate chloride from La Fossa Crater, Vulcano, Aeolian Islands, Italy. Mineralogical Magazine. 2014;78(1):203–213.

[85] Mees F, Hatertand F, Rowe R. Omongwaite, $Na_2Ca_5(SO_4)_6 \cdot 3H_2O$, a new mineral from recent salt lake deposits, Namibia. Mineralogical Magazine. 2008;72(6):1307–1318.

[86] Autenrieth H, Braune G. Ein neues Salzmineral, seine Eigenschaften, sein Auftreten und seine Existenzbedingungen im System der Salze ozeanischer Salzablagerungen (A new salt mineral, its properties, its occurence and the conditions for its existence in the system of salts of oceanic salt deposits). Naturwissenschaften. 1958;45(15):362–363.

[87] Demartin F, Campostrini I, Castellano C, Gramaccioli CM, Russo M. D'ansite-(Mn), $Na_{21}Mn^{2+}(SO_4)_{10}Cl_3$ and d'ansite-(Fe), $Na_{21}Fe^{2+}(SO_4)_{10}Cl_3$, two new minerals from volcanic fumaroles. Mineralogical Magazine. 2012;76(7):2773–2783.

[88] Demartin F, Gramaccioli CM, Campostrini I, Pilati T. Aiolosite, $Na_2(Na_2Bi)(SO_4)_3Cl$, a new sulfate isotypic to apatite from La Fossa crater, Vulcano, Aeolian Islands, Italy. American Mineralogist. 2010;95:382–385.

[89] Demartin F, Gramaccioli CM, Campostrini I. Adranosite, $(NH_4)_4NaAl_2(SO_4)_4Cl(OH)_2$, a new ammonium sulfate chloride from La Fossa crater, Vulcano, Aeolian Islands, Italy. The Canadian Mineralogist. 2010;48:315–321.

[90] Mitolo D, Demartin F, Garavelli A, Campostrini I, Pinto D, Gramaccioli, et al. Adranosite-(Fe), $(NH_4)_4NaFe_2(SO_4)_4Cl(OH)_2$, a new ammonium sulfate chloride from La Fossa crater, Vulcano, Aeolian Islands, Italy. The Canadian Mineralogist. 2013;51:57–66.

[91] Garavelli A, Pinto D, Mitolo D, Bindi L. Leguernite, $Bi_{12.67}O_{14}(SO_4)_5$, a new Bi oxysulfate from the fumarole deposit of La Fossa crater, Vulcano, Aeolian Islands, Italy. Mineralogical Magazine. 2014;78:1629–1645.

[92] Demartin F, Castellano C, Gramaccioli CM. Campostriniite, $(Bi^{3+},Na)_3(NH_4,K)_2Na_2(SO_4)_6 \cdot H_2O$, a new sulfate isostructural with görgeyite, from La

Fossa Crater, Vulcano, Aeolian Islands, Italy. Mineralogical Magazine. 2015;79(4):1007–1018.

[93] Vergouwen L. Eugsterite, a new salt mineral. American Mineralogist. 1981;66:632–636.

[94] Slyusareva MN. Hydroglauberite, a new mineral of the hydrous sulphate group. American Mineralogist. 1970;55:321.

[95] Alpers CN, Jambor JL, Nordstrom DK. Sulfate minerals – crystallography, geochemistry, and environmental significance. Reviews in Mineralogy and Geochemistry. 2000;40:22.

[96] Sarp H, Deferne J. Chessexite, a new mineral. American Mineralogist. 1984;69:406.

[97] Thordarson Th, Höskuldsson Á. Postglacial volcanism in Iceland. Jökull. 2008;58:197–228.

[98] Harðarson BS, Fitton JG, Hjartarson Á. Tertiary volcanism in Iceland. Jökull. 2008;58:161–178.

[99] Jakobsson S, Jónasson K, Sigurðsson IA. The three igneous rock series in Iceland. Jökull. 2008;58:117–138.

[100] Þórarinsson S, Einarsson Þ, Sigvaldason GE, Elísson G. The submarine eruption off the Vestman Islands 1963–1964. A preliminary report. Bulletin of Volcanology. 1964;27:435–445.

[101] Þórarinsson S. Sitt af hverju um Surtseyjargosið. (Some facts about the Surtsey eruption.) Náttúrufræðingurinn (Naturalist). 1966;35:153–181.

[102] Þórarinsson S. Síðustu þættir Eyjaelda. (The last phases of the Surtsey eruption.) Náttúrufræðingurinn (Naturalist). 1969;38:113–135.

[103] Jakobsson SP, Jónsson SS, Leonardsen ES. Encrustations from lava caves in Surtsey, Iceland. A preliminary report. Surtsey Research Progress Report. 1992;10:73–78.

[104] Þórarinsson S, Steinþórsson S, Einarsson Þ, Kristmannsdóttir H Óskarsson N. The eruption on Heimaey, Iceland. Nature. 1973;241:372–375.

[105] Jakobsson SP, Pedersen AK, Rønsbo JG, Larsen LM. Petrology of mugearite-hawaiite: early extrusives in the 1973 Heimaey eruption, Iceland. Lithos. 1973;6:203–214.

[106] Sigurðsson O. Jarðeldar á Heimaey. (Eruption in Heimaey.) Týli. 1974;4:5–26.

[107] Sigmundsson G, Hreinsdóttir S, Hooper A, Árnadóttir T, Pedersen R, Roberts MJ, et al. Intrusion triggering of the 2010 Eyjafjallajökull eruption. Nature. 2010;468:426–430.

[108] Sigmarsson O, Vlastelic I, Andreasen R, Bindeman I, Devidal J-L, Moune S, et al. Remobilization of silicic intrusion by mafic magmas during the 2010 Eyjafjallajökull eruption. Solid Earth. 2011;2:271–281.

[109] Jónasson K, Jakobsson SP. Encrustations from the 2010 Fimmvörðuháls eruption. In: 30th Nordic Geological Winter Meeting: Programme and Abstracts, 9–12. January 2012. Reykjavík: Geoscience Society of Iceland; 2012.

[110] Þórarinsson S. Course of events. In: The Eruption of Hekla 1947–1948. Vísindafélag Ísl. 1976;4(1): 1–33.

[111] Schythe JC. Hekla og dens sidste udbrud, den 2den September 1845 (Hekla and its latest eruption, the 2nd September 1845). Kjöbenhavn: Bianco Lunos Bogtrykkeri; 1847. 154 p.

[112] Guðmundsson Á., Óskarsson N, Grönvold K, Sæmundsson K, Sigurðsson O, Stefánsson R, et al. The 1991 eruption of Hekla, Iceland. Bulletin of Volcanology. 1992;54:238–246.

[113] Sigvaldason GE. Some geochemical and hydrothermal aspects of the 1961 Askja eruption. Beiträge zur Mineralogie und Petrographie (Contributions to Mineralogy and Petrography). 1964;10:263–274.

[114] Þórarinsson S. Sigvaldason GE. The eruption in Askja, 1961. A preliminary report. American Journal of Science. 1962;260:641–651.

[115] Þórarinsson S. Askja on fire. Reykjavík: Almenna bókafélagið; 1963. 54 p.

[116] Björnsson A. Dynamics of crustal rifting in NE Iceland. Journal of Geophysical Research. 1985;90:10151–10162.

[117] Piochi M, Pappalardo L, De Astis G. Geochemical and isotopical variations within the Campanian Comagmatic Province: implications on magma source composition. Annals of Geophysics. 2004;47(4):1485–1499.

[118] Piochi M, Mormone A, Balassone G, Strauss H, Troise C, De Natale G. Native sulfur, sulfates and sulfides from the active Campi Flegrei volcano (southern Italy): genetic environments and degassing dynamics revealed by mineralogy and isotope geochemistry. Journal of Volcanology and Geothermal Research. 2015;304:180–193.

[119] Sgavetti M, Pompilio L, Roveri M, Manzi V, Valentino GM, Lugli S, et al. Two geologic systems providing terrestrial analogues for the exploration of sulfate deposits on Mars: initial spectral characterization. Planetary and Space Science. 2009;57:614–627.

[120] Russo M. Realgar e pararealgar della solfatara di Pozzuoli (Napoli) (Realgar and pararealgar from the Pozzuoli solfatara (Neaples). Micro. 2004;2004:25–28.

[121] Rolandi G, Paone A, Di Lascio M, Stefani G. The 79 AD eruption of Somma: the relationship between the date of the eruption and the southeast tephra dispersion. Journal of Volcanology and Geothermal Research. 2007;169:87–98.

[122] Chiodini G, Marini L, Russo M. Geochemical evidence for the existence of high-temperature hydrothermal brines at Vesuvio volcano, Italy. Geochimica et Cosmochimica Acta. 2001;65:2129–2147.

[123] Caliro S, Chiodini G, Avino R, Minopoli C, Bocchino B. Long time-series of chemical and isotopic compositions of Vesuvius fumaroles: evidence for deep and shallow processes. Annals of Geophysics. 2011;54:137–149.

[124] De Astis G, Lucchi F, Dellino P, La Volpe L, Tranne C A, Frezzotti ML, et al. Geology, volcanic history and petrology of Vulcano (central Aeolian archipelago). Geological Society, London, Memoirs. 2013;37:281–349.

[125] Paonita A, Favara R, Nuccio PM, Sortino F. Genesis of fumarolic emissions as inferred by isotope mass balances: CO_2 and water at Vulcano Island, Italy. Geochimica et Cosmochimica Acta. 2002;66:759–772.

[126] Capasso G, D'Alessandro W, Favara R, Inguaggiato S, Parello F. Interaction between the deep fluids and the shallow groundwaters on Vulcano Island (Italy). Journal of Volcanology and Geothermal Research. 2001;108:187–198.

[127] Coltelli M, Del Carlo P, Vezzoli L. The discovery of a Plinian basaltic eruption of Roman age at Etna volcano, Italy. Geology. 1998;26:1095–1098.

[128] Neri M, Acocella V, Behncke B. The role of the Pernicana fault system in the spreading of Mt. Etna (Italy) during the 2002–2003 eruption. Bulletin of Volcanology. 2004;66:417–430.

[129] Branca S, Del Carlo P. Eruptions of Mt. Etna during the past 3200 years: a revised compilation integrating the historical and stratigraphical records. In: Bonaccorso A, Calvari S, Coltelli M, Negro CD, Falsaperla S, editors. Mt. Etna: Volcano Laboratory. Washington: American Geophysical Union; 2004. pp. 1–22.

[130] Liotta M, Paonita A, Caracausi A, Martelli M, Rizzo A, Favara R. Hydrothermal processes governing the geochemistry of the crater fumaroles at Mount Etna volcano (Italy). Chemical Geology. 2010;278:92–104.

[131] Papazachos BC, Comninakis PE. Geophysical and tectonic features of the Aegean Arc. Journal of Geophysical Research. 1971;76:8517–8533.

[132] Nicholls JA. Petrology of Santorini volcano, cyclades, Greece. Journal of Petrology. 1971;12(1):67–119.

[133] Keller J. Mediterranean island arcs. In: Thorpe RS, editor. Andesites. New York: Wiley; 1982. pp. 307–325.

[134] Fytikas M, Innocenti F, Manetti P, Mazzuoli R, Peccerillo A, Villari L. Tertiary to quaternary evolution of volcanism in the Aegean region. Geological Society London Special Publications. 1984;17(1):687–699.

[135] Fytikas M, Innocenti F, Kolios N, Manetti P, Mazzuoli R, Poli G, et al. Volcanology and petrology of volcanic products from the island of Milos and neighbouring islets. Journal of Volcanology and Geothermal Research. 1986;28:297–317.

[136] Pe-Piper G, Piper DJW. Volcanism at subduction zones; Aegean area. Bulletin of the Geological Society of Greece. 1972; 9:113–144.

[137] Pe-Piper G, Hatzipanagiotou K. The Pliocene volcanic rocks of Crommyonia, western Greece and their implications for the early evolution of the South Aegean arc. Geological Magazine. 1997;134:55–66.

[138] Liakopoulos A, Katerinopoulos A, Markopoulos T, Bouleègue, J. A mineralogical petrographic and geochemical study of samples from wells in the geothermal field of Milos Island (Greece). Geothermics. 1991;20(4):237–256.

[139] Tarney J, Barr SR, Mitropoulos P, Sideris K, Katerinopoulos A, Stouraiti H. Santorini: geochemical constraints on magmas sources and eruption mechanisms. The European Laboratory Volcanoes. 1996;EUR18161EN:89–112.

[140] Bagnato E, Tamburello G, Aiuppa A, Sprovieri M, Vougioukalakis GE, Parks M. Mercury emissions from soils and fumaroles of Nea Kameni volcanic centre, Santorini (Greece). Geochemical Journal. 2013;47:437–450.

[141] Chiodini G, Cioni R, Leonis C, Marini L, Raco B. Fluid geochemistry of Nisyros Island, Dodecanese, Greece. Journal of Volcanology and Geothermal Research. 1993;56:95–112.

[142] D'Alessandro W, Brusca L, Kyriakopoulos K, Michas G, Papadakis G. Hydrogen sulphide as a natural air contaminant in volcanic/geothermal areas: the case of Soussaki, Corinthia (Greece). Environmental Geology. 2009;57(8):1723–1728.

[143] D'Alessandro W, Brusca L, Martelli M, Rizzo A, Kyriakopoulos K. Geochemical characterization of natural gas manifestations in Greece. Bulletin of the Geological Society of Greece. 2010;43(5):2327–2337.

[144] Kiyosu Y, Kurahashi M. Origin of sulfur species in acid sulfate-chloride thermal waters, northeastern Japan. Geochimica et Cosmochimica Acta. 1983;47:1237–1245.

Section 4

Volcanism in the Geological Record

Chapter 12

Submarine Volcanism of the Cabo de Gata Magmatic Arc in the Betic-Rif Orogen, SE Spain: Processes and Products

Carles Soriano, Ray A.F. Cas, Nancy R. Riggs and Guido Giordano

Additional information is available at the end of the chapter

http://dx.doi.org/10.5772/63579

Abstract

Volcanic eruptions in subaqueous settings have been traditionally characterized by the study of ancient deposits and, more recently, by indirect observation of the sea floor with different geophysical means. Subaqueous volcanism is largely governed by the physical properties of water and the way water interacts with magma. Among the characteristic products of subaqueous volcanism are hyaloclastite breccias of dense clasts and of pumiceous clasts produced by the quench fragmentation of hot magma in effusive eruptions. Pumice breccias driven by fragmentation of magma in explosive eruptions are not infrequent. The Miocene volcanic zone of Cabo de Gata in southeastern Spain provides excellent exposures where to test the current understanding on subaqueous volcanism. In particular, submarine lavas with a coherent core and an outer carapace of vesicular hyaloclastite together with pumice breccias and crystal tuffs of the El Barronal Formation provide clues to understand transient conditions during explosive and effusive eruptions. Debris avalanches deposits are rather common in Cabo de Gata, such as those of the Los Frailes Formation and the Cerro Estorvillas Formation, and help to understand the instability processes of submarine volcanic edifices and the resultant mass flows. Interbedding of volcanic rocks with shallow water sedimentary rocks allows inferring water depth conditions for volcanism and the subsidence history of the volcano-sedimentary basin.

Keywords: hyaloclastite, submarine explosions, debris-avalanche, subsidence, infralittoral

1. Introduction

The Cabo de Gata volcanic zone is located in southeastern Spain and is a portion of the Neogene volcanic arc of the Betic-rif Orogen, an arcuate orocline formed by westward retreat of an east

dipping slab Orogen, (**Figure 1**). The zone includes a wide variety of volcanic facies, ranging from explosive to effusive and recording transient conditions during eruptions. Volcanic rocks of Cabo de Gata are calc-alkaline in composition and were erupted from submarine vents and deposited in submarine settings, although rare facies record the transition to subaerial settings. Therefore, volcanism in Cabo de Gata is essentially submarine, although some volcanic edifices and products may have risen from above sea level. In terms of rock chemistry, eruptive style, age and depositional setting, volcanic successions in Cabo de Gata can be compared with similar examples from the volcanic arc of Japan. The Cabo de Gata volcanic zone constitutes the best exposed, best preserved and most voluminous record of the volcanic arc of the Betic-Rif Orogen and is certainly the most important record of submarine volcanism in the western Mediterranean area.

Despite its significance, it has not been until very recently that systematic studies with a modern facies to processes approach were undertaken in the Cabo de Gata volcanic zone and for this reason this area has remain virtually unknown for most volcanologists. Previous studies were mainly focused on petrological aspects of the volcanic rocks and on the Rodalquilar gold epithermal deposits associated with volcanic rocks, without providing a comprehensive stratigraphic framework aimed to understand the processes and products of Cabo de Gata volcanism [1–6]. Comparison of Cabo de Gata volcanic rocks with other Miocene volcanic zones such as the Iblean Mountains in Sicily, Sulcis in Sardegna and volcanic islands in the Aegean Sea may provide a more comprehensive view on volcanism of similar age occurring in different geotectonic scenarios of the narrow Mediterranean area.

Here, we first present an introductory section on the principles of subaqueous volcanism and then a review of our research undertaken during the last five years in the Cabo de Gata volcanic zone. In particular, we focus on those facies and successions of facies that reveal transient conditions of eruptive styles during eruptions and on submarine volcanic debris-avalanche deposits, which constitute a unique opportunity for a direct study of this kind of deposits in the geological record. We also focus on the facies and the stratigraphic successions of sedimentary rocks interbedded with volcanic rocks, aiming to characterize the bathymetric conditions for sediment deposition and, indirectly, for volcanism. Using the evidence provided by facies analyses we typify the characteristic eruptive models in Cabo de Gata and their link to the tectonics of the Neogene volcano-sedimentary basin in which volcanic rocks are exposed.

2. Basic principles of subaqueous volcanism

Understanding volcanic processes in subaqueous environments has always been challenging because first, in most cases, they cannot be directly observed, and second the physical properties of water and the way that water interacts with erupting or intruding magma are still not fully understood. Despite many contributions to the subject, the major debate still seems to revolve around the factors that relate water depths and explosive eruptions.

In modern environments, one of the greatest limitations has been the inability to observe processes and seafloor volcanic topography as well as the distribution of different facies or

http://dx.doi.org/10.5772/63579

deposit types at scales that provide understanding of the characteristics, extent, scale and relations of processes and deposits. Local submersible and camera observations have been helpful, but are very limiting. However, recent advances in imaging technology, such as high-resolution side-scan sonar and bathymetry technology mounted on autonomous underwater vehicles (AUVs) such as Sentry, allow very high-resolution Digital Elevation Model imagery to be produced over large areas and whole submerged volcanoes that will open up a new world of understanding of subaqueous volcanic processes. In addition, new generation photographic videoing and sampling facilities on remotely operated vehicles (ROVs) such as Jason and Medea provided hitherto unparalleled opportunities to learn about modern sea floor processes, including volcanism.

In ancient volcanic successions, the principal approach for understanding volcanological processes and settings remains detailed mapping of the relations between facies and analysis of their characteristics to assess original water depths and the process origins of the facies. This has given rise to an ongoing need to quantify the physical processes associated with subaqueous eruptions, including the constraints on processes imposed by subaqueous environments, in order to understand the origins of different deposit types.

The most recent review of submarine volcanic processes has been by [7] (see for a listing of other reviews and major research contributions) in which they provided a summary of the essential physical properties of water and magma, as well as a conceptual overview of the processes and deposit characteristics. To illustrate the concepts, they cited examples from the Cabo de Gata volcanic succession that has been well described by [8–12] and is summarized below in this paper. Recently, [13] quantified many of the physical processes involved in the formation of volcanic glass and the quench fragmentation of volcanic glass in subaqueous settings based on the materials-science literature. These authors then related the characteristics of hyaloclastite deposits to those physical processes and rates of processes. In this section, we briefly review the main processes, principles and deposit types in subaqueous environments.

The major difference between subaerial volcanism and subaqueous volcanism is the aqueous medium in the latter and the different ways that magma and water can interact to influence the style of eruption and the types of deposits. Water has a significant impact on the cooling rates of magma that is erupted into it, as well as creating ambient confining-pressure constraints on the way that exsolving magmatic volatiles and superheated water behave. Water is a high-enthalpy substance. It has a high heat capacity (4.187 kJ/kg K) and high thermal conductivity (0.58 W/m Kelvin at 25°C for water and 0.61 W/mK at 25°C, and 0.68 W/mK at 120°C for seawater [14]). Water is therefore very thermodynamically responsive to changes in temperature, which allow it to readily absorb and release heat transmitted to it by magma, via conduction and radiative-heat transfer. This is particularly important when magma at temperatures from 700 to 1200°C comes into contact with liquid water (<20°C). Water acts as a heat sink and can cause the magma to instantaneously cool through the glass transition temperature, causing glass to form. If the rate of heat loss or cooling rate is high, the magma/glass is thermally shocked, causing contractional tensile stresses to form in the glass. If these exceed the tensile strength of the glass, it shatters in situ, leading to a formation of a network of contractional fractures that propagate inwards from the cooling margin of the magma body.

This process is called quench fragmentation and the breccia of glass debris that forms is called hyaloclastite [7, 13]. This process can occur at any water depth.

However, water can very quickly change state over a limited temperature range (0–100°C) when superheated by contact with magma (700–1200°C) and over a range of external pressures that are determined by water depth. The hydrostatic pressure gradient in a body of water is 1 bar (0.1 MPa)/10 m water depth. In particular, liquid water can readily transform into steam, which has a much lower thermal conductivity (0.016 W/m K at 125°C) and specific heat capacity (1.996 kJ/kg K [15]). If this occurs at the interface between magma and water in a process called film boiling (also known as the Leidenfrost Effect), a vapour film forms at the interface, which can insulate the magma from heat loss. Sustained and efficient film boiling can thus reduce the rate of heat loss or cooling of the magma, moderate the rate of contraction, and so minimize thermal tensile stresses in the cooling glass. As a result, the magma may remain coherent and be preserved as a coherent lava or a coherent intrusion in the case where magma intrudes water-saturated sediments.

The super-heating of liquid water at low confining pressures causes a phase transformation to steam and a consequent major volume expansion. At high, instantaneous, rates of expansion such transformations are explosive, driving phreatic and phreatomagmatic volcanic explosions. This is most likely to occur at shallow water depths up to several hundred metres [16].

However, at increasing water depths and hydrostatic pressures the hydrostatic pressure approaches the critical pressure of water. The critical point of water is the pressure (and temperature) at which there is no distinction between the liquid and the gaseous phases; the fluid is called a supercritical fluid and has the properties of both the gaseous and the liquid forms. For pure water, the critical pressure is ~218–221 bars or 21.8–22.1 MPa and for seawater, it is about 300 bars or 30 MPa [17]. Since the hydrostatic pressure gradient in water is 1 bar or 0.1 MPa/10 m water depths, at water depths of 2 or more kms steam that forms at the interface between magma and the water mass is highly compressed and cannot expand explosively unless it can be instantaneously decompressed, which is difficult to do at those water depths. The modern seafloor record and the geological record tell us that voluminous explosive eruptions (cf. subaerial plinian eruptions) that occurred at water depths of more than 1 km are rare, although there are many examples of deposits of variably vesiculated pumiceous debris that originated in shallower water but were then resedimented into deeper water by various processes.

On this point, however, it is important to stress that not all pumice is explosive in origin. Coherent pumice domains can be well developed in subaerial lavas, formed through slow volatile exsolution and vesicle growth at nonexplosive rates in lavas with a subcritical volatile content to drive explosive eruption. In relatively deep subaqueous environments, the hydrostatic confining pressure will hinder both the initial exsolution of volatiles and the vesicle-growth rates. Growth rates may, however, be high enough to form well-vesiculated lavas with coherent pumice domains, but not high enough to drive explosions [7, 13]. Quench fragmentation of such coherent pumice domains can produce large volumes of pumice hyaloclastite.

http://dx.doi.org/10.5772/63579

Another factor that suppresses the intensity of submarine explosive eruptions is the bulk modulus of water, which for pure water is 2.15 × 109 Pa and for seawater is 2.34 × 109 Pa. The bulk modulus of a fluid is a measure of its resistance to uniform compression, i.e., its compressibility or the degree to which it deforms. In comparison, the adiabatic bulk modulus of air is orders of magnitude less, at 1.42 × 105 Pa. Because water is much less compressible and deformable than air, explosions into water are much more suppressed, restricted and much less intense than in air [7].

We now focus on the principal findings of [13] about the principles involved in the fracture behavior of volcanic glass, based on assessment of the ceramics and glass literature in materials science.

- Cooling contraction cracks propagate perpendicular to the cooling surfaces, which initially are the margins of the magma body at its interface with water or water-saturated sediments.
- The distance between cooling cracks depends on the cooling rate, the temperature differential and gradient between magma and water and the level of thermal stress. This determines the first-order grain size of the resultant hyaloclastite breccia and explains why grain size is smaller at the margins of a magma body compared with the interior, where cooling rates and temperature gradients are lower.
- Once a cooling crack forms, it also becomes a cooling surface and other cracks will form perpendicular to it and then others perpendicular to the second-order fractures, etc.
- The spacing between propagating cracks is usually equal to the length of the crack.
- When a crack approaches another crack, it will try to change direction and approach at right angles.
- When a crack intersects another crack, it will usually stop because it cannot propagate across the space.
- Crack formation results in release of both thermal and mechanical energy and cracks may stop if the tensile stress falls below the strength of the glass, which increases as glass cools.
- Crack shape, and thus fragment shape, depends on cooling rate, the crack propagation velocities and the orientation of the cooling surfaces. At high crack velocities, which occur when the temperature differential is high, cracks tend to be straight and form under what is called the critical crack regime. Crack velocities can be >600 ms^{-1}. At crack velocities greater than 0.25 times the speed of sound in glass, cracks may bifurcate and form wedge to splinter-shaped fragments. Low-temperature differentials lead to low crack velocities (subcritical regime (<cm s^{-1}) and cracks may become curviplanar.
- Water not only plays a physical role in facilitating crack propagation by causing cooling contraction tensile stresses at the crack tip but also plays a chemical role in breaking chemical bonds in the glass in a propagating crack tip.
- Heterogeneous glass, with dispersed crystals, lithic fragments and vesicles, experiences complex fracture formation because of the variable properties of the various components of the glass.

- Glass with abundant dispersed crystals is stronger than aphyric glass, is more resistant to quench fragmentation and, should it fragment, it is likely to form coarse hyaloclastite breccia.
- The presence of abundant vesicles in glass weakens it and makes it more prone to quench fragmentation.
- Pumice hyaloclastite formed through nonexplosive quench fragmentation should be quite common in submarine settings. If the deposit is still in situ, it may still preserve jigsaw fit textures. However, if it is resedimented, it should be bedded and preserve characteristics of a variety of subaqueous mass flow processes (e.g., grain-flow, turbidity currents, debris flow, debris avalanches and rafted suspension transport).

These principles and processes help to explain many of the characteristics of quench-fragmented hyaloclastite deposits, as described above, but also including the following:

- Equant, blocky clast aggregates are likely to have formed under steady, slow, subcritical crack-propagation conditions. Equant clasts with curviplanar margins are likely to have formed at low temperatures and low temperature differentials.
- Elongate, splinter- and wedge-shaped clasts are likely to have formed under high crack velocity in critical crack-growth regimes at high temperature differentials.
- Perlite cracking may be a product of thermal stressing and quenching under slow-cooling, subcritical conditions.
- Fine hyaloclastite breccia is the product of a fast cooling rate and high temperature differential, which is why hyaloclastite grainsize may vary from fine at the margins of a body to coarser in the interior and even grade into a coherent interior.
- Jig-saw fit textures are indicative of in situ, nonexplosive, cooling contraction quench fragmentation.
- Clast-rotated textures indicate postcrack formation movement as a result of continued lava or intrusion movement or downslope resedimentation.
- The grainsize of quench-fragmented crystalline glass hyaloclastite is likely to be coarser than for aphyric glass hyaloclastite.
- Pumice hyaloclastite should not be unusual in subaqueous settings and not all pumice is pyroclastic in origin.

In the following sections, we illustrate how some of the processes of subaqueous volcanism, in particular those regarding magma fragmentation and transport and deposition of volcanic debris, are recorded in the submarine volcanic rocks of Cabo de Gata.

3. Geological setting of Cabo de Gata

The Betic-Rif is a complex orogenic system whose geodynamic evolution has been widely debated (e.g., for recent reviews [18–20]). This complexity partly arises from the need to

http://dx.doi.org/10.5772/63579

reconcile the structures and kinematics of geodynamic processes operating at different scales and times in the narrow area of the western Mediterranean with the large-scale and long-standing geodynamic scenario of African and Eurasian plate convergence.

The Betic-Rif Orogen is an arcuate mountain belt with a northern branch formed by the Betic cordillera in the Iberian Peninsula and a southern branch formed by the Rif chain in northern Africa. The orogen displays a tight arc with a westward concavity in the Gibraltar strait (**Figure 1**). Igneous rocks of tholeitic, calc-alkaline, shoshonitic and ultrapotassic compositions show enrichment in K with time and are exposed in the internal areas of the belt [19, 21, 22]. Igneous rocks are subduction-related in a broad sense and are partly coeval with the extension tectonics developed in the internal areas of the Betic-Rif during Neogene. Calc-alkaline rocks in particular, display a clear arc-related geochemical signature and are synchronous with the opening of the back-arc Alborán basin (**Figure 1**). Arc curvature, arc magmatism and back-arc extension were formed during Miocene time by the westward rollback of a narrow eastward-subducting slab fragmented from the African plate [20, 22, 23]. Westward retreat of the subducted slab was accompanied by thinning of the continental crust, formation of oceanic crust and extension, leading to the formation of Neogene intramontane basins in the internal areas of the Betic-Rif [20, 22, 24]. Extension ceased in Late Miocene and deformation in the internal areas of the Betic-Rif was dominated by the kinematics of African and Eurasian plate convergence. NNW convergence of Africa with Iberia compressed the Alborán basin and reactivated suitably oriented faults in the intramontane basins. The internal areas of the Betic-Rif became a diffuse plate boundary between Africa and Eurasia dominated by wrench tectonics processes that are still active, as shown by recent seismicity of the Carboneras fault and other similar strike-slip faults [20, 22, 25].

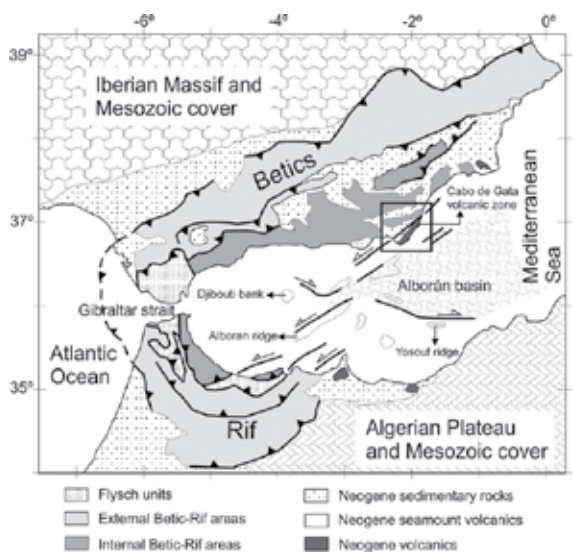

Figure 1. Geologic map of the Betic-Rif Orogen in the Western Mediterranean with location of the Cabo de Gata volcanic zone (modified from [24, 26]). Box shows location of **Figure 2**.

Due to the complex geodynamic evolution of the Betic-Rif Orogen and to the wrench tectonics established in the internal areas since Late Miocene time, the volcanic arc of the Betic-Rif appears distributed along fault-bounded seamounts in the Alborán Sea and onshore in volcano-sedimentary basins on both branches of the mountain belt (**Figure 1**). The Cabo de Gata volcanic zone corresponds to a portion of this volcanic arc exposed in the eastern part of the Almería-Níjar basin (**Figure 2**). This basin is structurally controlled by the Carboneras fault, which divides the basin into a western through dominated by Late Miocene to Pleistocene sedimentary rocks and an eastern through dominated by Miocene volcanic rocks (**Figure 2**). The Carboneras fault is an active structure with a complex kinematic history that includes contemporaneous strike-slip and dip-slip movements since Early Miocene time [27–29]. Basement to the Neogene succession of the Almería-Níjar basin are Paleozoic to Jurassic metamorphic rocks of the Maláguide, Alpujárride and Nevado-Filábride complexes that crop out in the mountain ranges bounding the basin (Sierra Cabrera, Sierra Alhamilla) and along the Carboneras fault strands (**Figure 2**). Gravimetric data and magnetic modeling suggest that volcanic rocks underlie Late Miocene to Pleistocene sedimentary rocks in the western part of the Almería-Níjar basin. The residual gravimetric anomaly together with well log data suggest that Neogene infill of the basin increases to the southwest (SW) and that the Neogene-basement boundary dips to the SW [30, 31]. The structure of the Almería-Níjar basin, of other intramontane basins of the Betic-Rif and of submarine promontories in the Alborán Sea consists of low-amplitude open folds with kilometer-scale wavelengths related to stepped normal faults, which are in turn associated with regional strike-slip faults [30, 32, 33].

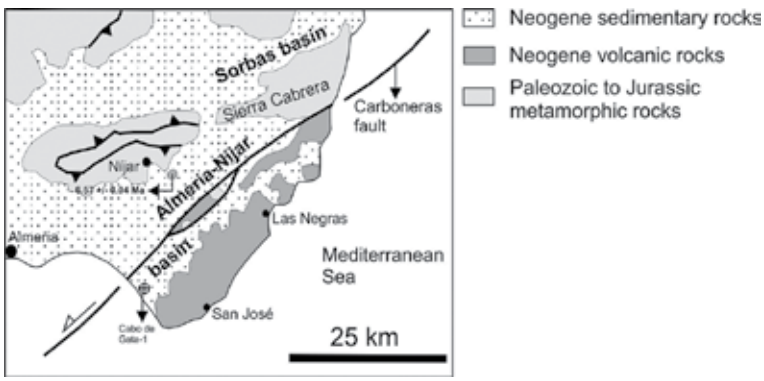

Figure 2. Simplified geologic map of the Almeria-Níjar basin and the Cabo de Gata volcanic zone (modified from [34]). Ar^{40}/Ar^{39} age corresponds to the Cerro del Hoyazo dacite [35].

4. Stratigraphy, geochronology, and structure of the Cabo de Gata volcanic zone

The Cabo de Gata volcanic zone is an area of semiarid climate in which rock exposure is virtually continuous both along the shoreline and the inland. Maximum elevation is nearly

http://dx.doi.org/10.5772/63579

500 m above sea level and the original morphologies of volcanic edifices are poorly preserved due to erosion. Nevertheless, excellent exposures of stratigraphic sections along marine cliffs and inland allow a precise reconstruction of the volcanic stratigraphy. Based on preserved exposures of deposits, Cabo de Gata can be understood as a volcanic field formed by dispersed small-scale lava domes and larger dome complexes and by larger volcanic seamounts. The stratigraphic succession of Cabo de Gata consists of volcanic rocks interbedded with sedimentary rocks, mainly carbonate and siliciclastic deposits. Bedding of volcanic and sedimentary rocks, dip of tabular lavas and overall disposition of volcanic bodies are subhorizontal or shallowly inclined to the northeast (NE), providing a general upward stratigraphic polarity toward the NE.

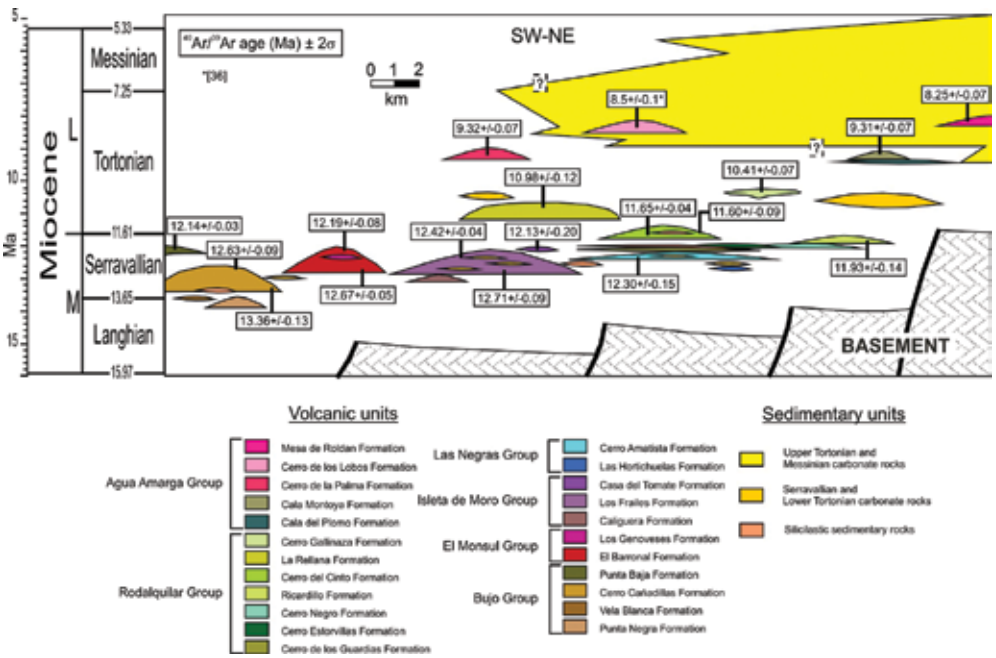

Figure 3. Chronostratigraphic scheme of the Cabo de Gata volcanic zone with distribution of the different lithostratigraphic units (modified from [10]). All Ar^{40}/Ar^{39} ages from [22] except [36].

The volcanic stratigraphy shown in **Figure 3** is a revision of that in [10] with some minor changes regarding the aggregation of formations into groups, in particular the Agua Amarga and Rodalquilar groups. Description, discussion and extended data on the Ar^{40}/Ar^{39} ages of formations are available in [22]. The lithostratigraphic units distinguished are formations formally defined that were subsequently divided into informal subunits when required [10]. The criteria used to divide the stratigraphic succession of Cabo de Gata into formations and to aggregate them into groups is based on lithology, stratigraphic position, age and geochemical affinity. Formations, groups and the informal units within formations are bounded by unconformities of different hierarchy. Volcanic units are interbedded with sedimentary units throughout the Cabo de Gata region with an overall trend of thicker and older volcanic units

toward the SW and thicker and younger sedimentary units toward the NE (**Figure 3**). Upper Tortonian to Messinian sedimentary rocks cap the volcano-sedimentary succession toward the NE. Sedimentary units are laterally discontinuous, in particular toward the SW of Cabo de Gata, which may result in the local amalgamation of thick piles of volcanic rocks separated by unconformities.

The main structural features in Cabo de Gata are subvertical normal faults that affect volcanic and sedimentary units and can be grouped into three sets based on their orientation: dominant NW-SE- to N-S-trending faults and subordinate NE-SW-trending faults (**Figure 4**). Fanning stratal dips and differences in bed thickness across fault blocks are thought to indicate that displacement along some faults is syndepositional to the emplacement of volcanic and sedimentary rocks [32]. Epithermal ore deposits of the Rodalquilar mine area result from hydrothermal fluids precipitated at high temperatures along N-S-trending faults [6]. Structures in Cabo de Gata are similar to those of other Neogene intramontane basins of the Betic Rif Orogen and of volcanic seamounts of the Alborán Sea. These structures are associated with the still active wrench tectonics established in the area since Late Miocene. This tectonic regime is ultimately responsible for the observed uplift-downlift displacements along some faults and for the present-day exposure above sea level of the submarine volcano-sedimentary successions of Cabo de Gata.

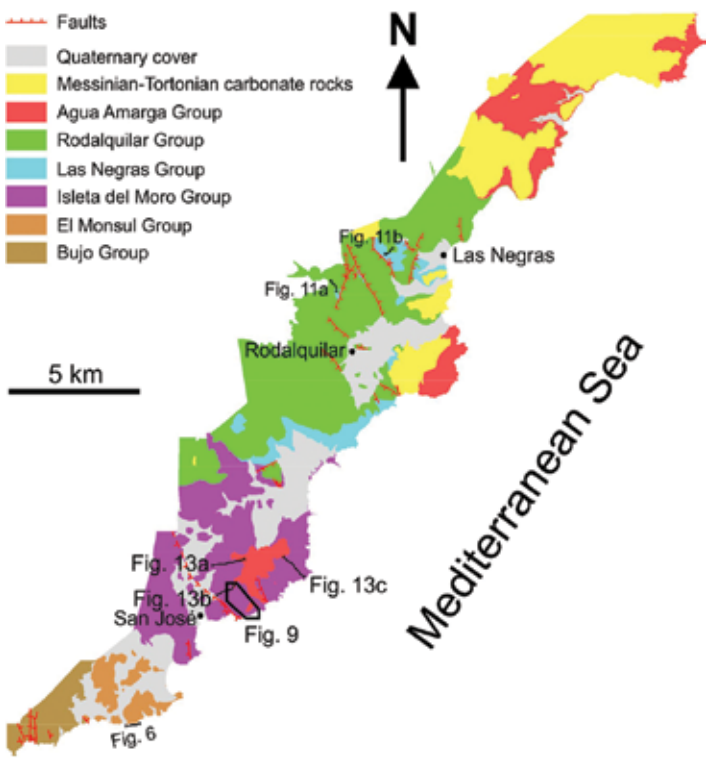

Figure 4. Simplified geologic map of the Cabo de Gata volcanic zone with the distribution of groups and location of figures (modified from [22]).

http://dx.doi.org/10.5772/63579

The chronostratigraphic position of volcanic units based on radio-isotopic ages indicates that volcanism in Cabo de Gata started in Serravalian and ended in Tortonian times (**Figure 3**). During this time, volcanism migrated toward the NE while hiatuses in the volcanic activity became increasingly significant (**Figure 5**). Geophysical and well-log data reveal the occurrence of volcanic rocks beneath the oldest dated unit of Cabo de Gata [30, 31]. Hence, given the Messinian age of the Cerro del Hoyazo dacite [35], the volcanic activity in the whole Almeria-Níjar basin may have encompassed Middle to Late Miocene time (**Figure 5**). Volcanic formations and informal subunits within them correspond to volcanic cycles in a wide sense, meaning that they include all the deposits associated with the volcanic activity during an eruptive period. The volcanic units are separated from each other either by distinct unconformities or by sedimentary rocks, indicating hiatuses in the volcanic activity and erosion of volcanic edifices and deposits. In the following sections, the relevant features of Cabo de Gata volcanism are illustrated with selected examples of deposits and stratigraphic successions.

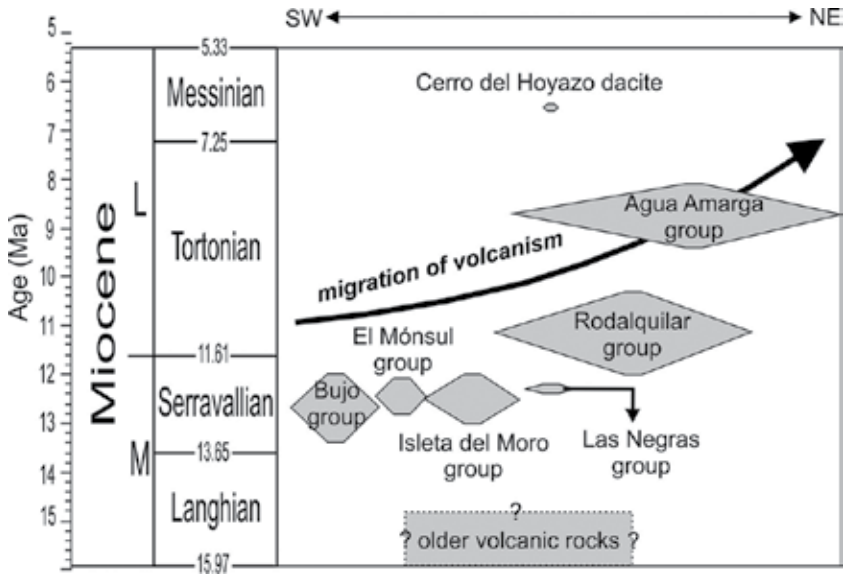

Figure 5. Chronologic timetable of the volcanic activity in the Almería-Níjar basin based on Ar^{40}/Ar^{39} ages of dated rocks approximately distributed from SW-NE (modified from [22]).

5. Transitions between explosive and effusive conditions during submarine eruptions

Transitions from explosive to effusive activity or vice versa are common during individual eruptions in most subaerial volcanoes (Teide, Soufrière Hills, Mount St. Helens, Monte Pilato, etc.). Transient conditions during eruptions have been either witnessed in active volcanoes or are well documented through the study of volcanic deposits. In subaqueous settings, however,

their study is certainly more problematic and the usually incomplete and fragmental nature of many submarine successions hampers a proper understanding of how these transitions are recorded. Here, transitions from explosive to effusive eruptive style during individual eruptions are illustrated with examples from the volcanic succession of the El Barronal Formation in southwestern Cabo de Gata (**Figure 4**). An extended description of the lihofacies succession of this unit is available in [9].

The El Barronal Formation consists of a succession of lavas interbedded with volcaniclastic rocks that is intruded by subvertical dikes (**Figure 6**). The lower boundary of this unit is an unconformity with the Cerro Cañadillas Formation while the upper limit is not exposed. The whole El Barronal Formation is composed of up to five lava units. The El Barronal Formation has been Ar^{40}/Ar^{39}-dated at 12.19 Ma for lava unit 4 and 12.67 Ma for lava unit 3 [9]. Interbedded between these two lava units is the rhyolitic dome of the Los Genoveses Formation and also carbonate rocks with shell fragments and polymictic siliciclastic rocks with rounded pebbles from the metamorphic basement of the Neogene succession of Cabo de Gata (**Figure 3**).

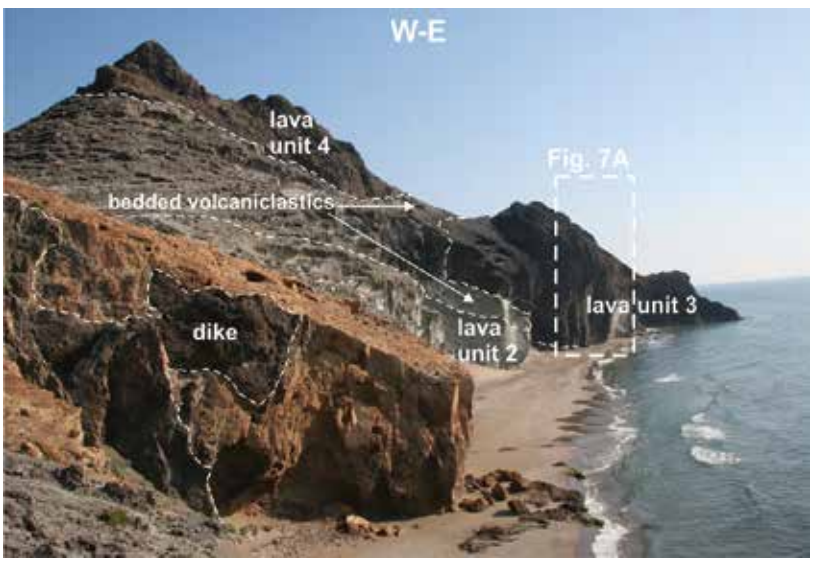

Figure 6. Panoramic view of the stratigraphic succession of the El Barronal Formation at Playa del Barronal. Note lava unit 3 pinching out into bedded volcaniclastic succession to the west (see **Figure 4** for location).

Lavas, volcaniclastic rocks and dikes of the El Barronal Formation have identical andesitic composition and mineralogy. Lavas are formed by a coherent core grading into an outer carapace of in situ to clast-rotated hyaloclastite breccia. The coherent core of lavas has colonnade columnar joints and entablature columnar joints usually forming rosette structures (**Figure 7A**). The outer carapace consists of massive hyaloclastite with dense clasts grading outward into massive and flow-banded hyaloclastite with vesicular clasts (~40% vesicles). Volcaniclastic rocks are bedded and consist of massive breccia with dense and vesicular clasts, diffusely bedded pumice-rich breccia, cross-bedded crystal-rich sandstone and thinly bedded

http://dx.doi.org/10.5772/63579

fine tuffaceous sandstone. These facies types contain outsized clasts and have rapid vertical and lateral transitions between them (**Figure 8**).

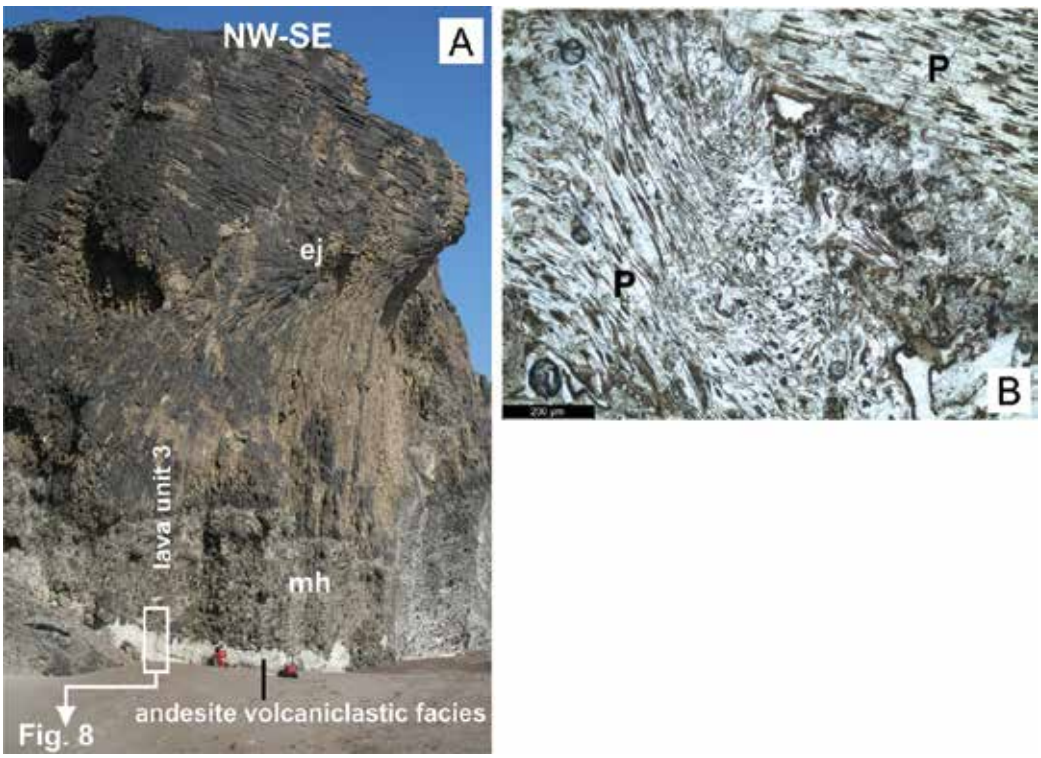

Figure 7. A: lava unit 3 of the El Barronal Formation with entablature jointed facies (ej) showing fan-like joints and grading downward into massive hyaloclastite with dense clasts (mh) and **B**: photomicrograph of finely bedded tuffaceous sandstone with tube-pumice clasts (P).

Volcaniclastic facies contain a variety of clasts indicating provenance from different sources: juvenile components (pumice clasts, glass shards and crystals), clasts derived from underlying lavas (dense rock clasts and vesicular clasts) and exotic well-rounded andesite cobbles likely derived from sources above wave base. Juvenile components are rare in massive breccia, whereas they are present in different amounts in the rest of volcaniclastic facies. Textural evidence of juvenile clasts (i.e., vesicularity >60%, tube-pumice clasts and bubble-wall shards) suggests fragmentation of magma in the conduit by magmatic explosions, whereas the blocky shape of crystals and lithics can be attributed to some degree of magma-water interaction in the fragmentation processes (**Figure 7B**). Finer-grained volcaniclastic facies show distorted bedding, small-scale faults, folds and dish structures, suggesting that they were water-saturated at emplacement. Soft-sediment deformation structures are invariably located at the contact between volcaniclastic facies and upper lavas indicating that volcaniclastic facies were wet and poorly consolidated at the emplacement of upper lavas (**Figure 8**). These contact relations suggest that the time encompassed between the deposition of volcaniclastic facies

and the emplacement of upper lavas was short and that lavas and volcaniclastic rocks were likely syn-eruptive.

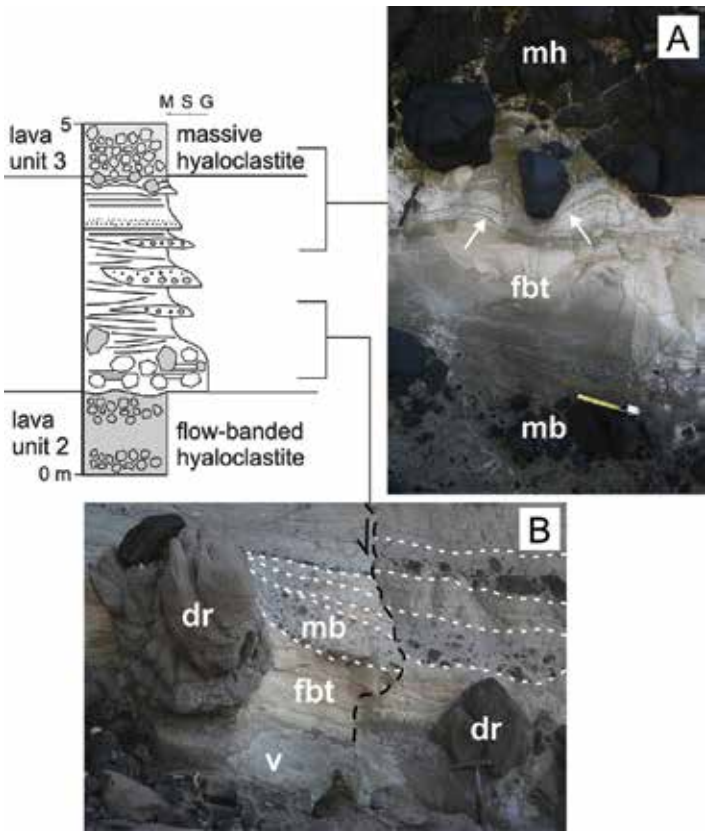

Figure 8. Stratigraphic log and contact relations of the volcaniclastic deposits located between lava unit 2 and 3 of the El Barronal Formation. mh, massive hyaloclastite; mb, massive breccia; tbt, thinly bedded fine tuffaceous sandstone; dr, dense rock clast; v, vesicular clast (see **Figure 7A** for log location).

The El Barronal Formation can be characterized as a succession of eruptive cycles, each of which started with explosive eruptions that yielded deposition of volcaniclastic facies and ended with the effusive emplacement of lavas. A hiatus in the andesite volcanic activity of El Barronal, with eventual deposition of carbonate sediments and emplacement of rhyolitic magma, separates each volcanic cycle. Explosive activity was complex as suggested by the rapid lateral and vertical transitions among volcaniclastic facies and by coexistence of textural evidences indicating fragmentation of magma by magmatic explosions and by magma-water interaction processes. The latter would have enhanced fragmentation efficiency yielding the grain size of finer volcaniclastic facies. Explosive eruptions may have mixed together the different types of juveniles, lithics and clasts from above-wave-base settings too. Steam-driven explosions would have been responsible for the fragmentation of blocks and smaller clasts and the deposition of massive breccia.

http://dx.doi.org/10.5772/63579

6. Submarine volcanic debris-avalanche deposits

Collapse of volcanic edifices and deposition of debris-avalanche deposits in submarine settings are common processes. They often partially affect ocean-island volcanoes such as Hawaii, Tenerife, Reunion and Augustine and also submarine volcanic edifices such as lava domes and stratovolcanoes. Most of the debris avalanches under the sea are inaccessible for obvious reasons and their study has to be undertaken indirectly by means of different geophysical techniques. To our knowledge, there is only one volcanic submarine debris avalanche deposit described in the literature that has been studied in detail by direct access to onshore exposures [37].

The volcanic debris avalanche deposits of Cabo de Gata are well exposed and fairly well constrained in terms of their submarine depositional setting. Therefore, they constitute a unique opportunity for a direct study of this kind of deposits. Here we summarize the main characteristics of two debris avalanche deposits in Cabo de Gata, one of which has been already described in a former work [8] and is the subject of ongoing research.

6.1. The debris avalanche deposits of the Los Frailes Formation

Submarine volcanic debris avalanche deposits crop out to the northeast of San José village in southern Cabo de Gata (**Figure 4**). These deposits are stratigraphically located in informal subunits 2 and 4 of the Los Frailes Formation. Ar^{40}/Ar^{39} ages of sampled blocks from the debris avalanche deposits in subunits 2 and 4 are 12.71 Ma and 12.42 Ma, respectively.

The debris avalanche deposit of subunit 2 is particularly well exposed and is bounded by upper and lower carbonate sedimentary rocks that are laterally discontinuous and contain oysters, corals, echinoderms, algae, and undifferentiated shell fragments (**Figure 9**). This debris avalanche deposit is laterally associated to the northwest with dacite lavas showing a flow-banded and columnar-jointed coherent core that grades outward into in situ to clast-rotated hyaloclastite breccia (**Figure 9**). Lavas and debris-avalanche deposit have identical dacite composition and mineralogy. The debris-avalanche deposit of subunit 2 is massive and monomictic and has an internal organization consisting of block facies "floating" in matrix facies or mixed facies (**Figure 10A**), which is consistent with the classical descriptions of debris avalanche deposits in the literature [38–40]. Some blocks are up to 10^4 cubic meters, although most of them are usually about an order of magnitude smaller and most blocks have a flow-banded and polyhedral-jointed interior (**Figure 10B**). The basal contact of megablocks is sharp, planar, and often fractured with dislocations showing stepped geometry. Shear planes with sigmoid shape form anastomosed lenses and are common at the base of megablocks (**Figure 10C**). Matrix consists of a clast-supported framework of centimeter- to decimeter-size angular clasts with randomly oriented internal flow banding (**Figure 10B**). The upper surface of the debris avalanche deposit in subunit 2 is flat, whereas the lower surface is more irregular, gently dipping to the SE in the northwestern part (**Figure 9**). The maximum thickness of this deposit is nearly 100 m. If a map view of the upper surface of the deposit was exposed rather than an oblique cross-section of the whole deposit, the positive

topography built up by megablocks would have likely resulted in the classical hummocky morphology of most debris avalanche deposits [38, 41, 42].

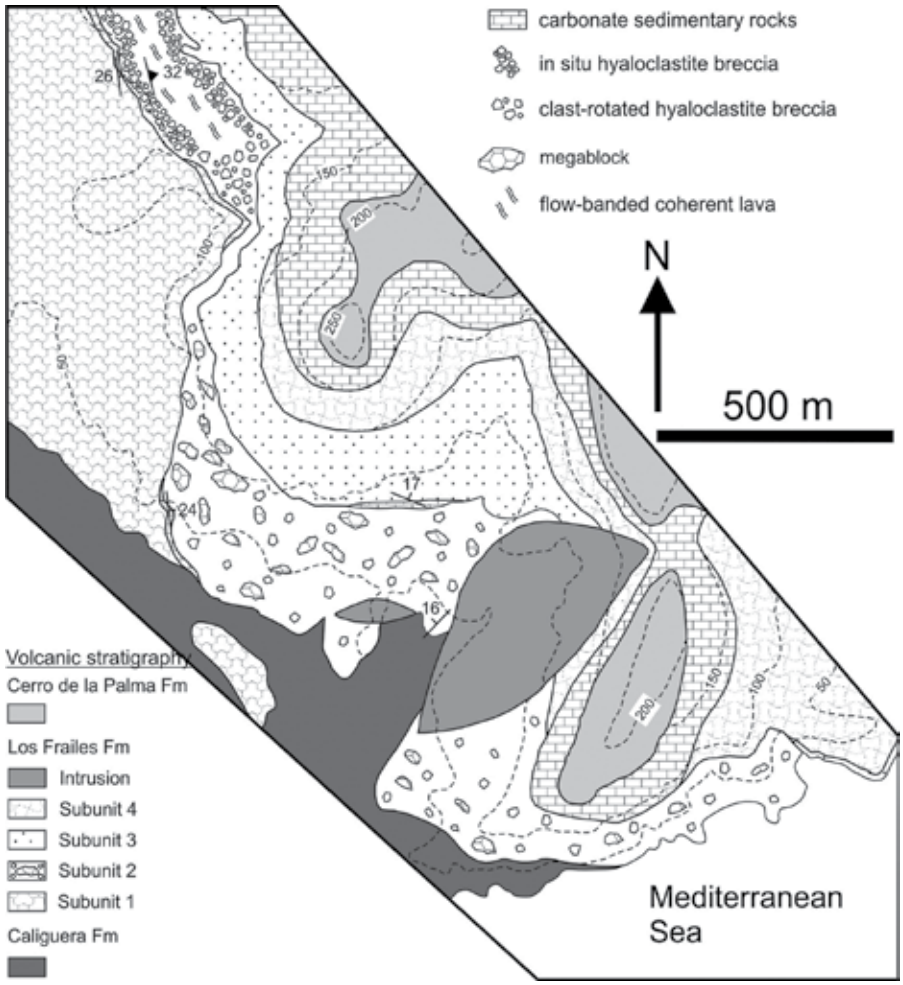

Figure 9. Geologic map of the Los Frailes Formation (see **Figure 4** for location).

The lateral association of the debris-avalanche deposit and lavas within subunit 2, together with their identical composition and mineralogy, indicates that dacite lavas are probably the source area for the volcanic debris of the avalanche deposit. Thickness and areal distribution of the debris-avalanche deposit in **Figure 6** and nearby areas suggests a volume <0.5 km^3 and run-out distance <5 km [8]. These factors together suggest that the debris avalanche is derived from the sector collapse of a submarine lava dome or a dome complex. In this view, megablocks correspond to the coherent core of the lava dome, whereas matrix facies corresponds to the hyaloclastite carapace surrounding the core. In spite of this general provenance for block and matrix facies, block disintegration and clast-to-clast friction during transport are not to be

http://dx.doi.org/10.5772/63579

excluded as mechanisms producing block and clast fragmentation [42, 43]. This is particularly evident by the shear deformation and stepped geometry at the base of megablocks.

The debris-avalanche deposit of subunit 4 is thinner and less extended laterally than that of subunit 2. It is massive, monomictic and dacitic in composition and is stratigraphically limited by lower and upper carbonate sedimentary rocks that contain marine fossils. The internal organization of the debris avalanche deposit of subunit 4 is similar to that of subunit 2, consisting of block and mixed facies.

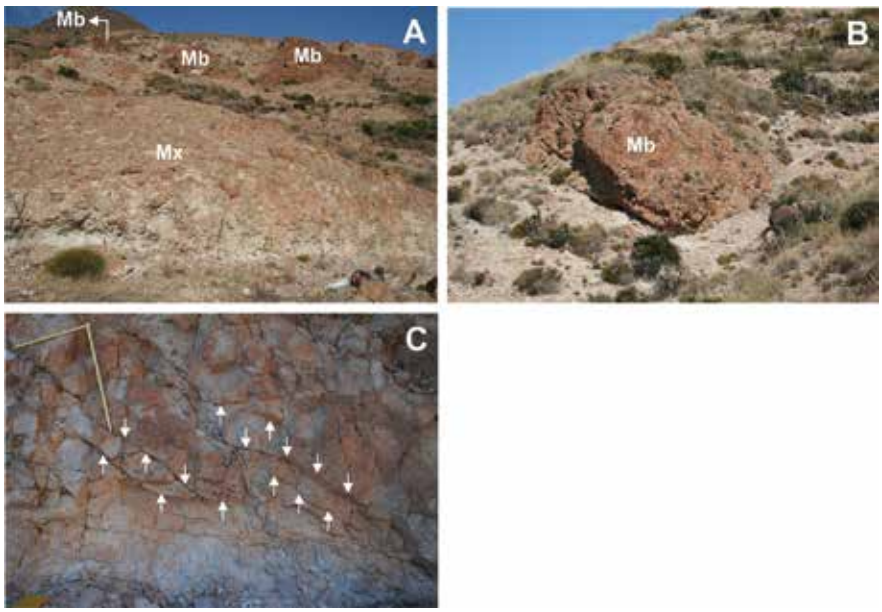

Figure 10. A: panoramic view of the debris-avalanche deposit of subunit 2 of the Los Frailes Formation with megablocks (Mb) and matrix (Mx). **B**: megablock with polyhedral-jointed interior and sharp basal contact. **C**: base of a megablock with anastomosed sigmoid shear planes (arrows).

6.2. The debris avalanche deposit of the Cerro Estorvillas Formation

Inland exposures to the west of Las Negras and to the north of Rodalquilar in the central Cabo de Gata area provide well-preserved profiles of the debris avalanche deposit of the Cerro Estorvillas Formation (**Figure 4**). This unit uncomformably overlies rhyolite bedded pumice breccia of the Cerro de los Guardias Formation and is unconformably overlain by flow banded dacite lavas of the Monte Cinto Formation and by andesite lavas and breccias of the Cerro Negro Formation. The age of the Cerro Estorvillas Formation is stratigraphically constrained between 12.30 Ma and 11.93 Ma (**Figure 3**). The Cerro Estorvillas Formation is dacitic in composition and monomictic and consists of a volcanic succession with a debris avalanche deposit at the base grading upward into bedded pumice breccia that in turn grades upward into bedded and massive breccia (**Figure 11**). To the west of Las Negras, the Cerro Estorvillas Formation also includes dacite lavas.

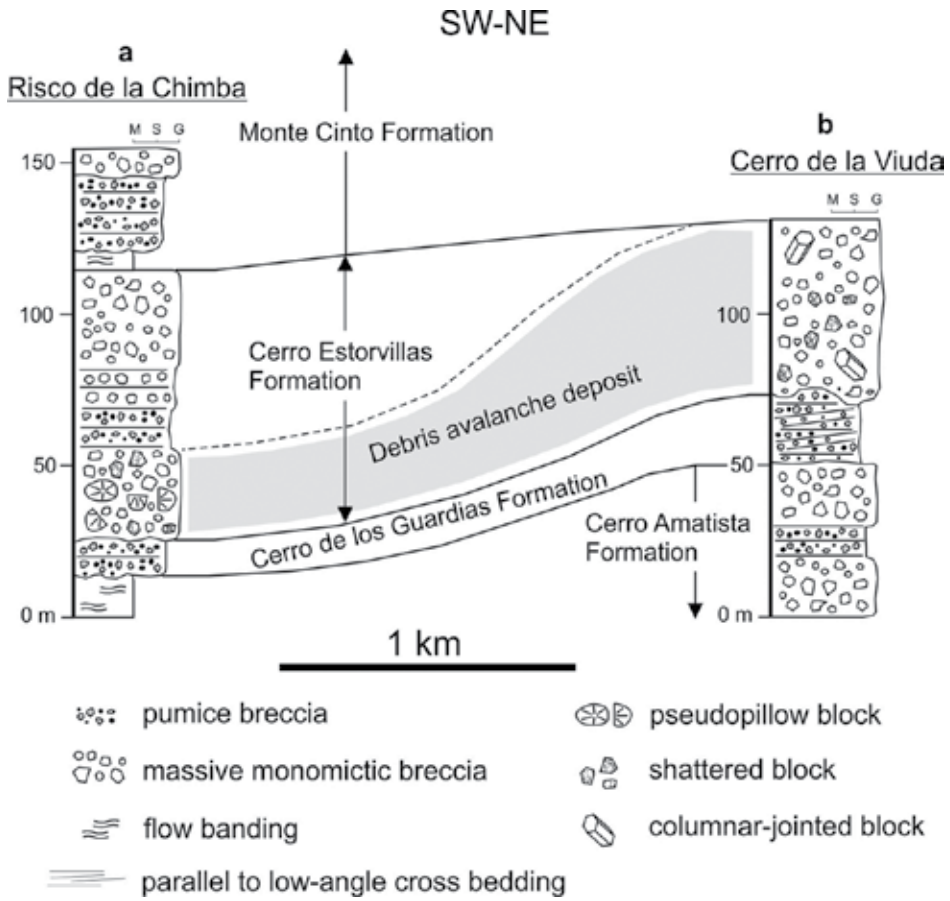

Figure 11. Stratigraphic logs of the Cerro Estorvillas Formation (see **Figure 4** for log location).

The debris avalanche deposit of the Cerro Estorvillas Formation is almost 100 m thick near Las Negras, whereas it is less than 50 m thick farther to the west. This deposit is massive and internally organized in block and mixed facies. Block facies consists of angular clasts up to 6 m across, including meter-size pseudopillow blocks that exhibit radial jointing and meter-size blocks with columnar jointing (**Figure 12A** and **B**). Mixed facies comprises a clast-supported framework of centimeter- to decimeter-size angular clasts of the same composition and mineralogy as the blocks. Blocks are usually shattered with a jigsaw-fit fracture framework. In the lower part of the debris-avalanche deposit, irregular domains with diffuse margins extend laterally for more than 10 m and are less than 5 m thick. These domains consist of well-rounded cobbles of dacite occasionally supported in a matrix of coarse sand that consists of dense rock fragments of dacite and crystals (**Figure 12C**). The contact of the debris avalanche deposit with the underlying Cerro de los Guardias Formation consists of an irregular zone in which clasts and small, usually vein-like, portions of the debris avalanche deposit are mixed with clasts and portions of the underlying pumice breccia deposit (**Figure 12D**). This mixing zone extends up to 2 m upward from the basal contact of the debris-avalanche deposit.

http://dx.doi.org/10.5772/63579

Figure 12. A: columnar-jointed block in the debris-avalanche deposit of the Cerro Estorvillas Formation; **B**: pseudopillow block with radial jointing; **C**: detailed of the cobble domain in the lower part of the debris-avalanche deposit. Note fracture pattern in shattered cobble clasts (arrows); **D**: basal mixed contact of the debris-avalanche deposit of the Cerro Estorvillas Formation to the pumice breccia of the Cerro de los Guardias Formation. Note shattered clasts in the debris-avalanche deposit.

Lack of sorting, massive character, internal organization in block and mixed facies and shattered blocks with jigsaw-fit fractures are usual features of debris avalanche deposits [38, 40, 44, 45]. Pseudopillow radial-jointed blocks may derive from pillows and lava lobes surrounded by hyaloclastite breccia originally deposited in subaqueous settings while the monomictic character indicates a homogenous source for the volcanic debris. Rounded cobbles must have been formed by long-term reworking in highly energetic settings rather than in a nearly instantaneous event like a debris-avalanche. Although marine fossils have not been observed in the cobble domains, rounding of the clasts and the coarse sand matrix fits well with original deposition in a beach environment and subsequent transport within the debris

avalanche. Transport and deposition of nearly intact parts of the volcano stratigraphy is a common feature observed in many debris avalanche deposits [39, 41]. Hence, the debris avalanche of the Cerro Estorvillas Formation may have involved the partial collapse of an emerged dacite lava dome likely located to the west of Las Negras, where dacite lavas of the same composition and mineralogy occur. Rhyolite pumice and andesite clasts and irregular portions of pumice breccia from the underlying Cerro de los Guardias Formation at the basal contact of the debris avalanche are interpreted to have been ripped up from the substrate during transport.

7. Tectonic controls on cyclic volcanism

The nearly continuous sedimentation in passive-margins and other types of sedimentary basins allows characterization of basin dynamics by use of the principles of sequence stratigraphy and techniques such as backstripping and decompaction on sedimentary successions. In contrast, the record of volcanism is discontinuous in the geologic history due to its episodic character, whereas volcanic rocks allow a reasonably good determination of absolute ages via radio-isotopic dating. Additionally, in the coherent lithofacies of volcanic successions, compaction effects on accumulated thicknesses are minor and can be likely disregarded.

In Cabo de Gata, volcanic units were emplaced in submarine settings at unknown depth and are interbedded with sedimentary units in which paleobathymetry can be better constrained by analyzing the lithofacies of sedimentary successions. Using the known thickness and ages of volcanic rocks and the better-constrained paleodepth deposition of sedimentary rocks, the paleobathymetric setting of volcanism can be indirectly constrained and the uplift-downdrop history of volcano-sedimentary successions in Cabo de Gata can be roughly assessed. In addition, lateral correlation of the different lithofacies forming subunits of the Los Frailes Formation allows characterization of the eruptive styles and interpretation of the constructive and destructive processes of volcanic edifices during the eruptive periods. This may serve to illustrate the tectonic controls on cyclic volcanism not only of the Los Frailes Formation but also of other units in Cabo de Gata.

Debris-avalanche deposits of subunits 2 and 4 are laterally associated toward the north with coherent lava that grade into hyaloclastite breccias (**Figure 13**). Subunit 1 is also made up of debris-avalanche deposits and coherent lava that grade into hyaloclastite breccia and have a similar dacitic composition and mineralogy to dacite of subunits 2 and 4. Subunit 3 is made up of pumice-rich and glass-shard-rich lithofacies (i.e., massive and bedded pumice breccia, massive pumice tuff and thinly bedded fine tuff). Lithofacies of subunit 3 are fines depleted, have low-angle cross bedding and soft-sediment-deformation structures and show similar dacitic composition and mineralogy to subunits 2 and 4. Although subunit 3 is laterally discontinuous, it constitutes a distinctive stratigraphic marker in the Los Frailes area that allows lateral correlation of subunits within the Los Frailes Formation (**Figure 13**).

http://dx.doi.org/10.5772/63579

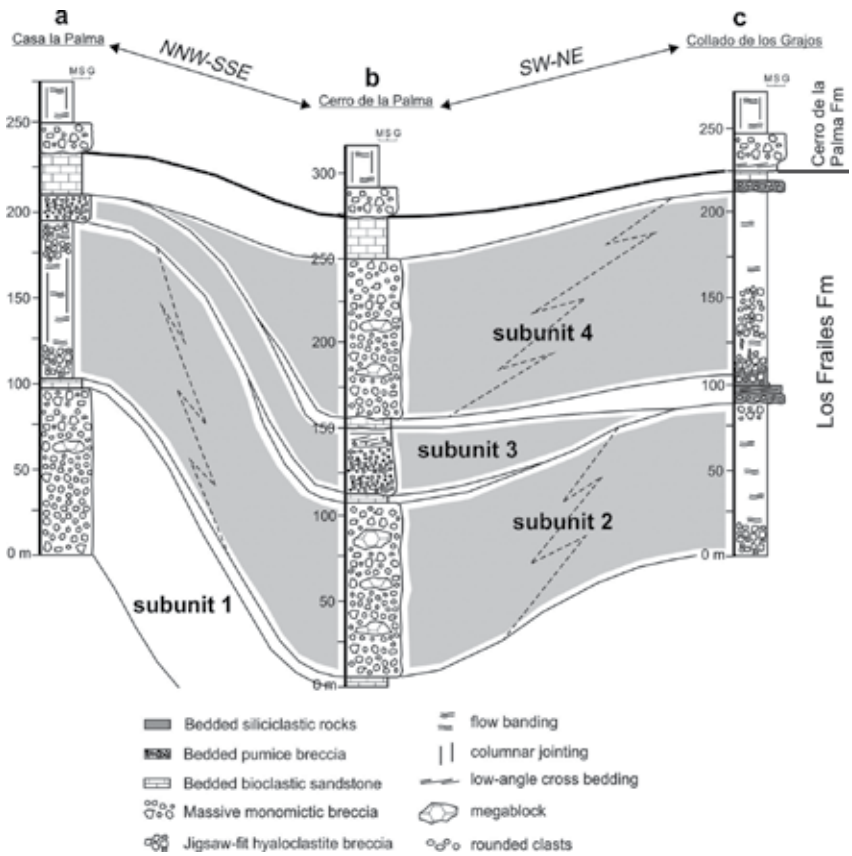

Figure 13. Correlation of volcanic subunits and sedimentary units of the Los Frailes Formation in the Los Frailes area (see **Figure 4** for log location).

At Collado de los Grajos, lava of subunit 2 is overlain by a fining-upward siliciclastic succession that, from base to top, consists of massive conglomerate with well-rounded pebbles of phyllite from the metamorphic basement to the Neogene succession of Cabo de Gata, low-angle cross-bedded coarse sandstone and cross-laminated fine sandstone to siltstone. The siliciclastic succession is overlain by lava of subunit 4, which consists of hyaloclastite breccia grading upward into coherent lava. Fine sandstone and siltstone of the upper siliciclastic succession fluidized and filled the space between clasts of in situ to clast-rotated hyaloclastite breccia of subunit 4. Coherent lava of subunit 4 is capped by a fining- and thinning-upward succession that, from base to top, includes a conglomerate bed, rhodolith-rich facies and cross-bedded sandstone (**Figure 14A**). The conglomerate bed is horizontal, up to 1 m thick and grades upward into a carbonate bed of up to 50 cm thick. The base of the conglomerate bed is irregular on the coherent dacite lava of subunit 4. Conglomerate is composed of well-rounded dacite cobbles with the free space among cobbles filled up with carbonate material infiltrated from the overlying carbonate bed (**Figure 14B**). Dacite cobbles and the underlying coherent lava are remarkably reddish. The upper carbonate bed is massive to crudely bedded and grades

upward into low-angle, cross-bedded bioclastic sandstone up to 25 cm thick. The carbonate bed is a rhodolith-rich rudstone that contains angular volcanic clasts, serpulids, bryozoan, bivalve fragments and other bioclasts (**Figure 14C**). Rhodoliths have a concentric algal framework around bioclastic nuclei and occasionally around volcanic clasts. The carbonate succession is overlain by cross-bedded monomict sandstone, massive monomict breccia and coherent lavas of the Cerro de la Palma Formation (**Figure 13**).

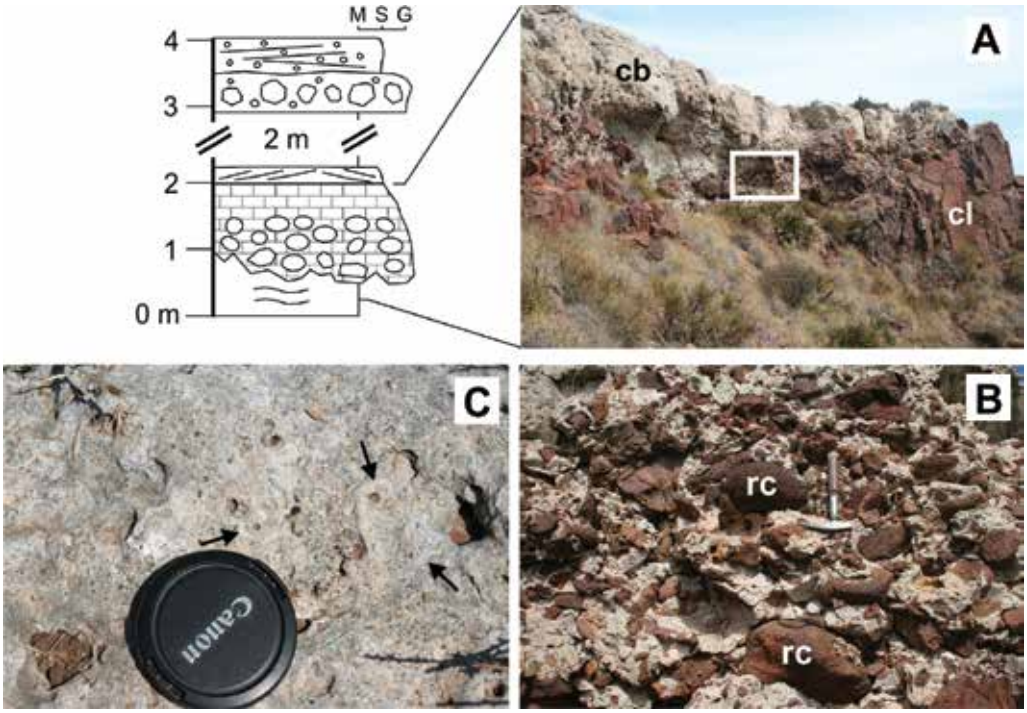

Figure 14. Detailed stratigraphic log of with the sedimentary sequence overlying coherent lava of subunit 4 in the Collado de Los Grajos log (see **Figure 13** for location). **A**: contact of subhorizontal conglomerate bed and carbonate bed (cb) on reddish coherent lava (cl). **B**: conglomerate bed with well-rounded cobbles (rc) and carbonate matrix infilling the the space among cobbles. **C**: top view of the carbonate bed with crustose rhodoliths forming concentric algae framework (arrows).

Fluidized sandstone and siltstone at the base of lava of subunit 4 indicates that the sediment was wet and nonconsolidated at the time of lava emplacement. The reddish color of the uppermost part of coherent lava of subunit 4 and of dacite cobbles of the upper conglomerate bed can be attributed to oxidizing conditions either at lava emplacement or after emplacement. Rhodoliths are encrusting coralline algae usually associated with above wave base environments, although they have been also described in deeper water settings [46, 47]. In terms of modern sequence stratigraphy, rhodolith-rich facies deposited on unconformities have been interpreted as condensed beds, indicating the onset of marine transgression ([48] and references therein). This interpretation fits well with the conglomerate bed on coherent lava of subunit 4 as deposited in a beach environment after lava emplacement and with rhodolith-

http://dx.doi.org/10.5772/63579

rich bed and cross-bedded sandstone as a deeper facies in an ongoing marine transgression. Hence, the fining and thinning-upward sedimentary sequence with the conglomerate bed at the base and the cross-bedded sandstone at the top is interpreted to have been deposited above wave base and to reflect deepening water conditions from the shoreface down to infralittoral settings. The depositional model of a Late Holocene clastic prograding wedge in the western Mediterranean has been studied in detail and shows that the mean storm wave base is 20 m below sea level [49]. The present-day configuration of the western Mediterranean was somewhat similar to the paleogeographic configuration in early Tortonian times, in which the Mediterranean Sea was connected to the Atlantic Ocean by narrow passages [50]. Hence, the mean storm wave base during Serravallian-Tortonian times can be reasonably assumed at 20 m below sea level (mbsl) and the exceptional storm wave base at 30 mbsl, both marking the slope break that separates infralittoral and littoral depositional settings from offshore deposition.

Subunits 2, 3, and 4 are separated by sedimentary successions in which silt grain size is minor and clay grain size is absent. These successions contain a variety of shallow-water marine fossils (bryozoan, echinoderms, bivalves, and coralline algae) and have low-angle cross stratification, rounded cobbles and pebbles and other evidence of above wave base settings as shown above. Therefore, the sedimentary units separating the volcanic subunits of the Los Frailes Formation can be collectively interpreted as mixed carbonate-siliciclastic platform-beach facies deposited in infralittoral to littoral settings. The fines-depleted character, soft-sediment deformation structures, low-angle cross-bedding and interbedding with sedimentary rocks from shallow-water settings suggest subaqueous deposition of volcanic subunit 3 of the Los Frailes Formation [8]. Hence, the composite stratigraphic succession obtained from lateral correlation in the Los Frailes area includes thin sedimentary units deposited in infralittoral to littoral settings (0–20 mbsl) and thicker volcanic units emplaced in deeper, likely offshore, settings (>20 mbsl). Based on these paleobathymetyric constraints, the relative sea-level curve can be obtained with hiatuses corresponding to the unconformities at the contacts between volcanic and sedimentary units (**Figure 15**). Fluidization of unconsolidated sediments into overlying lavas suggests that the time encompassed from deposition of sediments to lava emplacement was not very long. Based on the ages of volcanic subunits and on the number of volcanic subunits of the Los Frailes formation, the periodicity of volcanic cycles can be roughly approximated at 10^5 years. Volcanic activity during each volcanic cycle includes constructive and destructive events of volcanic edifices and is assumed to have occurred in a relatively short time span ($<10^4$ years). The Los Frailes area can be regarded as a volcanic field composed of individual, partly overlapping, domes that are active along a time span of about 5×10^5 years with periods of volcanic repose separating dome activity. A similar scenario has been proposed for Surtseyan volcanism of the Eocene-Oligocene Waiareka-Deborah volcanic field in New Zealand but encompassing a time span of several 10^6 years [51]. The accumulated thickness of the stratigraphic succession at Los Frailes is mainly derived from the volcanic activity while the sedimentary succession accumulated during repose periods has much smaller thickness (**Figure 15**). Sea-level oscillations can be explained by the progradation and retrogradation of mixed carbonate-siliciclastic platform-beach wedges after each volcanic cycle and by infilling of offshore settings with volcanic material during volcanic cycles. This

dynamics requires tectonic subsidence to accommodate the thickness of volcanic material accumulated during volcanic cycles in infralittoral to littoral sediments. Similar to other Neogene basins of the Betic-Rif Orogen [52–54], we propose that tectonic subsidence in Cabo de Gata is controlled by uplift-downdrop displacements along major strike-slip faults that bound the Almeria-Níjar basin (i.e., the Carboneras fault) and/or by vertical displacements along minor faults associated with these major faults.

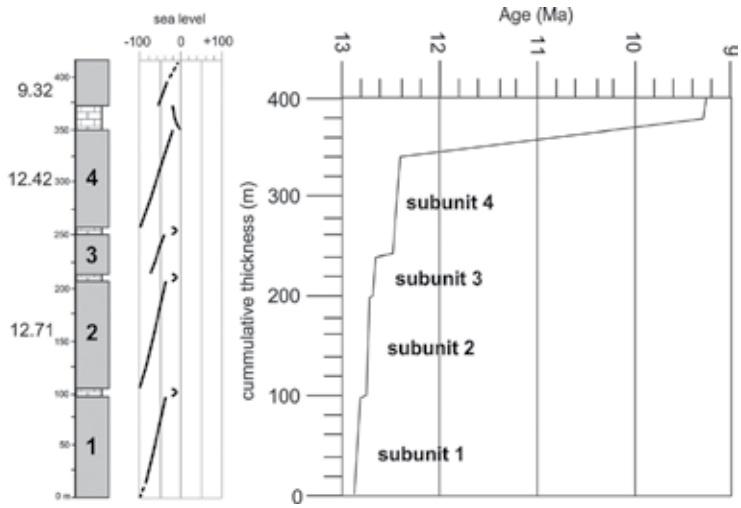

Figure 15. Composite stratigraphic log of the Los Frailes area based on the lateral correlation of **Figure 13** with sea-level curve based on the bathymetric constrains from sedimentary units and volcanic units (1–4) and cumulative thickness versus age.

8. Conclusion

Volcanism in Cabo de Gata is cyclic, with eruptive periods being characterized by both construction and partial dismantling of volcanic edifices, whereas noneruptive periods are characterized by volcanic repose, sedimentation of carbonate and siliciclastic rocks and erosion of volcanic edifices and deposits. The El Barronal Formation, the Los Frailes Formation and many other units in Cabo de Gata, which are divided into volcanic subunits separated by sedimentary units, are the geological record of this cyclic volcanism and volcanic hiatus history. Volcanic activity in Cabo de Gata includes effusive and explosive eruptions and syn-eruptive partial collapse of volcanic edifices yielding avalanches of volcanic debris deposited in submarine settings. The characteristic eruption model in Cabo de Gata likely began with explosive eruptions that produced juvenile and lithic fragments and deposition of pyroclastic density currents and ended with the effusion of lavas. Volcanic debris-avalanche deposits of the Los Frailes Formation and the Cerro Estorvillas Formation resulted from the sector collapse of submarine to emergent lava domes and were deposited in offshore settings. They constitute rare examples in the geological record of submarine volcanic debris avalanches that can be

http://dx.doi.org/10.5772/63579

studied by direct access on exposed outcrops. Based on depositional setting of sedimentary rocks and on thickness and ages of volcanic rocks, it is suggested that the volcanic pile produced during each volcanic cycle in infralittoral to littoral settings is accommodated by tectonic subsidence along major faults controlling the Almeria-Níjar basin.

Acknowledgements

We thank Miguel Garcés for comments and suggestions on a first version of the manuscript. This research has been partly funded by project 2014SGR1595 and by grant PRX14/00303 to Carles Soriano.

Author details

Carles Soriano[1*], Ray A.F. Cas[2*], Nancy R. Riggs[3*] and Guido Giordano[4*]

*Address all correspondence to: csoriano@ictja.csic.es, ray.cas@nau.edu, nancy.riggs@nau.edu and guido.giordano@uniroma3.it

1 Institute of Earth Sciences "Jaume Almera", Superior Council for Scientific Research c/ Lluís Solé Sabarís s/n, Barcelona, Spain

2 School of Earth, Atmosphere and Environment, Monash University, Monash University, Calyton Campus, Australia

3 Geology Program, School of Earth Sciences and Environmental Sustainability, Northern Arizona University, Flagstaff, USA

4 Department of Science, Geological Sciences Section, Roma Tre University, Largo S. Leonardo Murialdo, Roma, Italy

References

[1] Fuster JM, Aguilar MJ, García A. Las sucesiones volcánicas en la zona del Pozo de los Frailes dentro del vulcanismo cenozoico del Cabo de Gata (Almería). Estudios Geológicos. 1965; XXI: 199–222.

[2] Páez Carrión A, Sánchez Soria P. Vulcanología del Cabo de Gata, entre San José y Vela Blanca. Estudios Geológicos. 1965; XXI: 223–246.

[3] León C. Las formaciones volcánicas del Cerro de los Lobos (Almería, SE. de España). Estudios Geológicos. 1967; XXIII: 15–28.

[4] Di Battistini G, Toscani L, Iaccarino S, Villa IM. K/Ar ages and the geological setting of calc-alkaline volcanic rocks from Sierra de Gata, SE Spain. Neues Jahrbuch für Mineralogie, Monatshefte. 1987; H 8: 369–383.

[5] Cunningham CG, Arribas A Jr, Rytuba JJ, Arribas A. Mineralized and unmineralized calderas in Spain; Part 1, evolution of the Los Frailes caldera. Mineralium Deposita 1990; v. 25 (supp.): S21–S28.

[6] Arribas A Jr, Cunningham CG, Rytuba JJ, Rye RO, Kelly WC, Podwysocki MH, McKee EH, Tosdal RM. Geology, Geochronology, Fluid inclusions, and Isotope Geochemistry of the Rodalquilar Gold Alunite Deposit Spain. Economic Geology.1995; 90: 795–822.

[7] Cas RAF, Giordano G. Submarine volcanism: a review of the constrains, processes and products and relevance to the Cabo de Gata volcanic succession. Italian Journal of Geosciences. 2014; 133: 362–377.

[8] Soriano C, Riggs N, Giordano G, Porreca M, Conticelli S. Cyclic growth and mass wasting of submarine Los Frailes lava flow and dome complex in Cabo de Gata, SE Spain. Journal of Volcanology and Geothermal Research. 2012; 231–232: 72–86.

[9] Soriano C, Giordano G, Cas R, Riggs N, Porreca M. Facies architecture, emplacement mechanisms and eruption style of the submarine andesite El Barronal complex, Cabo de Gata, SE Spain. Journal of Volcanology and Geothermal Research. 2013; 264: 210–222.

[10] Soriano C, Giordano G, Riggs N, Porreca M, Bonamico A, Iosimi D, Cifelli F, Mattei M, De Benedetti A, Guarnieri L, Marchionni S. Geologic map, volcanic stratigraphy and structure of the Cabo de Gata volcanic zone, Betic-Rif Orogen, SE Spain. Italian Journal of Geosciences. 2014; 133: 325–340.

[11] Porreca M, Cifelli F, Soriano C, Giordano G, Romano C, Conticelli S, Mattei M. Hyaloclastite fragmentation below the glass transition: an example from El Barronal submarine volcanic complex (Spain). Geology. 2014; 42: 87–90.

[12] Porreca M, Cifelli F, Soriano C, Giordano G, Mattei M. Magma flow within dykes in submarine hyaloclastite environments: an AMS study of the Miocene Cabo de Gata volcanic units. In: Ort MH, Porreca M, Geissman JW, editors. The Use of Palaeomagnetism and Rock Magnetism to Understand Volcanic Processes. Geological Society, London, Special Publication, 396; 2015. p. 133–157.

[13] van Otterloo J, Cas RAF, Scutter C. The fracture behaviour of volcanic glass and relevance to quench fragmentation during formation of hyaloclastite and phreatomagmatism. Earth Science Reviews. 2015; 151: 79–116.

[14] Sharqawy M, Lienhard JH, Zubair SM. Thermophysical properties of seawater: a review of existing correlations and data. Desalination and water treatment. 2010; 16: 354–380.

[15] Höskuldsson A, Sparks RSJ. Thermodynamics and fluid dynamics of effusive subglacial eruptions. Bulletin of Volcanology. 1997; 59: 219–230.

[16] Zimanowski B, Buttner R. Phreatomagmatic explosions in subaqueous volcanism. In: White JDL, Smellie JL, Clague DA, editors. Submarine Explosive Volcanism. American Geophysical Union, Monograph, 140; 2003. pp. 51–60.

[17] Wohletz KH. Water/magma interaction: physical considerations for the deep submarine environment. In: White JDL, Smellie JL, Clague DA, editors. Submarine Explosive Volcanism. American Geophysical Union, Monograph, 140; 2003. pp. 25–49.

[18] Doblas M, López-Ruiz J, Cebriá JM. Cenozoic evolution of the Alboran Domain: a review of the tectonomagmatic models. In: Beccaluva L, Bianchini G, Wilson M, editors Cenozoic Volcanism in the Mediterranean area. Geological Society of America, Special Paper, 418; 2007. pp. 303–320.

[19] Lustrino M, Duggen S, Rosenberg C. The central-western Mediterranean: anomalous igneous activity in an anomalous collisional tectonic setting. Earth Science Reviews. 2011; 104: 1–40.

[20] Vergés J, Fernàndez M. Tethys-Atlantic interaction along the Iberia-Africa plate boundary: The Betic-Rif orogenic system. Tectonophysics. 2012; 579: 144–172.

[21] Conticelli S, Guarnieri L, Farinelli A, Mattei M, Avanzinelli R, Bianchini G, Boari E, Tommasini S, Tiepolo M, Prelevic D, Venturelli G. Trace elements and Sr-Nd-Pb isotopes of K-rich, shoshonitic, and calc-alkaline magmatism of the Western Mediterranean Region: genesis of ultrapotassic to calc-alkaline magmatic associations in a post-collisional geodynamic setting. Lithos. 2009; 107: 68–92.

[22] Mattei M, Riggs N, Conticelli S, Giordano G, Cifelli F, Soriano C, Jicha B, Marchionni S, Guarnieri L, Tommasini S, Jasim A, Franciosi L, Porreca M. Geochronology geochemistry and geodynamics of the Cabo de Gata volcanic zone, South Eastern Spain. Italian Journal of Geosciences. 2014; 133: 341–361.

[23] Faccenna C, Piromallo C, Crespo-Blanc A, Jolivet L, Rossetti F. Lateral slab deformation and the origin of the western Mediterranean arcs. Tectonics. 2004; 23: TC1012.

[24] Comas MC, Platt JP, Soto JI, Watts AB. The origin and tectonic history of the Alboran basin; insights from Leg 161 results. In: Zahn R, Comas MC, Klaus A, editors. Proceedings of the Ocean Drilling Program, Scientific Results, 161; 1999. pp. 555–580.

[25] McClusky HL, Conner ME, Smith LD, Holloway MV, Conover TA, Beasley DE. Mapping of the lateral flow field in typical subchannels of a support grid with vanes. Journal of Fluids Engineering. 2003; 125(6): 987–996.

[26] Iribarren L, Verges J, Camurri F, Fullea J, Fernandez M. The structure of the Atlantic–Mediterranean transition zone from the Alboran Sea to the Horseshoe Abyssal Plain (Iberia-Africa plate boundary). Marine Geology. 2007; 243: 97–119.

[27] Bell JW, Amelung F, King GCP. Preliminary late quaternary slip history of the Carboneras fault, Southeastern Spain. Journal of Geodynamics. 1997; 24: 51–66.

[28] Scotney P, Burgess R, Rutter EH. 40Ar/39Ar age of the Cabo de Gata volcanic series and displacements on the Carboneras fault zone, SE Spain. Journal of the Geological Society, London. 2000; 157: 1003–1008.

[29] Rutter EH, Burgess R, Faulkner DR. Constraints on the movement history of the Carboneras Fault Zone (SE Spain) from stratigraphy and ^{40}Ar-^{39}Ar dating of Neogene volcanic rocks. In: Llana-Fúnez S, Marcos A, Bastida F, editors. Deformation Structures and Processes within the Continental Crust. Geological Society, London, Special Publications, 394; 2014. pp. 79–99.

[30] Pedrera A, Marín-Lechado C, Galindo-Zaldívar J, Rodríguez-Fernández LR, Ruiz-Constán A. Fault and fold interaction during development of the Neogene-Quaternary Almería-Níjar basin (SE Betic Cordilleras). In: Moratti G, Chalouan A, editors Tectonics of the Western Mediterranean and North Africa. Geological Society, London, Special Publication, 262; 2006. pp. 217–230.

[31] Borehole dataset of the Instituto Geologico y Minero of Spain. Available from www.igme.es

[32] Brachert TC, Hultzsch N, Knoerich AC, Krautworst UMR, Stückrad OM. Climatic signature in shallow-water carbonates: high-resolution stratigraphic markers in carbonate build-ups (Late Miocene, southern Spain). Palaeogeography, Palaeoclimatology, Palaeoecology. 2001; 175: 211–237.

[33] Ballesteros M, Rivera J, Muñoz A, Muñoz-Martín A, Acosta J, Carbo A, Uchupi E. Aboran basin southern Spain-Part II. Neogen tectonic implications for the orogenic float model. Marine and Petroleum Geology. 2008; 25: 75–101.

[34] (IGME) Instituto Geológico y Minero de España. Mapa Geológico de España 1:50000, El Pozo de los Frailes 1060. Servicio de Publicaciones del Ministerio de Industria y Energía, Madrid. 1983.

[35] Duggen S, Hoernle K, van den Bogaard P, Harris C. Magmatic evolution of the Alboran region: The role of subduction in forming the western Mediterranean and causing the Messinian Salinity Crisis. Earth and Planetary Science Letters. 2004; 218: 91–108.

[36] Montgomery P, Farr MR, Franseen EK, Goldstein RH. Constraining controls of carbonate sequences with high-resolution chronostratigraphy: Upper Miocene, Cabo de Gata region, SE Spain. Palaeogeography, Palaeoclimatology, Palaeoecology. 2001; 176: 11–45.

[37] Trofimovs J, Cas RAF, Davis BK. An Archean submarine volcanic debris avalanche deposit, Yilgarn Craton, western Australia, with komatiite, basalt and dacite megablocks. The product of dome collapse. Journal of Volcanology and Geothermal Research. 2004; 138: 111–126.

[38] Crandell DR, Miller CD, Glicken HX, Christiansen RL, Newhall CG. Catastrophic debris avalanche from ancestral Mount Sashta, California. Geology. 1984; 12: 143–146.

[39] Glicken HX. Sedimentary architecture of large volcanic-debris avalanches. In: Smith GA., Fisher RV, editors. Sedimentation in volcanic settings. SEPM Tulsa Special Publication, 45; 1991. pp. 99–106.

[40] Palmer BA, Alloway BV, Neall VE. Volcanic-debris-avalanche deposits in New Zealand-Lithofacies organization in unconfined, wet-avalanche flows. In: Smith GA., Fisher RV, editors. Sedimentation in Volcanic settings. SEPM Tulsa Special Publication, 45; 1991. pp. 89–98.

[41] Stoopes GR, Sheridan MF. Giant debris avalanche from the Colima Volcanic Complex, México, implications for long runout landslides (<100°km) and hazard assessment. Geology. 1992; 20: 299–302.

[42] Roverato M, Cronin S, Procter J, Capra L. Textural features as indicators of debris avalanche transport and emplacement, Taranaki volcano. Geological Society of America bulletin. 2014. DOI:10.1130/B30946.1.

[43] Voight B, Komorowski JC, Belusov AB, Belusova M, Boudon G, Francis PW, Franz V, Heinrich P, Sparks RSJ, Young SR. The 26 December (Boxing Day) 1997 sector collapse and debris avalanche at Soufrière Hills Volcano, Montserrat. In: Druitt TH, Kokelaar BP editors. The eruption of Soufrière Hills Volcano, Montserrat, from 1995–1999. Geological Society London Memoir 21; 2002. pp. 363–407.

[44] Siebert L. Large volcanic debris avalanche: characteristics of source areas, deposits and associated eruptions. Journal of Volcanology and Geothermal Research. 1984; 22: 163–197.

[45] Ui T, Glicken HX. Internal structural characteristics of debris avalanche from Mount Sahsta, California, U.S.A. Bulletin of Volcanology. 1986; 48: 189–194.

[46] Flügel E. Microfacies of Carbonate Rocks. Springer Berlin Heidelberg; 2004. 976 p.

[47] Brandano M, Ronca S. Depositional processes of the mixed carbonate-siliciclastic rhodolith beds of the Miocene Saint-Florent Basin, northern Corsica. Facies. 2014; 60: 73–90.

[48] Nalin R, Nelson CS, Basso D, Massari F. Rhodolith-bearing limestones as transgressive marker beds: fossil and modern examples from North Island, New Zealand. Sedimentology. 2008; 55: 249–274.

[49] Hernández-Molina FJ, Fernández-Salas LM, Lobo F, Somoza L, Díaz-del-Río V, Alveirinho Dias JM. The infralittoral prograding wedge: a new large-scale progradational sedimentary body in shallow marine environments. Geo-Marine Letters. 2000; 20: 109–117.

[50] Martín JM, Braga JC, Aguirre J, Puga-Bernabéu A. History and evolution of the North-Betic Strait (Prebetic Zone, Betic Cordillera): A narrow, early Tortonian, tidal-domi-

nated, Atlantic-Mediterranean marine passage. Sedimentary Geology. 2009; 216: 80–90.

[51] Moorhouse BL, White JDL, Scott, J. Cape Wanbrow: A stack of Surtseyan-style volcanoes built over millions of years in the Waiareka-Deborah volcanic field, New Zealand. Journal of Volcanology and Geothermal Research. 2015; 298: 27–46.

[52] Soria J, Viseras C, Fernández J. Late Miocene-Pleistocene tectono-sedimentary evolution and subsidence history of the central Betic Cordillera (Spain): a case study of the Guadix intramontane basin. Geological Magazine. 1998; 135: 565–574.

[53] Garcés M, Krijgsman W, Agustí J. Chronostratigraphic framework and evolution of the Fortuna basin (Eastern Betics) since the Late Miocene. Basin Research. 2001; 13: 199–216.

[54] Rodríguez-Fernández J, Sanz de Galdeano C. Late orogenic intramontane basin development: the Granada basin, Betics (southern Spain). Basin Research. 2006; 18: 85–102.

Chapter 13

How Polygenetic are Monogenetic Volcanoes: Case Studies of Some Complex Maar-Diatreme Volcanoes

Boris Chako Tchamabé, Gabor Kereszturi,
Karoly Németh and Gerardo Carrasco-Núñez

Additional information is available at the end of the chapter

http://dx.doi.org/10.5772/63486

Abstract

The increasing number of field investigations and various controlled benchtop and large-scale experiments have permitted the evaluation of a large number of processes involved in the formation of maar-diatreme volcanoes, the second most common type of small-volume subaerial volcanoes on Earth. A maar-diatreme volcano is recognized by a volcanic crater that is cut into country rocks and surrounded by a low-height ejecta rim composed of pyroclastic deposits of few meters to up to 200 m thick above the syn-eruptive surface level. The craters vary from 0.1 km to up to 5 km wide and vary in depth from a few dozen meters to up to 300 m deep. Their irregular morphology reflects the simple or complex volcanic and cratering processes involved in their formation. The simplicity or complexity of the crater or the entire maar itself is usually observed in the stratigraphy of the surrounding ejecta rings. The latter are composed of sequences of successive alternating and contrastingly bedded phreatomagmatic-derived dilute pyroclastic density currents (PDC) and fallout depositions, with occasional interbedded Strombolian-derived spatter materials or scoria fall units, exemplifying the changes in the eruptive styles during the formation of the volcano. The entire stratigraphic sequence might be preserved as a single eruptive package (small or very thick) in which there is no stratigraphic gap or significant discordance indicative of a potential break during the eruption. A maar with a single eruptive deposit is quantified as monogenetic maar, meaning that it was formed by a single eruptive vent from which only a small and ephemeral magma erupted over a short period of time. The stratigraphy may also display several packages of deposits separated either by contrasting discordance surfaces or paleosoils, which reflect multiple phases or episodes of eruptions within the same maar. Such maars are characterized as complex polycyclic maars if the length of time between the eruptive events is relatively short (days to years). For greater length of time (thousands to millions of years), the complex maar will be quantified as polygenetic. These common depositional breaks interpreted as signs of temporal interruption of the eruptions for various timescales also indicate deep magma system processes; hence magmas of different types might erupt during the formation of

both simple and complex maars. The feeding dikes can interact with groundwater and form closely distributed small craters. The latter can coalesce to form a final crater with various shapes depending on the distance between them. This observation indicates the significant role of the magmatic plumbing system on the formation and growth of complex and polygenetic maar-diatreme volcanoes.

Keywords: maar-diatreme, polygenetic, monogenetic volcanism, complex maars, dike injection

1. Introduction

Monogenetic volcanoes represent the most common type of subaerial volcanoes not only on Earth but in the solar system [1–3]. These volcanoes, including maars, tuff rings, tuff cones and scoria cones, and sometimes short lava flows, are generally believed to form by a single short-lived eruption probably during a brief period of time (e.g., hours to days). The eruptions are typically fed by small volume of magma of any type, producing simple and small-volume volcanoes that predominantly clustered in lowland volcanic fields at the footprints of polygenetic volcanoes (e.g., [4–7]). The term polygenetic is often used to refer to volcanoes constructed by multiple eruptive events over a large timespan and characterized by complex volcanic and geochemical evolution such as stratovolcanoes (e.g., [8]). The same applies in this study. Most of the small volcanoes are generally characterized by simple and easy to understand volcanic sequences. However, the reality is different and that is what this book chapter tries to demonstrate. For instance, increasing investigations in several volcanic fields have shown that small volcanoes can exhibit, in special cases, a contrasting stratigraphy consisting of tephra units and other lava flows sometimes of different geochemical compositions (e.g., [8–10]). The eruptive units are sometimes deposited periodically with short or even prolonged inactive periods between eruptive events, indicating an evolution that cannot be explained with a single eruption (e.g., [11–13]). Additionally, such intricate trend of complexity is even more obvious with maar volcanoes that are the results of explosive magma-water interactions (molten-fuel-coolant interaction), a process causing fragmentation of both the magma and country rocks close to the surface (e.g., [14–19]. Their eruptive sequences are, therefore, heavily influenced by the magma internal (physicochemical) attributes as well as the environmental parameters that are largely expressed by the nature of the geologic substrate and the availability of external water to cause explosions. Maars are, therefore, probably the most complex and suitable bunch of small-volume volcanoes where complex sedimentary succession of their rim (and underground) architecture is expected. In this chapter, we intend to explore this diversity through some recent studies and own research. Examples will include recently documented small volcanoes showing complex stratigraphy, compound volcano edifice, and complex eruptive history, in various volcanic fields, including the Western Australian volcanic field (e.g., [10, 20]), the Coli Albani volcanic complex in Italy [13, 21], the Cameroon volcanic line [11, 22, 23], the Eiffel volcanic field [24, 25], the Trans-Mexican Volcanic Belt [26–28], the Central Volcanic Range of Costa Rica [12],

http://dx.doi.org/10.5772/63486

the Bakony-Balaton Highland Volcanic Field in Hungary [29–31], as well as Auckland volcanic field in New Zealand [32–34].

This chapter focuses on phreatomagmatic-derived volcanoes, especially maar-diatremes, for which an important number of field investigations and various types of controlled benchtop and large-scale experiments have permitted to constrain processes involved in their formation, such as the mechanism of explosion (e.g., [35–39]), the quantification and control of magma-water interactions during the fragmentation process in regard to the potential maximum energy release that such process can provide (e.g., [35, 40]), the cratering process (e.g., [17–19]), the resulting volcanic facies preserved in a volcanic edifice and depositional processes associated with the distal regions of such volcanoes in the inter-volcano region (e.g., [29, 41–47]), as well as the characterization of the changes in the eruptive styles in the course of their formation (e.g., [48–52]), and the geochemical processes associated with their formation from the melt extraction and deep fractionation prior to eruptions to the processes influencing the rising magma batches (e.g., [8, 21, 52–55]). The reader can therefore refer to [56–58] for detailed review on scoria cones. The main purpose of this chapter is to highlight the main features that could help to understand the formation of complex maars and how we can recognize and discriminate The latter from simple maar volcanoes. Thus, we will emphasize where poly-activity have been identified such as the Purrumbete Maar, Australia (e.g., [20]), Albano Maar, Colli Albani volcano, Italy (e.g., [13, 21]), Hule Maar, Costa Rica (e.g., [12]), or Barombi Mbo Maar, Cameroon [22, 59]. In the light of several previous discussions around the monogenetic volcanoes (e.g., [6, 58, 60]), we present some key similarities and dissimilarities within simple and complex small-volume volcanoes, especially maars, so that a better definition for those volcanic end members could be understood. We also discuss what processes might drive complex activity at maar volcanoes in order to propose a conceptual model that can summarize the origin and growth of this type of end-member volcano.

2. General features of maar-diatreme volcanoes

In many volcanic fields, it is usually common to see a low rim of bedded pyroclastic ejecta surrounding a dried or water-filled depression that cuts into the pre-eruptive ground (**Figure 1**). This structure is usually called maar. Maar is a German-derived word that means "crater lake," whose origin derived from the Latin word *mare* (sea). In 1819, in his book "Die erloschenen Vulkane in der Eifel und am Niederrheine," Johann Steininger was probably the first to coin the term maar to describe a volcanic feature while working in the Eifel volcanic area in Germany, in which the craters are usually occupied by lakes. The term was then widely used by Ollier [61] and Lorenz [62, 63] and others authors cited therein. These early papers put the term of maar into the scientific literature as an important volcanic landform formed through phreatomagmatic eruptions, which is now applied to similar craters (e.g., [12]). A maar stands for a volcanic crater that is cut into country rocks (a few meters or tens of meters above the preexisting ground surface) and surrounded by a low-height ejecta rim composed of pyroclastic deposits of few meters to up to 200 m thick above the syn-eruptive surface level (e.g., [64]). The term maar is sometimes also used only as a morphological term.

Figure 1. Photos showing the typical landform of some maar volcanoes. (**A**) Blue Lake Maar (Mount Gambier, South Australia), (**B**) Aci Golu Maar (Turkey), (**C**) Al Wahbah Maar (Harrat Khisb in western Saudi Arabia), (**D**) Cora Maar (Central Anatolia), and (**E**) Meke Gölü Maar (Turkey), (**F**) Alchichica Maar, (**G**) Aljojuca Maar, and (**H**) Atexcac Maar of the EMVB, Mexico.

Maar volcanoes are characterized by a relatively small crater size, hundred meters to up to 5 km in diameter [65], with few dozen of meters to up to 300 m deep [9]. The craters are mostly circular in shape, although in some cases an irregular morphology can be observed due to a formation through the injection of discrete dikes at several but closely spaced explosion craters/centers to the main crater (e.g., [55]). Examples of such simple maars are certainly the most widely spread in monogenetic volcanic fields, such as the Eifel volcanic field, western central Germany, where many maars are characterized by small crater diameters ranging from 83 to 1580 m [25] and low tephra deposit thickness, e.g., Ulmener Maar, 7.5 m thick, Pulvermaar, 27 m thick, or Meedelder Maar, 23 m thick[24]. The same feature is observed with some maars of the Trans-Mexican volcanic field (e.g., [66–68]) or those of the Quaternary Auckland Volcanic Field in New Zealand (e.g., [69]), as well as maars of the Sabatini Volcanic District in the Roman Province of Central Italy (e.g., [70]). The crater floor usually lies well below the surrounding ground level and frequently exhibits near-vertical crater wall escarpments (e.g., [6, 8, 71]). On the other hand, the ejecta rings of maars are characterized by sequences of successive alternation and contrastingly bedded pyroclastic deposits. Much of the bedding forms by dilute pyroclastic density currents (PDC), blast and fallout depositions after phreatomagmatic explosions. This produces a range of beds, typically changing from thick, structureless, and commonly block-rich near the vent to well-developed medial cross-bedding and dune-form

http://dx.doi.org/10.5772/63486

and thin distal planar beds [12, 34, 42, 72, 73]. In many cases, occasionally interbedded Strombolian-derived spatter material or scoria fall units are observed. This exemplifies the changes in the eruptive styles during the formation of a maar volcano (e.g., [45, 49, 74, 75]). The deposit sequence also commonly contains large amounts of lithic material that is entrained from the country rock basement and in some cases accretionary lapilli that is an indicator of free moisture or water droplets in the moving two- or three-phase current [76–78]. Bedding sags are common sedimentary features and their abundance usually reflects the violent excavation of blocks of country rock or magmatic bombs during the formation of the diatreme and the ballistic nature of eruptions (e.g., [55–57]) (**Figure 2**).

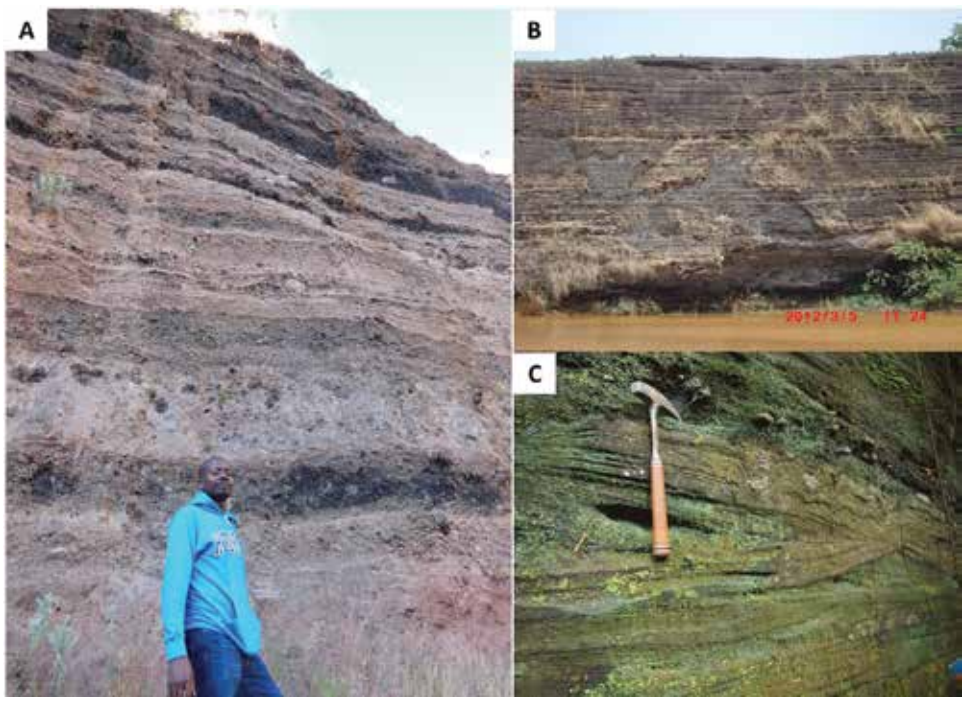

Figure 2. Some features observed on maar deposits. (**A**) Contrasting surge and fall units of the Alberca de Guadalupe maar deposits (Zacapu basin, Michoacán, Mexico); (**B**) thinly stratified surge deposits of Nyos Maar, Cameroon; (**C**) soft structure deformation and impact sags in a sequence of Barombi Mbo Maar deposit, Cameroon.

The estimated volumes of bulk-ejected tephra and the corresponding dense rock equivalent (DRE) using different methods such as isopach and/or juvenile content of the bulk deposits or by applying interpolation techniques on digital elevation models (DEM) along with rock textural data collected from the field (e.g., [69]) are usually very small (≤1 km^3). This suggests that maars are very small-volume volcanoes compared to the middle-size shield volcanoes (1–10 km^3) and the large polygenetic volcanoes (10–10,000 km^3). The latter ones have a stable melt source over prolonged periods, where shallow magma storage systems are expected to develop and form a well-defined and stable vent zone over a long time, producing large volumes of materials and potentially chemically diverse eruptive products [60]. The duration of volcanic

activity leading to their formation would therefore be probably short and even reduced to a single eruptive event (e.g., [6]).

Another feature that is usually associated to maars is a diatreme. Because of the occurrence in maar deposits of an important amount of accidental lithic fragments of the country rock, it was inferred that below a maar there is inevitably an extended subsurface inverted cone- or carrot-shaped structure called diatreme (e.g., [29, 79]). Many remnants of well-exposed diatremes have been identified in association with massifs of plutonic rocks of different compositions and also in ore deposits fields, where in the form of brecciated and pebbly pipes, they have frequently served as the most favorable ore- and diamond hosting structures. However, even if geophysical studies have demonstrated the presence of this structure beneath maars (e.g., [80, 81]) and that in rare occasions drill holes have reach the upper level of the diatreme facies of the maar-diatreme volcanoes (e.g., [62, 63]), the opportunity to examine a diatreme and an ejecta ring belonging to the same maar-diatreme volcano is rare, posing some difficulty to establish the direct relationships between the ejecta ring of a maar, the eruption processes, and the growth of its underlying diatreme. Nevertheless, the diatreme beneath maars might consist of deposits formed during eruptions that can be described collectively as "diatreme deposits," including bedded diatreme fill; un-bedded diatreme fill, including in zones that cut across bedded fill; as well as root zone deposits (e.g., [12], **Figure 3**).

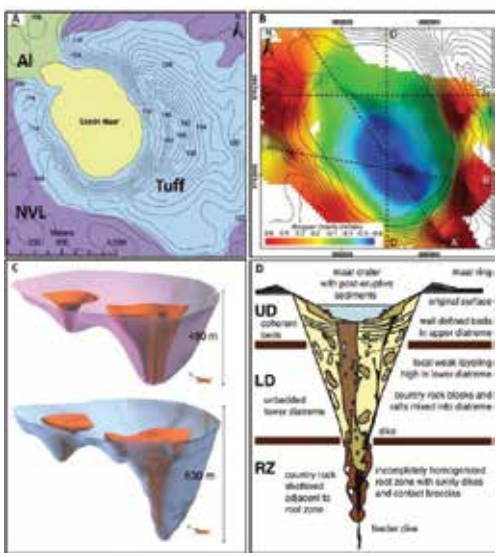

Figure 3. Example of geophysical response from the Ecklin Maar, Newer Volcanics Province, southeastern Australia, (images from Blaikie et al. [81]). (**A**) Simplified geology of the maar; (**B**) Bouguer anomaly with regional trend removed showing gravity low over the crater; (**C**) 3D model viewed from southwest (upper) and optimized geometry (lower) of the Ecklin diatreme. (**D**) Maar and diatreme structure with distinct parts of the diatremes defined by their typical lithofacies and structure (from White and Ross [82]).

These general features commonly characterize a simple maar volcano that is considered as monogenetic volcano sensu stricto. The latter corresponds to a volcano characterized by a

http://dx.doi.org/10.5772/63486

single eruptive vent (single crater for maars and tuff rings and unique and regular cone shape for scoria cones) through which only a small and temporal magma supply of single or various compositions erupted once in a brief period of time. This implies that all the pathways of magma supply should have cooled down and ascending routes are no longer favored for the next magma batch (e.g., [60]). In reference to maars or tuff rings, the tephra ring for monogenetic maars would have a relatively regular shape that might follows the morphology of the crater. The stratigraphic sequence is as simple as possible in terms of tephra succession (e.g., no stratigraphic gap or discordance indicative of a potential break in the eruption progression). This simplicity does not only refer to the small thickness or the relatively homogeneous type of deposits (e.g., PDC) that can be observed at some maars, because some monogenetic maars can have complex deposit sequences including dilute PDC, tephra fall and spatter, and sometimes rootless lava flows. The Barombi Koto Maar (Cameroon volcanic line) is an example of this type of maar volcanoes. The deposit sequence of this maar indicates a volcanic evolution comprising an initial phreatomagmatic stage, followed by a late sustained Strombolian activity that formed a small scoria phase, then another phreatomagmatic phase, and a late sustained Strombolian-style explosive eruption that formed a small scoria cone constructing an islet in the middle of the crater lake, without any break in the preserved eruptive sequence [23]. Nyos Maar in Cameroon could also be a good example. Nyos Maar is characterized by a lower lava flow unit (8 m thick) and an upper dilute PDC unit (~70–80 m thick on the eastern lakeshore), indicating an initial fire-fountaining phase [83] and a series of phreatomagmatic explosions [83] without gap between the eruptive sequences indicating a continuous eruption [84].

3. Features of complex maar volcanoes

As discussed above, maar-diatreme volcanoes are commonly composed of a crater, an ejecta ring, and an underlying diatreme structure that is filled by various fragments from the ascending magma and the country rock. In addition, they are characterized by small eruptive volumes that usually result in the simplicity of their volcanic edifice. The small eruptive volume is also interpreted as a result of a short volcanic activity and even reduced to a single eruptive event. However, even characterized by a small eruptive volume, all maar-diatreme volcanoes are dissimilar in terms of volcanic edifice morphology. Like their "cousins" tuff rings and scoria cones, which are usually considered as monogenetic volcanoes, these volcanoes are very complex especially when their stratigraphic sequences, the morphology of their craters and/or their ejecta rings, or the chemical composition throughout the sequence are examined in detail. For instance, Németh et al. [85] and Németh and Kereszturi [60] following earlier definitions of monogenetic volcanoes (e.g., [4]) highlighted different types of small volcanoes that can be encountered in monogenetic volcanic fields. These included monogenetic volcanoes sensu stricto and complex monogenetic volcanoes with multiple eruptive episodes, which in some cases are characterized by a complex magmatic feeding system. In the literature there are numerous examples for such eruptive behavior: Crater Hill [32], the long-lived scoria cone and lava flow complex of Rangitoto Auckland volcanic field, New Zealand [86], and Motukorea tuff ring in Auckland volcanic field, New Zealand [87, 88]; the Kissomlyó in Hungary

(e.g., [89]); the Udo, Songaksan, and Yangpory in South Korea (e.g., [8, 54, 90]); the Purrumbete Maar in Australia (e.g., [10]); Fekete-hegy [91], Bondoró [31], and Tihany [29] from the Bakony-Balaton Highland Volcanic Fields in Western Hungary; some maars in the Eifel volcanic field, Germany [92, 93]; the Cerro Negro scoria cone, Nicaragua [94, 95]; and El Volcancillo, Mexico [96]. All of these examples were likely constructed over a longer period of time (from Ky to My). This was inferred from the fact that those volcanoes, even having a small eruptive volume, have a complex stratigraphy and tephra ring architecture suggesting that multiple eruptive episodes contributed to the growth and destruction of the volcanic edifice (e.g., [85]). These volcano categories are revisited hereafter with an emphasis on maar-diatremes.

Figure 4. Textural unconformities in the Meke Gölü Maar deposit, Turkey (**A**), and laterally discontinuous thick cross-laminated beds in the Cora Maar deposit (**B**). (**C**) Complex well-marked discordant contacts and truncation surface between the deposit packages at Alchichica Maar, Easter Mexican Volcanic Belt (EMVB). Note the discordant contacts between the scoria cone, the lava flow, and the maar pyroclastic deposit sequence (PH). The left lower photo shows a sharp contact between the scoria cone and the pyroclastic level PH.

As with polygenetic volcanoes, multiple eruptive events have the capability to produce with time a large cumulative volume of tephra and/or lava products around a single or multiple volcanic vents. In the case of small volcanoes, this probably will result in the deposition of

http://dx.doi.org/10.5772/63486

thick eruptive sequences. However, the volume or the thickness of deposits might not be a common feature to all small volcanoes where multiple eruptions or polycyclic activity is observed. This is mainly because these parameters depend directly on the volume of magma involved in each eruptive cycle and, in the cases of maars and tuff rings, to the depths at which explosions took place to excavate an important fraction of country rocks that compose up to 90% of ejected materials (e.g., [12]). Nevertheless, the consequence of the poly-activity within small volcanoes is the construction of complex stratigraphic sequences. These complex volcanoes usually display packages or depositional units made of erupted materials that in some cases can be directly apparent on the field by deposit textural differences, chaotic deposits separated by a lava flow horizon (e.g., [97]), and/or a dike cutting through the deposit units (e.g., [98]). Textural differences in pyroclastic sequences can also show altered or palagonized juvenile-rich deposits that underlie a fresh surge or fall unit within the same eruptive sequence (e.g., [33, 97, 99]) or the presence of centimeter- to decimeter-thick light brown to yellowish pedogenized ash horizons in some deposits [21]. Well-marked structural discordant contacts or truncation surface or erosional limits between the deposit packages (e.g., [26, 34, 66, 76, 92, 100]) are some of the main features observed within the stratigraphic sequence. These are characterized by high-angle, laterally discontinuous or thick cross-laminated levels and angular unconformities between pyroclastic deposits, ranging in outcrop scale from centimeter to decameter long (**Figure 4**). In many other cases, one of the features that separate the eruptive packages is a paleosoil (e.g., [12, 22, 42, 101, 102]).

Because the formation of a soil requires a minimum time ranging from hundreds to millions of years depending on the climatic conditions (e.g., [103]), this feature highlights how long was the period of the eruptive activity and is therefore commonly used to distinguish between simple monogenetic and complex polygenetic small volcanoes. However, multiple eruptive events might occur within a short timescale without the formation of paleosoils between eruptive packages, and the surrounding deposits can display the same stratigraphic and structural complexity [9]. Note that in historic times only a few maar-diatreme volcanoes erupted. In 1954 the Nilahue Maar erupted in Chile during almost half a year, but the main eruptive phase ended after 10 days producing a maar crater of 300 m in diameter. In contrast, in 1977 the Ukinrek West Maar erupted only for 3 days and generated 10 m-thick tephra ring, a 170 m wide (rim to rim) and 30 m deep maar crater (e.g., [100, 104]). This information is certainly not enough to generalize about the duration of a sequence of maar-forming eruption, making it difficult to easily distinguish between the complex maars. Fisher et al. [105] suggested that an eruptive pulse is a single explosion or detonation that may last a few seconds to minutes producing an eruption column from which particles will sediment to form a single well-defined tephra bed. On the other hand, an eruptive phase consists of series of strong explosions that can last a few hours to days generating pulsating eruptions columns and formation of several well-defined beds. Depending on the style of magma fragmentation, an eruptive phase may alternate between explosive and effusive eruptive phases [106]. It is also important to note that the eruption here is fed by a single magma batch or multiple magma batches that could be of the same or different compositions (e.g., [60]). The eruptive episode or single eruption is composed of several eruptive phases, which may last a few days to months and in some volcanoes for years [105 ,106].

Following these definitions, (1) a complex monogenetic volcano can be categorized as the one where multiple eruptive phases have been identified. This implies that magma batch or batches feeding the system erupted almost at the same time, with a very short break (days to years [9]) insufficient to allow any significant erosion or alteration (palagonization) at the top of each eruptive package (deposits of one eruptive phase) and especially the formation of a paleosoil. This type can experience vertical and lateral vent migration and dike arrests which are very common processes in the formation of maar-diatreme volcanoes (e.g., [28, 107, 108]).

In contrast, (2) complex monogenetic volcanoes with polygenetic inheritance are those in which at least two eruptive episodes have been identified, i.e., where a paleosoil or any indication for time gap from the eruptive sequence can be established (time obtained by conventional dating methods) that separates two sequences of deposits, each composed of multiple packages (e.g., [22, 101]). This also implies that the time gap between the eruptive episodes is significant, several thousands of years as observed with the Albano Maar (e.g., [13, 21]), the Barombi Mbo Maar (e.g., [59]), the Bondoró Volcanic Complex [31], the Hule Maar (e.g., [12]), or Ilchulbong tuff cone [9].

While the erosional limits or the presence of paleosoils within the stratigraphic sequence would mainly indicate a time gap between eruptive cycles, structural truncation surfaces or discordant contacts usually result in complex tephra ring architectures, especially when deposit packages have different dipping angles (e.g., [9, 20]). This suggests an influence of the variation in the eruptive vents or some tectonic activity with the progression of eruptions that have been attributed to the formation of complex craters morphologies (e.g., [17, 20, 26, 27, 90, 91]). Experimental studies have even demonstrated that the size and shape of maar craters might vary depending on the positions and numbers of the explosion loci during their formation (e.g., [109–112]). For instance, according to [111], final crater shapes tend to be roughly circular if subsurface explosion epicenters occur within each other's footprints (i.e., the plan view area of reference crater produced by a single explosion) and elongate if an epicenter lies somewhat beyond the footprint of the previous explosion, such that their footprints overlap. But if epicenters are too far apart, the footprints do not overlap and separate craters result (e.g., [29, 113]). This is likely the process that occurred at the Tihany volcanic complex in Western Hungary, where successive eruptions created three separated volcanic centers (e.g., [29]). **Figure 5** shows this complexity of the crater shape for some maar volcanoes of both monogenetic (e.g., Atexcac; **Figure 5c**) and polygenetic natures (e.g., Albano and Purrumbete Maars; **Figure 5B** and **D**). These maars are characterized by many small craters a minimum of three for the Purrumbete Maar to up to nine for the Atexcac maar [27] that coalesced to form relatively regular or irregular crater morphologies. Many other maars with such complex eruptive evolution and crater morphology have been identified in different volcanic fields. Crater Hill in Auckland Volcanic Field, New Zealand, is characterized by a nearly circular tuff ring of 900–1100 m wide and only 9–15 m thick, surrounding an elliptic irregular crater [115]. The crater resulted from the coalescence of at least four vents spaced along a NNE trending, 600 m-long fissure [115]. Tecuitlapa Maar located in the eastern Central Volcanic Belt of Mexico [28] is characterized by a 1 km-diameter irregular crater which is an alignment of scoria cones. It is thought that activity there began in the eastern part of the crater with phreatomagmatic

http://dx.doi.org/10.5772/63486

eruption, where basaltic magma interacted with liquefied tuffaceous sediments. Then, the explosion locus gradually moved westward producing an elliptical crater. The eruptions then dried out and began to produce scoria/spatter cones with nested craters along the same alignment parallel to regional structural trends [28]. Chako Tchamabé et al. [11] demonstrated also that similar migration of explosion vent occurred at the polygenetic Barombi Mbo Maar, forming a very large, amalgamated maar crater with a total diameter of 2.5 km. A minimum of three and a maximum of five craters were suggested according to the three eruptive episodes identified and the potential implication of several dike injections within the progression of activity [55].

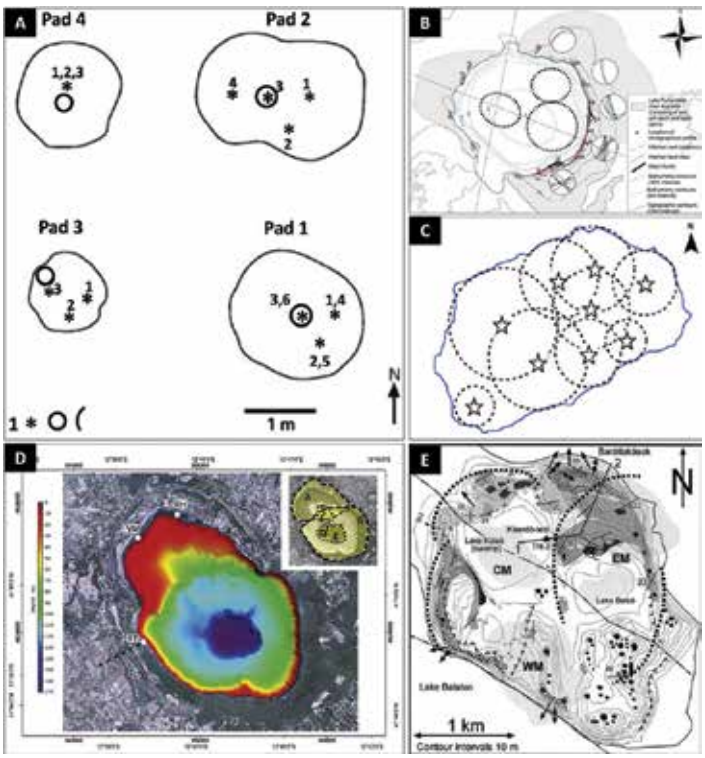

Figure 5. Complexity of crater morphology of maars. (**A**) Shapes of final crater rims resulting from experimental study showing the effect of vertical (Pad 4), lateral (Pads 2 and 3), and both (Pad 1) series of explosions (after Valentine et al. [111]). Bold circle, low point in each crater; 1, 2…, numbers of blast epicenters (asterisk). (**B**, **C** and **D**) Crater shapes and inferred number of vents (dash circles) for Purrumbete Maar (after Jordan et al. [20]), Atexcac Maar (after López-Rojas and Carrasco-Núñez [27]), and Albano Maar (after Anzidei et al. [114]) respectively. (**E**) Complex Tihany volcanic center where large distances between explosion vents have formed three distinct craters (after Németh et al. [29]).

Complex crater morphology (e.g., size and shape) could thus be considered as other useful features that characterize complex maars. However, distinguishing between simple maars and complex ones based on the morphology of the crater alone might be confusing. As noted earlier, simple monogenetic maars can present both regular (subcircular to circular) and irregular crater shapes, irrespective to their sizes. This is probably because multiple batches of magma

might cause explosions simultaneously at several locations near the main center of the crater (e.g., [37, 103]), resulting to the formation of an irregular crater-shaped and a complex but simple deposit sequence in which discordances are scarce. Sill complexes are present in some monogenetic volcanic fields and suggested to fed some maar-diatreme-forming eruptions (e.g., [18, 34, 116–119]). In addition, investigations have shown that the crater morphology and even the architecture of pyroclastic deposits and evolution of maar-diatreme volcanoes can be highly affected by the type of environment—hard substrate (rocks) or a soft substrate (unconsolidated volcaniclastic or sedimentary deposits)—in which they are emplaced (e.g., [82, 91, 120, 121]). In soft substrates, maar-diatreme volcanoes tend to have large and bowl-shaped craters, with gently dipping inner walls [91]. Recent analog experiments as well as field observations from classical diatremes cut into "soft substrate" showed that the diatreme wall can be steep for such maars that cut through soft substrate (e.g., [121–125]). This might be valid for the geometry of the upper part of the maar-diatreme volcano, especially for its crater, given that the number of individual eruptions can also heavily affect the final crater-diatreme morphology, and as many explosive events take place hence as large and old as your maar, the role of the substrate physical conditions will be reduced (e.g., [125]). In contrast, maars formed in hard-rock environment tend to be irregular, small in size and characterized by funnel-shaped and vertical (e.g., Joya Honda, Mexico [126], Nyos Maar, Cameroon [127]) to steeply dipping crater walls. For instance, in the Calatrava volcanic field in Spain, [120] measured and compared the crater sizes and shapes of 60 maars formed in hard substrate and 66 maars formed in soft-substrate basin-filling sediments. While the average crater radius of maars in hard substrate setting is ~ 339 m, those in the other setting have an average of 556 m, indicating that in this volcanic field, the size of the craters for soft-substrate maars is 64% larger on average than that of hard-substrate maars, though the average crater shape in aerial view is quite similar [121]. Maar crater shapes can also be strongly controlled by the presence of any pre-volcanic lithological situations, including older cones that might have been dissected by the maar-forming eruption, or when explosions occur in a preexisting crater form by previous activity (e.g., [128]). The initial shape of the crater might even change with time due to erosion and slumping of the walls and tephra ring (e.g., [18, 79, 129–131]), shallowing the crater slope and reducing the relief. Older maar basins, for example, could have strong erosion modification along their margins and also could be filled with post-eruptive debris, enlarging the original size of the crater. Unusually large maar lake with irregular boundary might certainly results from complex and migrating explosion locus in the area of the crater floor resulting in complex collapse event and scalloped crater wall architecture. Therefore, it is possible to wrongly interpret a maar with complex crater outline as complex maar as its erosion progresses. Large and complex crater outlines can equally mean either a complex eruptive history or long-lasting erosion history; then one has to check the eruptive sequence carefully not only the morphology of the crater. Correlations should be done between the sequence of activity, the different eruptive packages to the number of craters/vents, and probably the distance between them before using the crater morphology to characterize complex maars, as the crater morphology reflects the complexity on the growth of the volcano (**Table 1**).

http://dx.doi.org/10.5772/63486

Maars	Stratigraphy				Crater morphology				Genetic nature
	Thickness (m) of deposit rim (maximum section)	Number of eruptive units	Transition style between deposit packages	Geochemical composition of erupted materials	Size (km)	Number of vents or potential crater basins and relative distance between them	shape	Depth (m – under lake surface)	
BMM	126	3	Paleosoils	Bimodal	2.5	~5 small craters closely distributed	Subcircular	110	Polygenetic
Tecuitlapa	50–70	4	Facies transition	–	1.3 × 1	Undetermined but at least six cinder vents have been highlighted [28]. The positions of the explosion locus are unknown but are distributed laterally following a structural fault	Elliptical	–	Monogenetic
Purrumbete	40	4	Three major Structural discordances	Bimodal (polymagmatic)	3	Three craters closely distributed [10]	Subcircular	45	Polycyclic
Albano		3	Paleosoils	Complex		Five craters closely distributed	Elliptical		Polygenetic
Hule		3	Paleosoils and facies transition	Bimodal [12]	2.3 × 1.8	Three lakes separated by two intra-maar pyroclastic cones and lava flows [12]. Assuming	Sub circular for the whole basin,	Vary for each of the three lakes (Hule, 26.5; Congo, 14.6;	Polygenetic

Maars	Stratigraphy				Crater morphology				Genetic nature
	Thickness (m) of deposit rim (maximum section)	Number of eruptive units	Transition style between deposit packages	Geochemical composition of erupted materials	Size (km)	Number of vents or potential crater basins and relative distance between them	shape	Depth (m – under lake surface)	
						the lakes are lying in resulting craters, we may have three small craters among which the main Hule lake shows two vents for [116] located ~500 m from a basin to another (see **Figure 2** in [117])	elongated for the main Hule lake	unnamed, 4 m) [12]	
Atexcac	61	4	Facies transition	–	1.15 × 0.85	Nine potential craters randomly distributed [27]	Elliptical	120	Polycyclic
Crater Hill	9–15	7	Truncation surface and facies transition	Compositional variation due to clino pyroxene ± spinel fractionation	0.656	4 Aligned along a fissure	Elliptical	100–120	Polycyclic

Table 1. Some characteristics of complex maar volcanoes formed from multiple eruptive events. The number of eruptive units is based here on the number and style of transitions identified and in some case corresponds to the number of eruptive events.

http://dx.doi.org/10.5772/63486

4. Growth of complex monogenetic volcanoes

The eruptive mechanism associated with the formation and growth of monogenetic volcanoes is neither well known nor uniform actually and is somehow attributed to a wide range of magmatic and magma-water interaction-driven explosions at both shallow and deep levels vertically and laterally within the substrate [22, 23, 34, 88, 98, 99, 132, 133]. However, the eruptive timespan for the development of complex monogenetic volcanoes makes a big difference compared to the monogenetic sensu stricto end members. The time in this context is certainly related the timescale of magmatic process in the mantle beneath the volcano. In fact, it is much longer and it is sometimes comparable with large polygenetic volcanoes that are characterized by subsequent production of significant volumes of magma with time. Recent studies have shown that at monogenetic volcanoes, small volumes of melt can segregate from the mantle and readily ascend to the surface through dike or crack propagations (e.g., [8, 54, 55, 134–137]). The segregated melts can rise and erupt simultaneously. In such cases, a polymagmatic monogenetic volcano would form, assuming that the magma batches are of different chemical compositions, such as the Udo volcano in Korea (e.g., [8]). On the other hand, the melts can form with time (e.g., yrs to My), rise, and erupt sporadically. In this latter case, successive vents can be constructed and, depending on the distance between the feeder conduits in the system, can produce the nested or separated vents that characterize these relatively complex volcanoes (**Figure 5**). This process can occur in a typical intra-plate volcanic field such as Saudi Arabia [138] or at basaltic-andesitic polygenetic volcanoes such as Tongariro volcano in New Zealand [139] or at complex maars such as Albano Maar (e.g., [21]) or Barombi Mbo Maar [55] and is broadly accompanied by polymagmatic activity. At Tongariro volcanic Complex in New Zealand, for example, diverse lava flows and pyroclastic units with contrasting chemical and isotopic composition were deposited in a period of 275 Ky, constructing 17 small (>0.3 km^3) to large (>12 km^3) nested and overlapping volcanic cones in a non-systematic orderly progression in space for cone-building events and without any systematic distribution of the vents as well [139]. Freda et al. [21] demonstrated based on $^{40}Ar/^{39}Ar$ ages dating that volcanic activity at Albano Maar (Italy) was strongly discontinuous in time, with a first eruptive cycle at 69±1 ka producing at least two eruptive phases and a second cycle with two peaks at 39±1 and 36±1 ka producing at least four eruptive phases. All these cycles occurred in a narrow surface area centered from each other within only hundreds of meters away, forming a compound volcanic edifice. Using geochemical constraints, they also could demonstrate that each eruptive phase was fed by magmas with different compositions. The complexity in chemical composition was attributed either to the arrival of a new batch of magma during the different eruptive cycles, or to the feeding of the system by the same magma that continuously differentiated and erupted during the whole life of the activity. The eruptive activity at Barombi Mbo Maar in Cameroon follows also such complex volcanic and petrogenetic evolution [55]. In this case, three distinct eruptive events occurred subsequently at 0.5 Ma, 0.2 Ma, and 0.08 Ma [59], fed by magmas with different compositions (**Figure 6**). Petrogenetic constrains there also highlighted the segregation and rise of distinct magma batches with time. During the first eruptive event at Barombi Mbo, successive magma batches of same composition created a first crater, and after a significant reposed period of about 0.3 My, other

magma batches some with the same composition with the former one and other with distinct composition were involved. This indicates that during this second eruptive episode, at least two dikes contributed to the formation of another crater close to the first one. The same process occurred during the third episode after another repose period of about 0.1 My.

It can be observed that the production of magmas within these volcanoes is distributed in a longer timescale, covering a 500 ka range for the Barombi Mbo Maar, less than 300 ka at Tongariro, and only 30 ka at Albano Maar. These observations suggest that one of the main factors that might favor polygenetic activity at monogenetic volcanoes is certainly the time necessary for the segregation of small volumes of melt, mantle fertility, available melt, melting and discharge rates, and the quick potential of magma batches to rise to the surface through regional tectonic setting and stress distribution in the crust. It is important to note that beneath such polygenetic volcanoes, there could be several pockets of melting in the mantle.

Because the degree of partial melting may also vary in each pocket of melting depending on various factors (e.g., the P-T condition, mineral phases present and volume of volatile phases in the mantle zone, or the geotectonic context where the volcano is located), the melts can segregate simultaneously or individually in the different melting spots in the mantle and erupt with time. Still, it is not excluded that the same melting point can produce, with time, small but sufficient volumes of melt that can erupt at different locations near the previous vents due to the tectonic control in the volcanic area or following cracks produced during precedent eruptions. This also allows us to suggest that, if beneath a monogenetic volcanic field, there are conditions that can favor in a local mantle zone the existence of multiple melting spots; the melts might raise with time as they are produced to develop complex small volcanoes with multiple eruptions. If the rising magma batches encountered a wet zone near the surface, a complex maar-diatreme will develop (**Figure 6**).

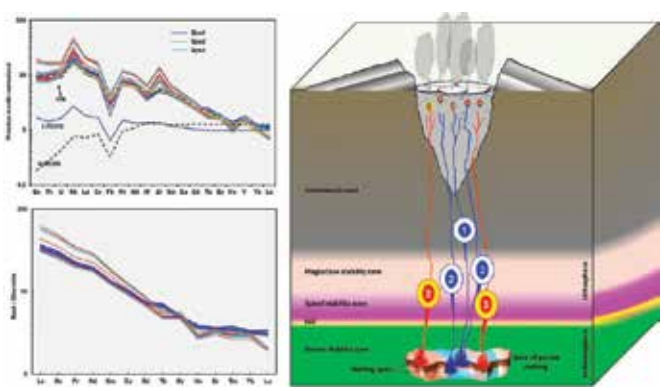

Figure 6. Example of complex compositional variation highlighting complex evolution at Barombi Mbo Maar in Cameroon. The schematic diagram (not to scale) presents the expected feeding system beneath the BMM complex. (1), (2), and (3) correspond to different magma batches feeding the system during the 1st, 2nd, and 3rd eruptive events, respectively, after Chako Tchamabé et al. [59]. The blue and red colors are used here to highlight the different magmas and not the melting loci. Note the involvement of at least two distinct dikes during the second and the third eruptive episodes (details in Chako Tchamabé [55]).

http://dx.doi.org/10.5772/63486

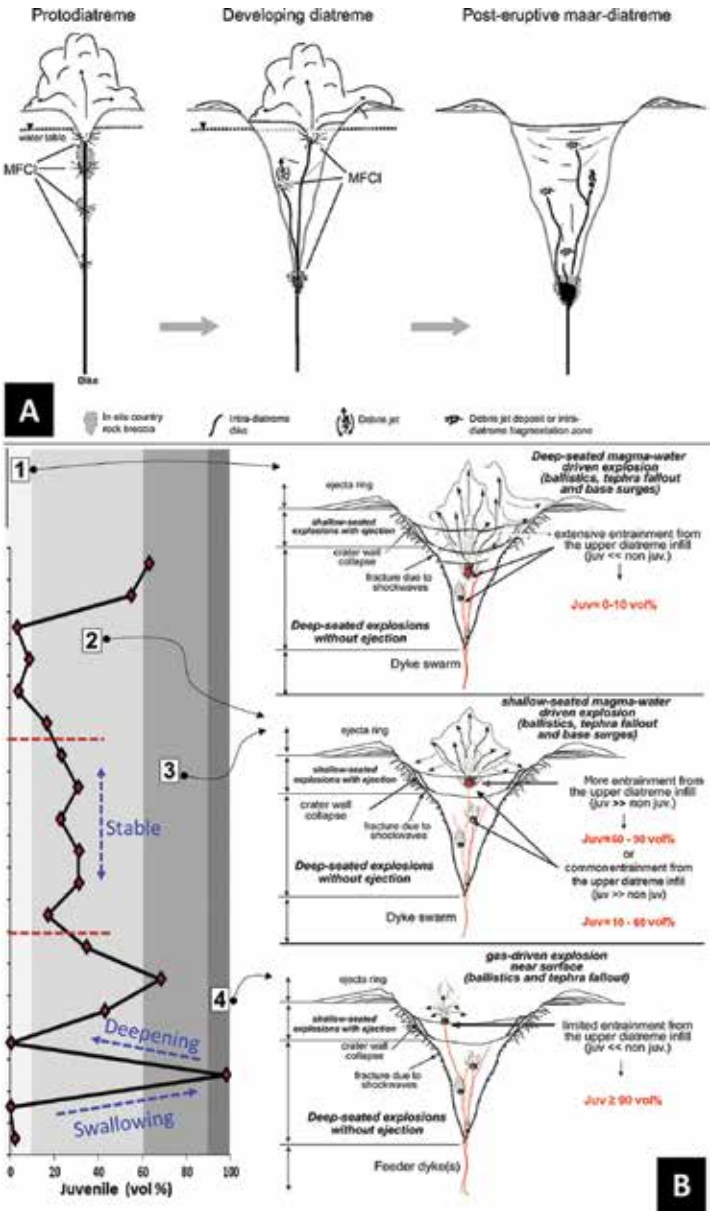

Figure 7. (**A**) Conceptual model after Valentine and White [148] showing explosive molten-fuel-coolant interactions (MFCI) that might take place over a range of depths, brecciating country rock where the explosions take place, but being most effective at shallow depths. (**B**) Comparative schematic model for interpreting the evolution and potential explosion sites (shallow or deep) at maars based on stratigraphic distribution of juvenile components in the BMM ejecta ring. From left to right we have the variation of juvenile populations with a delimitation of domains of juvenile proportion that might reflect a potential model of explosions during maar-diatreme formation. Dashed red lines represent the volcanic hiatus (paleosoils in the deposit) separating the different episodes. The different domains: 1 (juvenile ≤ 10 vol.%), 2 (juvenile = 10–60 vol.%), 3 (juvenile = 60–90 vol.%), and 4 (juvenile ≥ 90) are described in the text and more details in Chako Tchamabé et al. [11].

In the context of growth of such complex monogenetic volcanoes, these observations have an important consequence. The classical growth model of maar-diatremes has long been interpreted following the conceptual model of Lorenz [8], who suggested that the locus of subsurface phreatomagmatic explosions propagates downward with the deepening of a groundwater drawdown cone, as water is used and ejected by explosions [8]. This model implies that the diatremes widen due to slumping and subsidence of host material as their explosion loci deepen [140, 141]. As a result, near-surface occurring lithics would dominate the base of the ejecta rings, while lithics originating from deep-seated explosions location will be deposited on the upper parts of the ejecta ring. Many authors, however, have interpreted the variations in grain size and component distributions in tephra deposits of maars to reflect variations in the intensity of fragmentation during the phreatomagmatic explosions and/or intervening magmatic volatile-driven phases (e.g., [11, 20, 74, 142]) which in turn are often inferred to be related to magma-water ratios (e.g., [143]). It has thus been observed that some maars record intermediate and/or closing phases of magmatic volatile-driven activity in the form of lavas and/or scoria accumulations (e.g., Barombi Koto Maar [23], Tecuitlapa Maar [28]) which are interpreted to result from the absence of groundwater according to [8]. But, the presence of magmatic fragmentation with the evolution of a maar may certainly indicate shallow explosions (e.g., [74]). For instance, Valentine and White [29] propose an alternative model that allows multiple levels of country rock disruption and fragmentation, based on effective mixing by debris jets, an important subsurface transport phenomenon in phreatomagmatic vent complexes that is defined as an upward-moving stream of volcaniclastic debris, magmatic gases, and water vapor ± liquid water droplets, occurring on multiple vertical levels within a growing subsurface diatreme (e.g., [144]). This conceptual model is in accordance with the observed irregular distribution of accidental lithics in ejecta rings (e.g., [145]), field examples on diatreme geometry (e.g., [79]), but also on experimental cratering studies (e.g., [109, 124, 146]) and geophysical modeling (e.g., [80, 81, 147]). Chako Tchamabé et al. [11] also suggested that the variation of juvenile populations within the stratigraphic sequence of maars might reflect a potential mode of explosions during maar-diatreme formation (**Figure 7**). They proposed four domains varying from 0 to 100 vol.% of juvenile contain with the corresponding mode of explosion. For example, a juvenile content of ≤10 vol.% (domain 1) might suggest deep-seated explosions with limited ejection of juveniles and extensive entrainment of fragmented lithics. For 10–60 vol.% juvenile contents, deep- and shallow-seated explosions might occur, with a common entrainment of juveniles and more fragmented lithics, whereas juvenile contents of 60–90 vol.% would suggest shallow-seated explosions with more ejection of juvenile and limited entrainment of fragmented lithics. Up to 90 vol.% of juvenile indicates very shallow (near-surface) gas-driven explosions with ejection of more juveniles. This observation, supported by the conceptual model of [148] for the growth of maars and their diatremes (**Figure 7**), makes clear that explosions may occur at multiple levels, laterally and vertically, contributing to fragmentation and mixing of debris through a combination of upward-directed jets and downward subsidence (e.g., [109, 110, 124, 128, 149]).

However, while those models allow for understanding the diverse eruption scenarios within the formation of simple maars, it might be difficult to determine the growth of complex monogenetic volcanoes, especially complex maars that formed from multiple eruption

http://dx.doi.org/10.5772/63486

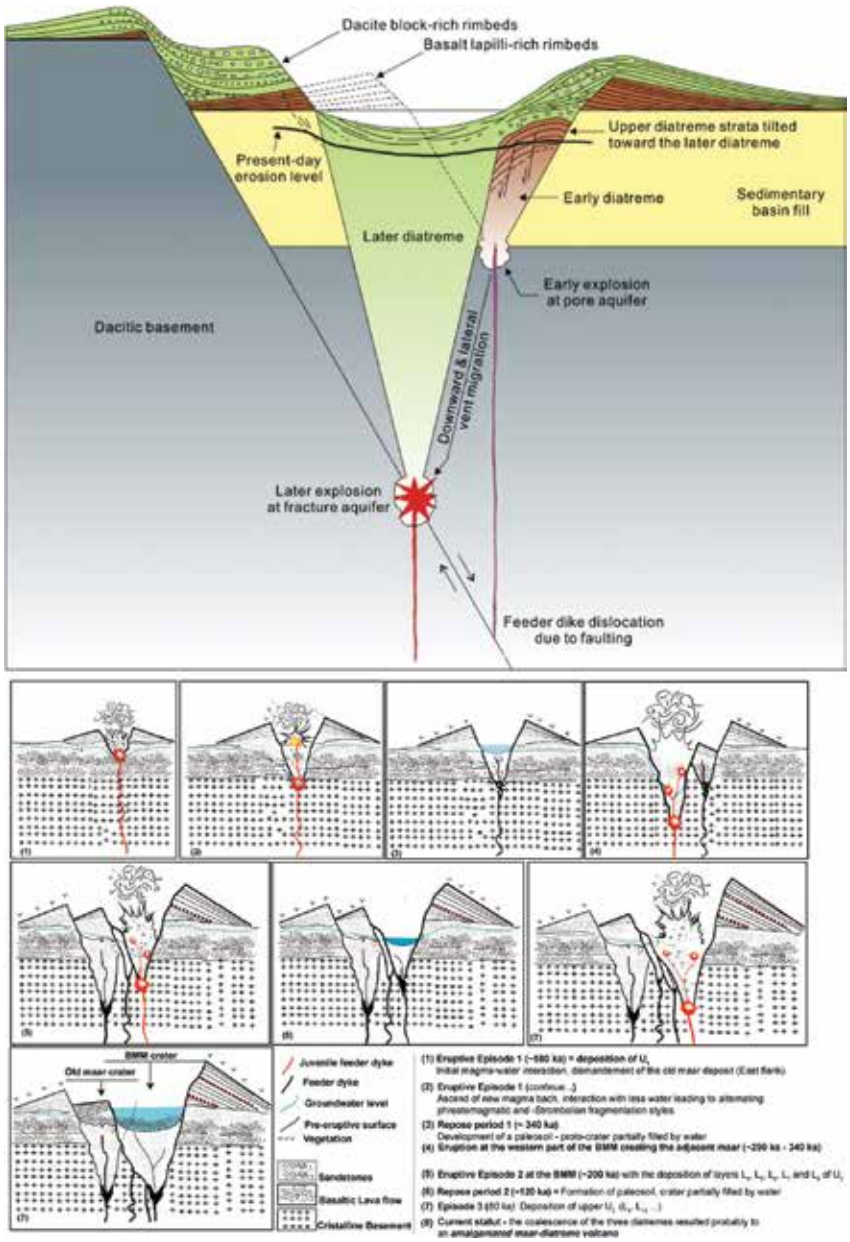

Figure 8. Schematic illustration of the cross-sectional geometry of the Yangpori diatreme (Son et al. [90]) consisting of two cross-cutting diatreme structures, which resulted from migration of the explosion locus associated with basin-margin fault movement (left). Sketch of the temporal evolution and growth of the BMM and its diatreme; here, the explosions started at shallow depth. Afterward, a vertical shift of explosion locus in the substrate followed, producing a scoria-rich layer through alternating phreatomagmatic- and Strombolian-type explosions. Explosions started again after a quiescent period of ~0.3 Ma and magma-water interactions occurring at deeper and at various lateral positions within the diatreme. These explosions widened the crater and deposited more tephra onto the ejecta ring. The explosion pattern may have been the same during the third eruptive episode, continuing to widen the crater and the diatreme (details in Chako Tchamabé et al. [11]).

episodes. Such volcanoes can have dramatic change in the eruption processes given to the overlapping nature of the eruptive products. These can also create truncation and bias in the sedimentary and stratigraphic record as a response of lateral and vertical variation of subsurface explosive loci. The formation of the Yangpori diatreme (South Korea), for example, occurred in two distinct eruption phases, punctuated by sudden lowering of the explosion locus [90]. The first phase of eruption was initiated and maintained at a relatively shallow level within the water-logged basin fills, whereas the second eruptive phase was generated by explosions within a fracture-controlled or joint aquifer within the dacitic basement. This generated two cross-cutting diatreme structures, which resulted from migration of the explosion locus associated with basin-margin fault movement (**Figure 8**). Similar processes were suggested for the Barombi Mbo Maar in Cameroon, but in contrast to the Yangpori diatreme where a tectonically controlled migration was highlighted, new diatremes grew close to the first one at Barombi Mbo due to the discrete injection of new dikes. This implies that the growth process of these complex volcanoes cannot be "predicted" using such growth models, because they are way too complicated in terms of eruptive evolution. A generalized model may not apply for these volcanoes. Each complex monogenetic or polygenetic small volcano should be treated independently, and the growth model for its formation should be done taking into consideration the number of vents identified, the discontinuities observed within the stratigraphy, the eruptive timespan, and probably the geochemistry of the erupted materials.

5. Conclusions

1. Maar-diatreme volcanoes are small volcanic landforms formed as a result of strong MFCI explosive eruptions and usually following a single evolution with a succession of eruptive phases all related to a single eruption, that is closely related in time, and therefore they are usually considered as simple monogenetic volcanoes. However, recent examples of maar volcanoes show a more complex evolution, involving important timescale and breaks in the eruptive activity, changes in the eruptive style, and variations in the magma composition, suggesting the injection of different magma batches during long periods of time. Such complex volcanoes can be grouped into two end members:

- Complex monogenetic volcanoes that are characterized by multiple eruptive phases but which evolved in a single eruptive episode. Here magma batches feeding the system erupt almost at the same time, with a very short break (months to years) insufficient to allow any significant erosion or alteration (e.g., palagonization) at the top of each eruptive package (deposits of one eruptive phase) and especially the formation of a paleosoil. These are polycyclic monogenetic volcanoes.

- If the volcano formed during a very large timescale (e.g., Ky to My) and if at least two eruptive episodes are identified with significant time gaps that can be measured by radiogenic dating methods, the volcano surely is a polygenetic volcano. In such cases, paleosoil layers or highly eroded or altered surfaces may separate the eruptive units.

http://dx.doi.org/10.5772/63486

It is also important to note that for such polygenetic volcanoes, all the eruptions should take place in very close vents that will form a final compound volcanic edifice with overlapping deposits. If the vents are distant ones from others, distinct, but very closely distributed monogenetic volcanic edifices might form.

2. Maars are characterized by composite stratigraphic sequences that are dominated by PDCs and minor fall beds and in some case spatter lava flows. However, for complex maars, sedimentological evidences to establish time gap during the growth of the edifice are crucial to establish the polygenetic nature of the volcano. Maars are also characterized by complex craters morphologies that reflect the complex eruptive evolution and the influence of numerous other factors such as the geologic and tectonic settings, the presence of any pre-volcanic lithological situations including older cones that might have been dissected by the maar-forming eruption or preexisting crater. Because the complexity of the crater morphology applies for both simple and complex maars, observed crater margin needs to be evaluated in respect to establish if the size and shape of the crater reflect the structural boundary of the maar or if this results from an erosion enlarged and/or lake overfilled boundary. In both cases, however, the structural boundary of the maar crater commonly results from the complex explosive excavation history, which is linked to multiple concomitant or timely spaced dike injections, and vent migration in the crater floor that can either be randomly distributed or followed by some structural element such as fissures.

3. The magmatic plumbing system also plays an important role on the growth of complex monogenetic volcanoes, especially maar volcanoes in which diatremes are present. Geochemical variations are sometimes noted at many simple and complex volcanoes. This either means that multiple but near-simultaneous magma batch rise took place or the chemical variations reflect magmatic differentiation en route or both. Thus, if no time gap can be established between the eruptive units, a polymagmatic monogenetic volcano will develop. In contrast, if the complex magmatic activity is correlated with many eruptive episodes, the volcano will be presented as a complex polymagmatic monogenetic volcano with polygenetic inheritance.

4. Though a significant number of large and complex maar volcanoes are known, many of them might really be a reflection of short-lived volcanic events taking place nearly in the same place over longer time (ka range). This chapter clearly demonstrates the detailed complexity of maar eruptions that also emerged from other recent studies on other small-volume volcanoes. Even if the low levels of magmatic differentiation within some of these volcanoes do not allow observation of contrasting magmas in any single volcanic construct, systematic stratigraphically constrained analysis of sample sets might bring significant information on the formation and growth of maars. A complex combination of controlled factors includes the nature of the magmatic plumbing system, the substrate and the influence of local tectonic settings, the melting and ascent rates, groundwater availability, and the multiple injections of magmas successively or, concomitantly during a single eruption, vent migration and establishment of multiple sequential or even possibly concurrent eruption sites. Such detailed investigation would be necessary to

understand each volcanic system and it is only at the end that the volcano may be declare monogenetic or polygenetic.

5. These complex monogenetic volcanoes occur more often than it was previously thought, which is perhaps the reflection of the source region complexity and ascent mechanism. This line of research should be systematically examined in the future because it might hold important clue to understand the geological evolution and volcanic hazard associated with these small-volume magmatic systems located usually far from tectonic boundaries.

Acknowledgements

We thank the book editor for inviting this contribution. The main idea of the work originated from CTB's PhD results, conducted in the framework of the SATREPS-Ny-Mo project entitled "Magmatic Fluid Supply into Lakes Nyos and Monoun, and Mitigation of Natural Disasters in Cameroon." The project organizers and the funding institutions, Japan Science and Technology (JST) and Japan International Cooperation Agency (JICA), are greatly thanked here. Postdoc scholarship supports from National University Autonomous of Mexico (UNAM) and funding from *Consejo Nacional de Ciencia y Tecnología* (CONACyT) through the CONACyT-0150900 project, led by G. Carrasco-Núñez, have given the opportunity to CTB to work on maars of the Eastern Mexican Volcanic Belt (EMVB). Review by B. van Wyk de Vries and language editing by D. Miggins (Oregon State University, USA) significantly increased the readability of the text.

Author details

Boris Chako Tchamabé[1*], Gabor Kereszturi[2], Karoly Németh[2] and Gerardo Carrasco-Núñez[1]

*Address all correspondence to: boris.chako@yahoo.fr

1 Centre for Geosciences, National University Autonomous of Mexico (UNAM), Campus UNAM Juriquilla, Querétaro, Mexico

2 Volcanic Risk Solutions, Massey University, Palmerston North, New Zealand

References

[1] Lorenz, V. (2007) Syn- and posteruptive hazards of maar–diatreme volcanoes. *J Volcanol Geotherm Res*, 159, 285–312. Doi:10.1016/j.jvolgeores.2006.02.015.

[2] Wilson, L. (2009) Volcanism in the Solar System. Nature Geoscience, vol. 2, p. 389–97. Doi:10.1038/ngeo529.

[3] Shoemaker, E.M., Robinson, M.S., Eliason, E.M. (1994) The south pole region of the moon as seen by clementine. *Science*, 266, 1851–54. Doi:10.1126/science.266.5192.1851.

[4] Takada, A. (1994) The influence of regional stress and magmatic input on styles of monogenetic and polygenetic volcanism. *J Geophys Res*, 99, 13563–73. Doi: 10.1029/94JB00494.

[5] Walker, G.P.L. (2000) Basaltic volcanoes and volcanic systems. In: Sigurdsson, H., Houghton, B., Rymer, H., Stix, J., and McNutt, S., editors. Encyclopedia of Volcanoes. Academic Press, p. 283–9.

[6] Nemeth, K. (2010) Monogenetic volcanic fields; origin, sedimentary record, and relationship with polygenetic volcanism. *Spec Paper Geol Soc Am*, 470, 43–66. Doi: 10.1130/2010.2470(04).

[7] Johnson, P.J., Valentine, G.A., Cortés, J.A., Tadini, A. (2014) Basaltic tephra from monogenetic Marcath Volcano, central Nevada. *J Volcanol Geotherm Res*, 281, 27–33. Doi: 10.1016/j.jvolgeores.2014.05.007.

[8] Brenna, M., Cronin, S.J., Smith, I.E.M., Sohn, Y.K., Németh, K. (2010) Mechanisms driving polymagmatic activity at a monogenetic volcano, Udo, Jeju Island, South Korea. *Contr Mineral Petrol*, 160, 931–50. Doi:10.1007/s00410-010-0515-1.

[9] Sohn, Y.K., Cronin, S.J., Brenna, M., Smith, I.E.M., Németh, K., White, J.D.L., et al. (2012) Ilchulbong tuff cone, Jeju Island, Korea, revisited: a compound monogenetic volcano involving multiple magma pulses, shifting vents, and discrete eruptive phases. *Bull Geol Soc Am*, 124, 259–74. Doi:10.1130/B30447.1.

[10] Jordan, S.C., Jowitt, S.M., Cas, R.A.F. (2015) Origin of temporal–compositional variations during the eruption of Lake Purrumbete Maar, Newer Volcanics Province, southeastern Australia. *Bull Volcanol*, 77, 883. Doi:10.1007/s00445-014-0883-x.

[11] Chako Tchamabé, B., Ohba, T., Kereszturi, G., Németh, K., Aka, F.T., Youmen, D., et al. (2015) Towards the reconstruction of the shallow plumbing system of the Barombi Mbo Maar (Cameroon) implications for diatreme growth processes of a polygenetic maar volcano. *J Volcanol Geotherm Res*, 301, 293–313. Doi:10.1016/j.jvolgeores. 2015.06.004.

[12] Alvarado, G.E., Soto, G.J., Salani, F.M., Ruiz, P., de Mendoza, L.H. (2011) The formation and evolution of Hule and Róo Cuarto maars, Costa Rica. *J Volcanol Geotherm Res*, 201, 342–56. Doi:10.1016/j.jvolgeores.2010.12.017.

[13] Giaccio, B., Marra, F., Hajdas, I., Karner, D.B., Renne, P.R., Sposato, A. (2009) $^{40}Ar/^{39}Ar$ and ^{14}C geochronology of the Albano maar deposits: implications for defining the age and eruptive style of the most recent explosive activity at Colli Albani Volcanic District, Central Italy. *J Volcanol Geotherm Res*, 185, 203–13. Doi:10.1016/j.jvolgeores.2009.05.011.

[14] Wohletz, K.H., McQueen, R.G. (1984) Volcanic and stratospheric dustlike particles produced by experimental water-melt interactions. *Geology*, 12, 591–4. Doi: 10.1130/0091-7613(1984)12<591:VASDPP>2.0.CO.

[15] Zimanowski, B., Fröhlich, G., Lorenz, V. (1995) Experiments on steam explosion by interaction of water with silicate melts. *Nucl Eng Des*, 155, 335–43. Doi:10.1016/0029-5493(94)00880-8.

[16] Zimanowski, B., Fröhlich, G., Lorenz, V. (1991) Quantitative experiments on phreatomagmatic explosions. *J Volcanol Geotherm Res*, 48, 341–58. Doi:10.1016/0377-0273(91)90050-A.

[17] Autin-Erickson, A., Büttner, R., Dellino, P., Ort, M.H., Zimanowski, B. (2008) Phreatomagmatic explosions of rhyolitic magma: experimental and field evidence. *J Geophys Res: Solid Earth*, 113, 1–12. Doi:10.1029/2008JB005731.

[18] Lorenz, V. (2003) Maar–diatreme volcanoes, their formation, and their setting in hard-rock or soft-rock environments. *Geolines*, 15, 72–83.

[19] White, J.D.L. (1996) Impure coolants and interaction dynamics of phreatomagmatic eruptions. *J Volcanol Geotherm Res*, 74, 155–70. Doi:10.1016/S0377-0273(96)00061-3.

[20] Jordan, S.C., Cas, R.A.F., Hayman, P.C. (2013) The origin of a large (>3 km) maar volcano by coalescence of multiple shallow craters: Lake Purrumbete maar, southeastern Australia. *J Volcanol Geotherm Res*, 254, 5–22. Doi:10.1016/j.jvolgeores.2012.12.019.

[21] Freda, C., Gaeta, M., Karner, D.B., Marra, F., Renne, P.R., Taddeucci, J., et al. (2006) Eruptive history and petrologic evolution of the Albano multiple maar (Alban Hills, Central Italy). *Bull Volcanol*, 68, 567–91. Doi:10.1007/s00445-005-0033-6.

[22] Chako Tchamabé, B., Youmen, D., Owona, S., Issa, Ohba, T., Nemeth, K., et al. (2013) Eruptive history of the Barombi Mbo Maar, Cameroon Volcanic Line, Central Africa: constraints from volcanic facies analysis. *Central Eur J Geosci*, 5, 480–96. Doi:10.2478/s13533-012-0147-2.

[23] Tamen, J., Nkoumbou, C., Mouafo, L., Reusser, E., Tchoua, F.M. (2007) Petrology and geochemistry of monogenetic volcanoes of the Barombi Koto volcanic field (Kumba graben, Cameroon volcanic line): implications for mantle source characteristics. *C R Geosci*, 339, 799–809. Doi:10.1016/j.crte.2007.09.007.

[24] Rausch, J., Grobéty, B., Vonlanthen, P. (2015) Eifel maars: quantitative shape characterization of juvenile ash particles (Eifel Volcanic Field, Germany). *J Volcanol Geotherm Res*, 291, 86–100. Doi:10.1016/j.jvolgeores.2014.11.008.

[25] Seib, N., Kley, J., Büchel, G. (2013) Identification of maars and similar volcanic landforms in the West Eifel Volcanic Field through image processing of DTM data: efficiency of different methods depending on preservation state. *Int J Earth Sci*, 102, 875–901. Doi: 10.1007/s00531-012-0829-5.

[26] Carrasco-Núñez, G., Ort, M.H., Romero, C. (2007) Evolution and hydrological conditions of a maar volcano (Atexcac crater, Eastern Mexico). *J Volcanol Geotherm Res*, 159, 179–97. Doi:10.1016/j.jvolgeores.2006.07.001.

[27] López-Rojas, M., Carrasco-Núñez, G. (2015) Depositional facies and migration of the eruptive loci for Atexcac axalapazco (central Mexico): implications for the morphology of the crater. Revista Mexicana de Ciencias Geológicas 377–94.

[28] Ort, M.H., Carrasco-Núñez, G. (2009) Lateral vent migration during phreatomagmatic and magmatic eruptions at Tecuitlapa Maar, east-central Mexico. *J Volcanol Geotherm Res*, 181, 67–77. Doi:10.1016/j.jvolgeores.2009.01.003.

[29] Németh, K., Martin, U., Harangi, S. (2001) Miocene phreatomagmatic volcanism at Tihany (Pannonian Basin, Hungary). *J Volcanol Geotherm Res*, 111, 111–35. Doi:10.1016/S0377-0273(01)00223-2.

[30] Németh, K., Martin, U., Harangi, S. (1999) Miocene maar/diatreme volcanism at the Tihany Peninsula (Pannonian Basin); the Tihany Volcano. *Acta Geol Hung*, 42, 349–77.

[31] Kereszturi, G., Csillag, G., Németh, K., Sebe, K., Balogh, K., Jáger, V. (2010) Volcanic architecture, eruption mechanism and landform evolution of a Plio/Pleistocene intracontinental basaltic polycyclic monogenetic volcano from the Bakony–Balaton Highland Volcanic Field, Hungary. *Central Eur J Geosci*, 2, 362–84. Doi:10.2478/v10085-010-0019-2.

[32] Houghton, B.F., Wilson, C.J.N., Rosenberg, M.R., Smith, I.E.M., Parker, R.J. (2000) Mixed deposits of complex magmatic and phreatomagmatic volcanism: an example from Crater Hill, Auckland, New Zealand. *Bull Volcanol*, 58, 59–66. Doi:10.1007/s004450050126.

[33] Németh, K., White, J.D.L. (2003) Reconstructing eruption processes of a Miocene monogenetic volcanic field from vent remnants: Waipiata Volcanic Field, South Island, New Zealand. *J Volcanol Geotherm Res*, 124, 1–21. Doi:10.1016/S0377-0273(03)00042-8.

[34] Agustín-Flores, J., Németh, K., Cronin, S.J., Lindsay, J.M., Kereszturi, G., Brand, B.D., et al. (2014) Phreatomagmatic eruptions through unconsolidated coastal plain sequences, Maungataketake, Auckland Volcanic Field (New Zealand). *J Volcanol Geotherm Res*, 276, 46–63. Doi:10.1016/j.jvolgeores.2014.02.021.

[35] Wohletz, K.H., Sheridan, M.F. (1983) Martian rampart crater ejecta: experiments and analysis of melt–water interaction. *Icarus*, 56, 15–37. Doi:10.1016/0019-1035(83)90125-2.

[36] Kokelaar, P. (1986) Magma–water interactions in subaqueous and emergent basaltic volcanism. *Bull Volcanol*, 48, 275–89.

[37] Büttner, R., Zimanowski, B. (1998) Physics of thermohydraulic explosions. *Phys Rev E*, 57, 5726–9. Doi:10.1103/PhysRevE.57.5726.

[38] Wohletz, K.H. (1986) Explosive magma–water interactions: thermodynamics, explosion mechanisms, and field studies. *Bull Volcanol*, 48, 245–64. Doi:10.1007/BF01081754.

[39] Büttner, R., Dellino, P., La Volpe, L., Lorenz, V., Zimanowski, B. (2002) Thermohydraulic explosions in phreatomagmatic eruptions as evidenced by the comparison between pyroclasts and products from Molten Fuel Coolant Interaction experiments. *J Geophys Res: Solid Earth*, 107, ECV 5–1–ECV 5–14. Doi:10.1029/2001JB000511.

[40] Sheridan, M.F., Wohletz, K.H. (1981) Hydrovolcanic explosions: the systematics of water–pyroclast equilibration. *Science*, 212, 1387–9. Doi:10.1126/science.212.4501.1387.

[41] Valentine, G.A. (1987) Stratified flow in pyroclastic surges. *Bull Volcanol*, 49, 616–30 Doi: 10.1007/BF01079967.

[42] Sohn, Y.K., Chough, S.K. (1989) Depositional processes of the Suwolbong tuff ring, Cheju Island (Korea). *Sedimentology*, 36, 837–55. Doi:10.1111/j.1365-3091.1989.tb01749.x.

[43] White, J.D.L., Schmincke, H.U. (1999) Phreatomagmatic eruptive and depositional processes during the 1949 eruption on La Palma (Canary Islands). *J Volcanol Geotherm Res*, 94, 283–304. Doi:10.1016/S0377-0273(99)00108-0.

[44] Sulpizio, R., Mele, D., Dellino, P., La Volpe, L. (2007) Deposits and physical properties of pyroclastic density currents during complex Subplinian eruptions: the AD 472 (Pollena) eruption of Somma-Vesuvius, Italy. *Sedimentology*, 54, 607–35. Doi:10.1111/j.1365-3091.2006.00852.x.

[45] Brand, B.D., Clarke, A.B., Semken, S. (2009) Eruptive conditions and depositional processes of Narbona Pass Maar volcano, Navajo volcanic field, Navajo Nation, New Mexico (USA). *Bull Volcanol*, 71, 49–77. Doi:10.1007/s00445-008-0209-y.

[46] Ngwa, C.N., Suh, C.E., Devey, C.W. (2010) Phreatomagmatic deposits and stratigraphic reconstruction at Debunscha Maar (Mt Cameroon volcano). *J Volcanol Geotherm Res*, 192, 201–11. Doi:10.1016/j.jvolgeores.2010.02.012.

[47] Gernon, T.M., Upton, B.G.J., Hincks, T.K. (2013) Eruptive history of an alkali basaltic diatreme from Elie Ness, Fife, Scotland. *Bull Volcanol*, 75, 1–20. Doi:10.1007/s00445-013-0704-7.

[48] Houghton, B.F., Hackett, W.R. (1984) Strombolian and phreatomagmatic deposits of ohakune craters, Ruapehu, New Zealand: a complex interaction between external water and rising basaltic magma. J Volcanol Geotherm Res. 21, 207–31.

[49] Clarke, H., Troll, V. (2005) Changing eruptive styles and textural features from phreatomagmatic to strombolian activity of basaltic littoral cones: Los Erales cinder cone, Tenerife, Canary Islands. *Estud Geol*, 134, 121–34.

[50] Clarke, H., Troll, V.R., Carracedo, J.C. (2009) Phreatomagmatic to Strombolian eruptive activity of basaltic cinder cones: Montaña Los Erales, Tenerife, Canary Islands. *J Volcanol Geotherm Res*, 180, 225–45. Doi:10.1016/j.jvolgeores.2008.11.014.

[51] D'Oriano, C., Poggianti, E., Bertagnini, A., Cioni, R., Landi, P., Polacci, M., et al. (2005) Changes in eruptive style during the A.D. 1538 Monte Nuovo eruption (Phlegrean Fields, Italy): the role of syn-eruptive crystallization. *Bull Volcanol*, 67, 601–21. Doi: 10.1007/s00445-004-0397-z.

[52] Nicholson, R.S., Gardner, J.E., Neal, C.A. (2011) Variations in eruption style during the 1931 A.D. eruption of Aniakchak volcano, Alaska. *J Volcanol Geotherm Res*, 207, 69–82. Doi:10.1016/j.jvolgeores.2011.08.002.

[53] Van Otterloo, J., Raveggi, M., Cas, R.A.F., Maas, R. (2014) Polymagmatic activity at the monogenetic Mt Gambier volcanic complex in the Newer Volcanics Province, SE Australia: new insights into the occurrence of intraplate volcanic activity in Australia. *J Petrol*, 55, 1317–51. Doi:10.1093/petrology/egu026.

[54] Brenna, M., Cronin, S.J., Németh, K., Smith, I.E.M., Sohn, Y.K. (2011) The influence of magma plumbing complexity on monogenetic eruptions, Jeju Island, Korea. *Terra Nova*, 23, 70–5. Doi:10.1111/j.1365-3121.2010.00985.x.

[55] Chako Tchamabé, B. (2015) Volcano-Stratigraphy and Geochemistry of Tephra Deposits and its Relevance for Understanding the Polygenetic Inheritance and Plumbing System of Maar–Diatreme Volcanoes: Clues for Hazards Prospective, A Case Study for the Barombi Mbo Maar, Cameroon, Central Africa. Tokai University. Doi:ci.nii.ac.jp/naid/500000935695.

[56] Keating, G.N., Valentine, G.A., Krier, D.J. Perry, F.V. (2008) Shallow plumbing systems for small-volume basaltic volcanoes. *Bull Volcanol*, 70, 563–82. Doi:10.1007/s00445-007-0154-1.

[57] Hintz, A.R., Valentine, G.A. (2012) Complex plumbing of monogenetic scoria cones: new insights from the Lunar Crater Volcanic Field (Nevada, USA). *J Volcanol Geotherm Res*, 239–240, 19–32. Doi:10.1016/j.jvolgeores.2012.06.008.

[58] Kereszturi, G., Nemeth, K. (2013) Monogenetic basaltic volcanoes: genetic classification, growth, geomorphology and degradation. *Update Volcanol New Adv Understand Volcan System*, 3–88. Doi:10.5772/51387.

[59] Chako Tchamabé, B., Ohba, T., Ooki, S., Youmen, D., Owona, S., et al. (2014) Temporal evolution of the Barombi Mbo Maar, a polygenetic maar–diatreme volcano of the Cameroon Volcanic Line. *Int J Geosci*, 5, 1315–23. Doi:10.4236/ijg.2014.511108.

[60] Németh, K., Kereszturi, G. (2015) Monogenetic volcanism: personal views and discussion. *Int J Earth Sci*, 104, 2131–46. Doi:10.1007/s00531-015-1243-6.

[61] Ollier, C.D. (1967) Maars their characteristics, varieties and definition. *Bull Volcanol*, 31, 45–73. Doi:10.1007/BF02597005.

[62] Lorenz, V. (1973) On the formation of maars. *Bull Volcanol*, 37, 183–204. Doi:10.1007/BF02597130.

[63] Lorenz, V. (1986) On the growth of maars and diatremes and its relevance to the formation of tuff rings. *Bull Volcanol*, 48, 265–74. Doi:10.1007/BF01081755.

[64] Németh, K. (2001) Deltaic density currents and turbidity deposits related to maar crater rims and their importance for palaegeographic reconstruction of the Bakony–Balaton Highland volcanic field, Hungary. *Spec Publs. Int Ass Sediment*, 31, 261–77. Doi: 10.1002/9781444304275.ch19.

[65] Begét, J.E., Hopkins, D.M., Charron, S.D. (1996) The largest known maars on earth, Seward Peninsula, Northwest Alaska. *Arctic*, 49, 62–9.

[66] Siebe, C., Salinas, S. (2014) Distribution of monogentic phreatomagmatic volcanoes (maars, tuff-cones and tuff-rings) in the Mexican Volcanic Belt and their tectonic and hydrogeologic environment. In: Carrasco-Núñez, G., Aranda-Gómez, J.J., Ort, M.H., Silva-Corona J.J., editor. *IAVCEI-5IMC-Meeting, Querétaro November 2014 (Mexico)*, p. 183–4.

[67] Kshirsagar, P., Siebe, C., Guilbaud, M.N., Salinas, S., Layer, P.W. (2015) Late Pleistocene Alberca de Guadalupe maar volcano (Zacapu basin, Michoacán): stratigraphy, tectonic setting, and paleo-hydrogeological environment. *J Volcanol Geotherm Res*, 304, 214–36. Doi:10.1016/j.jvolgeores.2015.09.003.

[68] Siebe, C., Macías, J.L., Abrams, M., Rodríguez, S., Castro, R., Delgado, H. (1995) Quaternary explosive volcanism and pyroclastic deposits in east central Mexico: implications for future hazards. *Guidebook of Geological Excursions: In Conjunction with the Annual Meeting of the Geol Soc Am,* New Orleans, Louisiana, November 6–9, 1995, p. 1–48.

[69] Kereszturi, G., Németh, K., Cronin, S.J., Agustín-Flores, J., Smith, I.E.M., Lindsay, J. (2013) A model for calculating eruptive volumes for monogenetic volcanoes—implication for the Quaternary Auckland Volcanic Field, New Zealand. *J Volcanol Geotherm Res*, 266, 16–33. Doi:10.1016/j.jvolgeores.2013.09.003.

[70] Sottili, G., Palladino, D.M., Gaeta, M., Masotta, M. (2012) Origins and energetics of maar volcanoes: examples from the ultrapotassic Sabatini Volcanic District (Roman Province, Central Italy). *Bull Volcanol*, 74, 163–86. Doi:10.1007/s00445-011-0506-8.

[71] Lorenz, V. (1970) Some aspects of the eruption mechanism of the big hole maar, central oregon. *Bull Geol Soc Am*, 81, 1823–30. Doi:10.1130/0016-7606(1970)81[1823:SAOTEM]2.0.CO;2.

[72] White, J.D. (1991) Maar–diatreme phreatomagmatism at Hopi Buttes, Navajo Nation (Arizona), USA. *Bull Volcanol*, 53, 239–58. Doi:10.1007/BF00414522.

[73] Vazquez, J.A., Ort, M.H. (2006) Facies variation of eruption units produced by the passage of single pyroclastic surge currents, Hopi Buttes volcanic field, USA. *J Volcanol Geotherm Res*, 154, 222–36. Doi:10.1016/j.jvolgeores.2006.01.003.

[74] Sottili, G., Taddeucci, J., Palladino, D.M., Gaeta, M., Scarlato, P., Ventura, G. (2009) Subsurface dynamics and eruptive styles of maars in the Colli Albani Volcanic District, Central Italy. *J Volcanol Geotherm Res*, 180, 189–202. Doi:10.1016/j.jvolgeores.2008.07.022.

[75] Kereszturi, G., Németh, K., Csillag, G., Balogh, K., Kovács, J. (2011) The role of external environmental factors in changing eruption styles of monogenetic volcanoes in a Mio/Pleistocene continental volcanic field in western Hungary. *J Volcanol Geotherm Res*, 201, 227–40. Doi:10.1016/j.jvolgeores.2010.08.018.

[76] Heiken, G.H. (1971) Tuff rings: examples from the Fort Rock-Christmas Lake Valley basin, south-central Oregon. *J Geophys Res*, 76, 1626–5615. Doi:10.1029/JB076i023p05615.

[77] Miyabuchi, Y., Ikebe, S., Watanabe, K. (2008) Geological constraints on the 2003–2005 ash emissions from the Nakadake crater lake, Aso Volcano, Japan. *J Volcanol Geotherm Res*, 178, 169–83. Doi:10.1016/j.jvolgeores.2008.06.025.

[78] Chough, S.K., Sohn, Y.K. (1990) Depositional mechanics and sequences of base surges, Songaksan tuff ring, Cheju Island, Korea. *Sedimentology*, 37, 1115–1135. Doi:10.1111/j.1365-3091.1990.tb01849.x.

[79] Kurszlaukis, S., Fulop, A. (2013) Factors controlling the internal facies architecture of maar–diatreme volcanoes. *Bull Volcanol*, 75, 1–12. Doi:10.1007/s00445-013-0761-y.

[80] Blaikie, T.N., Ailleres, L., Cas, R.A.F., Betts, P.G. (2012) Three-dimensional potential field modelling of a multi-vent maar–diatreme—the Lake Coragulac maar, Newer Volcanics Province, south-eastern Australia. *J Volcanol Geotherm Res*, 235–236, 70–83. Doi:10.1016/j.jvolgeores.2012.05.002.

[81] Blaikie, T.N., Ailleres, L., Betts, P.G., Cas, R.A.F. (2014) A geophysical comparison of the diatremes of simple and complex maar volcanoes, Newer Volcanics Province, south-eastern Australia. *J Volcanol Geotherm Res*, 276, 64–81. Doi:10.1016/j.jvolgeores.2014.03.001.

[82] White, J.D.L., Ross, P.S. (2011) Maar–diatreme volcanoes: a review. *J Volcanol Geotherm Res*, 201, 1–29. Doi:10.1016/j.jvolgeores.2011.01.010.

[83] Lockwood, J.P., Rubin, M. (1989) Origin and age of the Lake Nyos maar, Cameroon. *J Volcanol Geotherm Res*, 39, 117–24. Doi:10.1016/0377-0273(89)90052-8.

[84] Aka, F.T., Yokoyama, T., Kusakabe, M., Nakamura, E., Tanyileke, G., Ateba, B., et al. (2008) U-series dating of Lake Nyos maar basalts, Cameroon (West Africa): implications for potential hazards on the Lake Nyos dam. *J Volcanol Geotherm Res*, 176, 212–24. Doi:10.1016/j.jvolgeores.2008.04.009.

[85] Németh, K., Cronin, S.J., Haller, M.J., Brenna, M., Csillag, G. (2010) Modern analogues for Miocene to Pleistocene alkali basaltic phreatomagmatic fields in the Pannonian Basin: "soft-substrate" to "combined" aquifer controlled phreatomagmatism in intraplate volcanic fields. *Cent Eur J Geosci*, 2, 339–61 (Research Article). Doi:10.2478/v10085-010-0013-8.

[86] Shane, P., Gehrels, M., Zawalna-Geer, A., Augustinus, P., Lindsay, J., Chaillou, I. (2013) Longevity of a small shield volcano revealed by crypto-tephra studies (Rangitoto volcano, New Zealand): change in eruptive behavior of a basaltic field. *J Volcanol Geotherm Res*, 257, 174–83. Doi:10.1016/j.jvolgeores.2013.03.026.

[87] McGee, L.E., Millet, M.A., Smith, I.E.M., Németh, K., Lindsay, J.M. (2012) The inception and progression of melting in a monogenetic eruption: Motukorea Volcano, the Auckland Volcanic Field, New Zealand. *Lithos*, 155, 360–74. Doi:10.1016/j.lithos.2012.09.012.

[88] Agustín-Flores, J., Németh, K., Cronin, S.J., Lindsay, J.M., Kereszturi, G. (2015) Construction of the North Head (Maungauika) tuff cone: a product of Surtseyan volcanism, rare in the Auckland Volcanic Field, New Zealand. *Bull Volcanol*, 77, 97–120.. Doi:10.1007/s00445-014-0892-9.

[89] Jankovics, M.É., Harangi, S., Németh, K., Kiss, B., Ntaflos, T. (2015) A complex magmatic system beneath the Kissomlyó monogenetic volcano (western Pannonian Basin): evidence from mineral textures, zoning and chemistry. *J Volcanol Geotherm Res*, 301, 38–55. Doi:10.1016/j.jvolgeores.2015.04.010.

[90] Son, M., Kim, J.S., Jung, S., Ki, J.S., Kim, M.C., Sohn, Y.K. (2012) Tectonically controlled vent migration during maar–diatreme formation: an example from a Miocene half-graben basin in SE Korea. *J Volcanol Geotherm Res*, 223–224, 29–46. Doi:10.1016/j.jvolgeores.2012.02.002.

[91] Auer, A., Martin, U., Németh, K. (2007) The Fekete-hegy (Balaton Highland Hungary) "soft-substrate" and "hard-substrate" maar volcanoes in an aligned volcanic complex —implications for vent geometry, subsurface stratigraphy and the palaeoenvironmental setting. *J Volcanol Geotherm Res*, 159, 225–45. Doi:10.1016/j.jvolgeores.2006.06.008.

[92] Shaw, C.S.J., Woodland, A.B., Hopp, J., Trenholm, N.D. (2010) Structure and evolution of the Rockeskyllerkopf Volcanic Complex, West Eifel Volcanic Field, Germany. *Bull Volcanol*, 72, 971–90. Doi:10.1007/s00445-010-0380-9.

[93] Pirrung, M., Fischer, C., Büchel, G., Gaupp, R., Lutz, H, Neuffer, F.O. (2003) Lithofacies succession of maar crater deposits in the Eifel area (Germany). *Terra Nova*, 15, 125–32. Doi:10.1046/j.1365-3121.2003.00473.x.

[94] McKnight, S.B., Williams, S.N. (1997) Old cinder cone or young composite volcano? The nature of Cerro Negro, Nicaragua. *Geology*, 25, 339–42. Doi:10.1130/0091-7613(1997)025<0339:OCCOYC>2.3.CO;2.

[95] Courtland, L.M., Kruse, S.E., Connor, C.B., Connor, L.J., Savov, I.P., Martin, K.T. (2012) GPR investigation of tephra fallout, Cerro Negro volcano, Nicaragua: a method for constraining parameters used in tephra sedimentation models. *Bull Volcanol*, 74, 1409–24. Doi:10.1007/s00445-012-0603-3.

[96] Siebert, L., Carrasco-Núñez, G. (2002) Late-Pleistocene to precolumbian behind-the-arc mafic volcanism in the eastern Mexican Volcanic Belt; implications for future hazards. *J Volcanol Geotherm Res*, 115, 179–205. Doi:10.1016/S0377-0273(01)00316-X.

[97] Befus, K.S., Hanson, R.E., Lehman, T.M., Griffin, W.R. (2008) Cretaceous basaltic phreatomagmatic volcanism in West Texas: Maar complex at Peña Mountain, Big Bend National Park. *J Volcanol Geotherm Res*, 173, 245–64. Doi:10.1016/j.jvolgeores.2008.01.021.

[98] Muirhead, J.D., Van Eaton, A.R., Re, G., White, J.D.L., Ort, M.H. (2016) Monogenetic volcanoes fed by interconnected dikes and sills in the Hopi Buttes volcanic field, Navajo Nation, USA. *Bull Volcanol*, 78, 11. Doi:10.1007/s00445-016-1005-8.

[99] Valentine, G.A., Perry, F.V., WoldeGabriel, G. (2000) Field characteristics of deposits from spatter-rich pyroclastic density currents at Summer Coon volcano, Colorado. *J Volcanol Geotherm Res*, 104, 187–99. Doi:10.1016/S0377-0273(00)00206-7.

[100] Kienle, J., Kyle, P.R., Self, S., Motyka, R.J., Lorenz, V. (1980) Ukinrek Maars, Alaska, I. April 1977 eruption sequence, petrology and tectonic setting. *J Volcanol Geotherm Res*, 7, 11–37. Doi:10.1016/0377-0273(80)90018-9.

[101] Giordano, G. (1998) Facies characteristics and magma–water interaction of the White Trachytic Tuffs (Roccamonfina Volcano, southern Italy). *Bull Volcanol*, 60, 10–26. Doi: 10.1007/s004450050213.

[102] Valentine, G.A., Sottili, G., Palladino, D.M., Taddeucci, J. (2015) Tephra ring interpretation in light of evolving maar–diatreme concepts: Stracciacappa maar (central Italy). *J Volcanol Geotherm Res*, 308, 19–29. Doi:10.1016/j.jvolgeores.2015.10.010.

[103] Dosseto, A., Buss, H.L., Suresh, P.O. (2012) Rapid regolith formation over volcanic bedrock and implications for landscape evolution. *Earth Planet Sci Lett*, 337–338, 47–55. Doi:10.1016/j.epsl.2012.05.008.

[104] Self, S., Kienle, J., Huot, J.P. (1980) Ukinrek Maars, Alaska, II. Deposits and formation of the 1977 craters. *J Volcanol Geotherm Res*, 7, 39–65. Doi:10.1016/0377-0273(80)90019-0.

[105] Fisher, R.V., Heiken, G., Hulen, J.B. (1998) Volcanoes: Crucibles of Change. Princeton: Nature Publishing Group.

[106] Fisher, R.V., Schmincke, H.-U. (1984) Pyroclastic Rocks. Berlin, Heidelberg: Springer-Verlag. Doi:10.1007/978-3-642-74864-6.

[107] Lefebvre, N.S., White, J.D.L., Kjarsgaard, B.A. (2016) Arrested diatreme development: standing Rocks East, Hopi Buttes, Navajo Nation, USA. *J Volcanol Geotherm Res*, 310, 186–208. Doi:10.1016/j.jvolgeores.2015.12.007.

[108] Kereszturi, G., Németh, K. (2011) Shallow-seated controls on the evolution of the Upper Pliocene Kopasz-hegy nested monogenetic volcanic chain in the Western Pannonian Basin (Hungary). *Geol Carpath*, 62, 535–46. Doi:10.2478/v10096-011-0038-3.

[109] Graettinger, A.H., Valentine, G.A., Sonder, I., Ross, P.S., White, J.D.L., Taddeucci, J. (2014) Maar–diatreme geometry and deposits: subsurface blast experiments with variable explosion depth. *Geochem Geophys Geosyst*, 15, 740–64. Doi: 10.1002/2013GC005198.

[110] Graettinger, A.H., Valentine, G.A., Sonder, I. (2015) Circum-crater variability of deposits from discrete, laterally and vertically migrating volcanic explosions: experimental evidence and field implications. *J Volcanol Geotherm Res*, 308, 61–9. Doi:10.1016/j.jvolgeores.2015.10.019.

[111] Valentine, G.A., Graettinger, A.H., Macorps, É., Ross, P.S., White, J.D.L., Döhring, E., et al. (2015) Experiments with vertically and laterally migrating subsurface explosions with applications to the geology of phreatomagmatic and hydrothermal explosion craters and diatremes. *Bull Volcanol*, 77, 1–17. Doi:10.1007/s00445-015-0901-7.

[112] Sonder, I., Graettinger, A. H. Valentine, G. A. (2015) Scaling multiblast craters: general approach and application to volcanic craters." *Journal of Geophys Res: Solid Earth*, 120, 6141–6158. Doi: 15 10.1002/2015JB012018

[113] Abrams, M.J., Siebe, C. (1994) Cerro Xalapaxco: an unusual tuff cone with multiple explosion craters, in central Mexico (Puebla). *J Volcanol Geotherm Res*, 63, 183–99. Doi: 10.1016/0377-0273(94)90073-6.

[114] Anzidei, M., Carapezza, M.L., Esposito, A., Giordano, G., Lelli, M., Tarchini, L. (2008) The Albano Maar Lake high resolution bathymetry and dissolved CO_2 budget (Colli Albani volcano, Italy): constrains to hazard evaluation. *J Volcanol Geotherm Res*, 171, 258–68. Doi:10.1016/j.jvolgeores.2007.11.024.

[115] Houghton, B.F., Wilson, C.J.N., Smith, I.E.M. (1999) Shallow-seated controls on styles of explosive basaltic volcanism: a case study from New Zealand. *J Volcanol Geotherm Res*, 91, 97–120. Doi:10.1016/S0377-0273(99)00058-X.

[116] Francis, E.H. (1968) Effect of sedimentation on volcanic processes, including neck-sill relationships, in the British Carboniferous. *PROC 23RD INT GEOL CONGR PRAGUE 2*, Czech Republic, 1968, p. 163–74.

[117] Stollhofen, H. (1997) Regional European Meeting of Sedimentology. Heidelberg.

[118] Lorenz, V., Haneke, J. (2004) Relationship between diatremes, dykes, sills, laccoliths, intrusive-extrusive domes, lava flows, and tephra deposits with unconsolidated water-saturated sediments in the late Variscan intermontane Saar-Nahe Basin, SW Germany. *Geol Soc Lond Special Publ*, 234, 75–124. Doi:10.1144/gsl.sp.2004.234.01.07.

[119] Németh, K., Martin, U. (2007) Shallow sill and dyke complex in western Hungary as a possible feeding system of phreatomagmatic volcanoes in "soft-rock" environment. *J Volcanol Geotherm Res*, 159, 138–52. Doi:10.1016/j.jvolgeores.2006.06.014.

[120] Martín-Serrano, A., Vegas, J., García-Cortés, A., Galán, L., Gallardo-Millán, J.L., Martín-Alfageme, S., et al. (2009) Morphotectonic setting of maar lakes in the Campo de

Calatrava Volcanic Field (Central Spain, SW Europe). *Sediment Geol*, 222, 52–63. Doi: 10.1016/j.sedgeo.2009.07.005.

[121] Ross, P.S., Delpit, S., Haller, M.J., Németh, K., Corbella, H. (2011) Influence of the substrate on maar–diatreme volcanoes—an example of a mixed setting from the Pali Aike volcanic field, Argentina. *J Volcanol Geotherm Res*, 201, 253–71. Doi:10.1016/j.jvolgeores.2010.07.018.

[122] Delpit, S., Ross, P.S., Hearn, B.C. (2014) Deep-bedded ultramafic diatremes in the Missouri River Breaks volcanic field, Montana, USA: 1 km of syn-eruptive subsidence. *Bull Volcanol*, 76, 1–22. Doi:10.1007/s00445-014-0832-8.

[123] Valentine, G.A., van Wyk de Vries, B. (2014) Unconventional maar diatreme and associated intrusions in the soft sediment-hosted Mardoux structure (Gergovie, France). *Bull Volcanol*, 76, 1–16. Doi:10.1007/s00445-014-0807-9.

[124] Ross, P.S., White, J.D.L., Valentine, G.A., Taddeucci, J., Sonder, I., Andrews, R.G. (2013) Experimental birth of a maar–diatreme volcano. *J Volcanol Geotherm Res*, 260, 1–12. Doi: 10.1016/j.jvolgeores.2013.05.005.

[125] Macorps, É., Graettinger, A.H., Valentine, G.A., Ross, P.-S., White, J.D.L., Sonder, I. (2016) The effects of the host–substrate properties on maar–diatreme volcanoes: experimental evidence. *Bull Volcanol*, 78, 26. Doi:10.1007/s00445-016-1013-8.

[126] Aranda-Gómez, J.J., Luhr, J.F. (1996) Origin of the Joya Honda maar, San Luis Potosí, México. *J Volcanol Geotherm Res*, 74, 1–18. Doi:10.1016/S0377-0273(96)00044-3.

[127] McCord, S., Schladow, S.G. (1998) Numerical simulations of degassing scenarios for CO_2-rich Lake Nyos, Cameroon. *J Geophys Res*, 103, 12355–64.

[128] Taddeucci, J., Valentine, G.A., Sonder, I., White, J.D.L., Ross, P.S., Scarlato, P. (2013) The effect of pre-existing craters on the initial development of explosive volcanic eruptions: an experimental investigation. *Geophys Res Lett*, 40, 507–10. Doi:10.1002/grl.50176.

[129] Carn, S.A. (2000) The Lamongan volcanic field, East Java, Indonesia: physical volcanology, historic activity and hazards. *J Volcanol Geotherm Res*, 95, 81–108. Doi:10.1016/S0377-0273(99)00114-6.

[130] Gençalioğlu-Kuscu, G., Atilla, C., Cas, R.A.F., Kuscu, I. (2007) Base surge deposits, eruption history, and depositional processes of a wet phreatomagmatic volcano in Central Anatolia (Cora Maar). *J Volcanol Geotherm Res*, 159, 198–209. Doi:10.1016/j.jvolgeores.2006.06.013.

[131] Németh, K., Cronin, S.J., Smith, I.E.M., Agustín-Flores, J. (2012) Amplified hazard of small-volume monogenetic eruptions due to environmental controls, Orakei Basin, Auckland Volcanic Field, New Zealand. *Bull Volcanol*, 74, 2121–37. Doi:10.1007/s00445-012-0653-6.

[132] Smith, I.E.M., Blake, S., Wilson, C.J.N., Houghton, B.F. (2008) Deep-seated fractionation during the rise of a small-volume basalt magma batch: Crater Hill, Auckland, New Zealand. *Contr Miner Petrol*, 155, 511–27. Doi:10.1007/s00410-007-0255-z.

[133] Martin, U., Németh, K. (2005) Eruptive and depositional history of a Pliocene tuff ring that developed in a fluvio-lacustrine basin: Kissomlyó volcano (western Hungary). *J Volcanol Geotherm Res*, 147, 342–56. Doi:10.1016/j.jvolgeores.2005.04.019.

[134] Valentine, G.A., Graettinger, A.H., Sonder, I. (2014) Explosion depths for phreatomagmatic eruptions. *Geophys Res Lett*, 41, 3045–51. Doi:10.1002/2014GL060096.

[135] Valentine, G.A., Perry, F. V. (2007) Tectonically controlled, time-predictable basaltic volcanism from a lithospheric mantle source (central Basin and Range Province, USA). *Earth Planet Sci Lett*, 261, 201–16. Doi:10.1016/j.epsl.2007.06.029.

[136] Rasoazanamparany, C., Widom, E., Valentine, G.A., Smith, E.I., Cortés, J.A., Kuentz, D. et al. (2015) Origin of chemical and isotopic heterogeneity in a mafic, monogenetic volcanic field: a case study of the Lunar Crater Volcanic Field, Nevada. *Chem Geol*, 397, 76–93. Doi:10.1016/j.chemgeo.2015.01.004.

[137] Tadini, A., Bonali, F.L., Corazzato, C., Cortés, J.A., Tibaldi, A., Valentine, G.A. (2014) Spatial distribution and structural analysis of vents in the lunar crater volcanic field (Nevada, USA). *Bull Volcanol*, 76, 1–15. Doi:10.1007/s00445-014-0877-8.

[138] Camp, V.E., Roobol, M.J., Hooper, P.R. (1991) The Arabian continental alkali basalt province: part II. Evolution of Harrats Khaybar, Ithnayn, and Kura, Kingdom of Saudi Arabia. *Geol Soc Am Bull*, 363–91. Doi:10.1130/0016-7606(1991)103<0363:TA-CABP>2.3.CO;2.

[139] Hobden, B.J., Houghton, B.F., Davidson, J.P., Weaver, S.D. (1999) Small and short-lived magma batches at composite volcanoes: time windows at Tongariro volcano, New Zealand. *J Geol Soc*, 156, 865–8. Doi:10.1144/gsjgs.156.5.0865.

[140] Valentine, G.A., Shufelt, N.L., Hintz, A.R.L. (2011) Models of maar volcanoes, Lunar Crater (Nevada, USA). *Bull Volcanol*, 73, 753–65. Doi:10.1007/s00445-011-0451-6.

[141] Lorenz, V., Kurszlaukis, S. (2007) Root zone processes in the phreatomagmatic pipe emplacement model and consequences for the evolution of maar–diatreme volcanoes. *J Volcanol Geotherm Res*, 159, 4–32. Doi:10.1016/j.jvolgeores.2006.06.019.

[142] van Otterloo, J., Cas, R.A.F., Sheard, M.J. (2013) Eruption processes and deposit characteristics at the monogenetic Mt. Gambier Volcanic Complex, SE Australia: implications for alternating magmatic and phreatomagmatic activity. *Bull Volcanol*, 75, 1–21. Doi:10.1007/s00445-013-0737-y.

[143] Wohletz, K.H., Sheridan, M.F. (1983) Hydrovolcanic explosions. II. Evolution of basaltic tuff rings and tuff cones. *Am J Sci*, 385–413. Doi:10.2475/ajs.283.5.385.

[144] Ross, P.S., White, J.D.L. (2006) Debris jets in continental phreatomagmatic volcanoes: a field study of their subterranean deposits in the Coombs Hills vent complex, Antarctica. *J Volcanol Geotherm Res*, 149, 62–84. Doi:10.1016/j.jvolgeores.2005.06.007.

[145] Valentine, G.A. (2012) Shallow plumbing systems for small-volume basaltic volcanoes, 2: evidence from crustal xenoliths at scoria cones and maars. *J Volcanol Geotherm Res*, 223–224, 47–63. Doi:10.1016/j.jvolgeores.2012.01.012.

[146] Valentine, G.A., White, J.D.L., Ross, P.S., Amin, J., Taddeucci, J., Sonder, I., et al. (2012) Experimental craters formed by single and multiple buried explosions and implications for volcanic craters with emphasis on maars. *Geophys Res Lett*, 39. L20301. Doi: 10.1029/2012GL053716.

[147] Blaikie, T.N., Ailleres, L., Betts, P.G., Cas, R.A.F. (2014) Interpreting subsurface volcanic structures using geologically constrained 3-D gravity inversions: examples of maar–diatremes, Newer Volcanics Province, southeastern Australia. *J Geophys Res: Solid Earth*, 119, 3857–78. Doi:10.1002/2013JB010751.

[148] Valentine, G.A., White, J.D.L. (2012) Revised conceptual model for maar–diatremes: subsurface processes, energetics, and eruptive products. *Geology*, 40, 1111–4. Doi: 10.1130/G33411.1.

[149] McClintock, M., White, J.D.L., Houghton, B.F., Skilling, I.P. (2008) Physical volcanology of a large crater-complex formed during the initial stages of Karoo flood basalt volcanism, Sterkspruit, Eastern Cape, South Africa. *J Volcanol Geotherm Res*, 172, 93–111. Doi:10.1016/j.jvolgeores.2005.11.012.

Chapter 14

Ordovician and Carboniferous Volcanism/Plutonism in Central Inner Mongolia, China and Paleozoic Evolution of the Central Asian Orogenic Belt

Yuruo Shi

Additional information is available at the end of the chapter

http://dx.doi.org/10.5772/62303

Abstract

Adakite was originally proposed as a genetic term to define intermediate to high silica, high Sr/Y and La/Yb volcanic and plutonic rocks derived from melting of young, subducted lithosphere. However, most volcanic rocks in modern island arcs and continental arcs are probably derived from melting in the mantle wedge. Trace element chemistry with high Sr/Y ratios is a distinguishing characteristic of adakites. Ordovician and Carboniferous volcanic/plutonic rocks with high Sr/Y ratios occur in Central Inner Mongolia, which is situated on the southern margin of the Central Asian Orogenic Belt (CAOB). The samples are mostly granodiorite, tonalite and quartz-diorite in composition with intermediate to high-silica, high Na_2O (3.08–4.26 wt.%), low K_2O (0.89–2.86 wt.%) and high Na_2O/K_2O and Sr/Y ratios. Their chondrite-normalized REE patterns are characterized by LREE enrichment. In mantle-normalized multi-element variation diagrams, they show typical negative Nb anomalies, and all samples display positive $\varepsilon_{Hf}(t)$ and $\varepsilon_{Nd}(t)$ values, and low I_{Sr}. The Ordovician rocks, however, show higher Sr/Y and La/Yb ratios than the Carboniferous samples, implying that the older granitoids represent adakitic granitoids, and the Carboniferous granitoids are typical subduction-related arc granitoids but also with adakite-like compositions. The results are compatible with the view that the Central Asian Orogenic Belt (CAOB) in Inner Mongolia evolved through operation of several subduction systems with different polarities: an early-middle Paleozoic subduction and accretion system along the northern margin of the North China Craton and the southern margin of the Mongolian terrane, and late Paleozoic northward subduction along the northern orogen and exhumation of a high-pressure metamorphic terrane on the northern margin of the North China Craton.

Keywords: Adakitic, Ordovician and Carboniferous, Geochemistry, Hf-in-zircon isotopes, Central Inner Mongolia, CAOB

1. Introduction

It is generally agreed that the Solonker suture zone represents the southernmost termination of the Central Asian Orogenic belt (CAOB; [1–5]). However, there are a lot of controversies about the timing of the amalgamation of the Central Asian Orogenic belt with continental blocks to the south [1–9]. It is still debated whether the CAOB evolved through subduction and accretion of a single, long-lasting, subduction system [10] or through several subduction systems with different polarities and through collision/accretion of arcs and microcontinents [11–15].

Adakite was originally proposed as a genetic term to define intermediate to high-silica, high Sr/Y and La/Yb volcanic and plutonic rocks derived from melting of young, subducted lithosphere [16]. However, most volcanic rocks in modern island arcs and continental arcs are probably derived from melting in the mantle wedge [17]. Trace element chemistry with high Sr/Y ratios is a distinguishing characteristic of adakites [16, 18]. Ordovician and Carboniferous volcanic/plutonic rocks with high Sr/Y ratios occur in Central Inner Mongolia, which is situated on the southern margin of the Central Asian Orogenic Belt (CAOB, [19]). Early Paleozoic [6–9, 20–22] and Late Paleozoic [2–4, 23] arc volcanism/plutonism as part of trench-island arc-basin systems occurred along the southern margin of South Mongolian microcontinent and the northern margin of North China Craton, suggesting concurrent two-way subduction towards opposing continental margins. The chapter focuses on early and late Paleozoic volcanic/plutonic rocks with high Sr/Y ratios in Central Inner Mongolia, and contributes geochemical data to the evolution of the CAOB.

2. Geotectonic situation

Central Asian Orogenic Belt (CAOB, [19]) is a giant accretionary orogen [15], bounded by the Siberian, Tarim and North China Craton ([19, 24]; **Figure 1**), and reflects a complex evolution from the late Mesoproterozoic to late Palaeozoic [1, 6, 8, 14, 26, 27].

In Central Inner Mongolia and adjacent southern Mongolia, the Solonker suture zone can be traced for ca. 1000 km by dismembered ophiolite fragments (**Figure 1**) and represents a major paleo-plate boundary in Central Asia that stretches northeastwards for more than 2500 km in Mongolia and China [28]. It has been variably interpreted as the southernmost limit of the Altaids ([10]) or the southernmost termination of the CAOB [1]. The Solonker suture zone separates two continental blocks (**Figure 1**) [3]. The Northern Block consists of the Southern Mongolia (or Hutag Uul) block (gneissic granite, 1784 ± 7 Ma, Shi et al., unpublished data) and the Northern Orogen, which includes metamorphic complex (an orthogneiss has a zircon age of 437 ± 3 Ma, [29]), an ophiolitic mélange with blueschist, a near-trench granitoid (ca. 498–461 Ma) and a juvenile arc (ca. 484–469 Ma, [3]). The Southern Block comprises the southern orogen and the northern margin of the North China Craton.

http://dx.doi.org/10.5772/62303

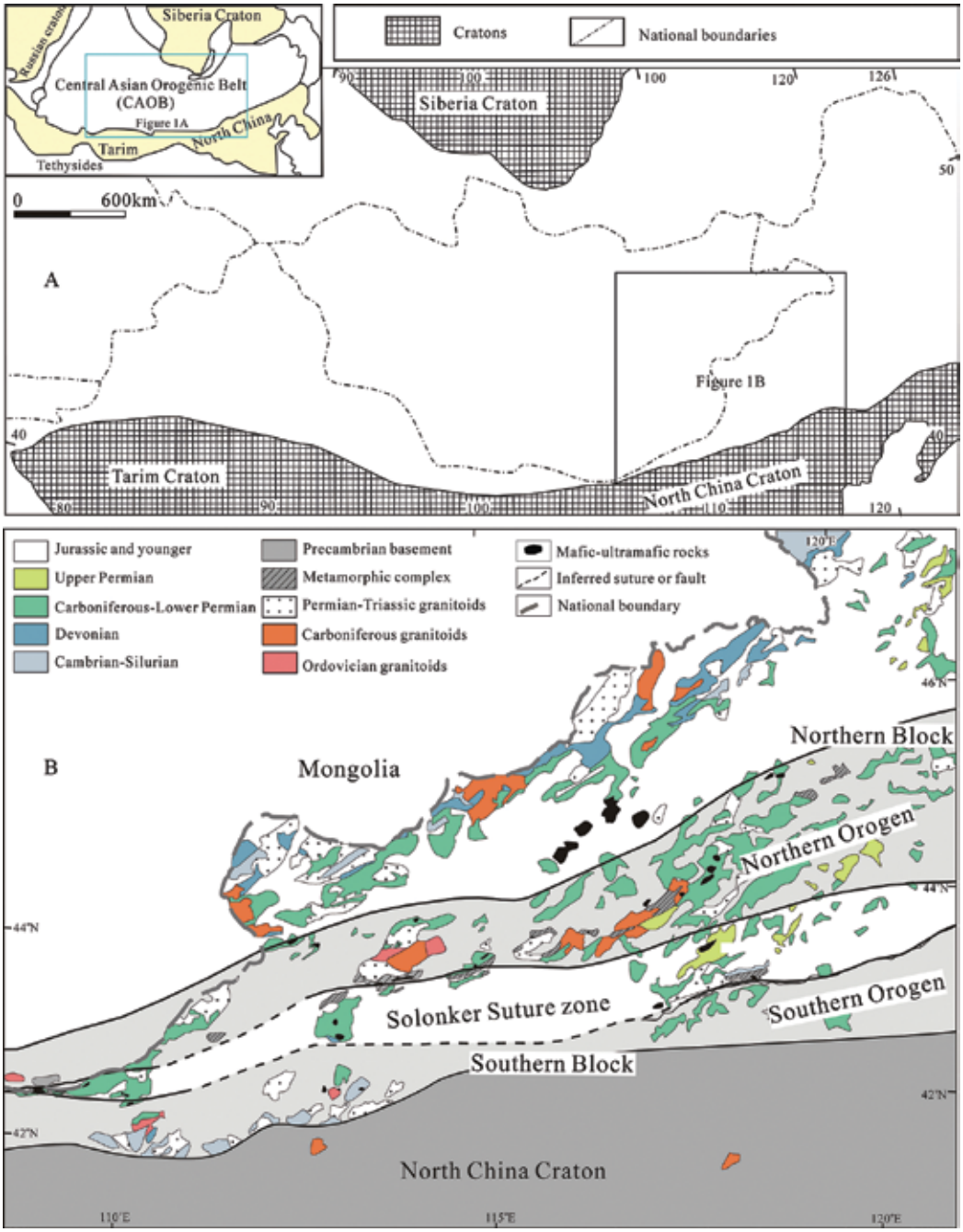

Figure 1. Geological sketch map of the southeastern CAOB (the inset map of **Figure 1A** compiled after [19]; **Figure 1B** after [3, 25]). In **Figure 1B**, the Solonker suture zone represents the tectonic boundary between the northern and the southern continental blocks [3].

Paleozoic volcanic rocks and granitoids are widely distributed along the margin of the Solonker suture zone. Ordovician granitoids (quartz-diorite, granodiorite, diorite, tonalite, and trondjemite; **Table 1** and **Figure 2**) occur in the northern and southern orogen [7, 8, 20, 21, 42, 43]; **Figure 1**), whereas Carboniferous volcanic rocks and granitoids (quartz-diorite, granodiorite, tonalite, and granite; **Table 1** and **Figure 2**) are mainly distributed in the northern orogen ([2, 23, 30, 31, 35, 37, 38, 40, 41]; **Figure 1**), and scattered along the northern margin of the North China Craton [44, 45]. The geochemical data of representative rocks are listed in **Table 2**.

Unit	Episode	Lithology	Zircon age (Ma)	Method	$\varepsilon_{Hf(t)}$ (Zircon)	$\varepsilon_{Nd(t)}$ (Whole rock)	Initial $^{87}Sr/^{86}Sr$ (whole rock)	Reference
Northern Orogen	Ordovician	Quartz diorite	490 ± 8	SHRIMP				[23]
		Tonalite	479 ± 8	SHRIMP		+1.5	0.7053	[7]
		Quartz diorite	475 ± 6	SHRIMP				[7]
		Granodiorite	472 ± 3	SHRIMP	+7.4 to +10.7	+2.2	0.7060	This study
		Tonalite	464 ± 8	SHRIMP		+1.4	0.7053	[7]
	Carboniferous	Tonalite	329 ± 3	SHRIMP		+5.1	0.7043	This study
		Quartz diorite	325 ± 3	SHRIMP				[30]
		Quartz diorite	323 ± 4	SHRIMP				[31]
		Quartz diorite	322 ± 3	SHRIMP				[30]
		Monzogranite	322 ± 1	LA-ICP-MS	+10.6 to +14.0			[32]
		Quartz diorite	320 ± 3	SHRIMP	+8.1 to +12.3	+2.1	0.7051	This study
		Granodiorite	320 ± 8	SHRIMP		+1.0	0.7055	This study
		Andesite	320 ± 7	SHRIMP				[33]
		Granite	319 ± 4	LA-ICP-MS				[34]
		Granodiorite	319 ± 3	SHRIMP				[35]
		Basalt	318 ± 3	LA-ICP-MS				[4]
		Granite	317 ± 2	LA-ICP-MS				[36]
		Garnet bearing granite	316 ± 3	SHRIMP				[29]
		Granodiorite	316 ± 1	LA-ICP-MS	+3.0 to +12.6			[32]
		Quartz diorite	315 ± 4	SHRIMP				[31]
		Basalt	315 ± 4	LA-ICP-MS				[4]
		Monzonitic granite	314 ± 2	LA-ICP-MS				[37]
		Quartz diorite	313 ± 5	SHRIMP				[31]
		Granodiorite	312 ± 1	LA-ICP-MS				[38]

http://dx.doi.org/10.5772/62303

Unit	Episode	Lithology	Zircon age (Ma)	Method	$\varepsilon_{Hf(t)}$ (Zircon)	$\varepsilon_{Nd(t)}$ (Whole rock)	Initial $^{87}Sr/^{86}Sr$ (whole rock)	Reference
		Monzonitic diorite	312 ± 4	SHRIMP				[39]
		Diorite	311 ± 2	SHRIMP				[35]
		Gabbroic diorite	310 ± 5	SHRIMP	+5.4 to +11.5	+2.5	0.7052	[2]
		Quartz diorite	310 ± 2	SHRIMP				[35]
		Volcanic rock	310 ± 1	LA-ICP-MS				[38]
		Quartz diorite	309 ± 8	SHRIMP		−0.2	0.7056	[23]
		Volcanic rock	309 ± 2	LA-ICP-MS				[40]
		Monzonitic granite	308 ± 2	LA-ICP-MS				[36]
		Monzonitic granite	307 ± 2	SHRIMP				[41]
		Volcanic rock	307 ± 6	LA-ICP-MS				[40]
		Rhyolite	303 ± 6	SHRIMP				[33]
Mongolia Hutag Uul		Gneissic granite	1784 ± 7	SHRIMP				Shi et al., unpublished
		Granodiorite	454 ± 10	SHRIMP				Shi et al., unpublished
Southern Orogen	Ordovician	Tonalite	491 ± 8	SHRIMP		+5.2	0.7047	[8]
		Diorite	472					[42]
		Dacite	459 ± 8	SHRIMP				[43]
		Dacite	458 ± 3	SHRIMP		+7.1	0.7058	[8]
		Quartz diorite	454 ± 4	SHRIMP		+2.0	0.7056	[8]
		Diorite	452 ± 3	SHRIMP				[8]
		Trondjemite	451 ± 7	SHRIMP				[43]
		Granodiorite	450					[42]
Northern margin of NCC	Carboniferous	Biotite K-feldspar granite	342 ± 5	SHRIMP				[44]
		Quartz diorite	324 ± 6	SHRIMP				[45]
		Quartz diorite	311 ± 2	SHRIMP				[45]
		Granodiorite	310 ± 5	SHRIMP				[45]
		Quartz diorite	302 ± 4	SHRIMP				[45]
Ophiolitic block								
Erlianhot-Hegenshan		Gabbro	354 ± 7	SHRIMP		+9.8	0.7043	[3]
		Gabbro	298 ± 9	SHRIMP		+8.1	0.7037	[25]
Jiaoqier-		Gabbro	483 ± 2	SHRIMP				[8]

Unit	Episode	Lithology	Zircon age (Ma)	Method	$\varepsilon_{Hf(t)}$ (Zircon)	$\varepsilon_{Nd(t)}$ (Whole rock)	Initial $^{87}Sr/^{86}Sr$ (whole rock)	Reference
Xilinhot								
Solonker-Linxi		Trondjemite	324 ± 3	SHRIMP		+8.4	0.7039	[3]
		Plagiogranite	288 ± 6	SHRIMP		+7.8	0.7039	[3]
		Gabbro	284 ± 4	SHRIMP		+6.8	0.7043	[3]
Wenduermiao-Xar Moron		Gabbro	480 ± 3	SHRIMP		+9.2	0.7059	[8]

Table 1. Summary of zircon ages, Hf isotopic data and whole-rock Sr-Nd isotopic data.

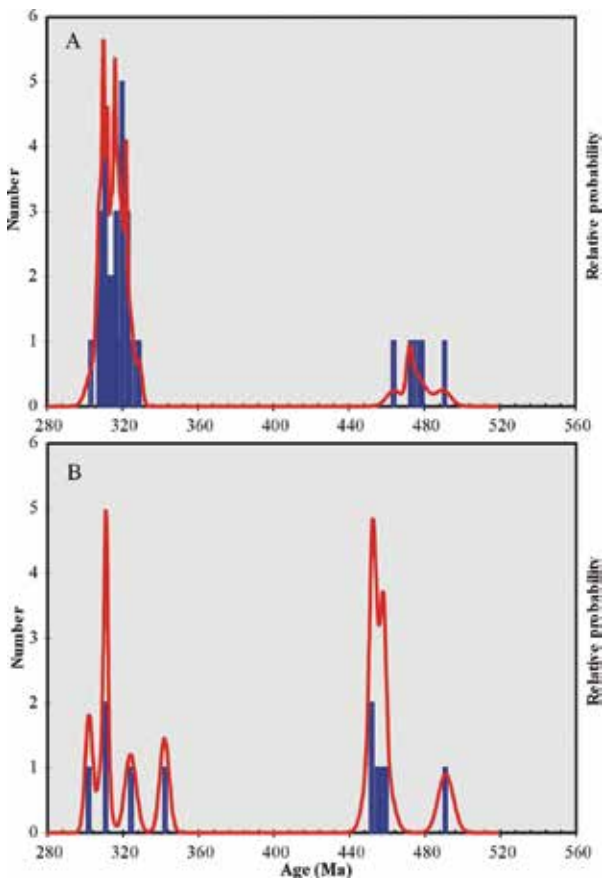

Figure 2. Cumulative plot for zircon U-Pb ages of Ordovician and Carboniferous rocks from Central Inner Mongolia (data and references are in **Table 1**). A for rocks from the Northern Block, which consists of the Southern Mongolia (or Hutag Uul) block and the northern orogen; and B for rocks from the Southern Block, which is composed of the northern margin of North China Craton and the southern orogen [3].

http://dx.doi.org/10.5772/62303

Sample	**MS02-7**	**MB1-3**	**MS3-5**	**MB1-6**	**MB1-1**	**MB1-5**	**MB1-2**	**MB1-4**
Lithology	**Tonalite**	**Granodiorite**	**Tonalite**	**Tonalite**	**Granodiorite**	**Quartz-diorite**	**Granite**	**Granite**
Age (Ma)	**479 ± 8**	**472 ± 3**	**464 ± 8**	**329 ± 3**	**ca. 320**	**320 ± 3**	**297 ± 2**	**--**
SiO_2	61.13	67.37	61.62	61.98	66.47	54.96	75.19	71.94
TiO_2	0.42	0.25	0.41	0.59	0.43	0.68	0.18	0.17
Al_2O_3	17.05	16.31	16.56	16.22	15.63	18.80	13.76	15.68
TFe_2O_3	5.88	3.68	5.62	5.82	4.17	7.98	1.92	1.30
MnO	0.14	0.08	0.14	0.08	0.06	0.12	0.02	0.02
MgO	2.34	1.14	2.27	2.95	1.69	3.65	0.70	0.47
CaO	5.69	3.91	5.78	4.93	3.43	6.25	0.39	1.54
Na_2O	3.56	4.26	3.08	3.22	3.37	3.14	3.92	5.47
K_2O	1.34	1.37	1.74	1.49	2.86	0.89	2.62	2.89
P_2O_5	0.19	0.12	0.18	0.16	0.14	0.22	0.09	0.11
LOI	1.84	1.40	2.78	2.48	1.81	2.95	1.32	0.73
TOTAL	99.58	99.89	100.18	99.92	100.06	99.64	100.11	100.32
Na_2O/K_2O	2.66	3.11	1.77	2.16	1.18	3.53	1.50	1.89
Sc	12.8	5.60	13.4	17.1	9.5	20.0	2.69	0.60
V	115	64	107	123	83	151	33.9	25.1
Cr	20.44	5.0	79.5	45	21	26	8.8	8.1
Co	12.1	6.0	10.6	17.3	10.7	21.8	3.23	2.80
Ni	10.3	3.6	18	29.1	11.4	19.8	7.0	3.9
Cu	5.4	9.1	6.2	38.7	10.3	51.4	23.0	15.8
Zn	51.5	39.2	49.5	55.9	42.7	87.8	18.3	30.9
Ga	16.5	17.4	16.3	16.9	16.1	19.4	12.7	18.1
Ge	1.38	1.48	1.42	1.45	1.17	1.28	1.21	0.78
Rb	32.26	51.1	42.09	69.08	96.9	24.05	99.6	66.5
Sr	649	711	604	304	373	473	198	581
Zr	84.8	78.3	81.9	149.4	171	52.6	75.1	104.4

Sample	MS02-7	MB1-3	MS3-5	MB1-6	MB1-1	MB1-5	MB1-2	MB1-4
Lithology	**Tonalite**	**Granodiorite**	**Tonalite**	**Tonalite**	**Granodiorite**	**Quartz-diorite**	**Granite**	**Granite**
Age (Ma)	**479 ± 8**	**472 ± 3**	**464 ± 8**	**329 ± 3**	**ca. 320**	**320 ± 3**	**297 ± 2**	**--**
Nb	3.64	4.73	3.2	5.23	6.20	4.96	6.12	1.96
Cs	0.55	0.794	0.8	1.25	1.12	1.54	1.82	1.27
Ba	685.0	471.8	862.4	241.8	687.1	173.8	487.8	511.8
Hf	2.43	2.09	2.43	3.59	4.50	1.33	2.18	2.88
Ta	0.24	0.26	0.23	0.45	0.55	0.25	0.61	0.19
Th	3.78	10.46	2.76	5.83	11.26	0.49	11.83	2.31
U	1	1.48	1.05	1.277	2.16	0.264	0.58	1.11
La	10.92	25.5	7.35	14.67	19.3	9.45	8.91	5.41
Ce	22.7	49.3	17.01	29.3	37.9	20.9	28.4	14.3
Pr	2.85	4.58	2.11	3.78	4.23	2.63	1.97	1.25
Nd	11.85	15.8	9.03	16.2	16.2	11.6	7.12	5.11
Sm	2.67	2.19	2.32	3.63	3.09	2.61	1.33	1.00
Eu	0.84	0.61	0.77	1.00	0.81	0.88	0.32	0.38
Gd	2.57	2.09	2.26	3.84	2.81	2.72	1.45	0.93
Tb	0.42	0.23	0.38	0.64	0.40	0.42	0.22	0.11
Dy	2.39	1.32	2.26	3.77	2.31	2.54	1.46	0.72
Ho	0.52	0.26	0.51	0.87	0.48	0.53	0.33	0.12
Er	1.52	0.78	1.39	2.32	1.29	1.41	0.95	0.35
Tm	0.25	0.12	0.23	0.39	0.20	0.22	0.16	0.038
Yb	1.64	0.95	1.61	2.61	1.42	1.50	1.18	0.37
Lu	0.27	0.15	0.28	0.44	0.24	0.24	0.18	0.028
Y	16.2	9.1	14.5	27.0	14.1	16.9	11.1	4.68
La/Yb	6.7	26.8	4.6	5.6	13.6	6.3	7.6	14.6
Sr/Y	40	78	42	11	27	28	18	124

Table 2. Major oxide (wt.%) and trace element (ppm) composition of representative samples.

http://dx.doi.org/10.5772/62303

Figure 3 shows the photographs of field occurrences and photomicrographs of some representative samples. **Figure 3A** was taken from Central Inner Mongolia to show the beautiful landscape; **Figure 3B** shows the Carboniferous volcanic rocks which are located in the Southern Block.

Granodiorite sample MB1-3 (**Figure 3C** and **3D**), collected from Baiyinbaolidao, southern Sonidzuoqi, which is located in the Northern Block, is medium-grained, foliated and consists of plagioclase (45–50 vol.%), quartz (20–25%), K-feldspar (10–15), biotite (5–10%), hornblende (1–5%), accessory zircon, apatite and sphene. Plagioclase is partially epidotized, sericitized and biotite grains are chloritized.

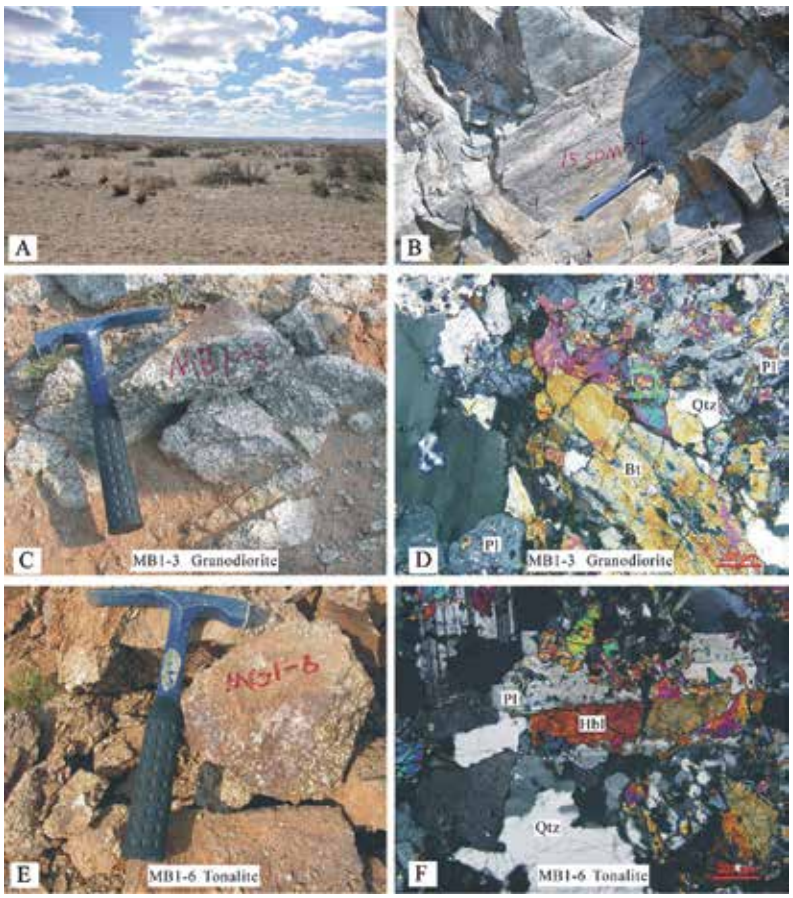

Figure 3. Photographs to show field occurrences and photomicrographs of some representative samples.

Tonalite sample MB1-6 (**Figure 3E** and **3F**), which is also collected from Baiyinbaolidao, Southern Sonidzuoqi, is medium-grained and consists of plagioclase (60–65%), quartz (20–25%), hornblende (10–15%) and biotite (1–5%) with trace amounts of zircon, apatite and sphene. Plagioclase is partially epidotized, and biotite grains are chloritized.

3. Petrogenesis of the Ordovician and Carboniferous volcanic rocks and granitoids

The Ordovician granitoid samples have intermediate to high-silica (61.13–67.37 wt.%), high Al_2O_3 (mostly >15 %), higher Na_2O than K_2O ($Na_2O > K_2O$, Na_2O/K_2O = 1.77–3.11), low MgO (<3%), low HREE (**Figure 4**), depleted HFSE (**Figure 5**), Y and Yb (Y < 18 ppm, Yb < 1.9 ppm), high Sr (604–711 ppm), Sr/Y mostly >40 (40.1–78.1) (**Table 2**; **Figure 6**) and low I_{Sr} with positive $\varepsilon_{Nd}(t)$ isotope ratios (**Table 1**; **Figure 7**). The Ordovician granitoid samples therefore represent adakitic compositions ([16, 48]; **Table 3**).

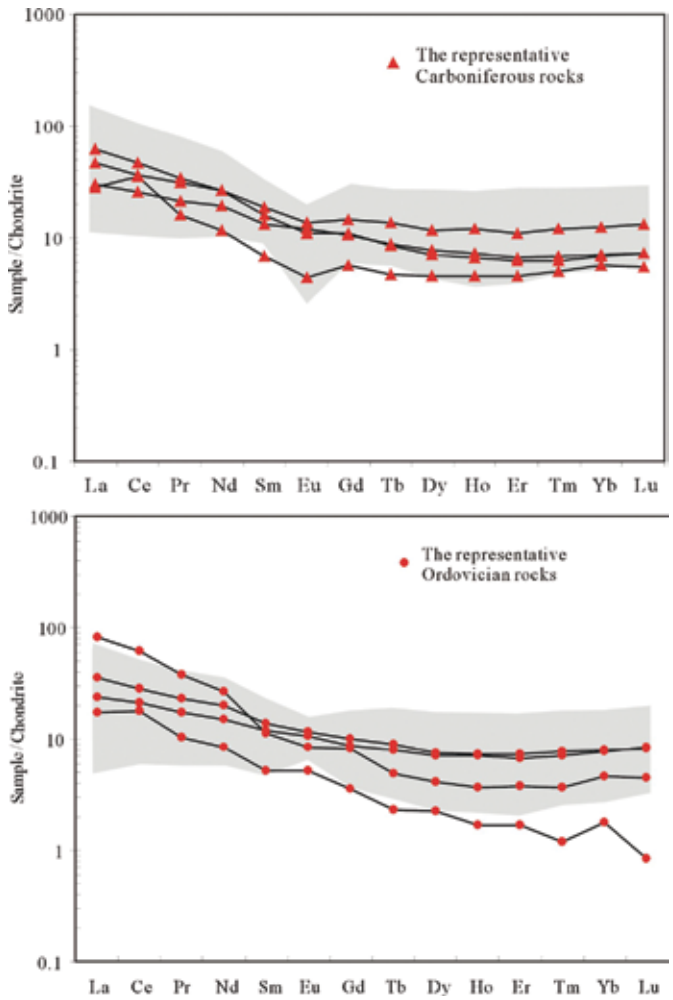

Figure 4. Chondrite (CHON)-normalized REE patterns for representative samples (grey fields show data from [7, 8, 43] for Ordovician granitoids; and from [23, 30, 32, 34, 36, 37] for Carboniferous granitoids). Chondrite values are from [46].

http://dx.doi.org/10.5772/62303

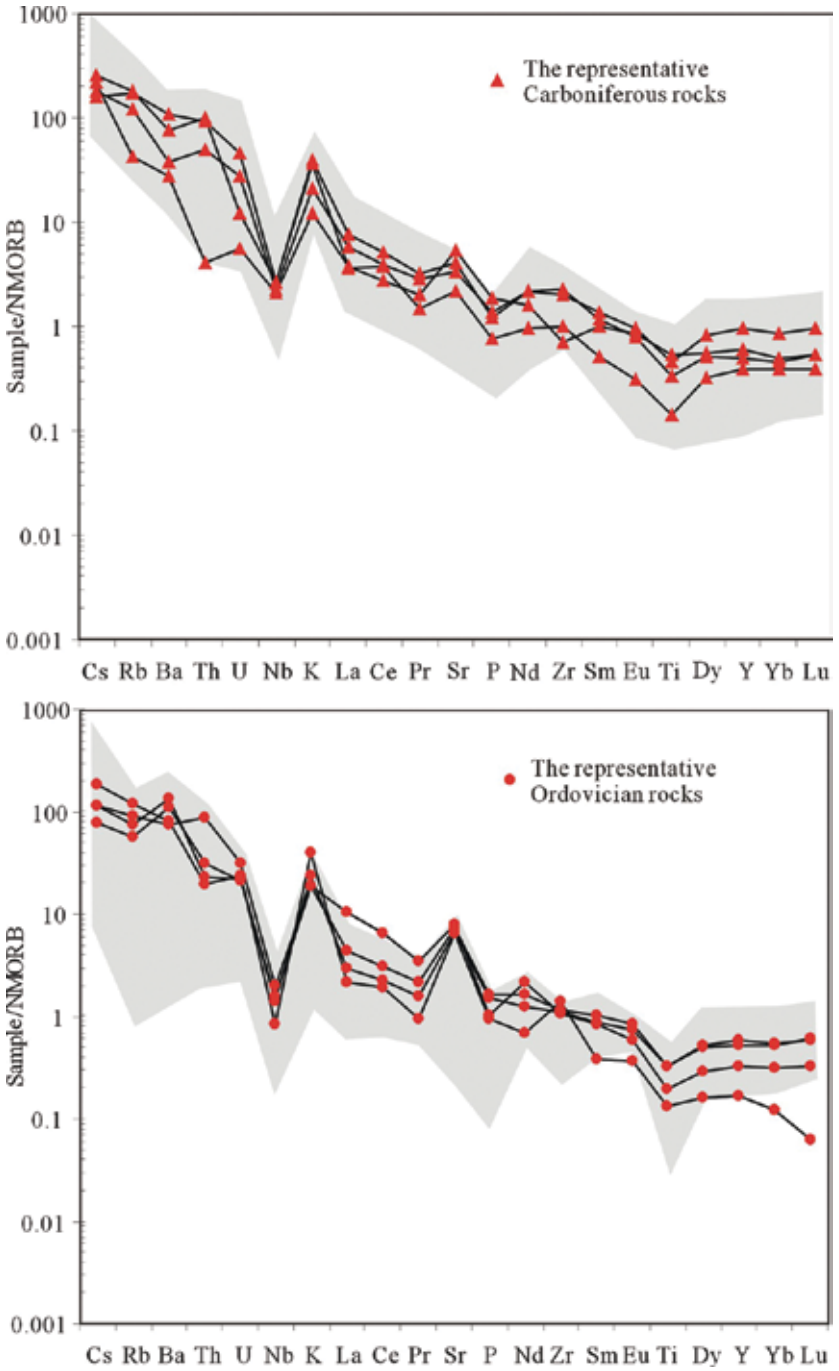

Figure 5. N-MORB-normalized trace element variation diagrams for representative samples (grey fields show data from [7, 8, 43] for Ordovician granitoids; and from [23, 30, 32, 34, 36, 37] for Carboniferous granitoids). N-MORB values are from [47].

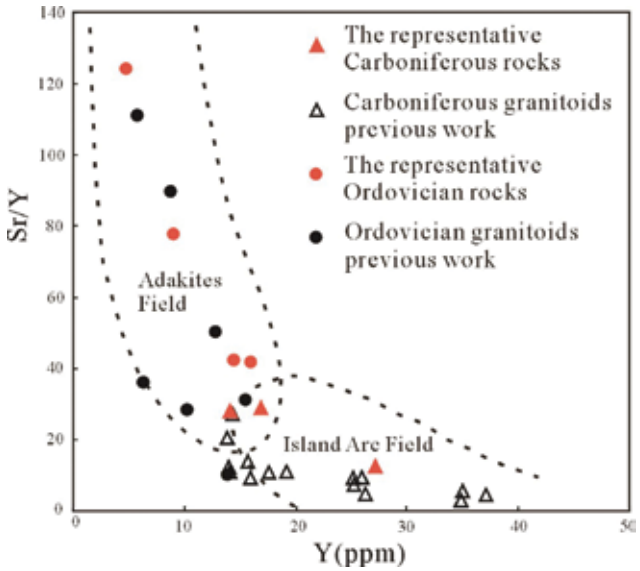

Figure 6. Y vs. Sr/Y plot showing adakitic rocks (after [18]) (data from [7, 8, 43] for Ordovician rocks; and from [23, 30, 32, 34, 36, 37] for Carboniferous rocks).

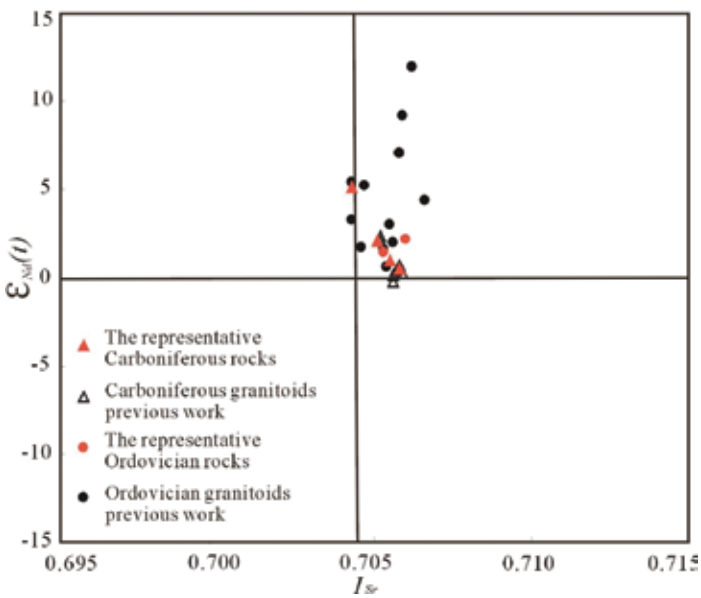

Figure 7. I_{Sr} vs. $\varepsilon_{Nd(t)}$ for some typical Ordovician and Carboniferous rocks with high Sr/Y ratio from Central Inner Mongolia (data from [8, 23]).

http://dx.doi.org/10.5772/62303

	Adakites			**MS02-7 Tonalite**	**MB1-3 Granodiorite**	**MS3-5 Tonalite**	**Oceanic arc granites**			**Active continental margin arc granites**	**MB1-6 Tonalite**	**MB1-1 Granodiorite**	**MB1-5 Quartz-diorite**
	Adakites[a]	**Cook island[b]**	**Cerro Pampa[c]**				**Oman[d]**	**Little Port[d]**	**Jamaica[d]**	**Chile[d]**			
SiO_2 (%)	≥56.0	61.4	62.6	61.13	67.37	61.62	70.1	69.5	68.4	74.5	61.98	66.47	54.96
Al_2O_3 (%)	≥15.0	18.4	17.3	17.05	15.68	16.56	12.0	14.60	14.44	12.52	16.22	15.63	18.80
Na_2O/K_2O	>1.00	7.75	3.82	2.66	3.11	1.77	15.75	4.37	1.18	0.65	2.16	1.18	3.53
MgO (%)	<3			2.34	1.14	2.27					2.95	1.69	3.65
Y (μg/g)	≤18.00	6		16.2	9.1	14.5	44	19	10	30	27.0	14.1	16.9
Yb (μg/g)	≤1.90	0.85	0.72	1.64	0.15	1.61	4.54		1.37	3.12	2.61	1.42	1.50
Sr (μg/g)	>400	1910	1886	649	711	604	200	274	210	93	304	373	473
Sr/Y	>20	319		40	78	42	4.6	14.4	21.0	3.1	11	26	28
Sr anomaly	Positive	Positive		Positive	Positive	Positive					Positive	Positive	Positive
Eu anomaly	Positive or weakly negative			Weakly negative	Negative	Positive					Negative	Negative	Weakly positive
Age (Ma)	<25 Ma	<24 Ma	ca. 12 Ma	479 ± 8	472 ± 3	464 ± 8					329 ± 3	ca. 320	320 ± 3

[a] [16, 49].
[b] Cook island adakites [50].
[c] Cerro Pampa adakites [51].
[d] [52].

Table 3. The comparison of geochemical characteristics between the rocks from Central Inner Mongolia, the typical adakitic and arc rocks.

The genesis of adakites is extensively debated, and there are four proposed origins, namely partial melting of young subducted lithosphere [16], melting of newly underplated lower continental crust [53], differentiation of a parental basaltic magma [54, 55] and melting of foundered mafic lower continental crust [56]. High-Al, high Na_2O and calc-alkaline adakites are generally interpreted to have formed due to the melting of subducted oceanic crust and are different from high-K, high total alkali ($Na_2O + K_2O$) and low Al_2O_3 adakites that form through melting of thickened basaltic lower continental crust [16, 51, 53, 57–60].

The Inner Mongolian Ordovician granitoids of this study have depleted HREE, Nb, positive Sr anomalies, low Y and Yb contents and positive to weakly negative Eu anomalies. These characteristics are consistent with the loss of plagioclase and the presence of garnet as residual phases, probably related to partial melting of the source material under eclogite-facies conditions [61, 62]. The petrology and geochemistry of the Ordovician adakitic granitoids indicate a contribution from melting of subducted oceanic crust in their formation rather than melting of thickened basaltic lower continental crust.

The Carboniferous samples in this area have intermediate to high-silica (54.96–66.47 wt.%), high Al_2O_3 (15.63–18.80 %), higher Na_2O than K_2O ($Na_2O > K_2O$, Na_2O/K_2O = 1.18–3.53), low HREE (**Table 2**; **Figure 4**), and with low I_{Sr} (0.7043–0.7060), positive $\varepsilon_{Nd}(t)$ (+1.0 to +5.1) and $\varepsilon_{Hf}(t)$ (+8.1 to +12.3) isotope ratios (**Table 1**; **Figures 7** and **8**). However, most of them have lower Sr and Sr/Y ratio than those of Ordovician adakitic granitoids in this area (**Table 2**; **Figure 6**), which are typical subduction-related arc granitoids [52, 63, 64] although still with adakite-like compositions [16, 48].

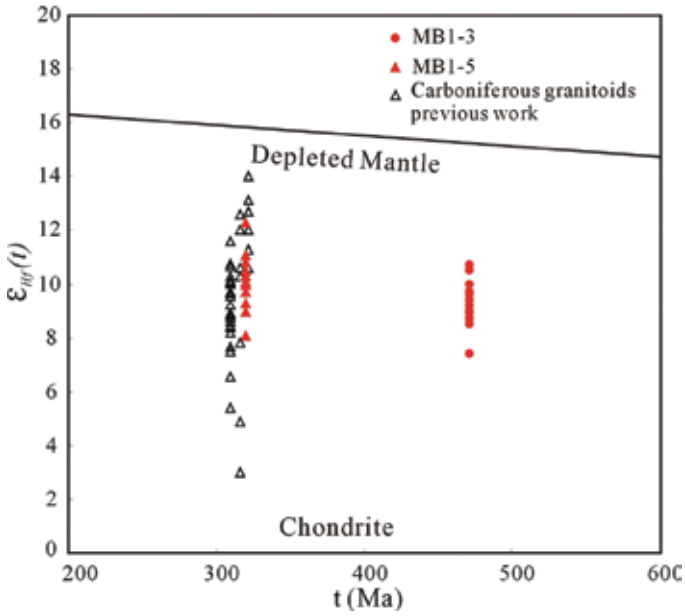

Figure 8. U-Pb age vs. $\varepsilon_{Hf(t)}$ for zircons from (data from [2], and [32] for Carboniferous granitoids).

http://dx.doi.org/10.5772/62303

4. Geodynamic significance of the Ordovician and Carboniferous volcanic rocks and granitoids

A subduction-accretion complex usually forms along a convergent plate boundary where an oceanic plate subducts beneath another oceanic or continental plate [65]. Early Paleozoic arc plutonism as part of trench-island arc-basin systems ([6, 8, 21, 22]; **Table 2**) occurred in the southern orogen, along the northern margin of the North China Craton, and late Silurian molasse deposits unconformably overlie these rocks [6, 66]. Coeval adakitic plutonism is emplaced in the northern orogen, along the southern margin of the Mongolian terrane [20]. Silurian high-pressure metamorphic rocks [67] and Silurian syncollisional magmatism in the northern orogen along the Solonker suture [68] were also reported. All these features indicate an early-middle Paleozoic subduction and accretion system along the northern margin of the North China Craton and the southern margin of the Mongolian terrane. After demise of the ocean in the southern orogen, caused by subduction of a ridge crest and by ridge collision with supra-subduction zone ophiolite in the Silurian [8], the southern orogen became tectonically consolidated and turned into a post-orogenic setting [69].

There has been some debate about whether the Carboniferous calc-alkaline granitoids formed in a subduction zone [23, 30] or in a late- to post-orogenic setting [31]. Carboniferous calc-alkaline plutonic rocks (ca. 328–308 Ma) in the northern orogen were suggested by [2, 23, 30] as subduction genesis, which can be related to the northward subduction of Asian ocean slab. Bao et al. [31], however, thought these Carboniferous granitoids formed in a Late Paleozoic rift area because of Permian bimodal volcanic rocks. These Carboniferous granitoids include variably foliated gabbro, diorite, quartz diorite, granodiorite, tonalite and granite [23, 30], which belong to low-K tholeiitic and calk-alkaline series, and are enriched in large ion lithophile elements (LILE) and depleted in high field strength elements (HFSE) [2, 23, 30], low I_{Sr}, positive $\varepsilon_{Nd}(t)$ and $\varepsilon_{Hf}(t)$ isotope ratios ([23]) showing subduction-related arc granitoids characteristics [52, 63, 64].

Additionally, a subduction-accretion complex was identified from previously defined late Carboniferous and early Permian strata in the Daqing pasture, southern Xiwuqi, Inner Mongolia [4]. In addition to this subduction-accretion complex, most magmatic rocks are considered to have formed in a subduction setting [23, 30], and the spatial configuration of both geological units indicates that the subduction polarity was from south to north [4] along the northern orogen.

Carboniferous granitoids on the northern margin of North China craton also have the composition of tholeiitic and calk-alkaline island-arc rocks and adakitic compositions [45], however, low negative whole-rock $\varepsilon_{Nd}(t)$ and zircon $\varepsilon_{Hf}(t)$ isotope ratios indicate that they were derived mainly from anatectic melting of the ancient lower crust with some involvement of mantle materials [70]. The Carboniferous plutons were interpreted as subduction-related and emplaced in an Andean-style continental-margin arc [70].

On the northern margin of the North China craton, however, Carboniferous eclogites are exposed at least 200 km south of the Solonker suture zone and have tholeiitic protoliths (MORB

and IAT), and eclogite-facies metamorphism reflects deep subduction of oceanic lithosphere [71]. The granitoids (330–298 Ma) of this area were emplaced and deformed during, and/or shortly after eclogite-facies metamorphism (ca. 331–319 Ma) [71]. This close temporal relationship indicates that magmatism closely followed the exhumation of the high-pressure metamorphic terrane [3].

5. A possible model for the discrete evolution of CAOB

The southeastern CAOB was formed by the concurrent two-way subduction of Paleo-Central Asian Ocean towards opposing continental margins in the early Paleozoic (**Figure 9A**). In the south is an arc-trench complex, which can be regarded as an analogue of the Izu-Bonin-Mariana arc [72], and in the north a product of ridge-trench interaction [8]. In the late Paleozoic, however, Andean-type orogenesis was induced by subduction of Central Asian Ocean beneath either the northern (e.g. [4]) or southern (e.g. [45]) continental blocks (**Figure 9B**). Plutonic magmatism [45] was accompanied by exhumation of a high-pressure metamorphic terrane [71] in the south; and a subduction-accretion complex [4], together with most arc-related magmatic rocks [23, 30] was formed along the northern orogen.

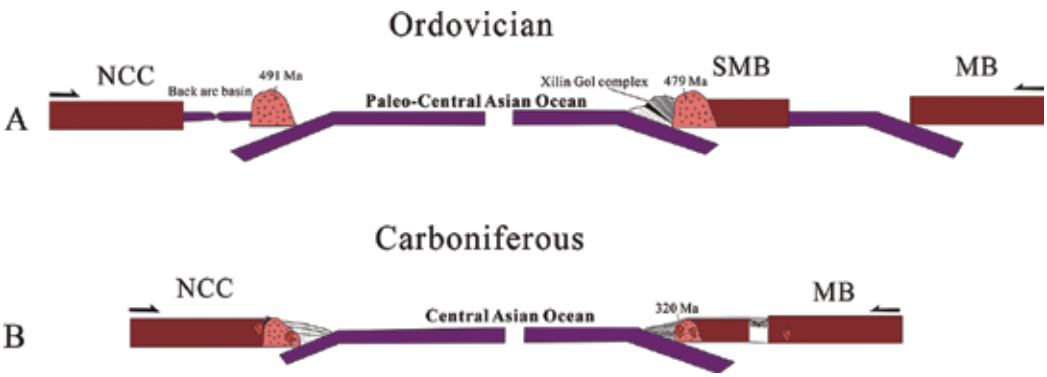

Figure 9. A possible model for Ordovician and Carboniferous evolution of Central Inner Mongolia. Abbreviation: NCC, North China Craton; SMB, South Mongolia Block; MB, Mongolia Block.

6. Modern equivalent

6.1. Cook Island and Cerro Pampa adakites

Cenozoic andesitic to dacitic rocks collected from Cerro Pampa [51] and andesites from Cook Island [50] have intermediate to high-silica, high Al_2O_3, higher Na_2O than K_2O, low HREE,

http://dx.doi.org/10.5772/62303

depleted HFSE, Y and Yb, high Sr, and high Sr/Y ratios (**Table 3**), and low I_{Sr} with positive ε_{Nd} isotope ratios. The samples, therefore, represent adakites [50, 51]. Cerro Pampa adakitic magmas formed in response to melting of hot slab that was subducting beneath South America [51], and similar petrogenesis for the Austral Volcanic Zone adakites [50]. Ordovician adakitic rocks from Central Inner Mongolia show similar petrogenesis and geotectonic setting with the Cenozoic adakites from Cook Island [50], Cerro Pampa [51] and Aleutian arc [16].

6.2. Oman and Chile volcanic arc granites

Volcanic arc granites from Oman and Chile have high-silica, intermediate Al_2O_3, low HREE [52] (**Table 3**), and with low Sr and Sr/Y ratios than the adakites (**Table 3**), which are typical subduction-related arc granitoids derived from melting in the mantle wedge. Most Carboniferous volcanic rocks and granitoids present similar petrogenesis and geotectonic setting with the Cenozoic subduction-related arc granitoids.

7. Conclusions

1. The Ordovician and Carboniferous volcanic rocks and granitoids are mostly intermediate to high-silica, high Na_2O/K_2O ratio, high Sr/Y ratios. They are characterized by LREE enrichment and exhibit typical negative Nb anomalies. All samples show positive $\varepsilon_{Hf}(t)$, $\varepsilon_{Nd}(t)$ values and low I_{Sr}.
2. The Ordovician rocks show higher Sr/Y ratio than the Carboniferous rocks, suggesting that the former represent adakitic rocks and the latter are typical subduction-related arc rocks with adakite-like compositions.
3. The Central Asian Orogenic Belt evolved through several subduction systems with different polarities in Central Inner Mongolia, namely an early-middle Paleozoic subduction and accretion system along the northern margin of the North China Craton and the southern margin of the Mongolian terrane, and late Paleozoic northward subduction along the northern orogen and exhumation of a high-pressure metamorphic terrane on the northern margin of the North China Craton.

Acknowledgements

The editorial patience and the comments of Dr. Karoly Nemeth are appreciated. This study was financially supported by the National Natural Science Foundation of China (Grant nos. 40703012) and Geological Survey of China (Grant nos. 1212011121075, 12120114020901, 12120114064301, and 1212011120332).

Author details

Yuruo Shi

Address all correspondence to: shiyuruo@bjshrimp.cn

Beijing SHRIMP Center, Institute of Geology, Chinese Academy of Geological Sciences, Beijing, China

References

[1] Xiao W.J., Windley B.F., Hao J., Zhai M.G., 2003. Accretion leading to collision and the Permian Solonker suture, Inner Mongolia, China: termination of the Central Asian orogenic belt. Tectonics 22, 8–20.

[2] Chen B., Jahn B.M., Tian W., 2009. Evolution of the Solonker suture zone: constraints from zircon U-Pb ages, Hf isotopic ratios and whole-rock Nd–Sr isotope compositions of subduction- and collision-related magmas and forearc sediments. Journal of Asian Earth Sciences 34, 245–257.

[3] Jian P., Liu D.Y., Kröner A., Windley B.F., Shi Y.R., Zhang W., ZhangF.Q., MiaoL.C., ZhangL.Q., Tomurhuu D., 2010. Evolution of a Permian intraoceanic arc–trench system in the Solonker suture zone, Central Asian Orogenic Belt, China and Mongolia. Lithos 118(1), 169–190.

[4] Liu J.F., Li J.Y., Chi X.G., Qu J.F., Hu Z.C., Fang S., Zhang Z., 2013. A late-Carboniferous to early early-Permian subduction–accretion complex in Daqing pasture, southeastern Inner Mongolia: evidence of northward subduction beneath the Siberian paleoplate southern margin. Lithos 177, 285–296.

[5] Shi Y.R., Liu C., Deng J.F., Jian P., 2014. Geochronological frame of granitoids from Central Inner Mongolia and its tectonomagmatic evolution. Acta Petrologica Sinica 30 (11), 3155–3171 (in Chinese with English abstract).

[6] Tang K.D., 1990. Tectonic development of Paleozoic foldbelts at the north margin of the Sino-Korean craton. Tectonics 9, 249–260.

[7] Shi Y.R., Liu D.Y., Zhang Q., Jian P., Zhang F.Q., Miao L.C., ShiG.H., ZhangL.Q., Tao H., 2004. SHRIMP dating of diorites and granites in southern Suzuoqi, Inner Mongolia. Acta Geologica Sinica 78(6), 789–799. (in Chinese with English abstract).

[8] Jian P., Liu D.Y., Kröner A., Windley B.F., Shi Y.R., Zhang F.Q., Shi G.H., Miao L.C., Zhang W., Zhang Q., 2008. Time scale of an early to mid-Paleozoic orogenic cycle of the long-lived Central Asian Orogenic Belt, Inner Mongolia of China: Implications for continental growth. Lithos 101, 233–259.

http://dx.doi.org/10.5772/62303

[9] Xu B., Zhao P., Wang Y.Y., Liao W., Luo Z.W., Bao Q.Z., Zhou Y.H., 2015. The pre-Devonian tectonic framework of Xing'an-Mongolia orogenic belt (XMOB) in north China. Journal of Asian Earth Sciences 97, 183–196.

[10] Sengör A.M.C., Natal'in B.A., Burtman V.S., 1993. Evolution of the Altaid tectonic collage and Paleozoic crustal growth in Eurasia. Nature 364, 299–307.

[11] Coleman R.G., 1989. Continental growth of Northwest China. Tectonics 8, 621–635.

[12] Mossakovskii A.A., Ruzhentsev S.V., Samygin S.G., Kheraskova T.N., 1993. Central Asian Foldbelt: geodynamic evolution and formation history. Geotektonika 6, 3–32 (in Russian).

[13] Kröner A., Windley B.F., Badarch G., Tomurtogoo O., Hegner E., Jahn B.M., Gruschka S., Khain E.V., Demoux A., Wingate M.T.D., 2007, Accretionary growth and crust formation in the Central Asian Orogenic Belt and comparison with the Arabian-Nubian-Shield. Geological Society of America, Memorials 200, 181–209.

[14] Kröner A., Kovach V., Belousova E., Hegner E., Armstrong R., Dolgopolova A. Seltmann R., Alexeiev D.V., Hoffmann J.E., Wong J., Sun M., Cai K., Wang T., Tong Y., Wilde S.A., Degtyarev K.E., Rytsk E., 2014. Reassessment of continental growth during the accretionary history of the Central Asian Orogenic Belt. Gondwana Research 25, 103–125.

[15] Windley B.F., Alexeiev D., Xiao W.J., Kröner A., Badarch G., 2007. Tectonic models for accretion of the Central Asian Orogenic Belt. Journal of the Geological Society 164 (1), 31–47.

[16] Defant M.J., Drummond M.S. 1990. Derivation of some modern arc magmas by melting of young subducted lithosphere. Nature 347, 662–665.

[17] Gill J.B., 1981. Orogenic Andesites and Plate Tectonics. Springer, Berlin.

[18] Defant M.J., Drummond M.S., 1993. Mount St. Helens: potential example of the partial melting of the subducted lithosphere in a volcanic arc. Geology 21(6), 547–550.

[19] Jahn B.M., Wu F.Y., Chen B., 2000. Granitoids of the Central Asian Orogenic Belt and continental growth in the Phanerozoic. Transactions Royal Society of Edinburgh: Earth Sciences 91, 181–193.

[20] Shi Y.R., Liu D.Y., Zhang Q., Jian P., Zhang F.Q., Miao L.C., Shi G.H., Zhang L.Q., Tao H., 2005a. The petrogenesis and SHRIMP dating of the Baiyinbaolidao adakitic rocks in south Suzuqi, Inner Mongolia. Acta Petrologica Sinica 21, 143–150 (in Chinese with English abstract).

[21] Zhang W., Jian P., 2008. SHRIMP dating of Early Paleozoic granites from North Damaoqi, Inner Mongolia. Acta Geologica Sinica 82, 778–787 (in Chinese with English abstract).

[22] Zhang W., Jian P., Kröner A., Shi Y.R., 2013. Magmatic and metamorphic development of an early to mid-Paleozoic continental margin arc in the southernmost Central Asian Orogenic Belt, Inner Mongolia, China. Journal of Asian Earth Sciences 72, 63–74.

[23] Chen B., Jahn B.M., Wilde S., Xu B., 2000. Two contrasting Paleozoic magmatic belts in northern Inner Mongolia, China: petrogenesis and tectonic implications. Tectonophysics 328, 157–182

[24] Badarch G., Cunningham W.D., Windley B.F., 2002. A new terrane subdivision for Mongolia: implications for the Phanerozoic crustal growth of Central Asia. Journal of Asian Earth Sciences 21 (1), 87–110.

[25] Miao L.C., Fan W.M., Liu D.Y., Zhang F.Q., Sh,i Y.R., Guo, F., 2008. Geochronology and geochemistry of the Hegenshan ophiolitic complex: Implications for late-stage tectonic evolution of the Inner Mongolia-Daxinganling Orogenic Belt, China. Journal of Asian Earth Sciences 32: 348–370.

[26] Dobretsov N.L., Berzin N.A., Buslov M.M., 1995. Opening and tectonic evolution of the Paleo-Asian Ocean. International Geology Review 37 (4), 335–360.

[27] Jian P., Shi Y.R., Zhang F.Q., Miao L.C., Zhang L.Q., Kröner A., 2007. Geological excursion to Inner Mongolia, China, to study the accretionary evolution of the southern margin of the Central Asian Orogenic Belt. Structural and tectonic correlation across the Central Asia Orogenic Collage: Implications for continental growth and intracontinental deformation (Abstracts and Excursion guidebook). The Third International workshop and field excursions for IGC Project 480: 49–72.

[28] Li J.Y., 2006. Permian geodynamic setting of Northeast China and adjacent regions: closure of the Paleo- Asian Ocean and subduction of the Paleo-Pacific Plate. Journal of Asian Earth Sciences 26, 207–224.

[29] Shi G.H., Liu D.Y., Zhang F.Q., Jian P., Miao L.C., Shi Y.R., Tao H., 2003. Zircon SHRIMP U-Pb geochronology and significance of the Xilinhot metamorphic complex, Inner Mongolia, China. Chinese Science Bulletin 48(20), 2187–2192 (in Chinese).

[30] Liu J.F., Chi X.G., Zhang X.Z., Ma Z.H., Zhao Z., Wang T.F., Hu Z.C., Zhao X.Y., 2009. Geochemical characteristic of Carboniferous quartz-diorite in the southern Xiwuqi area, Inner Mongolia and its tectonic significance. Acta Geologica Sinica 83 (3), 365–376 (in Chinese with English abstract).

[31] Bao Q.Z., Zhang C.J., Wu Z.L., Wang H., Li W., Sang J.H., Liu Y.S., 2007. SHRIMP U-Pb zircon geochronology of a Carboniferous quartz-diorite in Baiyingaole area, Inner Mongolia and its implications. Journal of Jilin University (Earth Science Edition) 37 (1), 15–23 (in Chinese with English abstract).

[32] Hu C.S., Li W.B., Xu C., Zhong R.C., Zhu F., 2015. Geochemistry and zircon U-Pb-Hf isotopes of the granitoids of Baolidao and Halatu plutons in Sonidzuoqi area, Inner

http://dx.doi.org/10.5772/62303

Mongolia: Implications for petrogenesis and geodynamic setting. Journal of Asian Earth Sciences 97, 294–306.

[33] Xin H.T., Teng X.J., Cheng Y.H., 2011. Stratigraphic Subdivision and Isotope Geochronology Study on the Baoligaomiao Formation in the East Ujimqin County, Inner Mongolia. Geological Survey and Research 34, 1–8 (in Chinese with English abstract).

[34] Liang Y.W., Yu C.L., Shen G.Z., Sun Q.R., Li J.W., Yang Y.C., She H.Q., Zhang B., Tan G., 2013. Geochemical characteristics of granites in the Suonaga Pb-Zn-Ag deposit of Dong Ujimqin Banner, Inner Mongolia, and their tectonic and ore-forming implications. Geology in China 40, 767–779 (in Chinese with English abstract).

[35] Xue H.M., Guo L.J., Hou Z.Q., Tong Y., Pan X.F., Zhou X.W., 2010. SHRIMP zircon U-Pb ages of the middle Neopaleozoic unmetamorphosed magmatic rocks in the southwestern slope of the DaHinggan Mountains, Inner Mongolia. Acta Petrologica et Mineralogica 29, 811–823 (in Chinese with English abstract).

[36] Xu L.Q., Ju W.X., Liu C., He H.Y., Li M.Y., 2012. Sr-Yb classification and genesis of late Carboniferous granites in Arenshaobu area of Erenhot, Inner Mongolia. Geological Bulletin of China 31, 1410–1419 (in Chinese with English abstract).

[37] He F.B., Xu J.X., Gu X.D., Cheng X.B., Wei B., Li Z., Liang Y.N., Wang Z.L., Huang Q., 2013. Ages, origin and geological implication of the Amuguleng composite granite in East Ujimqin Banner, Inner Mongolia. Geological Review 59, 1150–1164 (in Chinese with English abstract).

[38] Li K., Zhang Z.C., Feng Z.S., Li J.F., Tang W.H., Luo Z.W., C.Y., 2015. Two-phase magmatic events during late Paleozoic in the north of the Central Inner Mongolia-Da Hinggan orogenic belt and its tectonic significance. Acta Geologica Sinica 89, 272–288 (in Chinese with English abstract).

[39] Yun F., Nie F.J., Jiang S.H., Liu Y., Zhang W.Y., 2011. Zircon SHRIMP U-Pb age of Monuogechin monzodiorite of Inner Mongolia and its geological significance. Mineral Deposits 30, 504–510 (in Chinese with English abstract).

[40] Li K., Zhang Z.C., Feng Z.S., Li J.F., Tang W.H., Luo Z.W., 2014. Zircon SHRIMP U-Pb dating and its geological significance of the Late-Carboniferous to Early-Permian volcanic rocks in Bayanwula area, the central of Inner Mongolia. Acta Petrologica Sinica 30, 2041–2054 (in Chinese with English abstract).

[41] Cheng Y.H., Teng X.J., Xin H.T., Yang J.Q., Ji S.P., Zhang Y., Li Y.F., 2012. SHRIMP zircon U-Pb dating of granites in Mahonondor area, East Ujimqin Banner, Inner Mongolia. Acta Petrologica et Mineralogica 31, 323–334 (in Chinese with English abstract).

[42] Xu L.Q., Deng J.F., Chen Z.Y., Tao J.X. 2003. The identification of Ordovician adakites and its signification in northern Damao,Inner Mongolia. Geoscience 17, 428–434 (in Chinese with English abstract).

[43] Liu D.Y., Jian P., Zhang Q., Zhang F.Q., Shi Y.R., Shi G.H., Zhang F.Q., Tao H., 2003. SHRIMP dating of adakites in the Tulingkai ophiolite,Inner Mongolia: evidence for the early Paleozoic subduction. Acta Geologica Sinica 77, 318–327 (in Chinese with English abstract).

[44] Zhang C., Liu S.W., Han B.F., He G.Q. Huang B.L., 2007a. SHRIMP U-Pb dating of Dashigou biotite-K-felspar granites in Shangdu, Inner Mongolia, and its significance. Acta Petrologica Sinica 23(3), 591–596 (in Chinese with English abstract).

[45] Zhang S.H., Zhao Y., Song B., Yang Z.Y., Hu J.M., Wu H., 2007b. Carboniferous granitic plutons from the northern margin of the North China block: Implications for a Late Paleozoic active continental margin. Journal of the Geological Society London 164, 451–463.

[46] Boynton W.V., 1984. Geochemistry of the rare earth elements: meteorite studies. In: Henderson P. (Ed.), Rare Earth Element Geochemistry. Elsevier, 63–114.

[47] Sun S.S., McDonough W.F., 1989. Chemical and isotope systematics of oceanic basalts: implications for mantle composition and processes. Geological Society, London, Special Publications 42, 313–345.

[48] Martin H., 1986. Effect of steeper Archean geothermal gradient on geochemistry of subduction-zone magmas. Geology 14(9), 753–756.

[49] Drummond M.S., Defant M.J., 1990. A model for trondhjemite-tonalite-dacite genesis and crustal growth via slab melting: Archean to modern comparisons. Journal of Geophysical Research: Solid Earth (1978–2012), 95(B13), 21503–21521.

[50] Stern C.R., Kilian R., 1996. Role of the subducted slab, mantle wedge and continental crust in the generation of adakites from the Andean Austral Volcanic Zone. Contributions to Mineralogy and Petrology 123(3), 263–281.

[51] Kay S.M., Ramos V.A., Marquez M., 1993. Evidence in Cerro Pampa volcanic rocks of slab melting prior to ridge trench collision in southern South America. Journal of Geology 101, 703–714.

[52] Pearce J.A., Harris N.B.W., Tindle A.G., 1984. Trace-element discrimination diagrams for the tectonic interpretation of granitic rocks. Journal of Petrology 25, 956–983.

[53] Atherton M.P., Petford N., 1993. Generation of sodium-rich magmas from newly underplated basaltic crust. Nature 362, 144–146.

[54] Castillo P.R., Janney P.E., Solidum R.U., 1999. Petrology and geochemistry of Camiguin Island, southern Philippines: insights to the source of adakites and other lavas in a complex arc setting. Contributions to Mineralogy and Petrology 134, 33–51.

[55] Castillo P.R., 2006. An overview of adakite petrogenesis. Chinese Science Bulletin 51, 257–268.

http://dx.doi.org/10.5772/62303

[56] Gao S., Rudnick R.L., Yuan H.L., Liu X.M., Liu Y.S., Xu W.L., LingW.L., AyersJ., WangX.C., Wang Q.H., 2004. Recycling lower continental crust in the North China craton. Nature 432, 892–897.

[57] Peacock S.M., Rushmer T., Thompson A.B., 1994. Partial melting of subducting oceanic crust. Earth and Planetary Science Letters 121, 227–244.

[58] Drummond M.S., Defant M.J., Kepezhinskas P.K., 1996. Petrogenesis of slab derived trondhjemite-tonalite-dacite/adakite magmas. Geological Society of America Special Papers 315, 205–215.

[59] Defant M.J., Xu J.F., Kepezhinskas P., Wang Q., Zhang Q., Xiao L., 2002. Adakites: some variations on a theme. Acta Petrologica Sinica 18, 129–142.

[60] Kay S.M., Mpodozis C., 2002. Magmatism as a probe to the Neogene shallowing of the Nazca plate beneath the modern Chilean flat-slab. Journal of South American Earth Sciences 15, 39–57.

[61] Rapp R.P., Watson E.B., Miller C.F., 1991. Partial melting of amphibolite/eclogite and the origin of Archean trondhjemites and tonalites. Precambrian Research 51, 1–25.

[62] Rapp R.P., Watson E.B., 1995. Dehydration melting of metabasalt at 8–32 kbar: implications for continental growth and crust-mantle recycling. Journal of Petrology 36, 891–931.

[63] Harris N.B.W., Pearce J.A., Tindle A.G., 1986. Geochemical characteristics of collision zone magmatism. In: Coward M.P., Ries A.C. (Eds.), Collision Tectonics: Geological Society Special Publications 19, 67–81.

[64] Pearce J.A., 1996. Sources and settings of granitic rocks. Episodes 19, 120–125.

[65] Isozaki Y., 1996. Anatomy and genesis of a subduction-related orogen: A new view of geotectonic subdivision and evolution of the Japanese Islands. Island Arc 5, 289–320.

[66] Zhang Y., Tang K., 1989. Pre-Jurassic tectonic evolution of intercontinental region and the suture zone between the North China and Siberian platforms. Journal of South East Asian Earth Sciences 3, 47–55.

[67] Yan Z.Y., Tang K.D., Bai J.W., Mo Y.C., 1989. High pressure metamorphic rocks and their tectonic environment in northeastern China. Journal of Southeast Asian Earth Sciences 3, 303–313.

[68] Shi Y.R., Liu D.Y., Jian P., Zhang Q., Zhang F.Q., Miao L.C., Shi G.H., Zhang L.Q., Tao H., 2005b. Zircon SHRIMP dating of K-rich granites in Sonid Zuoqi. Central Inner Mongolia. Geological Bulletin of China 25, 424–428 (in Chinese with English abstract).

[69] Shi Y.R., Liu D.Y., Miao L.C., Zhang F.Q., Jian P., Zhang W., HouK.J., Xu J.Y., 2010. Devonian A-type granitic magmatism on the northern margin of the North China Craton: SHRIMP U-Pb zircon dating and Hf-isotopes of the Hongshan granite at Chifeng, Inner Mongolia, China. Gondwana Research 17(4), 632–641.

[70] Zhang S.H., Zhao Y., Song B., Hu J.M., Liu S.W., Yang Y.H., 2009. Contrasting Late Carboniferous and Late Permian-Middle Triassic intrusive suites from the northern margin of the North China craton: Geochronology, petrogenesis, and tectonic implications. Geological Society of America Bulletin 121(1–2), 181–200.

[71] Ni Z.Y., Zhai M.G., Wang R.M., Tong Y., 2006. Late Paleozoic retrograded eclogites from within the northern margin of the North China Craton: evidence for subduction of the Paleo-Asian ocean. Gondwana Research 9, 209–224.

[72] Stern R.J., Bloomer S.H., 1992. Subduction zone infancy: examples from the Eocene Izu-Bonin-Mariana and Jurassic California arcs, Geological Society of America Bulletin 104, 1621–1636.

Edited by Karoly Nemeth

Updates in Volcanology - From Volcano Modeling to Volcano Geology is a new book that is based on book chapters offered by various authors to provide a snapshot of current trends in volcanological researches. Following a short Introduction, the book consists of three sections, namely, ''Understanding the Volcano System from Petrology, Geophysics to Large Scale Experiments,'' ''Volcanic Eruptions and Their Impact to the Environment,' and ''Volcanism in the Geological Record.'' These sections collect a total of 13 book chapters demonstrating clearly the research activity in volcanology from geophysical aspects of volcanic systems to their geological framework. Each chapter provides a comprehensive summary of their subject's current research directions. This book hence can equally be useful for students and researchers.

ISBN 978-953-51-5079-4

Photo by Sergey_Krasnoshchokov / iStock

IntechOpen